



DEVELOPMENT OF A NEW DESIGN METHOD FOR STEEL HOLLOW SECTION MEMBERS RESISTANCE

A thesis

Submitted in fulfillment of the requirements for the degree

Of

Doctor in Applied Sciences

By

MARIELLE HAYECK

29 July 2016

'It always seems impossible until it is Done'

'Nelson Mandela'

ACKNOWLEDGEMENTS

The work accomplished in this thesis would not have been possible without the constant support and guidance of my supervisor M. Nicolas Boissonnade. It was his strategic cognizance and expertize that allowed me the opportunity to pursue this research project. I deeply thank his constant encouragement and guidance every step of the way.

I would also like to express my sincerest gratitude to my directors, M. Jean-Pierre Jaspard and M. Fadi Geara for their encouragements and valuable advices necessary for my progress through my doctoral program.

I am thankful for the members of the jury who dedicate their time and lend me their expertise in order to accomplish this work.

One major part of my PhD was experimental and the tests were performed in the Structural Engineering Laboratory of the University Of Applied Sciences Of Western Switzerland – Fribourg. I would like to commend the laboratory staff for their efficient help that largely contributed to the feasibility of the experiments.

Furthermore, I am thankful for the generous financial contribution of CIDECT and AUF through their direct funding and scholarships. I also owe a debt of gratitude to Voestalpine and V&M who supplied the various specimens for my work.

I am also thankful to all my colleagues in the civil department in Switzerland for their friendly assistance and enjoyable presence.

Many thanks to my family and friends, it was their encouragements and sacrifices that helped me overcome a lot of obstacles along the way.

Marielle Hayeck

July 2016

ABSTRACT

This dissertation presents research done in the field of enhancing the performance and the carrying capacity of tubular members, through the development of an original design approach based on the “Overall Interaction Concept” (O.I.C.). The proposed approach makes use of the interaction between the two ideal behaviours of structural members (resistance and instability) and includes the influence of initial imperfections (out-of straightness, residual stresses, non-homogenous material), to calculate the resistance of a structure through a single parameter: λ “relative slenderness”.

A test program was carried out as a part of a European project named ‘HOLLOPOC’ to determine the experimental behaviour of beam-columns loaded by bi-axial bending with axial force. Twelve buckling tests, consisting of hot-rolled and cold-formed rectangular and circular hollow section members were conducted. These tests were accompanied by preliminary measurements of cross-section geometry, material properties, geometrical imperfections, residual stresses as well as stub column tests. Besides, a finite element model was calibrated on the basis of these tests. For both the present test series and another one from the literature, it was shown that the FE models were capable of replicating accurately the response and resistance of the experiments. Accordingly, the validated FE models have been further used in extensive numerical studies, and a database comprising more than seventy thousand results was built consecutively. Based on these computations, design proposals were made, by considering identified governing parameters, within the context of the Overall Interaction Concept, using an extension of the Ayrton-Perry approach. Finally, a safety evaluation was completed to check the proposed formulae against the results of current Eurocode 3 rules.

TABLE OF CONTENTS

ACKNOWLEDGEMENTS.....	i
ABSTRACT.....	ii
NOTATIONS.....	x
1. INTRODUCTION.....	1
2. STATE OF THE ART.....	6
2.1. Introduction.....	6
2.2. Members in compression.....	6
2.2.1. History of buckling studies.....	6
2.2.2. European buckling curves.....	12
2.2.3. Analytical formulation for European buckling curves.....	15
2.2.3.1. Bounds of European curves.....	15
2.2.3.2. Mathematical formulations.....	17
2.2.3.3. Merchant-Rankine formulation.....	19
2.2.3.4. Ayrton-Perry format.....	20
2.2.4. Adopted analytical formulation.....	23
2.2.5. Current developments in the design of thin-walled hollow members.....	26
2.2.5.1. Method with interaction of faces.....	26
2.2.5.2. Method without interaction of faces.....	27
2.3. Members in bending and axial compression.....	30
2.3.1. Member under compression and mono-axial bending: $N_{Ed}+M_{Ed}$	31
2.3.2. Member under compression and biaxial bending: $N_{Ed}+M_{y,Ed}+M_{z,Ed}$	33
2.3.3. Design formulae for Method 1.....	34
2.3.3.1. Member with class 1 and 2 cross-sections.....	35
2.3.3.2. Member with class 3 and 4 cross-sections.....	36
2.3.4. Design formulae for Method 2.....	36
2.3.4.1. Member with class 1 and 2 cross-sections.....	38
2.3.4.2. Member with class 3 and 4 cross-sections.....	38
2.3.5. Extension of the Ayrton-Perry formulations to combined loading situations.....	39

2.4.	Shortcoming of actual codes	43
2.5.	Conclusion	44
3.	EXPERIMENTAL INVESTIGATIONS	46
3.1.	Introduction	46
3.2.	Test program	47
3.2.1.	Selection of test specimens	49
3.2.2.	Adopted parameters	56
3.3.	Preliminary measurements	58
3.3.1.	Cross-sectional dimensions	58
3.3.2.	Tensile tests	61
3.3.3.	Geometrical imperfections	69
3.3.3.1.	LVDT measurements	69
3.3.3.2.	Topometric measurements	80
3.3.4.	Residual stresses	85
3.3.4.1.	Specimen preparation	85
3.3.4.2.	Mechanical measurements	87
3.3.4.2.1.	Flexural residual stresses	88
3.3.4.2.2.	Membrane residual stresses	90
3.3.4.3.	Strain gauges measurements	90
3.3.5.	Stub column tests	95
3.4.	Buckling tests	100
3.4.1.	Test setup	103
3.4.2.	Measurements acquisition	111
3.5.	Validation of numerical vs. experimental member response	116
3.5.1.	UAS Western Switzerland – Fribourg test series	116
3.5.1.1.	Finite element model assumptions	116
3.5.1.2.	Validation: F.E. vs. test results	119
3.5.2.	European project “Semi-Comp” test series	125
3.5.2.1.	General scope of the study	125
3.5.2.2.	Finite element model assumptions	126

3.5.2.3.	Validation: F.E. vs. test results	129
3.6.	Summary	131
4.	NUMERICAL PARAMETRIC STUDY ON HOT-ROLLED MEMBERS.....	133
4.1.	Introduction	133
4.2.	Description of F.E. models	133
4.2.1.	Material behaviour and residual stresses.....	134
4.2.2.	Shell models	139
4.2.2.1.	Mesh refinement	139
4.2.2.2.	Loading and support conditions.....	143
4.2.2.3.	Geometrical imperfections.....	144
4.2.2.3.1.	Selection and definition of local imperfections.....	144
4.2.2.3.2.	Selection and definition of global imperfections	150
4.2.2.4.	Load-path sensitivity.....	153
4.2.3.	Beam models	163
4.3.	Parametric study on hot-rolled hollow section members.....	166
4.3.1.	Cases and parameters considered	166
4.3.2.	Determination of R-factors involved in the O.I.C. approach	169
4.3.2.1.	Determination of R_{RESIST} (resistance).....	170
4.3.2.2.	Determination of $R_{STAB,CS}$ (cross-section instability)	172
4.3.2.3.	Determination of $R_{STAB,MB}$ (member instability)	176
4.3.3.	Analysis of results	178
4.3.3.1.	Influence of cross-section shape and slenderness	182
4.3.3.2.	Influence of yield stress	185
4.3.3.3.	Influence of bending moment distribution.....	187
4.3.3.4.	Influence of axial force level	190
4.3.3.5.	Influence of biaxial bending	193
4.4.	Comparison of F.E. results with Eurocode 3 predictions	196
4.5.	Conclusions.....	198
5.	NUMERICAL PARAMETRIC STUDY ON COLD-FORMED MEMBERS	200

5.1. Introduction	200
5.2. Description of F.E. models	201
5.2.1. Material behaviour and residual stresses.....	201
5.2.2. Modelling assumptions adopted for the F.E. model.....	204
5.3. Cases and parameters considered	205
5.4. Analyses of results	209
5.4.1. Influence of cross-section shape and slenderness	209
5.4.2. Influence of yield stress.....	210
5.4.3. Influence of bending moment distribution	212
5.4.4. Influence of axial force level.....	214
5.4.5. Influence of biaxial bending.....	216
5.5. Conclusions.....	218
6. O.I.C. – BASED DESIGN PROPOSAL.....	219
6.1. Introduction	219
6.2. Influence of strain-hardening on a beam-column member	220
6.3. Additional tests collected from literature.....	226
6.3.1. Characterization by means of the O.I.C.	226
6.3.2. Use of O.I.C. plotting – Analyses and conclusions.....	226
6.3.3. Gathered experimental data vs. F.E. results	232
6.4. Proposal of design “interaction” curves – parametric studies	235
6.4.1. Simple case of pure compression	235
6.4.1.1. Hot-rolled sections	235
6.4.1.2. Cold-formed sections	238
6.4.1.3. Coupled instabilities in highly slender sections.....	241
6.4.1.3.1. Influence of second-order effects.....	243
6.4.1.3.2. Case of exaggeratedly slender sections.....	247
6.4.2. Members under compression and triangular bending moment distribution.....	253
6.4.2.1. Compression and minor-axis bending cases	255

6.4.2.1.1.	Hot-rolled square sections.....	255
6.4.2.1.2.	Hot-rolled rectangular sections	257
6.4.2.1.3.	Cold-formed square sections.....	260
6.4.2.1.4.	Cold-formed rectangular sections	262
6.4.2.2.	Compression and major-axis bending cases	263
6.4.2.2.1.	Hot-rolled square sections.....	263
6.4.2.2.2.	Hot-rolled rectangular sections	264
6.4.2.2.3.	Cold-formed square sections.....	266
6.4.2.2.4.	Cold-formed rectangular sections	266
6.4.2.3.	Compression and biaxial bending.....	268
6.4.2.3.1.	Hot-rolled square sections.....	270
6.4.2.3.2.	Hot-rolled rectangular hollow sections	273
6.4.2.3.3.	Cold-formed square sections.....	278
6.4.2.3.4.	Cold-formed rectangular sections	280
6.4.3.	Members under compression and constant bending moment distribution.....	285
6.4.3.1.	Compression and minor-axis bending cases	285
6.4.3.1.1.	Hot-rolled square sections.....	285
6.4.3.1.2.	Hot-rolled rectangular sections	291
6.4.3.1.3.	Cold-formed square sections.....	295
6.4.3.1.4.	Cold-formed rectangular hollow sections	299
6.4.3.2.	Compression and major-axis bending cases	303
6.4.3.2.1.	Hot-rolled square sections.....	303
6.4.3.2.2.	Hot-rolled rectangular sections	303
6.4.3.2.3.	Cold-formed square sections.....	308
6.4.3.2.4.	Cold-formed rectangular sections	308
6.4.3.3.	Compression and biaxial bending.....	313
6.4.3.3.1.	Hot-rolled square sections.....	315
6.4.3.3.2.	Hot-rolled rectangular sections	323
6.4.3.3.3.	Cold-formed square sections.....	332
6.4.3.3.4.	Cold-formed rectangular sections	339
6.4.4.	Influence of bending moment distribution.....	347
6.4.5.	Influence of the section shape	356

6.5. Accuracy of proposed models – Comparison with actual Eurocode 3 rules 357

6.6. Summary of proposal	366
6.7. Simplified proposal.....	374
6.8. Worked examples	380
6.8.1. Cold-formed rectangular hollow section: RHS 200x100x5	380
6.8.1.1. Member geometry and loading	380
6.8.1.2. Cross-section classification.....	381
6.8.1.3. Cross-section verification	383
6.8.1.4. Member verification according to Eurocode 3 Method 2.....	383
6.8.1.5. Member verification according to the O.I.C. approach	385
6.8.2. Cold-formed square hollow section: SHS 120x120x8.....	387
6.8.2.1. Member geometry and loading	387
6.8.2.2. Cross-section classification.....	388
6.8.2.3. Cross-section verification	389
6.8.2.4. Member verification according to Eurocode 3 Method 2.....	389
6.8.2.5. Member verification according to the O.I.C. approach	391
6.8.3. Hot-rolled square hollow section: SHS 120x120x8.....	392
6.8.3.1. Member geometry and loading	392
6.8.3.2. Cross-section classification.....	393
6.8.3.3. Cross-section verification	393
6.8.3.4. Member verification according to Eurocode 3 Method 2.....	393
6.8.3.5. Member verification according to the O.I.C. approach	395
6.8.4. Cold-formed square hollow section: SHS 300x300x6.3	396
6.8.4.1. Member geometry and loading	396
6.8.4.2. Cross-section classification.....	397
6.8.4.3. Cross-section verification	398
6.8.4.4. Member verification according to Eurocode 3 Method 2.....	400
6.8.4.5. Member verification according to the O.I.C. approach	401
6.9. Conclusions.....	403
7. CONCLUSION AND FUTURE DEVELOPMENTS.....	405
8. REFERENCES.....	410

9. ANNEXES	416
9.1. Annex 1: Collection of existing buckling beam-column test results	416
9.2. Annex 2: Determination of appropriate material law for cold-formed tubes..	421
9.2.1. Cold-formed sections with normal steel grades	421
9.2.1.1. Collection of existing experimental tensile test results.....	421
9.2.1.2. Simple Ramberg-Osgood formulation	422
9.2.1.3. Double Ramberg-Osgood formulation	425
9.2.1.4. Influence of R.-O. coefficients on the resistance of cold-formed tubes ...	427
9.2.2. Cold-formed sections with high steel grades	429
9.3. Annex 3: Selection of the loading combinations adopted in the experimental main buckling tests	432
9.4. Annex 4: Load path sensitivity – $L = 5500\text{ mm}$	433
9.5. Annex 5: Application steps of the Overall Interaction Concept for members.	437
9.6. Annex 6: Detailed results of beam-column tests	438
10. LISTE OF FIGURES	530
11. LISTE OF TABLES	546

NOTATIONS

Abbreviations:

AISC	American Institute of Steel Construction
CF	Cold-Formed
CHS	Circular Hollow Section
D	Diameter of circular sections
EC3	Eurocode 3
EN	European Standard
FE	Finite Element
GMNIA	Geometrically, materially nonlinear analysis with imperfections
HF	Hot-Finished
HR	Hot-Rolled
LBA	Linear buckling analysis
LC	Load Case
LVDT	Linear Variable Displacement Transducer
MNA	Materially nonlinear analysis
O.I.C.	Overall Interaction Concept
RHS	Rectangular Hollow Section
R.-O.	Ramberg-Osgood
R_{max}	Largest corner radius
R_{min}	Smallest corner radius
AS ₁	LVDT at position 1

AS ₂	LVDT at position 2
AS ₃	LVDT at position 3
AS ₄	LVDT at position 4
HSS	High strength steel

Latin letters:

A	Area of the cross-section
a	Initial local imperfection amplitude (only used in section 4.2.2.3.1.)
a	measured deflection of the strip (only used in section 3.3.4.2.)
B	Section width
C_{ii}, C_{ij}	Interaction factors
C_m	Equivalent moment factor
d_z, d_y	Distance between LVDTs along z -axis and y -axis respectively
e_y	Excentricity in y -axis direction
e_z	Excentricity in z -axis direction
E	Young's modulus of elasticity
E_m	Young's modulus of elasticity, mean
E_{LVDT}	Young's modulus from LVDTs
E_{SG}	Young's modulus from strain gauges
$e_{0,d}$	Initial deflection at mid-span
f	Stress
f_{u_flat}	Material ultimate stress of the flat region
f_{u_corner}	Material ultimate stress of the corner region
$f_{u,m}$	Average ultimate stress
f_y	Material yield stress
f_{u_flat}	Material yield stress of the flat region

f_{u_corner}	Material yield stress of the corner region
f_{ym}	Material yield stress, mean of yield plateau
f_u	Material ultimate stress
f_{max}	Ultimate tensile stress
F_{exp}	Applied force at ultimate load for experimental tests
F_{FE}	Applied force at ultimate load for Finite Element simulations
h_w	height of the web
H	Section depth
I_y	Moment of inertia about the strong axis
I_z	Moment of inertia about the weak axis
k	Correction factor (only used in section 3.3.5)
k, k_σ	plate buckling coefficient
K	amplification factor
K_{ib}, K_{ij}	Interaction factors
l_{final}	Final length measured by the extensometer
$l_{initial}$	Initial length measured by the extensometer
L	Length
L_{arc_i}	Arc length at the inner surface
L_{arc_e}	Arc length at the outer surface
$L_{arc_e_or_i}$	Arc length at the inner or the outer surface
L_{arc_m}	Arc length at the neutral axis
L_{arc_final}	final arc length
m_y	Normalized major-axis bending moment
m_z	Normalized minor-axis bending moment
M_{Ed}	Design value of the acting bending moment

M_{el}	Elastic cross-section resistance for pure bending moment
M_{pl}	Plastic cross-section resistance for pure bending moment
M_y	Bending moment about the strong axis (y - y)
M_z	Bending moment about the weak axis (z - z)
M^{II}	Second order bending moment
n, m	Ramberg-Ogood parameters
n	Normalized axial force, equal to $N / N_{b,Rd}$
N	Axial force
N_{pl}	Plastic cross-section resistance for pure axial force
N_{eff}	Effective cross-section resistance for pure axial force
N_{Ed}	Design value of the acting axial force
N_u	ultimate compression load
N_u	ultimate compression load
$N_{b,Rd}$	Buckling resistance for pure compression
N_{pl_actual}	Plastic load based on actual properties
N_{pl_nom}	Plastic load based on nominal properties
N_{cr}	Critical load
r	Corner radius
R_e	External curvature radius
R_i	Internal curvature radius
R_m	curvature radius at the neutral axis
R_{m_final}	Final mid-thickness radius of curvature
R_{ULT}	Ultimate load multiplier
R_{RESIST}	Resistance load multiplier
R_{STAB}	Critical load multiplier

$R_{STAB,CS}$	Cross-section critical load multiplier
$R_{STAB,CS}$	Member critical load multiplier
t	Thickness
t_f	Thickness of the flange
t_w	Thickness of the web
v	Half strip thickness
v_{max}	Maximum deflexion reached at peak load
W_{pl}	Plastic section modulus
W_{el}	Elastic section modulus
Greek letters:	
α	Angle of curvature
$\alpha_{\text{biaxiality}}$	Degree of bi-axiality
α	Imperfection factor
α_{CS}	Cross-section imperfection factor
β	Factor relative to the instability limit
α^* and β^*	Plasticity factors
Δ	Displacement
δ_c	Corrected stub column end-shortening
δ_{LVDT}	End-shortening recorded by LVDTs
Δ_{TOT}	Total displacement
ε	Strain of $\sqrt{\frac{235}{f_y}}$
ε_f	Failure strain
ε_u	Material ultimate strain

ε_y	Material yield strain
ε_{ym}	Average material yield strain
ε_{um}	Average material ultimate strain
η	Generalized imperfection factor
θ_y	Rotation around y -axis
θ_z	Rotation around z -axis
λ	relative slenderness
λ_0	End of plateau slenderness
λ_{cs}	Cross-section slenderness
λ_{MB}	Member slenderness
λ_{CS+MB}	Member slenderness considering local instability
λ_v	plate slenderness
ξ	Clamping coefficient
σ	Stress
$\sigma_{0.2}$	0.2% proof stress
σ_{cr}	Critical stress
σ_{ext}	External stress
σ_{max}	Maximum stress
σ_{rc}	Stress due to residual stresses
σ_{ult}	Ultimate stress
σ_y	Yield stress
$\sigma_{flexural}$	Flexural stress
ν	Poisson's ratio
ϕ	Variable accounted for in the Ayrton-Perry formula

χ	Buckling reduction factor
χ_{cs}	Cross-section reduction factor
χ_{MB}	Member reduction factor
χ_{CS+MB}	Member reduction factor considering local instability
ψ	Ratio between end moments
ψ_y, ψ_z	Ratio between end moments about y - y and z - z axes respectively
γ_{M1}	Partial factor for resistance of members to instability
$\Omega_{y/z}$	Degree of biaxiality
η_y	Ratio between normalized major-axis bending moment and axial force
η_z	Ratio between normalized minor-axis bending moment and axial force

1. Introduction

The research works presented herein addresses the behaviour, resistance and design of steel hollow section members. The intention is here to propose an original design approach based on the Overall Interaction Concept (O.I.C.) [1]. The proposed approach is based on the interaction between the two ideal behaviours of structural members: resistance and instability. The classical concept of ‘Resistance’ mainly characterizes the cross-sectional capacity of the member, whereas the concept of ‘Stability’ describes the tendency of an ideal member to buckle under the applied loading. None of these concepts does really describe the real behaviour of structural members. The concept of ‘Resistance’ assumes that no instability phenomena can occur while the concept of ‘Stability’ considers an ideal member, i.e. a geometrically perfect member made of a material characterized by a linear elastic constitutive law and having an infinite resistance.

The Overall Interaction Concept makes use of both aspects ‘Resistance’ and ‘Stability’ and includes the influence of initial imperfections (out-of straightness, residual stresses, non-homogenous material) which makes the member’s real resistance results from an interaction between cross-section resistance and instability, as illustrated in Figure 1.

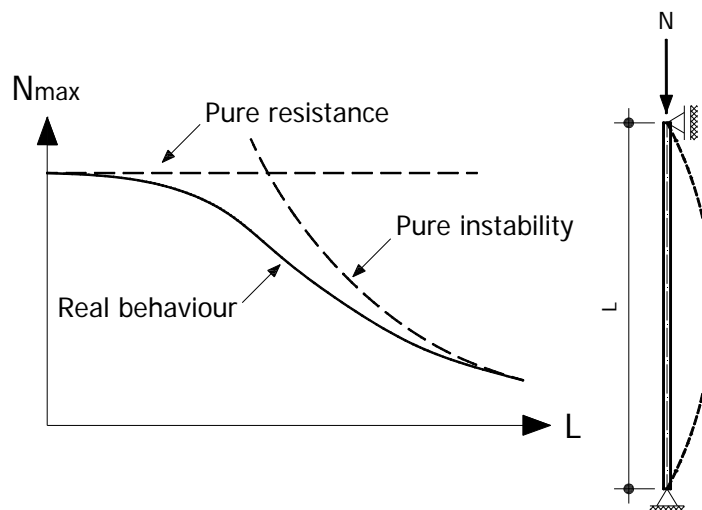


Figure 1 – Resistance – stability interaction for flexural buckling

The member’s real resistance develops specific load-carrying behaviour in the different ranges of slenderness. At very low slenderness, the cross-sectional resistance dominates and the effect of local buckling is mainly highlighted. With increasing slenderness, the elements fail because of both local (i.e. cross-section) and global (i.e. member) instabilities. The

member behaviour is significantly influenced by both geometrical imperfections and residual stresses. In the high slenderness range, member buckling is dominated by elastic behaviour; the larger the slenderness the greater the dominance. The effect of global buckling is mainly highlighted regardless of the section slenderness and local buckling that may occur.

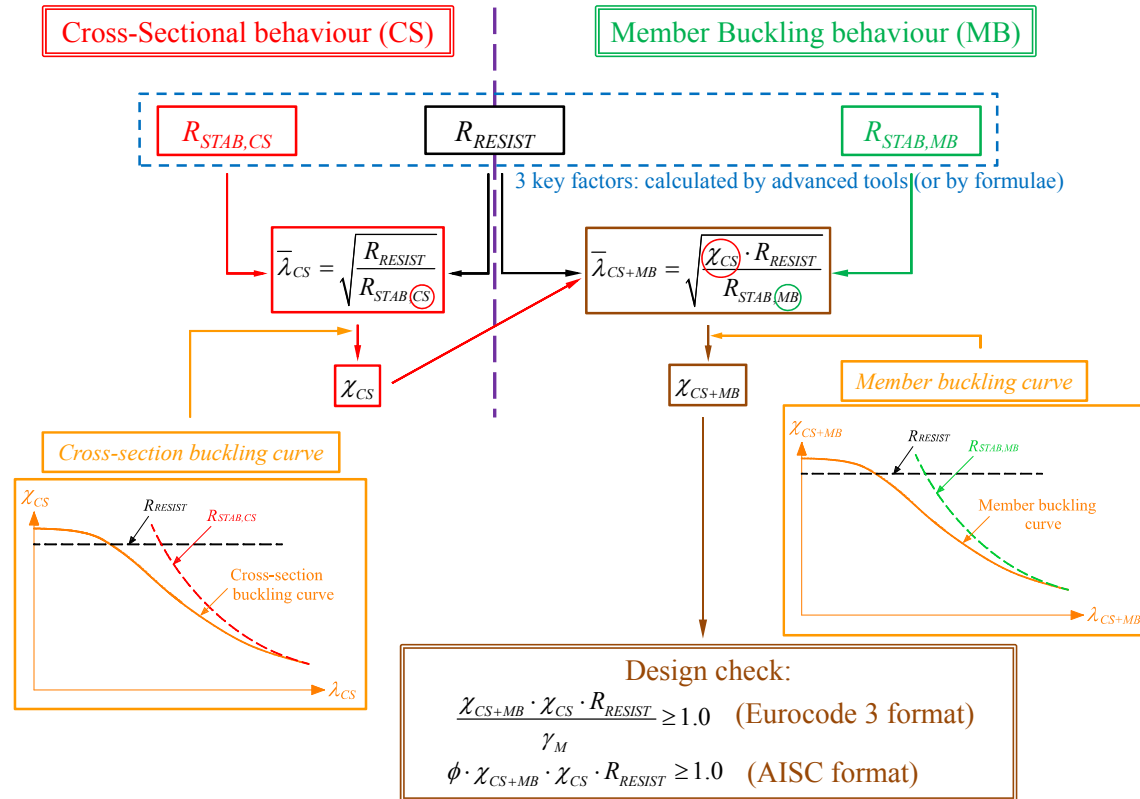


Figure 2 – Principles and application steps of proposed “Overall Interaction Concept”

The proposed O.I.C. approach relies on the generalization of the relative slenderness notion defined as $\lambda = \sqrt{R_{RESIST} / R_{STAB}}$, where R_{RESIST} represents the factor by which the initial loading has to be multiplied to reach the pure resistance limit and R_{STAB} is the equivalent factor used to reach the buckling load (instability) of the ideal member. Doing so, makes it capable of dealing with complex loading situations, as well as with various problems (e.g. member or cross-section resistance-instability interaction, non-linear material behaviour...). The relative slenderness value “ λ ” would lead to the determination of a “ χ ” value (Figure 2) called “reduction factor” that represents the penalty due to instability effects on the pure resistant behaviour. The interaction curve, by means of the λ -value, accounts for all resistance and instability aspects, rules the interaction, and further includes the effect of imperfections.

In the proposed approach, cross-sectional and member resistances are based on extended Ayrton-Perry approaches [2], providing reduction χ factors that account for potential local and global (member) instabilities.

Preliminary research works [3] at the cross-sectional level (i) allowed to evidence the suitability and ease of application of the concept, (ii) established a new overall cross-section slenderness λ_{CS} capable of handling plate interactions within the section, (iii) identified the key parameters affecting the resistance in an $\chi_{CS} - \lambda_{CS}$ format at the cross-section level, (iv) and proposed so-called $\chi_{CS} = f(\lambda_{CS})$ resistance functions that were shown to be significantly more accurate and safe than EC3 predictions.

The present work further extends the application of the O.I.C. to members with hollow section shapes. They address their inelastic beam-column response, and include possible local-global interaction under simple and combined loading situations – one of the most complex element's responses.

Many existing such design approaches have been developed in the past decades and have been implemented in design standards (EC3, AISC LRFD, BS 5950, DIN 18 800, AS 4100...). As detailed in ECCS 9, EC3 design rules for beam-columns are certainly the most advanced and accurate beam-column formulae; in particular, tubular sections were deeply considered and received specific treatment. Consequently, they have been kept as an analytical reference for the present study.

From a practical point of view, actual codes and methods still suffer from a series of problems and inadequacies. In current design codes, buckling curves exist for the design of tubular members, for pure compression load-case (and also for the design of open sections unbraced beams experiencing lateral torsional buckling); these curves depend on the cross-section geometry, the manufacturing process, the plane of buckling considered etc. As a first attempt, such buckling curves are hereafter generalized to take into account combined load combinations; the curves are drawn according to the O.I.C. concept which relies on the generalization of the relative slenderness concept.

Moreover, in Eurocode 3 for example, local instability is accounted for through an additional step prior to the verification process that consists in the classification of the cross-section. According to the class of the section, different sets of formulae are to be used for the design

checks of both sections and members, i.e. plastic or elastic equations. The determination of the effective section for class 4 cross-sections, require tedious long calculations with iterations. It has been shown [4] that several values of the b/t limit ratios of Eurocode 3 are often misleading and suffer from a lack of mechanical background. Moreover, this concept of classes generates a gap of resistance at the class 2-3 border, which is mechanically meaningless. Another important limitation embedded with the b/t limit ratios found in standards lies in the assumed “ideal support conditions” of the various plates of the section, thus each plate is assumed to behave independently of adjacent plates which disregard the interaction between elements.

Since continuous strength functions are proposed in the O.I.C. approach, no cross-section classification steps or section effective properties determination are needed. Also, the method is built such that combined load cases can be as easily treated as simple ones.

In the following, the results of experimental, numerical and theoretical investigations are reported. Chapter 3 first describes the series of 12 beam-column tests performed on rectangular and circular hollow section shapes. Detailed preliminary measurements are also described such as material and stub column tests, residual stresses and initial geometrical imperfections measurements. Chapter 3 then reports on the development and validation of purposely-designed shell FE models; both the present test series and another series [4] are used as experimental references to assess the FE models.

Chapter 4 and chapter 5 report on the results of extensive numerical parametric studies performed on hot-rolled and cold-formed beam-column members respectively. Key parameters such as the bending moment distribution, axial force ratio, degree of biaxial bending and steel grade were identified. These results have been further used to assess the merits of the proposed new design approach.

Continuous interaction curves were derived in chapter 6, for hot-rolled and cold-formed steel hollow beam-column members along the slenderness range, by considering all the identified governing parameters. With the adoption of the Ayrton-Perry extended format, locally fitted factors were defined; the proposed design curves for simple and combined load cases are presented. Chapter 6 illustrates as well the accuracy of the proposed design formulae. Statistical results of the comparison between F.E., Eurocode 3 and proposal calculations are presented. The resistance estimates were significantly improved by the new proposal, with

mean and standard deviation values indicating a far better level of accuracy and consistency. A summary of the proposed design formulae and recommendations for practical design are presented, followed by a description of worked examples illustrating the effectiveness, the simplicity and the economic benefit of the newly developed design proposals.

Chapter 7 summarizes the research, presents the original contributions of this work and gives aspects and suggestions for further investigations.

2. State of the Art

2.1. Introduction

In the following chapter, special attention is paid to earlier research on the buckling of steel beam-column members and to the theoretical studies undertaken since 1956 by the European convention on metallic structures (CECM) on the determination of the buckling curves. A brief review of the analytical ways of formulating the design curves is presented along with the adopted mathematical Ayrton-Perry formulations that were found to describe the best the buckling behaviour of beam-column members.

Then, the current design specifications, incorporated in the latest version of Eurocode 3: EN 1993–1–1 [5], are presented for the verification of members subjected to compression and to combined bending and compression.

It should be noted that, the rules are mainly related here to rectangular and square cross-sections shapes.

The following chapter can be subdivided into two sub-sections (sections 2.2 and 2.3) presenting the research work, and the detailed historical review of “beam-columns” subjected to:

- pure compression load case;
- bending and axial compression.

Section 2.4 presents the shortcoming of the currently used design approaches. Eventually, summary and conclusions are addressed in section 2.5.

2.2. Members in compression

2.2.1. History of buckling studies

The buckling of stone and wood columns has been first studied by the mathematician Héron d’Alexandrie followed by Leonardo Da Vinci in the XV^{th} century. It was not until 1729 that a physician Petrus Van Musschenbroek noticed that the critical load of a column is inversely proportional to the square of its length. Consequently, empirical approaches were developed for this purpose.

In 1778 Leonard Euler, inspired by Bernoulli's work, proposed a general, precise formula for calculating the critical load of ideal pin-ended column of constant inertia:

$$N_{cr} = \frac{\pi^2 EI}{L^2} \quad (1)$$

To be able to determine the critical buckling load, buckling is assumed to have occurred with a deflection y at mid span.

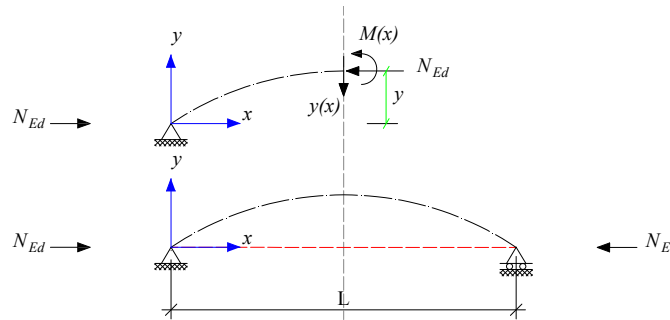


Figure 3 – Deflection column due to applied compressive load

The moment equation at the cut end at mid-span can be written as:

$$\sum M = 0 = N \cdot y + M(x) = 0 \quad (2)$$

which leads to:

$$EI \frac{d^2 y}{dx^2} = -N \cdot y \quad (3)$$

and simplifies to:

$$\frac{d^2 y}{dx^2} + \left(\frac{N}{EI} \right) y = 0 \quad (4)$$

The solution for this equation is:

$$N = n^2 \frac{\pi^2 EI}{L^2} \quad (5)$$

where the values of n define the buckling mode shapes (see Figure 4)

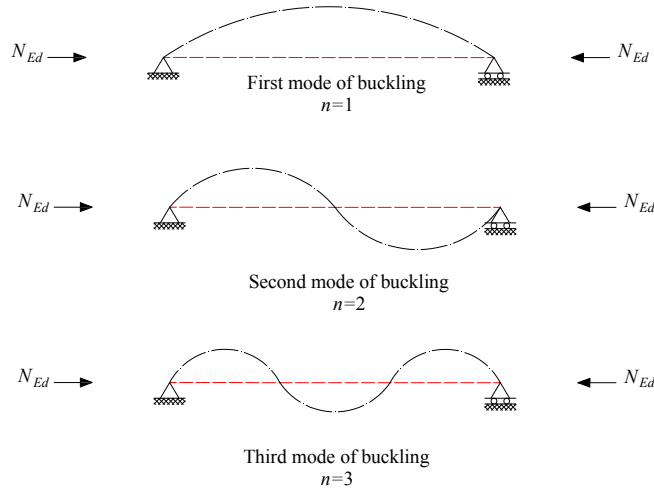


Figure 4 – First three modes of buckling load

The column buckles at the first buckling load mode leading to Euler's famous formula (see Equation (1)) and never reach greater mode unless bracing is placed at the points where no deflection occurs.

Euler's formulation made no allowance for geometric and structural imperfections. This explains why many researchers failed to reconcile the theory with actual test results.

In 1826, L. Navier [6] showed that the Euler formulation presents the upper bound of column buckling loads, based on experimental results.

Two lines of investigations were undertaken at the time:

- the inelastic approach considering an ideal perfect element. This line was undertaken by Engesser, Considère, Jasinski, Von Karman and Shanley;
- the elastic approach including the influence of imperfections on the resistance of the actual member. This line was undertaken by Young, Ayrton-Perry, Robertson and Duthiel.

In Euler's formula the inelastic approach falls back on substituting a variable quantity for the modulus of elasticity. According to E. Engesser [7] the tangent modulus E_t should be used, whereas Considère [8] and Jasinski [9] introduced the reduced modulus E_r given as follow:

$$E_r = \frac{4E \cdot E_t}{(\sqrt{E} + \sqrt{E_t})^2} \quad (6)$$

In 1947, F.R. Shanley demonstrated that the buckling load of an ideal column is given by the application of the reduced modulus concept while for real members having initial imperfections, the buckling load slightly exceeds the one given by the tangent modulus concept.

Figure 5 illustrates the historical review of buckling as proposed by Rondal [10].

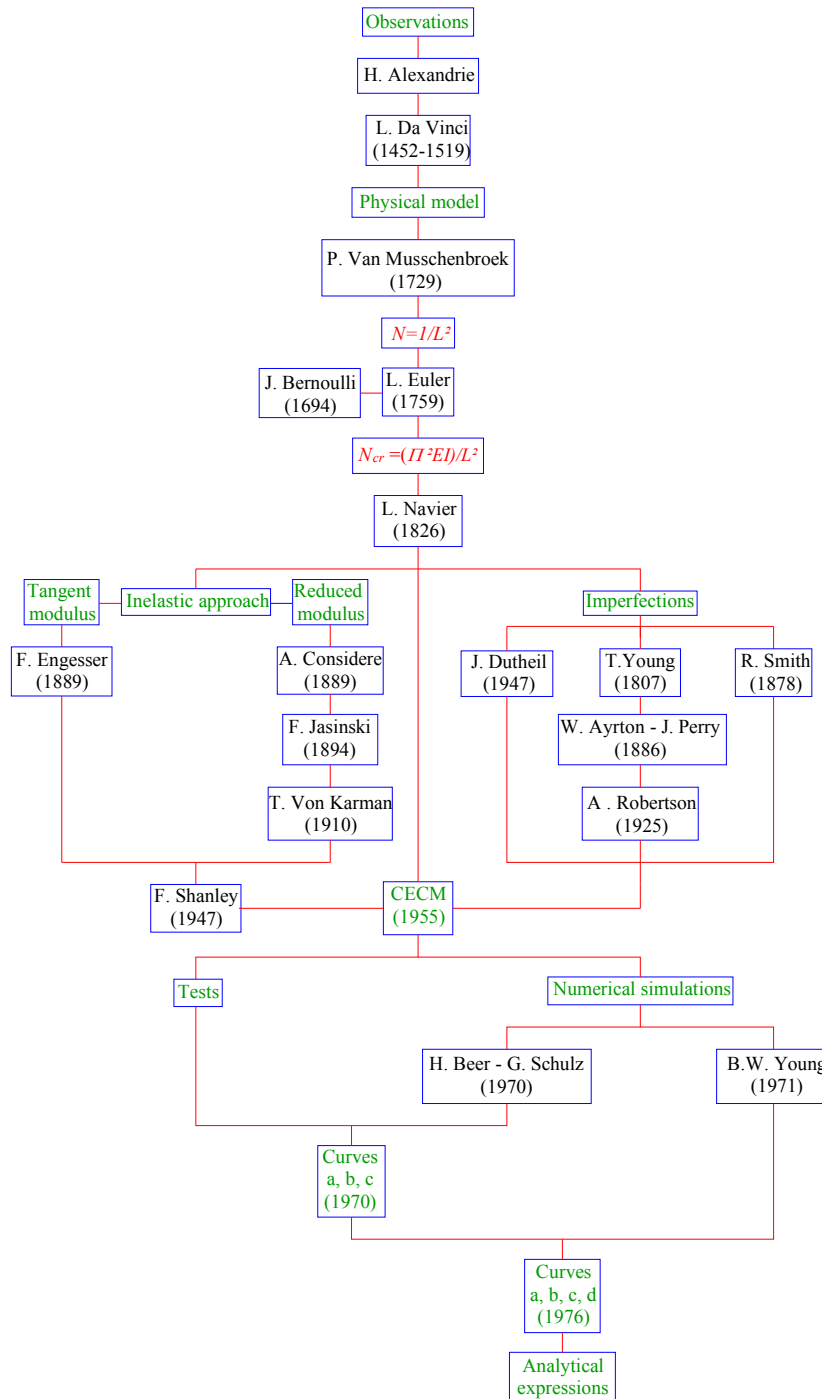


Figure 5 – Historical review of buckling

Thomas Young [11] showed in 1807 that the compression of the real member is influenced by geometric imperfections such as initial out of straightness, eccentrically applied forces... In the case of simply supported member, he demonstrated that the geometric imperfections created a bending moment which is amplified by a coefficient K , expressed as follows [12]:

The initial sinusoidal geometrical imperfection is referred to as $v_0(x)$ and $e_{0,d}$ is the corresponding maximum amplitude at mid-span:

$$v_0(x) = e_{0,d} \sin \frac{\pi x}{L} \quad (7)$$

An additional deflection $v(x)$ appears when the compression load N_{Ed} is applied:

$$v(x) = A \sin \frac{\pi x}{L} \quad (8)$$

where A is the maximum value of the additional deflection as illustrated in Figure 6.

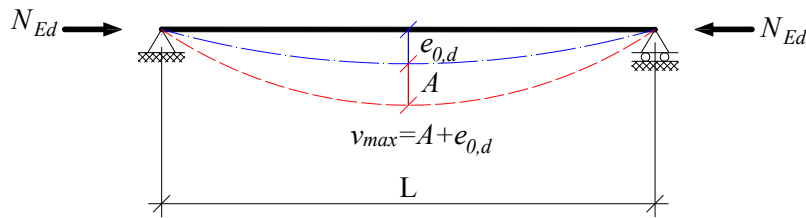


Figure 6 – Simply supported member with initial imperfection

The elastic flexural equilibrium equation, accounting for the initial imperfection, becomes:

$$v'' + \frac{N_{Ed}}{EI} (v_0 + v) = 0 \quad (9)$$

where I represents the second moment of area in the plane of bending.

The value of A can be calculated by replacing Equations (7) and (8) in Equation (9) giving the following expression:

$$A = \frac{N_{Ed}}{N_{cr} - N_{Ed}} e_{0,d} \quad (10)$$

where N_{cr} is the critical flexural buckling load calculated according to (1).

Then, the maximum deflection v_{max} at mid-span can be expressed as:

$$v_{\max} = \frac{N_{cr}}{N_{cr} - N_{Ed}} e_{0,d} = \frac{1}{1 - N_{Ed} / N_{cr}} e_{0,d} \quad (11)$$

The amplification factor K can be expressed as follows for the case of sinusoidal bending moment:

$$K = \frac{1}{1 - N_{Ed} / N_{cr}} \quad (12)$$

In the case of a constant bending moment, the amplification factor can be written as follow:

$$K^* = \frac{1}{\cos \frac{\pi}{2} \sqrt{N_{Ed} / N_{cr}}} \quad (13)$$

Ayrton and Perry indicated, 80 years after Young's approach, that for the usual values of the ratio N/N_{cr} , the expressions (12) and (13) give very similar results and since then the initial curvature was considered as a generalized geometric imperfection.

Taking this as a starting point and agreeing that the failure criteria is based on the attainment of the yield limit f_y , the stability of a member subjected to an axial compression N_{Ed} is written:

$$\frac{N_{Ed}}{A} + \frac{M^I}{W_{el}} = f_y \quad (14)$$

Young demonstrated that the second order bending moment is obtained by multiplying the first order moment:

$$M^I = N_{Ed} e_{0,d} \quad (15)$$

by the amplification factor K :

$$M^I = K N_{Ed} e_{0,d} = N_{Ed} v_{\max} = \frac{N_{Ed}}{1 - N_{Ed} / N_{cr}} e_{0,d} \quad (16)$$

Substitution of Equation (16) into Equation (14) gives the expression of a second-order in-plane elastic check of the most heavily loaded cross-section on the member:

$$\frac{N_{Ed}}{N_{Rd}} + \frac{1}{1 - N_{Ed} / N_{cr}} \frac{N_{Ed} e_{0,d}}{M_{Rd}} \leq 1 \quad (17)$$

Equation (17) can be rearranged into the Ayrton-Perry format as follows:

$$(1 - \chi)(1 - \chi\lambda^2) = e_{0,d} \frac{A}{W_{el}} \chi = \eta\chi \quad (18)$$

where χ is the flexural buckling reduction factor and η is the factor accounting for generalized imperfections, and can be expressed as follows:

$$\eta = e_{0,d} \frac{A}{W_{el}} \quad (19)$$

Many researchers proposed different expressions for the parameter η [13] which is linked to the member's length. Some expressions can be briefly cited here:

- Robertson [14] proposal retained in the British Standards BSI 153 and 449 up to 1962:

$$\eta_R = 0.003\lambda \quad (20)$$

- G.B. Godfrey's [15] proposal adopted in the standard BS 449:

$$\eta_G = 0.03(\lambda / 100)^2 \quad (21)$$

- Dutheil's [16] [17] proposal retained by the French regulations CM56, where $C=1/12$ was experimentally determined:

$$\eta_D = \frac{C}{\pi^2 E} f_y \lambda^2 \quad (22)$$

2.2.2. European buckling curves

In 1960, the CECM noted a large discrepancy in the shape of the buckling curves employed in different regulations and arranged therefore for a series of tests under D. Sfintesco's [18] direction and for a series of numerical simulations carried out by Beer and Schultz.

As a result, in 1970 the CECM proposed three non-dimensional curves (see Figure 7) as functions of the different types of sectional shape and the considered plane of buckling (see Table 1).

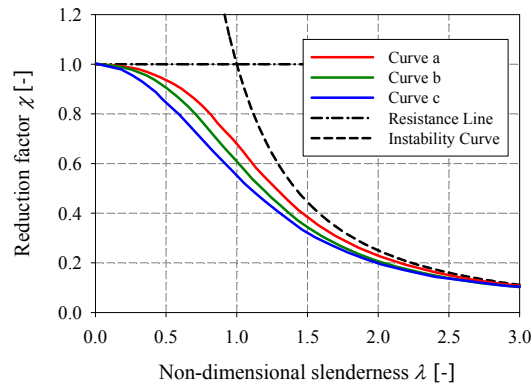




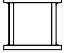

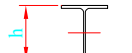


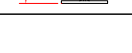
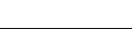
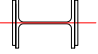
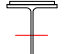
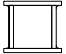
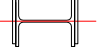
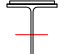




Figure 7 – Curves proposed by the CECM in 1970

Table 1 – Cross-sectional shapes corresponding to the curves a, b and c proposed by the CECM in 1970

Classification of columns				Curve
Rolled hot-finished tubes				<i>a</i>
Welded hot-finished tubes				<i>a</i>
Welded box sections				<i>b</i>
Rolled I beams		Buckling about the minor axis	$h/b > 1.2$	<i>b</i>
		Buckling about the major axis	$h/b \leq 1.2$	<i>c</i>
Welded I beams		gas cut flanges		<i>b</i>
		rolled flanges		<i>c</i>
		gas cut flanges		<i>b</i>
		rolled flanges		<i>b</i>
Rolled I-beam with welded on reinforcing plates		minor axis		<i>a</i>
		major axis		<i>b</i>
Annealed box sections				<i>a</i>
Annealed I-Beams		minor axis		<i>b</i>
		major axis		<i>a</i>
Tee-section or channel sections				<i>c</i>

Simultaneously, Baar [19] developed a simplified analytical formulation of these three curves, without a plateau. He found that the following form gives satisfactory results:

$$\chi = \frac{1}{(0.5 + \alpha\lambda^2) + \sqrt{(0.5 + \alpha\lambda^2) + \beta\lambda^2}} \quad (23)$$

The factors α and β are chosen according to Table 2.

Table 2 – Parameters proposed by Baar for buckling curves

Curve	α	β
<i>a</i>	0.514	-0.795
<i>b</i>	0.554	-0.738
<i>c</i>	0.552	-0.377

Equation (23) was derived based on Dutheil's approach and differs by the introduction of the parameter β . This expression has been introduced into two French documents [20] [21].

The bucking curves proposed in 1970 showed some inconsistencies and were accordingly modified:

- for low values of relative slenderness, the strain hardening of the material prevails over local buckling. This requires the adoption of curves with plateau for low values of slenderness;
- the three curves were established for most used steel grades and for sections of nominal thicknesses not exceeding 40 mm. However, higher steel grades members and profiles with thicknesses exceeding 40 mm were increasingly used.

The need for adapted buckling curves, taking into account the listed factors became inevitable. In 1978, the CECM proposed five new buckling curves [22], containing a plateau for the values of the reduced slenderness ratio between 0 and 0.2 (see Figure 8). The proposed curves take into account the influence of the material yield stress: when f_y is greater or equal to 430 N/mm², the adopted curve is the one located above the one defined for $f_y < 430$ N/mm², i.e. taking a_0 instead of a , a instead of b ...For sections of thickness exceeding 40 mm, the residual stresses are more significant than those used for the proposition of the buckling curves. Thus, an additional curve d was introduced (located under curve c) and proposed for

welded I-sections buckling about the minor axis and for rolled I-sections no matter the considered plane of buckling.

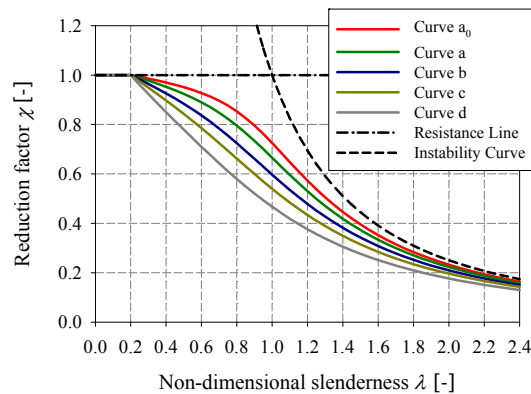


Figure 8 – Curves proposed by the CECM in 1978

2.2.3. Analytical formulation for European buckling curves

2.2.3.1. Bounds of European curves

It would be interesting to discuss about the upper and lower bounds of the European buckling curves. The upper bound of buckling curves is based on the interaction between the two ideal behaviours of structural members: resistance and instability. The classical concept of ‘resistance’ mainly characterizes the cross-sectional capacity of the member and the concept of ‘stability’ describes the tendency of members and sections to buckle under the applied loading. None of these concepts does really describe the real behaviour of structural members. The concept of ‘resistance’ assumes that no instability phenomena can occur while the concept of ‘stability’ considers an ideal member, i.e. a geometrically perfect member made of material characterized by a linear elastic constitutive law and having an infinite resistance. The upper bound is represented accordingly in the $\chi = f(\lambda)$ axes, by an horizontal straight line $\chi = 1$ (i.e. the resistance line) for $\lambda < 1$ and by the curve $\chi = \frac{1}{\lambda^2}$ for $\lambda \geq 1$ (i.e. the instability curve), which is, in fact, the Euler curve.

In the $\chi = f(\chi\lambda^2)$ axes, the upper bound is represented by an horizontal straight line $\chi = 1$ and by a vertical straight line $\chi = \frac{1}{\lambda^2}$.

The equation of the upper bound limit can be written as follow:

$$\chi + \chi\lambda^2 - \chi^2\lambda^2 = 1 \quad (24)$$

As for the lower bound of buckling curves, Merchant was the first to suggest an interaction formula for member buckling, hereafter referred to as the Rankine Equation (25):

$$\frac{\sigma_{ult}}{\sigma_{cr}} + \frac{\sigma_{ult}}{\sigma_y} = 1 \quad (25)$$

where σ_{ult} and σ_{cr} refer to the ultimate and to the critical buckling stresses respectively. σ_y is the corresponding yield stress.

For columns, σ_{cr} would be relative to the Euler curve:

$$\sigma_{cr} = \pi^2 E / \lambda^2 \quad (26)$$

In a non-dimensional form, Equation (25) could be written as follows:

$$\chi + \chi\lambda^2 = 1 \quad (27)$$

Possibilities for a ‘plastic plateau’ in the reduction curve can be easily introduced in the Merchant-Rankine type of formula with the following equation for $\chi \leq 1$ and $\lambda \leq \lambda_0$:

$$\chi + \chi\lambda^2 - \chi\lambda_0^2 = 1 \quad (28)$$

However, with member buckling curves, it turned out that the Merchant-Rankine is not truly respected since the member buckling curve *d* happened to be situated below the Merchant-Rankine curve.

The lower bound of buckling curves is given by Rondal [10] according to equation (29):

$$\chi^2\lambda^2 - \chi\lambda_0^2 = 0 \quad (29)$$

The lower bound curve, gives a measure of the relative effect of various imperfections. For example, the buckling resistance of welded profiles can be located under curve *d* due to the unfavorable residual stresses induced by the welding.

The European curves as well as the upper and lower bounds curves are illustrated in Figure 9, in the axes $\chi = f(\chi\lambda^2)$ and $\chi = f(\lambda)$.

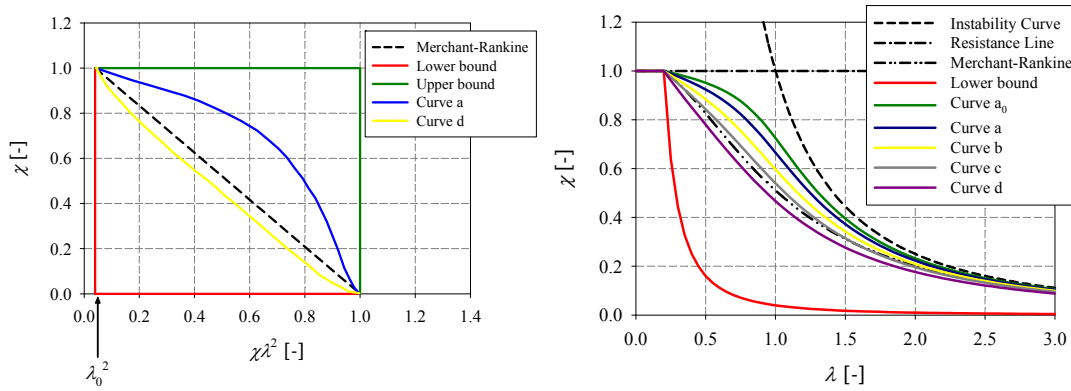


Figure 9 – Upper and lower bounds of buckling curves

2.2.3.2. Mathematical formulations

Now that the limiting bounds of the proposed buckling curves, have been discussed and detailed, a brief review of the analytical ways of formulating the design curves are presented. Many researchers have proposed simplified analytical expressions for the European curves proposed by CECM. According to Rondal [10], three analytical ways of formulating the design curves can be considered:

- Mathematical formulations;
- Merchant-Rankine formulation;
- Ayrton-Perry format.

Many authors have proposed analytical relations falling within these three ways. For instance, for flexural member buckling, the most famous purely empirical relationships are the formulae of Baar [19], Young [11] and Bjorhovde [23].

It is clear that the development of the series presented in Equation (30) can enable a rigorous representation of almost any curve, provided that the number n is sufficiently high, which will involve a large number of parameters a_i and make impractical the use of this kind of formulation:

$$\chi = \sum_{i=0}^n a_i \lambda^i \quad (30)$$

Attempts made by Baar, by considering $n=4$, to propose analytical representation for the curves proposed by the CECM in 1970, revealed inaccurate. The tested mathematical series are the following:

$$\chi = 1 + \sum_{i=1}^4 a_i \lambda^i \quad (31)$$

$$\chi = \frac{1}{1 + \sum_{i=1}^4 a_i \lambda^i} \quad (32)$$

$$\chi = \frac{1 + a_4 \lambda}{1 + \sum_{i=1}^3 a_i \lambda^i} \quad (33)$$

However, a satisfactory formulation was made by Baar, when considering two-parameters approach derived from Dutheil (see section 2.2.2), which seem to prove that it is preferable to use a mathematical approach based on the actual behaviour of the buckling member.

In 1972, Young proposed an inverse mathematical equation for the derivation of slightly different member buckling curves compared to CECM proposed curves, with the a_i coefficients given according to Table 3.

$$\lambda^2 = \sum_{i=1}^4 a_i \chi^{i-2} \quad (34)$$

Table 3 – Parameters proposed by Young for buckling curves

Curve	a_1	a_2	a_3	a_4
a	1.07	-1.15	2.97	-2.83
b	0.97	-0.46	0.84	-1.30
c	0.92	-0.08	-1.14	0.34
d	0.87	0	-1.71	0.87

This proposal presented a major inconvenient for practical applications, since the determination of χ required successive approximations.

Eventually, Bjorhovde used polynomial equations for the determination of the member buckling curves of the Structural Stability Council (SSRC), however with a discontinuous description, i.e. 4 polynomial equations per curve. Also, his proposals presented many inconvenients, since a large number of parameters were required and the discontinuities caused unnecessary complexity.

2.2.3.3. Merchant-Rankine formulation

Lindner [24] and Unger [25] proposed a generalization of the Merchant-Rankine equation detailed in (27), with the use of the Equation (35). Various values of n corresponding to the different member curves (a_0 , a , b , c and d) are detailed in Table 4.

$$\chi = \left(\frac{1}{1 + \lambda^{2n}} \right)^{1/n} \quad (35)$$

Table 4 – Parameters proposed by Unger and Linder for buckling curves

Curve	n_{Unger}	n_{Linder}
a_0	1.90	1.810
a	1.60	1.486
b	1.20	1.138
c	1.05	1.038
d	0.90	0.881

The authors of the project revision of DIN 4114 [26], adopted a polynomial equation for the determination of the n parameter with given a_i values (see Table 5):

$$n = \sum_{i=0}^4 a_i \lambda^i \quad (36)$$

Table 5 – Parameters proposed by the project revision of DIN 4114

Curve	a_0	a	b	c	d
a_3	0.2054	0.1000	0.0439	-0.0005	-0.0153
a_2	-1.3000	-0.6547	-0.2759	-0.0147	-0.0677
a_1	2.1355	1.0586	0.3307	0.0296	0.1230
a_0	1.0275	1.1639	1.2087	1.1559	0.9889

None of these three proposals take account of the plateau for $\lambda \leq 0.2$ and the proposed analytical representation revealed inaccurate when compared to the CECM curves.

The plastic plateau was introduced in the Merchant-Rankine type of formula according to Equation (37) with given n values (see Table 6):

$$\chi = \left(\frac{1}{1 + \lambda^{2n} - \lambda_0^{2n}} \right)^{1/n} \quad (37)$$

Table 6 – Parameters proposed the Merchant-Rankine with plateau formula

Curve	n
a_0	2.05
a	1.58
b	1.17
c	1.05
d	0.85

Equation (37) gives satisfactory approximation to the CECM buckling curves, except for Curve d .

2.2.3.4. Ayrton-Perry format

The Ayrton-Perry [2] approach was found the mathematical formulation describing the best the buckling behaviour of beam-column members.

The physical basis of the Ayrton-Perry formulation lies in the adoption of a failure criteria based on the attainment of the yield limit, with the following equation of a column subjected to a pure compression with an initial curvature amplitude e_0 :

$$\frac{N}{A} + \frac{M''}{W_{el}} = f_y \quad (38)$$

Equation (38) can be rearranged in terms of stresses, where σ_{ult} represents the ultimate stress and W_{el} the elastic modulus:

$$\sigma_{ult} + \frac{\sigma_{ult} \cdot e_0}{\left(1 - \frac{\sigma_{ult}}{\sigma_{cr}}\right)} \cdot \frac{A}{W_{el}} = \sigma_y \quad (39)$$

which in turn can be represented in the following form:

$$\sigma_{ult} (\sigma_{cr} - \sigma_{ult}) + \sigma_{ult} \sigma_{cr} e_0 \frac{A}{W_{el}} = \sigma_y (\sigma_{cr} - \sigma_{ult}) \quad (40)$$

$$\sigma_y (\sigma_{cr} - \sigma_{ult}) - \sigma_{ult} (\sigma_{cr} - \sigma_{ult}) = \sigma_{ult} \sigma_{cr} e_0 \frac{A}{W_{el}} \quad (41)$$

$$(\sigma_{cr} - \sigma_{ult}) (\sigma_y - \sigma_{ult}) = \eta \sigma_{cr} \sigma_{ult} \quad (42)$$

with $\eta = \frac{e_0 A}{W_{el}}$

Taking $e_0 = \frac{l}{\gamma}$, η can be written in the form of:

$$\eta = \frac{\lambda}{\gamma(i/\nu)} \quad (43)$$

Maquoi and Rondal demonstrated that the ratio i/ν is almost constant for each of the principal buckling planes of the classical sections. Therefore different buckling behaviours can be expected depending on the two planes of buckling.

In a non-dimensional form, Equation (42) can be written as follows, by multiplying both sides of it by $1/f_y$:

$$(1 - \chi)(1 - \chi\lambda^2) = \eta\chi \quad (44)$$

where χ is the reduction factor, λ is the relative slenderness and η is the factor accounting for generalized imperfections.

Figure 10 shows the schematic representation of the Ayrton-Perry approach, where a set of curves can be obtained by giving different values to the parameter η taking as upper limit ($\eta = 0$)

- the resistance horizontal straight line $\chi = 1$;
- the instability curve defined with Euler curve $\chi = 1/\lambda^2$.

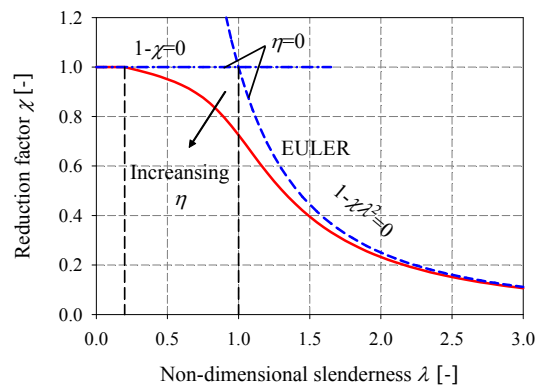


Figure 10 – Schematic representation of the Ayrton-Perry approach.

Seven propositions have been performed to define a simple formulation of the parameter η which is linked with the length of the member:

$$\eta_1 = \alpha_1(\lambda - 0.2) \quad (45)$$

$$\eta_2 = \alpha_2\sqrt{\lambda^2 - 0.04} \quad (46)$$

$$\eta_3 = \alpha_3(\lambda - 0.2)^2 \quad (47)$$

$$\eta_4 = \alpha_4(\lambda^2 - 0.04) \quad (48)$$

$$\eta_5 = \alpha_5(\chi\lambda^2 - 0.04) \quad (49)$$

$$\eta_6 = \alpha_6(\lambda^2(1 + \chi) - 0.08) \quad (50)$$

$$\eta_7 = \alpha_7\chi(\lambda - 0.2) \quad (51)$$

Dwight [27] proposed to use Equation (45) to determine the generalized imperfection η .

A numerical study performed to find the α -value, making Equation (52) minimal, showed that only Equations (45) and (46) lead to satisfactory solutions.

$$\sum_{i=1}^{35} (\chi_i^{CECM} - \chi_i^{Calculated})^2 \rightarrow \text{minimum} \quad (52)$$

It was also found that, the η_1 expression is the most representative of the steel behaviour whereas η_2 expression is more suitable for aluminium alloys.

For the direct calculation of the χ factor, Equation (44) can be rearranged as follow, by using Equation (45) for the determination of the generalized imperfection η :

$$\chi = \frac{1 + \alpha(\lambda - 0.2) + \lambda^2}{2\lambda^2} - \frac{1}{2\lambda^2} \sqrt{[1 + \alpha(\lambda - 0.2) + \lambda^2]^2 - 4\lambda^2} \quad (53)$$

Equation (53) can be written as the following by introducing the intermediate factor ϕ :

$$\chi = \frac{\phi - \sqrt{\phi^2 - \lambda^2}}{\lambda^2} \quad (54)$$

$$\phi = 0.5 \left[1 + \alpha(\lambda - 0.2) + \lambda^2 \right] \quad (55)$$

Equation (54) can now be multiplied by the complement of $\phi - \sqrt{\phi^2 - \lambda^2}$:

$$\chi = \frac{\phi - \sqrt{\phi^2 - \lambda^2}}{\lambda^2} \left[\frac{\phi + \sqrt{\phi^2 - \lambda^2}}{\phi + \sqrt{\phi^2 - \lambda^2}} \right] \quad (56)$$

This finally leads to the following form of the Ayrton-Perry formula:

$$\chi = \frac{1}{\phi + \sqrt{\phi^2 - \lambda^2}} \quad (57)$$

2.2.4. Adopted analytical formulation

Maquoi and Rondal [28] proposed to adopt the Ayrton-Perry expression to represent the European curves:

$$(1 - \chi)(1 - \chi\lambda^2) = \eta\chi = \alpha(\lambda - 0.2)\chi \quad (58)$$

where

$$\eta = e_{0,d} \frac{A}{W_{el}} = \alpha(\lambda - 0.2) \quad (59)$$

As already mentioned, the left side of this equation represents a simple multiplication of two polynomials; the first one represents the plastic resistance of a perfect stub column, and the second represents the instability curve which is the limit of a perfect column. The behaviour of a real column lies below these curves and the right term of the equation describes the loss of strength (the α parameter provides the curves below the two defined limits) due to geometrical and mechanical imperfection effects. The end-of-plateau limit $\lambda_0 = 0.2$ adopted by the CECM is provided as well.

This equation was retained by the German, Austrian, Belgian, French, Swiss and in Eurocode 3 regulations [29].

According to [29], the influence of the material yield stress f_y can be taken into account by considering the following equation for the generalized imperfections factor:

$$\eta = \alpha(\lambda - 0.2)\left(\frac{235}{f_y}\right)^{0.8} \quad (60)$$

The factor α depends on:

- the cross-sectional shape;
- the plane of buckling;
- the steel grade;
- the thickness of the cross-section;
- the manufacturing process.

The α -values proposed by Maquoi and Rondal were obtained by optimum adjustment of the analytical formulations by the CECM proposed curves, and are taken according to Table 7 and Table 8.

Table 7 – Imperfection factor for buckling curves

Buckling curve	a_0	a	b	c	d
Imperfection factor α	0.13	0.21	0.34	0.49	0.76

Once determined, the reduction factor χ and the reduced slenderness λ are calculated using Equations (57) and (61) respectively:

$$\lambda = \sqrt{\frac{Af_y}{N_{cr}}} \quad (61)$$

The buckling verification of member subjected to axial compression is finally written as:

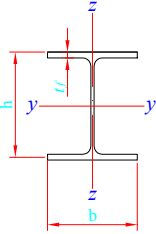
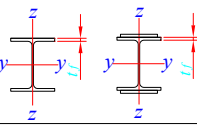

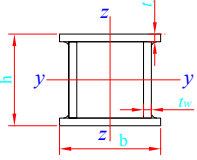
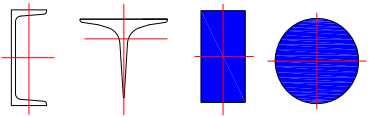

$$\frac{N_{Ed}}{N_{b,Rd}} \leq 1 \quad (62)$$

where N_{Ed} is the design value of the compression force; $N_{b,Rd}$ is the design buckling resistance of the compression member calculated as follows:

$$N_{b,Rd} = \frac{\chi A f_y}{\gamma_{M1}} \quad (63)$$

The cross sectional area A introduced in Equations (61) and (63), corresponds to the actual structural sections for class 1, 2 and 3 cross-sections and to the effective area for class 4 sections.

Table 8 – Imperfection factor for buckling curves

Cross-section	Limits	Buckling about axis	Buckling curve	
			S 235 S 275 S 355 S 420	S 460
Rolled I-sections 	$h/b > 1.2$ $t_f \leq 40 \text{ mm}$	y-y z-z	a b	a_0 a_0
	$40 \text{ mm} < t_f \leq 100 \text{ mm}$	y-y z-z	b c	a a
	$h/b \leq 1.2$ $t_f \leq 100 \text{ mm}$	y-y z-z	b c	a a
	$t_f > 100 \text{ mm}$	y-y z-z	d d	c c
Welded I-sections 	$t_f \leq 40 \text{ mm}$	y-y z-z	b c	b c
	$t_f > 40 \text{ mm}$	y-y z-z	c d	c d
Hollow sections 	hot-rolled	any	a	a_0
	cold-formed	any	c	c
Welded box sections 	generally (except as below)	any	b	b
	thick welds: $a > 0.5 t_f$ $b/t_f < 30$ $h/t_w < 30$	any	c	c
U-, T- and solid sections 		any	c	c
L-sections 		any	b	b

2.2.5. Current developments in the design of thin-walled hollow members

Nowadays, the engineering structures made of thin-walled steel elements have widespread practical applications. Thin-walled elements fail by premature local buckling of their plates, and never attain the plastic compression load. In this section, the maximum attained load by class 4 cross-sections is referred to as N_v . Various methods for calculating the buckling strength of slender sections rely on the effective width method, which require tedious and long calculations. In this section, special attention has been paid to the interpretation of the local-global coupling phenomenon without resorting to the effective widths method concept. According to the Liège method [13], the interaction between local and global instabilities may be taken into account by the mathematical well-known Ayrton-Perry expression, by replacing the compression yield load N_{pl} by the failure load N_v of a thin-walled stub column.

The Ayrton-Perry expression is written in the form of:

$$(1 - \chi')(1 - \chi' \lambda'^2) = \eta \chi = \alpha(\lambda' - 0.2)\chi' \quad (64)$$

with $\chi' = N / N_v = N / A f_v$ and $\lambda' = \sqrt{\frac{N_v}{N_{cr}}}$

The cross sectional area A and inertia I introduced in Equation (64), are those of the actual structural sections without any effective width reduction.

The maximum load N_v of a stub column taking account of the local buckling of the faces can be determined through two analytical methods as described below.

2.2.5.1. Method with interaction of faces

According to Bleich [30], the buckling stress of the whole cross-section can be calculated as follows:

$$\sigma_{cr} = k \frac{\pi^2 E}{12(1 - \nu^2)} \left(\frac{t}{h_m} \right)^2 \quad (65)$$

where k is the plate buckling coefficient given according to Equation (66) and b_m and h_m are the dimensions of the cross-section as illustrated in Figure 11.

$$k = \left(2 + \frac{2}{10\xi + 3} \right)^2 \quad (66)$$

$$\xi = \frac{0.38}{1 - \left(\frac{b_m}{h_m} \right)^2} \quad (67)$$

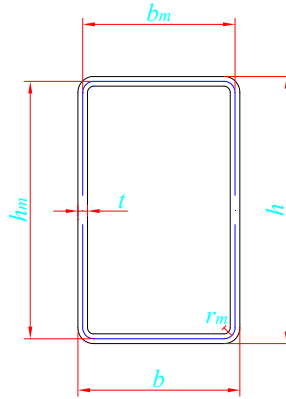


Figure 11 – Section notation and designation

The equivalent slenderness ratio can be related to the structural section according to the following equation:

$$\lambda_v = \sqrt{\frac{f_y}{\sigma_{cr}}} \quad (68)$$

Then local buckling curves (such as Chilver, Hanovre, CECM curves...) can be used for determining the ultimate load of the stub column. This method which has been applied by some researchers, in particular Chilver [31], presents some inconsistencies and shortcoming. It does not rest on a justifiable theoretically valid basis, since it associates the critical-elastic concept to take into account the interaction of the faces, with the failure-type concept in the search of a failure curve.

2.2.5.2. Method without interaction of faces

The second method [13] is based on the assumption that there is no interaction between the stub columns faces on failure. This hypothesis was held by several researchers such as Dwight [32].

The failure load N_v of a thin-walled stub column can be obtained by adding the failure loads of the corresponding faces and corners, leading to the following expression:

$$N_v = 2 \cdot \sigma_{v1} \cdot b_{f1} \cdot t + 2 \cdot \sigma_{v2} \cdot b_{f2} \cdot t + \sigma^* A_{corners} \quad (69)$$

where b_f is the flat width of the tube face, $A_{corners}$ is the total area of the corners, σ_v is the failure stress of one-face and σ^* is the maximum stress supported by the corners.

Braham [13] proposed to use the average of the stresses σ_{v1} and σ_{v2} to determine the maximum stress σ^* . The failure stresses σ_v are obtained by using local buckling curves. For instance, many important, theoretical and experimental works were performed in Cambridge in the field of plate local buckling. Also, extensive developments have been conducted to derive buckling curves for different loading conditions and types of sections taking into account the cross-section as a whole and not plates separately. It shall be mentioned that the residual stresses taken into account to derive the Cambridge curves are those of welded profiles. A numerical study performed by Gilson [33] showed that the residual stress pattern of tubular profiles is more favorable for slenderness ratio values $\lambda_v \leq 2$ than the residual stresses adopted in Cambridge.

Accordingly, more reasonable local buckling curves, proposed at Liège (see Figure 12) were adopted to determine the failure stresses σ_{v1} and σ_{v2} of the faces of square or rectangular hollow sections. These buckling curves have the following characteristics:

- the Ayton-Perry formulations were used reflecting the two failure modes (resistance limit from one hand and instability limit from another hand: the curves lie below the plastic plateau and the well-known Von Karman curve ($\chi = 1/\lambda$) defining the failure stress of an ideal plate, free from imperfections;
- a distinction between heat treated and non-heat treated structural sections was made;
- an appropriate end of plateau was adopted as the limit to the local buckling range of plates $\lambda_{v0} = 0.8$ as requested by the CECM.

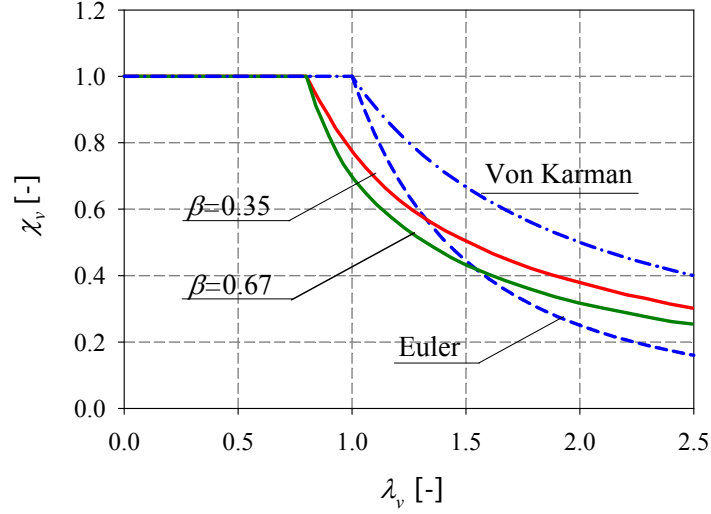


Figure 12 – Local buckling curves

The Ayton-Perry approach can be written as follows:

$$(1 - \chi_v)(1 - \chi_v \lambda_v) = \beta(\lambda_v - 0.8)\chi_v \quad (70)$$

where the reduction coefficient χ_v and the slenderness ratio of the face λ_v are given by:

$$\chi_v = \frac{\sigma_v}{f_y} \quad (71)$$

$$\lambda_{v,h} = \mu \frac{h_m / t}{1.9} \sqrt{f_y / E} \quad (72)$$

$$\lambda_{v,b} = \frac{b_m / t}{1.9} \sqrt{f_y / E} \quad (73)$$

where the coefficient μ is given by Bleich according to the following equation:

$$\mu = \frac{6.9 - 3(b_m / h_m)^2}{7.9 - 4(b_m / h_m)^2} \quad (74)$$

For the direct calculation of the χ_v factor, Equation (70) can be rearranged as follows:

$$\chi_v = \frac{1 + \beta(\lambda_v - 0.8) + \lambda_v}{2\lambda_v} - \frac{1}{2\lambda_v} \sqrt{[1 + \beta(\lambda_v - 0.8) + \lambda_v]^2 - 4\lambda_v} \quad (75)$$

The imperfection factor β has been adjusted with actual test results and is given according to Table 9.

Table 9 – Imperfection factor β

Section	Heat treated	Non-heat treated
Imperfection factor β	0.35	0.67

The width b_m used in the calculation of the slenderness ratio is replaced by an equivalent value b_{eq} , allowing for the stabilizing action of the corners according to Equation (76) and Figure 13.

$$b_{eq} = b_f = b_m - 2r_m \quad (76)$$

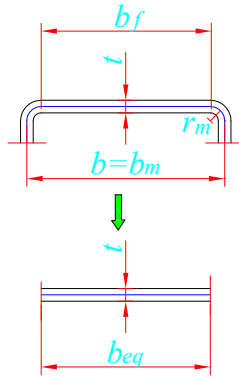


Figure 13 – Definition of equivalent width value

A numerical study has led to adopt, for values of r_m / b_m lower than 0.12 the following relation:

$$\frac{b_{eq}}{b_m} = 1 - \left(2.45 \frac{b_m}{t} - 50 \right) \left(\frac{r_m}{b_m} \right)^3 \quad (77)$$

2.3. Members in bending and axial compression

As detailed in ECCS 9, Eurocode 3 design rules for beam-columns are certainly the most advanced and accurate beam-column formulae; in particular, tubular sections were deeply considered and received specific treatment. Consequently, in the following section, a description of the methods used nowadays in the latest version of Eurocode 3 (EN 1993-1-1) to deal with the most complex behaviour of a span member subjected to bending and axial compression is made. In the present approach of EN 1993-1-1, the effects of the axial force

and the bending moments are summed and the non-linear effects are accounted for by specific interaction factors. Two different formats of the interaction formulae are provided:

- Method 1 which has been developed by M. Villette, J.P. Jaspart, N. Boissonnade and J.P. Muzeau, is adaptable to identify and account for the structural effects. Each coefficient of the formulae represents a single physical effect (material and geometrical non linearities and interactions between loading components). This method is detailed in Annex A of EN 1993–1–1;
- Method 2 which has been developed by R. Greiner, R. Ofner, G. Salzgeber, P. Kaim, J. Lindner, A. Rusch, S. Heyde and J.Wang Kunming, is mainly focused on the direct design of standard cases and uses a reduced number of factors. This method is detailed in Annex B of EN 1993–1–1.

It should be noted that, both methods have been validated by numerical simulations and experimental tests with open sections and very few experimental tests on hollow section columns have been considered [34].

In the following, section 2.3.1 details the basic format of the formulae developed for the design of members subjected to compression and mono-axial bending. This format is extended in section 2.3.2 to the complex load case: compression and biaxial bending. Sections 2.3.3 and 2.3.4 present the coefficients and interaction factors adopted by both Methods 1 and 2 respectively. More details concerning the background of the interaction formulas presented hereafter can be found in [12].

Finally, the extension of the Ayrton-Perry formulation for member subjected to compression and biaxial bending moment is detailed in section 2.3.5.

2.3.1. Member under compression and mono-axial bending: $N_{Ed}+M_{Ed}$

As already mentioned in section 2.2.1, the stability of a member subjected to an axial compression load N_{Ed} is given by:

$$\frac{N_{Ed}}{N_{Rd}} + \frac{1}{1 - N_{Ed} / N_{cr}} \frac{N_{Ed} e_{0,d}}{M_{el,Rd}} \leq 1 \quad (78)$$

The expression for compression and additional first order moment M_{Ed} is given by Equation (79) which represents a second-order cross-sectional check of the most heavily loaded section.

$$\frac{N_{Ed}}{N_{Rd}} + \frac{1}{1 - N_{Ed} / N_{cr}} \frac{N_{Ed} e_{0,d}}{M_{el,Rd}} + \frac{M_{Ed \max}^{II}}{M_{el,Rd}} \leq 1 \quad (79)$$

where $M_{Ed \max}^{II}$ is the second-order maximum bending moment induced by the first order bending moment and can be expressed as:

$$M_{Ed \max}^{II} = \frac{C_m M_{Ed}}{1 - N_{Ed} / N_{cr}} \quad (80)$$

The equivalent moment concept [12] is used in order to avoid the determination of the location of the most heavily loaded cross-section. It consists of replacing the actual first order bending system by a sinusoidal equivalent first order bending moment that produces the same amplified bending moment (see Figure 14). The latter is usually expressed as $C_m M_{Ed}$. The primary bending moment is induced by end moments and/or transverse loading.

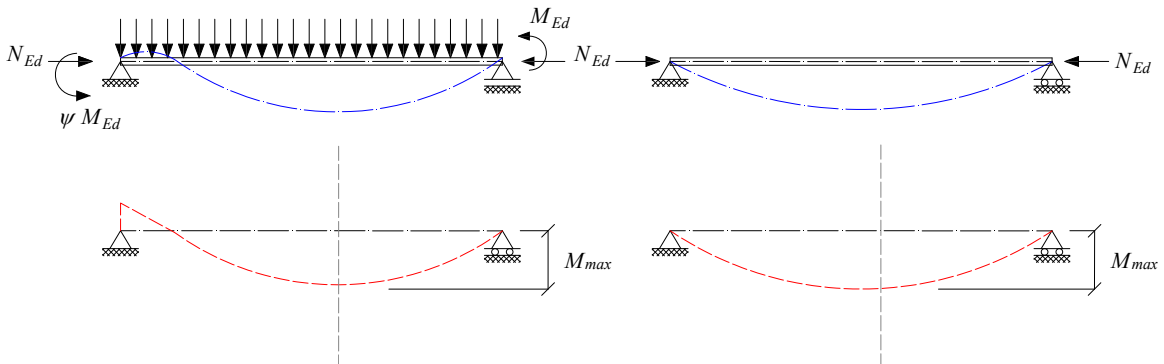


Figure 14 – Actual 2nd order bending moment and the associated sinusoidal equivalent

Equation (79) can be written as follow:

$$\frac{N_{Ed}}{N_{Rd}} + \frac{1}{1 - N_{Ed} / N_{cr}} \frac{N_{Ed} e_{0,d}}{M_{el,Rd}} + \frac{1}{1 - N_{Ed} / N_{cr}} \frac{C_m M_{Ed}}{M_{el,Rd}} \leq 1 \quad (81)$$

With the inclusion of the factor μ , the general elastic format can be written:

$$\frac{N_{Ed}}{\chi N_{Rd}} + \mu \frac{1}{1 - N_{Ed} / N_{cr}} \frac{C_m M_{Ed}}{M_{el,Rd}} \leq 1 \quad (82)$$

where:

$$\mu = \frac{1 - N_{Ed} / N_{cr}}{1 - \chi N_{Ed} / N_{cr}} \quad (83)$$

The elastic-plastic check for one plane behaviour is obtained by replacing $M_{el,Rd}$ by $C M_{pl,Rd}$. The full plastic bending resistance $M_{pl,Rd}$ may not be reached because of instability effects and only an intermediate elastic-plastic value $C M_{pl,Rd}$ is reached.

$$\frac{N_{Ed}}{\chi N_{pl,Rd}} + \mu \frac{1}{1 - N_{Ed} / N_{cr}} \frac{C_m M_{Ed}}{C M_{pl,Rd}} \leq 1 \quad (84)$$

2.3.2. Member under compression and biaxial bending: $N_{Ed} + M_{y,Ed} + M_{z,Ed}$

Biaxial bending is accounted for by adding a second bending term in Equation (82) to give the general elastic formats (Equations (85) and (86)) allowing to check the member resistance about both principal planes (strong and weak axes respectively):

$$\frac{N_{Ed}}{\chi_y N_{pl,Rd}} + \mu_y \left[\frac{C_{my} M_{y,Ed}}{(1 - N_{Ed} / N_{cr,y}) M_{el,y,Rd}} + \frac{C_{mz} M_{z,Ed}}{(1 - N_{Ed} / N_{cr,z}) M_{el,z,Rd}} \right] \leq 1 \quad (85)$$

$$\frac{N_{Ed}}{\chi_z N_{pl,Rd}} + \mu_z \left[\frac{C_{my} M_{y,Ed}}{(1 - N_{Ed} / N_{cr,y}) M_{el,y,Rd}} + \frac{C_{mz} M_{z,Ed}}{(1 - N_{Ed} / N_{cr,z}) M_{el,z,Rd}} \right] \leq 1 \quad (86)$$

where

$$\mu_y = \frac{1 - N_{Ed} / N_{cr,y}}{1 - \chi_y N_{Ed} / N_{cr,y}} \quad (87)$$

$$\mu_z = \frac{1 - N_{Ed} / N_{cr,z}}{1 - \chi_z N_{Ed} / N_{cr,z}} \quad (88)$$

When sections of class 1 or 2 are of concern, the following equations are used:

$$\frac{N_{Ed}}{\chi_y N_{pl,Rd}} + \mu_y \left[\frac{C_{my} M_{y,Ed}}{(1 - N_{Ed} / N_{cr,y}) C_{yy} M_{pl,y,Rd}} + \alpha^* \frac{C_{mz} M_{z,Ed}}{(1 - N_{Ed} / N_{cr,z}) C_{yz} M_{pl,z,Rd}} \right] \leq 1 \quad (89)$$

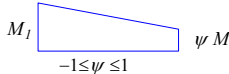
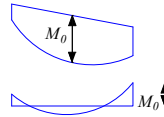
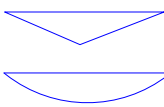
$$\frac{N_{Ed}}{\chi_y N_{pl,Rd}} + \mu_z \left[\beta^* \frac{C_{my} M_{y,Ed}}{(1 - N_{Ed} / N_{cr,y}) C_{zy} M_{pl,y,Rd}} + \frac{C_{mz} M_{z,Ed}}{(1 - N_{Ed} / N_{cr,z}) C_{zz} M_{pl,z,Rd}} \right] \leq 1 \quad (90)$$

where α^* and β^* are factors taking into account the material non-linear behaviour; C_{ii} and C_{ij} are the interaction factors dealing with the plasticity effects: The factors C_{ii} and C_{ij} are used respectively when the bending plane is the same or perpendicular to the plane of buckling.

2.3.3. Design formulae for Method 1

Method 1 [35], [36], [37], [38] adopts different expressions for the equivalent uniform moment factors C_m depending on the corresponding moment diagram (see Table 10).

Table 10 – Equivalent uniform moment factors C_m

Moment diagram	C_m
	$C_m = 0.79 + 0.21\psi + 0.36(\psi - 0.33) \frac{N_{Ed}}{N_{cr}}$
	$C_m = 1 + \left(\frac{\pi^2 EI v_0 }{ M_0 L^2} - 1 \right) \frac{N_{Ed}}{N_{cr}}$
	$C_m = 1 - 0.18 \frac{N_{Ed}}{N_{cr}}$ $C_m = 1 + 0.03 \frac{N_{Ed}}{N_{cr}}$

When the bending moment is due to transverse loads or to end moments with transverse loads, the C_m factor can be written according to the following equation, with M_0 and v_0 representing the first order maximum bending moment and deflection respectively.

$$C_m = 1 + \left(\frac{\pi^2 EI |v_0|}{|M_0| L^2} - 1 \right) \frac{N_{Ed}}{N_{cr}} \quad (91)$$

For the case of a concentrated load at mid-span, it can be written:

$$C_m = 1 - 0.18 \frac{N_{Ed}}{N_{cr}} \quad (92)$$

For a uniformly distributed load:

$$C_m = 1 + 0.03 \frac{N_{Ed}}{N_{cr}} \quad (93)$$

For the case of linearly distributed bending moments, Villette ([39], [40]) expression is used:

$$C_m = 0.79 + 0.21\psi + 0.36(\psi - 0.33) \frac{N_{Ed}}{N_{cr}} \quad (94)$$

Concerning the plasticity coefficients C_{ii} and C_{ij} , taking account of the plasticity effects in the interaction between mono-axial bending and axial force, the following expressions are proposed:

$$C_{ii} = 1 + (w_i - 1) \left[2 - \frac{1.6}{w_i} C_{m,i}^2 (\lambda_{\max} + \lambda_{\max}^2) \right] \frac{N_{Ed}}{N_{pl,Rd}} \geq \frac{W_{el,j}}{W_{pl,i}} \quad (95)$$

$$C_{ij} = 1 + (w_j - 1) \left[2 - 14 \frac{C_{m,j}^2 \lambda_{\max}^2}{w_j^5} \right] \frac{N_{Ed}}{N_{pl,Rd}} \geq 0.6 \sqrt{\frac{w_j}{w_i}} \frac{W_{el,j}}{W_{pl,i}} \quad (96)$$

The axial force plays a role in the extent of yielding at the ultimate limit state. Because of instability effects, the beam may not reach the full plastic bending resistance $M_{pl,Rd}$. This effect is accounted for through the presence of the highest relative slenderness $\lambda_{\max} = \max(\lambda_y; \lambda_z)$ and $N_{Ed} / N_{pl,Rd}$. The contribution of bending moments along the member is included by the C_m factors.

2.3.3.1. Member with class 1 and 2 cross-sections

The buckling capacity is predicted by Equations (89).and (90) for class 1 and 2 cross-sections, where α^* and β^* give the best fit with the non-linear interaction equation for cross-section properties and can be written as:

$$\alpha^* = 0.6 \sqrt{\frac{w_z}{w_y}} \quad (97)$$

$$\beta^* = 0.6 \sqrt{\frac{w_y}{w_z}} \quad (98)$$

where the ratio between the plastic and the elastic modulus w should be lower than 1.5 which represents the maximum value for the range of realistic structural sections:

$$w = \frac{W_{pl}}{W_{el}} \leq 1.5 \quad (99)$$

2.3.3.2. Member with class 3 and 4 cross-sections

The buckling capacity of class 3 sections is obtained by replacing the elastic-plastic bending resistances $C M_{pl,Rd}$ by the elastic ones $M_{el,Rd}$ in Equations (89).and (90). In addition, a linear interaction between $M_{y,Ed}$ and $M_{z,Ed}$ is considered (i. e. $\alpha^* = \beta^* = 1$).

$$\frac{N_{Ed}}{\chi_y N_{pl,Rd}} + \mu_y \left[\frac{C_{my} M_{y,Ed}}{(1 - N_{Ed} / N_{cr,y}) M_{el,y,Rd}} + \frac{C_{mz} M_{z,Ed}}{(1 - N_{Ed} / N_{cr,z}) M_{el,z,Rd}} \right] \leq 1 \quad (100)$$

$$\frac{N_{Ed}}{\chi_z N_{pl,Rd}} + \mu_z \left[\frac{C_{my} M_{y,Ed}}{(1 - N_{Ed} / N_{cr,y}) M_{el,y,Rd}} + \frac{C_{mz} M_{z,Ed}}{(1 - N_{Ed} / N_{cr,z}) M_{el,z,Rd}} \right] \leq 1 \quad (101)$$

For class 4 cross-sections, the buckling capacity becomes as follows:

$$\frac{N_{Ed}}{\chi_y N_{pl,Rd}} + \mu_y \left[\frac{C_{my} (M_{y,Ed} + e_{N,y} N_{Ed})}{(1 - N_{Ed} / N_{cr,y}) M_{eff,y,Rd}} + \frac{C_{mz} (M_{z,Ed} + e_{N,z} N_{Ed})}{(1 - N_{Ed} / N_{cr,z}) M_{eff,z,Rd}} \right] \leq 1 \quad (102)$$

$$\frac{N_{Ed}}{\chi_z N_{pl,Rd}} + \mu_z \left[\frac{C_{my} (M_{y,Ed} + e_{N,y} N_{Ed})}{(1 - N_{Ed} / N_{cr,y}) M_{eff,y,Rd}} + \frac{C_{mz} (M_{z,Ed} + e_{N,z} N_{Ed})}{(1 - N_{Ed} / N_{cr,z}) M_{eff,z,Rd}} \right] \leq 1 \quad (103)$$

where $M_{eff,Rd}$ represents the effective bending resistance of the cross-section, and e_N , the shift of centroid due to effective cross-section concept.

2.3.4. Design formulae for Method 2

The interaction formula of Method 2 is derived from an elastic in-plane flexural buckling check extended to allow for plasticity:

$$\frac{N_{Ed}}{N_{pl,Rd}} + \frac{1}{1 - N_{Ed} / N_{cr}} \frac{C_m M_{Ed} + N_{Ed} e_{0,d}}{M_{pl,Rd}} \leq 1 \quad (104)$$

The Ayrton-Perry Equation (18) can be rearranged for the determination of the maximum amplitude $e_{0,d}$:

$$e_{0,d} = \left(\frac{1}{\chi} - 1\right)(1 - \chi\lambda^2) \frac{W_{pl}}{A} \quad (105)$$

Replacing Equation (105) in Equation (104) allows the determination of the buckling interaction formula expressed as follows:

$$\frac{N_{Ed}}{\chi N_{pl,Rd}} + k \frac{C_m M_{Ed}}{M_{pl,Rd}} \leq 1 \quad (106)$$

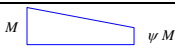
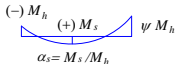
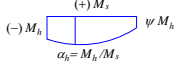
$$\text{where } k = \frac{1}{1 - \frac{N_{Ed}}{N_{pl,Rd}} \chi \lambda^2} \quad (107)$$

It is to be noticed that the theoretical formula of k is not fully appropriate due to the elastic second-order theory and linear cross-section interaction used and interacting with each other. Therefore, numerical simulations were performed on different sections and moment diagrams including different values of the parameters λ_i , η_i and C_{mi} to derive the k -factor. Additional G.M.N.I.A. calculations were performed to derive the C_m -factors given in Table 11.

Austin-formula [41] proposed the following expression of C_m for members tested under linearly varying moment diagrams:

$$C_m = 0.6 + 0.4\psi \geq 0.4 \quad (108)$$

Table 11 – Equivalent moment factor C_m

Moment diagram	Range		C_{my} and C_{mz}	
			Uniform load	Concentrated load
	$-1 \leq \psi \leq 1$		$0.6 + 0.4\psi \geq 0.4$	
 $\alpha_s = M_s/M_h$	$0 \leq \alpha_s \leq 1$	$-1 \leq \psi \leq 1$	$0.2 + 0.8\alpha_s \geq 0.4$	$0.2 + 0.8\alpha_s \geq 0.4$
	$-1 \leq \alpha_s < 0$	$0 \leq \psi \leq 1$	$0.1 - 0.8\alpha_s \geq 0.4$	$-0.8\alpha_s \geq 0.4$
$-1 \leq \psi \leq 0$		$0.1(1 - \psi) - 0.8\alpha_s \geq 0.4$	$-0.2(-\psi) - 0.8\alpha_s \geq 0.4$	
 $\alpha_h = M_h/M_s$	$0 \leq \alpha_s \leq 1$	$-1 \leq \psi \leq 1$	$0.95 + 0.05\alpha_h$	$0.9 + 0.1\alpha_h$
	$-1 \leq \alpha_s \leq 0$	$0 \leq \psi \leq 1$	$0.95 + 0.05\alpha_h$	$0.9 + 0.1\alpha_h$
		$-1 \leq \psi \leq 0$	$0.95 + 0.05\alpha_h(1 + 2\psi)$	$0.9 + 0.1\alpha_h(1 + 2\psi)$
<i>For members with sway mode the equivalent uniform moment factor</i>				

should be taken $C_{my} = 0.9$ or $C_{mz} = 0.9$ respectively.

C_{my} , C_{mz} and shall be obtained according to the bending moment diagram between the relevant braced points as follows:

Moment factor	Bending axis	Points braced in direction
C_{my}	y – y	z – z
C_{mz}	z – z	y – y

2.3.4.1. Member with class 1 and 2 cross-sections

Biaxial bending is accounted for by adding a second bending term in Equation (104), to give the general formats for Method 2 formulations (Equations (109) and (110)), allowing to check the member resistance about both principal planes (strong and weak axes respectively):

$$\frac{N_{Ed}}{\chi_y N_{pl,Rd}} + k_y \frac{C_{my} M_{y,Ed}}{M_{pl,y,Rd}} + 0.6k_z \frac{C_{mz} M_{z,Ed}}{M_{pl,z,Rd}} \leq 1 \quad (109)$$

$$\frac{N_{Ed}}{\chi_z N_{pl,Rd}} + 0.6k_y \frac{C_{my} M_{y,Ed}}{M_{pl,y,Rd}} + k_z \frac{C_{mz} M_{z,Ed}}{M_{pl,z,Rd}} \leq 1 \quad (110)$$

where:

$$k_y = 1 + (\lambda_y - 0.2)n_y \leq 1 + 0.8n_y \quad (111)$$

$$k_z = 1 + (\lambda_z - 0.2)n_z \leq 1 + 0.8n_z \quad (112)$$

$$n_y = \frac{N_{Ed}}{\chi_y N_{pl}} \quad (113)$$

$$n_z = \frac{N_{Ed}}{\chi_z N_{pl}} \quad (114)$$

$$C_{my} = C_{mz} = 0.6 + 0.4\psi \geq 0.4 \quad (\text{see Table 11}) \quad (115)$$

2.3.4.2. Member with class 3 and 4 cross-sections

According to Method 2, the buckling about the strong and weak axis respectively is predicted by Equations (116).and (117) for class 3 cross-sections.

$$\frac{N_{Ed}}{\chi_y N_{pl,Rd}} + k_y \frac{C_{my} M_{y,Ed}}{M_{el,y,Rd}} + k_z \frac{C_{mz} M_{z,Ed}}{M_{el,z,Rd}} \leq 1 \quad (116)$$

$$\frac{N_{Ed}}{\chi_z N_{pl,Rd}} + 0.8k_y \frac{C_{my} M_{y,Ed}}{M_{el,y,Rd}} + k_z \frac{C_{mz} M_{z,Ed}}{M_{el,z,Rd}} \leq 1 \quad (117)$$

where:

$$k_y = 1 + 0.6\lambda_y n_y \leq 1 + 0.6n_y \quad (118)$$

$$k_z = 1 + 0.6\lambda_z n_z \leq 1 + 0.6n_z \quad (119)$$

For class 4 sections the section properties $N_{pl,Rd}$ and $M_{el,y,Rd}$, $M_{el,z,Rd}$ are replaced by the effective section properties.

It should be noted that, numerical simulations and tests confirmed that a pure elastic buckling behaviour does not exist and a certain amount of plastic capacity is always expected. For this reason the reduction factor 0.8 was applied to the strong-axis bending moment for buckling about the weak axis (see Equation (117)). This factor reduces the effect of the bending moment M_y , which has been found by some research weak in plastic sections.

2.3.5. Extension of the Ayrton-Perry formulations to combined loading situations

Agreeing that the failure criteria are based on the attainment of the yield limit f_y , the stability of a member subjected to an axial compression N_{Ed} and biaxial bending moment about the strong axis plane is written:

$$\frac{N_{Ed}}{A} + \frac{1}{1 - N_{Ed} / N_{cr,y}} N_{Ed} \left(\frac{e_{0,d} + e_y}{W_{el,y}} \right) + \frac{1}{1 - N_{Ed} / N_{cr,z}} N_{Ed} \left(\frac{e_z}{W_{el,z}} \right) = f_y \quad (120)$$

where e_y and e_z are the axial compression load eccentricities. For the case of member subjected to different values of eccentricities at both ends (e_1 and e_2 with $e_2 > e_1$), the equivalent eccentricity is used according to Austin formula [41] for both principal planes:

$$e_{eq} = 0.6e_2 + 0.4e_1 \geq 0.4e_2 \quad (121)$$

In a non-dimensional form, Equation (120) can be written as follows:

$$(1 - \chi)(1 - \chi\lambda_y^2)(1 - \chi\lambda_z^2) = \eta_{yy}\chi(1 - \chi\lambda_z^2) + \eta_{zy}\chi(1 - \chi\lambda_y^2) \quad (122)$$

with:

$$\eta_{yy} = \alpha(\lambda_y - 0.2)\left(\frac{235}{f_y}\right)^{0.8} + e_y \frac{A}{W_{el,y}} \quad (123)$$

$$\eta_{zy} = e_z \frac{A}{W_{el,z}} \quad (124)$$

The reduction factor χ and the reduced slenderness λ_y and λ_z are calculated using the following equations:

$$\chi = \frac{N_{Ed}}{Af_y} \quad (125)$$

$$\lambda_y = \sqrt{\frac{Af_y}{N_{cr,y}}} = \frac{l_y}{\pi i_y \sqrt{E/f_y}} \quad (126)$$

$$\lambda_z = \sqrt{\frac{Af_y}{N_{cr,z}}} = \frac{l_z}{\pi i_z \sqrt{E/f_y}} \quad (127)$$

where i_y , i_z , l_y , l_z being the radius of gyration and the buckling length about both principle planes.

The stability of a member subjected to an axial compression N_{Ed} and biaxial bending moment about the minor axis plane is expressed as follows:

$$\frac{N_{Ed}}{A} + \frac{1}{1 - N_{Ed}/N_{cr,y}} N_{Ed} \left(\frac{e_y}{W_{el,y}}\right) + \frac{1}{1 - N_{Ed}/N_{cr,z}} N_{Ed} \left(\frac{e_{0,d} + e_z}{W_{el,z}}\right) = f_y \quad (128)$$

In a non-dimensional form, Equation (128) can be written as follows:

$$(1 - \chi)(1 - \chi\lambda_y^2)(1 - \chi\lambda_z^2) = \eta_{zz}\chi(1 - \chi\lambda_y^2) + \eta_{yz}\chi(1 - \chi\lambda_z^2) \quad (129)$$

with:

$$\eta_{zz} = \alpha(\lambda_z - 0.2)\left(\frac{235}{f_y}\right)^{0.8} + e_z \frac{A}{W_{el,z}} \quad (130)$$

$$\eta_{yz} = e_y \frac{A}{W_{el,y}} \quad (131)$$

The solution for Equations (122) and (129) is given by Cardan [42] and can be written as:

$$\chi = \frac{1}{a} \left[b + 2\sqrt{b^2 - ac} \cdot \cos \left(\frac{1}{3} \arccos \frac{a^2 + 2b^3 - 3abc}{2(b^2 - ac)^{3/2}} + 120 \right) \right] \leq 1 \quad (132)$$

When the member buckle about the major-axis plane the coefficients a , b and c are expressed:

$$a = \lambda_y^2 \lambda_z^2 \quad (133)$$

$$b = \frac{1}{3} (\lambda_y^2 + \lambda_z^2 + \lambda_y^2 \lambda_z^2 + \eta_{zy} \lambda_y^2 + \eta_{yy} \lambda_z^2) \quad (134)$$

$$c = \frac{1}{3} (1 + \lambda_y^2 + \lambda_z^2 + \eta_{zy} + \eta_{yy}) \quad (135)$$

When the member buckle about the minor-axis plane the coefficients a , b and c are expressed:

$$a = \lambda_y^2 \lambda_z^2 \quad (136)$$

$$b = \frac{1}{3} (\lambda_y^2 + \lambda_z^2 + \lambda_y^2 \lambda_z^2 + \eta_{yz} \lambda_z^2 + \eta_{zz} \lambda_y^2) \quad (137)$$

$$c = \frac{1}{3} (1 + \lambda_y^2 + \lambda_z^2 + \eta_{yz} + \eta_{zz}) \quad (138)$$

For the particular case of hollow structures made of thin-walled steel elements, the interaction between local and global instabilities may be taken into account by the mathematical Ayrton-Perry expression, by replacing the compression yield load N_{pl} by the failure load N_v of a thin-walled stub column.

For the case of thin-walled members buckling about the strong axis plane, Equation (122) can be written as follows:

$$(1 - \chi')(1 - \chi' \lambda_y'^2)(1 - \chi' \lambda_z'^2) = \eta'_{yy} \chi'(1 - \chi' \lambda_z'^2) + \eta'_{zy} \chi'(1 - \chi' \lambda_y'^2) \quad (139)$$

The reduction factor χ' and the reduced slenderness λ_y' and λ_z' are calculated using the following equations:

$$\chi' = \frac{N_{Ed}}{N_v} = \frac{N_{Ed}}{Af_v} \quad (140)$$

$$\lambda_y' = \sqrt{\frac{Af_v}{N_{cr,y}}} = \frac{l_y}{\pi i_y \sqrt{E/f_v}} \quad (141)$$

$$\lambda_z' = \sqrt{\frac{Af_v}{N_{cr,z}}} = \frac{l_z}{\pi i_z \sqrt{E/f_v}} \quad (142)$$

The factors accounting for generalized imperfections can be expressed as follows:

$$\eta'_{yy} = \alpha(\lambda_y' - 0.2) \left(\frac{235}{f_y}\right)^{0.8} + e_y \frac{A}{W'_{el,y}} \frac{f_v}{f_y} \quad (143)$$

$$\eta'_{zy} = e_z \frac{A}{W'_{el,z}} \frac{f_v}{f_y} \quad (144)$$

Equation (129) can be written as follows for the case of thin-walled members buckling about the weak axis plane:

$$(1 - \chi')(1 - \chi' \lambda_y'^2)(1 - \chi' \lambda_z'^2) = \eta'_{zz} \chi'(1 - \chi' \lambda_y'^2) + \eta'_{yz} \chi'(1 - \chi' \lambda_z'^2) \quad (145)$$

with:

$$\eta'_{zz} = \alpha(\lambda_z' - 0.2) \left(\frac{235}{f_y}\right)^{0.8} + e_z \frac{A}{W'_{el,z}} \frac{f_v}{f_y} \quad (146)$$

$$\eta'_{yz} = e_y \frac{A}{W'_{el,y}} \frac{f_v}{f_y} \quad (147)$$

$W'_{el,y}$ and $W'_{el,z}$ are the reduced section modulus about strong and weak axes respectively and are determined according to [29] as follows:

$$W'_{el,y} = W_{el,y} \frac{h_m (2 - \frac{h_m + \chi_{v,b} \cdot b_m}{h_m + b_m}) + 3\chi_{v,b} \cdot b_m}{h_m + 3b_m} \quad (148)$$

$$W'_{el,z} = W_{el,z} \frac{b_m (2 - \frac{b_m + \chi_{v,h} \cdot h_m}{h_m + b_m}) + 3\chi_{v,h} \cdot h_m}{b_m + 3h_m} \quad (149)$$

The solution for Equations (139) and (145) is given by Cardan's expression detailed previously in Equation (132).

2.4. Shortcoming of actual codes

Actual codes and methods still suffer from a series of problems and inadequacies. Some shortcomings can be cited in the following:

- the CECM proposed five buckling curves for pure compression load case, depending on the cross-section geometry, the manufacturing process, the plane of buckling considered... These buckling curves do not take into account combined load combinations;
- present design rules provide class-dependent interaction factors: according to the class of the section, different sets of formulae are to be used for the design checks of both sections and members, i.e. plastic or elastic equations;
- the determination of the effective section for class 4 cross-sections, require tedious long calculations with iterations;
- It has been shown [3] that the cross-section classification presents a lot of inconsistencies such as the gap of resistance at the class 2-3 borders, the assumed ideal support conditions of the section's plates...;
- the sets of formulae proposed by both methods (Method 1 and Method 2) appear to be long and complicated;
- the calibrated coefficients for both methods have been derived based on numerical and experimental tests on open sections (I and H cross-sections) and only a limited amount of experimental and numerical data on tubular members was available;

- in a same element, a section can have different classes depending on the load case combination.

All the shortcomings listed in this section emphasize the necessity of alternative design approach. The O.I.C. has been shown to be a fully appropriate alternative to the current well-known design rules to account for the interaction between resistance and instability effects, although being based on simple principles with straightforward application steps. The definition of the generalized relative slenderness brings simplicity to the method since all sections are treated in a unique procedure (open, hollow...); it also allows combined loading conditions to be treated as easily as simple ones and therefore avoiding resorting to complex interaction formulae, no cross-section classification steps or section effective properties determination are needed and “slender” sections are designed in the same way as others. In addition, the O.I.C. allows the use of a unique concept to characterize the resistance of sections as well as the resistance of members.

2.5. Conclusion

In this chapter a comprehensive survey concerning the field of the beam-column resistance was conducted. A detailed history of the buckling handling and development was made, along with an actual description of the methods used in nowadays standards to get the resistance of columns subjected to simple (pure compression) or combined loading (compression with bending moment). Then, the shortcomings of actual codes were listed and detailed. All of these sections and sub-sections would be of a great importance for the derivation of the O.I.C. design curves, since an adequate method has been selected, after getting a strong basis and overview on the global buckling.

In summary, this state of the art would serve the author through the following listed aspects:

- a deep understanding of global buckling background is of a prime importance since it is one of the aspects which should be treated in this work. In this chapter, special attention was paid to earlier research on the buckling of steel beam-column members and to the theoretical studies undertaken since 1956 by the European convention on metallic structures (CECM) on the determination of the buckling curves;
- a brief review of the analytical ways of formulating the design curves is presented along with the adopted mathematical Ayrton-Perry formulations that were found to

describe the best the buckling behaviour of beam-column members and thus will be developed and derived using numerical results in next chapters;

- the actual methods of treating and getting the ultimate buckling loads of hollow members covering all section classes, and tested under simple and combined loadings were presented in this chapter, since this is the main target of this work;
- a better understanding of the need to remove the actual codes and methods was presented through listing their various shortcomings. It was clearly seen that these codes still suffer from series of problems and inadequacies.

3. Experimental investigations

3.1. Introduction

A series of 12 buckling tests have been performed on rectangular and circular hollow section beam-columns of nominal steel grade S355. The columns were fabricated by either the hot-rolling or the cold-forming process, and were loaded under combined compression and bending by varying axial compression load eccentricities e_y and e_z . Two column lengths were chosen so as inelastic buckling to be governing (4000 mm and 4900 mm).

Preliminary measurements of cross-section geometry, material properties, geometrical imperfections, residual stresses as well as stub column tests are reported in detail within present chapter. The (imperfect) initial geometry of each buckling specimen was measured along the whole column by means of two different procedures. The first method relied on the use of a set of equally spaced **L**inear **V**ariable **D**isplacement **T**ransducers (**LVDTs**) displaced on each specimen's plates; the second method consisted in scanning the specimen's plates by means of a laser Tracker *AT401*. Residual stresses were also examined experimentally: the sectioning technique was used to get the deformations of the released material; these results have been compared to measurements taken with electrical strain gauges.

Further to the results of the tests themselves, the main goal was here to collect sufficient information for the validation of F.E. numerical tools, in order to launch extensive numerical parametric studies on hot-rolled and cold-formed sections, including a wide scope of parameters (such as cross-section shape, steel grade, load case...). Additional similar test data from European project “Semi-Comp” [4] have been added to the present results, where a test program was established to determine the influence of semi-compact class 3 sections on member buckling behaviour. The experimental results were compared to the results of the F.E. computations and the validity of the proposed model was ensured.

Following section 3.2 first describes the experimental test program (selection of the test specimens, element lengths, adequate load cases...). Section 3.3 then describes the preliminary measurements performed prior to testing and section 3.4 describes the series of the 12 buckling tests. Section 3.5 then reports on the development and validation of finite elements models (by

both the present test series and the one from the literature) and provides detailed information on the boundary conditions and loading procedure, the modeling of the measured material laws, residual stresses and geometrical dimensions. Finally, the results of the FE vs. experimental validation procedure are provided. Eventually, summary and conclusions are addressed in section 3.6.

3.2. Test program

Twelve 6000 mm beams involving 4 different cross-section shapes of nominal steel grade S355 were delivered at the Structural Engineering Laboratory of the University Of Applied Sciences Of Western Switzerland – Fribourg: two hot-rolled **C**ircular **H**ollow **S**ection shapes (**CHS** 159x5 and **CHS** 159x6.3) as well as two cold-formed **R**ectangular **H**ollow **S**ection shapes (**RHS** 200x100x4 and **RHS** 220x120x6). Table 12 summarizes the delivered cross-section shapes and lengths, their fabrication process and their cross-section classification in pure compression according to Eurocode 3. It should be noted that Voestalpine supplied the necessary rectangular section and V&M supplied the circular ones.

Hollow sections were chosen so as to cover stocky to slender section ranges, fabricated through either the hot-rolling or the cold-forming process. In order to investigate the cross-section shape on the beam-column resistance, different values of the B/t and D/t ratios¹ were considered for each section type. For example, two cross-section rectangular sizes were chosen: RHS 220x120x6 and RHS 200x100x4. RHS 200x100x4 corresponds to a class 4 (slender) section and was selected in an attempt to examine the application of the O.I.C. approach to slender sections, where both local (i.e. cross-section instability) and global (i.e. member instability) buckling modes are likely to occur and interact (so-called coupled instabilities).

Class 1 CHS, with different ratios of D/t were chosen (CHS 159x5 and CHS 159x6.3) to only witness global buckling modes. In total, three specimens were selected for each cross-section shape and size so as to investigate the influence of different loading situations on the same section.

¹ B/t represents the width-to-thickness ratio of a rectangular section and D/t represents the diameter-to-thickness ratio of a circular one.

Table 12 – Delivered sections properties

Specimen #	Cross-section shape	Length [mm]	Total number of specimens	Fabrication process	Cross-section classification in compression
1	RHS S355 200x100x4	6000	3	CF	4
2	RHS S355 220x120x6	6000	3	CF	3
3	CHS S355 159x5	6000	3	HR	1
4	CHS S355 159x6.3	6000	3	HR	1

Two column lengths ($L = 4000 \text{ mm}$ and $L = 4900 \text{ mm}$) were considered for the main beam-column tests; a portion (of approximately $L = 1000 \text{ mm}$) was kept for the preliminary measurements of residual stresses, stub column and tensile tests. Figure 15 represents the typical cutting plan of a 4900 mm member.

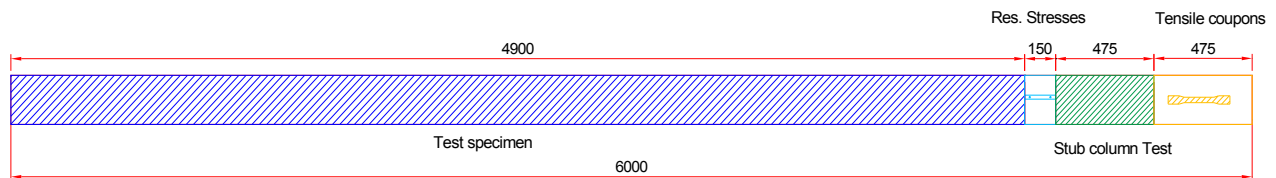

 Figure 15 – Cutting plan and use of a 4900 mm , CHS 159x5 column

Figure 16 illustrates the specimens cutting's procedure.



Figure 16 – Cutting procedure

In total, twelve beam-column tests were carried out with different member slenderness. Different load cases were considered through the application of eccentric compression: mono-axial (M_y) or bi-axial bending ($M_y + M_z$) combined with axial compression (N); different values of M/N ratios were adopted as well.

3.2.1. Selection of test specimens

In order to (i) examine the influence of the load case introduction on the member resistance and to (ii) select adequate load cases and element lengths for the twelve tested specimens, different load cases were considered, based on different combinations described as follows:

- 5 different member lengths: $L = 3500 \text{ mm}$, $L = 4000 \text{ mm}$, $L = 4500 \text{ mm}$, $L = 4700 \text{ mm}$ and $L = 4900 \text{ mm}$;
- different loading situations with different configurations as described in Table 13:
 - o pure compression N ;
 - o compression with major-axis bending $N+M_y$;
 - o compression with biaxial bending $N+M_y+M_z$.

A distinction has been made between the different loading situations, namely with respect to the bending moment distribution. Two coefficients² $\psi = 1$ and $\psi = 0$ were adopted to consider constant and triangular bending moment distributions, respectively.

Table 13 – Proportion of adopted loadings

n [-]	m_y [-]	m_z [-]	N [%]	M_y [%]	M_z [%]
0.80	0.20	–	80	20	–
0.70	0.30	–	70	30	–
0.60	0.40	–	60	40	–
0.50	0.50	–	50	50	–
0.40	0.60	–	40	60	–
0.20	0.80	–	20	80	–
0.80	–	0.20	80	–	20
0.60	–	0.40	60	–	40
0.50	–	0.50	50	–	50
0.40	–	0.60	40	–	60
0.20	–	0.80	20	–	80

² ψ_y and ψ_z indicate the ratios between end moments about y - y and z - z axes respectively.

0.60	0.20	0.20	60	20	20
0.50	0.25	0.25	50	25	25
0.40	0.30	0.30	40	30	30
0.33	0.33	0.33	33	33	33
0.20	0.40	0.40	20	40	40

Table 13 represents the proportion of adopted loading, where n represents the relative axial force ratio defined according to EN 1993-1-1 as $n = N / N_{b,Rd}$ where:

$$N_{b,Rd} = \chi A f_y / \gamma_{M1} \text{ for class 1, 2 and 3 cross-sections;}$$

$$N_{b,Rd} = \chi A_{eff} f_y / \gamma_{M1} \text{ for class 4 cross-sections;}$$

$N_{b,Rd}$, represents the buckling resistance of the member; A and A_{eff} represent respectively the actual and effective cross-sectional areas; χ and γ_{M1} represent respectively the reduction factor and partial factors for resistance of members to instability ($\gamma_{M1} = 1.0$ for this study);

Different values of the relative axial force ratio n were adopted ranging from 0.2 (i.e. the load case becoming thus a compression of 20% $N_{b,Rd}$ with monoaxial or biaxial bending), to 0.8 (i.e. the load case becoming thus a compression of 80% $N_{b,Rd}$ with monoaxial or biaxial bending).

m_y and m_z represent the relative bending moment ratios about y - y and z - z axis and were defined as $m_y = K.M_y / M_{y,Rk}$ and $m_z = K.M_z / M_{z,Rk}$ according to EN 1993-1-1 method 2 for members, where:

K represents the interaction factor;

$$M_{Rk} = M_{pl} / \gamma_{M1} \text{ for class 1 and 2 cross-sections;}$$

$$M_{Rk} = M_{el} / \gamma_{M1} \text{ for class 3 cross-sections;}$$

$$M_{Rk} = M_{eff} / \gamma_{M1} \text{ for class 4 cross-sections;}$$

Depending on the cross-section shape and on the end plate dimensions, the eccentricities were sometimes limited to a maximum value as illustrated in Figure 17, for practical convenience.

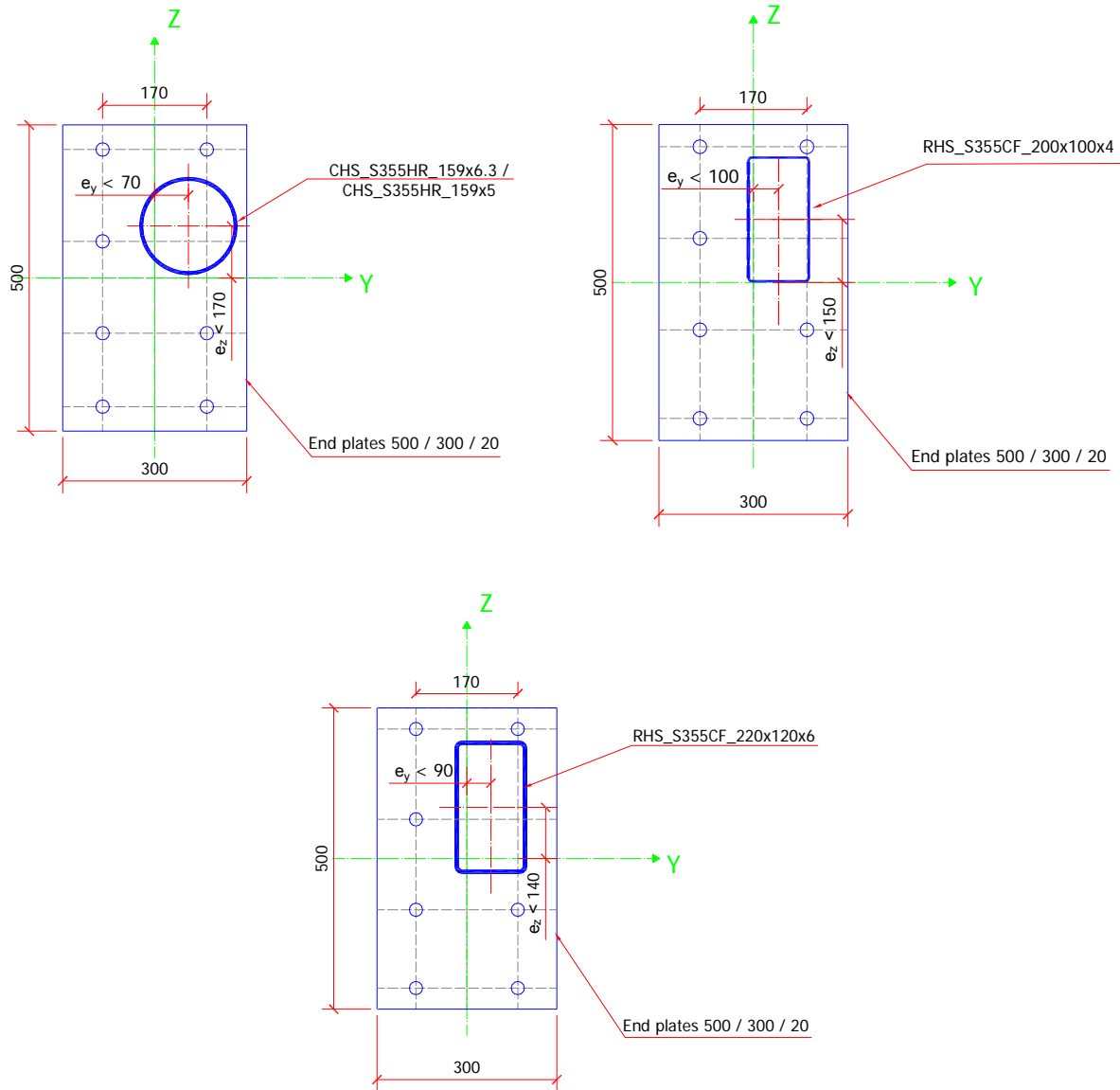


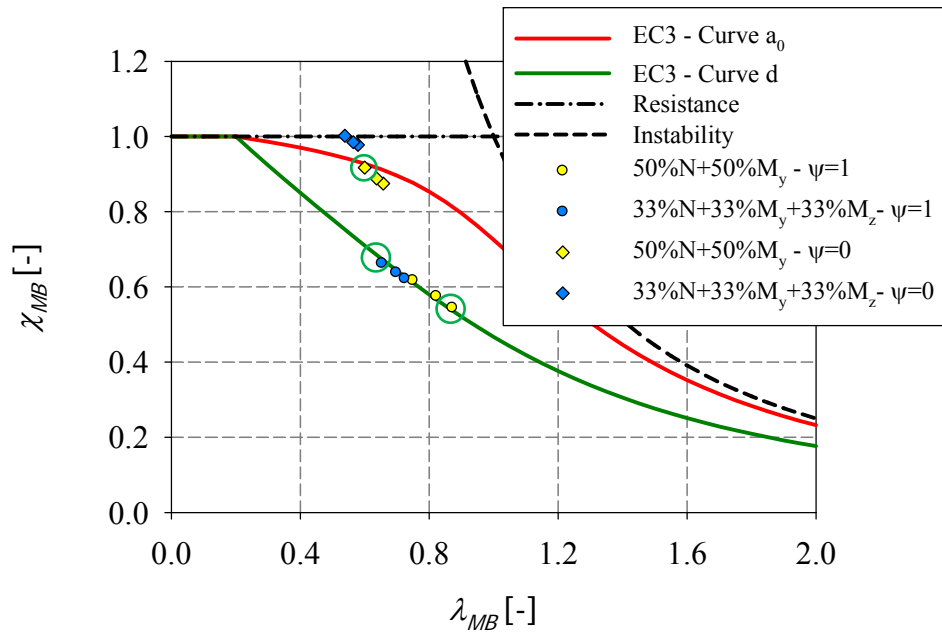
Figure 17 – Eccentricities limitations depending on the cross-section shape and end plates dimensions – a) CHS 159x5 / CHS 159x6.3 – b) RHS 200x100x4 – c) RHS 220x120x6

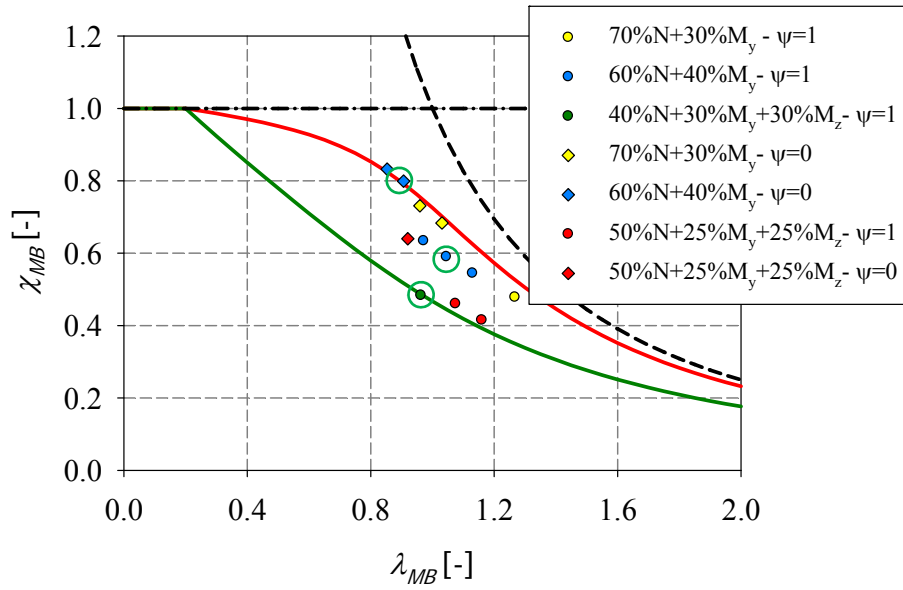
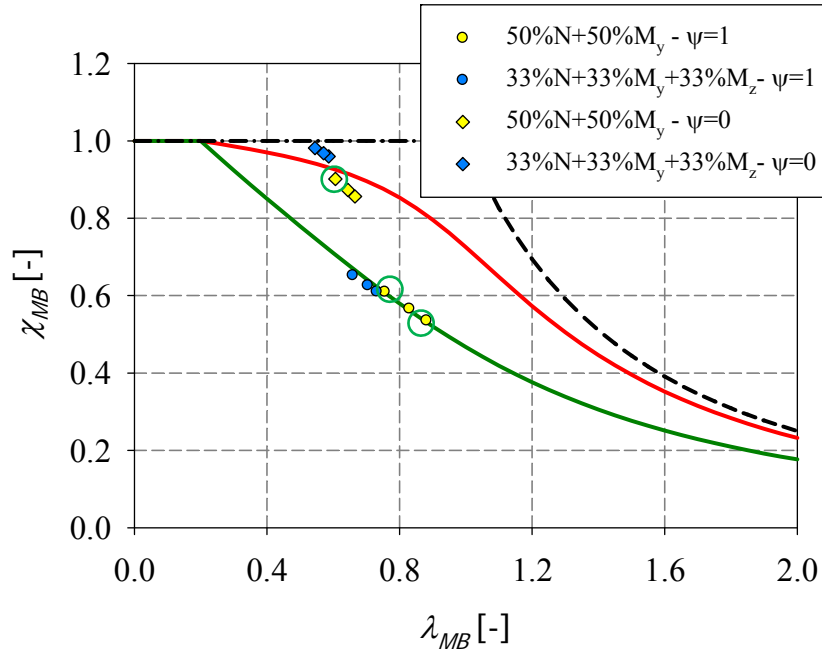
In total, 45 combinations of loading, cross-section shapes and elements lengths, were considered and can be found in Annex 3; the ultimate resistances R_{FE} of the considered members were determined numerically by mean of suitable shell elements so that F.E. results would involve the interaction between cross-section and member resistance, in order to be able to characterize the interaction between local and global instabilities. The obtained F.E. results were used as a basis to generate the initial loading that was increased proportionally to obtain the corresponding critical load multipliers $R_{STAB,CS}$ and $R_{STAB,MB}$, and the plastic load multiplier R_{RESIST} which was

computed using a dedicated Matlab tool developed to calculate the exact plastic load ratio of the section. $R_{STAB,CS}$ is computed using FINELg shell models for cross-sections in order to characterize local buckling modes and $R_{STAB,MB}$ is computed using Abaqus beam models so as to witness global buckling modes only; hence, if using shell elements, local buckling phenomenon may be visible and may potentially affect the value of the critical load for a member. All obtained results were plotted in an O.I.C. format (see Figure 18), where the horizontal axis represents the generalized slenderness λ_{MB} while the vertical axis reports the reduction factor χ_{MB} defined in Equation (150) and Equation (151), respectively.

$$\lambda_{MB} = \sqrt{\frac{R_{RESIST}}{R_{STAB,MB}}} \quad (150)$$

$$\chi_{MB} = \frac{R_{FE}}{R_{RESIST}} \quad (151)$$





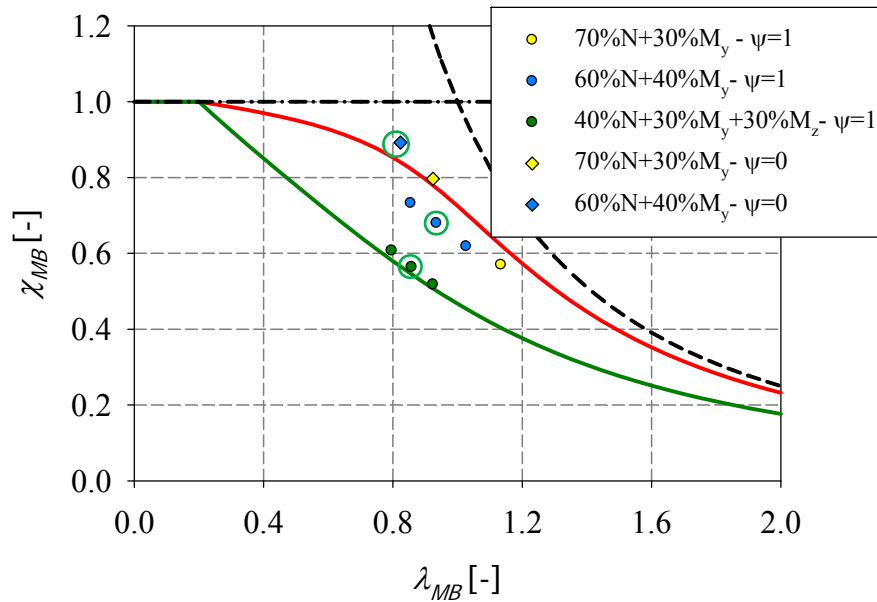


Figure 18 – Numerical member results tested under combined loadings for – a) CHS 159x6.3 – b) CHS 159x5 – c) RHS 200x100x4 – d) RHS 220x120x6

Figure 18 provides the following informations:

- as expected, no matter what the load cases are, member subjected to a triangular bending moment distribution ($\psi = 0$) exhibit a higher resistance than member subjected to a constant moment distribution ($\psi = 1$);
- members subjected to combined loading $N+M_y$ reach higher resistances than those with loading combinations of $N+M_y+M_z$. This is due to the fact that weak axis bending penalises flexural buckling instability of a beam-column member;
- members subjected to a high level of compression have a higher generalized relative slenderness λ_{MB} . This is mainly due to the fact that for a high level of compression, global buckling becomes predominant, leading to higher values of λ_{MB} . Overall buckling then occurs before cross-section full yielding, resulting in the failure of the element due to instability and not because of a lack of cross-sectional resistance. However, for a lower level of compression, lower values of λ_{MB} are reported. In such cases, bending is

predominant. The hollow sections exhibit little influence of instability due to their high resistance against lateral torsional buckling, and exhibit little influence of global instability due to the low level of compression, thus leading to lower λ_{MB} values;

- members subjected to a constant bending moment have higher values of generalized relative slenderness λ_{MB} than similar members subjected to a triangular bending moment distribution. This is due to the fact that the relative axial force ratio n has a bigger influence on the member resistance if it is loaded under compression with constant bending moment than under compression with triangular bending moment. In the latest case, a part of the section is less loaded in bending and provides a level of restraint to the entire member, thus the influence of the bending moment is reduced along the member length. Accordingly, the deflection induced by the bending moment, is bigger when a constant moment is applied (all the member fibers are subjected to the bending moment) and thus leads to a higher second order effect and to a premature column buckling;
- the rather large vertical dispersion noticed (i.e. results are distributed from above Eurocode 3 curve a_0 to below curve d) is associated to the bending moment distribution and to the combined load cases adopted. As mentioned previously, member subjected to a triangular bending distribution ($\psi = 0$) exhibit a higher resistance than member subjected to a constant moment distribution ($\psi = 1$), and members subjected to combined loading $N+M_y$, behave better than those with loading combinations of $N+M_y+M_z$;
- rectangular hollow sections with lower values of B/t ratios (i.e. RHS 220x120x6) exhibit a better behaviour than slender ones (i.e. RHS 200x100x4), when tested under the same combined load case. The same tendencies are observed for circular hollow sections, where stocky ones with lower values of D/t ratios (i.e. CHS 159x6.3) reach better relative resistance compared to slender ones (i.e. CHS 159x5).

One the influence of the load case, the bending moment distribution, the cross-section shape, the member slenderness... were examined, the twelve buckling tests were chosen as described in the following section.

3.2.2. Adopted parameters

Eventually, twelve load combinations have been chosen and are represented by the green circles on the O.I.C. curves of Figure 18. They allow to asses and choose:

- penalty factor χ_{MB} values well distributed along the vertical axis of the O.I.C. graph ($0.5 \leq \chi_{MB} \leq 1$);
- slenderness factor λ_{MB} values suitably distributed along the horizontal axis of the O.I.C. graph.

The chosen buckling tests also allow to overcome the following experimental limitations:

- axial shortening obtained numerically less than 150 mm since it is the maximum displacement of the hydraulic jack;
- eccentricities limitations depending on the end plate dimensions and cross-section shape (see Figure 17).

Table 14 summarizes the type and shape of the sections, the load cases and the lengths of the corresponding chosen specimens. The test specimens have been labeled so that the section type (RHS or CHS), the fabrication process³ (CF or HR) and the cross-section geometry can be identified from the label. A subsequent letter (T) is used, followed by an identification number ranging from 1 to 12, denoting the test number.

Table 14 – Test program for buckling tests

Cross-section shape	Fabrication process	Load case	Bending moment distribution	Length [mm]
RHS CF 200x100x4 T1	Cold-formed	60%N+40%M _y	Constant	4000
RHS CF 200x100x4 T2	Cold-formed	40%N+30%M _y +30%M _z	Constant	4000
RHS CF 200x100x4 T3	Cold-formed	60%N+40%M _y	Triangular	4000
RHS CF 220x120x6 T4	Cold-formed	60%N+40%M _y	Constant	4000
RHS CF 220x120x6 T5	Cold-formed	40%N+30%M _y +30%M _z	Constant	4000

³ CF: cold-formed, HR: Hot-rolled.

RHS CF 220x120x6 T6	Cold-formed	$60\%N+40\%M_y$	Triangular	4000
CHS HR 159x5 T7	Hot-rolled	$50\%N+50\%M_y$	Constant	4000
CHS HR 159x5 T8	Hot-rolled	$50\%N+50\%M_y$	Constant	4900
CHS HR 159x5 T9	Hot-rolled	$50\%N+50\%M_y$	Triangular	4000
CHS HR 159x6.3 T10	Hot-rolled	$50\%N+50\%M_y$	Constant	4900
CHS HR 159x6.3 T11	Hot-rolled	$33\%N+33\%M_y+33\%M_z$	Constant	4000
CHS HR 159x6.3 T12	Hot-rolled	$50\%N+50\%M_y$	Triangular	4000

Preliminary measurements were performed before each buckling test and consisted in:

- cross-section dimensions measurements using a digital caliper;
- material testing through classical tensile tests extracted from the flat faces and from the corners of the corresponding specimens;
- geometrical imperfections measurements by means of two different procedures. The first method consisted in a set of equally spaced linear variable displacement transducers (LVDTs), fixed on an aluminum bar that was displaced laterally on each specimen's plates. The second method consisted in scanning the specimen's plates by means of a laser Tracker *AT401*;
- residual stresses determination through the sectioning method to measure the deformations experienced by the released material. Measurements taken with electrical strain gauges were compared to the ones obtained by the mechanical procedure;
- stub column tests for the determination of cross-sectional load carrying capacities under pure compression.

A numerical model was developed so as to represent accurately the experimental behaviour of the tested columns. Every measured data was incorporated in the F.E. models used to get predictions before each test. The preliminary measurements mentioned are detailed hereafter.

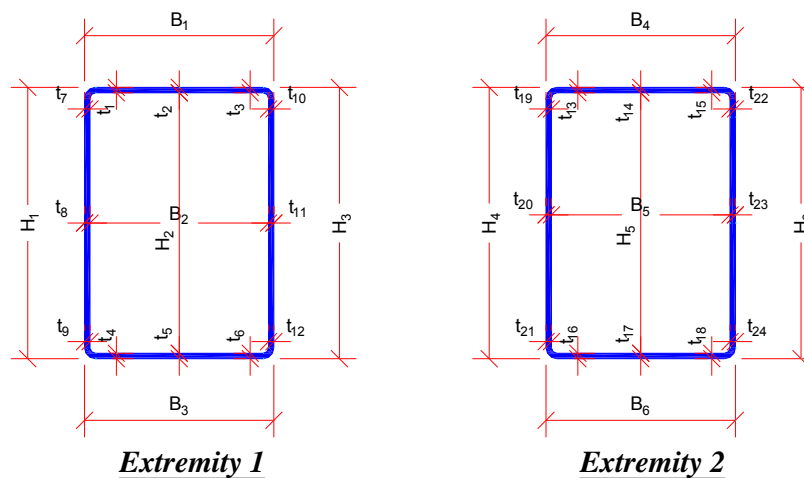
3.3. Preliminary measurements

3.3.1. Cross-sectional dimensions

The actual cross-section dimensions (i.e. such as the depth H , the width B and the thickness t for the rectangular specimens, whereas the diameter D and the thickness t for the circular sections) were measured using a digital caliper with an accuracy of 0.01 mm , as illustrated in Figure 19. These measurements were performed several times and at both sides of the specimens' ends before welding the end plates. The definitions of the measured parameters are illustrated in Figure 20 for both rectangular and circular sections.



Figure 19 – Measurement of cross-section dimensions of circular and rectangular sections



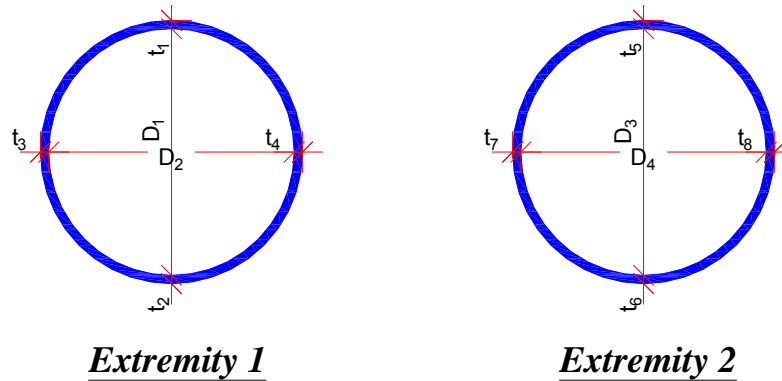


Figure 20 – Measured dimensions for various cross-sections

Figure 21 and Figure 22 represent the measured dimensions of the rectangular section RHS CF 200x100x4 T1 and of the circular section CHS HR 159x6.3 T12; comparison with corresponding tolerances according to EN 10210-2 [43] for hot-formed sections and EN 10219-2 [44] for cold-formed sections are also reported.

The following conclusions can be drawn from the figures:

- all measured dimensions oscillate very closely around the characteristic line with a minor deviation;
- some of the measured dimensions even resulted in values constantly exceeding the characteristic values;
- there are no out-of tolerance results.

Detailed measurement for all tested sections can be found in Annex 6. It should be mentioned that the same trends are observed in all other measured sections.

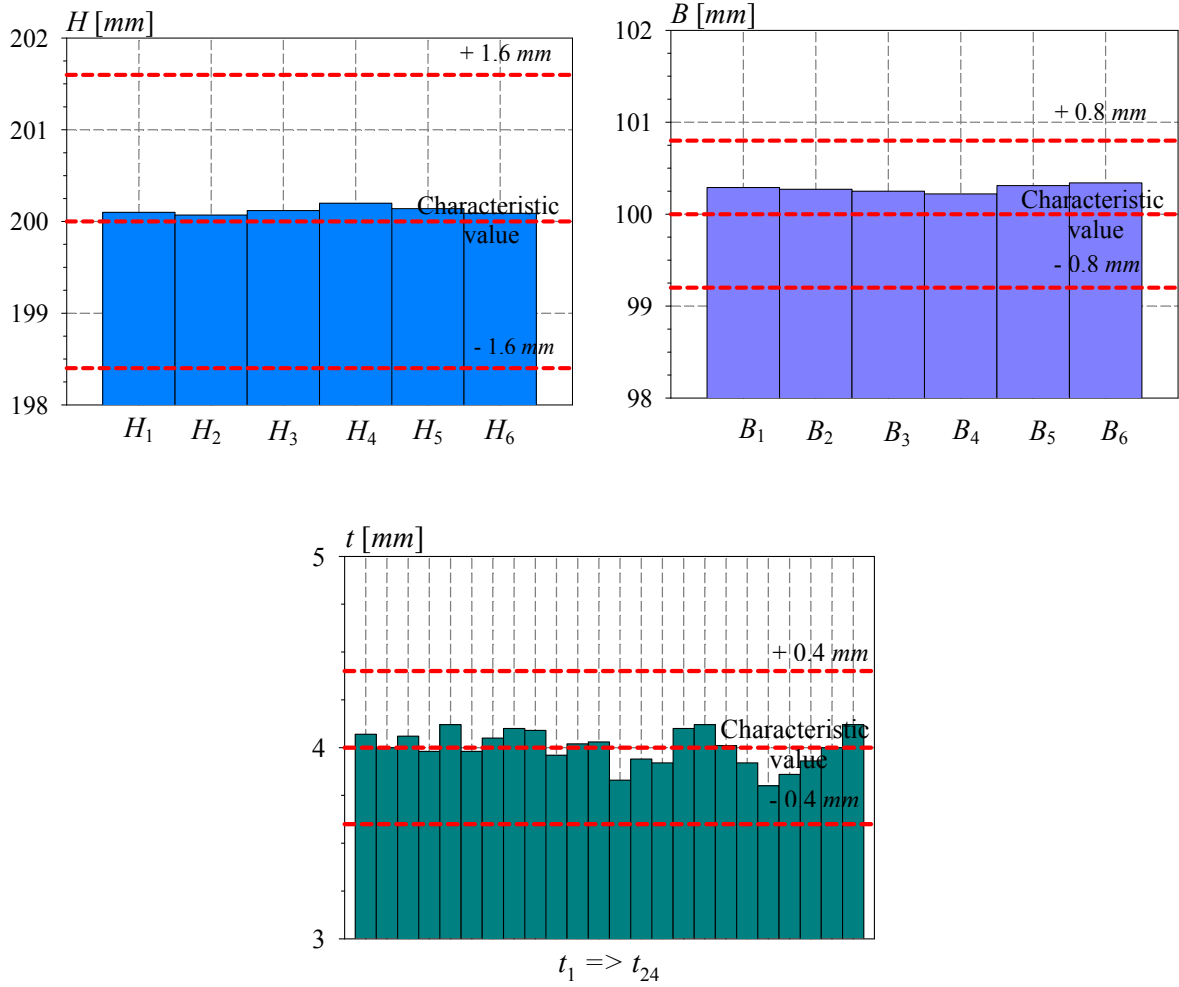


Figure 21 – Measured cross-sectional dimensions and tolerances – RHS CF 200x100x4 T1

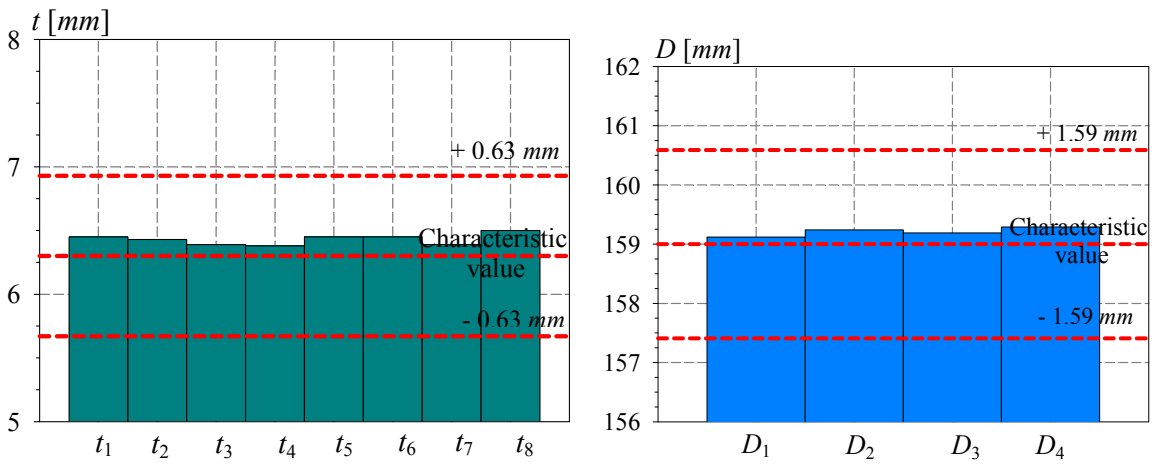


Figure 22 – Measured cross-sectional dimensions and tolerances – CHS HR 159x6.3 T12

3.3.2. Tensile tests

The material properties of all rectangular and circular hollow sections were characterized by means of classical tensile tests. Series of coupons were extracted from the middle of two opposite flat faces – not containing the weld – of the six cold-formed rectangular hollow sections, as well as from the two opposite corners, in an attempt to characterize the expected increase in strength stemming from cold-forming effects. Two tensile coupons were also extracted from each section of the six CHS (see Figure 23). The RHS flat coupons were 270 mm long with nominal gauge width of $10.t$, where t represents the thickness of the corresponding plate. The corner prismatic coupons as well as the CHS coupons were 150 mm long with coupon dimensions of 3 mm x 3 mm cut within the cross-section thickness in order to avoid creating eccentric loads while testing (see Figure 24 and Figure 25).



Figure 23 – Extraction of coupons from – a) CHS sections – b) RHS sections



Figure 24 – Tensile coupons extracted from – a) flat faces of cold-formed RHS sections – b) corners of cold-formed RHS sections – c) corners of hot-rolled CHS

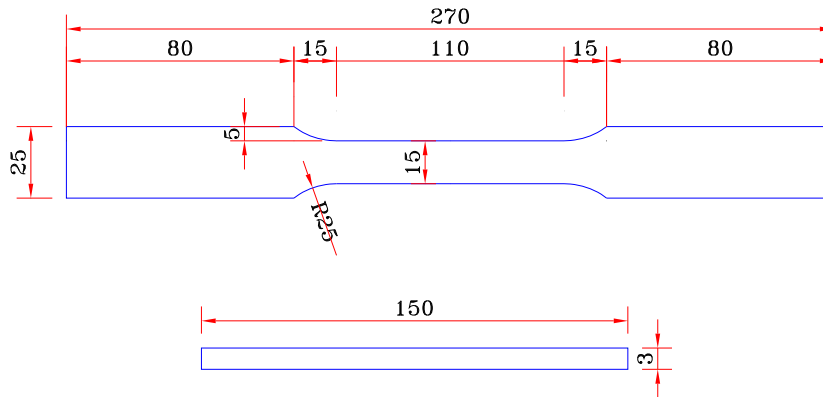


Figure 25 – Typical dimensions of tensile coupons (dimensions in *mm*)

A 100 *kN* testing machine with hydraulic grips was used to test the necked coupons. The corner and CHS coupons were tested in a smaller 10 *kN* testing machine due to their smaller size and cross-section. The coupons were placed in the testing rig and a calibrated extensometer of 20 *mm*

was mounted at the middle of each coupon. Tensile load was applied by a constant rate of strain (0.045 %/s) until fracture. In total, 36 coupon tests have been performed; some of the tested specimens are shown in Figure 27.

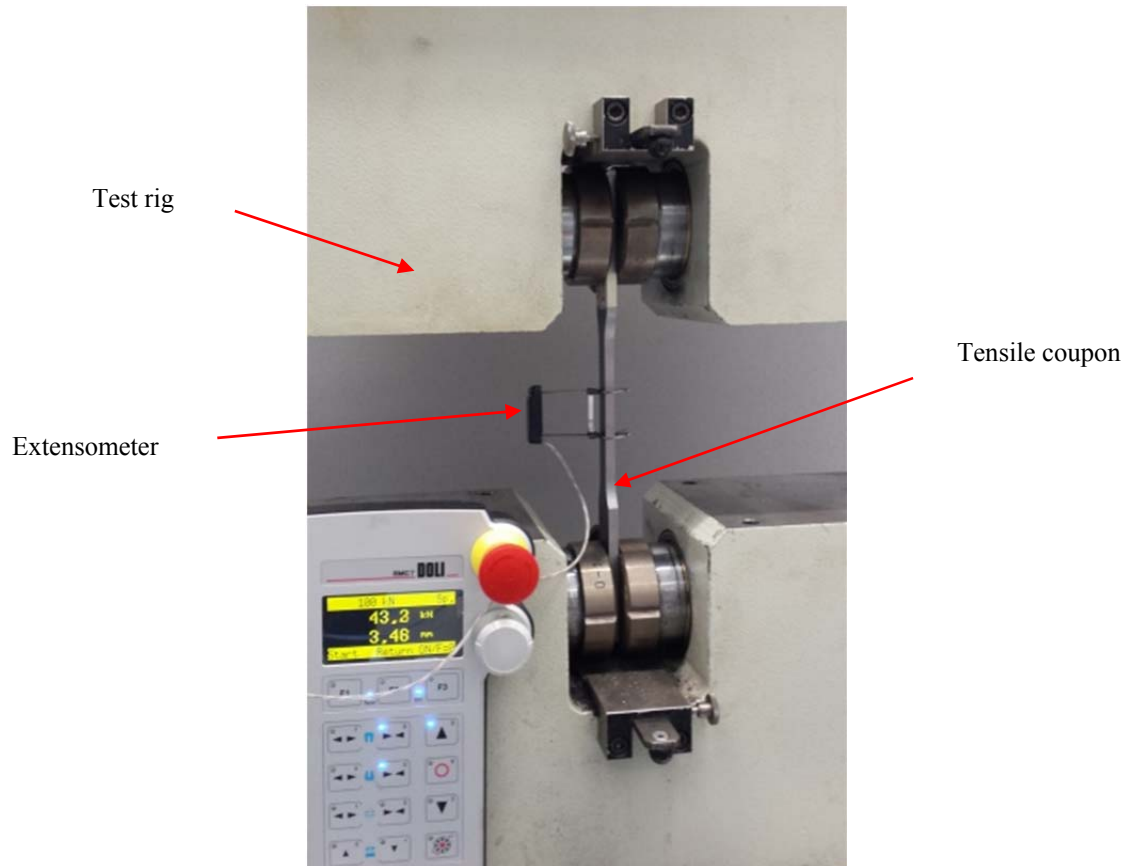


Figure 26 – Setup of tensile coupon tests





Figure 27 – Example of some tested coupons

The location of the coupons extracted from the RHS and CHS sections are illustrated in Figure 28. All stress-strain curves from the tested coupons were plotted, and Figure 29 proposes representative examples of stress-strain curves obtained for the hot-rolled section CHS 159x5 and the cold-formed section RHS 220x120x6. As expected, hot-rolled sections exhibit classic stress-strain behaviour, with distinct yield plateau and strain hardening effects. The finally-kept yield stress value f_y was taken as the average of the yield plateau stress for hot-rolled sections; 0.2 % proof stress was used as a convenient equivalent yield stress for cold-formed sections where the material response showed a pronounced non-linear behaviour. The Young's modulus E was taken as the gradient between 20% and 80% of f_y in the elastic part using a linear regression analysis.

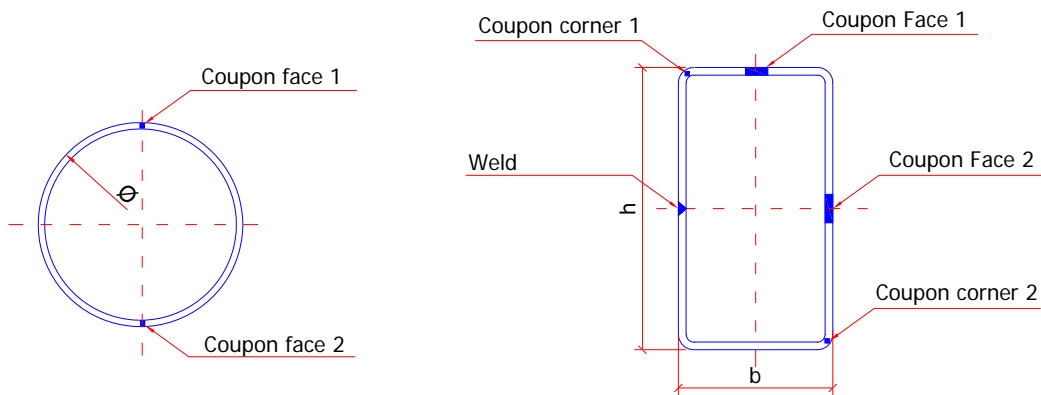


Figure 28 – Tensile coupons locations

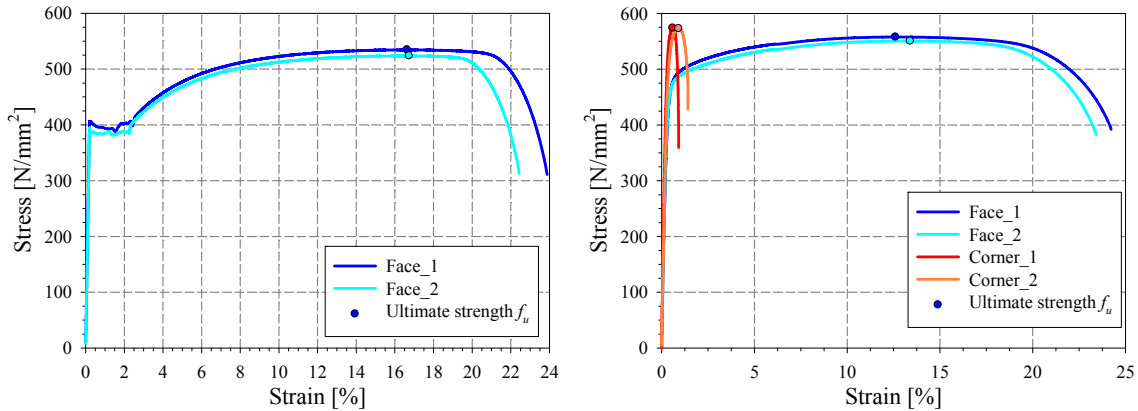


Figure 29 – Typical example of engineering stress-strain curves for – a) hot-rolled CHS 159x5 – b) cold-formed RHS 220x120x6

The Young's modulus E , the values of the yield, ultimate and fracture stresses (f_y^4 , f_u , f_t) along with the corresponding values of elongation (ε_y , ε_u and ε_t) were determined from the stress-strain curves, for each tested coupon. The average values of these parameters have been finally kept for each section and used in the finite element calculations. Resistance results are presented in Table 15 where E_m represents the mean value of the measured section Young's modulus while (f_{ym} , f_{um} , f_{tm}) represent the average values of yield, ultimate and fracture stresses along with the corresponding average values of elongation (ε_{ym} , ε_{um} and ε_{tm}), respectively. The following points can be noted:

- all the tested coupons extracted from the flat faces of the considered specimens fulfill the requirement specified by EN 1993-1-1:

$$\frac{f_u}{f_y} \geq 1.10 \quad (152)$$

- important increases in yield and ultimate strengths are observed in the corner regions of cold-formed sections, associated with a lower level of ductility at fracture. In some tests, the stresses were localized in the grips' zone and premature failure occurred in this region, leading to an overly reduced ductility (1% ultimate strain) as well as to a smaller ultimate strength. It should be mentioned that the uniform geometry of the prismatic

⁴ For hot-rolled profiles, the value of f_y was determined as the mean between the onset of yielding, which was the upper yield strength, and the onset of strain hardening for each coupon.

manufactured coupon reduces the ultimate strength of the considered corner coupons as well;

- for cold-formed sections, the average ultimate strengths in the corners is 8.3 % higher than the average ultimate strengths in the flat faces; however, the average yield strengths in the corners is 20.5 % higher than the average one in the corresponding flat faces;
- the low values of the Young's modulus coefficients are due to the laboratory measuring inconsistencies, thus $E = 210000 \text{ N/mm}^2$ was adopted for the numerical validation. Tabulated data, measured stress-strain curves and details can be found in Annex 6.

Table 15 – Measured material properties

Coupon	Cut from section	Position	E [GPa]	f_y [N/mm ²]	ε_y [%]	f_u [N/mm ²]	ε_u [%]	f_t [N/mm ²]	ε_t [%]	f_u/f_y [-]	E_m [N/mm ²]	f_{ym} [N/mm ²]	ε_{ym} [%]	f_{um} [N/mm ²]	ε_{um} [%]	f_{tm} [N/mm ²]	ε_{tm} [%]	$(f_u/f_y)_m$ [-]
T1-1	RHS 200x100x4	Face 1	236.3	475.0	0.20	594.2	16.78	442.6	28.25	1.25	233135	475	0.203	583	15.7	434	27.7	1.23
T1-2		Face 2	230.0	475.0	0.21	571.7	14.61	425.5	27.16	1.20								
T1-3		Corner 1	206.9	580	0.28	615.1	1.91	397.5	4.817	1.06								
T1-4		Corner 2	208.8	605	0.29	635.5	1.05	372.8	2.242	1.05								
T2-1	RHS 200x100x4	Face 1	172.0	440.0	0.46	574.8	13.50	423.7	23.14	1.31	193837	450	0.335	566	13.3	410	23.2	1.26
T2-2		Face 2	215.7	460.0	0.21	556.5	13.05	395.4	23.34	1.21								
T2-3		Corner 1	232.9	560	0.24	616.8	1.86	366.0	4.211	1.10								
T2-4		Corner 2	201.3	585	0.29	605.7	0.64	356.7	1.121	1.04								
T3-1	RHS 200x100x4	Face 1	190.5	483.3	0.25	601.1	11.50	437.4	19.43	1.24	206437	480	0.234	589	12.0	421	21.1	1.23
T3-2		Face 2	222.3	477.0	0.21	577.0	12.56	404.3	22.76	1.21								
T3-3		Corner 1	198.3	590	0.30	615.5	2.39	397.2	5.79	1.04								
T3-4		Corner 2	162.4	585	0.36	620.6	2.46	414.4	2.64	1.06								
T4-1	RHS 220x120x6	Face 1	192.7	460.0	0.24	559.1	14.48	403.8	25.40	1.22	184036	450	0.245	542	14.6	389	25.9	1.20
T4-2		Face 2	175.4	440.0	0.25	524.6	14.69	373.2	26.46	1.19								
T4-3		Corner 1	199.3	590	0.30	636.8	1.46	377.84	3.10	1.08								
T4-4		Corner 2	210.9	590	0.28	646.15	1.41	498.73	2.52	1.10								
T5-1	RHS 220x120x6	Face 1	187.4	463.1	0.25	557.7	12.60	392.1	24.22	1.20	182608	462	0.253	554	13.0	387	23.8	1.20
T5-2		Face 2	177.8	459.9	0.26	550.5	13.39	382.5	23.43	1.20								
T5-3		Corner 1	214.8	560	0.26	573.98	0.59	359.41	0.91	1.02								
T5-4		Corner 2	162.8	545	0.33	573.05	0.91	428.55	1.42	1.05								
T6-1	RHS 220x120x6	Face 1	210.0	455.0	0.22	576.3	14.36	403.9	26.44	1.27	196156	448	0.229	553	14.6	395	26.1	1.24
T6-2		Face 2	182.3	440.0	0.24	529.5	14.80	386.6	25.80	1.20								
T6-3		Corner 1	173.8	590	0.34	622.36	1.00	331.11	1.80	1.05								
T6-4		Corner 2	192.6	580	0.30	626.16	1.98	377.94	4.86	1.08								
T7-1	CHS 159x5	Face 1	203.0	393.0	0.19	545.5	15.92	324.7	22.91	1.39	205050	399	0.195	543	16.3	316	23.6	1.36
T7-2		Face 2	207.1	404.9	0.20	541.0	16.72	307.3	24.39	1.34								

Member resistance – Experimental tests and validation of F.E. models

T8-1	CHS 159x5	Face 1	202.5	399.7	0.20	534.5	16.63	311.0	23.88	1.34	198508	393	0.198	529	16.7	312	23.2	1.35
T8-2		Face 2	194.5	386.1	0.20	523.6	16.74	313.0	22.42	1.36								
T9-1	CHS 159x5	Face 1	203.8	405.8	0.20	536.9	15.45	318.3	23.22	1.32	202187	405	0.201	537	16.2	320	23.4	1.32
T9-2		Face 2	200.6	405.1	0.20	536.7	16.88	322.0	23.55	1.33								
T10-1	CHS 159x6.3	Face 1	193.8	407.8	0.21	551.9	16.54	334.4	22.79	1.35	198884	396	0.199	539	16.4	324	22.5	1.36
T10-2		Face 2	203.9	383.5	0.19	525.4	16.34	313.7	22.27	1.37								
T11-1	CHS 159x6.3	Face 1	200.7	390.8	0.19	522.3	16.14	320.6	21.33	1.34	202739	389	0.192	522	16.1	321	21.5	1.34
T11-2		Face 2	204.8	386.5	0.19	522.5	16.10	320.7	21.63	1.35								
T12-1	CHS 159x6.3	Face 1	196.8	391.4	0.20	527.5	16.41	313.5	21.80	1.35	206449	394	0.191	529	14.9	325	19.9	1.34
T12-2		Face 2	216.1	395.8	0.18	529.7	13.41	337.3	17.95	1.34								

3.3.3. Geometrical imperfections

The measurement of initial imperfections was performed by means of two different procedures. The first method was based on the measurements of a set of equally spaced linear variable displacement transducers (LVDTs) fixed on an aluminium bar that was displaced laterally on each specimen's plates in order to get a grid of out-of-plane imperfections on each plate's surface.

The second method consisted in scanning the specimen's plates by means of a laser Tracker *AT401* capable of measuring positions of scattered points very accurately. These points were then post-treated with a specific software to get the out-of-plane defaults of each specimen's plate.

3.3.3.1. LVDT measurements

Imperfections were measured using an aluminum frame comprising a sideways-movable aluminum bar drilled at 10 equally-spaced locations, containing 10 vertical displacements LVDTs spaced at 10 *cm* intervals (yellow arrow in Figure 30). In order to record data over the complete specimen, the frame was moved along the beam's length (see green arrow in Figure 30). All transducer readings were taken simultaneously as the frame travelled along the length of the specimen – measurements were not dynamic, though. Different beam segments were measured separately with an overlapping purposely considered to ensure the accuracy of the measurements. Three different transversal displacements were recorded for each RHS plate: one at mid-width and two at a distance of 20 *mm* from either side of the plate's corners. The transversal positions are denoted: *Position A*, *B* and *C*. Figure 31 to Figure 33 illustrate the positions of the LVDTs during the test. A flat, perfectly plane reference beam that have been specially manufactured in order to be considered perfectly horizontal, was used to reset the LVDTs to zero at the beginning of each test as shown in Figure 35.

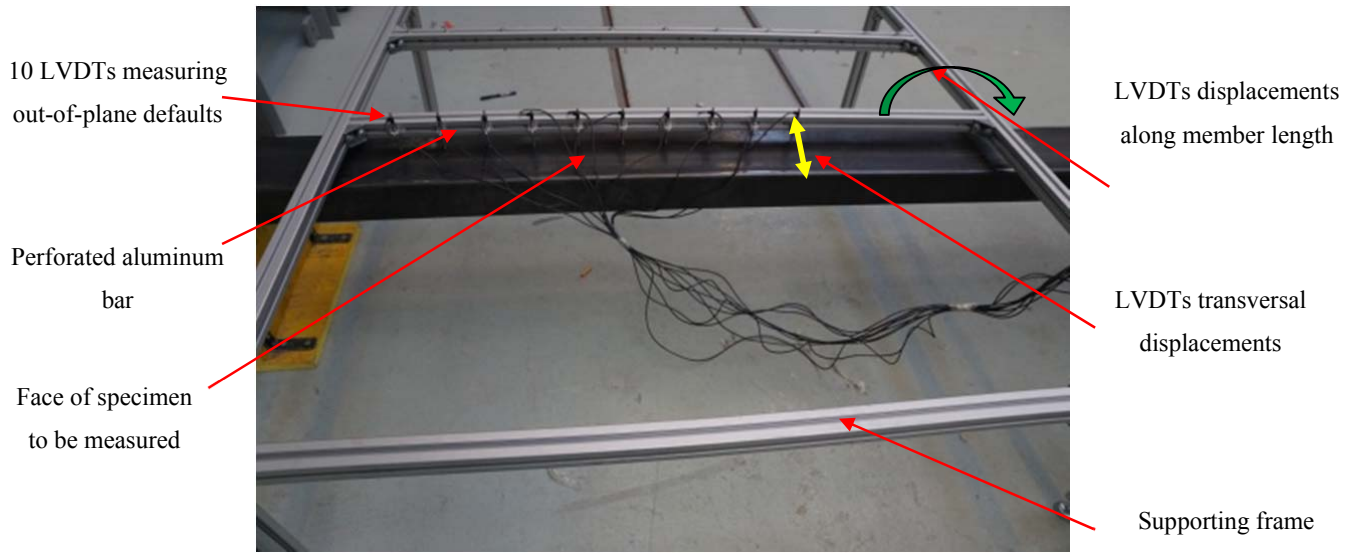
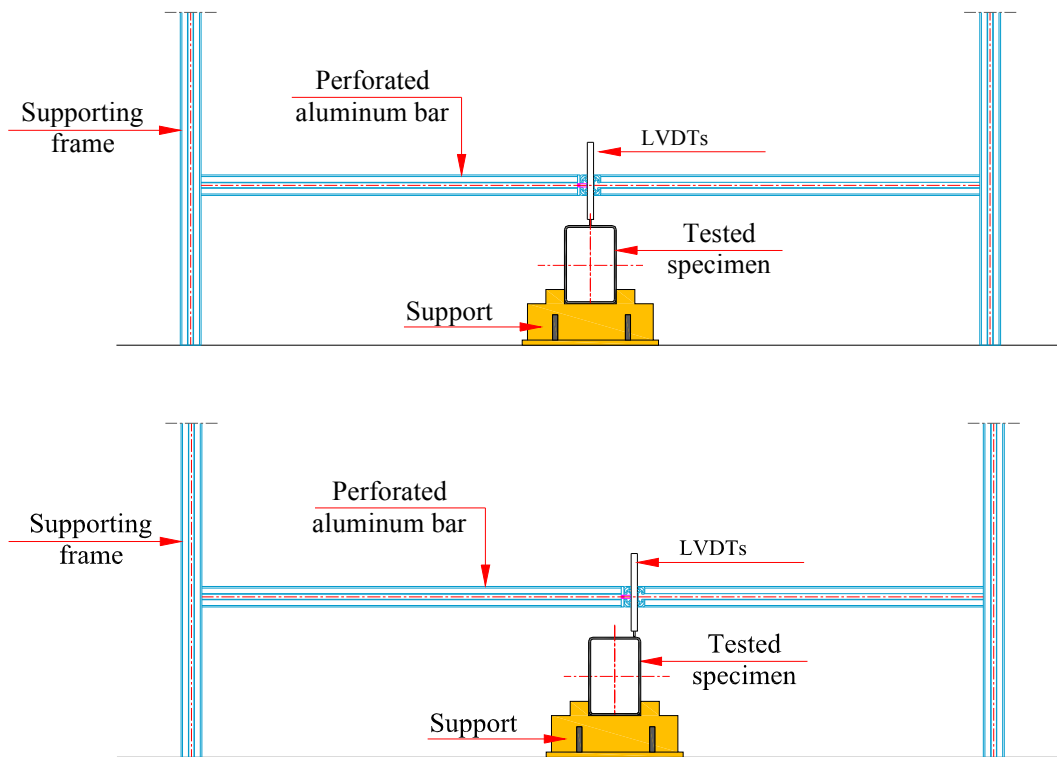


Figure 30 –Initial geometrical imperfections measuring procedure



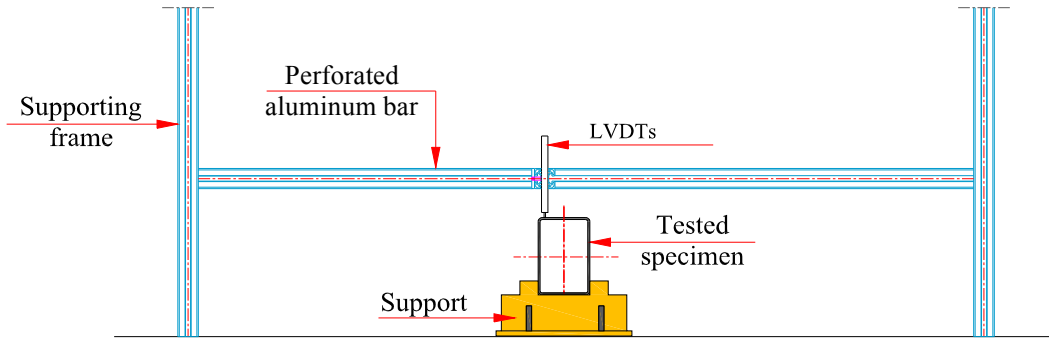


Figure 31 – LVDTs transversal displacements – a) Position A – b) Position B – c) Position C

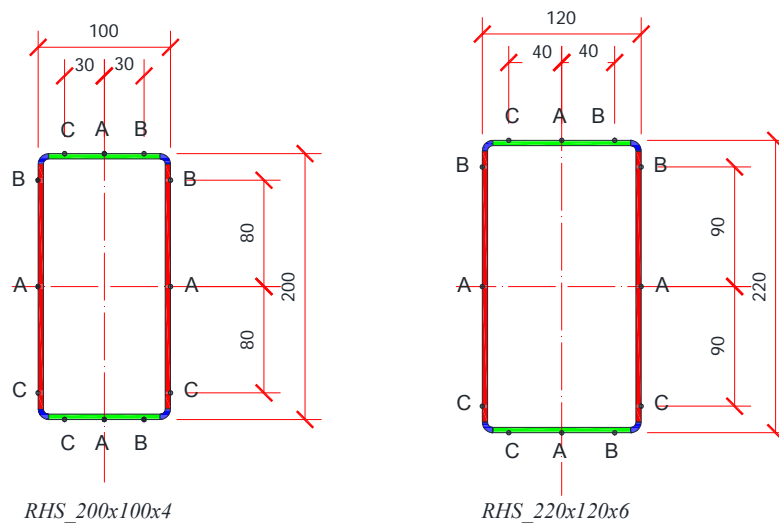


Figure 32 – LVDTs transversal displacements for – a) RHS 200x100x4– b) RHS 220x120x6

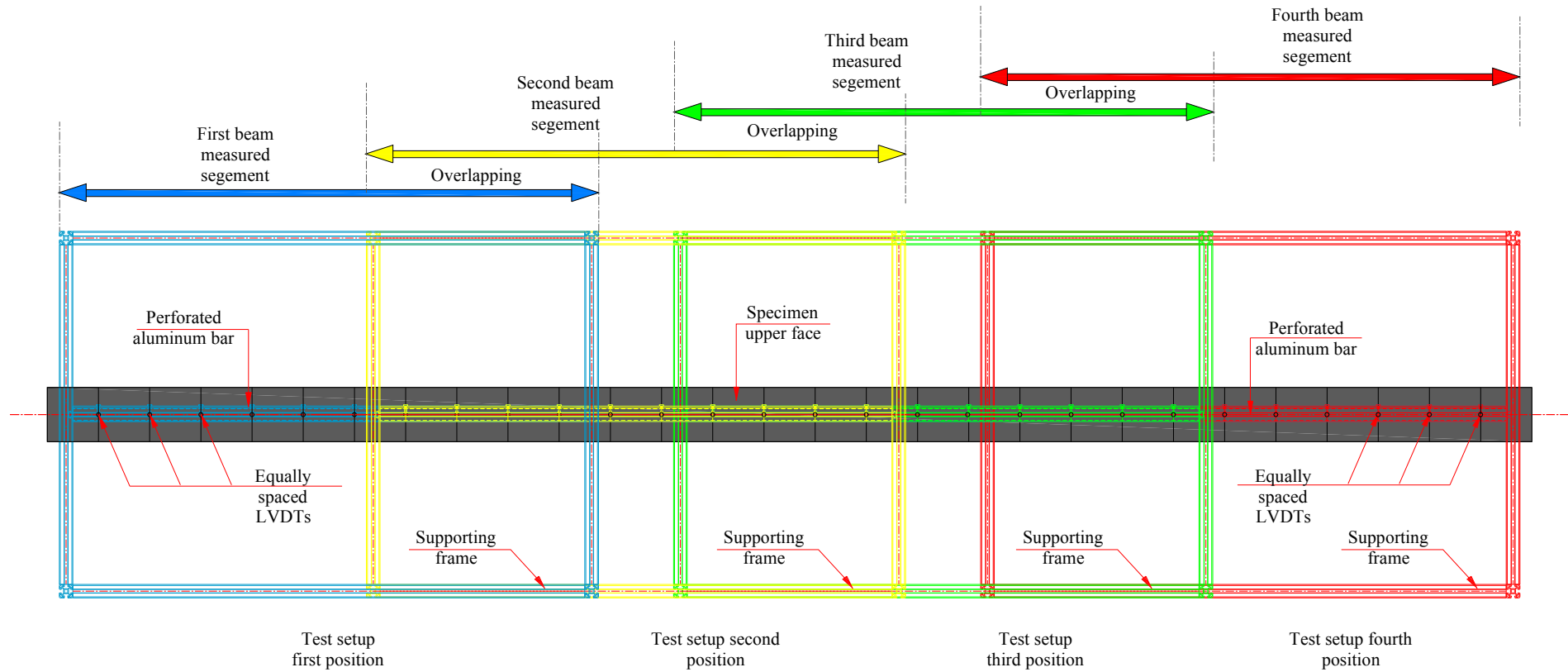


Figure 33 – LVDTs displacements along the beam length (top view)

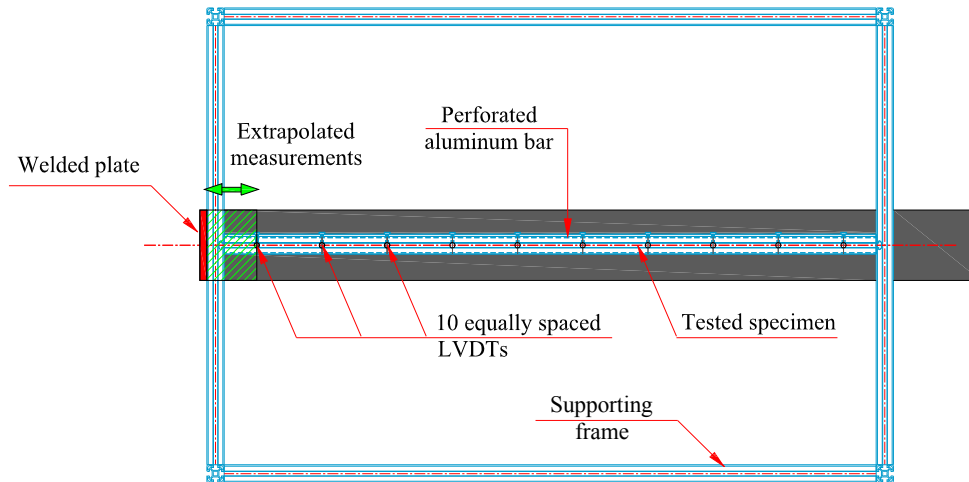


Figure 34 – Extrapolated measurements near the loading plates

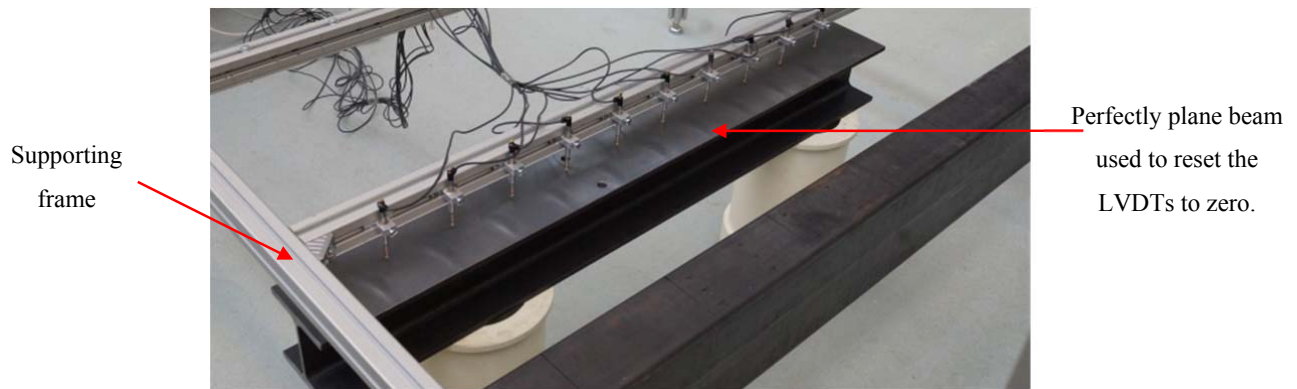


Figure 35 – Measurement of geometrical imperfections - Resetting the LVDTs to zero

The collected measurements were treated computationally and corrected by an 8-steps procedure in order to get the beam initial deflections as described below. An example of measurements for RHS CF 200x100x4 T1 is illustrated herein. The measurements in this case are performed on the bottom flange of the specimen, on the mid-width of the plate.

Step 1: The initial measurements collected from the LVDT are first plotted for each segment without any modification;

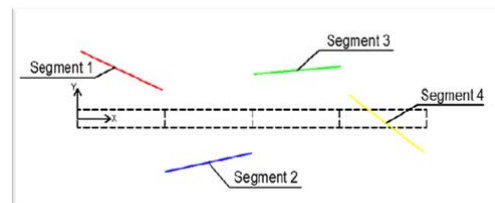


Figure 36 – Step 1 procedure

Step 2: The slopes of the overlapping part between two adjacent beam segments are matched (i.e. in this example, the measurements of the last four recordings of one segment and the first four recordings of the adjacent segment);

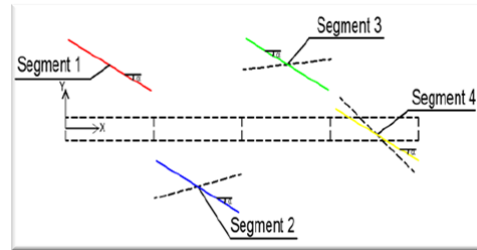


Figure 37 – Step 2 procedure

Step 3: Measurement series are connected to each other;

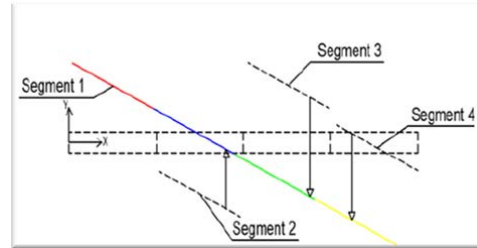


Figure 38 – Step 3 procedure

Step 4: After calculating the general slope of the connected measurement series, all measured displacements are reported to the horizontal axis;

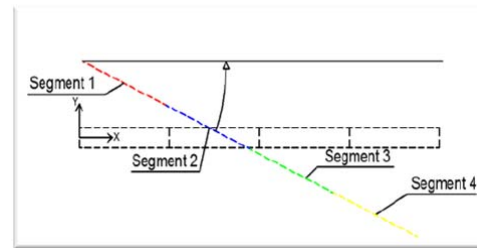


Figure 39 – Step 4 procedure

Step 5: A reference point at the beginning of each profile was selected, allowing setting this first value as a zero reference point, and all the other data were relative to this reference;

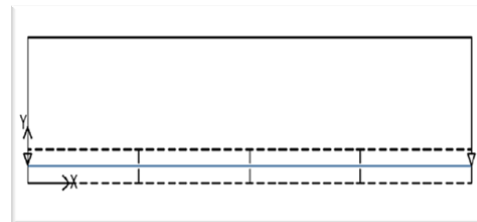


Figure 40 – Step 5 procedure

Step 6: the measurements are extrapolated⁵ to the length of the profile (see Figure 34);

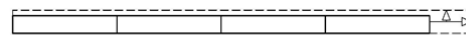
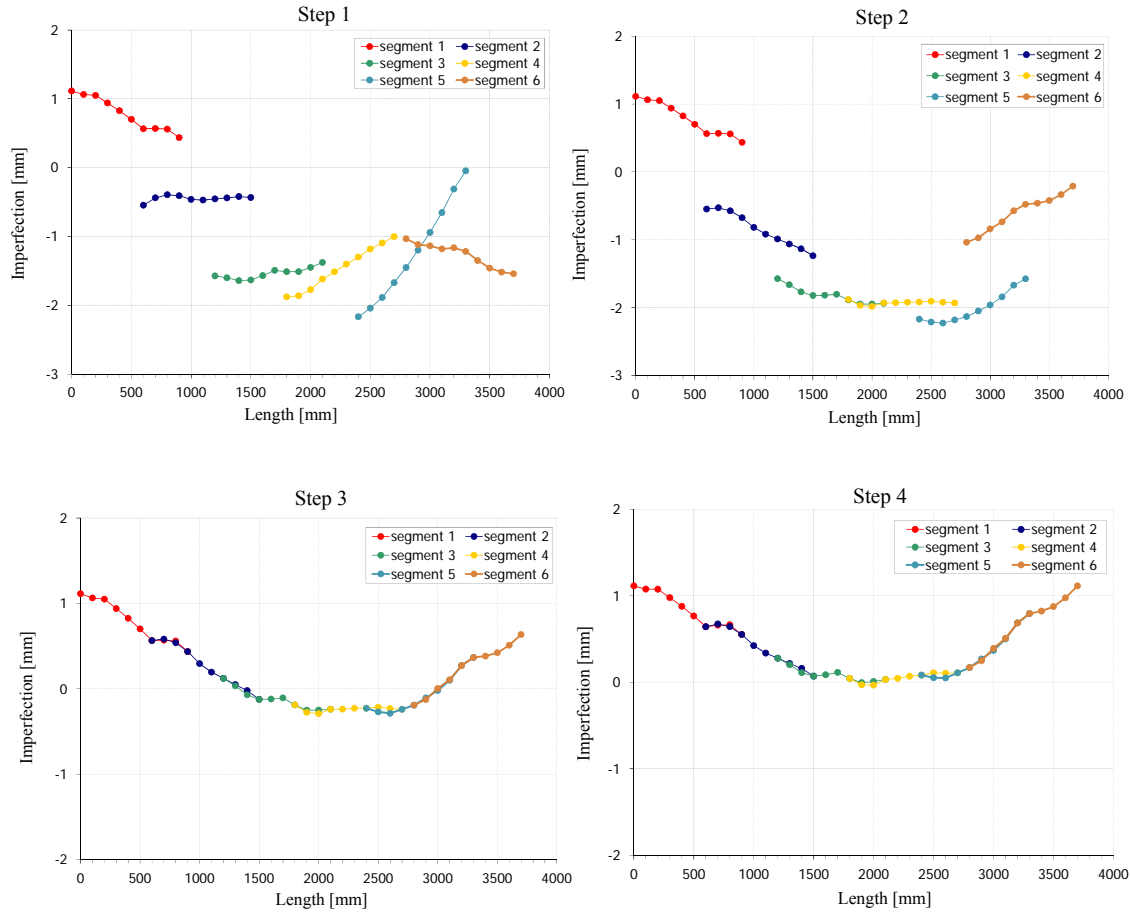


Figure 41 – Step 6 procedure

⁵ Due to geometrical constraints, it was difficult to measure the imperfections accurately near the loading plates. Thus, extrapolation on the obtained data was needed on both extremities of each specimen to get initial imperfection along the complete specimen's length.

Step 7: the displacement measurements of the points corresponding to the beam segment overlaps are replaced by their mean values. The obtained curve then still contains the beam initial geometrical imperfections and the deformed configuration caused by self-weight;

Step 8: the deformed configuration caused by the self-weight is removed from the total one in order to keep only the beam initial geometrical imperfections of a specimen’s face, for a given position in the plate’s width (i.e. center or extremity).



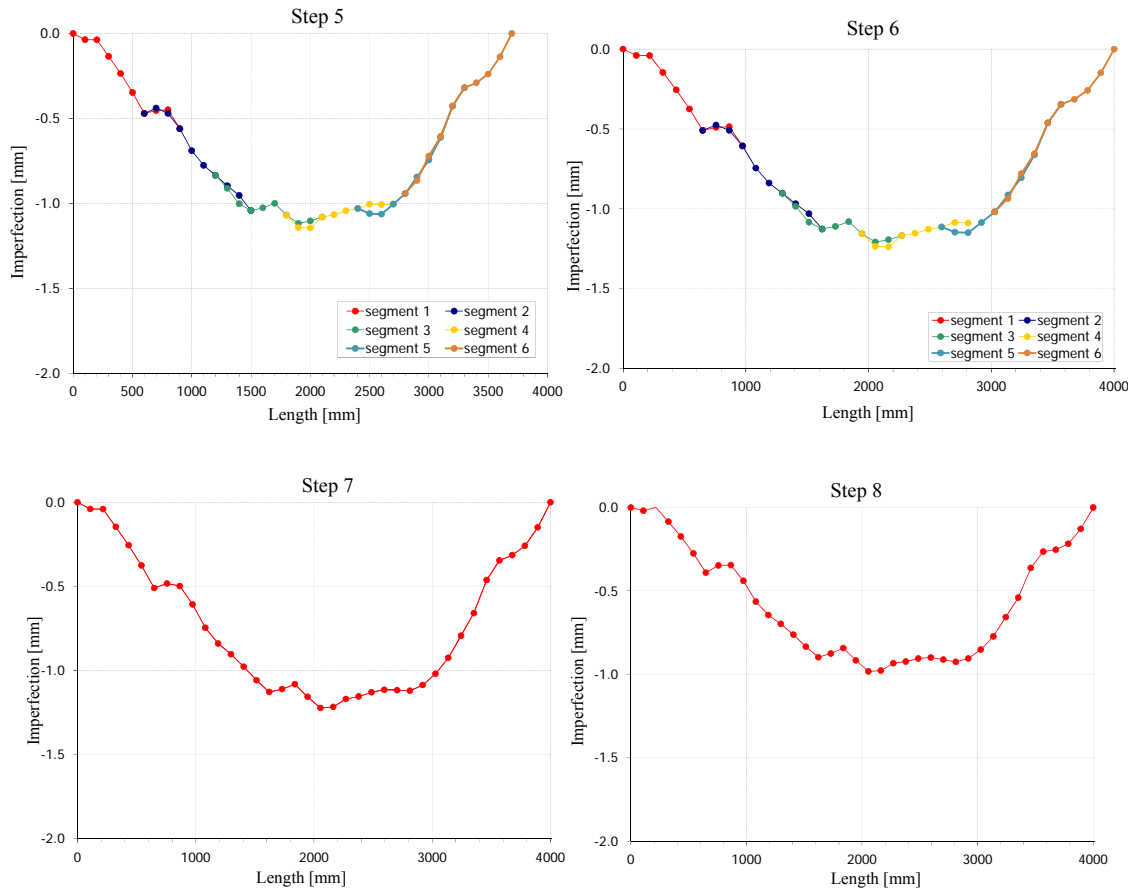


Figure 42 – Correction of measured geometrical imperfections by an 8-steps procedure

The 8-steps procedure was performed for the three defined positions (*Position A, B and C*) of each plate of the specimens. The corners could not be measured by means of the LVDTs and were assumed perfect. The initial imperfections measured were then introduced in the F.E. models for validation purposes. Figure 43 proposes an example of the (magnified) imperfect shape of a portion selected at mid span of the specimen RHS CF 200x100x4 T2 as implemented in the finite elements models.

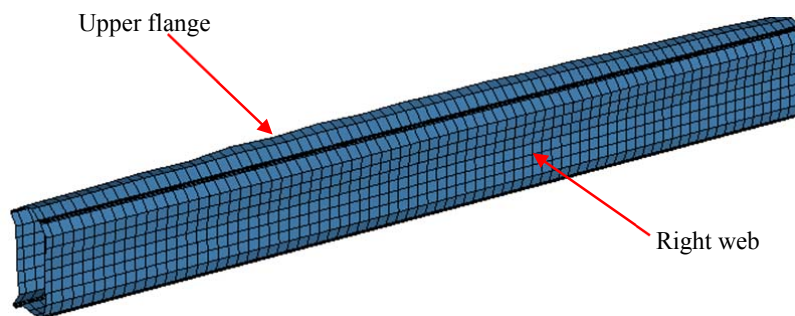


Figure 43 – Imperfect shape of specimen RHS CF 200x100x4 T2 (magnified)

Table 16 summarizes the maximum local magnitudes of initial imperfections measured along the member length. ‘Denom. local web’ and ‘Denom. local flange’ refer to the *denominator* in the ratios ‘ $h - 2r - t / denominator$ ’ and ‘ $b - 2r - t / denominator$ ’ equations, which is such that these ratios are equal to the measured maximum local magnitude of web and flange respectively. The measured imperfections are compared to the reasonable and realistic amplitude of imperfections chosen as a per plate amplitude $a / 200$ with ‘ a ’ equal to $(b-t-2r)$ or $(h-t-2r)$.

Table 17 summarizes the maximum global magnitudes of initial imperfections measured along the member length. ‘Denom. global web’ and ‘Denom. global flange’ refer to the *denominator* in the ratio ‘ $L / denominator$ ’ equation which is such that this ratio is equal to the measured maximum global magnitude of web and flange respectively. The measured imperfections are compared to the realistic average value of global imperfection amplitude equal to $L / 1000$.

Table 16 – Initial local maximum out-of-plane magnitude measured along the member length

Specimen	$h - 2r - t / 200$	$b - 2r - t / 200$	Average	Measured local magnitude web	Measured local magnitude flange	Measured local magnitude average	Denom. local web	Denom. local flange	Denom. local average
	[mm]	[mm]	[mm]	[mm]	[mm]	[mm]	[-]	[-]	[-]
RHS CF 200x100x4 T1	0.91	0.41	0.66	0.288	0.300	0.294	289	277	283
RHS CF 200x100x4 T2	0.92	0.41	0.66	0.435	0.689	0.562	190	120	155
RHS CF 200x100x4 T3	0.90	0.40	0.65	0.374	0.153	0.263	217	531	374
RHS CF 220x120x6 T4	0.97	0.47	0.72	0.280	0.120	0.200	337	788	562
RHS CF 220x120x6 T5	0.96	0.47	0.71	0.654	0.192	0.423	142	486	314
RHS CF 220x120x6 T6	0.97	0.47	0.72	0.206	0.522	0.364	459	181	320
Mean	0.94	0.44	0.69	0.373	0.329	0.351	272	397	334

Table 17 – Initial global maximum out-of-plane magnitude measured along the member length

Specimen	$L / 1000$	Measured global magnitude web	Measured global magnitude flange	Measured global magnitude average	Denom. global web	Denom. global flange	Denom. global average
	[mm]	[mm]	[mm]	[mm]	[-]	[-]	[-]
RHS CF 200x100x4 T1	4.00	0.259	0.743	0.501	15479	5385	10432
RHS CF 200x100x4 T2	4.00	0.805	0.462	0.633	4972	8667	6820
RHS CF 200x100x4 T3	4.00	1.048	0.579	0.814	3817	6909	5363
RHS CF 220x120x6 T4	4.00	1.395	0.763	1.079	2868	5246	4057
RHS CF 220x120x6 T5	4.00	1.377	0.669	1.023	2905	5984	4445
RHS CF 220x120x6 T6	4.00	0.622	1.411	1.016	6429	2835	4632
Mean	4.00	0.917	0.771	0.844	6078	5838	5958

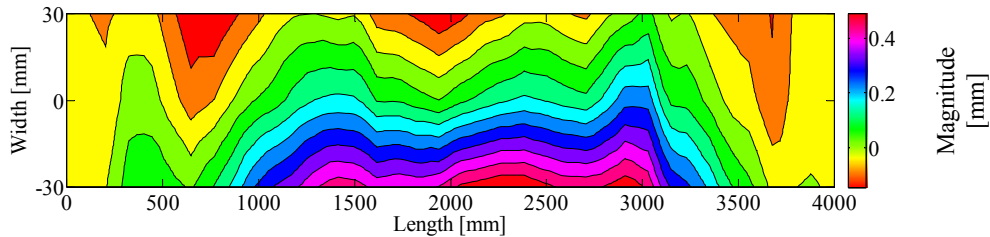
The following conclusions can be drawn from these tables:

- the maximum measured local magnitudes vary widely for the different considered tests and ranged from 0.2 to 0.56 with an average of 0.35;
- the same tendency is observed for the global buckling measurements, where the maximum magnitude ranged from 0.5 to 1 with an average of 0.85;
- the realistic magnitude of local imperfections $a / 200$ is seen to provide safe results when compared to the experimental one for all the tested columns; the average measured local magnitude being equal to $a / 334$;
- the realistic magnitude of global imperfections $L / 1000$ is seen to provide safe results when compared to the experimental one for all the tested columns; the average measured global magnitude being equal to $a / 5958$.

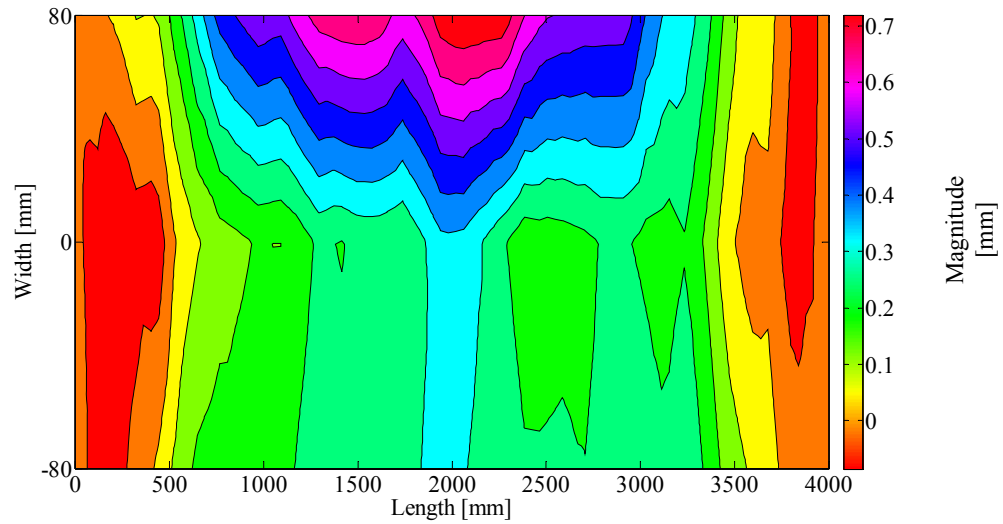
Accordingly, the realistic magnitudes can be safely adopted to represent the initial magnitude of tested beam-column members; the measured ones were seen to vary considerably depending on the tested column.

Figure 44 represents the corresponding out-of-flatness isolines of imperfection magnitudes obtained for each plate of the specimen RHS CF 200x100x4 T2 separately. All measured data with general imperfect shapes can be found in Annex 6.

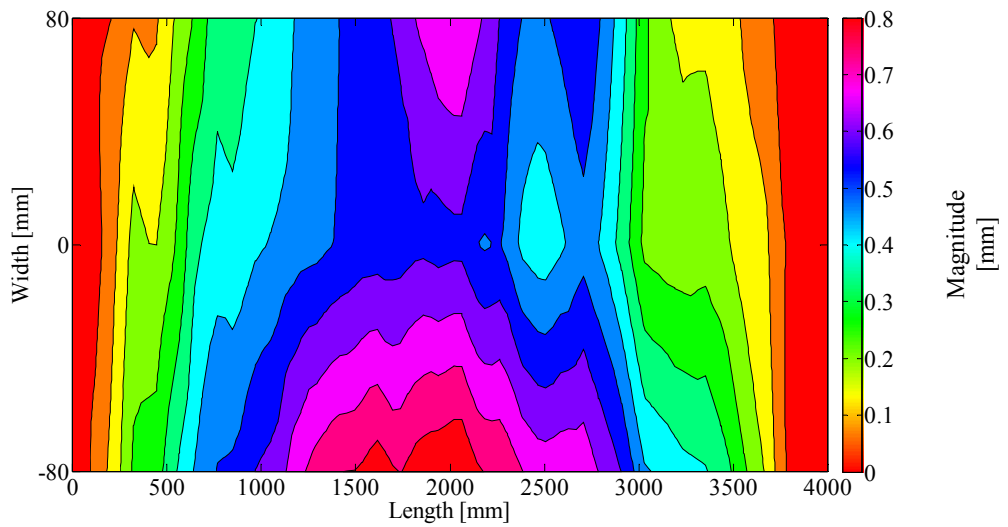
Bottom flange:



Left web:



Right web:



Upper flange:

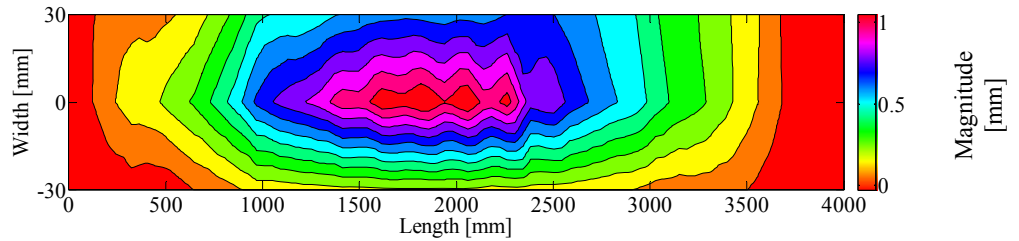


Figure 44 – Measured out-of-flatness isolines of imperfection magnitudes obtained for each plate of the RHS CF 200x100x4 T2 specimen.

3.3.3.2. Topometric measurements

Before each test, the initial geometrical imperfections were also measured for the six cold-formed RHS by means of a laser Tracker AT401 with a general accuracy of 0.5 mm and an improved accuracy of 0.2 mm in the expected failure zone. The columns were placed horizontally and marked with a series of targets; marks were more densely distributed at the expected location of local buckling (see Figure 45).

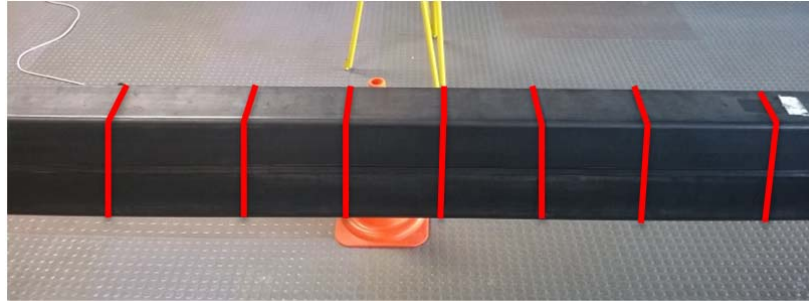


Figure 45 – Beam positions and measured sections

Approximately, 25 sections were measured for each beam and 22 points were measured for each corresponding section. In total 550 points were measured for each beam (see Figure 46).

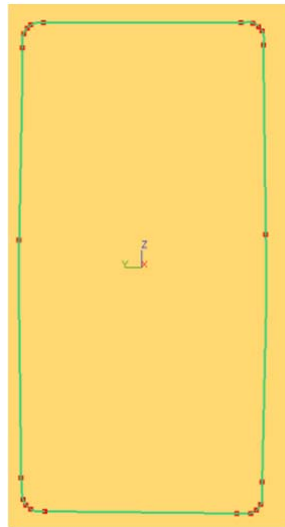


Figure 46 – Points distribution for each beam section

This technique consists in moving a light source along predefined longitudinal lines for each plate, and very accurately recording consecutive positions. The "tracker" technology allows the instrument to detect the reflector as illustrated in Figure 47. The remote measurements were then treated by a specific software (SA "Spatial Analyzer" of New River Kinematics) adapted to the measuring instrument.



Figure 47 – Measurement of geometrical imperfections – Topometric procedure

Figure 48 proposes an example of the (magnified) imperfect shape of a portion selected at mid span of the specimen RHS CF 200x100x4 T1 as implemented in the finite elements models. Figure 49 represents the corresponding out-of-flatness isolines of imperfection magnitudes obtained for each plate of the specimen RHS CF 200x100x4 T1 separately. All measured data with general imperfect shapes can be found in Annex 6.

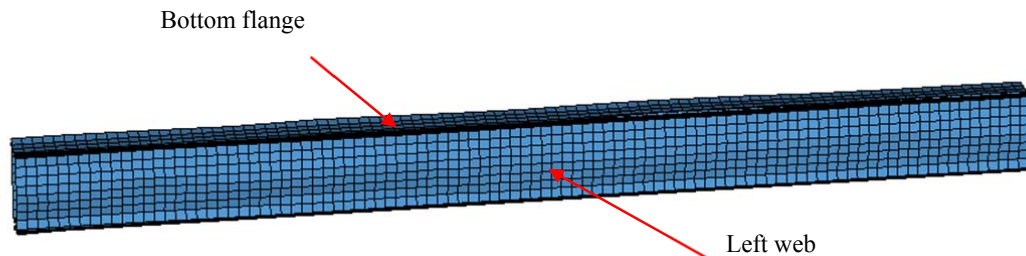
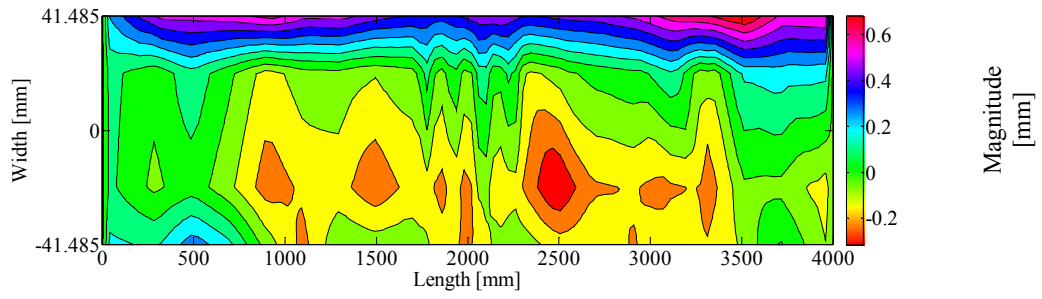
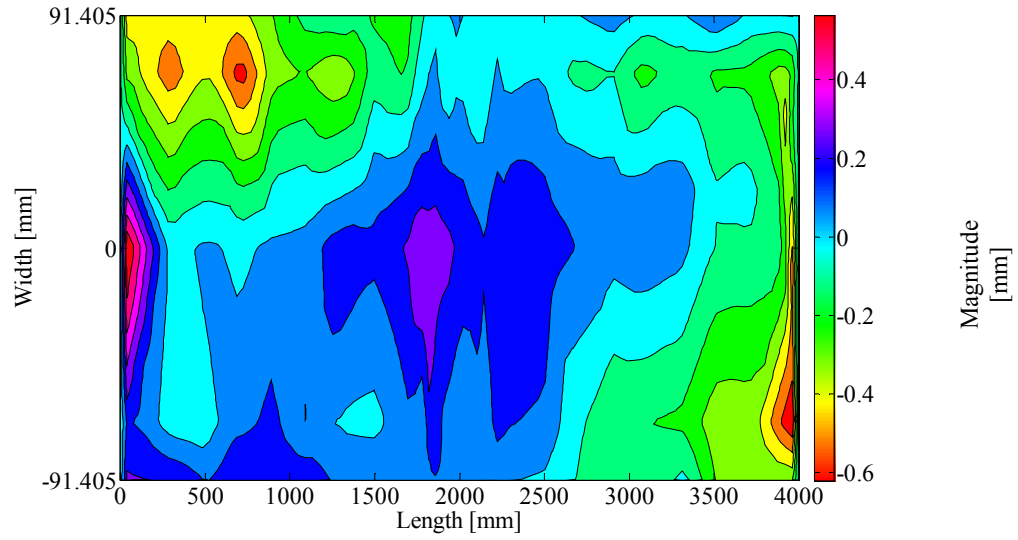


Figure 48 – Imperfect shape of specimen RHS CF 200x100x4 T1 (magnified)

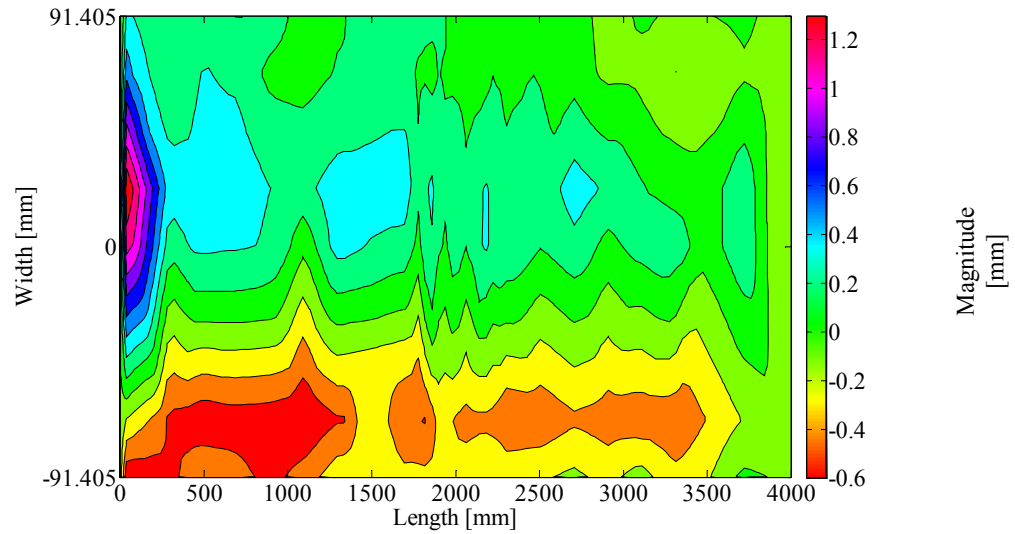
Bottom flange:



Left web:



Right web:



Upper flange:

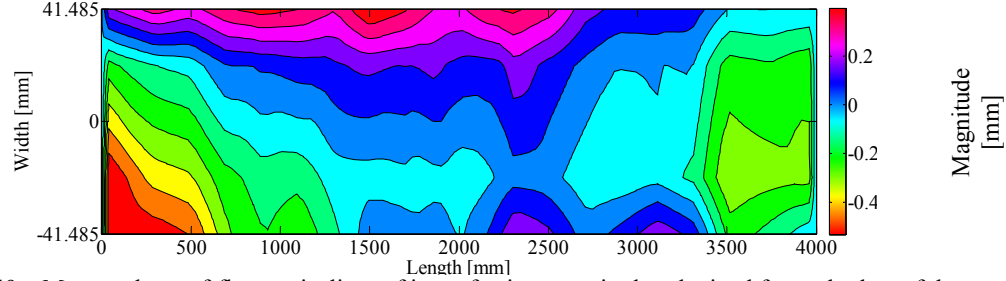


Figure 49 – Measured out-of-flatness isolines of imperfection magnitudes obtained for each plate of the RHS CF 200x100x4 T1 specimen.

Table 18 to Table 21 provide a comparison between maximum initial imperfection magnitude at mid-width of each specimen's plate, obtained by using the set of LVDTs and the laser Tracker AT401 for each plate of each specimen.

Table 18 – Maximum out-of-plane magnitude measured at mid-width of the upper flange plate

<i>Upper flange: maximum magnitude measurements at mid-width [mm]</i>		
Specimen	LVDT	AT401
RHS CF 200x100x4 T1	0.907	0.132
RHS CF 200x100x4 T2	1.150	0.179
RHS CF 200x100x4 T3	-0.647	-0.144
RHS CF 220x120x6 T4	0.597	0.091
RHS CF 220x120x6 T5	-0.159	-0.140
RHS CF 220x120x6 T6	-0.889	-0.136

Table 19 – Maximum out-of-plane magnitude measured at mid-width of the right web plate

<i>Right web: maximum magnitude measurements at mid-width [mm]</i>		
Specimen	LVDT	AT401
RHS CF 200x100x4 T1	0.307	0.429
RHS CF 200x100x4 T2	0.586	0.188
RHS CF 200x100x4 T3	1.095	0.510
RHS CF 220x120x6 T4	1.521	2.158
RHS CF 220x120x6 T5	1.490	1.871
RHS CF 220x120x6 T6	0.828	1.440

Table 20 – Maximum out-of-plane magnitude measured at mid-width of the bottom flange plate

<i>Bottom flange: maximum magnitude measurements at mid-width [mm]</i>		
Specimen	LVDT	AT401
RHS CF 200x100x4 T1	0.982	0.203
RHS CF 200x100x4 T2	0.264	0.098
RHS CF 200x100x4 T3	-0.696	-0.063
RHS CF 220x120x6 T4	-0.643	-0.123
RHS CF 220x120x6 T5	-0.757	-0.149
RHS CF 220x120x6 T6	-1.518	-0.073

Table 21 – Maximum out-of-plane magnitude measured at mid-width of the left web plate

<i>Left web: maximum magnitude measurements at mid-width [mm]</i>		
Specimen	LVDT	AT401
RHS CF 200x100x4 T1	0.546	0.343
RHS CF 200x100x4 T2	0.370	0.343
RHS CF 200x100x4 T3	0.674	0.558
RHS CF 220x120x6 T4	1.115	0.276
RHS CF 220x120x6 T5	0.723	0.373
RHS CF 220x120x6 T6	0.586	0.341

The figures below report on the measured initial imperfections along the length of the RHS CF 200x100x4 T2 specimen at the mid-width of the bottom flange and left web plates, by using the LVDT and the laser tracker procedures. One may notice that there was some extra initial deformation induced into the specimen near the end plates, caused by welding of the plates. It was difficult to measure such imperfections accurately by means of the LVDT procedure, since the measurements were extrapolated near both ends of the specimen.

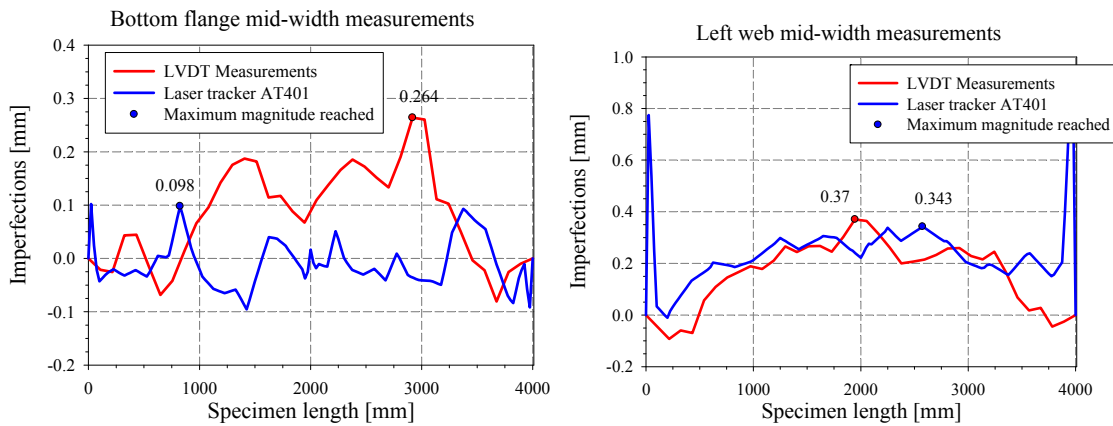


Figure 50 – Initial deformations along the length of the RHS CF 200x100x4 T2 specimen at the mid-width of each plate obtained by using the LVDT and the laser tracker procedures.

Disparities in measurements are credited to the insufficient accuracy of the LVDT method. The LVDTs procedure indeed typically slightly overestimated the initial defaults. A higher level of confidence and reliability are provided by the laser AT401 measurements. Both sets of measured initial imperfections were introduced in suitably-built shell F.E. models, along with all measured data, and were shown to lead to nearly identical numerically-predicted failure loads, indicating that the observed differences in imperfection patterns shall be deemed acceptable and sufficient.

3.3.4. Residual stresses

The development of residual stresses occurs primarily during the section production process and is associated with differential cooling and non-uniform plastic deformation. The general influence of residual stresses on structural members is to cause premature yielding, leading to a loss of stiffness and a reduction in load-carrying capacity [45].

The distribution of residual stresses induced by the forming process was investigated for two cross-sections shapes RHS CF 200x100x4 and RHS CF 220x120x6. Both specimens were manufactured through the cold-forming process. The sectioning technique was used to measure the deformations experienced by the released material (see Figure 51). More rigorously, material relaxation is such that each strip, after cutting, exhibits an axial displacement due to the membrane residual stresses relaxation and a curvature originating from the bending residual stresses. In cold-formed sections, bending residual stresses are generally dominant and the membrane stresses are relatively low. However, the opposite is expected in welded and hot-rolled sections where the membrane residual stresses are dominant.

Measurements were taken with electrical strain gauges and compared to the ones obtained by the mechanical procedure, as detailed in the following paragraphs.

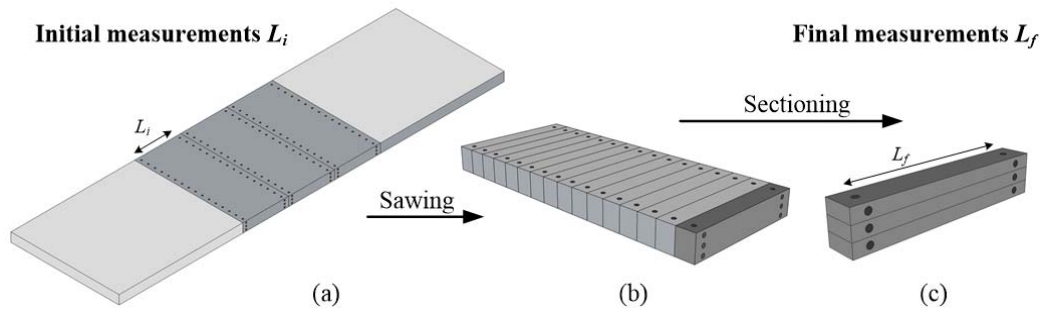


Figure 51 – Principles of the sectioning method

3.3.4.1. Specimen preparation

The portion kept for the residual stresses measurements was centered between sufficient materials (length $> 2.H$) from both sides to ensure a representative stress distribution and prevent the stress released due to the neighbourhood of the specimen edges (see Figure 52). The goal is to fulfill Saint-Venant's principle, i.e. keep far from big changes in geometry and section, i.e. from cut edges.

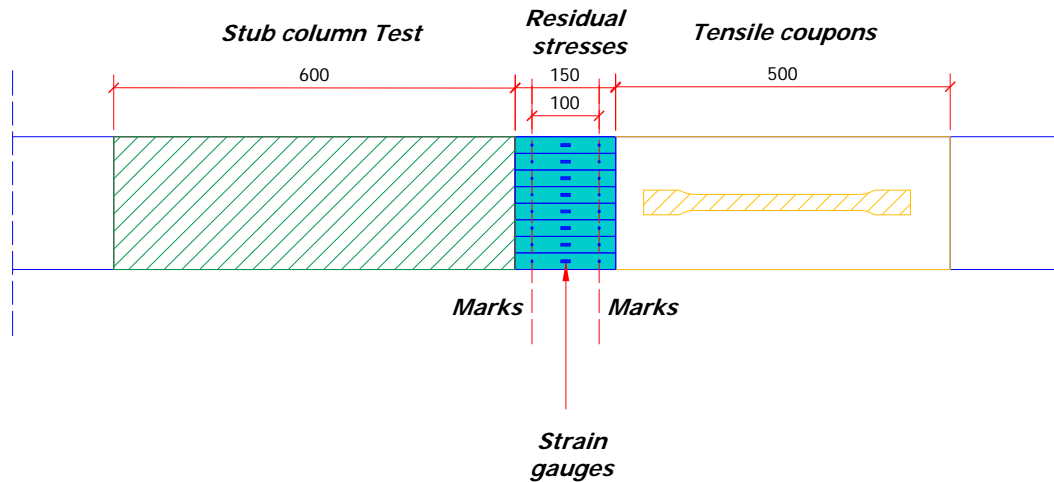


Figure 52 – Use of material for different preliminary tests and measurements

The specimens were divided into strips of 150 mm length and 30 mm width as shown in Figure 54, large enough to ensure a better accuracy of results. Actually, during the cutting, additional residual stresses are created due to the heating generated by the saw. The strip width was large enough in order to consider this effect negligible, but small enough to have sufficient measurement points. Regardless of the adopted strip width, the speed of sawing and the thickness of the plate will also affect the additional stress creation [3]. An effective liquid cooling system was used during the sawing, enabling the neglect of the sawing effects. Thus the heat generated by the saw was shown to have negligible impact on the measured residual stresses.

Two little 100 mm-spaced circular imprints were punched on each strip of the cross-section (see Figure 53). These marks were used as a reference to measure the length and curvature's variations mechanically. After recording all initial lengths and curvatures, a series of strain gauges were glued to the external surface of each strip in the longitudinal direction. Figure 54 illustrates the location of the strips in the RHS 200x100x4 and RHS 220x120x6 sections along with the adopted numbering convention. The first letter of the label is either A or B denoting an RHS 200x100x40 or an RHS 220x120x6 respectively, followed by an identification number (i.e. from 1 to 22).

A specific covering agent “PU140” was applied to securely protect the strain gauges measuring points against moisture, water, oil...

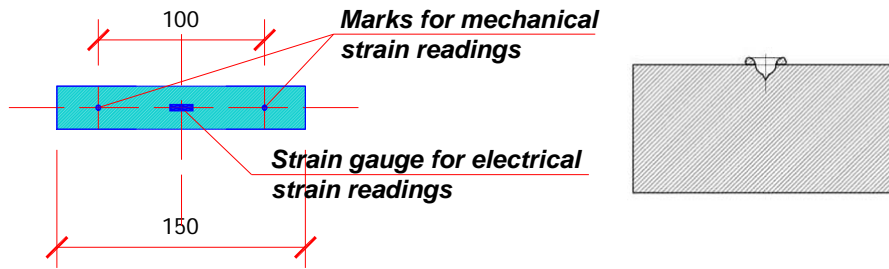


Figure 53 – Strain gauges and 100 mm-spaced circular marks locations – Circular imprint

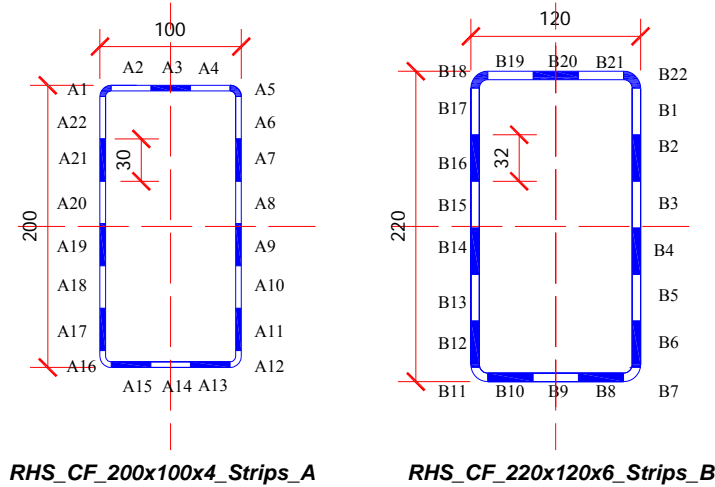


Figure 54 – Location of the strips in the hollow sections with the adopted labeling system

3.3.4.2. Mechanical measurements

Released residual stresses were first measured by mechanical means. Prior to cutting, the length of the strips was measured by an extensometer calibrated before each measurement with an ‘invar’ bar⁶ with a 100 mm basis (see Figure 55), whilst the curvature reference was measured by means of a curvature dial. Cutting of the strips was then performed on an automated milling machine followed by additional measurements of lengths and curvatures of the released strips (see Figure 56). The differences between initial and final strips length are linked to membrane stresses, while the curvature variations are due to flexural – through

⁶ The ‘invar’ bar has a thermal coefficient 10 times smaller than the steel coefficient. It was marked by two 100 mm spaced circular marks identical to the spaced circular marks punched on each strip of the cross-section. The bar served as a reference for each measure.

thickness – stresses. For both initial and final readings, a mean value was determined from five consecutive readings.



Figure 55 – Invar' bar with 100 mm basis

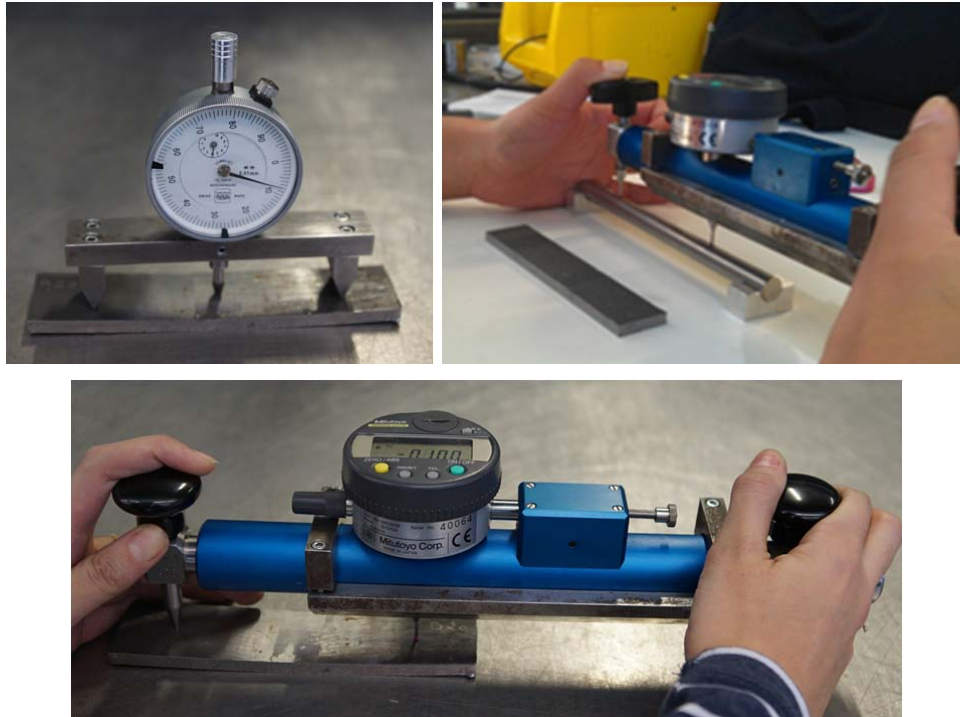


Figure 56 – Strip length and curvature measurements.

3.3.4.2.1. Flexural residual stresses

For sake of simplicity, bending residual stresses were initially determined by assuming a linearly-varying through-thickness stress distribution. This assumption was adopted in this study owing to the small thicknesses of the tested sections, and flexural stresses were thus calculated by means of the following equation:

$$\sigma_{flexural} = E \frac{L_{arc_e_or_i} - L_{arc_m}}{L_{arc_m}} \quad (153)$$

where E is the Young's modulus, $L_{arc_e_or_i}$ is the arc length at the inner or outer surface of the strip and L_{arc_m} stands for the neutral axis arc length as illustrated in Figure 57.

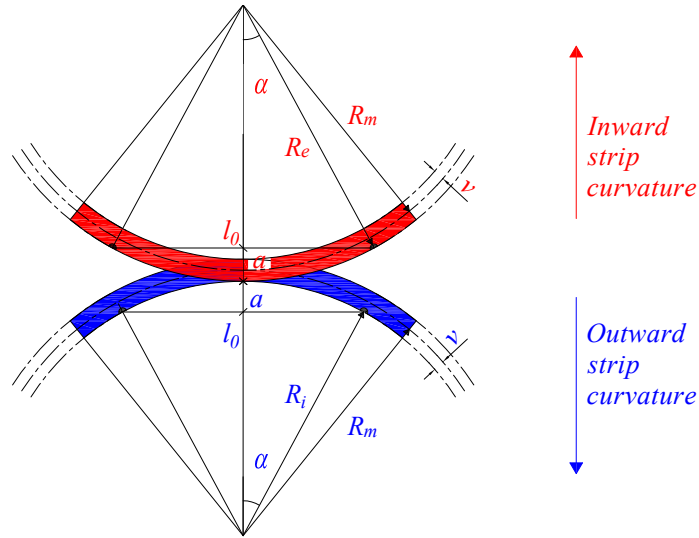


Figure 57 – Geometrical deformation due to residual stresses

Equation (153) can be rewritten in the following way:

$$\sigma_{flexural} = E \frac{\alpha R_{i_or_e} - \alpha(R_m)}{\alpha R_m} = E \frac{v}{R_m} \quad (154)$$

where α is the angle of curvature; R_m is the curvature radius at the neutral axis; R_i and R_e stands for external or internal radius curvature and v is the half strip thickness $t / 2$.

The angle of curvature α is calculated from the following expression:

$$\alpha = \arcsin \left(\frac{l_{final} - l_{initial}}{2R_{i_or_e}} \right) \quad (155)$$

l_{final} and $l_{initial}$ are the lengths measured by the extensometer before and after the strip cutting. The curvature radius at the neutral axis R_m is calculated by means of the following equation involving the addition or subtraction of the half strip thickness v :

$$R_m = R_{i_or_e} \pm v \quad (156)$$

The change in radius of curvature R_m (as well as for R_e and R_i) of the strips was calculated based on basic geometrical equations (assuming that the curvature was constant along the length of the strips):

$$(R - \Delta a)^2 + \left(\frac{L_0}{2}\right)^2 = R^2 \quad (157)$$

$$R = \frac{L_0^2}{8\Delta a} + \frac{\Delta a}{2} \quad (158)$$

where L_0 is the length over which the deflection is measured (here 100 mm corresponding to the curvature measuring device), Δa is the difference between the initial deflection of the strip and the final deflection of the strip.

$$\Delta a = a_{final} - a_{initial} \quad (159)$$

3.3.4.2.2. Membrane residual stresses

The determination of membrane residual stresses is more complex, since the measurements made by the extensometer must be corrected in order to remove the effects of strip curvature caused by the existence of flexural residual stresses [45]. Therefore, the stress measured through the extensometer is considered as a total stress in which a part is associated with the shortening due to the membrane stresses and the other part is associated with the curvature due to the flexural stresses.

Using the radius of curvature of the strips measured to the neutral axis R_{m_final} and the angle of curvature α (see Figure 57), the length along the arc can be calculated by means of the following equation:

$$L_{arc} = R_m \times \alpha \quad (160)$$

Therefore, the membrane residual stresses can be calculated by using the following equation:

$$\sigma_{membrane} = E \frac{L_{arc_f} - L_{arc_i}}{L_{arc_i}} \quad (161)$$

where L_{arc_i} and L_{arc_f} are the initial and final arc length calculated as mentioned above.

3.3.4.3. Strain gauges measurements

Strain gauges were glued to the external surface of each strip in the longitudinal direction, followed by initial electrical readings. The strips were then cut and final readings were taken.

During cutting, the strips exhibited both axial deformation and curvature due to the membrane and bending components of the unloading stress. The measurement procedure is illustrated in Figure 58. The total residual stresses measured from the outer surfaces combine both bending and membrane stresses. Consequently, the membrane residual stresses were obtained by subtracting the bending stresses determined mechanically from the curvature dial, and compared to values obtained with the extensometer. Patterns of through-thickness residual stresses variations for both the electrical and the mechanical readings and presented in Figure 59 and Figure 60 for the RHS CF 220x120x6 and RHS CF 200x100x4 specimens, respectively. One may note that the bending stresses were dominant while the membrane stresses were relatively low, as typically recorded for cold-formed tubes. These patterns have been introduced in the F.E. model to validate it. Suitable auto-equilibrated formulae are then derived to launch the extensive set of parametric study. Measured membrane stresses were introduced for the hot-rolled profiles, whereas both measured flexural and membrane residual stresses were introduced for cold-formed profiles. As for the circular hot-rolled profiles, only flexural residual stresses were introduced.

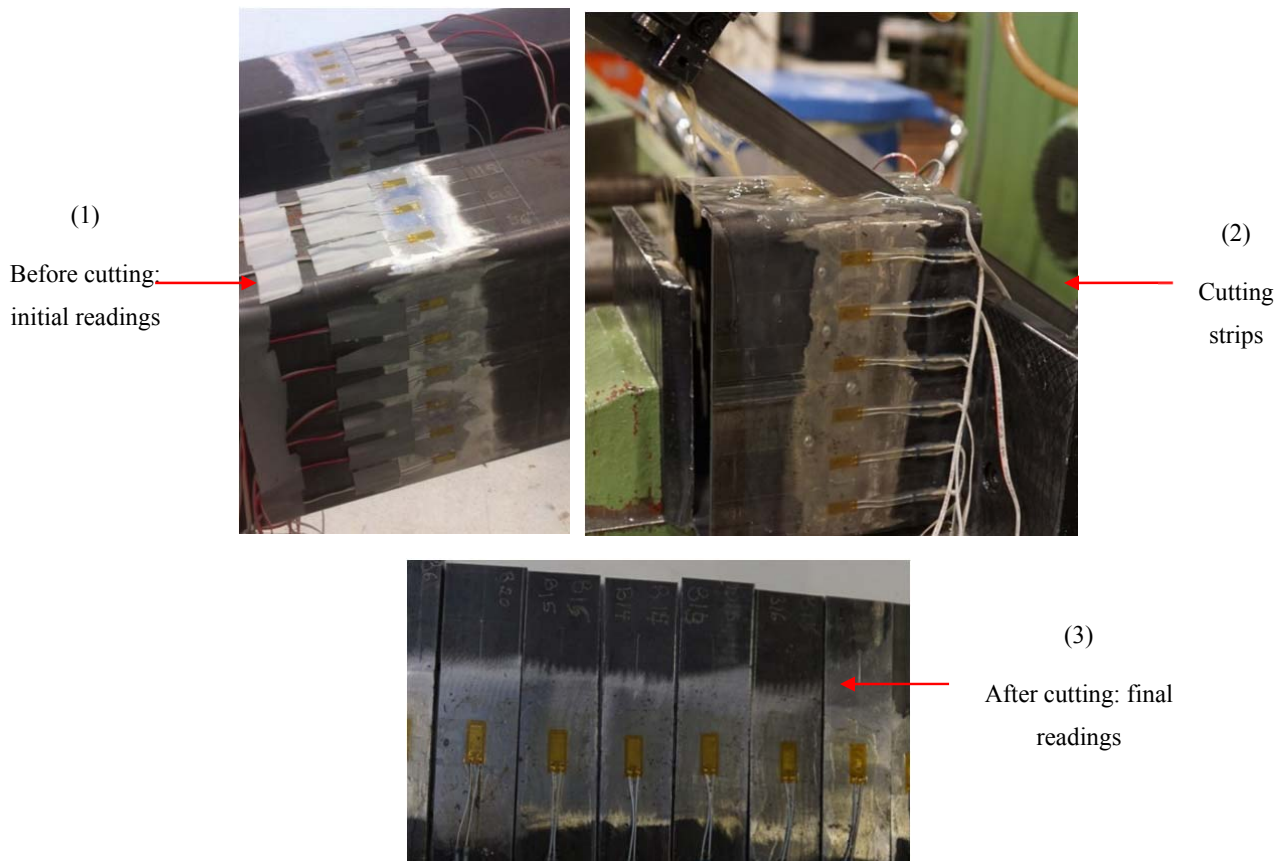


Figure 58 – Electrical strain measurements

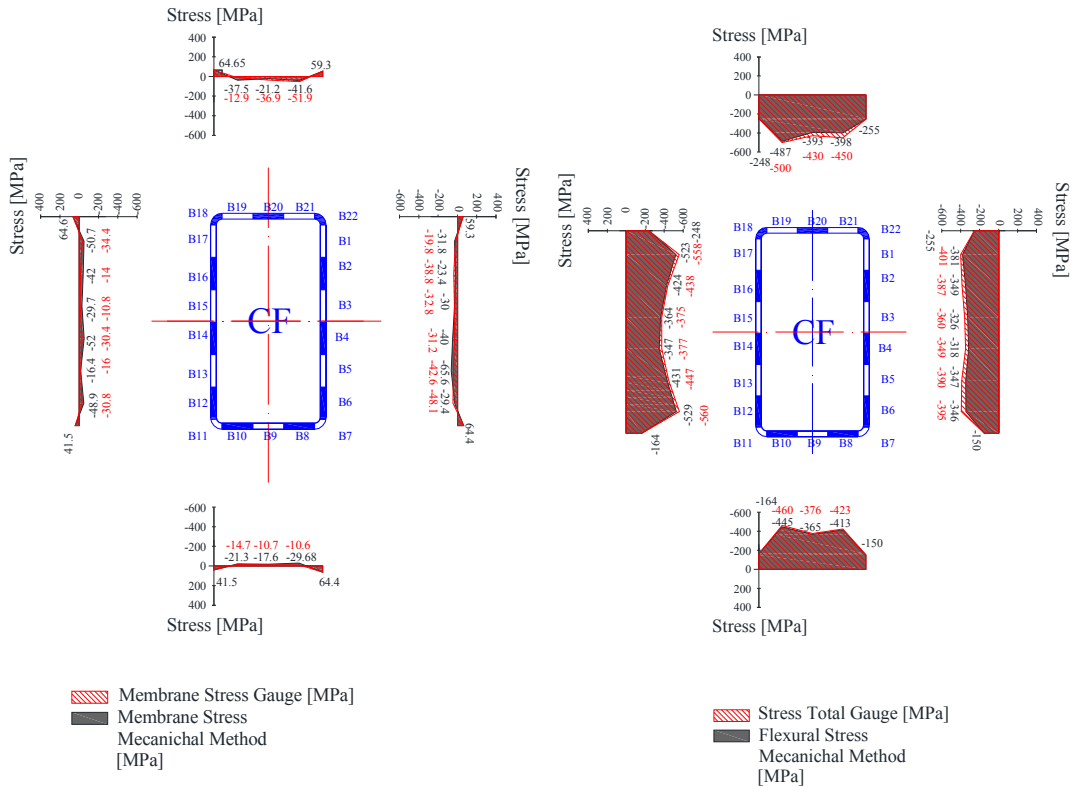


Figure 59 – Mechanical and electrical measured stresses – a) membrane (right column) – b) flexural/total (left column) stresses of RHS CF 220x120x6

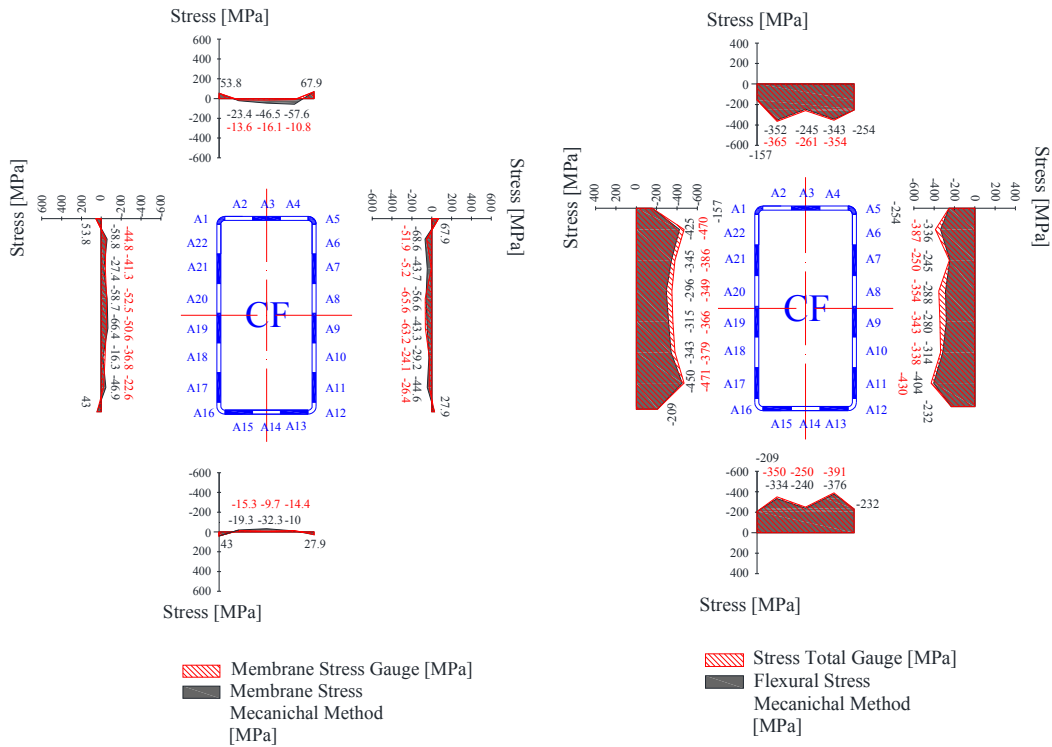


Figure 60 – Mechanical and electrical measured stresses – a) membrane (right column) – b) flexural/total (left column) stresses of RHS CF 200x100x4

The measured magnitudes were inevitably affected by several testing uncertainties, explaining the differences between the membrane residual stresses obtained mechanically and their counterparts obtained through electrical strain gauges. The main reasons behind these differences are laboratory measurements errors, especially the way of holding the extensometer, the variation of the inclination of the extensometer before and after cutting, etc. The extensometer had also an accuracy of $\pm 5 \mu m$. This precision value did not affect significantly the residual stresses in the corners as much as those found in the flat faces, because of the small magnitudes measured in the flat faces, especially with respect to membrane residual stresses measurements.

As previously mentioned, the distribution of residual stresses induced by the forming process was investigated for two cross-sections shapes RHS CF 200x100x4 and RHS CF 220x120x6. For both considered sections, an attempt to quantify the non-equilibrated membrane stresses has been made through the calculation of the ratio representing the percentage of non-equilibrated stresses over the total stresses:

$$\frac{\sum (b_i \sigma_{tension_i} + b_i \sigma_{compression_i})}{\sum (|b_i \sigma_{tension_i}| + |b_i \sigma_{compression_i}|)} \quad (162)$$

where b_i represents the strip width and $\sigma_{tension_i}$, $\sigma_{compression_i}$ the tension and compressive stresses measured on each strip.

This ratio calculated herein represents a quantitative way to evaluate and assess the reliability of the measurements. It helps getting an idea of how accurate the measurements are, i.e. assess the level of confidence of these values.

A constant (measured) stress value was considered over the strip width based on the measurement of one single point on the whole strip. Figure 61 illustrates the adopted block representation for the calculation of the non-equilibrated stresses for both cross-sections shapes considered.

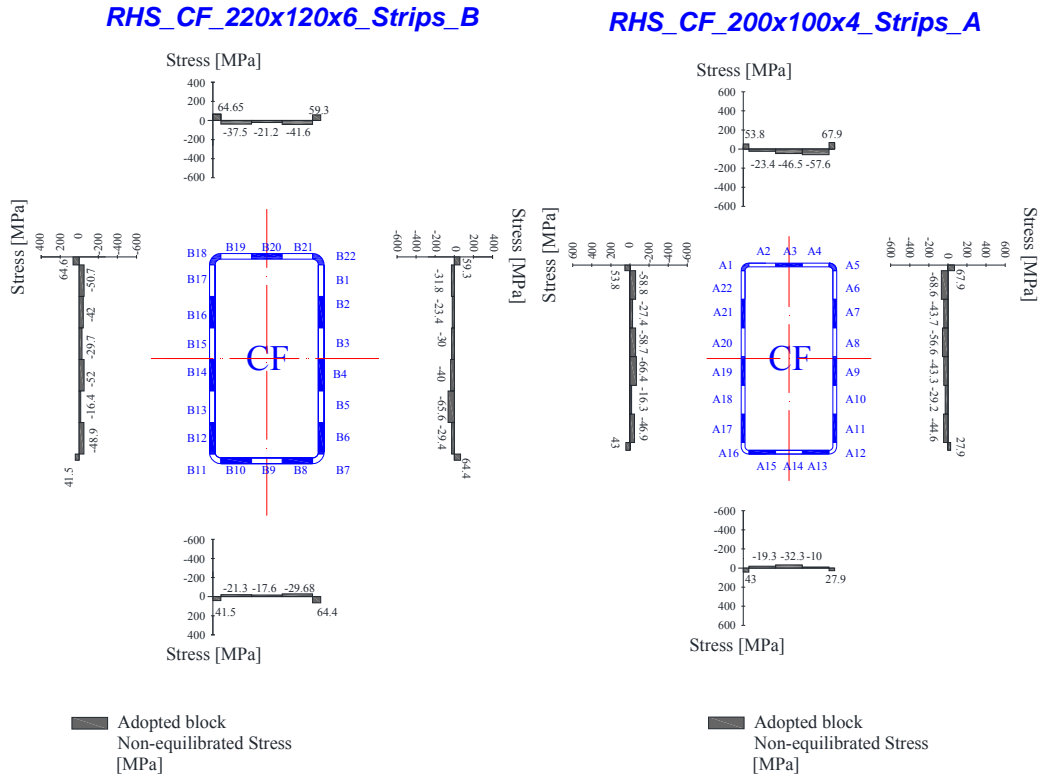


Figure 61 – Adopted block representation for the calculation of the non-equilibrated stresses for specimens – a) RHS CF 220x120x6 – b) RHS CF 200x100x4

Table 22 summarizes the obtained percentages of non-equilibrated stresses obtained and the lowest percentage that can be reached depending on the influence of the precision factor for both RHS sections by using Equation (162).

Table 22 – Percentage of non-equilibrated stresses

Profile	% of non-equilibrated stresses	Lowest % of non-equilibrated stresses
RHS CF 220x120x6	46.46	6.86
RHS CF 200x100x4	57.02	13.72

One may observe from the table that the percentages obtained are quite high. However, this does not necessarily indicate poor results. The main reasons behind these differences are laboratory measurement errors, especially the way of holding the extensometer, the variation of the inclination of the extensometer before and after cutting, etc. The extensometer had also an accuracy of $\pm 5 \mu m$. Therefore, the corresponding measured membrane values might decrease or increase depending on the precision factor; thus, the obtained percentage of non-equilibrated stresses would vary as well. One may notice that the high percentage (46.46 %)

reached for the profile RHS CF 220x120x6 might decrease to (6.86 %) and the percentage (57.02 %) reached for the profile RHS CF 200x100x4 might decrease to (13.72 %) along with the corresponding measured values.

It is to be noted that mechanical measurements have a better level of reliability when the strips were subjected to high values of residual stresses and therefore had a large variation in length (the influence of the accuracy of $\pm 5 \mu m$ is less pronounced for large variation in length), while electrical measurements give more accurate results for the low values of released stresses. Accordingly, electrical and mechanical measurements' pairs complete each other and improve confidence in the measurements.

3.3.5. Stub column tests

Twelve compression tests were performed on stub columns extracted from all different cross-section shapes. The length of the tested specimens was chosen equal to three times the largest cross-sectional dimension, based on the principle that the length is sufficiently small to prevent member buckling while long enough to avoid an important influence of the boundary conditions and leave the development of buckling waves free [46]. Prior to testing, each member length, dimensions and weight were measured and used for the calculation of the area assuming a density of 7850 kg/m^3 . The maximum loads obtained during the tests were then compared to the actual expected N_{pl,f_y} (i.e. obtained in combining the measured value of f_y to the measured section area), and to the nominal expected load $N_{pl,355}$ (i.e. obtained in combining the nominal value of f_y to the nominal section area). The ends of each stub were carefully manufactured. A flat marble stone was used to ensure that the faces were parallel and were as plane as possible to avoid minor and major axis rotations as well as twist rotations and warping.

The specimens were set in a 5000 kN hydraulic machine to apply compressive axial force to the stub column specimens. Two milled flat plates $250 \times 250 \times 150$ have been placed to the ends of each specimen in order to protect the testing machine surface and to ensure a uniform distribution of the load. Four transducers were positioned on the stub ends to measure the axial shortening of the specimens, and two strain gauges were attached at the mid-length of the specimen's adjacent plates. The attached strain gauges provided the load displacement behaviour of the specimen in the elastic range in order to assess the (indirect) corresponding Young's modulus. Figure 62 shows an example of a stub column during testing and

Figure 63 illustrates the failure shapes of all tested specimens. For stocky sections, local buckling occurred near the ends of the specimens.

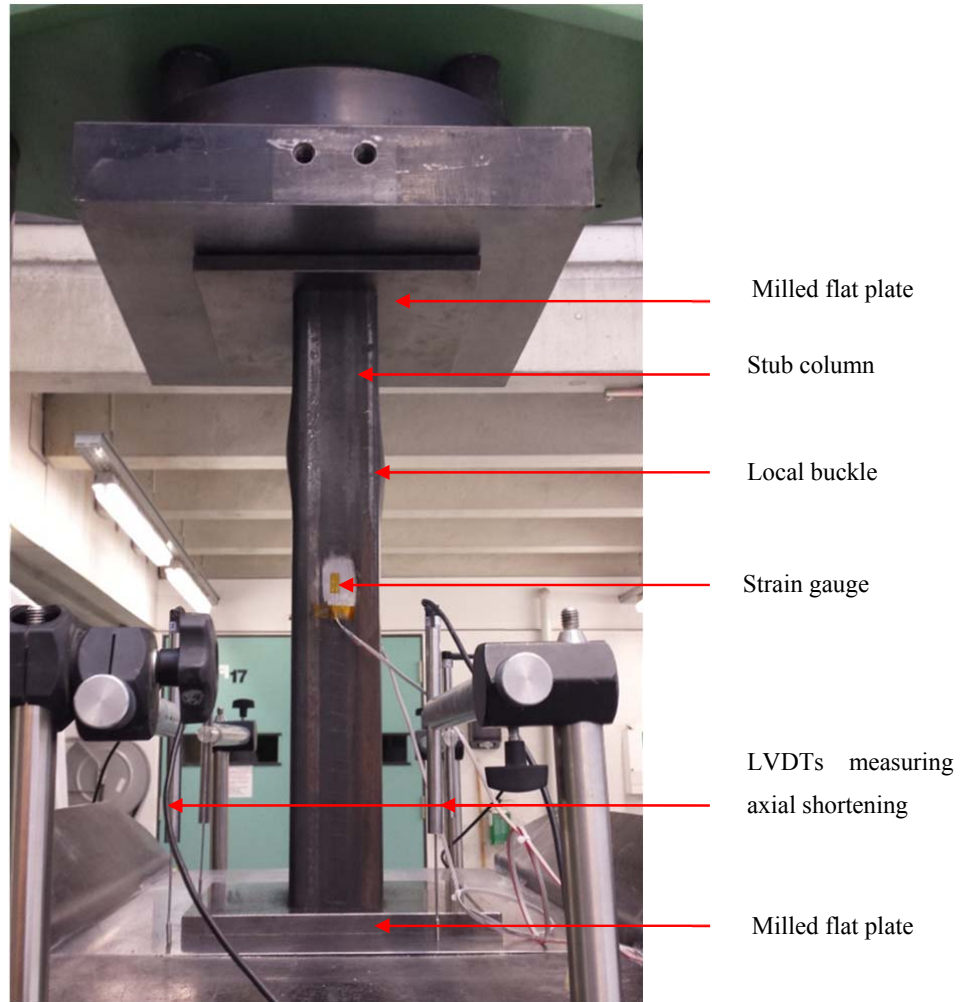


Figure 62 – General stub-column test setup

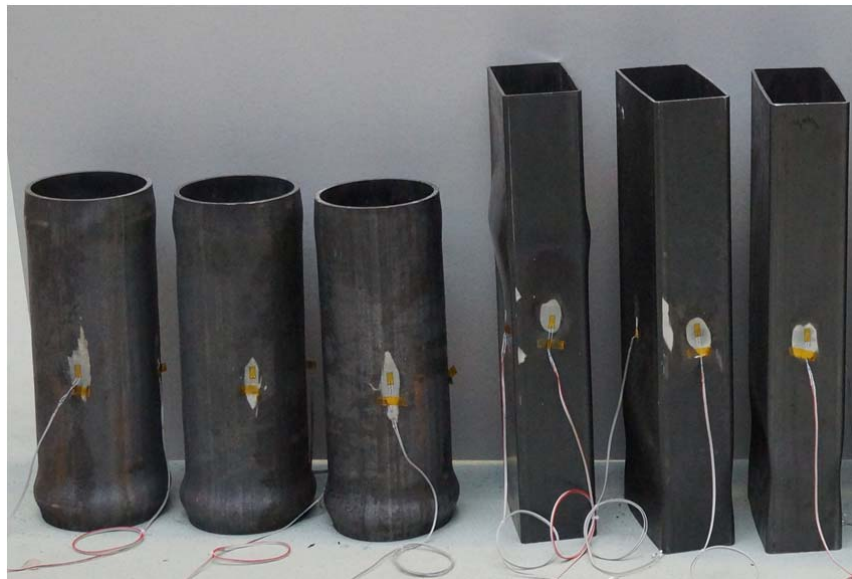




Figure 63 – Failure shapes of all stub columns

The recorded deformations obtained from the LVDTs were different from the ones registered by the strain gauges. A correction combining both sets of measurements described by the Centre for Advanced Structural Engineering ([47], [48] & [49]) was required. The strain gauges provide the correct initial Young's modulus slope since they were directly in contact with the column faces; however, the LVDTs provide good post-yield information but include the elastic deformation of the end plates leading to an incorrect initial Young's modulus value. The method consists in a correction factor k that represents the undesired displacement, which is then deduced from the end displacement:

$$k = \frac{L}{2} \left(\frac{1}{E_{LVDT}} + \frac{1}{E_{SG}} \right) \quad (163)$$

$$\delta_c = \delta_{LVDT} - 2kf \quad (164)$$

In Equation (163), E_{LVDT} represents the initial Young's modulus calculated from the LVDTs readings and E_{SG} is the initial Young's modulus calculated from the strain gauges. In Equation (164), f represents the applied stress N/A . The corrected end displacement δ_c is then the difference between the LVDT displacements δ_{LVDT} and the set-up displacement. Table 23 reports the obtained stub column failure loads and also allows to compare the maximum capacity obtained during the tests with the actual load $N_{pl, actual}$ and with the nominal expected load $N_{pl, nominal}$.

Table 23 – Stub column test results

Specimen	Length [mm]	Weight [kg]	Calculated area ¹ [mm ²]	$N_{pl, actual}$ [kN]	$N_{pl, nominal}$ [kN]	N_{exp} [kN]	$N_{exp} / N_{pl, actual}$	$N_{exp} / N_{pl, nominal}$
RHS_Stub_CF_200x100x4	603	10.4	2197	1044	780	770	0.74	0.99
RHS_Stub_CF_200x100x4	601	10.4	2204	992	783	765	0.77	0.98
RHS_Stub_CF_200x100x4	598	10.3 5	2205	1058	783	775	0.73	0.99
RHS_Stub_CF_220x120x6	660	19.15	3696	1663	1312	1608	0.97	1.23
RHS_Stub_CF_220x120x6	657	19.05	3694	1705	1311	1622	0.95	1.24
RHS_Stub_CF_220x120x6	659	19.1	3692	1652	1311	1611	0.98	1.23
CHS_Stub_HR_159x5	475	10	2682	1070	952	1233	1.15	1.29
CHS_Stub_HR_159x5	478	10	2665	1047	946	1220	1.16	1.29
CHS_Stub_HR_159x5	475	9.95	2668	1082	947	1162	1.07	1.23
CHS_Stub_HR_159x6.3	474	11.65	3131	1240	1111	1481	1.19	1.33
CHS_Stub_HR_159x6.3	474	11.41	3066	1191	1089	1437	1.21	1.32
CHS_Stub_HR_159x6.3	476	11.5	3078	1211	1093	1470	1.21	1.35

¹ The calculated areas were determined by dividing the weight of the specimens by their measured lengths and density ($G = 78.5 \text{ kNm}^3$).

Figure 64 plots the load N versus the stubs end shortening δ before and after correction and Figure 65 represents the normalized axial load N / N_{pl}^7 versus the measured strain $\varepsilon / \varepsilon_y$ (ε_y being the strain level at first yield).

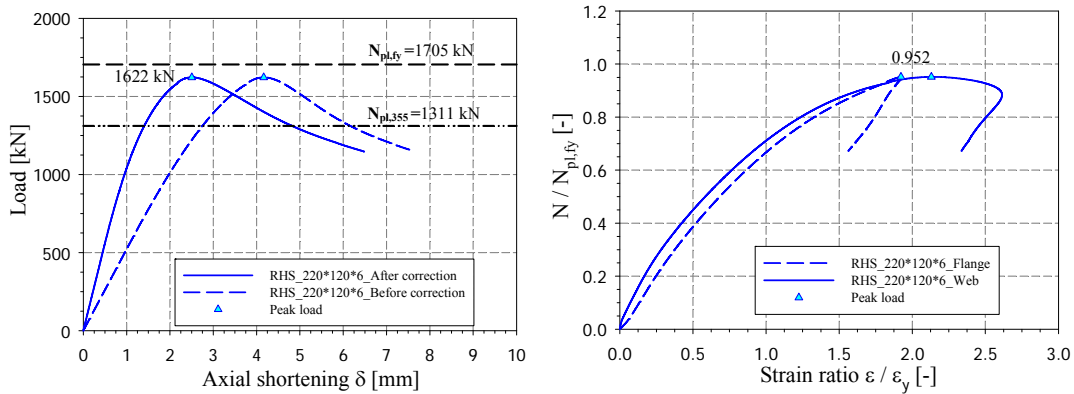


Figure 64 – Stub column test results – RHS CF 220x120x6 T5 – a) load displacement curve before and after correction – b) strain gauges measurements

⁷ N_{pl} is the product of the cross-section area A and the tensile coupon yield stress f_y .

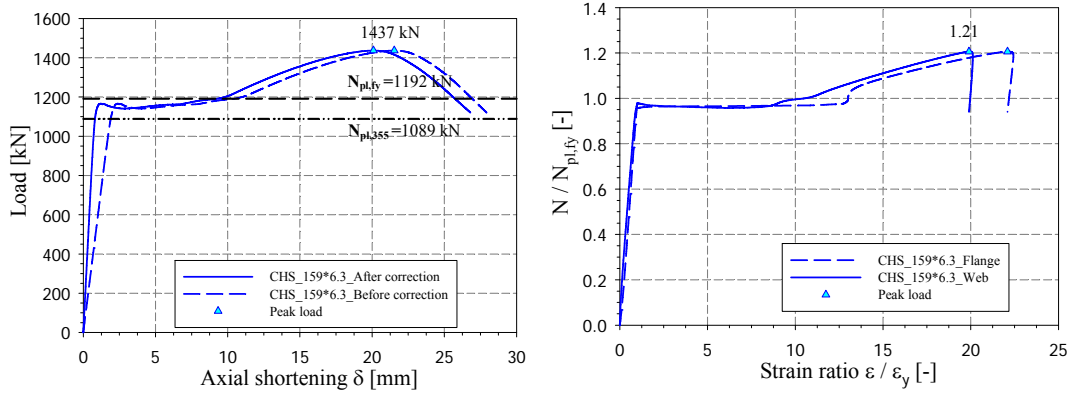


Figure 65 Stub column test results – CHS HR 159x6.3 T11 – a) load displacement curve before and after correction – b) strain gauges measurements

All stub columns failed by local buckling either prior to or subsequent to the onset of yielding. For the non-slender cases, deviation from the material curve occurred approximately at ultimate load where there is the onset of local buckling. For the slender cases, local buckling occurred in the elastic range, and deviation from the stress-strain curve may be followed by considerable post-buckling deformation. Deviations for the material stress-strain are obviously also due to other several effects including geometric imperfections, inelastic material behaviour and post-buckling response [3]. Some examples of material stress-strain and stub-strain responses are shown Figure 66 and more details can be found in Annex 6.

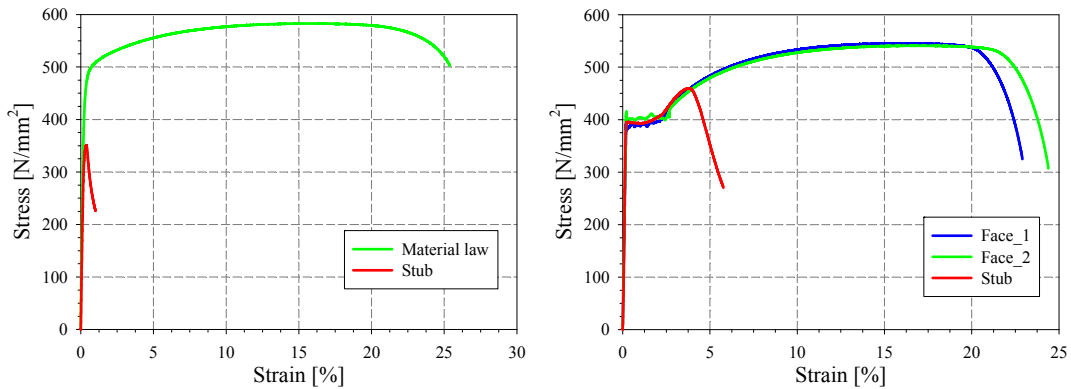


Figure 66 – Material vs. stub stress-strain curves – a) RHS CF 200x100x4 T1 – b) CHS HR 159x5 T7

3.4. Buckling tests

As previously mentioned, six hot-rolled CHS as well as six cold-formed RHS shapes were tested (see Figure 67). Table 24 summarizes the test program of the twelve buckling tests. The ends of the tested columns were milled flat and welded to end plates of 20 *mm* thickness with different eccentricities, according to the desired load case. Mono-axial and bi-axial-bending with axial compression load cases were obtained by applying eccentric compression. The bending moment distributions applied on the members were therefore linear, either constant (equal and same direction eccentricities applied at both end of the specimen) or triangular (eccentricities applied at one end of the specimen only). The end plates were bolted to two hemispherical bearings (hinges) specially designed to provide pinned-pinned end restraints for the test specimens. Each of the two bearings contained two T-shaped grooves, which enabled adjustment of the specimen when bolted to the endplates to achieve loading at the specified eccentricities. The bolts were pre-tensioned in order to prevent uplift or detachment of the specimen endplates from the hemispherical bearings. Figure 68 and Figure 69 illustrate typical specimens' arrangements for the case of a constant and a triangular bending moment distributions.

All twelve columns were tested up to and beyond failure and all readings were taken using an electronic data acquisition system recording at 2 *Hz* pace.

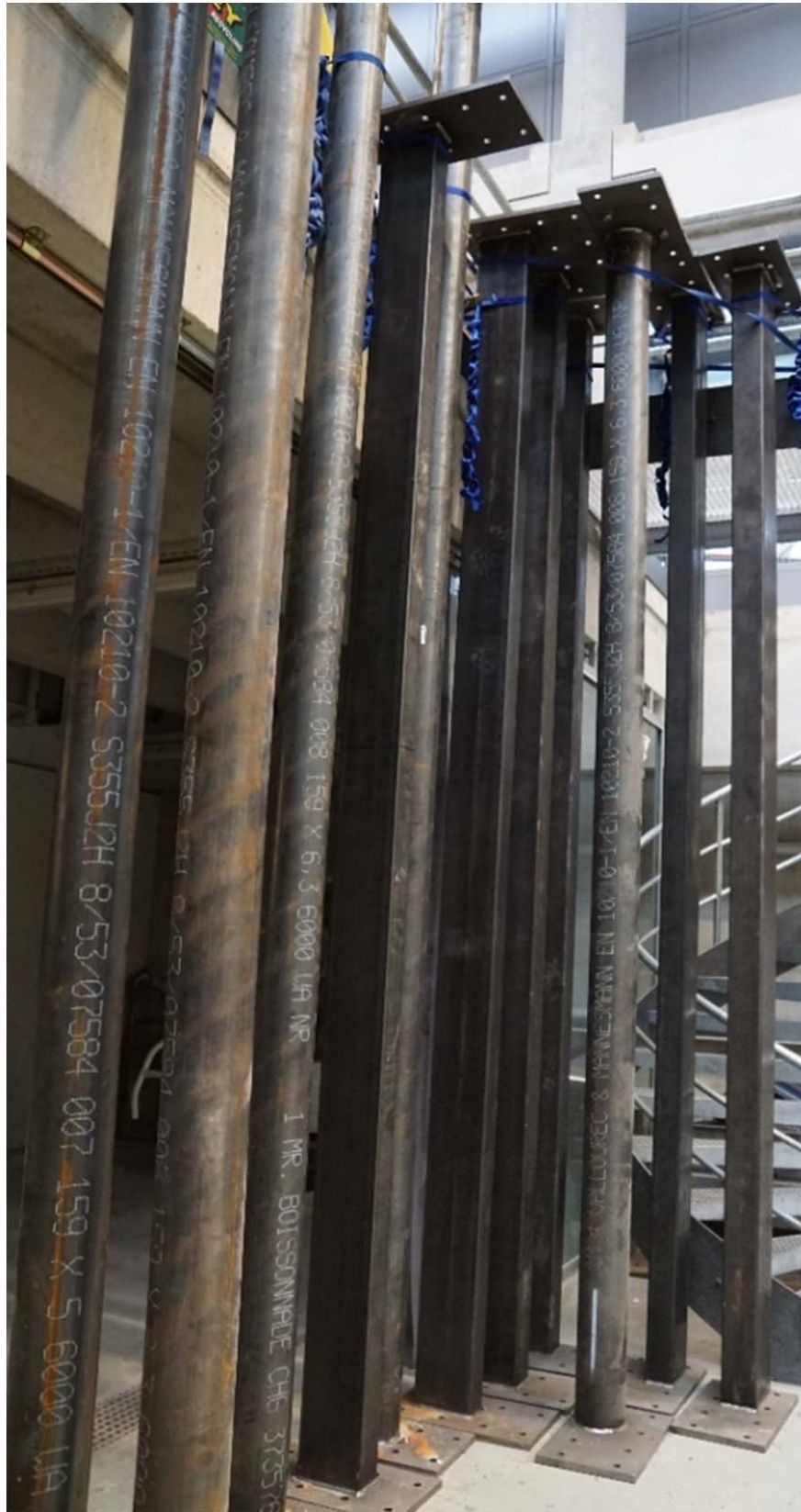


Figure 67 – Beam-column profiles

Table 24 – Test program summary

Cross-section shape	Load case ⁸	Bending moment distribution	Length [mm]	e_z [mm]	e_y [mm]
RHS CF 200x100x4 T1	60%N+40%M _y	Constant	4000	80	0
RHS CF 200x100x4 T2	40%N+30% M _y +30%M _z	Constant	4000	100	40
RHS CF 200x100x4 T3	60%N+40%M _y	Triangular	4000	140	0
RHS CF 220x120x6 T4	60%N+40%M _y	Constant	4000	70	0
RHS CF 220x120x6 T5	40%N+30%M _y +30%M _z	Constant	4000	85	40
RHS CF 220x120x6 T6	60%N+40%M _y	Triangular	4000	120	0
CHS HR 159x5 T7	50%N+50%M _y	Constant	4000	65	0
CHS HR 159x5 T8	50%N+50%M _y	Constant	4900	75	0
CHS HR 159x5 T9	50%N+50%M _y	Triangular	4000	130	0
CHS HR 159x6.3 T10	50%N+50%M _y	Constant	4900	75	0
CHS HR 159x6.3 T11	33%N+33%M _y +33%M _z	Constant	4000	85	55
CHS HR 159x6.3 T12	50%N+50%M _y	Triangular	4000	130	0

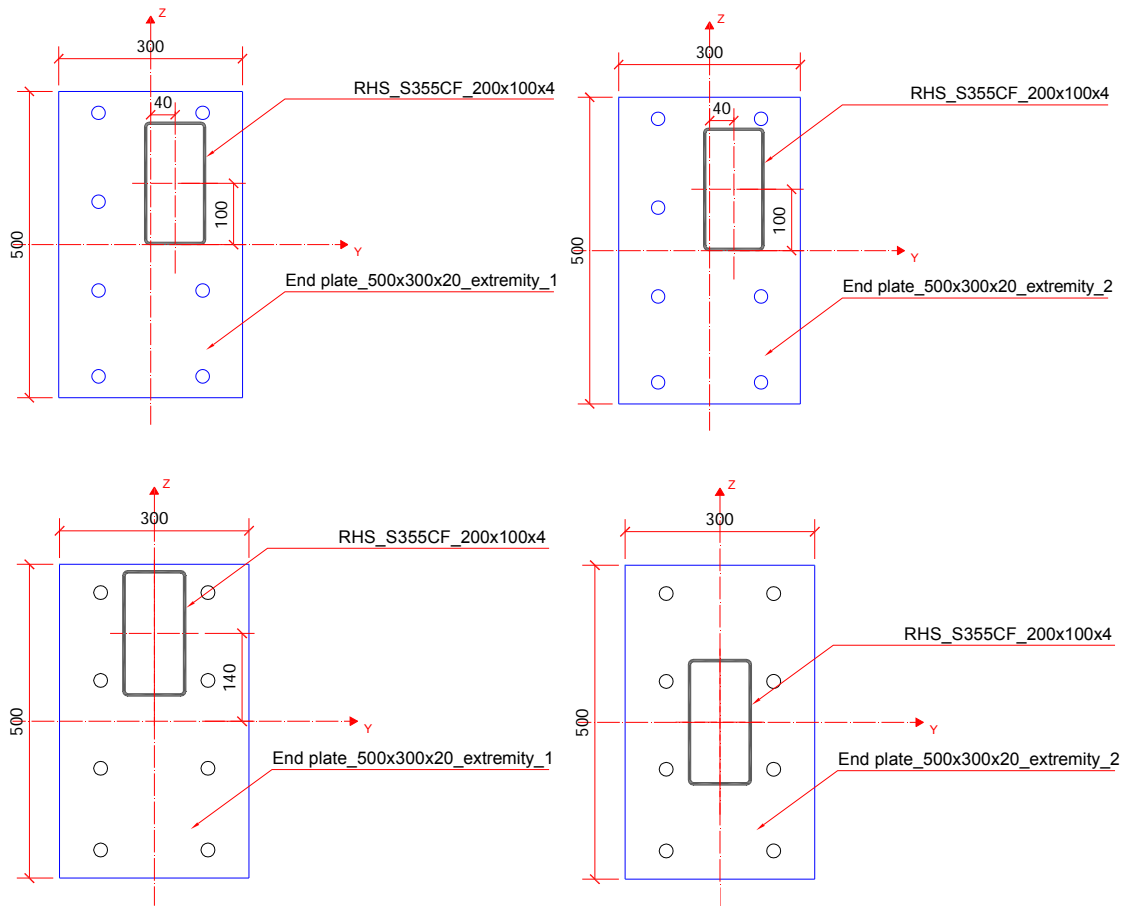


Figure 68 – End plates welded at both extremities – a) RHS CF 200x100x4 T2 (constant bending moment distribution) – b) RHS CF 200x100x4 T3 (triangular bending moment distribution)

⁸ The percentages reported here are relative to the force ratios n , m_y and m_z where $n = N / N_{b,Rd}$, $m_y = K.M_y / M_{y,Rk}$ and $m_z = K.M_z / M_{z,Rk}$.

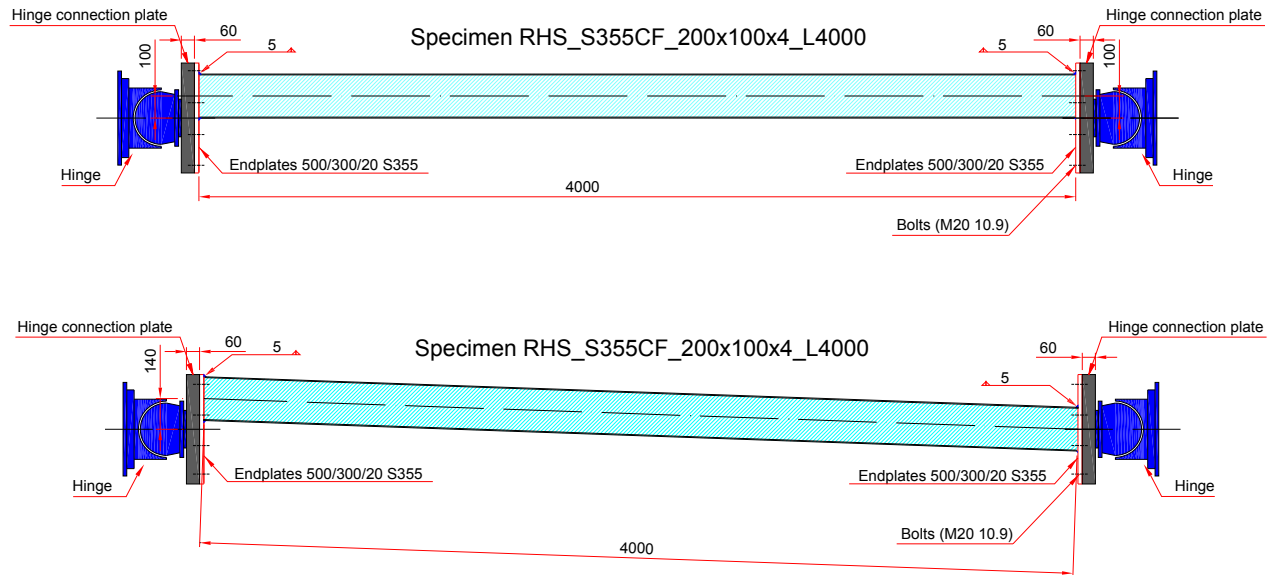


Figure 69 – Typical example of column positioning for the cases of – a) constant bending moment distribution – b) triangular bending moment distribution

3.4.1. Test setup

The test setup is presented in Figure 70 to Figure 72. A purposely-designed rigid frame was built to ensure sufficient bracing of the tested column. The loading rig consisted in a hydraulic jack HDCR 430-160 / 150⁹ fixed at the bottom of the column and used to generate upwards compressive force. Four load cells were located under the jacks to record the force applied. The end plates of the specimen were centered at their bottom and top to two spherical supports¹⁰ (i.e. hinges) specially designed to provide nearly pinned end conditions (see Figure 74). A connecting plate was placed at the bottom of the hinges with two rails (170 mm spaced) meant for bolts retaining the specimen end plates. The bolts were adequately pre-stressed in order to prevent uplift or detachment of the specimens' end plates.

⁹ The hydraulic jack type HDCR 430-160 / 150 has the following properties: lifting capacity = 4,310 kN, stroke = 150 mm.

¹⁰ The hinges were sprayed and greased with Teflon. Preliminary measurements showed that friction could be neglected.

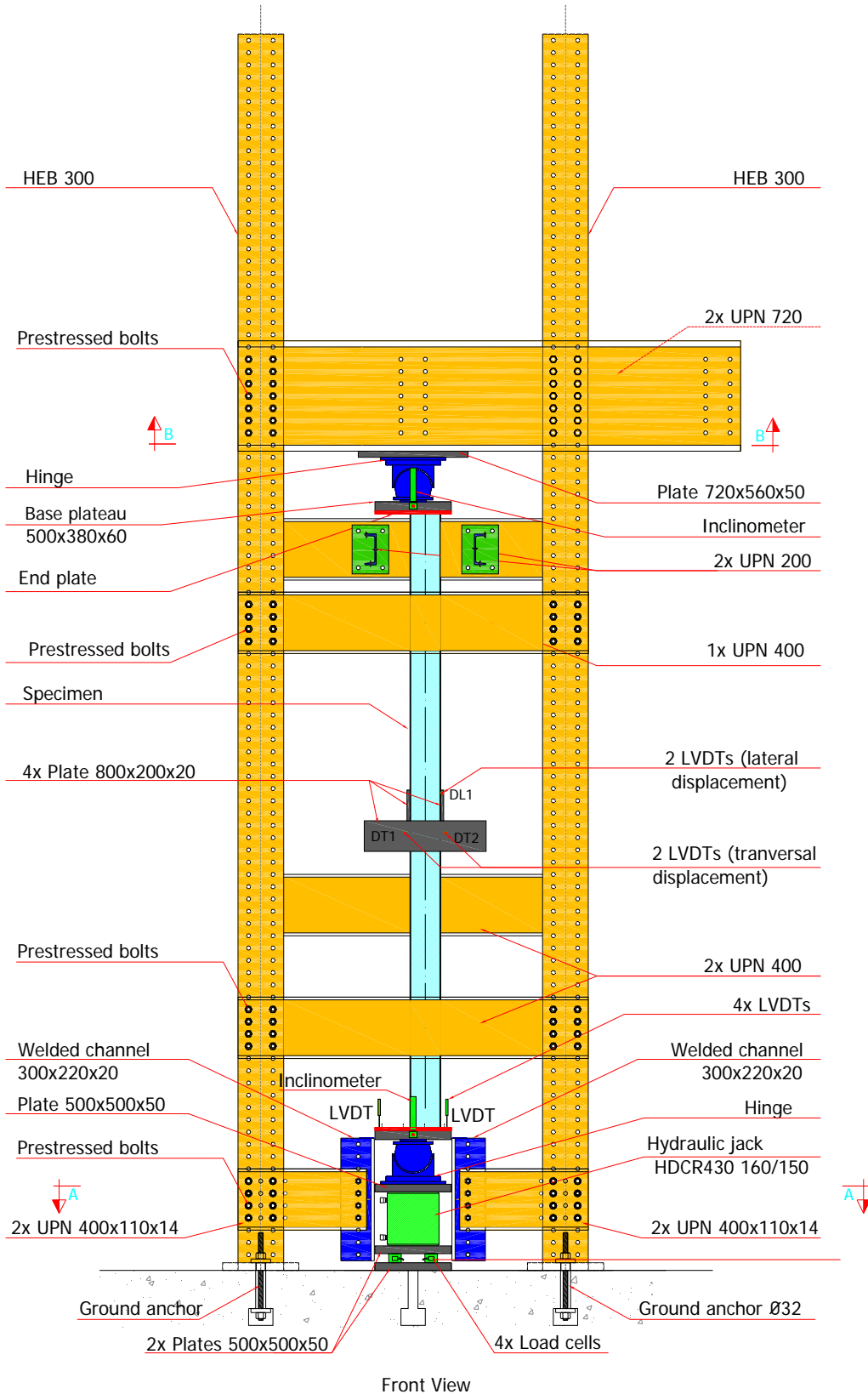


Figure 70 – Front view of test setup

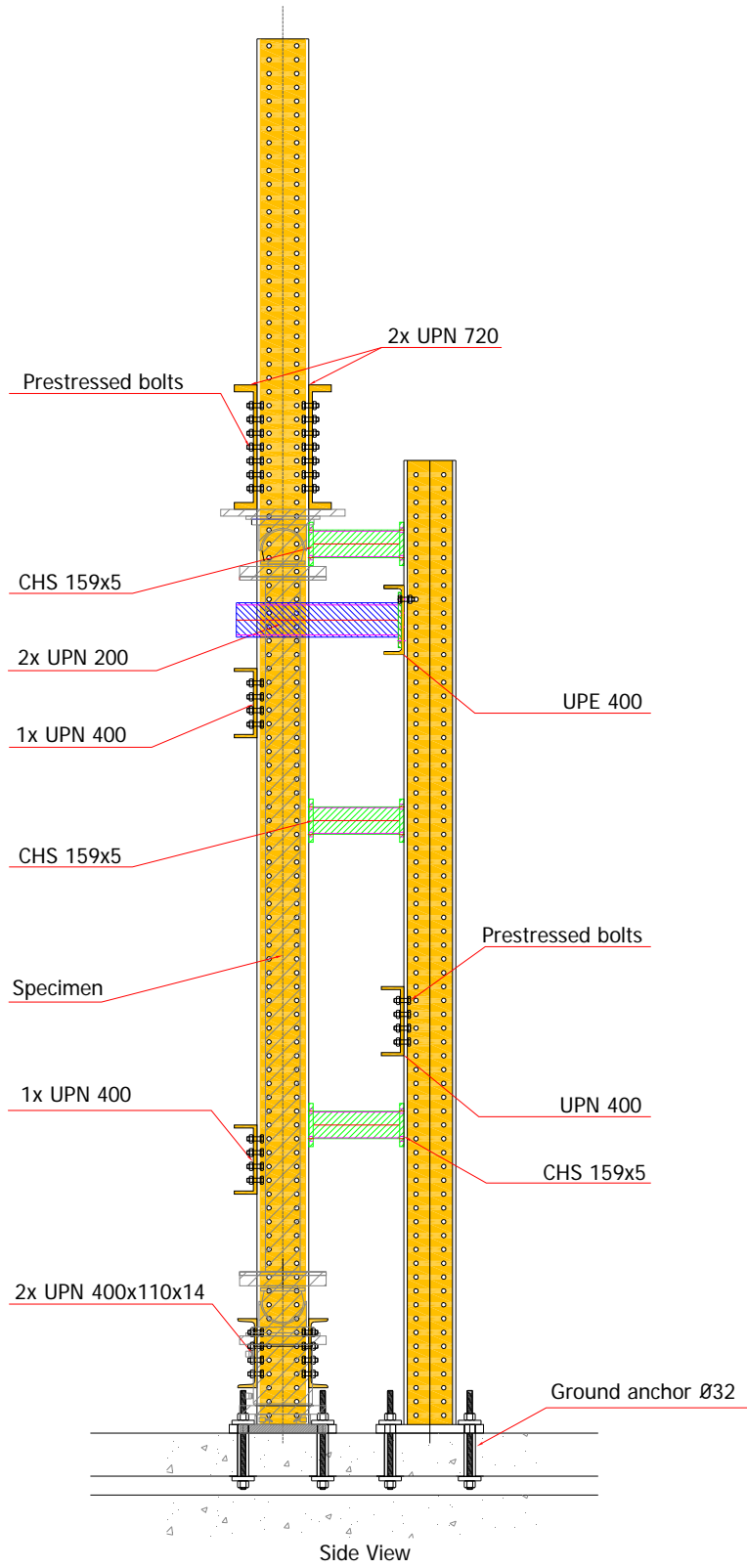


Figure 71 – Side view of test setup

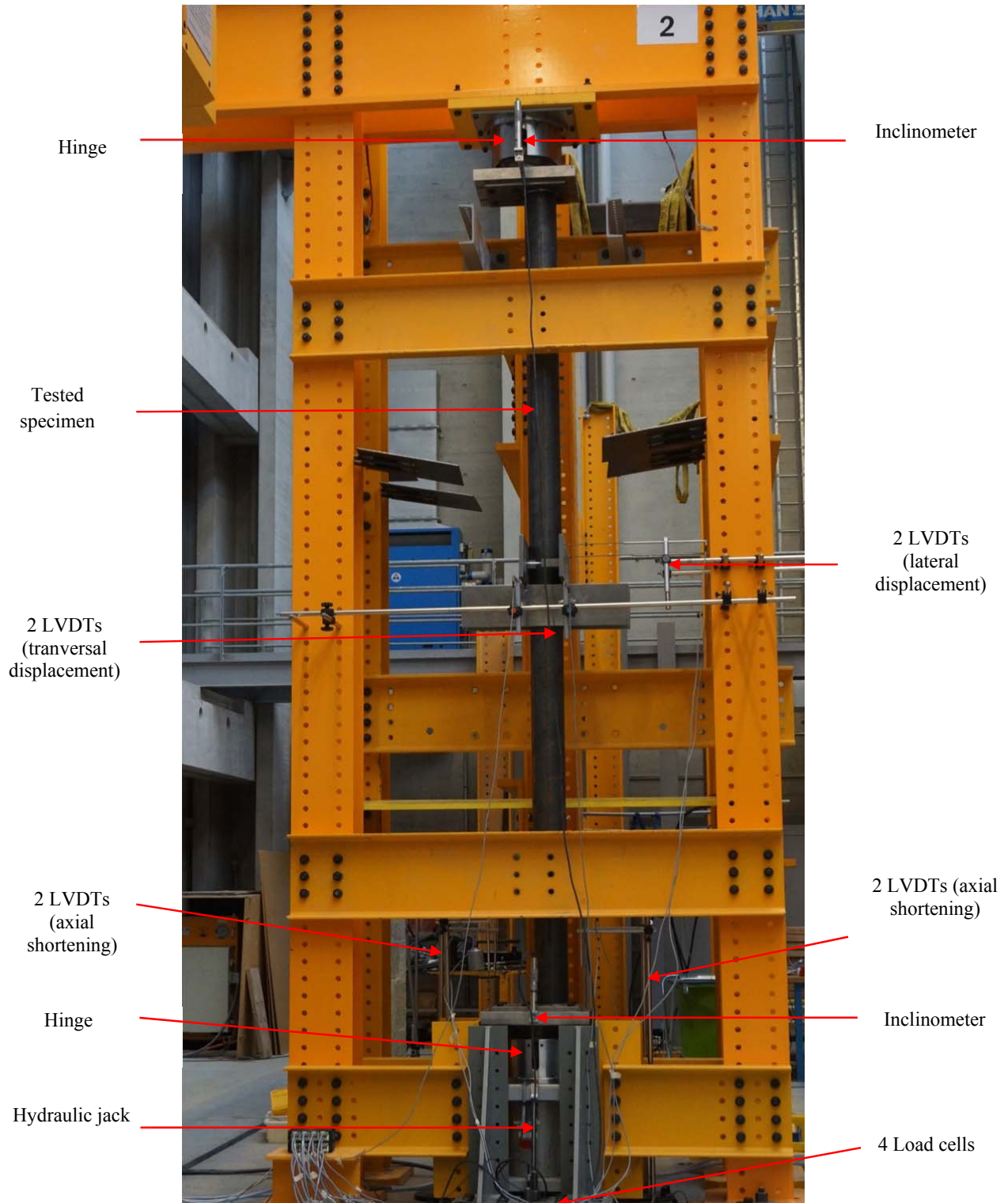


Figure 72 – Overall view of test setup

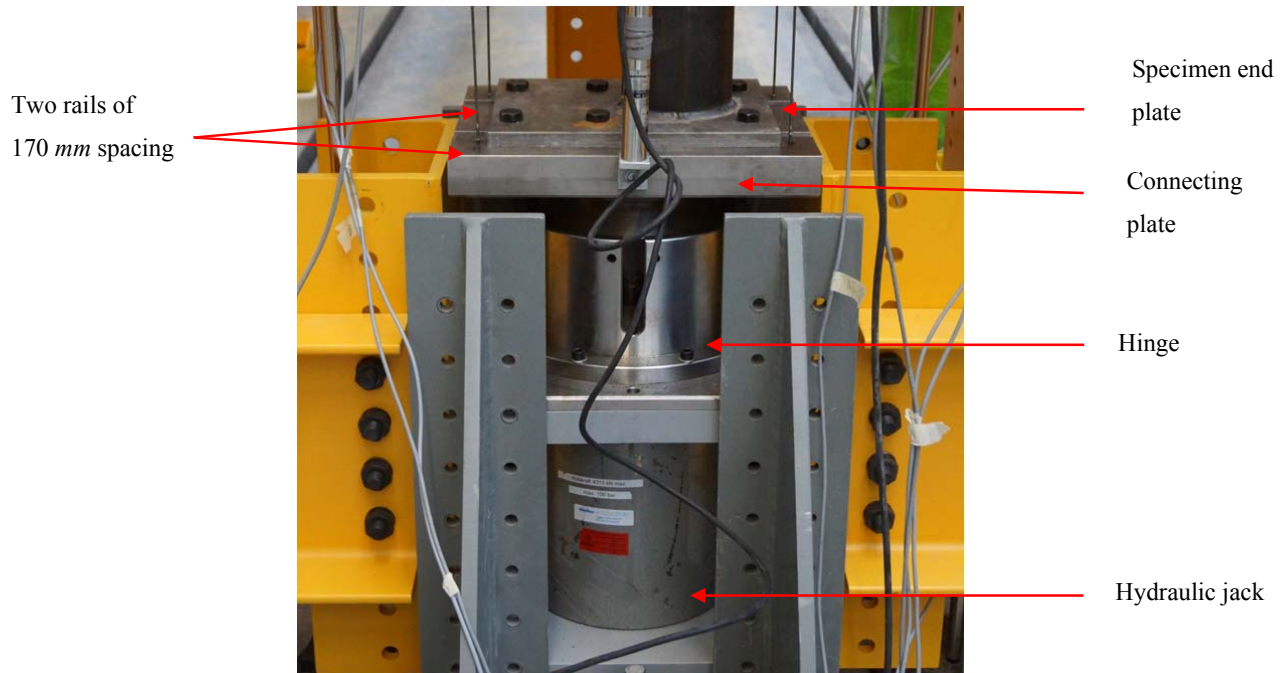


Figure 73 – End plate fixed to bottom hinge plate

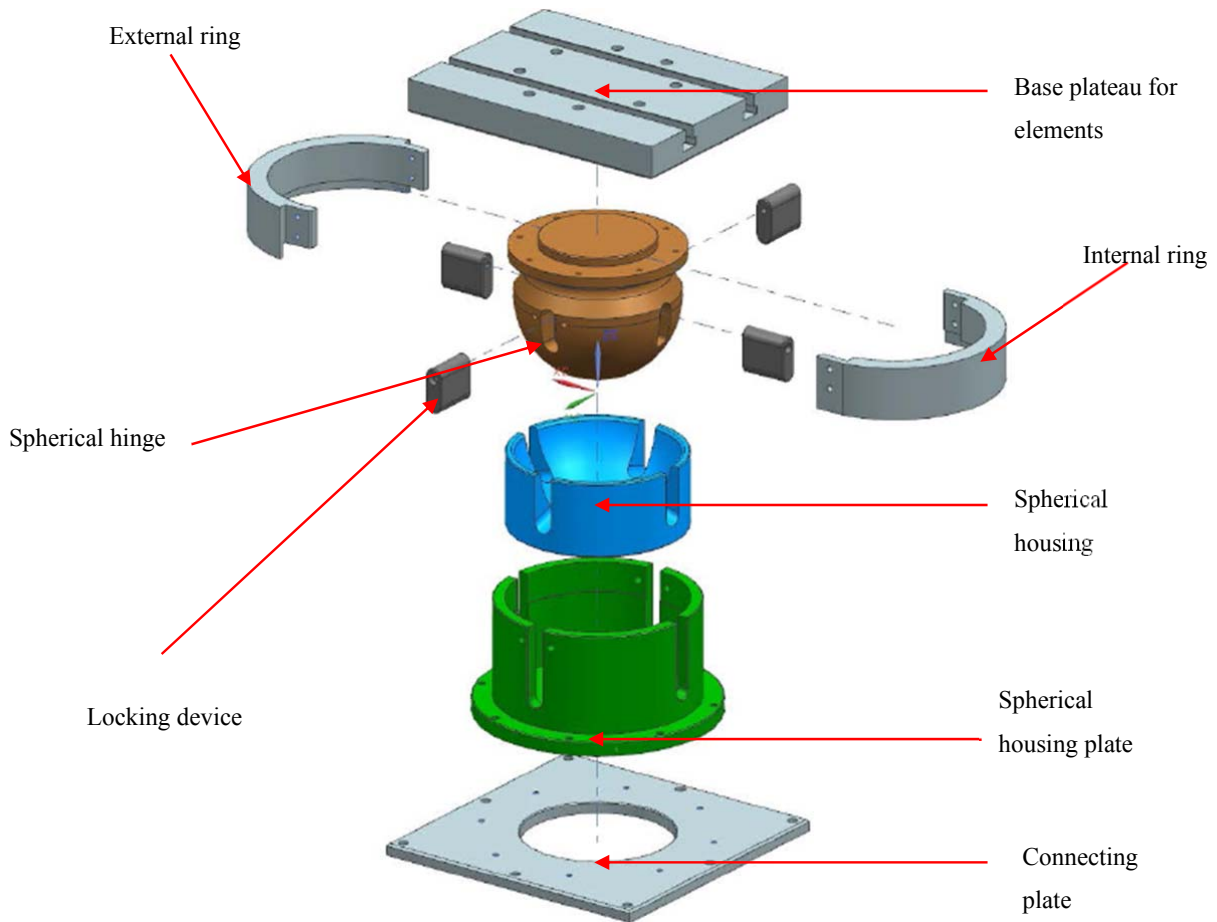
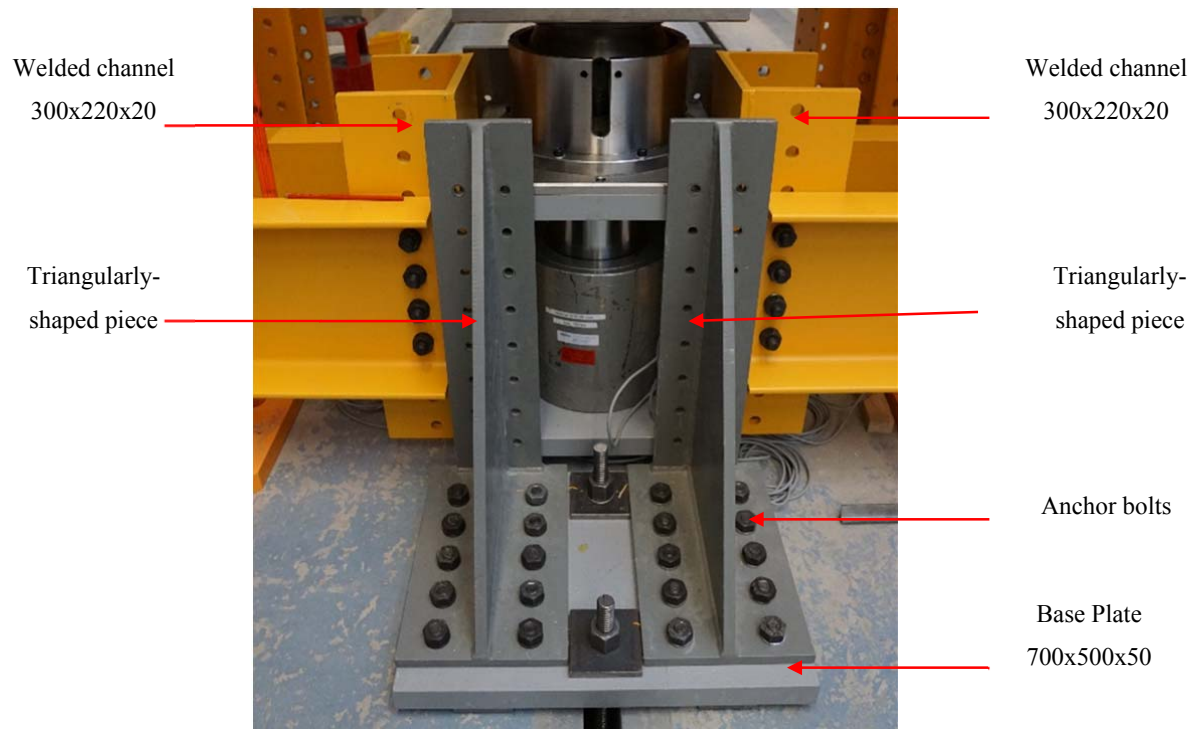
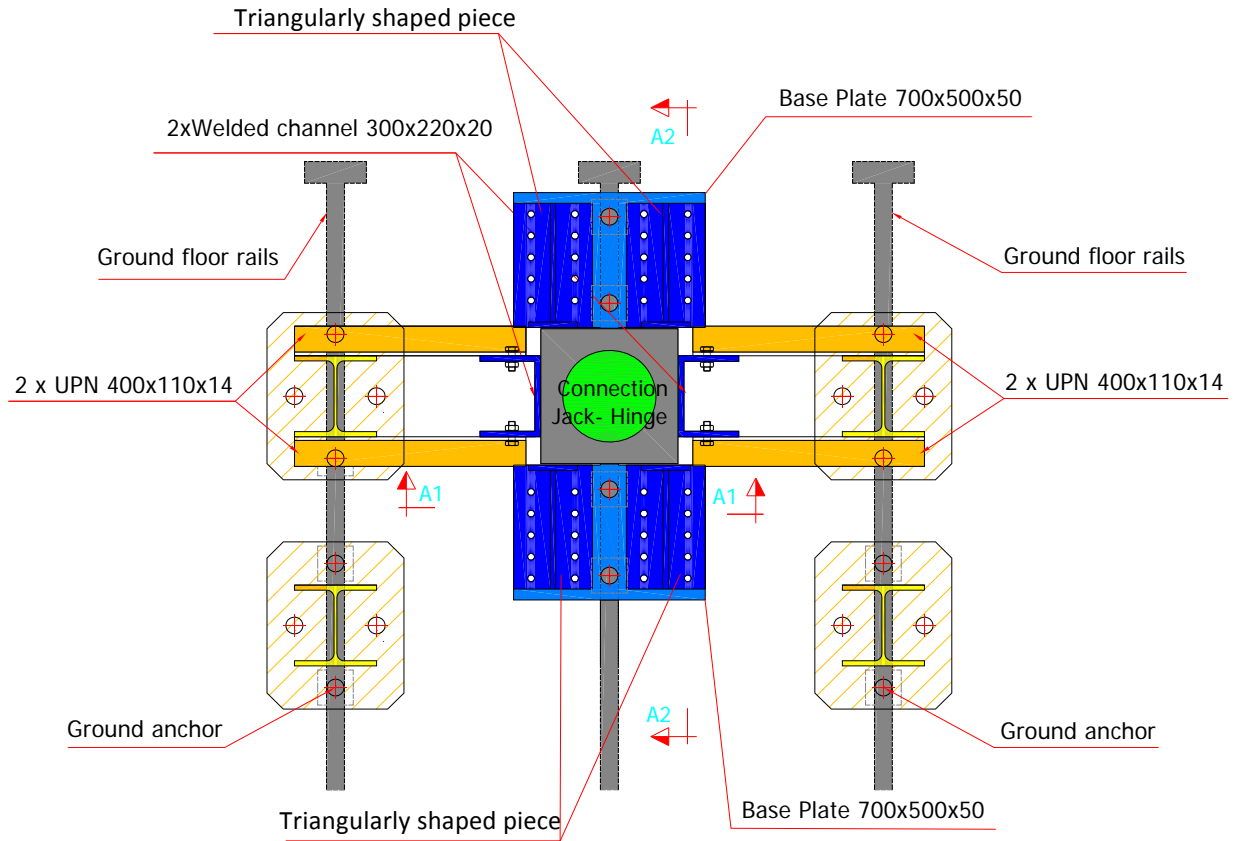


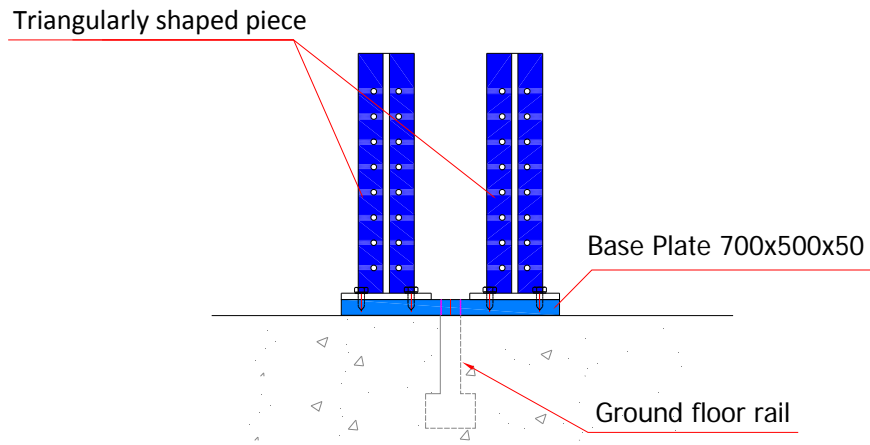
Figure 74 – Hinge detail

Since the hydraulic jack was placed at the bottom extremity, this extremity was free to move vertically. Therefore, and in order to resist to the shear forces arising when the column is tested under compression with triangular bending moment distributions, an additional supporting system aimed at resisting horizontal forces was specially designed, as illustrated in Figure 75. In one direction, these supports were formed by two triangularly-shaped pieces and anchored by threaded bolts to a base plate of dimensions 700x500x50 at each side of the specimen. In the other direction, the supports were made with welded channels 300x220x20 connected at each side of the specimen. Steel pieces were added between the welded channel 300x220x20 and the jack-hinge connection then greased, in order to fill installation gaps and to prevent friction and ensure the vertical displacement of the column during testing.





SECTION A-A



SECTION A1-A1

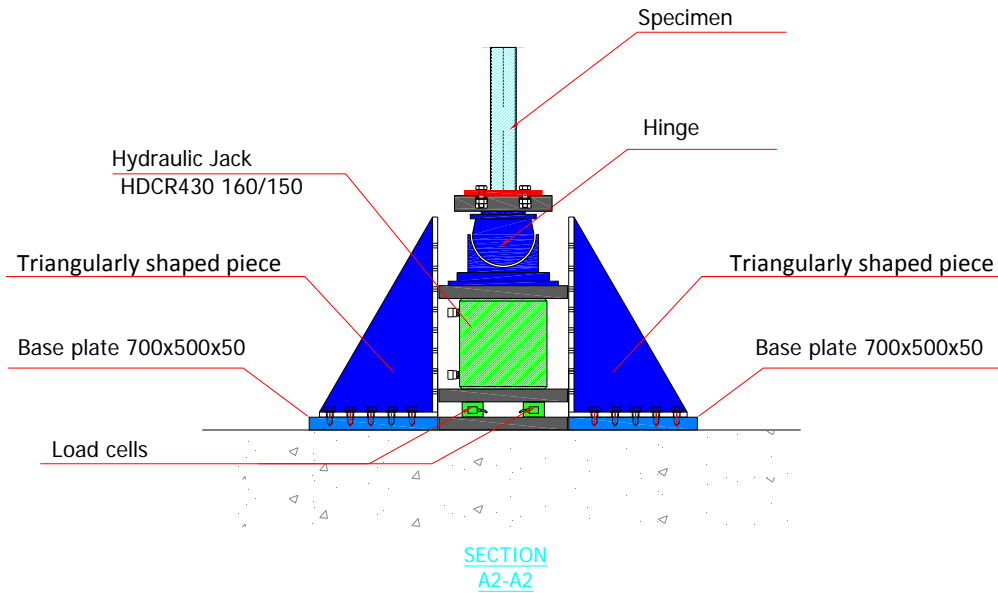


Figure 75 – Embedded support designed to resist shear forces

Figure 76 illustrates the column top end connection where the hinge end plate was anchored to a 720x560x50 plate by threaded bolts, and the plate itself was connected to the two UPN 720 by 8 bolts. In this case, the bolts were designed to resist the shear forces.

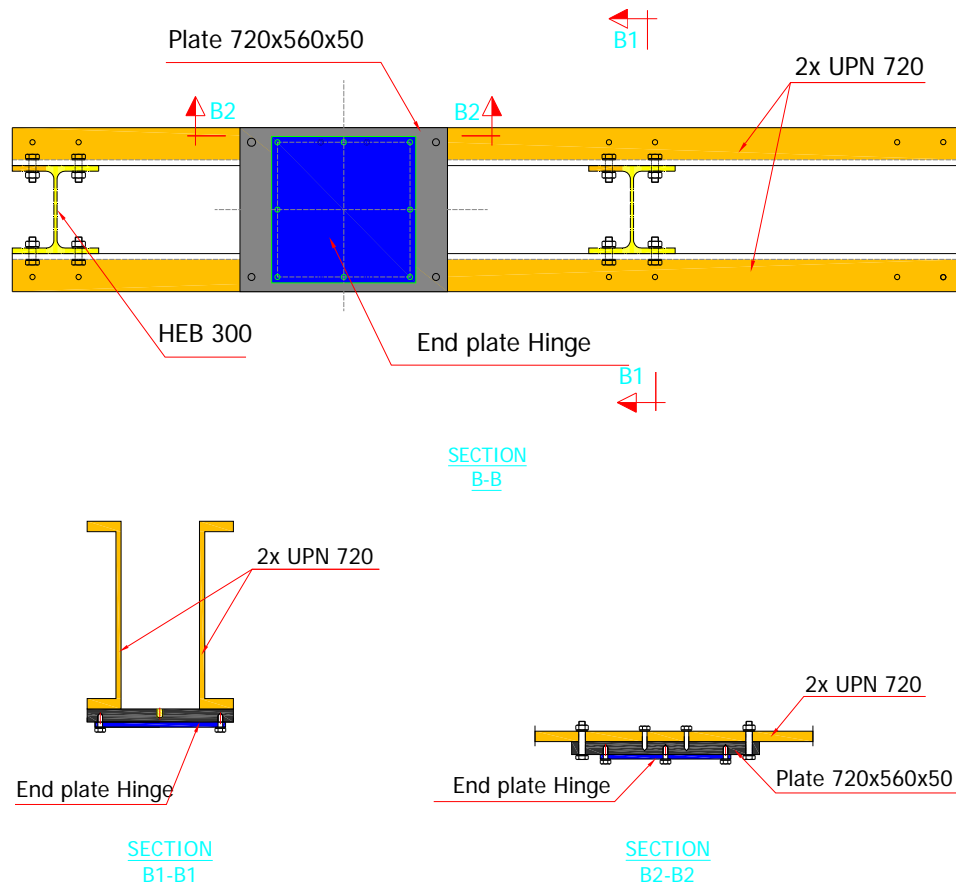


Figure 76 – Upper column end connection

3.4.2. Measurements acquisition

Various transducers were used to monitor the beam's response:

- 4 load cells were located under the jacks to record the applied force;
- inclinometers were fixed at both ends of the column to measure the column end rotations in both principal bending planes;
- 4 linear variable displacement transducers were positioned on the mid-span cross-section, to measure lateral and transversal displacements by means of two independent systems (Figure 77);
- 4 linear variable displacement transducers were positioned on the bottom end plate of the specimen to record the axial shortening and rotations during testing (see Figure 78 and Figure 79).

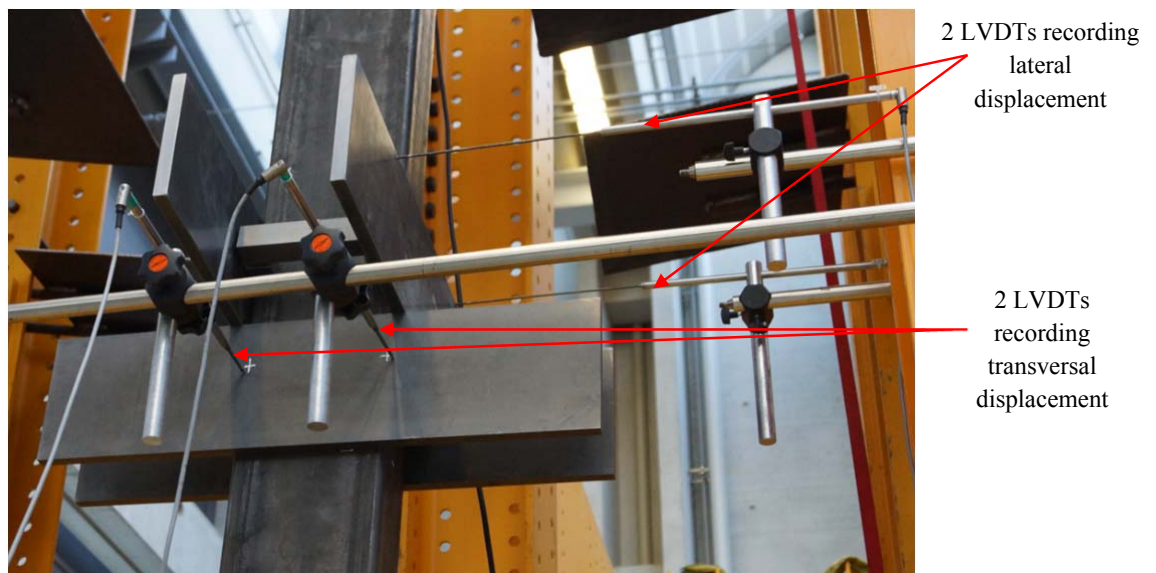


Figure 77 –Measurement of displacements in mid-span cross-section

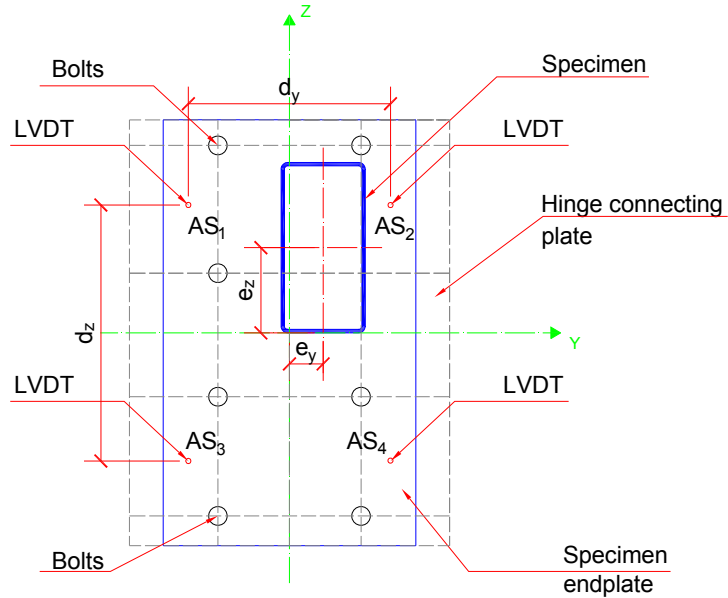


Figure 78 – LVDTs and specimen positions on bottom end plates

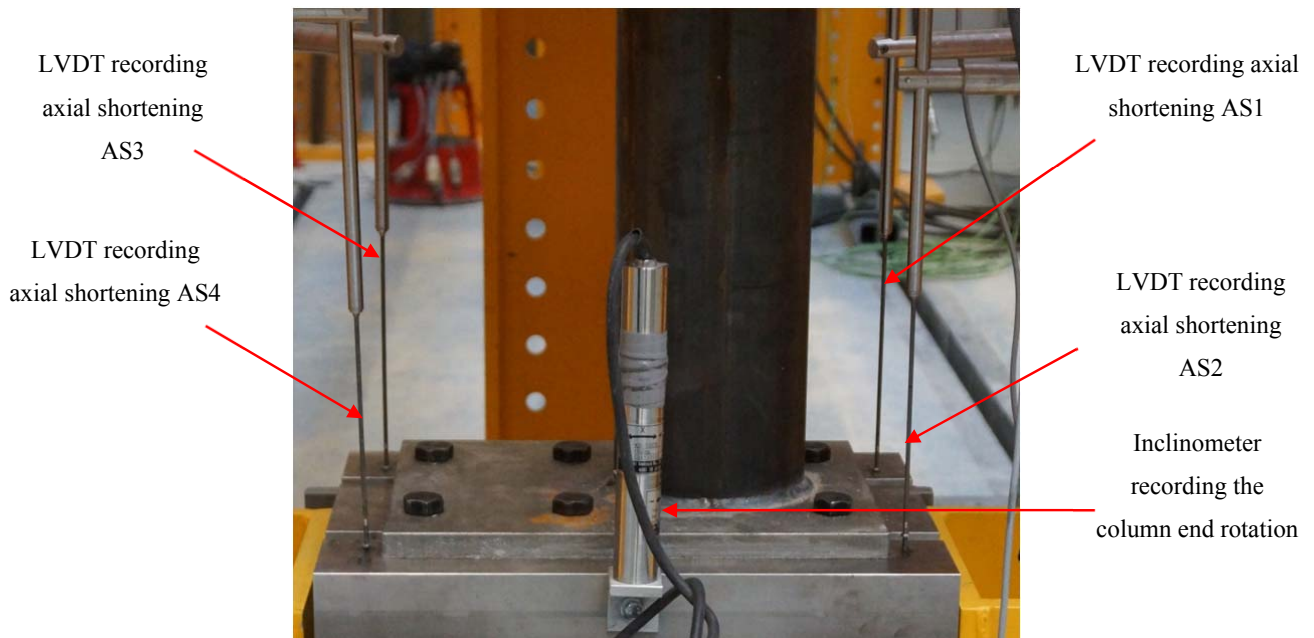


Figure 79 – Measurement of axial shortening

The bottom displacement was calculated as the following average:

$$\Delta = \frac{AS_1 + AS_2 + AS_3 + AS_4}{4} \quad (165)$$

where AS_1, AS_2, AS_3, AS_4 are the displacements of the bottom LVDTs (see Figure 78).

The rotations about major and minor axes at the bottom plate were calculated using Equation (166):

$$\theta_z = \frac{1}{d_y} \left[\frac{AS_1 + AS_3}{2} - \frac{AS_2 + AS_4}{2} \right] \text{ and } \theta_y = \frac{1}{d_z} \left[\frac{AS_3 + AS_4}{2} - \frac{AS_1 + AS_2}{2} \right] \quad (166)$$

where d_z , d_y are the distances respectively between the LVDTs in both principal directions, and θ_z , θ_y are the bottom rotations around Z and Y axes.

The values recorded with the LVDTs had to be geometrically corrected, with respect to the level of rotation reached. The corrections were quite negligible for almost all specimens since no important rotations were developed. LVDT rotations were compared to the rotations obtained with the inclinometers. Figure 80 illustrates the displacements measured by the four bottom LVDTs as well as the corresponding average displacement for the specimen CHS HR 159x6.3 T11. The complete set of results is provided in Annex 6.

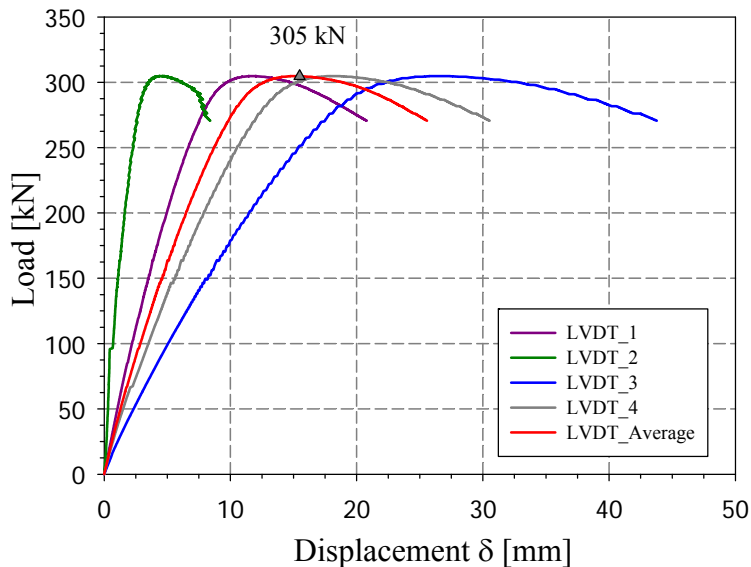


Figure 80 – Typical axial shortening curves (CHS HR 159x6.3 T11)

Figure 81 shows the rotations recorded along major and minor axes respectively and compared with the rotations obtained with the inclinometers for the same test. Since the column was tested under compression and constant bending moment, the same rotation was expected to occur at both ends of the column. However, a small difference in stiffness was observed between the end rotations measured by both upper and lower inclinometers. This difference is due to several experimental uncertainties such as the variation of eccentricities at

both ends due to the welding of the end plates, the column positioning... One may also notice small disparities in stiffness between the LVDTs and the inclinometers measurements which are credited to the insufficient accuracy of the LVDT method. A higher level of confidence and reliability are provided by the inclinometers measurements.

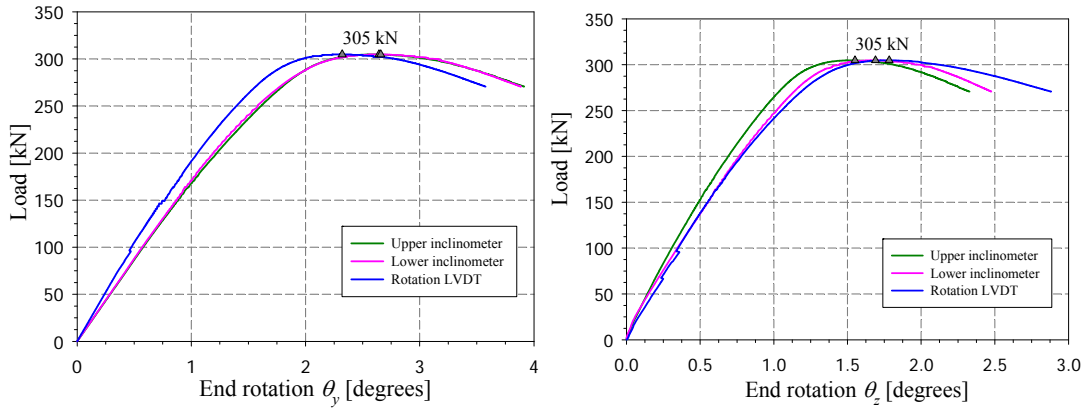


Figure 81 – Typical load-rotation curves along major and minor axes (CHS HR 159x6.3 T11)

The same procedure was applied to determine the lateral and transversal displacements as well as to check that no lateral torsional buckling occurred. As expected, negligible torsional rotations of the mid-span cross-section were measured for all tested specimens ($\theta < 0.5$ degrees), due to the high torsional stiffness of hollow sections. Figure 82 presents the mid-span cross-section lateral and transversal displacements for the specimen RHS CF 220x120x6 T6.

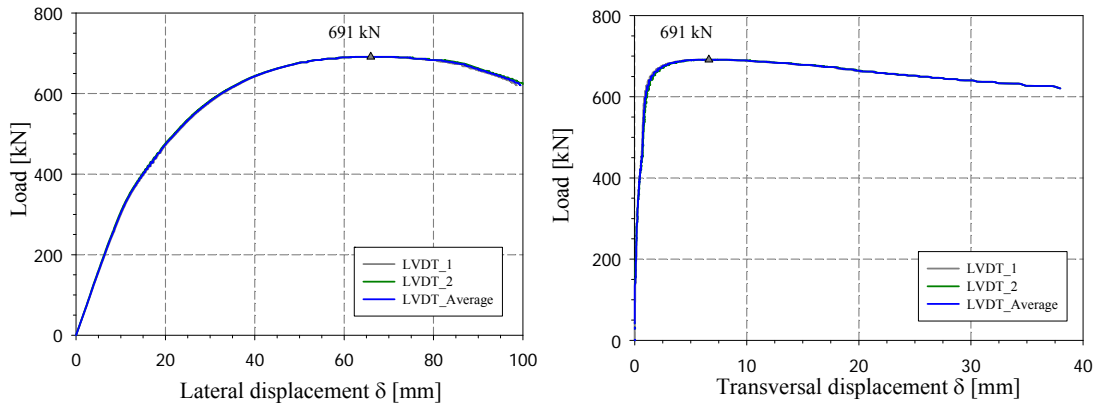


Figure 82 – Mid-span cross-section lateral and transversal displacements (RHS CF 220x120x6 T6)

Figure 83 displays the deformed shape of the specimen obtained after the test and numerically. The measured eccentricities and maximum forces of all tested specimens are listed in Table 25.

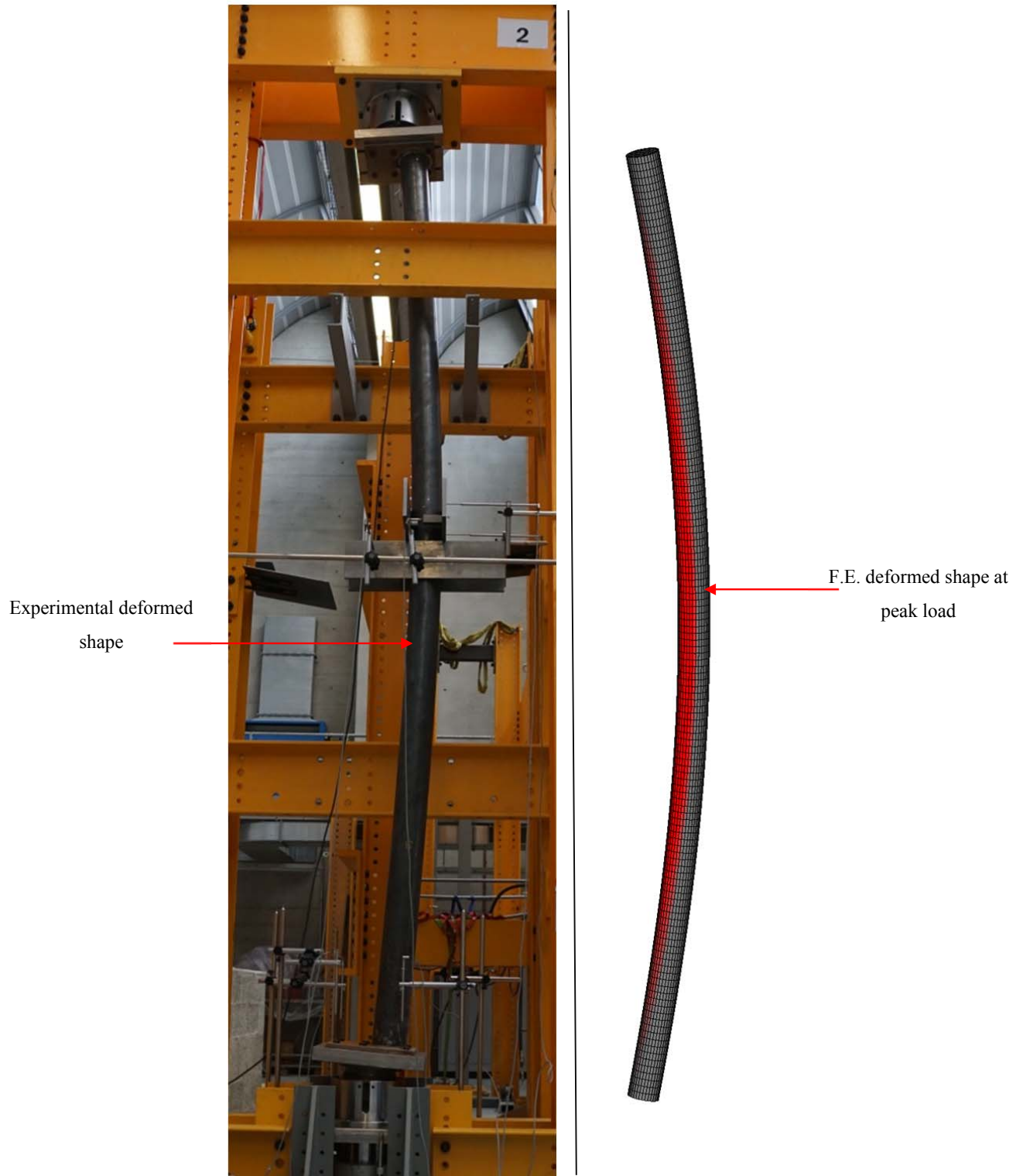


Figure 83 – Deformed shape of specimen CHS HR 159x5 T8

Table 25 – Measured specimens' dimensions and obtained ultimate loads for all tested specimens

Specimen	Measured dimensions							F_{TEST} [kN]
	$Length$	H	B	t	D	e_z [mm]	e_y	
	[mm]	[mm]	[mm]	[mm]	[mm]	[mm]	[mm]	
RHS CF 200x100x4 T1	4001.22	200.12	100.28	4.00	–	84.6	0	351.9
RHS CF 200x100x4 T2	3999.61	200.42	100.08	4.05	–	88.9	41.6	213.5
RHS CF 200x100x4 T3	4000.30	198.66	99.93	3.85	–	141.0	0	365.1
RHS CF 220x120x6 T4	4000.09	220.09	119.77	5.90	–	72.2	0	700.0
RHS CF 220x120x6 T5	4000.33	219.91	120.27	5.86	–	85.4	43.8	478.2
RHS CF 220x120x6 T6	3998.58	219.90	119.78	5.83	–	120.3	0	691.4
CHS HR 159x5 T7	3999.70	–	–	5.42	159.80	68.9	0	345.4
CHS HR 159x5 T8	4895.00	–	–	5.30	159.30	77.5	0	288.5
CHS HR 159x5 T9	4000.05	–	–	5.30	159.40	130.0	0	317.8
CHS HR 159x6.3 T10	4900.05	–	–	6.51	159.20	78.5	0	319.6
CHS HR 159x6.3 T11	4000.10	–	–	6.53	159.40	88.4	58.7	304.7
CHS HR 159x6.3 T12	4000.00	–	–	6.40	159.20	130.0	0	363.0

3.5. Validation of numerical vs. experimental member response

3.5.1. UAS Western Switzerland – Fribourg test series

3.5.1.1. Finite element model assumptions

Series of numerical computations have been led with the use of non-linear F.E.M. FINELg, continuously developed at the University of Liège and Greisch Engineering Office since 1970 [50]. This software offers almost all types of F.E.M. analyses, and present investigations have mainly been resorting to so-called M.N.A. (Materially Non-linear Analysis), L.B.A. (Local Buckling Analysis) and G.M.N.I.A. (Geometrically and Materially Nonlinear Analysis with Imperfections). The cross-sections were modelled with the use of quadrangular 4-nodes plate-shell finite elements with typical features (corotational total Lagrangian formulation, Kirchhoff's theory for bending). The corners of square and rectangular profiles were modeled with four shell elements per corner (Figure 85). Mesh *Type II* was selected (see Figure 84), on the basis of the case studies detailed in chapter 4, where series of G.M.N.I.A. F.E. calculations were performed on rectangular and square hollow sections by considering 4 different mesh densities. *Type II* mesh was seen to provide accurate results in terms of peak load and led to satisfactory results with reasonable computational effort.

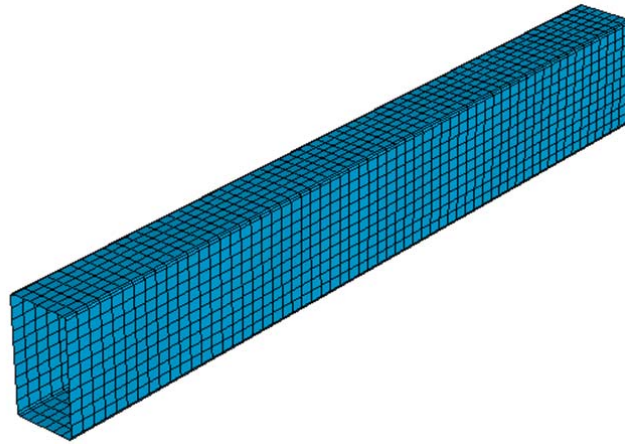
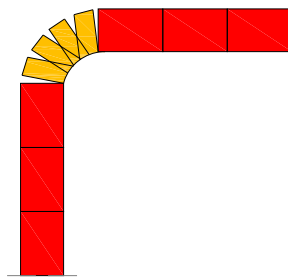
Figure 84 – Mesh *Type II* selected for G.M.N.I.A. calculations

Figure 85 – Detail view of the corner modelling

A numerical model was developed so as to represent accurately the experimental behaviour of the tested columns. End plates were modelled through rigid plates having an equivalent thickness of 80 mm (which is equal to the width of the hinge connecting plate and the specimen's end plate together), with shell elements that remained elastic during loading. The plates' stiffness allowed an even distribution of the applied load at the ends of the sections and prevented the cross-sectional deformation at both ends. Truss elements were used to simulate the (assumed) rigid spherical hinges at both ends, and allowing free rotations. All trusses were connected to the end plates nodes and to the centroid of the hinge. The load was applied at the centroid of the hinge, and the cases of combined bending with compression were simulated through an axial load applied at the centroid of the hinge with the corresponding measured eccentricities [3]. The buckling length which corresponds to the distance between the centres of the spherical hinges was respected in the numerical models as well (see Figure 86).

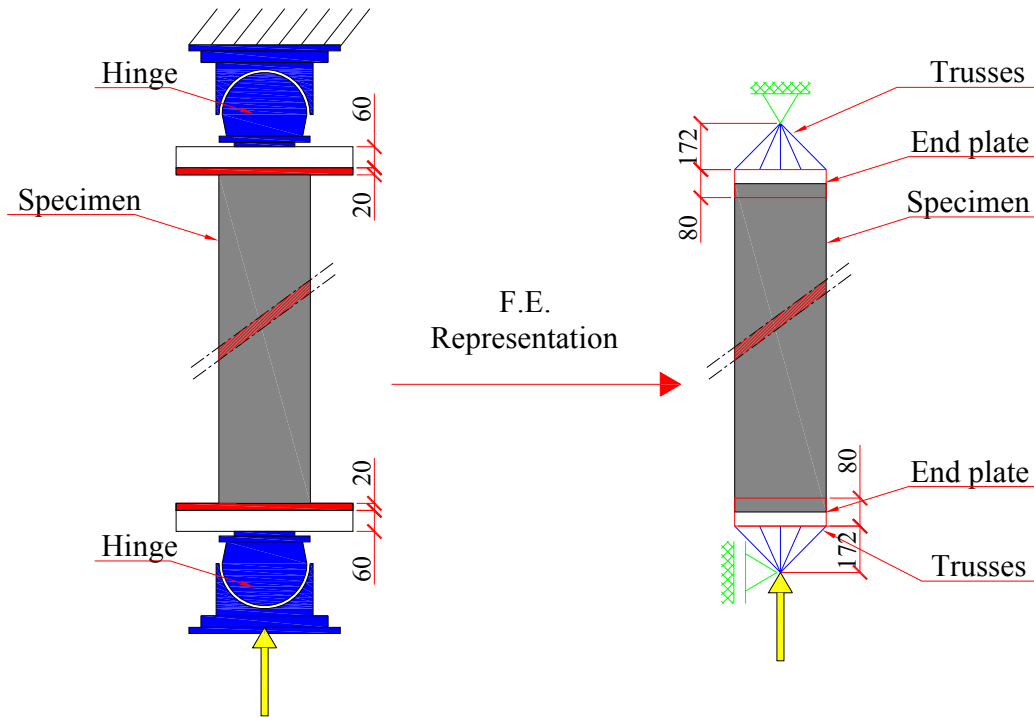


Figure 86 – Finite element model assumptions

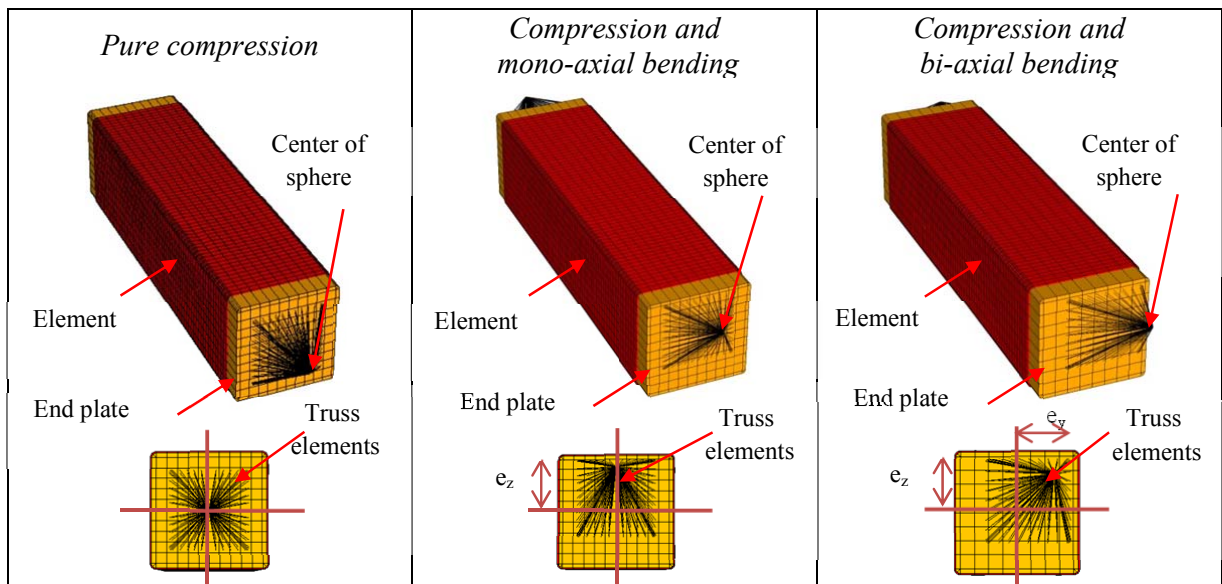


Figure 87 – Applied load with shifted truss center corresponding to different load cases [3]

Every measured data was taken into account for the validation of the F.E. models as closely as possible to the experimental conditions. In particular, the actual dimensions (section geometry and length) and material behaviour of the tested specimens were introduced in the F.E. models, as well as the measured geometrical imperfections. Since the membrane residual

stresses are insignificant in the cold-formed section, flexural stresses were only considered. As for the circular hot-rolled profiles, only flexural residual stresses were introduced. Averaged measured material stress-strain behaviour including strain-hardening effects was also included. An elastic-perfectly plastic with 2% strain hardening material law was implemented for hot-rolled profiles. Regarding the cold-formed tubular profiles, two material laws have been defined: one for the base material and one for the corner regions. A simple Ramberg-Osgood material law was used for the flat regions and a multi-linear law was adopted for the corners region as illustrated in Figure 88.

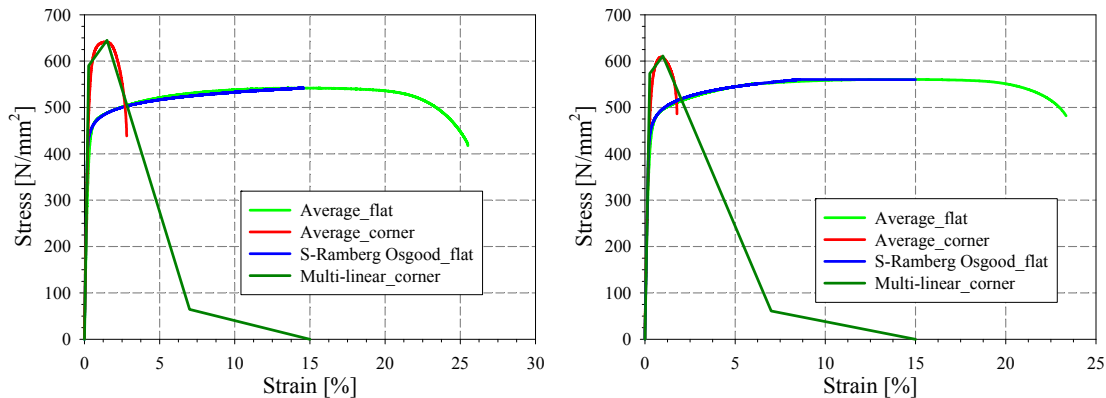


Figure 88 – Material stress strain laws adopted in F.E. calculations for specimens – a) RHS CF 220x120x6 T4 –
b) RHS CF 200x100x4 T2

A simple Ramberg-Osgood law was shown to be not suitable to represent the corners region [3], since this material law is characterized by a small ductility and a maximum strain of 2.5 %. Therefore, once the section reached that level of strain, the corners would find themselves ineffective leading to the failure of the entire section and no more strains could be achieved beyond this value of 2.5% strain.

3.5.1.2. Validation: F.E. vs. test results

The twelve beam-column tests were modeled using FINELg F.E. software, and the predicted ultimate loads were compared to the experimental ones. The initial imperfections measured by means of the LVDTs were introduced: a double interpolation in both directions was performed on the processed data by using a specific code specially developed for this purpose. Therefore, the F.E. desired mesh for each plate of every profile was adapted to the measured grids obtained during the test. For the RHS, the measured imperfections obtained by mean of the laser Tracker AT401 were also introduced.

Table 26 provides the numerical ultimate loads obtained by considering initial imperfections by means of equally spaced LVDTs, the experimental ultimate loads and the ratio of the experimental ultimate loads to their numerical counterparts for all investigated columns. It can be observed from the table that the numerical models could accurately predict the ultimate carrying capacities and represent the beam-column’s response conveniently, whatever the profile cross-section, loading arrangement, length...the mean and standard deviation values further highlight the accuracy and consistency of the numerical model which provides excellent accordance with the test results in terms of ultimate loads.

It should be noted that the numerical models are seen to sometimes provide slightly unsafe results, however not more than 4 % on the unsafe side. This may be due to the laboratory uncertainties that exist during the preliminary measurement processes. Furthermore, the numerical models are widely affected by the introduced cross-section dimensions, eccentricities values, material properties, geometrical imperfections, residual stresses...the complete test setup stiffness was also not modelled in the numerical simulations. These inconsistencies can also explain the maximum deviation of 11%.

Table 26 – Comparison of numerical and experimental ultimate loads

Cross-section shape	Load case	ψ	L [mm]	F_{TEST} [KN]	F_{FE_LVDT} [KN]	$\frac{F_{TEST}}{F_{FE_LVDT}}$ [-]
RHS CF 200x100x4 T1	60%N+40% M_y	1	4001.2	352	348	1.01
RHS CF 200x100x4 T2	40%N+30% M_y +30% M_z	1	3999.6	214	219	0.98
RHS CF 200x100x4 T3	60%N+40% M_y	0	4000.3	365	336	1.09
RHS CF 220x120x6 T4	60%N+40% M_y	1	4000.1	700	669	1.05
RHS CF 220x120x6 T5	40%N+30% M_y +30% M_z	1	4000.3	478	448	1.07
RHS CF 220x120x6 T6	60%N+40% M_y	0	3998.6	691	670	1.03
CHS HR 159x5 T7	50%N+50% M_y	1	3999.7	345	308	1.12
CHS HR 159x5 T8	50%N+50% M_y	1	4895.0	289	267	1.08
CHS HR 159x5 T9	50%N+50% M_y	0	4000.0	318	306	1.04
CHS HR 159x6.3 T10	50%N+50% M_y	1	4900.0	320	332	0.96
CHS HR 159x6.3 T11	33%N+33% M_y +33% M_z	1	4000.1	305	313	0.97
CHS HR 159x6.3 T12	50%N+50% M_y	0	4000.0	363	366	0.99
Mean						1.03
Standard deviation						0.05

Table 27 summarizes the experimental ultimate loads of the six RHS compared to their numerical counterparts obtained by considering initial imperfections by means of equally

spaced LVDTs and by mean of the laser Tracker AT401. Numerical simulations obtained by considering initial imperfections by means of the two considered methods give good predictions of the experimental ultimate loads, where a maximum difference of 6 % is obtained when considering the AT401 procedure whereas a maximum difference of 8 % is obtained when considering the LVDTs procedure. Both sets of measured initial imperfections, introduced in suitably-built shell F.E. models, along with all measured data, lead to nearly identical numerically-predicted failure loads, with a maximum difference of 5 %, indicating that the observed differences in imperfection patterns shall be deemed acceptable and sufficient.

Table 27 – Comparisons of F_{FE_AT401} with F_{FE_LVDT} and F_{TEST}

Specimen	$Length$	F_{TEST}	F_{FE_AT401}	F_{FE_LVDT}	F_{TEST}/F_{FE_AT401}	F_{TEST}/F_{FE_LVDT}	F_{FE_AT401}/F_{FE_LVDT}
	[mm]	[kN] _T	[kN]	[kN]	[-]	[-]	[-]
RHS CF 200x100x4 T1	4000	351.9	349.0	348.2	1.01	1.01	1.00
RHS CF 200x100x4 T2	4000	213.5	207.6	218.8	1.03	0.98	0.95
RHS CF 200x100x4 T3	4000	365.1	347.2	336.2	1.05	1.09	1.03
RHS CF 220x120x6 T4	4000	700.0	676.8	669.3	1.03	1.05	1.01
RHS CF 220x120x6 T5	4000	478.2	449.4	448.4	1.06	1.07	1.00
RHS CF 220x120x6 T6	4000	691.4	673.0	670.0	1.03	1.03	1.00

A graphical comparison of the ultimate loads obtained numerically by using the initial imperfections measured by means of the LVDTs and the experiments is shown in Figure 89 for all the tested specimens. Figure 90 presents a comparison of the test results and numerical results obtained by considering initial imperfections by means of the two considered methods for the RHS. The red lines presented in the graphical comparisons indicate a deviation of +/- 10% from equality. It can be seen that all numerical simulations give good predictions of the ultimate loads of loaded columns. All values oscillate very closely around the continuous $F_{TEST} / F_{F.E.M.} = 1.0$ ideal line, which indicates a very good accordance between test and numerical results obtained by considering initial imperfections by means of both described methods. Thus, the validity of the proposed model is ensured.

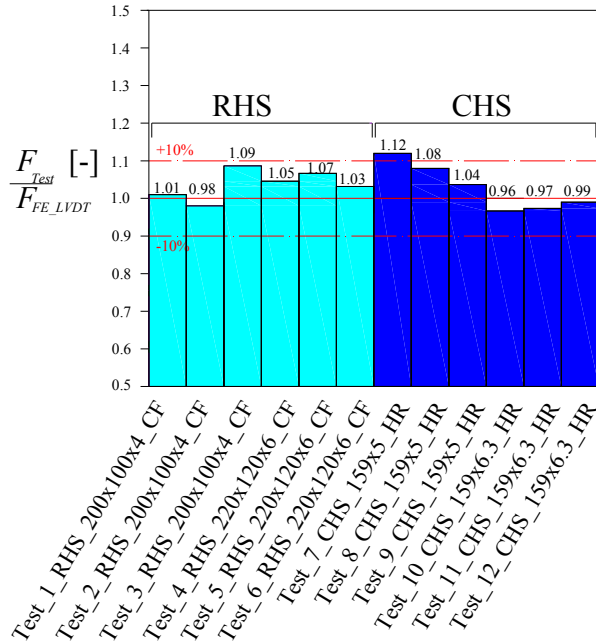


Figure 89 – F.E. peak loads vs. experimental loads.

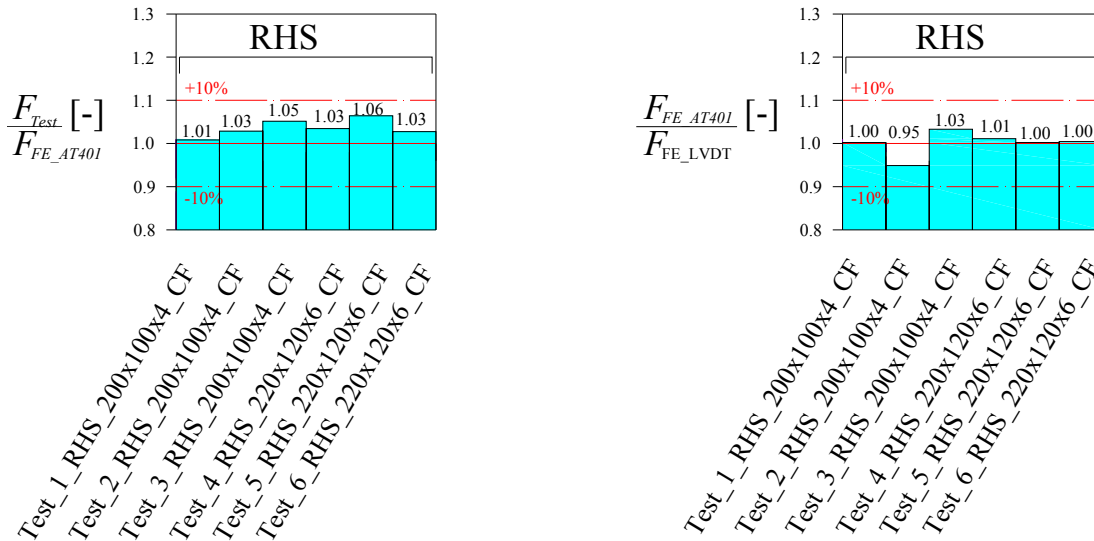
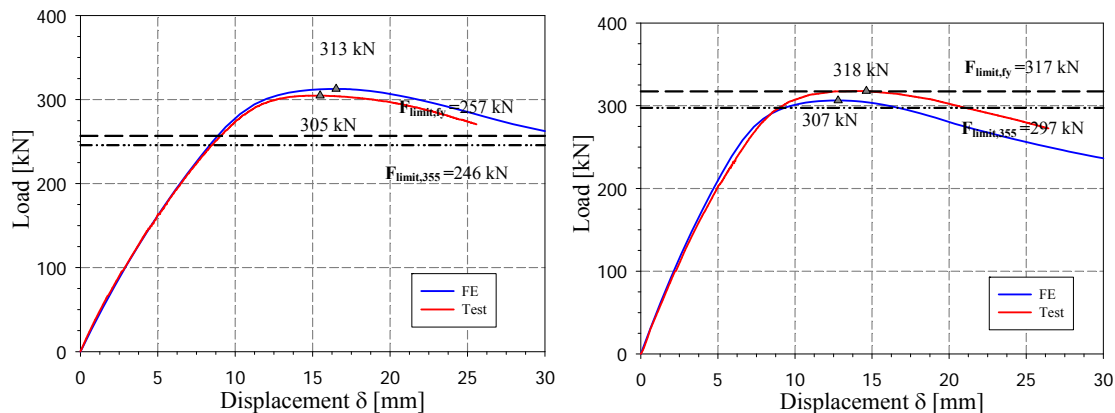


Figure 90 – Graphical representation of – a) F_{TEST} / F_{FE_AT401} – b) $F_{FE_AT401} / F_{FE_LVDT}$

Figure 91 to Figure 93 compares the results obtained numerically to the experimental ones: Figure 91 gives examples of experimental and numerical axial load-displacement curves; Figure 92 illustrates an example of the experimental mid-span lateral and transversal displacements compared with their numerical counterpart. Figure 93 compares the experimental beam end rotation along major and minor axis, to the corresponding numerical

rotations. The complete set of results is provided in Annex 6. It can be seen that all numerical simulations provide excellent accordance with the test results in terms of ultimate loads, displacements, columns end rotations, initial stiffness, failure modes... The minor differences in initial stiffness, ultimate load and post-peak behaviour between numerical and experimental results are mainly caused by non-explicitly modelled sources, such as a little friction in the hinges (i.e. the boundary conditions are never as ideal as in the computational model and are far more complicated than assumed numerically) [3], inconsistencies in the imperfections measurements and unexpected measured eccentricities¹¹. The complete test setup stiffness was also not modelled numerically for sake of simplicity (i.e. for example the whole designed frame ensuring the bracing, the embedded support located at the column bottom formed by the triangularly-shaped pieces and the welded channels, the column top end connection to the UPN 720...). It is to be noted that vertical displacements were not allowed on the upper extremity of the tested column, therefore LVDTs were only positioned on the bottom end plate of the specimens and inclinometers were fixed at both ends of the column... thus, absolute measured axial displacements were recorded during the test including the whole frame displacements. These inconsistencies can also explain the deviation between test and numerical assumptions in term of peak loads and initial stiffness. Since a maximum deviation of 11% is reported between the test and their numerical counterparts, the F.E. model can successfully predict the ultimate load of the columns and its validity is ensured.



¹¹ Before each test the corresponding eccentricities were measured. No strain gauges were attached on the specimen, therefore no back-calculations were performed to determine the corresponding eccentricities.

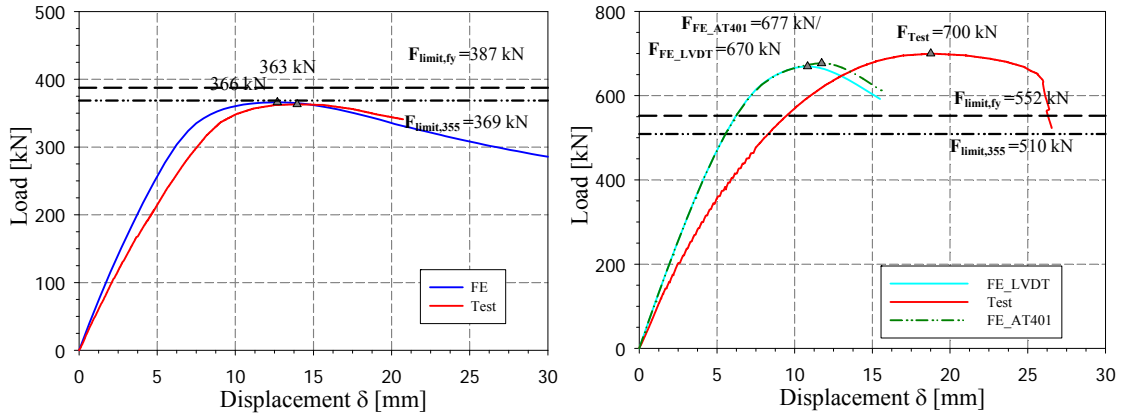


Figure 91 – Numerical vs. experimental axial load displacement curves of specimens – a) CHS HR 159x6.3 T11 – b) CHS HR 159x5 T9 – c) CHS HR 159x6.3 T12 – d) RHS CF 220x120x6 T4

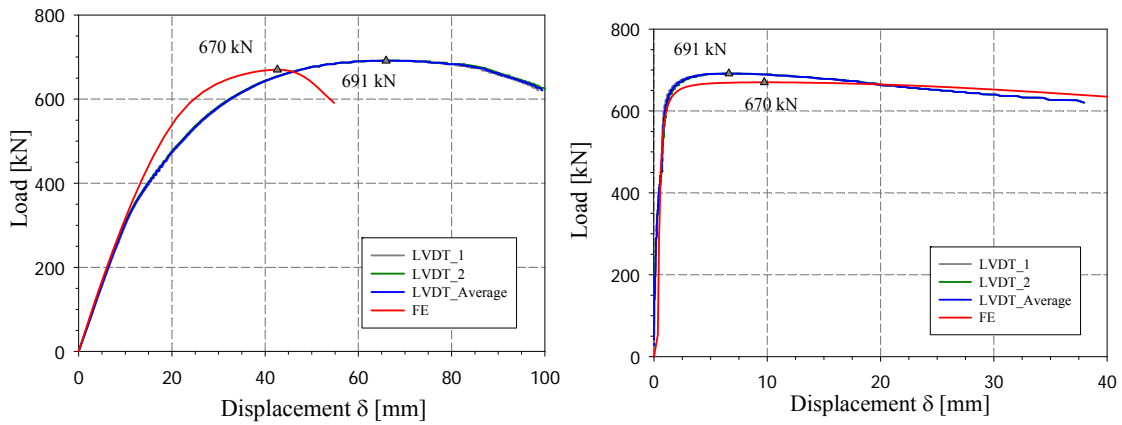


Figure 92 – Numerical vs. experimental mid-span displacements for specimen RHS CF 220x120x6 T6– a) lateral displacement – b) transversal displacement

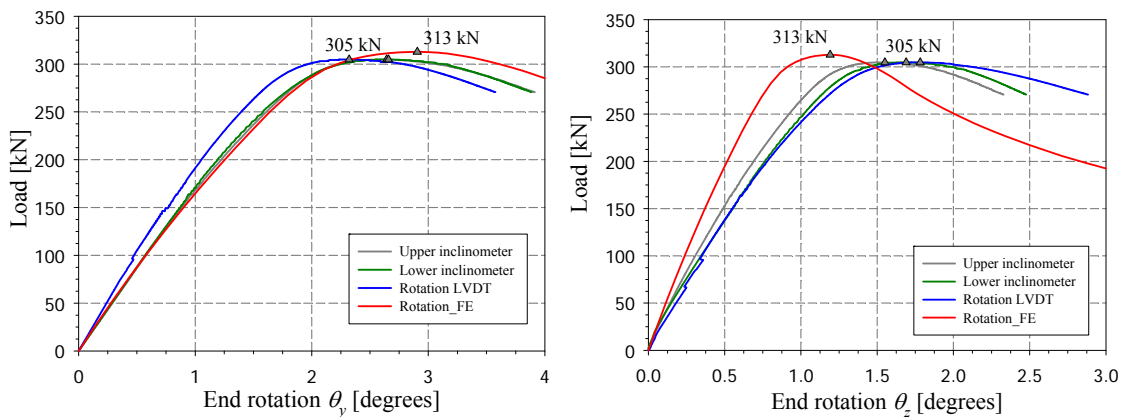


Figure 93 – Numerical vs. experimental beam end rotation for specimen CHS HR 159x6.3 T11 along – a) major-axis bending – b) weak-axis bending

3.5.2. European project “Semi-Comp” test series

3.5.2.1. General scope of the study

Additional well-documented similar test data from European project “Semi-Comp” [4] have been added to the present results, where a test program was established to determine the influence of semi-compact class 3 sections on member buckling behaviour. The test program comprised beam-column member buckling tests on 3.5 m to 4.5 m length profiles with hot-rolled H-shaped as well as cold-formed tubular cross-sections. The columns were tested under mono-axial or biaxial bending with axial compression. Linear bending moment diagrams were selected for each test as summarized in Table 28 for the tubular sections, where ψ_y and ψ_z represent the ratios between end moment about y - y and z - z axes, respectively. The member buckling tests eccentricities adopted are presented in Table 28 as well. The combined load cases were obtained through an eccentric load applied at the ends of the specimens through welded thick end plates. The support conditions of the members during the tests may be assumed to be “pinned conditions”: the end sections bending rotations can be assumed to be free. The full test program can be found in [4]. Figure 94 provides a general view of the test setup.



Figure 94 – General view of test setup

Table 28 – “Semi-Comp” test program for member buckling

RHS 200x120x4 (S275) $L = 4\text{ m}$	ψ_y	ψ_z	e_y [mm]	e_z [mm]	SHS 180x5 (S355) $L = 4\text{ m}$	ψ_y	ψ_z	e_y [mm]	e_z [mm]
R275_BU_1	1	/	55	0	S355_BU_1	1	/	55	0
R275_BU_2	0	/	55	0	S355_BU_2	0	/	55	0
R275_BU_3	/	1	0	45	S355_BU_3	-0.455	/	55	0
R275_BU_4	/	0	0	45	S355_BU_4	1	1	55	55
R275_BU_5	1	1	55	45	S355_BU_5	0	0	55	55
R275_BU_6	0	0	55	45	S355_BU_6	-0.455	-0.5	55	55

Besides the main member buckling tests, the material properties, residual stresses and initial geometrical imperfections were determined and incorporated in the numerical model in order to achieve the validation in a correct way. Accordingly, tensile coupon tests were extracted from the flat faces and the corners (where an increase of f_y is expected) of the tubular profiles for each type of cross-section. Concerning the measurement of residual stresses, the cutting strip technique had been used. A rather low level of membrane stresses was observed compared to the level of flexural stresses for the cold-formed tubular profiles. The initial geometrical imperfections were also measured since it has an influence on the carrying capacity of the members.

3.5.2.2. Finite element model assumptions

A similar F.E. model has been developed so as to fit with the test arrangements as closely as possible. Pinned-end conditions were applied and an additional rigid end plate, modeled with shell elements with an elastic material law, was linked to the specimen on both sides. The load was applied through nodal forces at the middle of the endplates, corresponding to the test conditions [4]. The thick plates allowed an even distribution of the applied load with no out-of-plane deformations. Figure 95 represents a rectangular hollow section with end plate, tested under compression and biaxial bending moment. All loading was increased proportionally up to and beyond failure.

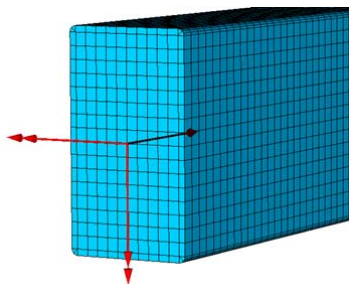


Figure 95 – Rectangular shape model with end plate

Mesh *Type II* was again selected. Every measured data was taken into account for the validation of the F.E. models as closely as possible to the experimental conditions. Table 29 represents the measured dimensions of each tubular specimen as well as some of the measured material properties introduced to the numerical model.

Table 29 – Measured dimensions and material properties

Profile	H [mm]	B [mm]	t [mm]	f_y [N/mm ²]	f_u [N/mm ²]	E [N/mm ²]
RHS200x120x4	199.8	120.8	3.7	378	486	177000
SHS180x180x5	180.2	180.2	4.7	413	538	178000

Averaged material stress-strain behaviour including strain hardening effects was used. Two material laws have been defined: one for the flat regions where a simple Ramberg-Osgood material law was used, and one for the corner regions where a multi-linear law was adopted. The low values of the measured Young's modulus coefficients are due to the laboratory measuring inconsistencies, thus $E = 210000 \text{ N/mm}^2$ was adopted for the numerical validation.

The adopted membrane residual stresses pattern for the numerical validation has been taken as an approximation of the measured residual stresses with respect to an auto-equilibrated pattern. The measured initial geometrical imperfections were also introduced. Again, the measured grid was adapted to the desired F.E. mesh, with the use of a double interpolation in both directions of the plates of each profile. This was done to represent as closely as possible the experimental conditions.

Table 30 summarizes the maximum local magnitudes of initial imperfections measured along the member length. 'Denom. local web' and 'Denom. local flange' refer to the *denominator* in the ratios ' $h - 2r - t / \text{denominator}$ ' and ' $b - 2r - t / \text{denominator}$ ' equations, which is such that these ratios are equal to the measured maximum local magnitude of web and flange respectively. The measured imperfections are compared to the reasonable and realistic amplitude of imperfections chosen as a per plate amplitude $a / 200$ with ' a ' equal to $(b-t-2r)$ or $(h-t-2r)$.

Table 31 summarizes the maximum global magnitudes of initial imperfections measured along the member length. 'Denom. global web' and 'Denom. global flange' refer to the *denominator* in the ratio ' $L / \text{denominator}$ ' equation which is such that this ratio is equal to the measured maximum global magnitude in both strong and weak axes respectively. The

measured imperfections are compared to the realistic average value of global imperfection amplitude equal to $L / 1000$.

The following conclusions can be drawn from these tables:

- the maximum measured local magnitudes vary widely for the different considered tests and ranged from 0.27 to 0.68 with an average of 0.43;
- the same tendency is observed for the global buckling measurements, where the maximum magnitude ranged from 0.35 to 0.64 with an average of 0.47;
- the realistic magnitude of local imperfections $a / 200$ is seen to provide safe results when compared to the experimental one for all the tested columns; the average measured local magnitude being equal to $a / 375$;
- the realistic magnitude of global imperfections $L / 1000$ is seen to provide safe results when compared to the experimental one for all the tested columns; the average measured global magnitude being equal to $a / 9660$.

Accordingly, the realistic magnitudes can be safely adopted to represent the initial magnitude of tested beam-column members; the measured ones were seen to vary considerably depending on the tested column.

Table 30 – Initial local maximum magnitude measured along the member length

Profile	$\frac{h - 2r}{t} -$	$\frac{b - 2r}{t} -$	Average	Measured	Measured	Measured	Denom.	Denom.	Denom.
	$\frac{t}{200}$	$\frac{t}{200}$		local	local	local	local	local	local
	[mm]	[mm]	[mm]	magnitude	magnitude	magnitude	web	flange	average
				web	flange	average	[-]	[-]	[-]
R275_BU_1	0.90	0.51	0.70	0.601	0.164	0.383	300	616	458
R275_BU_2	0.90	0.51	0.70	0.713	0.181	0.447	253	559	406
R275_BU_3	0.90	0.51	0.70	0.372	0.168	0.270	484	602	543
R275_BU_4	0.90	0.51	0.70	0.451	0.242	0.347	399	418	409
R275_BU_5	0.90	0.51	0.70	0.529	0.144	0.337	340	702	521
R275_BU_6	0.90	0.51	0.70	0.482	0.480	0.481	374	211	293
S355_BU_1	0.90	0.51	0.70	0.498	0.703	0.601	362	144	253
S355_BU_2	0.90	0.51	0.70	0.541	0.374	0.458	333	270	302
S355_BU_3	0.90	0.51	0.70	0.346	0.292	0.319	521	346	434
S355_BU_4	0.90	0.51	0.70	0.369	0.435	0.402	488	232	360
S355_BU_5	0.90	0.51	0.70	0.562	0.349	0.456	320	290	305
S355_BU_6	0.90	0.51	0.70	0.651	0.707	0.679	277	143	210
Mean	0.90	0.51	0.70	0.510	0.353	0.432	371	378	375

Table 31 – Initial global maximum magnitude measured along the member length

Profile	$L / 1000$	Measured global magnitude strong axis	Measured global magnitude weak axis	Measured global amplitude average	Denom. global strong axis	Denom. global weak axis	Denom. Global average
	[mm]	[mm]	[mm]	[mm]	[-]	[-]	[-]
R275_BU_1	4.05	0.382	0.601	0.492	10602	6739	8671
R275_BU_2	4.05	0.537	0.713	0.625	7542	5680	6611
R275_BU_3	4.05	0.337	0.372	0.355	12018	10887	11453
R275_BU_4	4.05	0.282	0.451	0.367	14362	8980	11671
R275_BU_5	4.05	0.421	0.529	0.475	9620	7656	8638
R275_BU_6	4.05	0.266	0.482	0.374	15226	8402	11814
S355_BU_1	4.05	0.304	0.38	0.342	13322	10658	11990
S355_BU_2	4.05	0.637	0.246	0.442	6358	16463	11411
S355_BU_3	4.05	0.559	0.446	0.503	7245	9081	8163
S355_BU_4	3.99	0.74	0.421	0.581	5392	9477	7435
S355_BU_5	4.05	0.629	0.245	0.437	6439	16531	11485
S355_BU_6	4.02	0.514	0.753	0.634	7821	5339	6580
Mean	4.04	0.47	0.47	0.47	9662	9658	9660

3.5.2.3. Validation: F.E. vs. test results

As mentioned before, every measured data was taken into account in the numerical model. The predicted ultimate loads were compared to the experimental ones and are presented in Table 32 for each beam-column test, where the agreement between the finite element predictions and its experimental counterpart seen to be very good for all considered cases. Figure 96 shows a graphical comparison of the ultimate loads from F.E. results with the experimental results. Figure 97 gives typical examples of experimental and numerical axial load-displacement curves.

Table 32 – Comparison of numerical and experimental ultimate loads from “Semi-Comp” project [4]

Test #	Specimen	Section	L [mm]	F_{TEST} [KN]	F_{FE} [KN]	F_{TEST}/F_{FE} [-]
1	S355_BU_1	SHS_S355CF_180x180x5	4050	563	580	0.97
2	S355_BU_2	SHS_S355CF_180x180x5	4050	656	698	0.94
3	S355_BU_3	SHS_S355CF_180x180x5	4050	708	747	0.95
4	S355_BU_4	SHS_S355CF_180x180x5	3990	460	483	0.95
5	S355_BU_5	SHS_S355CF_180x180x5	4050	600	605	0.99
6	S355_BU_6	SHS_S355CF_180x180x5	4020	629	643	0.98
7	R275_BU_1	RHS_S275CF_200x120x4	4050	404	394	1.03
8	R275_BU_2	RHS_S275CF_200x120x4	4050	451	465	0.97
9	R275_BU_3	RHS_S275CF_200x120x4	4050	261	254	1.03
10	R275_BU_4	RHS_S275CF_200x120x4	4050	331	314	1.06

11	R275_BU_5	RHS_S275CF_200x120x4	4050	268	243	1.10
12	R275_BU_6	RHS_S275CF_200x120x4	4050	307	301	1.02
					Mean	1.00
					Standard deviation	0.05

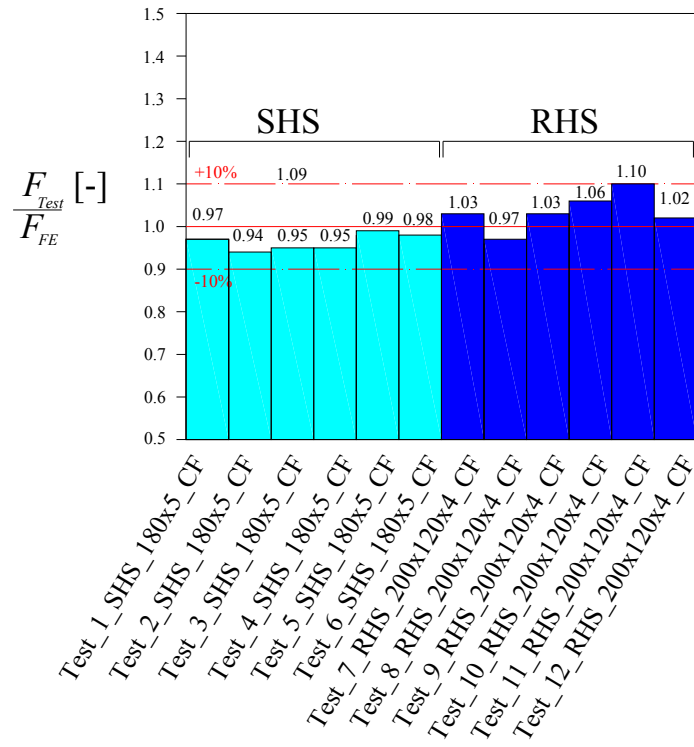
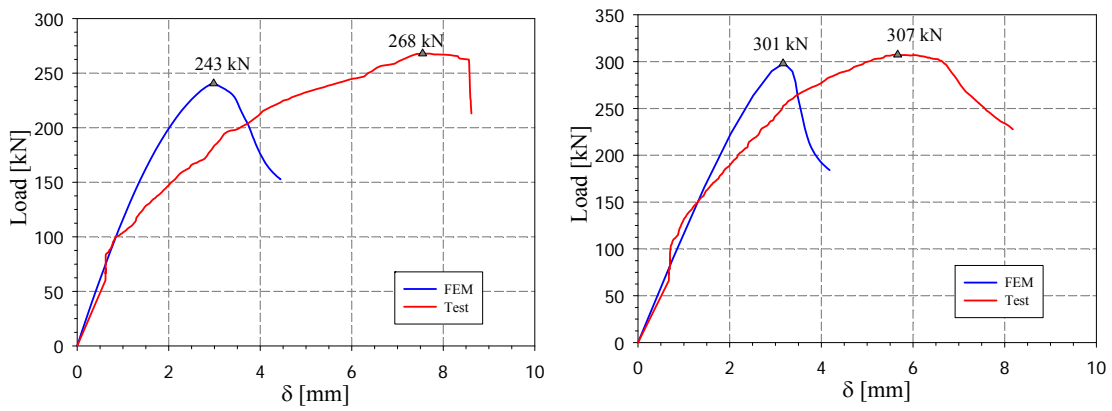


Figure 96 – F.E. peak loads vs. experimental loads.



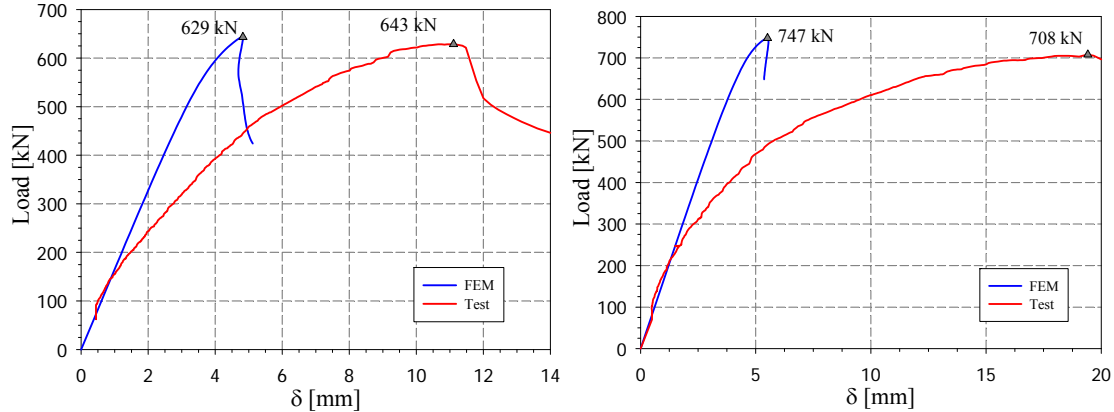


Figure 97 – Numerical vs. experimental axial load displacement curves of specimens – a) R275_BU_5– b) R275_BU_6– c) S355_BU_6 – d) S355_BU_3

These results again show that the numerical models could accurately predict the ultimate carrying capacities and represent the beam-column's response conveniently. The mean and standard deviation values further highlight the accuracy and consistency of the numerical model. It should be noted that the slightly safe or unsafe results obtained numerically are due to the laboratory inconsistencies that exist during the preliminary measurement processes¹².

The complete test setup stiffness was also not modeled in the numerical simulations. These inconsistencies can also explain the maximum deviation of 10%. The agreement between the finite element predictions and the tests is however considered to be very acceptable.

3.6. Summary

Experimental investigations on tubular rectangular and circular hollow sections have been presented in this chapter. The test program included 12 beam-columns buckling tests subjected to various load cases through the application of eccentric compression. In total, four different cross-section shape profiles of nominal yield stress $f_y = 355 \text{ N/mm}^2$ manufactured through hot-rolled and cold-formed processes were investigated.

Preliminary measurements prior to testing were also described in detail. They consisted in:

- measurements of cross-section dimensions;
- measurements of geometrical imperfections;

¹² Previous investigations [51] have found that the determination of yield and ultimate strengths are sensitive to the loading rate. Actual codes specify a range of loading rate for tensile coupon tests. However, the lower bound and upper bound of the loading rate provide quite different results in terms of the yield and ultimate strengths.

- determination of material properties;
- measurements of the residual stresses;
- testing of stub column tests.

Besides, numerical shell models simulating the test conditions as closely as possible were developed. For both the present test series and another one from literature, it was found that the F.E. models were capable of replicating accurately the response and resistance of the experiments.

Accordingly, the F.E. model safely considered able to provide reliable numerical references results, was adopted in order to launch the totality of an extensive parametric study (i.e. performed on hot-rolled and cold-formed sections, including a wide scope of key parameters such as cross-section shape, steel grade, load cases...).

Following the present experimental series, both numerical and analytical investigations are addressed, with the intention of developing better practical formulations for beam-columns member design.

4. Numerical parametric study on hot-rolled members

4.1. Introduction

Present chapter describes extensive F.E. studies performed on hot-rolled hollow section members, based on previously validated numerical models. More than 39 500 non-linear F.E. simulations have been performed and the results were plotted in O.I.C. format, i.e. with specific $\lambda - \chi$ axes (see section 4.3.3 for the description of the O.I.C. approach).

Following section 4.2 first describes the modelling assumptions: meshing, loading and support conditions, material and geometrical imperfections, adopted material law... for both shell model – in which both local (i.e. cross-section instabilities) and global (i.e. member instabilities) buckling modes are likely to occur and interact –, as well as beam models in which only global instabilities may occur. Section 4.3 then describes the parameters adopted in the numerical simulations and provides results for member behaviour in analysing the influence of various parameters on the member's response and resistance (yield stress, cross-section shape and load case). A comparison between the F.E. and Eurocode 3 calculations for different load cases are presented in section 4.4. Eventually, summary and conclusions are addressed in section 4.5.

4.2. Description of F.E. models

Numerical computations have been led with the use of non-linear F.E. software FINELg [50], continuously developed at the University of Liège and Greisch Engineering Office since 1970. This software offers almost all types of F.E. analyses, and present investigations have made use of so-called G.M.N.I.A. analyses (Geometrically and Materially Non-linear with Imperfections) to determine the ultimate resistance of sections or members [52].

The F.E. models have been developed in a manner to best fit the properties of a real member. In order to determine the ultimate resistance of a member numerically, beam models have first been used as to witness global instabilities only, regardless of the section slenderness and local buckling that may occur (i.e. local buckling is a phenomenon that can be represented by shell models but not by beam models, which can only report on global buckling). Moreover, to be able to quantify the interaction between local and global buckling, members have also

been modelled in shell elements where potential interactions between local and global instabilities are considered.

Finally, to determine the ultimate resistance of a cross-section, shell modelling has been used to witness local buckling of the cross-section; in such cases, the length of the specimens was chosen equal to three times the largest cross-sectional dimension in order to avoid global buckling.

4.2.1. Material behaviour and residual stresses

An elastic-perfectly plastic material law with strain-hardening have been adopted in the numerical models as illustrated in Figure 98 for normal steel grades, following ECCS recommendations [53].

The usual characteristics requirements for normal strength steel are as follows:

- $f_u / f_y > 1.1$;
- Elongation at failure $\varepsilon_{fr} > 15\%$;
- $\varepsilon_u > 15 \varepsilon_y$.

Consistently, an elastic-plateau-strain hardening material response was adopted. The strain hardening slope accounted for in the simulations was set equal to 2% E , following DIN 18800 part 2 recommendations [54].

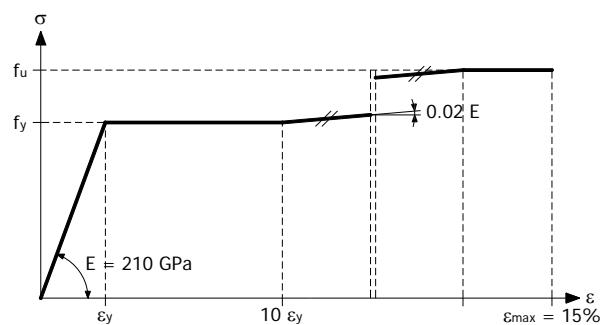


Figure 98 – Elastic-perfectly plastic with 2% strain hardening adopted material law

The Eurocode standard proposal prEN 1993-1-12 [55] extends the rules to steels up to S700 in order to benefit from the weight and cost savings of high strength steel thin plates [56] (see Figure 99).

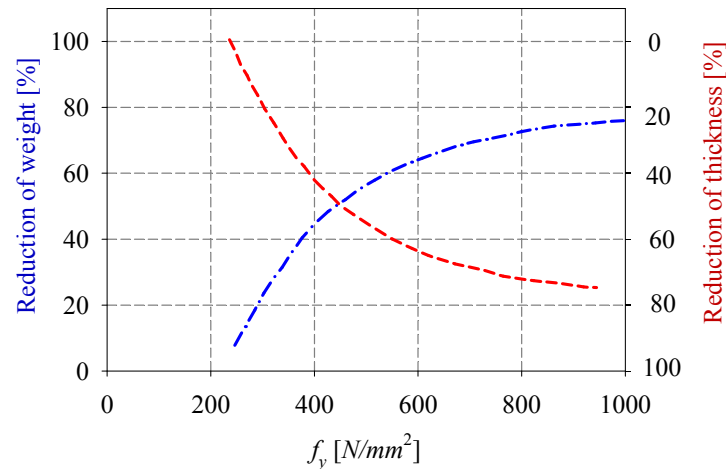


Figure 99 – Reductions of wall thickness and weight with increasing strength of steel

The characteristics of the recommended design values for high strength steel are as follows:

- $f_u / f_y > 1.05$;
- Elongation at failure $\varepsilon_{fr} > 10\%$;
- $\varepsilon_u > 15 \varepsilon_y$.

As shown in Figure 100, the typical stress-strain curve of low steel grades (S235 to S460) exhibits a classic behaviour with distinct yield plateau and strain-hardening effects. However, the material response of high strength steels ($f_y \geq 460 N/mm^2$) shows a pronounced non-linear behaviour and thus has no identifiable yield plateau, and strain-hardening immediately follows first yield. Typically, the 0.2% proof stress is used as a convenient equivalent yield stress. It can also be noted that the increase in yield stress is shown to be associated with a lower level of ductility at fracture.

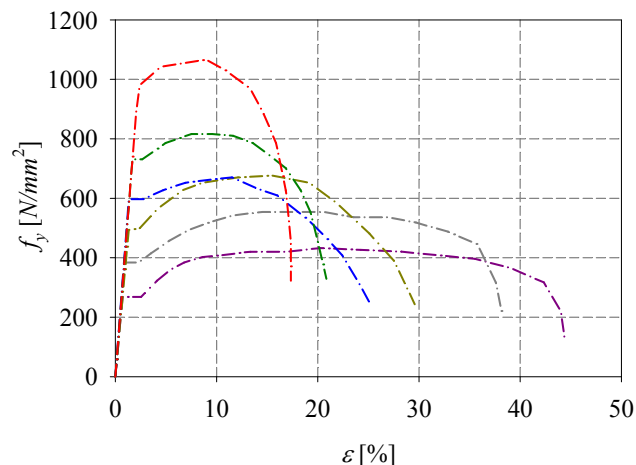


Figure 100 – Typical stress-strain curves for different steel grades

In order to adopt a suitable and realistic stress-strain curve for high strength steel, a numerical dedicated sub-study was performed using finite element software FINELg. Different class 1 sections were considered in the study, so as to focus on material response on cross-section resistance. Load cases N , $N+M_y$ and M_y were considered. The lengths of the profiles have been fixed to be about three times the height of the cross-section, in an attempt to avoid global buckling.

For the parametric study 54 G.M.N.I.A. calculations have been carried out, accounting for the following parameters:

- 3 hot-rolled RHS: RHS 50x30x4, RHS 60x40x5 and RHS 150x80x10;
- 3 hot-rolled SHS: SHS 40x40x3, SHS 80x80x5 and SHS 150x150x10;
- steel grade: S690;
- 3 material laws:
 - o *Type I*: elastic-perfectly plastic;
 - o *Type II*: elastic with 1% E strain hardening;
 - o *Type III*: elastic-plateau with 2% E strain hardening (see Figure 101).

These 3 material laws are frequently used in numerical studies since they represent in a suitable way the actual behaviour of structural steel. Table 33 illustrates the obtained results in terms of ratios $R_{REAL_TYPE I} / R_{REAL_TYPE II}$, $R_{REAL_TYPE II} / R_{REAL_TYPE III}$, where $R_{REAL_TYPE I}$, $R_{REAL_TYPE II}$ and $R_{REAL_TYPE III}$ represent the ultimate load multiplier obtained by using material laws *Type I*, *Type II* and *Type III*, respectively, being given an identical initial loading in all cases. One may notice that similar results are obtained by using *Type I* and *Type III* stress-strain curves, where an identified plateau is considered. In both cases, instability occurs at an early stage, before reaching the strain hardening zone. However, higher ultimate loads were reached by using *Type II* stress-strain curves, as expected, since no plateau was considered in this case, and due to strain hardening effects. *Type II* was excluded from the study because it only represents the behaviour of ultra-high strength steel ($f_y > 1100$ MPa) where the stress strain curves show no more yield plateau anymore.

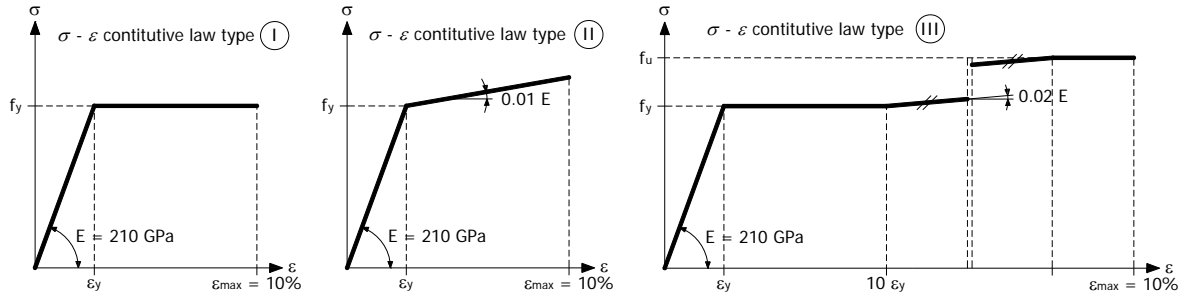


Figure 101 – Investigated stress-strain laws

Table 33 – Obtained results for tubular sections

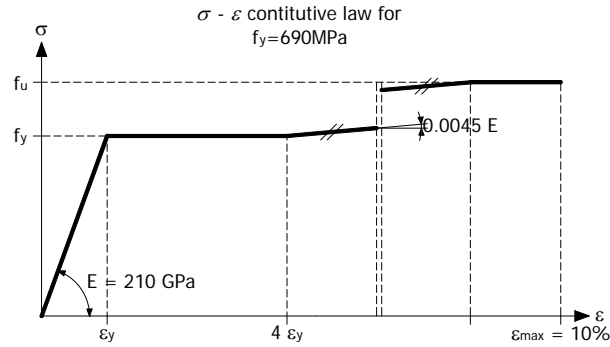
Load case	Pure compression: N			
Cross-section	Constitutive law	Ultimate compressive load [kN]	$R_{REAL_TYPE I} / R_{REAL_TYPE II}$	$R_{REAL_TYPE I} / R_{REAL_TYPE III}$
RHS_50x30x4	Type I	333.74	0.96	0.99
	Type II	349.12		
	Type III	336.87		
RHS_60x40x5	Type I	576.26	0.98	1.00
	Type II	589.77		
	Type III	576.29		
RHS_150x80x10	Type I	2677.55	0.98	1.00
	Type II	2721.61		
	Type III	2677.92		
SHS_40x40x3	Type I	285.61	0.97	1.00
	Type II	294.52		
	Type III	285.65		
SHS_80x80x8	Type I	1471.45	0.95	1.00
	Type II	1543.72		
	Type III	1471.54		
SHS_150x150x10	Type I	3657.73	0.98	1.00
	Type II	3727.94		
	Type III	3657.89		

Load case	Combined loading: $N+M_y$				
Cross-section	Constitutive law	Ultimate compressive load [kN]	Ultimate moment [kN.m]	$R_{REAL_TYPE I} / R_{REAL_TYPE II}$	$R_{REAL_TYPE I} / R_{REAL_TYPE III}$
RHS_50x30x4	Type I	151.71	3.79	0.93	0.98
	Type II	163.83	4.1		
	Type III	155.45	3.89		
RHS_60x40x5	Type I	282.26	7.06	0.95	1.00
	Type II	295.96	7.4		
	Type III	282.37	7.06		

RHS_150x80x10	Type I	1911.7	47.79	0.97	1.00
	Type II	1975.93	49.4		
	Type III	1912.14	47.8		
SHS_40x40x3	Type I	104.02	2.6	0.98	0.98
	Type II	106.1	2.65		
	Type III	106.08	2.65		
SHS_80x80x8	Type I	828.85	20.72	0.95	1.00
	Type II	874.6	21.87		
	Type III	829.16	20.73		
SHS_150x150x10	Type I	2617.12	65.43	0.97	1.00
	Type II	2695.73	67.39		
	Type III	2617.74	65.44		

Load case	Bending moment: M_y			
Cross-section	Constitutive law	Ultimate moment [kN.m]	$R_{REAL_TYPE I} / R_{REAL_TYPE II}$	$R_{REAL_TYPE I} / R_{REAL_TYPE III}$
RHS_50x30x4	Type I	5.37	0.92	0.99
	Type II	5.85		
	Type III	5.44		
RHS_60x40x5	Type I	10.64	0.95	1.00
	Type II	11.25		
	Type III	10.65		
RHS_150x80x10	Type I	134.88	1.00	1.00
	Type II	135.03		
	Type III	134.43		
SHS_40x40x3	Type I	3.87	0.99	1.00
	Type II	3.9		
	Type III	3.87		
SHS_80x80x8	Type I	38.71	0.96	1.00
	Type II	40.16		
	Type III	38.73		
SHS_150x150x10	Type I	189.26	1.01	1.00
	Type II	187.81		
	Type III	189.33		

Accordingly, for the particular case $f_y = 690 \text{ N/mm}^2$, constitutive law *Type III* was selected and the stress-strain material curve adopted is presented in Figure 102. The $\sigma - \varepsilon$ relationship respects the conditions $\varepsilon_u > 15 \varepsilon_y$ and $f_u / f_y = 1.05$ according to EC3-Part 1-12, with a smaller yield plateau (width set as $4 \varepsilon_y$ instead of $10 \varepsilon_y$); the obtained slope is equal to $0.45\% E$ in this case and the elongation at failure ε_{\max} was limited to 10 %.


 Figure 102 – Stress-strain curve for $f_y = 690 \text{ N/mm}^2$

Concerning the distribution of residual stresses, a specific attention was paid to the modelling of these material imperfections. For both shell and beam modelling, auto equilibrated membrane residual stresses patterns were generated with constant values equal to $0.5 f_y$ at corners and the corresponding values needed to reach equilibrium in flanges and webs (again, constant “block” distributions). The residual stresses are therefore defined so that the various stresses distributions are in auto-equilibrium in a plate-per-plate basis, as illustrated in Figure 103.

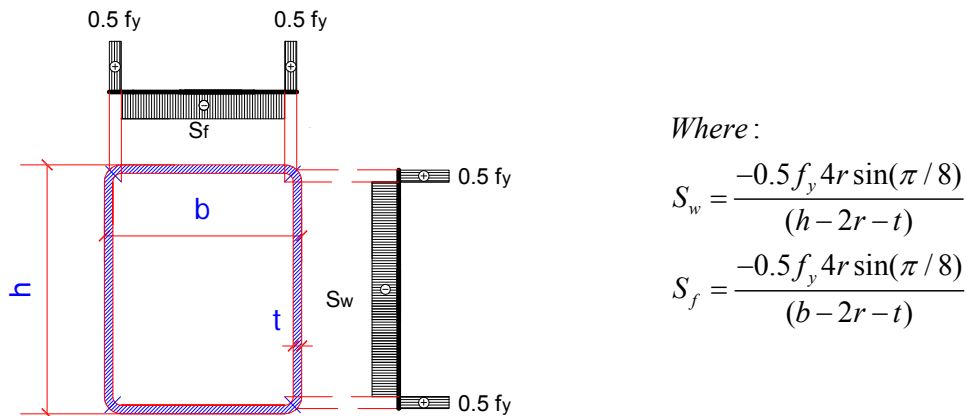


Figure 103 – Residual stresses distribution (ensuring auto equilibrium) for tubular hot-formed profiles – shell model

4.2.2. Shell models

4.2.2.1. Mesh refinement

To determine the ultimate resistance of a member, shell modelling has been used to characterize a potential influence of local buckling at the cross-section level; the sections were modelled by means of quadrangular 4-nodes plate-shell finite elements with typical features

(corotational total lagrangian formulation, Kirchhoff's theory for bending). Specimens have been modelled with a regular mesh of *Type II* all over the length, with corners modelled with two shell elements per corner (see Figure 104 and Figure 105). Case studies as detailed below shows that *Type II* mesh can predict with reasonable accuracy the structural behaviour of the members and was thus adopted in order to launch the totality of the parametric study.

Different types of mesh densities were tested for rectangular and square sections as shown in Figure 105, where the selected meshing types ranged from fine (*Type I* meshing) to coarse (*Type IV* meshing), in order to examine the influence of the mesh refinement on members' resistance. The purpose of this study is to adopt the most appropriate mesh density, able to provide an accurate numerical prediction of the member's behaviour at reasonable computation costs.

Therefore, a series of G.M.N.I.A. F.E. calculations were performed on rectangular and square hollow sections by considering the following parameters:

- Four rectangular cross-section shapes: RHS_220x120x10, RHS_300x200x8, RHS_200x100x5 and RHS_450x250x8 and four square sections: SHS_120x120x8, SHS_260x260x7.1, SHS_200x200x5 and SHS_300x300x6.3. Their respective classes are well-distributed along the class 1 to class 4 range;
- Two different element lengths: $L = 1500 \text{ mm}$ and $L = 3000 \text{ mm}$;
- Two different loading conditions: pure compression and major-axis bending with a constant moment distribution along the member;
- Yield stress: $f_y = 235 \text{ N/mm}^2$;
- 4 different mesh densities, as previously explained.

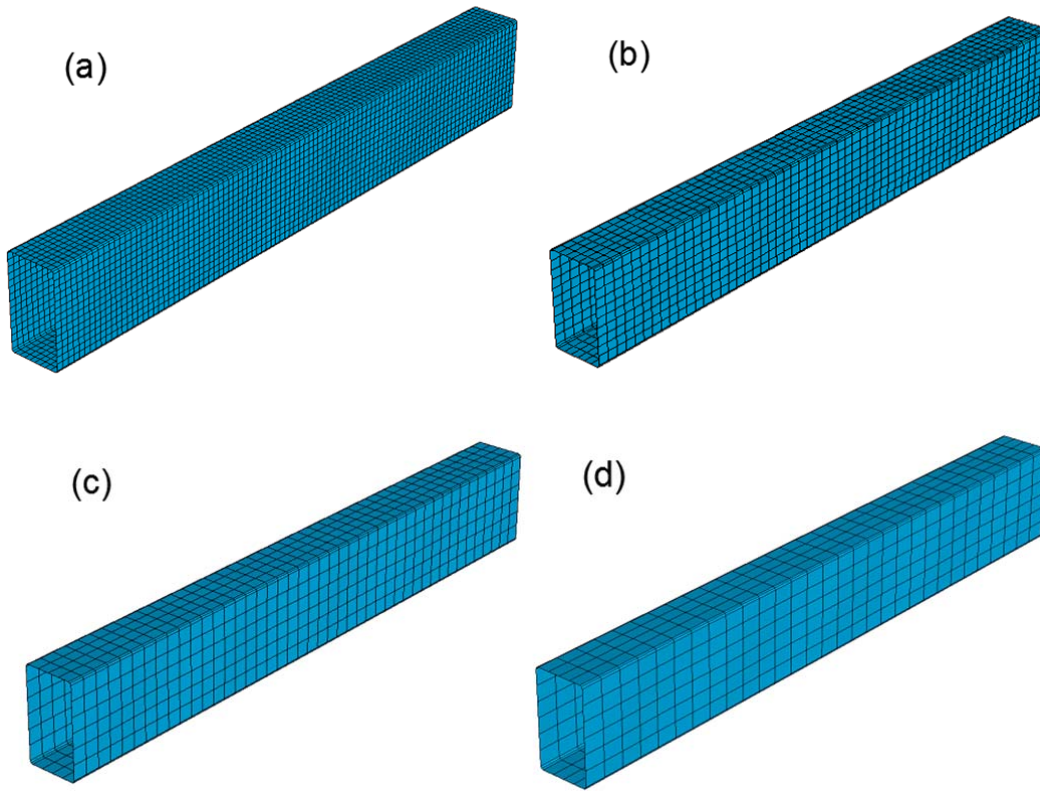


Figure 104 – Mesh density study for rectangular sections – a) *Type I* – b) *Type II* – c) *Type III* – d) *Type IV*

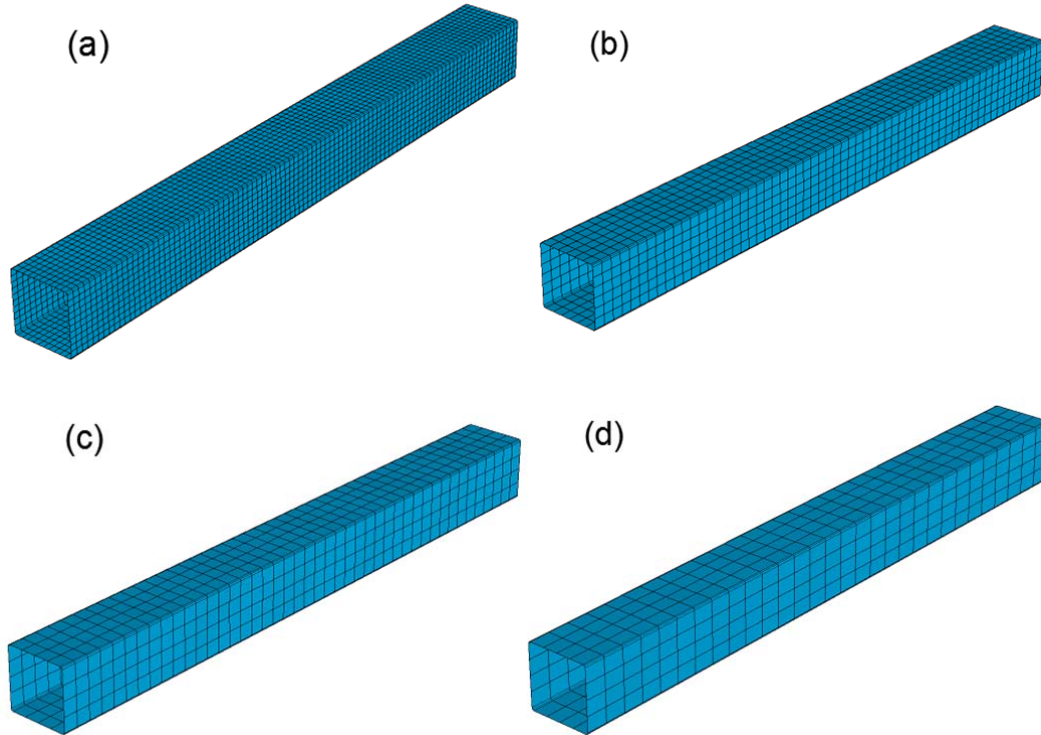


Figure 105 – Mesh density study for square sections – a) *Type I* – b) *Type II* – c) *Type III* – d) *Type IV*

Obtained results are shown in Figure 106 and Figure 107 for both rectangular and square sections, respectively. One directly observes that coarse meshes (*Type III* and *Type IV*) do not lead to acceptable results, being by as much as 13% lower than those of *Type I* mesh in the worst cases; therefore, these meshes have not been considered. Further, reasonable results and negligible differences are observed for more dense meshes (*Type I* and *Type II*) for all sections and load cases. Accordingly, mesh *Type II* was selected as it leads to satisfactory results with minimal computational effort.

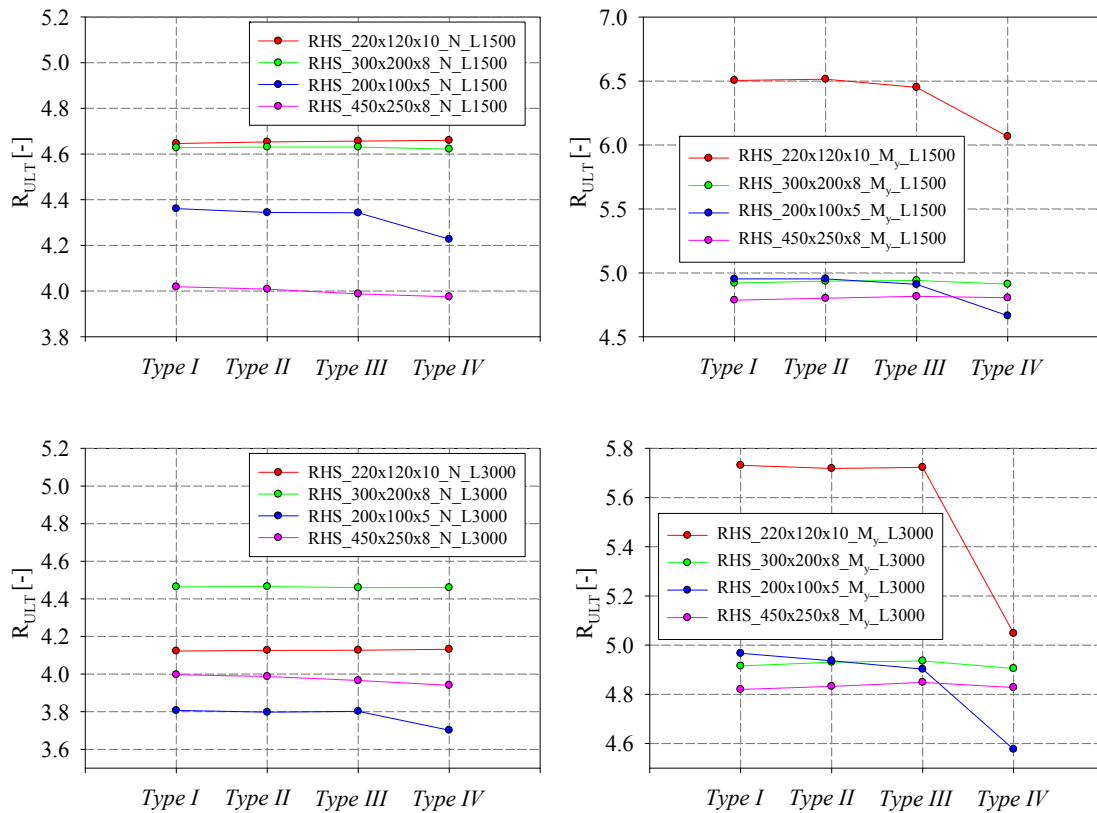
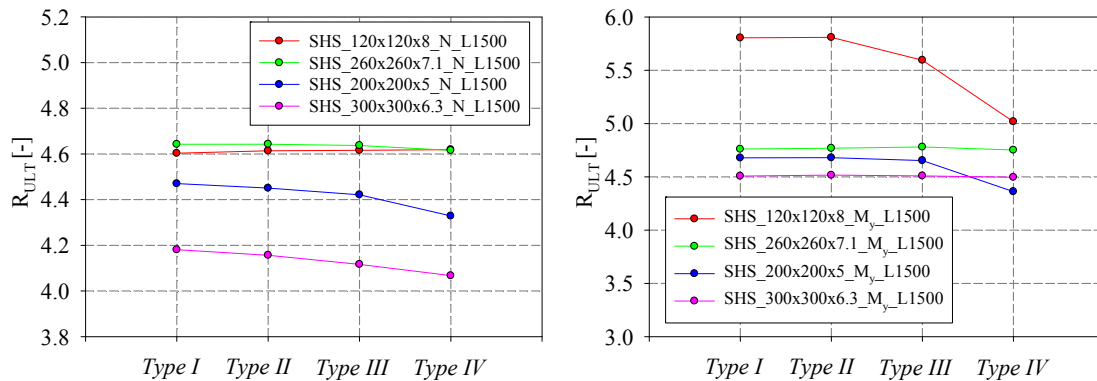


Figure 106 – Mesh density studies – Results for RHS sections



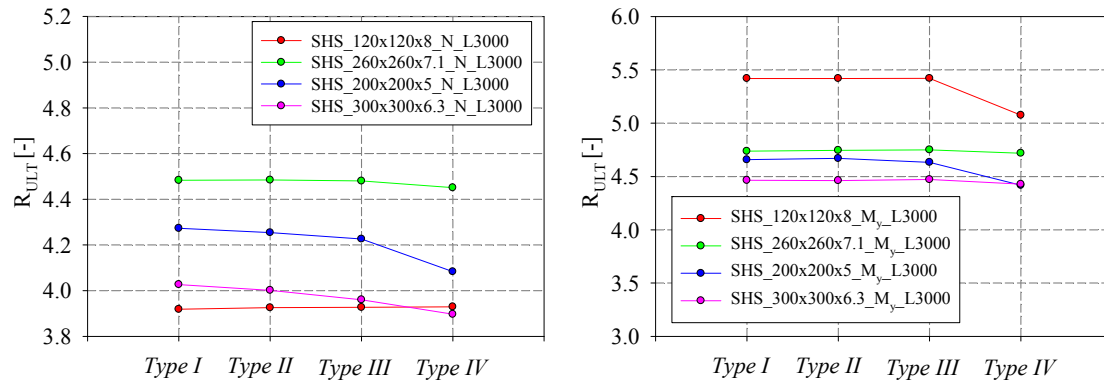


Figure 107 – Mesh density studies – Results for SHS sections

4.2.2.2. Loading and support conditions

The support conditions and the introduction of applied loads received particular attention, and use of so-called kinematic linear constraints has been made to ensure a “plane-sections-remain-plane” behaviour of the end sections. Following ideal simply-supported “fork” support conditions, the end cross-section can only exhibit a maximum of three degrees of freedom: axial global displacement, rotation about the strong axis and rotation about the weak axis. Only three different nodes are then necessary to describe the displacement of any point in the cross-section once the linear relationships for axial displacements are established. In other words, a maximum of three nodes may experience a “free” longitudinal displacement; all other nodes’ x-displacements linearly depend on the longitudinal displacements of the “x-free” nodes to respect a global cross-sectional displaced configuration. The three nodes were chosen at the plate edges (near different corners) of the cross-section, and all the nodes in between were constrained to the three main nodes with linear relationships. Additional fictitious nodes have been defined at the centroids of the end-cross-sections for the definition of the support conditions, and transverse supports preventing from local buckling have also been implemented in each plate. External loading was applied through four concentrated forces at the member’s ends (i.e. strong, weak axis bending moments and axial forces) and has been implemented at the flanges’ plates as shown in Figure 108.

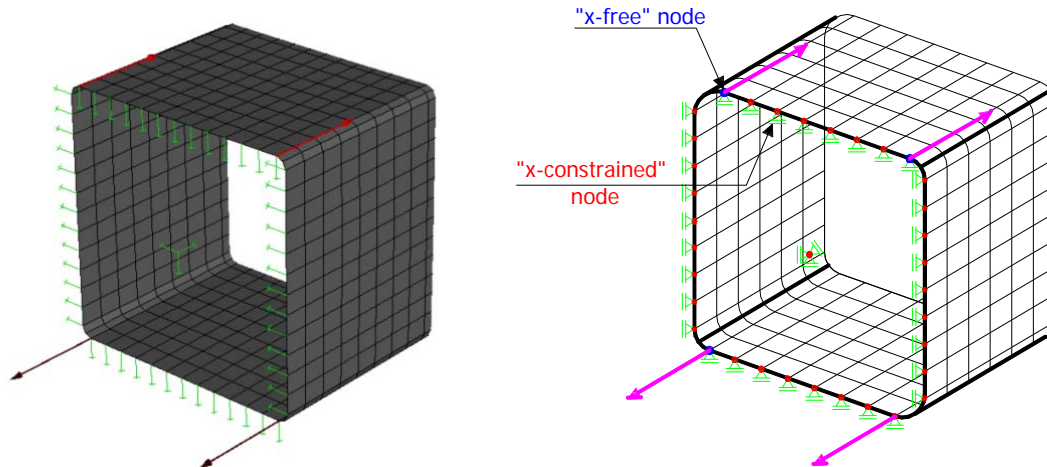


Figure 108 – Loading and support conditions

4.2.2.3. Geometrical imperfections

A specific attention was paid to the introduction of initial imperfections in the F.E. models, where both global and local defaults were taken into account through an appropriate modification of node coordinates.

4.2.2.3.1. Selection and definition of local imperfections

In order to examine the influence of local initial imperfection on the member resistance, different *shapes* and *amplitudes* of initial local geometric imperfections were examined.

Local imperfections *shapes* were introduced through an appropriate modification of node coordinates of the considered plate (i.e. web or flange) with a combination of sine waves in both directions in square half-waves patterns (see Figure 109). Suitable inward-outward directions have been adopted to keep a certain continuity in the overall pattern.

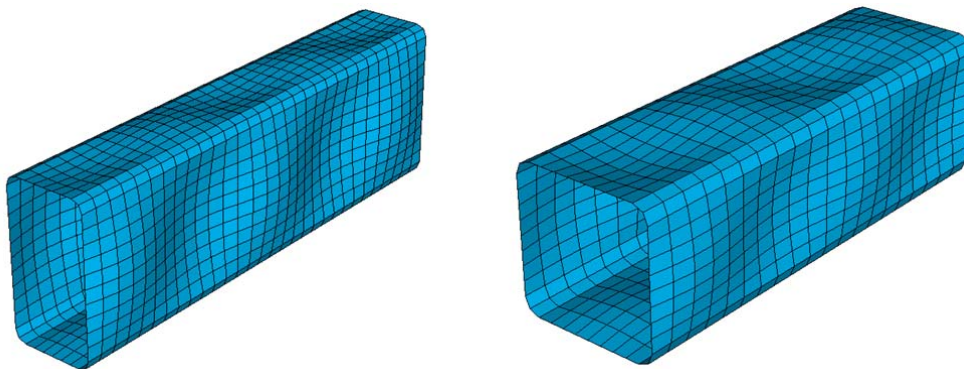


Figure 109 – Local geometrical imperfections adopted for both square and rectangular hollow sections
(magnified view)

Two types of longitudinal sine period were defined:

- Type 1: sine period is equal to the *average period* of both constitutive plates of the section;
- Type 2: sine period is equal to the *corresponding plate* width of the section. The flanges and webs therefore have independent initial imperfection *shapes* in this case; thus, the continuity of local imperfections between the flanges and the webs is lost.

For each type of shape defined, four values of the amplitude $a/200$ were adopted, where a stands as the corresponded plate width:

- *Average* refers to an ' a ' equal to $[(b - t - 2r) + (h - t - 2r)]/2$; ' a ' is equal to the *average* width of both constitutive plates of the section;
- *Per plate* refers to an ' a ' equal to $(b - t - 2r)$ or $(h - t - 2r)$; ' a ' is equal to the *corresponding plate* width of the section. The flanges and webs have independent initial imperfection *amplitudes* in this case;
- *Bigger* refers to an ' a ' equal to $(h - t - 2r)$; ' a ' is equal to the *corresponding bigger plate* width of the section;
- *Smaller* refers to an ' a ' equal to $(b - t - 2r)$; ' a ' is equal to the *corresponding smaller plate* width of the section.

Figure 110 represents the imperfections *shapes* and *amplitudes* used for each plate element individually; Figure 111 shows a magnified view of local imperfections introduced through adequate sine curve in both directions with respect to averaged or per plate periods.

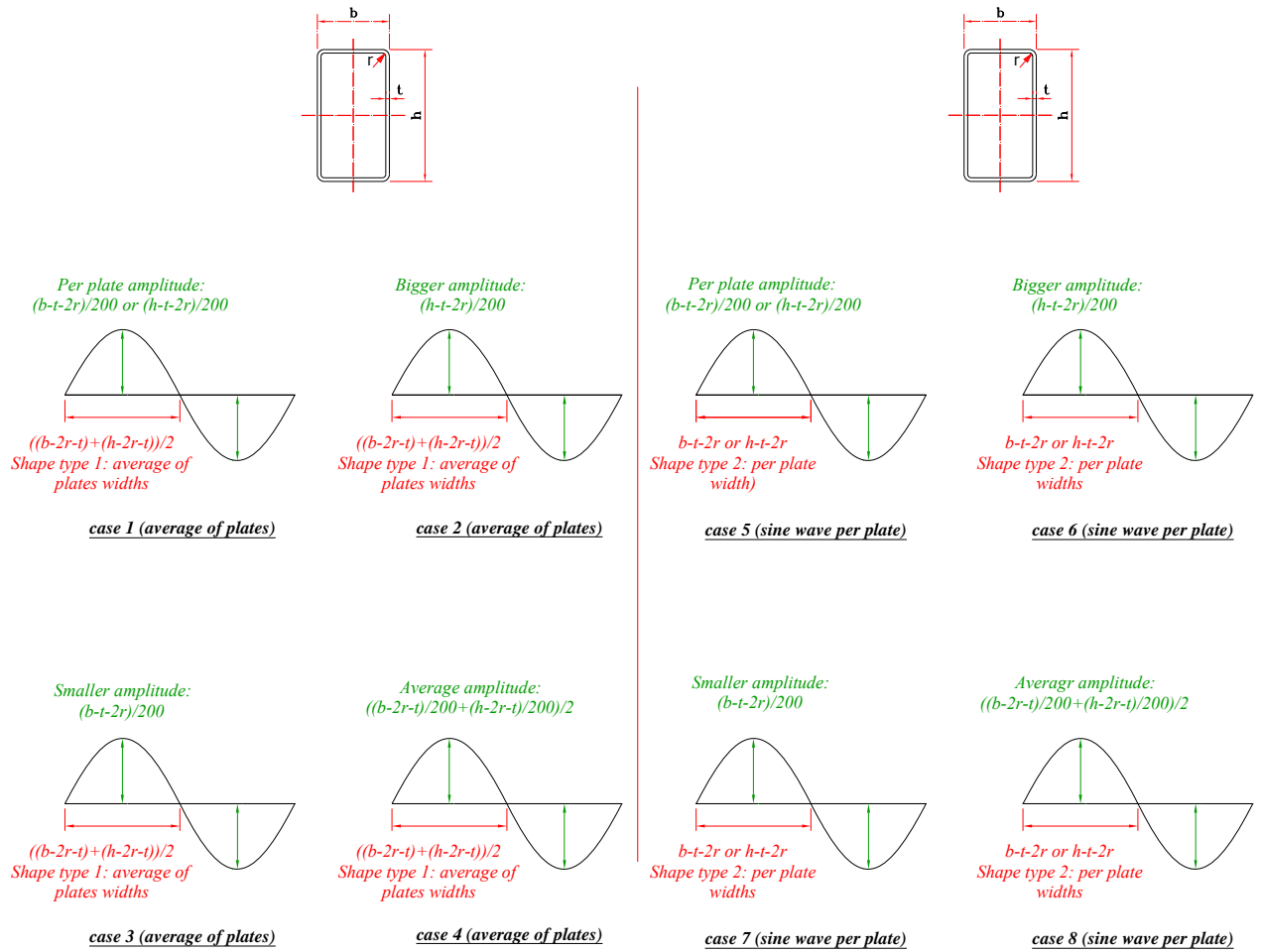


Figure 110 – Imperfections *shapes* and *amplitudes* cases adopted – a) Type 1: Sine period equal to the average of plates – b) Type 2: Sine wave per-plate

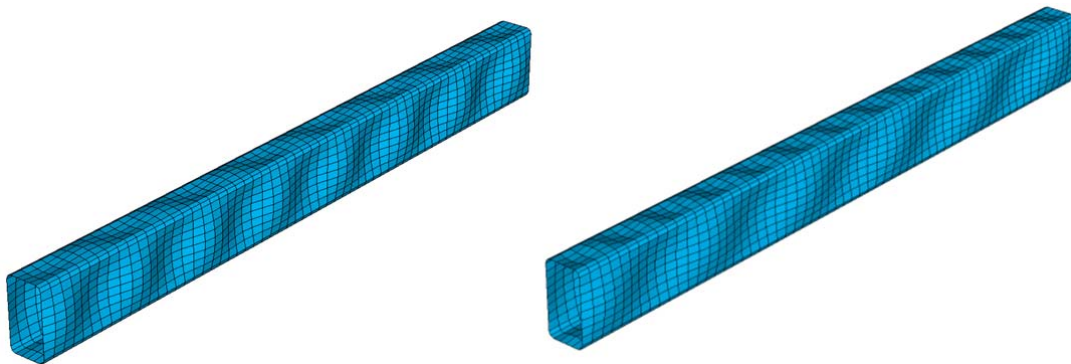
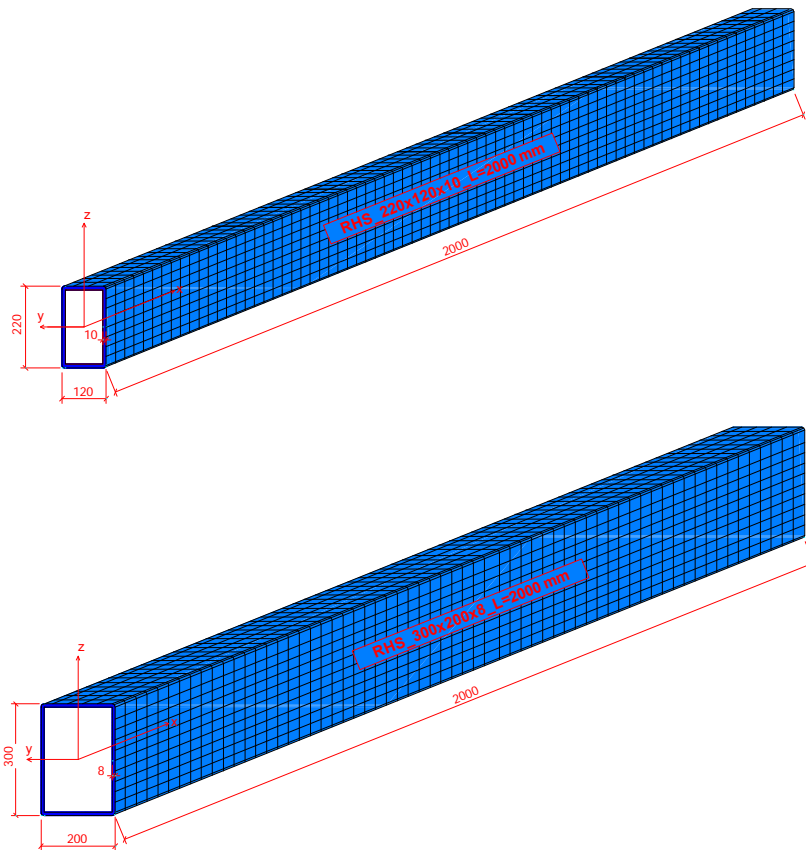


Figure 111 – Magnified view of local imperfections introduced through sine curve with respect to – a) averaged period – b) per-plate periods

In order to characterize their influence on the resistance, a series of F.E. calculations were carried out on rectangular hollow sections by considering the following parameters:

- Four cross-section shapes with the corresponding cross-sectional classes well-distributed along class 1 and class 4: RHS_220x120x10, RHS_300x200x8, RHS_200x100x5 and RHS_450x250x8 (see Figure 112);
- Two different element lengths: $L = 2000 \text{ mm}$ and $L = 6000 \text{ mm}$;
- Two different loading conditions: pure compression and major-axis bending with a constant moment distribution along the member;
- Yield stress: $f_y = 235 \text{ N/mm}^2$;
- Constant initial global imperfection with a sinusoidal shape varying along the member's length with maximum amplitude of $L / 1000$ at mid-span.

All cases (i.e. 1 to 8) as defined in Figure 110 have been investigated, in addition to case 9 corresponding to no local initial imperfections.



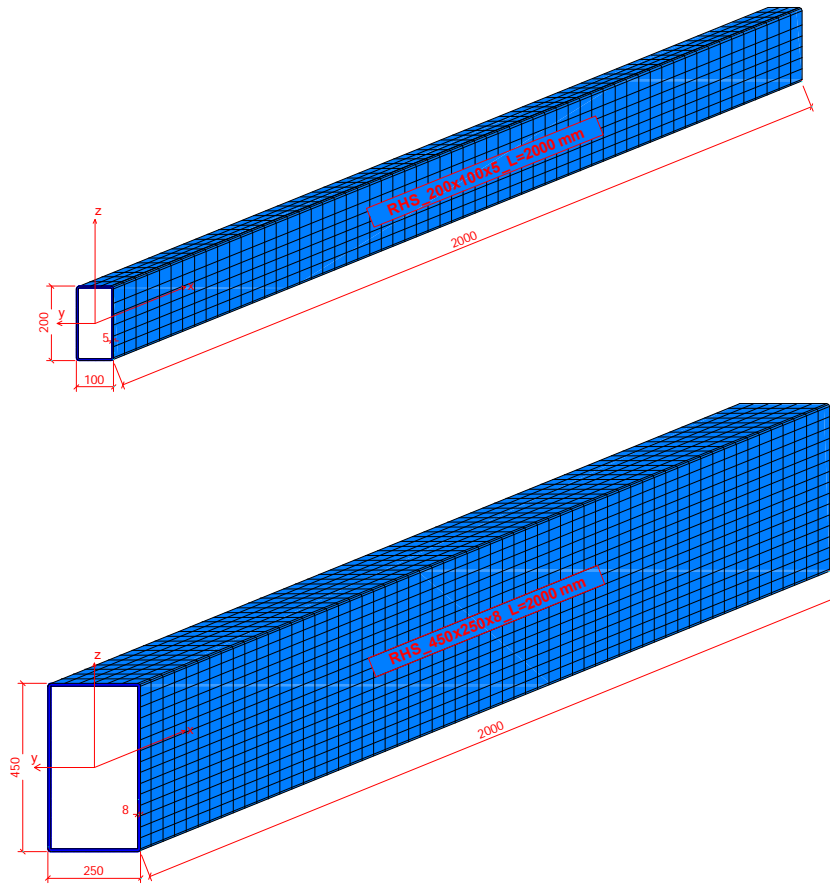


Figure 112 – Members dimensions and geometry – a) RHS_220x120x10 – b) RHS_300x200x8 – a) RHS_200x100x5 – b) RHS_450x250x8

Obtained results are illustrated in Figure 113 and Figure 114 for sections in compression and under major-axis bending, respectively.

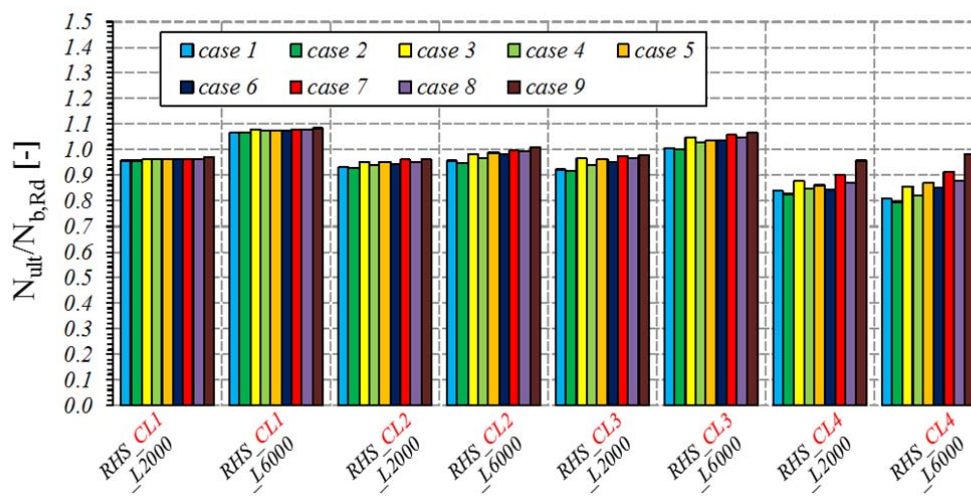


Figure 113 – Local imperfection sensitivity under pure compression

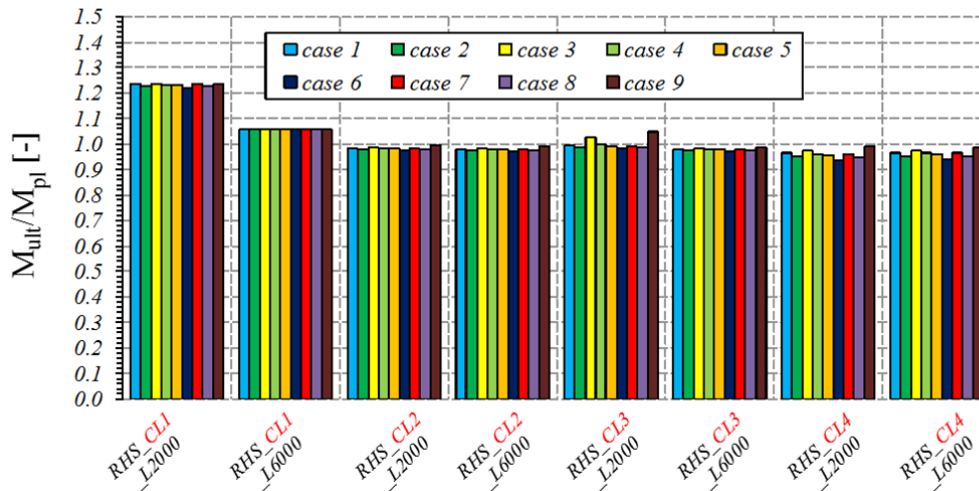


Figure 114 – Local imperfection sensitivity under major-axis bending

The following conclusions can be drawn from these figures:

- the results showed a minor difference between all the adopted initial imperfections for class 1 and class 2 sections as expected, since the corresponding cross-sections comprise highly stocky components (i.e. webs and flanges), so that the member is not significantly subjected to local instabilities before plastic deformations occur; the influence of local buckling on the global behaviour remains negligible, as expected. This difference is slightly more visible for class 3 and class 4 sections where the cross-sections comprise more slender components. Local instability for these sections occurs at an early stage and the handling of local buckling becomes crucial;
- as expected by comparing cases 2, 3, 4 that correspond to type 1 shape, one may notice that the section exhibits the highest resistance in case 3 (i.e. which correspond to the lowest local amplitude $a = (b - t - 2r) / 200$); the lowest one in case 2 (which correspond to the highest local amplitude $a = (h - t - 2r) / 200$); and an averaged capacity between the 2 cases is obtained in case 4 (where the amplitude corresponds to the average between flange and webs: $a = (\text{average}(h - t - 2r), (b - t - 2r)) / 200$ in this case). These results show how several initial imperfection *amplitudes* may affect the resistance which tends to increase with decreasing of the adopted *amplitudes*;
- the same tendencies are obtained in cases 6, 7 and 8 which correspond to type 2 shape;

- long members (length $L = 6000 \text{ mm}$) are less sensitive to the adopted type of local imperfection than the shorter ones ($L = 2000 \text{ mm}$). In the high slenderness range, member buckling dominates (the larger the slenderness of the member the greater the dominance), regardless of the section slenderness and local buckling that may occur;
- although all considered cases led to very close results, the *Bigger* amplitude, (i.e. corresponding to case 2 and case 6 and representing the highest local amplitude adopted) presented unfavourable initial amplitude, leading to a drop in capacity compared to the other cases, and was therefore considered to be too severe for being used in the F.E. simulations;
- the *Smaller* amplitude, (i.e. corresponding to case 3 and case 7 and representing the lowest local amplitude adopted) was also omitted from the F.E. studies. The cross-section capacities can be shown to be overestimated in these cases [58];
- *Per plate* and *Average* amplitudes are seen to have an almost similar effect on the cross-section capacity. Therefore, cases 1 and 4 representing both type 1 imperfection shape and having respectively *Per plate* and *Average* initial amplitudes, are seen to have almost equivalent effect on the cross-section capacity. The same conclusions are drawn for cases 5 and 8 representing both type 2 imperfection shape.

It is to be recalled that the definition of the sine waves periods must be dependent of both the web and flanges widths, so that rectangular sections can possess a consistent (equal) number of half-waves in both webs and flanges. Thus, the local imperfections in the flanges and webs will be continuous and coherent, with the corner remaining unaffected, i.e. if the web buckles in an outward direction, the flanges' buckles should be inward and vice versa [59].

Based on the previously-mentioned conclusions, the adopted local imperfection is type 1 that represents a sine period equal to the average period of both constitutive plates of the section, with the most reasonable and realistic amplitude of imperfections chosen as a per plate amplitude $a / 200$ with 'a' equal to $(b - t - 2r)$ or $(h - t - 2r)$.

4.2.2.3.2. Selection and definition of global imperfections

A similar approach was used in the numerical investigations launched to examine the influence of *global* imperfections on member capacity. However, in this case the local

imperfections were kept constant and the global imperfections varied following different *shapes* and *amplitudes*. Two main types of global imperfections were considered:

- Type 1: the global initial imperfection was introduced for both strong and weak axis (i.e. lateral default) with a so-called sinusoidal shape varying along the member length with a maximum amplitude at mid-span. Three different values of amplitude were chosen: $L / 500$, $L / 1000$ and $L / 2000$, designated as cases 1, 2 and 3 respectively, where L is the length of the corresponding element;
- Type 2: modal imperfections based on the first eigenmode of a linear buckling analysis with scaled amplitude taken as $L / 500$, $L / 1000$ and $L / 2000$, designated as cases 4, 5 and 6 respectively.

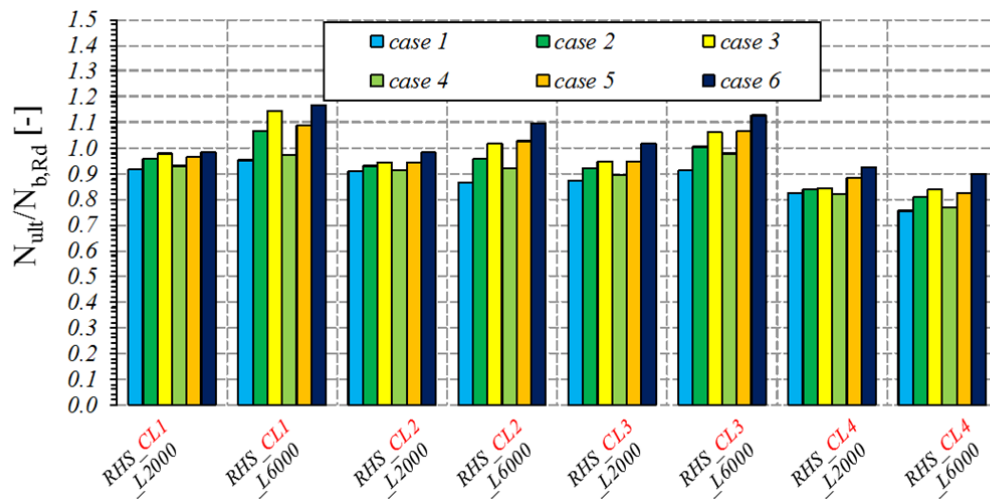


Figure 115 – Global imperfection sensitivity under pure compression

The obtained results shown in Figure 115 clearly demonstrate the following points:

- as expected in the case of pure compression, an increase in the imperfection's amplitude (from $L / 2000$ to $L / 500$) decreases the resistance;
- the eigenmode cases gave higher results than the hand-defined sine curve cases when the section is subjected to pure compression;
- the short members (length $L = 2000$ mm) are less sensitive to the adopted type of imperfection than the longer one ($L = 6000$ mm), since it is known that, in the $\chi - \lambda$

diagram, the effect of imperfection have larger influence on slenderness values λ_{CS+MB} ranging from 0.5 to 1.3.

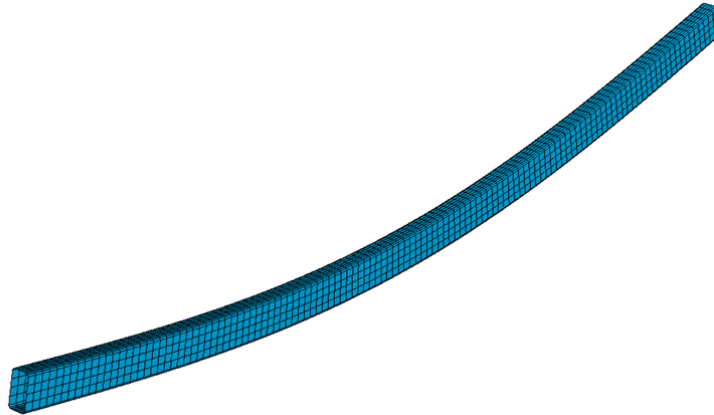


Figure 116 – Magnified view of imperfections introduced as based on the first eigenmode

The approach consisting in introducing imperfection patterns by means of the first eigenmode analysis seems to be slightly less severe; the hand-defined sine curve cases lead to more conservative results. The amplitude of $L / 500$ drops the $L / 1000$ resistance down to 11% in the worst cases, and is considered to be too severe and therefore is not adopted in the F.E. parametric study. The amplitudes of $L / 1000$ and $L / 2000$ lead to more realistic results compared to the amplitude of $L / 500$, and can safely represent the real (measured) amplitudes of members [60]. A maximum difference between these cases is reported to be equal to 6%. It is to be noted that experimental measurements show that within Europe's production, a realistic average value of steel member's initial imperfection amplitude lies around $L / 1000$; however the amplitude of $L / 500$ is outside fabrication tolerances [52].

Therefore, initial geometrical imperfections have been basically introduced through adequate modifications of node coordinates following sine shapes in both major and minor-axes with the realistic average value of global imperfection amplitude equal to $L / 1000$ in both principal planes as illustrated in Figure 117.

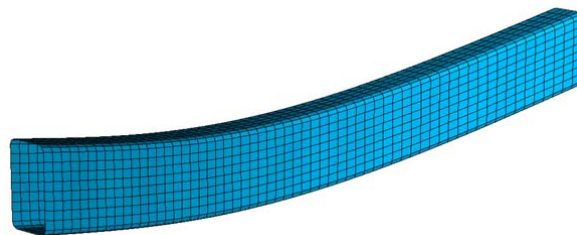


Figure 117 – Magnified initial global geometric imperfections

4.2.2.4. Load-path sensitivity

In order to examine the influence of the introduction of loading on the member resistance, 4 different loading sequences were examined, based on different combinations described as follows:

- case 1: one-stage loading: applying N , M_y and M_z simultaneously (*cyan* load-path in Figure 118);
- case 2: two-stages loading: applying N in a first stage, then continue with M_y+M_z simultaneously in the second stage (*red* load-path in Figure 118);
- case 3: two-stages loading: applying M_y in a first stage then continue with $N+M_z$ simultaneously in the second stage (*blue* load-path in Figure 118);
- case 4: applying M_z in a first stage, then continue with $N+M_y$ simultaneously in the second stage (*green* load-path in Figure 118).

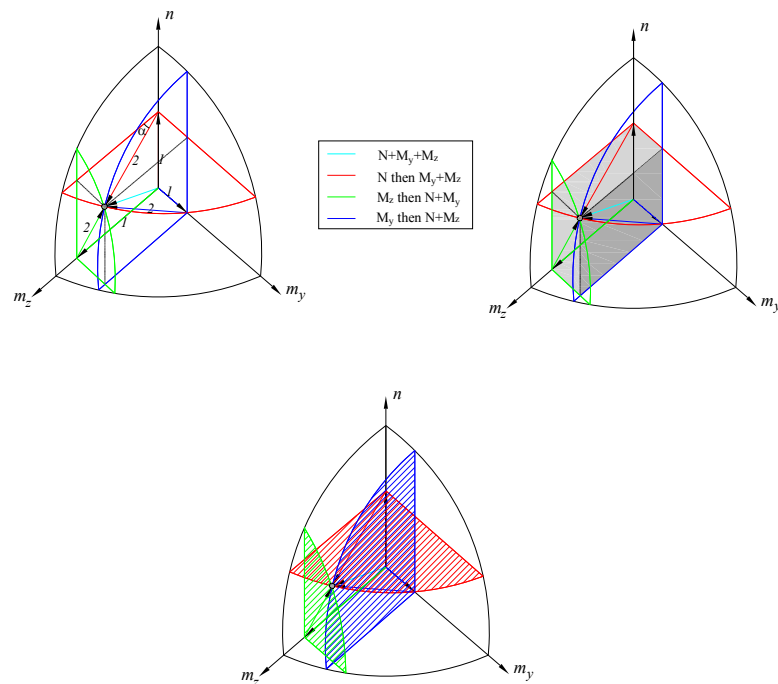


Figure 118 – Load path representation¹³

¹³ Figure 118 is only an illustrative drawing of the adopted load paths, in which n refers to the applied level of axial forces, m_y and m_z are respectively the applied levels of major and minor-axis bending.

Fictitious interactive curves have been drawn in Figure 118 for illustrative purposes of showing a target grey dot that all load-paths should lead to if they would give identical responses.

A series of F.E. calculations were carried out on rectangular and square hollow sections with the following parameters:

- four rectangular cross-section shapes (RHS_220x120x10, RHS_300x200x8, RHS_200x100x5 and RHS_450x250x8) and four square cross-section shapes (SHS_120x120x8, SHS_260x260x7.1, SHS_200x200x5, SHS_300x300x6.3) with the corresponding cross-sectional classes well-distributed along class 1 and class 4 section as illustrated in Figure 119;
- combined loading situations with a constant bending moment distribution along the member defined as follows:
 - o type 1: corresponds to a relative axial force ratio $n = 0.3$ (i.e. the load case becoming thus a compression of 30% $N_{b,Rd}$ where $N_{b,Rd}$ represents the buckling resistance of the member. In this case, the sections exhibit little influence of instability due to the low level of compression and the bending moment is predominant), with $\alpha_{biaxiality} = 50^\circ$ representing the biaxial bending ratio in a m_y - m_z diagram (see Figure 120 for illustration);
 - o type 2: corresponds to a relative axial force ratio $n = 0.7$ (global buckling becomes determinant due to the high level of compression) with a biaxial bending ratio $\alpha_{biaxiality} = 50^\circ$;
 - o type 3: corresponds to a relative axial force ratio $n = 0.7$ with biaxial bending ratio $\alpha_{biaxiality} = 70^\circ$.
- yield stress: $f_y = 235 \text{ N/mm}^2$;
- 4 different load sequences as previously explained;
- 3 different member's lengths: $L = 4000 \text{ mm}$, $L = 5500 \text{ mm}$ and $L = 7000 \text{ mm}$.

Additional calculations were simulated with the same parameters mentioned before with a length equal to three times the height of the section in order to determine the cross-section resistance.

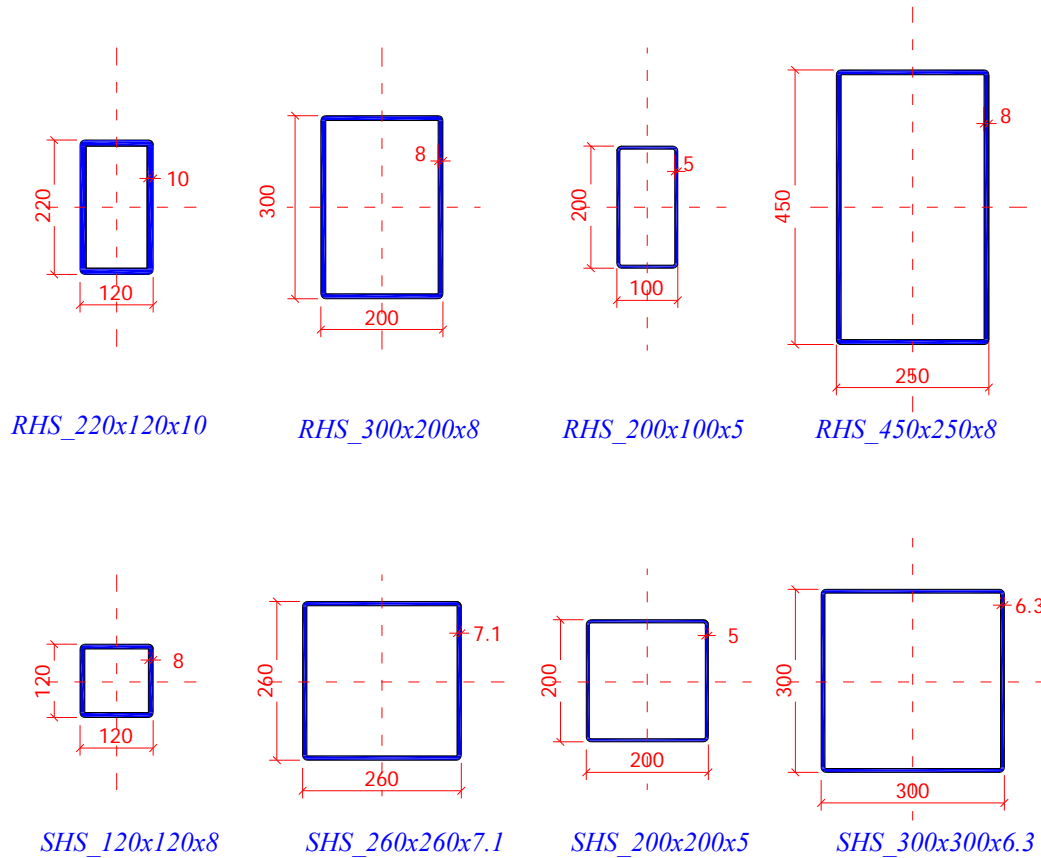


Figure 119 – Cross-section dimensions adopted in the load-path sensitivity

Obtained G.M.N.I.A. results for square sections are compared with Eurocode 3 predictions and presented in Figure 120 to Figure 127 and results obtained for rectangular ones are shown in Figure 128 to Figure 135. For sake of simplicity, the results obtained for $L = 5500 \text{ mm}$ are not presented in this section, and can be found in Annex 4. The graphs on the left column represent the interaction diagrams $m_y = M_y / M_{y,Rk}$ vs. $m_z = M_z / M_{z,Rk}$ and the ones on the right side represent $n = N_{Ed} / N_{b,Rd} = N_{Ed} / \chi \cdot N_{Rk}$ vs. m_y where M_{Rk} and N_{Rk} are the moment and normal force resistances, respectively. Note that, EC3_pl., EC3_el. and EC3_eff. represent the Eurocode 3 plastic, elastic and effective interaction curves. The intention is here to visualize the degree of reached axial forces for each load-path on one hand and the interaction $M_y - M_z$ in each load-path on another hand. Even though all load sequences would not follow the same

path, the interaction diagrams m_y vs. m_z illustrates close responses for all load sequences. The interaction diagram n vs. m_y compares the radial distances of the considered load-cases.

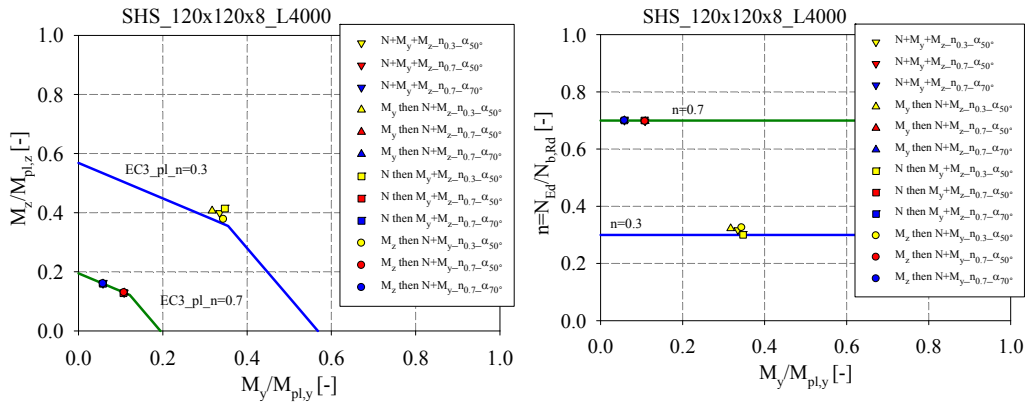


Figure 120 – Comparison of G.M.N.I.A. results for the SHS_120x120x8 of $L = 4000$ – a) m_z vs. m_y diagram – b) n vs. m_y diagram

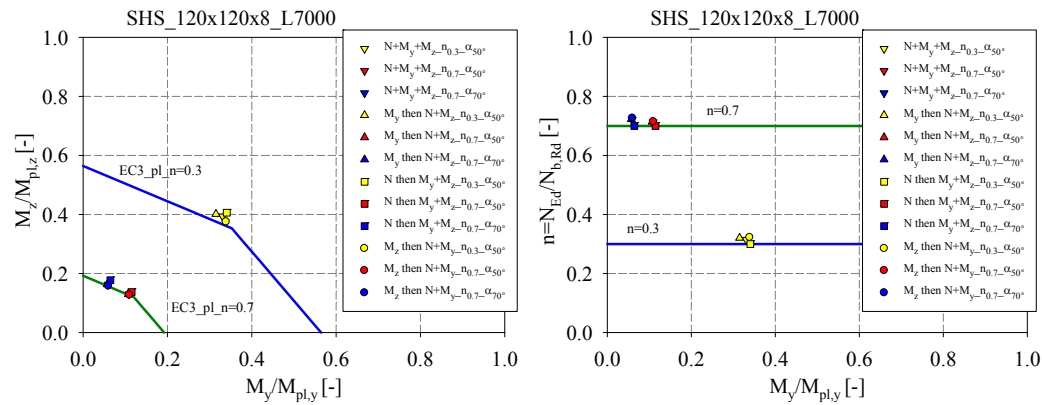


Figure 121 – Comparison of G.M.N.I.A. results for the SHS_120x120x8 of $L = 7000$ – a) m_z vs. m_y diagram – b) n vs. m_y diagram

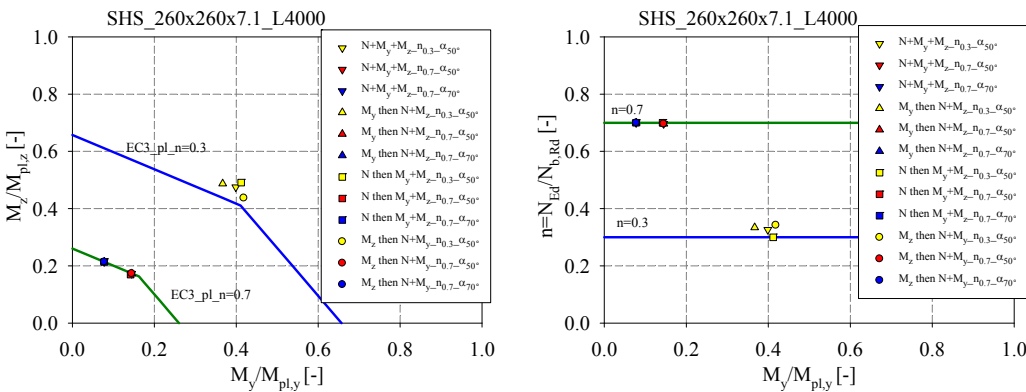


Figure 122– Comparison of G.M.N.I.A. results for the SHS_260x260x7.1 of $L = 4000$ – a) m_z vs. m_y diagram – b) n vs. m_y diagram

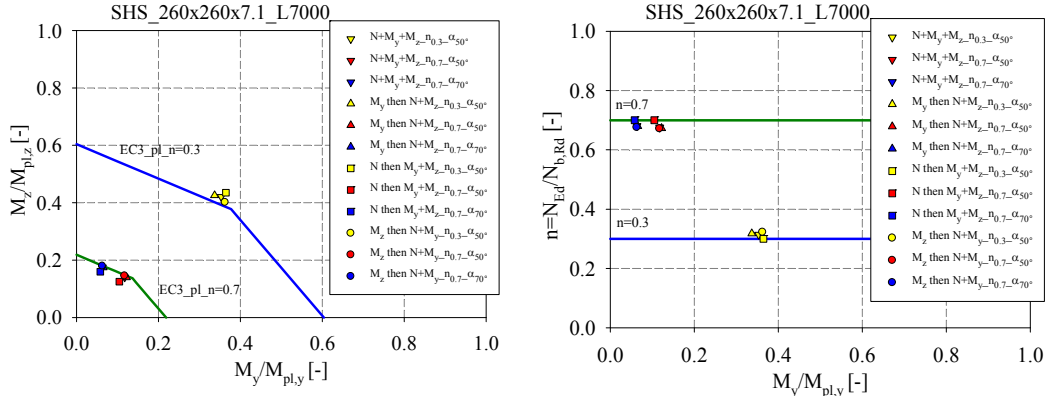


Figure 123 – Comparison of G.M.N.I.A. results for the SHS_260x260x7.1 of $L = 7000$ – a) m_z vs. m_y diagram – b) n vs. m_y diagram

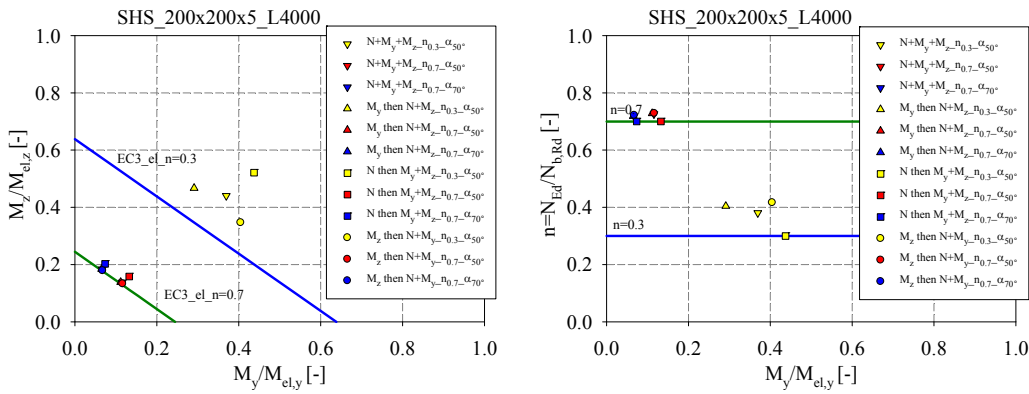


Figure 124 – Comparison of G.M.N.I.A. results for the SHS_200x200x5 of $L = 4000$ – a) m_z vs. m_y diagram – b) n vs. m_y diagram

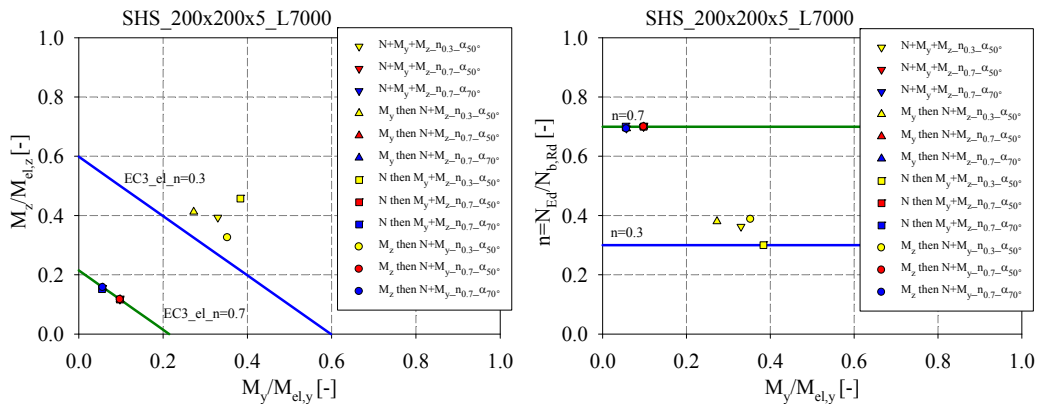


Figure 125 – Comparison of G.M.N.I.A. results for the SHS_200x200x5 of $L = 7000$ – a) m_z vs. m_y diagram – b) n vs. m_y diagram

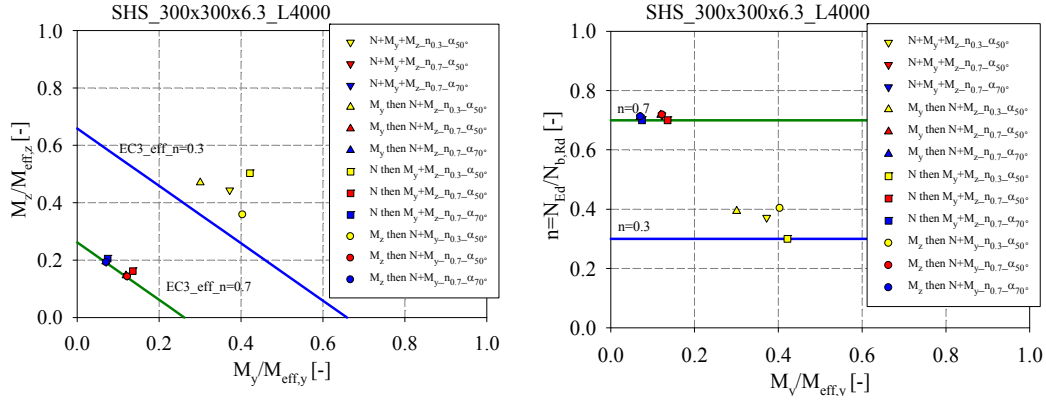


Figure 126– Comparison of G.M.N.I.A. results for the SHS_300x300x6.3 of $L = 4000$ – a) m_z vs. m_y diagram – b) n vs. m_y diagram

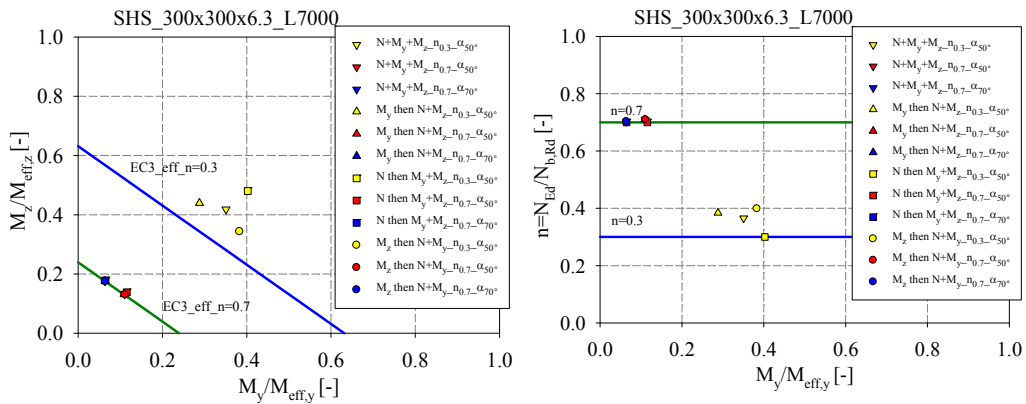


Figure 127 – Comparison of G.M.N.I.A. results for the SHS_300x300x6.3 of $L = 7000$ – a) m_z vs. m_y diagram – b) n vs. m_y diagram

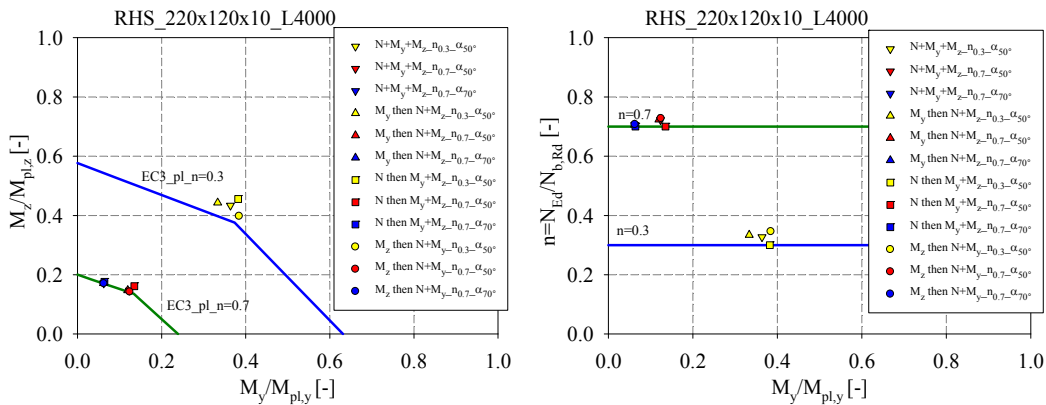


Figure 128– Comparison of G.M.N.I.A. results for the RHS_220x120x10 of $L = 4000$ – a) m_z vs. m_y diagram – b) n vs. m_y diagram

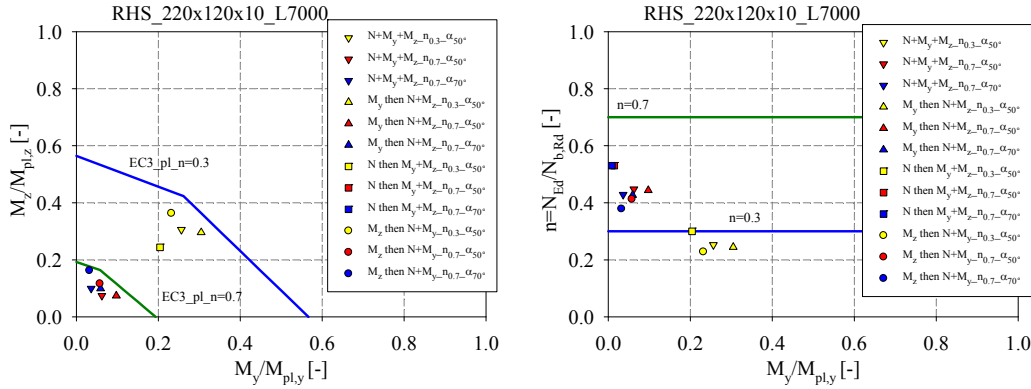


Figure 129 – Comparison of G.M.N.I.A. results for the RHS_220x120x10 of $L = 7000$ – a) m_z vs. m_y diagram – b) n vs. m_y diagram

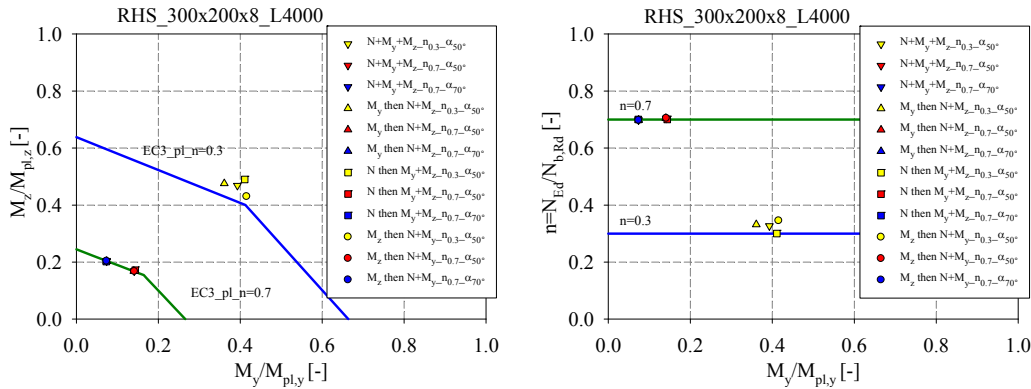


Figure 130– Comparison of G.M.N.I.A. results for the RHS_300x200x8 of $L = 4000$ – a) m_z vs. m_y diagram – b) n vs. m_y diagram

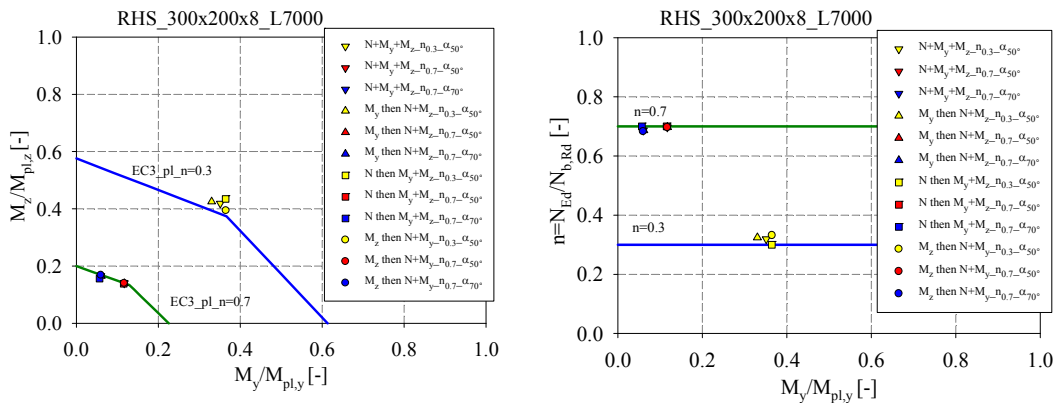


Figure 131 – Comparison of G.M.N.I.A. results for the RHS_300x200x8 of $L = 7000$ – a) m_z vs. m_y diagram – b) n vs. m_y diagram

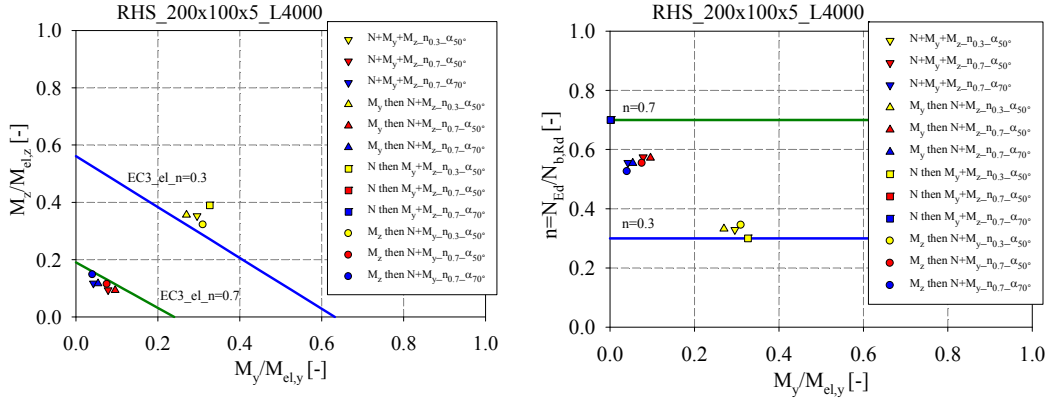


Figure 132 – Comparison of G.M.N.I.A. results for the RHS_200x100x5 of $L = 4000$ – a) m_z vs. m_y diagram – b) n vs. m_y diagram

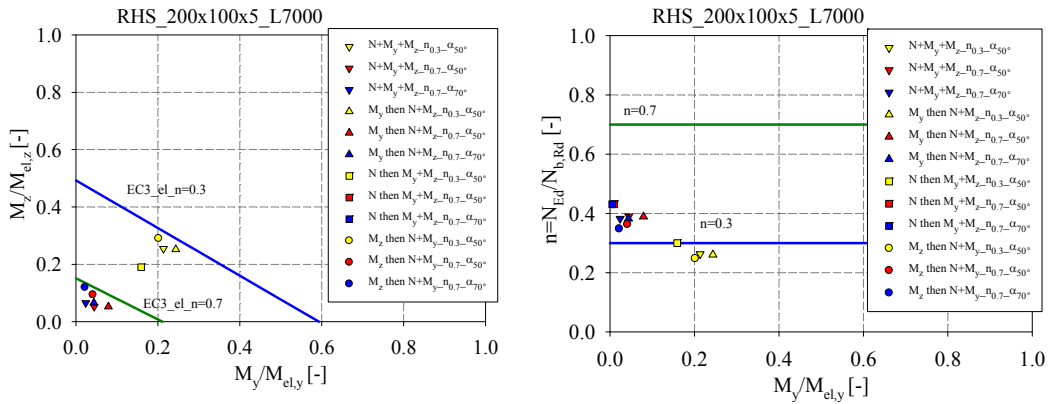


Figure 133 – Comparison of G.M.N.I.A. results for the RHS_200x100x5 of $L = 7000$ – a) m_z vs. m_y diagram – b) n vs. m_y diagram

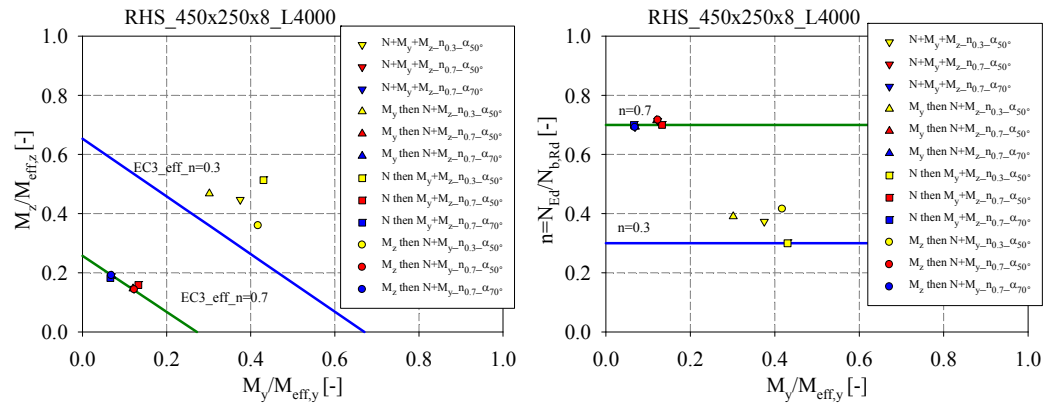


Figure 134 – Comparison of G.M.N.I.A. results for the RHS_450x250x8 of $L = 4000$ – a) m_z vs. m_y diagram – b) n vs. m_y diagram

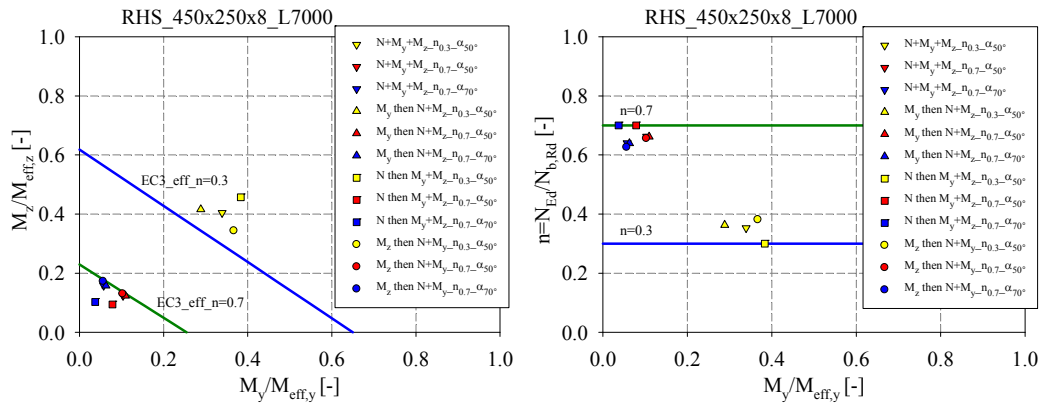


Figure 135 – Comparison of G.M.N.I.A. results for the RHS_450x250x8 of $L = 7000$ – a) m_z vs. m_y diagram – b) n vs. m_y diagram

The following conclusions can be drawn from these figures:

- all load sequences showed close results for a high level of compression ($n = 0.7$) and slightly scattered ones for small level of compression ($n = 0.3$);
- for short lengths ($L = 4000$ mm), the case 2 combination, i.e. N applied in a first stage followed by M_y+M_z (represented with square dots on the figures above), reaches the highest degree of bi-axiality at failure m_y - m_z (see diagrams on the left), and reaches the defined degrees of axial forces ($n = 0.3$ and $n = 0.7$) (right diagram), (see Figure 134);
- some of the long elements ($L = 7000$ mm), having a high relative axial force ratio ($n = 0.7$), reach the smallest degree of biaxial bending at failure. In this case, the failure is mostly due to the normal force. For the case of the slender section RHS_200x100x5 of $L = 7000$ mm for example, the defined relative axial force ratios were not reached and the section failed before the end of stage 1. Both local (i.e. cross-section instabilities) and flexural buckling (i.e. member instabilities) modes occur and interact in this case due to the high level of axial force and to the highly slender components of the corresponding elements;
- for all section types and lengths, the load case 1, i.e. applying $N+M_y+M_z$ simultaneously exhibits the most conservative responses compared to other load cases. The differences between all load sequences results remain very acceptable. For scientific consistency, load case 1 was used to launch the totality of the parametric study;

- short elements ($L=4000\text{ mm}$) with small levels of compression ($n = 0.3$) tested under load case 2 (i.e. the axial level was defined in the first load sequence), could reach lower levels of axial forces than the other load cases at the expense of higher levels of strong and minor-axis bending;
- for all section types and lengths, load path 4 exhibits the highest level of axial forces for all load cases, in comparison with load path 2 and 3.

All obtained results were drawn in an O.I.C. format, as presented in Figure 136 to Figure 138, where the horizontal axis represents the generalized slenderness λ_{CS+MB} defined in Equation (167) as the member's relative slenderness including the cross-sectional penalty, while the vertical axis reports the reduction factor χ_{CS+MB} .

$$\lambda_{CS+MB} = \sqrt{\frac{\chi_{CS} \cdot R_{RESIST}}{R_{STAB,MB}}} \quad (167)$$

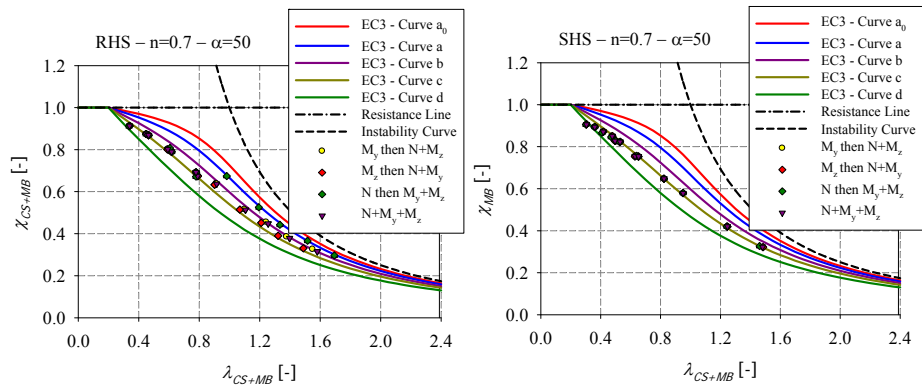


Figure 136 – G.M.N.I.A. results for the load case $n = 0.7$ $\alpha = 50^\circ$ – a) Rectangular hollow sections – b) Square hollow sections

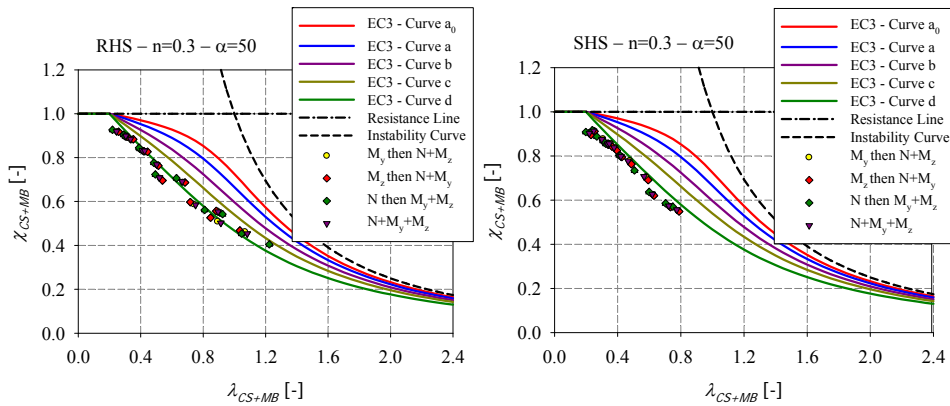


Figure 137 – G.M.N.I.A. results for the load case $n = 0.3$ $\alpha = 50^\circ$ – a) Rectangular hollow sections – b) Square hollow sections

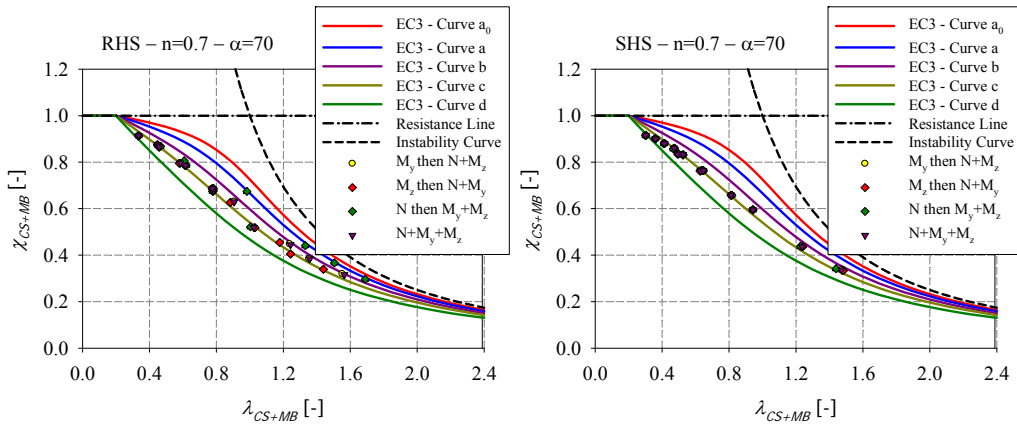


Figure 138 – G.M.N.I.A. results for the load case $n = 0.7$ $\alpha = 70^\circ$ – a) Rectangular hollow sections – b) Square hollow sections

The way the critical load multiplier $R_{STAB,MB}$ and the plastic load multiplier R_{RESIST} are calculated by introducing an initial loading based on the G.M.N.I.A. calculations (i.e. the obtained ultimate results were used as a basis to generate the initial loading that was increased proportionally to obtain the corresponding R_{RESIST} and $R_{STAB,MB}$ factors). Thus, these factors were calculated through a one-stage procedure (i.e. N , M_y and M_z being applied simultaneously) unlike the corresponding G.M.N.I.A. calculations (i.e. with two stages).

One may notice that almost similar results are obtained, no matter the load case adopted. For a high relative axial force ratio, differences in results are noticed. These differences are mainly due to the different values of the axial force ratio reached at failure, depending on the adopted load-sequence. It is known that, the member is greatly affected by the axial force ratio n (see section 4.3.3.4.). Thus, different values of the axial force ratio n , leads to a different member resistance.

Consequently, case 1 loading was adopted for the complete F.E. parametric study since it leads to safe but realistic results for all load cases. It represents the most useful and appropriate way of load application.

4.2.3. Beam models

Similarly to the shell numerical computations, beam models used for this parametric study were also developed with the use of the non-linear software FINELg and followed the same principles.

Obviously, the assumptions behind the beam element led to some adaptations, i.e. the boundary conditions simply consist in nodal constraints, and so are the loading forces nodal as

well, (see Figure 139). Furthermore, specimens have been modelled with longitudinal meshes comprising 28 elements. The nodes were tightly spaced near the supports and at the middle span area as illustrated in Figure 140 in order to allow a good representation of the beam yielding at the border and at mid span where the maximum moment is more likely to occur.

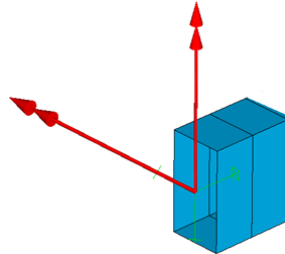


Figure 139 – Loading and support conditions (note that corners are also precisely accounted for in the beam models, however not represented in the above picture)

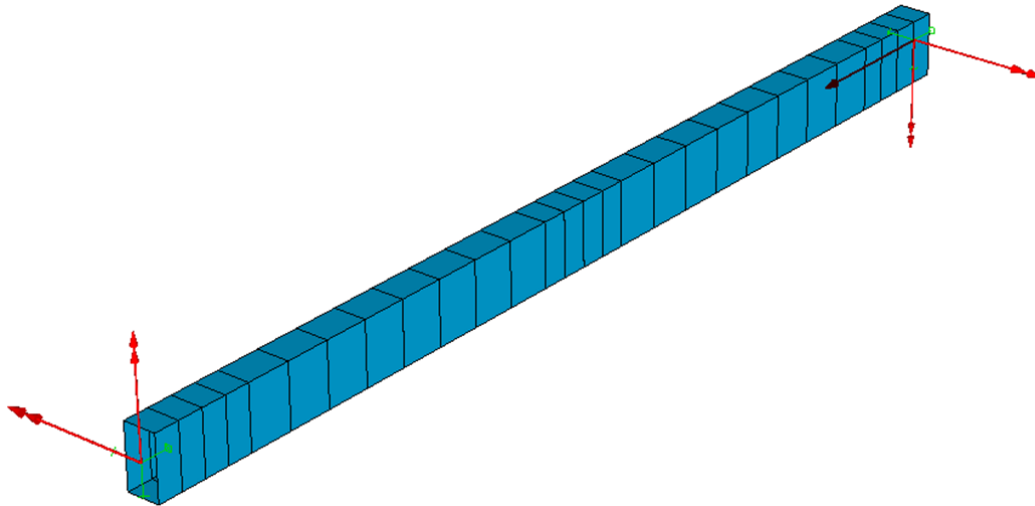


Figure 140 – Beam model in FINELg

Regarding the material adopted, the $\sigma - \varepsilon$ constitutive laws were obviously chosen identical to the shell modelling; typical elastic-perfectly plastic constitutive laws with 2% strain hardening slope have been adopted for the case of normal steel grades, and an elastic-perfectly plastic law with 0.45% strain hardening slope for the case of $f_y = 690 \text{ N/mm}^2$ as illustrated in Figure 141.

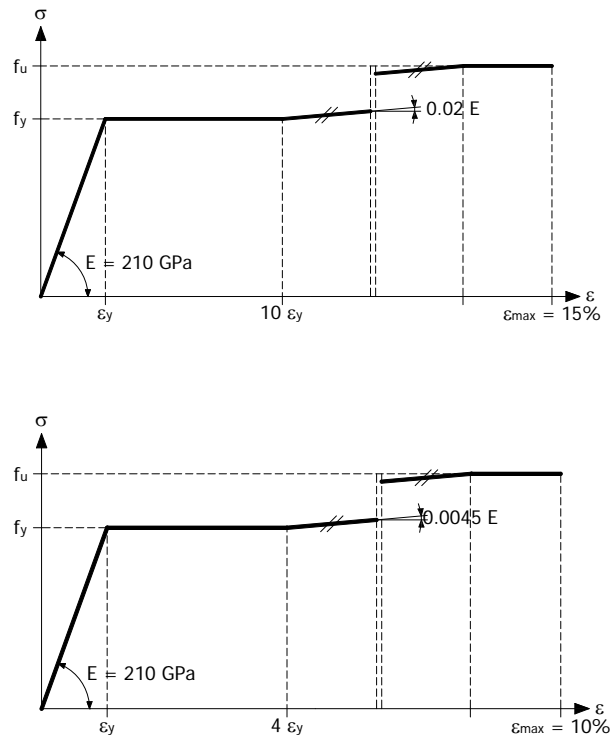
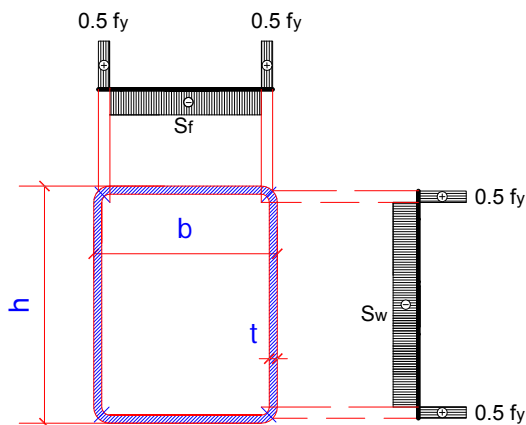


Figure 141 – Elastic-perfectly plastic hardening adopted material law with – a) 2% strain for normal steel grade – b) 0.45% strain for $f_y = 690 \text{ N/mm}^2$

Global initial deformations and residual stresses have been introduced. The residual stresses are defined in Figure 142 so that the various stresses distributions are in auto-equilibrium within each plate. The initial geometrical imperfections have been basically introduced through adequate modifications of node coordinates in both major and minor-axes with the realistic average value of global imperfection amplitude equal to $L / 1000$ as illustrated in Figure 143.



Where :

$$S_f = \frac{-0.5 f_y \pi (2r - t)}{4(b - 2r)}$$

$$S_w = \frac{-0.5 f_y \pi (2r - t)}{4(h - 2r)}$$

Figure 142 – Residual stresses distribution (ensuring auto equilibrium) for hot-formed profiles – beam model

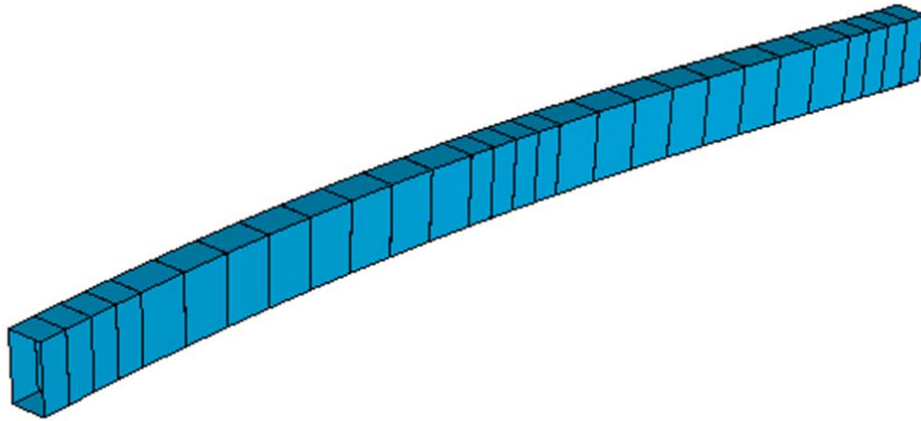


Figure 143 – Magnified view of global initial imperfections introduced in the beam F.E. model

A typical example of deformed shape at failure with the associated load-displacement response is illustrated in Figure 144.

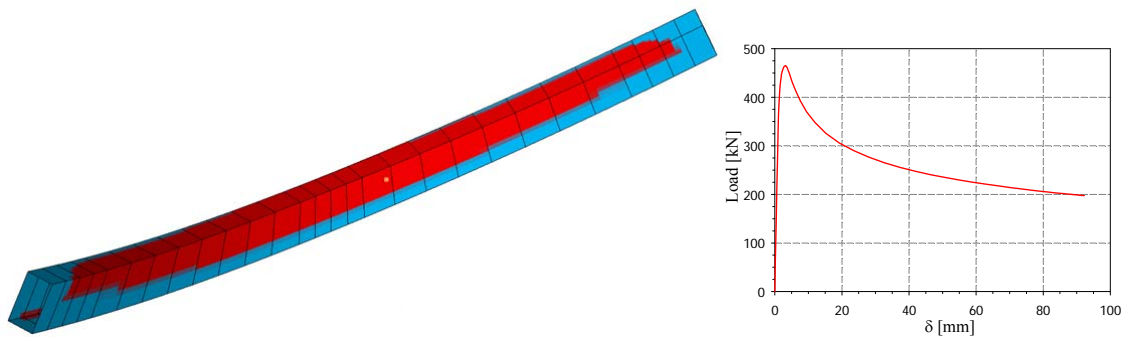


Figure 144 – Deformed shape and yield pattern at failure and load-shortening behaviour using beam models

4.3. Parametric study on hot-rolled hollow section members

4.3.1. Cases and parameters considered

In order to investigate how different key parameters may affect the structural response of a beam-column hollow section members, a first series of numerical computations on hot-formed tubes have been led, covering the following parameters:

- 13 different element lengths varying from 1500 *mm* to 15000 *mm* in order to represent the whole practical range of member slenderness;
- 3 different steel grades: S235, S355, S690;

- 8 cross-section shapes: rectangular and square hollow sections with the corresponding cross-sectional classes well-distributed along class 1 and class 4 according to EN 1993-1-1;
- Numerical calculations were performed through both beam (i.e. the member interactions curves would only take into account global instabilities and this would be regardless of local buckling instability) and shell element models (i.e. the member interactions curves would take into account the interaction between local and global instabilities);
- different loading conditions:
 - o pure compression N ;
 - o compression with major-axis bending $N+M_y$;
 - o compression with minor-axis bending $N+M_z$;
 - o compression with biaxial bending $N+M_y+M_z$.

A distinction has been made between the different loading situations, namely with respect to:

- linear bending moments distributions defined as the ratio between applied end moments: 2 coefficients were adopted $\psi_y = \psi_z = 1$ and $\psi_y = \psi_z = 0$ to consider constant and triangular distributions, respectively;
- the relative axial force ratio defined according to EN 1993-1-1 as $n = N / N_{b,Rd}$ ¹⁴ where:

$$N_{b,Rd} = \chi N_{pl} \text{ for class 1, 2 and 3 cross-sections;}$$

$$N_{b,Rd} = \chi N_{eff} \text{ for class 4 cross-sections;}$$

$N_{b,Rd}$, N_{pl} and N_{eff} represent respectively the buckling, plastic and effective resistance of the member; χ represents the reduction factor for instability; 3 values of the relative axial force ratio n were adopted going from 0.3 (i.e. the load case becoming

¹⁴ $\gamma_{M1} = 1.0$ for this study.

thus a compression of 30% $N_{b,Rd}$ with monoaxial or biaxial bending), to 0.7 (i.e. the load case becoming thus a compression of 70% $N_{b,Rd}$ with monoaxial or biaxial bending) to 1.0 (i.e. the load case becoming thus 100% $N_{b,Rd}$, a pure compression one);

- the degree of biaxial bending defined for combined load cases as the ratio M_y / M_z . This ratio was varied on the basis of an angle $\alpha_{biaxiality}$ in order to investigate the influence of the proportion of the major and minor-axis bending on the member resistance. For each load case, 10 values of the degree of biaxial bending were adopted varying from $\alpha_{biaxiality} = 0^\circ$ (i.e. the load case becoming compression with major-axis bending $N+M_y$) to $\alpha_{biaxiality} = 90^\circ$ (i.e. the load case becoming compression with minor-axis bending $N+M_z$), as shown in Figure 145 for different types of cross-section classification.

Additional calculations were performed with the same parameters mentioned before with a length equal to three times the height of the section in order to determine the cross-section resistance.

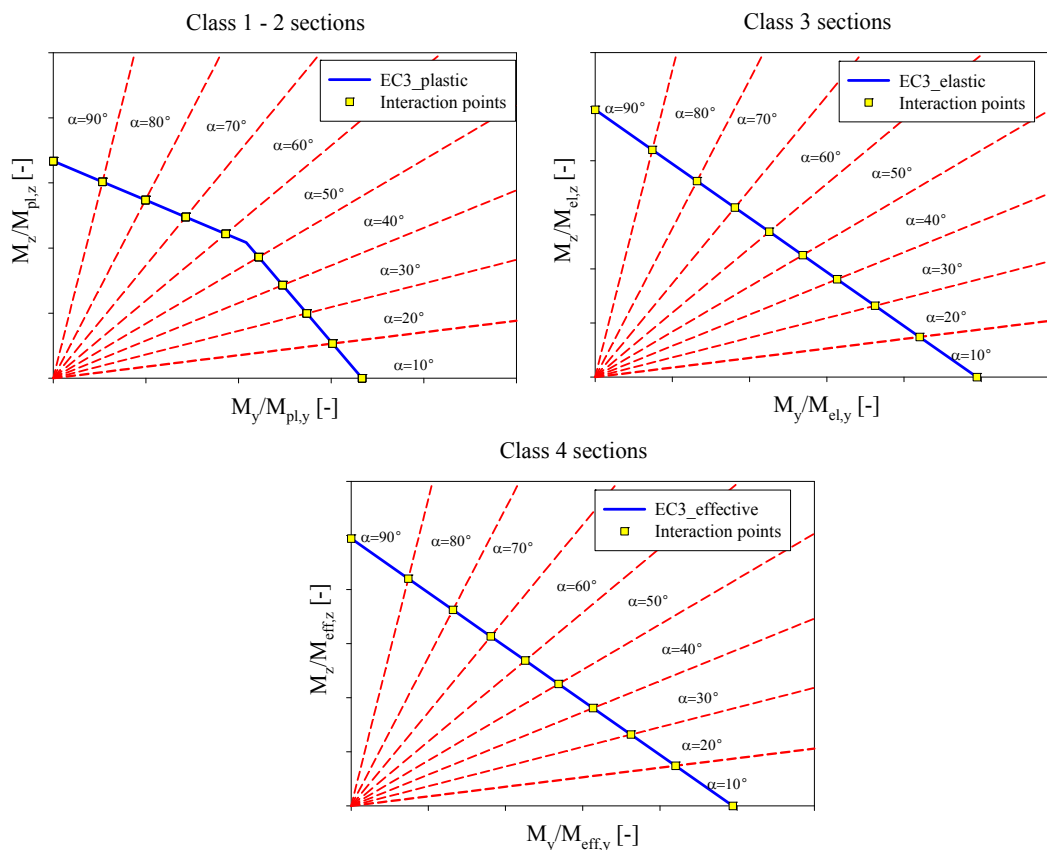


Figure 145 – Selection of load cases for $N+M_y+M_z$ combined situations – a) class 1-2 – b) class 3 – c) class 4

In order to derive the interaction curves for members, three parameters need to be computed: R_{RESIST} , R_{STAB} , and R_{REAL} (where R_{REAL} represents the ultimate load multiplier). These factors can be calculated either by hand or by numerical tools. For sake of accuracy, specialized developed tools were used to get the R-factors involved in the O.I.C. approach.

To determine the ultimate resistance of a member, FINELg beam model have been used so that only global instabilities would develop, regardless of the section slenderness and local buckling that may occur; all sections can therefore reach their plastic capacities, no matter the cross-section classification. In this case; the corresponding penalty factor and generalised member slenderness are denoted χ_{MB} and λ_{MB} , respectively.

Besides, to determine the ultimate resistance of a cross-section, shell models have been used to capture local buckling of the cross-section. The length of the cross-section specimen was chosen equal to three times the largest cross-sectional dimension based on the principle that the length is sufficiently small to prevent member buckling while long enough to avoid the influence of the boundary conditions. The corresponding penalty factor and slenderness definition are denoted χ_{CS} and λ_{CS} , respectively. Finally, to be able to account for the coupling between local and global buckling, members have also been modelled with FINELg shell elements so that results would involve the interaction between cross-section and member resistance. The corresponding penalty factor and slenderness definition are denoted χ_{CS+MB} and λ_{CS+MB} , respectively.

In total, some 39 500 non-linear G.M.N.I.A. F.E. computations have been performed for hot-rolled tubular sections. In order to get the R_{REAL} factors of hot-rolled sections, 8 500 non-linear F.E. computations for members were obtained by using beam models; 15 600 shell calculations for members were performed as well as 15 600 shell calculations for cross-sections. In addition, 15 600 simulations were performed to get $R_{STAB,CS}$; another 15 600 were performed to get $R_{STAB,MB}$ and 15 600 to get R_{RESIST} .

4.3.2. Determination of R-factors involved in the O.I.C. approach

As explained previously, the proposed O.I.C. approach relies on the generalization of the relative slenderness concept, establishing this parameter as the key to rule the interaction between resistance and instability. The proposed generalized slenderness is based on the calculation of “R-factors” (load ratios).

In the following paragraphs, the way the ‘R-factors’ are determined is explained in details: R_{RESIST} is computed using a dedicated Matlab tool developed to compute the exact ratio of the section [61]. $R_{STAB,CS}$ is computed using FINELg shell models for cross-sections and software Abaqus with beam modelling for members was used to calculate $R_{STAB,MB}$.

4.3.2.1. Determination of R_{RESIST} (resistance)

R_{RESIST} is computed using a specially-developed Matlab tool which is capable of taking into account precisely the effect of the cross-section corners, unlike Eurocode 3 formulae. The cross-section plates elements and corners are discretized into n fibres (see Figure 146).

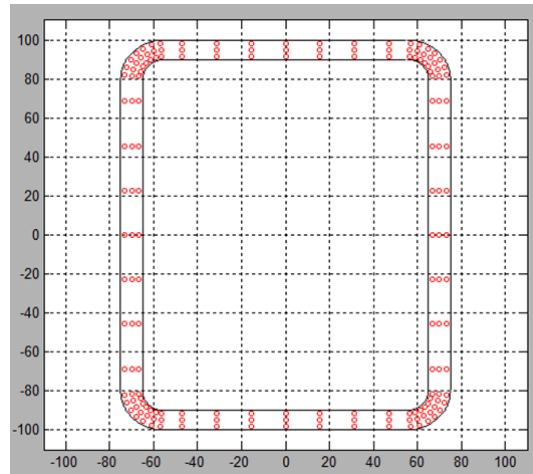


Figure 146 – Discretization in fibres for a rectangular hollow section by Matlab tool (each circle represents the centroid of a fibre)

The “exact” plastic resistance of a section is calculated through iterative computations. Calculations are based on the Bernoulli assumption (i.e. plane sections remain plane and normal to the deflected neutral axis) which leads to the conclusion that deformation diagrams remain linear. The strain is monitored on 4 characteristic points (that in our case coincide on the 4 corner of the section) and the strain diagram is assumed linear for any fibre in between. Following this assumption, the plastic resistance of sections under simple or combined loading situations can be computed.

The first step of the calculation of R_{RESIST} is to vary the deformation on the 4 corners of the section until the initial load that has been introduced by the user is matched; the second step is to increase the deformation value at the four characteristic point by a small amount and then, after the new strain diagram is determined, the stress corresponding to each fibre is then calculated from the material law that was preliminary introduced. Then, the stress in each

fibre is adequately summed to obtain the compression value N and integrated around the major and minor plastic axis of the section in order to determine the corresponding moment values M_y and M_z . This step is repeated until the strain at one point of the section reaches the ultimate strain value defined by the user. The N , M_y and M_z values and thus the R_{RESIST} load multiplier calculated at this ultimate step is considered the plastic ratio of the section. R_{RESIST} could also be determined by means of empirical formulae proposed in Eurocode 3 or, alternatively, from Lescouarch [62].

A small sub-study was conducted on square and rectangular sections covering all section classes, in order to compare the plastic ratio obtained by means of the 3 methods. The specimens were tested under compression with biaxial bending with $n = 0.3$; $n = 0.7$ and $\alpha_{biaxiality} = 20^\circ$; $\alpha_{biaxiality} = 60^\circ$ where n and $\alpha_{biaxiality}$ represent the relative axial force and the biaxial bending ratios, respectively. The obtained results are illustrated in Table 34 in terms of the ratios $R_{RESIST_EC3} / R_{RESIST_MATLAB}$, $R_{RESIST_LESCOUARCH} / R_{RESIST_MATLAB}$ and $R_{RESIST_EC3} / R_{RESIST_LESCOUARCH}$.

 Table 34 – Comparisons of R_{RESIST_EC3} with R_{RESIST_MATLAB} and $R_{RESIST_LESCOUARCH}$

Load case	$n = 0.3 / \alpha_{biaxiality} = 20^\circ$			$n = 0.7 / \alpha_{biaxiality} = 20^\circ$		
Cross-section	$R_{RESIST_EC3} / R_{RESIST_Matlab}$ [-]	$R_{RESIST_Lescouarch} / R_{RESIST_Matlab}$ [-]	$R_{RESIST_EC3} / R_{RESIST_Lescouarch}$ [-]	$R_{RESIST_EC3} / R_{RESIST_Matlab}$ [-]	$R_{RESIST_Lescouarch} / R_{RESIST_Matlab}$ [-]	$R_{RESIST_EC3} / R_{RESIST_Lescouarch}$ [-]
RHS_220x120x10	0.99	1.01	0.98	0.98	1.05	0.93
RHS_300x200x8	1.00	1.01	0.99	0.98	1.02	0.96
RHS_200x100x5	0.98	1.01	0.96	0.98	1.02	0.96
RHS_450x250x8	0.98	1.01	0.97	0.98	1.02	0.97
SHS_120x120x8	0.99	1.00	0.99	0.98	1.05	0.93
SHS_260x260x7.1	1.00	1.00	1.00	0.99	1.02	0.97
SHS_200x200x5	0.99	1.00	0.99	0.99	1.02	0.98
SHS_300x300x6.3	1.00	1.01	0.99	1.00	1.02	0.98

Load case	$n = 0.3 / \alpha_{biaxiality} = 60^\circ$			$n = 0.7 / \alpha_{biaxiality} = 60^\circ$		
Cross-section	$R_{RESIST_EC3} / R_{RESIST_Matlab}$ [-]	$R_{RESIST_Lescouarch} / R_{RESIST_Matlab}$ [-]	$R_{RESIST_EC3} / R_{RESIST_Lescouarch}$ [-]	$R_{RESIST_EC3} / R_{RESIST_Matlab}$ [-]	$R_{RESIST_Lescouarch} / R_{RESIST_Matlab}$ [-]	$R_{RESIST_EC3} / R_{RESIST_Lescouarch}$ [-]
RHS_220x120x10	1.03	1.02	1.01	1.01	1.05	0.96
RHS_300x200x8	1.02	1.01	1.01	1.01	1.03	0.98

RHS_200x100x5	1.02	1.01	1.01	1.01	1.03	0.98
RHS_450x250x8	1.01	1.00	1.02	1.01	1.02	0.99
SHS_120x120x8	0.99	1.00	0.98	0.99	1.06	0.93
SHS_260x260x7.1	1.00	1.00	1.00	0.99	1.02	0.97
SHS_200x200x5	0.99	1.02	0.97	1.00	1.02	0.98
SHS_300x300x6.3	0.99	1.00	0.99	1.00	1.02	0.98

The biggest difference between the 3 methods is seen to be equal to 7% for $n = 0.7$, and to 3% for $n = 0.3$ in the worst cases. The differences between the 3 methods is mainly due to the influence of the corner areas on the plastic resistance, rigorously taken into account in the Matlab tool and not considered accurately in Eurocode 3 and Lescouarch' equations – note that both unsafe and safe predictions are observed. Based on the previously-mentioned conclusions, the Matlab tool was adopted for all R_{RESIST} calculations presented in the following, for sake of accuracy.

4.3.2.2. Determination of $R_{STAB,CS}$ (cross-section instability)

The differential equation for elastic buckling of a plate of width c and thickness t results in the elastic local buckling stress given by:

$$\sigma_{cr} = \frac{k_{\sigma} \pi^2 E}{12(1-\nu^2)} \left(\frac{t}{c} \right)^2 \quad (168)$$

where k_{σ} is the plate buckling coefficient accounting for the support conditions and stress distributions across the plate. Typical cases are elements in compression supported on one edge ($k_{\sigma} = 0.425$), elements in compression supported on both edges ($k_{\sigma} = 4.0$) and elements in bending supported on both edges ($k_{\sigma} = 23.9$). The local buckling capacity of cross-sections as determined by the theoretical approach assumes that the plate elements are hinged along their boundaries. The buckling stress of each plate element can then be determined with the appropriate use of k_{σ} -value, and the lowest obtained stress can be considered as the buckling stress of the section [3]. Once the buckling stress of the section was obtained, the critical load of the section was determined in order to get the critical ratio $R_{STAB,CS}$.

In the following, a comparison is made between $R_{STAB,CS}$ critical ratios obtained by means of 3 different procedures: L.B.A. calculations using the non-linear numerical software FINELg, semi-analytical finite strip method CUFSM and the theoretical calculation of $\sigma_{cr,min}$ for

elastic buckling of a plate. Rectangular and square hollow sections corresponding to all cross-section classifications are investigated under compression and under major-axis bending. The obtained results are summarized in Table 35 and illustrated in Figure 147.

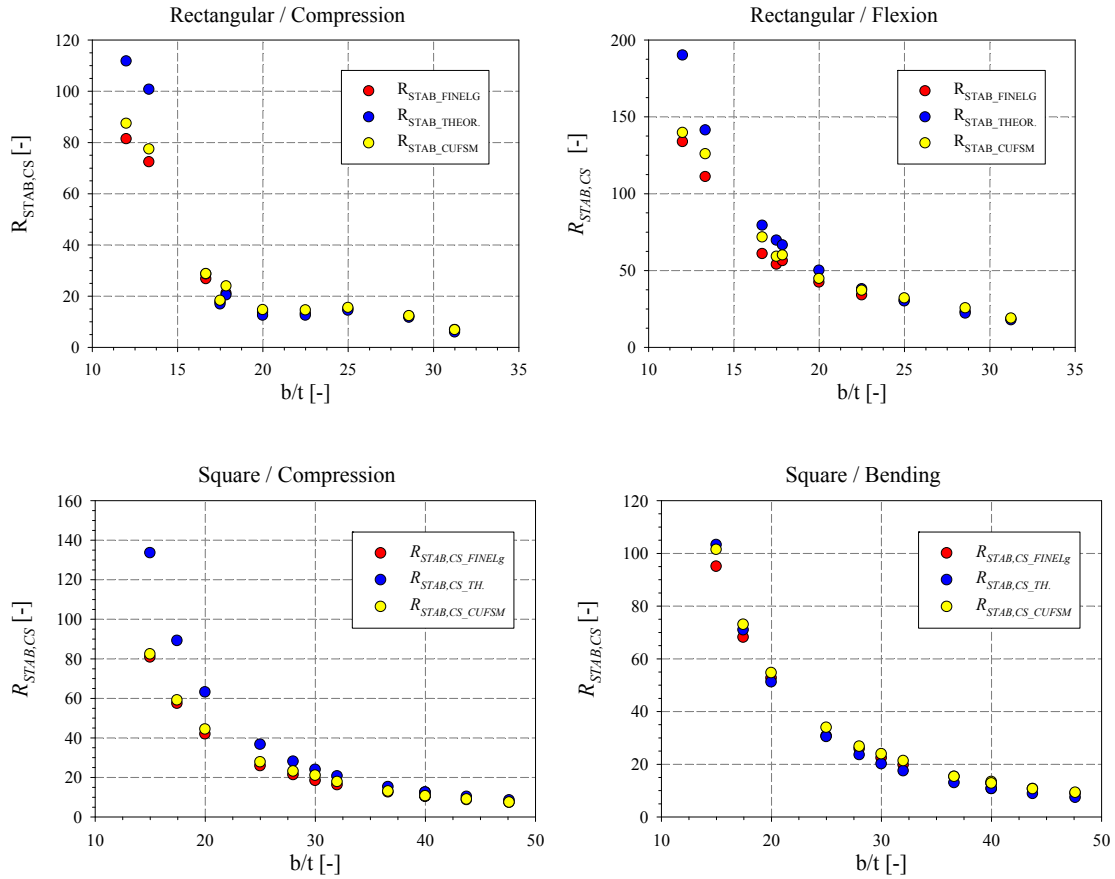


Figure 147 – R_{STAB,CS_FINELG} , R_{STAB,CS_CUFSM} and R_{STAB,CS_TH} graphical representation in function of b/t ratio

Table 35 – Comparison of R_{STAB,CS_TH} with R_{STAB,CS_FINELG} and R_{STAB,CS_CUFSM}

Loading	Compression		Bending	
	$R_{STAB,CS_TH} / R_{STAB,CS_CUFSM}$ [-]	$R_{STAB,CS_FINELG} / R_{STAB,CS_CUFSM}$ [-]	$R_{STAB,CS_TH} / R_{STAB,CS_CUFSM}$ [-]	$R_{STAB,CS_FINELG} / R_{STAB,CS_CUFSM}$ [-]
RHS_220x120x10_Cl.1	1.28	0.93	1.36	0.96
RHS_100x80x6_Cl.1	1.30	0.93	1.12	0.88
RHS_100x60x3.6_Cl.1	1.00	0.93	1.11	0.85
RHS_300x200x8_Cl.2	0.93	0.97	0.94	0.95
RHS_150x50x4_Cl.2	0.85	0.93	0.95	0.94
RHS_140x70x4_Cl.1	0.92	0.96	1.18	0.91
RHS_180x100x5.6_Cl.1	0.85	0.88	1.11	0.94
RHS_200x100x5_Cl.3	0.85	0.94	1.12	0.95

RHS_160x90x4_CI.3	0.86	0.91	1.03	0.92
RHS_260x180x6.3_CI.4	0.95	0.98	0.86	0.91
RHS_450x250x8_CI.4	0.87	1.00	0.94	0.97
SHS_120x120x8_CI.1	1.62	0.98	1.02	0.94
SHS_110x110x6.3_CI.1	1.51	0.97	0.97	0.93
SHS_60x60x3_CI.1	1.42	0.95	0.94	0.96
SHS_90x90x3.6_CI.1	1.32	0.93	0.90	0.91
SHS_140x140x5_CI.1	1.21	0.92	0.88	0.97
SHS_150x150x5_CI.1	1.14	0.88	0.84	0.94
SHS_160x160x5_CI.1	1.16	0.91	0.82	0.93
SHS_260x260x7.1_CI.2	1.17	0.96	0.85	1.00
SHS_200x200x5_CI.3	1.18	0.98	0.80	0.94
SHS_400x400x10_CI.3	1.18	0.99	0.84	1.00
SHS_350x350x8_CI.4	1.15	0.98	0.83	1.00
SHS_300x300x6.3_CI.4	1.15	0.99	0.79	0.96

It can be seen that small and negligible differences are obtained by using CUFSM and FINELg models, although CUFSM always provides slightly higher results compared to FINELg. These differences remain very acceptable and both models can be used. A bigger disparity is seen between the theoretical critical ratios from one hand (R_{STAB,CS_TH}) and CUFSM and FINELg ratios on the another hand (R_{STAB,CS_CUFSM} and R_{STAB,CS_FINELg}); this divergence reaches its highest values for stocky sections and the results are almost similar for slender ones. This can be explained by the fact that the theoretical formulae disregard the corner regions, whereas CUFSM and FINELg take them into account accurately, leading to higher $R_{STAB,CS}$ factors. Consequently, the relative influence of the corners compared to the “section-as-a-whole” for slender sections is almost negligible as expected; therefore, the divergence between results is reduced.

For stocky sections, the relative corner area is bigger than for slender sections, and its effect is more significant. This is shown at the range of relatively small slenderness values in Figure 147. The theoretical approach can lead to quite conservative results (SHS under compression) or to unconservative results (SHS in bending), depending on the cross-section shape and slenderness.

The theoretical approach – based on the plate slenderness formulations with the plates considered as simply supported – considers that any interaction that may exist between the flange and the web of a cross-section remains the same (i.e., k_σ values do not change), for any

given cross-section type, and disregard the corner regions. This may lead sometimes to unconservative results (SHS under compression or RHS in bending, where the support conditions are worse than simply supported) or to conservative results (i.e. the case of rectangular under compression or square in bending, where the support conditions are better than simply supported). Actually, for rectangular section under compression, the level of restraint offered by the narrow faces to the wider ones provides an increased cross-section resistance, particularly in the slender range. Therefore, the resistance in the webs will be considerably higher than a plate with simply supported edges and the buckling stress will be subsequently higher.

It is interesting to note that there is a big difference between the assumed k_σ values in standards and those calculated with finite strips. Numerical software such as CUFSM and FINELg, dedicated to elastic buckling calculations taking the elements' interactions into account in a quite accurate way, are more realistic than the theoretical approach. The theoretical approach assumes that the plate elements are simply supported. However, the edge conditions could differ from one section to another. For example, a rectangular section, made up of four plates with stiff flanges, would not have a k_σ value equal to that of a section with simply supported plates. The stiff flanges would prevent the rotation of the corners and the web plates will behave as if their longitudinal edges were fixed. Therefore, the resistance offered by the transverse strips in the webs shall be considerably higher than a plate with simply supported edges and the buckling stress will be subsequently higher. However, if the flanges are less stiff and prone to local buckling just like the webs, then the corners will not be fixed anymore and will rotate. Hence, in that case, the buckling stress will be the same as for a plate with simply supported longitudinal edges. Therefore, when using the theoretical equations, the determination of k_σ values could lead to conservative or unconservative results depending on the cross-section shape and slenderness, since all plates are connected with rigid joints and buckle simultaneously at an intermediate stress between the lowest and the highest calculated buckling stresses of each element separately. Additional research need to be done concerning the theoretical approach. For this study, no more developments have been undertaken because of a lack of time.

In general, when a cross-section is especially weak owing to local buckling, one of the constitutive elements of the cross-section is mainly responsible for the instability, i.e. when the critical value is reached, this element needs support and restraint from the adjacent elements since it is no longer capable of supporting the imposed loads. This restraint will

provide an additional “delay” before buckling occurs, until the cross-section as a whole becomes unstable [3]. The theoretical formulae disregard the interaction between the constitutive plates of the section and assume that a unique plate buckling coefficient k_σ exists for each element. In reality, as demonstrated herein with finite strip analysis, the plate buckling coefficient vary widely for a given section geometry and loading. Several other authors (Schafer, Kato) have evidenced equivalent conclusions for open sections [63] [64].

Consequently, the way of getting the critical load multiplier theoretically R_{STAB,CS_TH} was eliminated and not adopted in calculations. However, both CUFSM and FINELg sources lead to accurate, realistic and satisfactory results. $R_{STAB,CS}$ values were eventually calculated by FINELg, as it leads to satisfactory results with a minimal computational effort and time.

4.3.2.3. Determination of $R_{STAB,MB}$ (member instability)

R_{STAB} factors have been typically computed with FINELg for cross-sections and with ABAQUS for members ($R_{STAB,MB}$ can be also computed with FINELg beam models). The support conditions of the member are assumed to be simply supported with fork conditions, thus the effective length is equal to the member length.

Another small study was conducted on members of different lengths varying from 3500 mm to 7000 mm in order to compare the critical ratios obtained by using ABAQUS and FINELg on the member behaviour. Beam modelling was used in both cases so as to only witness global buckling. Different sections covering all cross-section classes were investigated under a combined loading $n = 0.3 / \alpha_biaxiality = 20^\circ$. The obtained results are summarized in Table 36.

Table 36 – Comparisons of R_{STAB,MB_ABAQUS} with R_{STAB,MB_FINELg} for different section shapes

Cross-section	RHS_220x120x10 Class 1	RHS_300x200x8 Class 2	RHS_200x100x5 Class 3	RHS_450x250x8 Class 4
Length [mm]	$R_{STAB,MB_ABAQUS} / R_{STAB,MB_FINELg}$ [-]	$R_{STAB,MB_ABAQUS} / R_{STAB,MB_FINELg}$ [-]	$R_{STAB,MB_ABAQUS} / R_{STAB,MB_FINELg}$ [-]	$R_{STAB,MB_ABAQUS} / R_{STAB,MB_FINELg}$ [-]
3500	0.98	0.98	0.99	0.91
4000	0.98	0.98	0.99	0.96
4500	0.98	0.99	0.99	0.98
5000	0.99	0.99	0.99	0.98
5500	0.99	0.99	0.99	0.99
6000	0.99	0.99	0.99	0.99

6500	0.99	0.99	0.99	0.99
7000	0.99	0.99	0.99	0.99

Cross-section	SHS_120x120x8 Class 1	SHS_260x260x7.1 Class 2	SHS_200x200x5 Class 3	SHS_300x300x6.3 Class 4
Length [mm]	$\frac{R_{STAB,MB_ABAQUS}}{R_{STAB,MB_FINELg}}$ [-]	$\frac{R_{STAB,MB_ABAQUS}}{R_{STAB,MB_FINELg}}$ [-]	$\frac{R_{STAB,MB_ABAQUS}}{R_{STAB,MB_FINELg}}$ [-]	$\frac{R_{STAB,MB_ABAQUS}}{R_{STAB,MB_FINELg}}$ [-]
3500	0.98	0.97	0.98	0.95
4000	0.98	0.97	0.99	0.97
4500	0.98	0.98	0.99	0.97
5000	0.98	0.98	0.99	0.98
5500	0.98	0.99	0.99	0.98
6000	0.99	0.99	0.99	0.99
6500	0.99	0.99	0.99	0.99
7000	0.99	0.99	0.99	0.99

The obtained results show minor differences (usually around 1%) between R_{STAB,MB_FINELg} and R_{STAB,MB_ABAQUS} , although FINELg gives always higher critical ratios compared to ABAQUS. The results are illustrated in Figure 148 where the x-axis represents the element's length and the y-axis bears the ratio $R_{STAB,MB_FINELg} / R_{STAB,MB_ABAQUS}$.

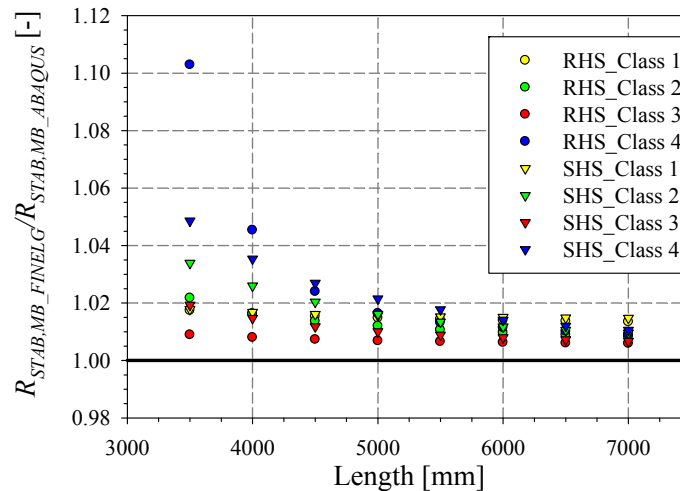


Figure 148 – $R_{STAB,MB_FINELg} / R_{STAB,MB_ABAQUS}$ graphical representation as a function of member length

This ratio is seen to be always higher than 1.0 whatever the length and shape of the element. However, the disparity between both models reaches its highest values for short elements and this divergence decrease when the length of the element increases. Actually, when performing

the L.B.A. simulations with ABAQUS software, the beam section was approximated by a "fictitious section" based on its geometric properties. The analyses are based on ABAQUS's beam general section and defined directly by the following properties: A , I_y , I_z , I_t (where A represents the area of the section; I_y is the moment of inertia about the strong axis, I_z is the moment of inertia about the weak axis, I_t is the torsional inertia). The cross-section properties introduced in ABAQUS are calculated based on a section with two elements per corner in order to match the FINELg shell assumption. Nevertheless, in FINELg, when using beam elements, the rectangular and square hollow section are predefined and modelled with a continuous, circular corner.

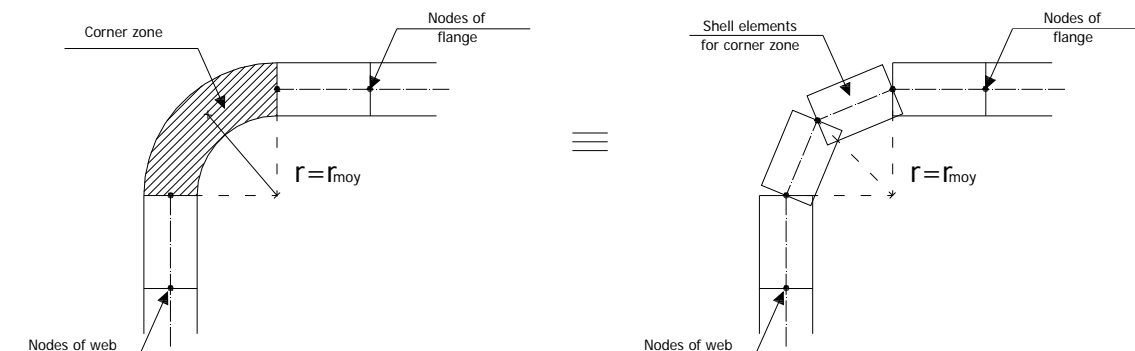


Figure 149 – FEM-treatment of corners zones for hollow sections – a) beam models – b) shell models

Due to these differences, it is shown in Figure 148 that results between ABAQUS and FINELg diverge by a small amount and this divergence is more pronounced in the small length range where higher $R_{STAB,MB}$ value are noticed with ABAQUS. Hence, for small elements, the cross-section properties have more impact on the critical load whereas for long elements, it is the element length that determines the critical buckling load $R_{STAB,MB}$. It is also to be noted that computational algorithms are different for each software, which may lead to small differences. Nevertheless, altogether, the differences between results (except for small elements) do not exceed a value of 4%, which remain very acceptable and ABAQUS was adopted for the calculation of $R_{STAB,MB}$ for members.

4.3.3. Analysis of results

The present paragraph analyses the influence of various parameters on the resistance of member, by means of F.E. numerical results. The figures presented hereafter show results obtained by using the shell and the beam model. Different loading conditions, sections, steel grades...were adopted in the numerical results, which explain the large dispersion

immediately noticed. Further analyses are then conducted to sort these results by load distributions, proportions of loads on one another... The goal is to identify the key parameters that should be accounted for in design proposal (see chapter 6). For small slenderness values, the strain hardening effect is remarkable, the members exhibiting an interesting reserve of resistance ($\chi_{MB} \geq 1.0$).

Figure 150 represents results obtained with the beam model (only global buckling occurs). The horizontal axis represents the generalized slenderness λ_{MB} while the vertical axis reports the reduction factor χ_{MB} defined in Equation (169) and Equation (170), respectively. $R_{ult,FE,BEAM}$ is the ultimate load multiplier obtained with the beam model. Note that all factors associated with cross-sectional behaviour and instability are obviously excluded from Equations (169) and (170), consistently.

$$\lambda_{MB} = \sqrt{\frac{R_{RESIST}}{R_{STAB,MB}}} \quad (169)$$

$$\chi_{MB} = \frac{R_{ult,FE,BEAM}}{R_{RESIST}} \quad (170)$$

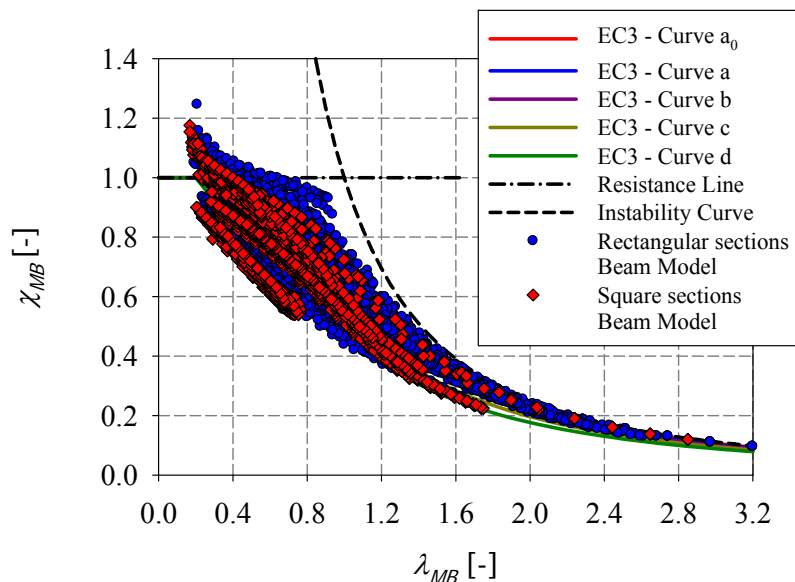


Figure 150 – Numerical results for beam members (global instabilities accounted for)

Nevertheless, and in order to determine the interaction between local and global instabilities, shell elements computations were also performed in Figure 151 so that these results would

involve the interaction between cross-section and member resistance. The horizontal axis represents the generalized slenderness λ_{SHELL} while the vertical axis reports the reduction factor χ_{SHELL} defined in Equation (171) and Equation (172), respectively. $R_{ult,FE,SHELL}$ is the ultimate load multiplier obtained with the shell model.

$$\lambda_{SHELL} = \sqrt{\frac{R_{RESIST}}{R_{STAB,MB}}} \quad (171)$$

$$\chi_{SHELL} = \frac{R_{ult,FE,SHELL}}{R_{RESIST}} \quad (172)$$

By comparing the results obtained by means of shell F.E. models where both local and global instabilities are accounted for (see Figure 151) with the results obtained by mean of beam F.E. models (Figure 150), it is obvious that the influence of the section sensitivity to local buckling is important. The effect of local buckling is mainly highlighted for low values of relative slenderness ($\lambda_{MB} < 0.8$) where the failure of the element is due to a lack of resistance and to cross-section buckling and not because of member instability. As expected, beam models reach higher resistance (i.e. all the sections reach their plastic resistance) than shell ones (i.e. different values of resistance are reached: plastic, elastic or effective depending on the cross-section classification); strain hardening effects are obviously more remarkable in the beam model, for the same reasons. Slender sections exhibiting an important influence of local buckling have a lower resistance when modelled with shell elements rather than with beam elements especially at low values of relative slenderness. The vertical scatter observed in the shell model is mainly due to different section classes: stocky sections (i.e. class 1 sections) exhibit a better behaviour than slender ones (i.e. class 4 sections).

For higher values of member relative slenderness ($0.8 < \lambda_{MB} < 1.6$), the elements fail because of instability, combined with the imperfections' level. Both local (i.e. cross-section instabilities) and global (i.e. member instabilities) buckling modes are likely to occur and interact (so-called coupled instabilities) in the shell models leading to a lower resistance than in the beam models. For high values of the relative slenderness, shell and beam models are only able to witness global buckling regardless of the section slenderness and local buckling that may occur.

One may also notice, by comparing the results obtained by the shell models with the results obtained by mean of the beam models, an horizontal shift in the shell results, where different beam-column lengths were tested varying from 1500 mm to 15000 mm; whereas with the beam models, the column lengths varied from 3500 mm to 7000 mm.

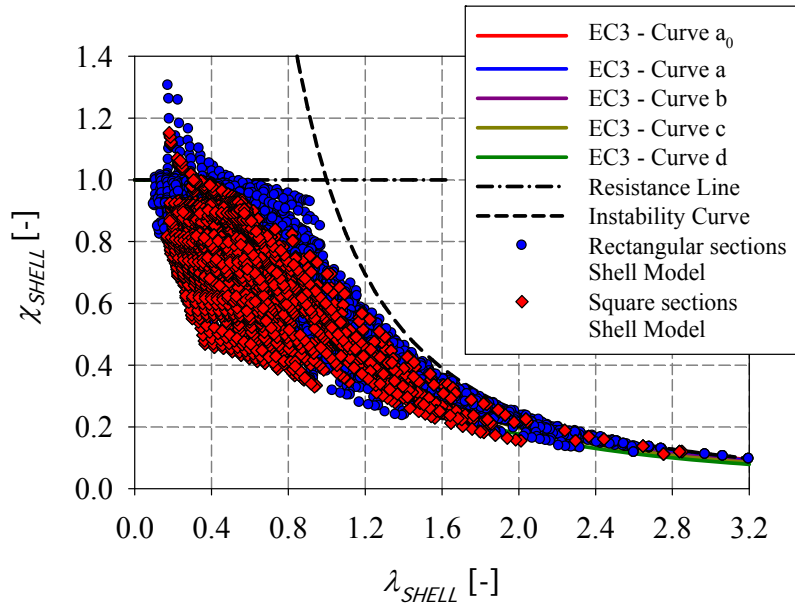


Figure 151 – Numerical results for shell members (both local and global instabilities accounted for)

Figure 152 proposes results obtained by substituting the member interaction curve by a global interaction curve that considers local instability. The horizontal axis represents the generalized slenderness λ_{CS+MB} while the vertical axis reports the reduction factor χ_{CS+MB} defined in Equation (173) and Equation (174), respectively:

$$\lambda_{CS+MB} = \sqrt{\frac{\chi_{CS} \cdot R_{RESIST}}{R_{STAB,MB}}} \quad (173)$$

$$\chi_{CS+MB} = \frac{R_{ult,FE,SHELL}}{\chi_{CS} \cdot R_{RESIST}} \quad (174)$$

In Equation (173) and Equation (174), χ_{CS} represents the cross-section reduction factor calculated numerically. Analytical expressions were developed to get χ_{CS} and can be found in [3].

The final resistance factor $R_{ult,FE,SHELL}$ is computed using shell elements in this case so that local and global instabilities interact; $R_{ult,FE,SHELL}$ is affected by resistance and instability as well as by initial imperfections (i.e. residual stresses, geometrical imperfections), by the material law, load cases, section geometries, boundary conditions...). Figure 152 displays close tendencies with member results computed using beam models (see Figure 150). At first sight, one would expect the member and global interaction curve to give identical results since the effect of local buckling is deducted for the latter. Nevertheless, and even if same tendencies are shown for both cases, it can be noticed that beam results attain higher values especially for low values of slenderness ($\lambda_{CS+MB} < 1.6$). This is due to the fact that, in the beam model, no local instabilities occur whereas the global interaction curve is computed by deducting the cross-section instabilities from the real behaviour. Hence, cross-section results includes the non-linear effect of geometrical and material imperfection and also for some cases the occurrence of distortional buckling modes. This non-linearity at the cross-section level is neglected in the beam model which causes the shell and beam result to diverge. Moreover and since it is known that the effect of imperfection have larger influence on slenderness values λ_{CS+MB} ranging from 0.8 to 1.6, it can also be seen in Figure 150 and Figure 152 that beam and shell result diverge the most in this part.

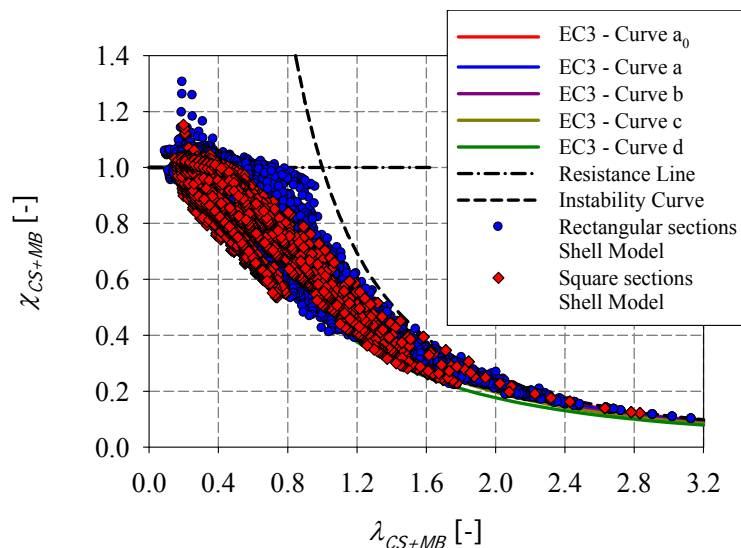


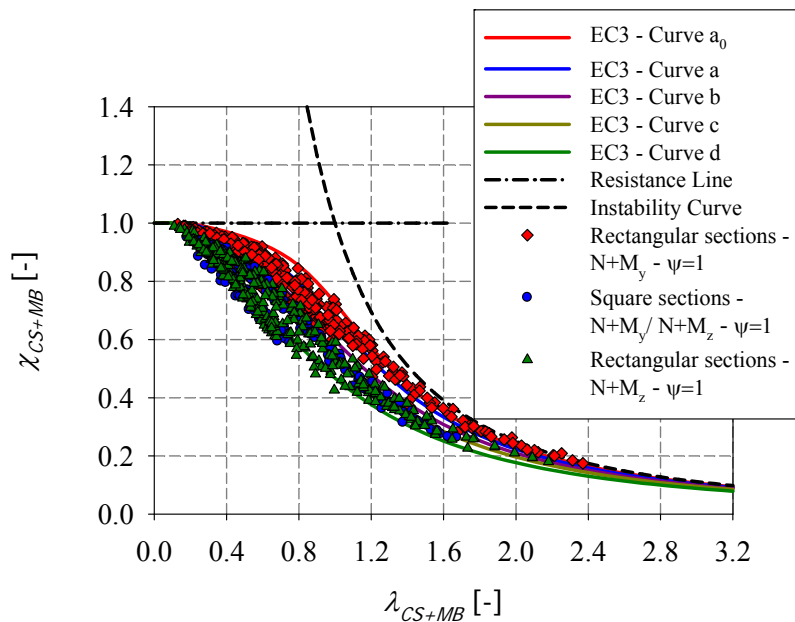
Figure 152 – Shell numerical results including the interaction formula linking both local and global instabilities

4.3.3.1. Influence of cross-section shape and slenderness

As can be noticed in the results displayed in Figure 153, the cross-section geometry is a key parameter that influences the member resistance. These results clearly evidence that

rectangular sections under combined loading behave better than square ones. This is due to the interaction between the constituent plates of the section: instability first occurs in the slender plates of a rectangular profile so that narrow ones provide buckling restraints, unlike for square profiles where buckling happens simultaneously in the four constitutive plates¹⁵; also, it is clearly shown that these members are less affected by instability and have a better behaviour under compression with major-axis bending than under compression with minor-axis bending.

The rather large vertical dispersion noticed in the figures is associated with different loading conditions, sections, steel grades... Further analyses are conducted in the following to sort these results according to the governing parameters (such as the influence of the bending moment distribution, the degree of biaxial bending, the level of compression...).



¹⁵ Explanations are here given for compression only, for sake of clarity.

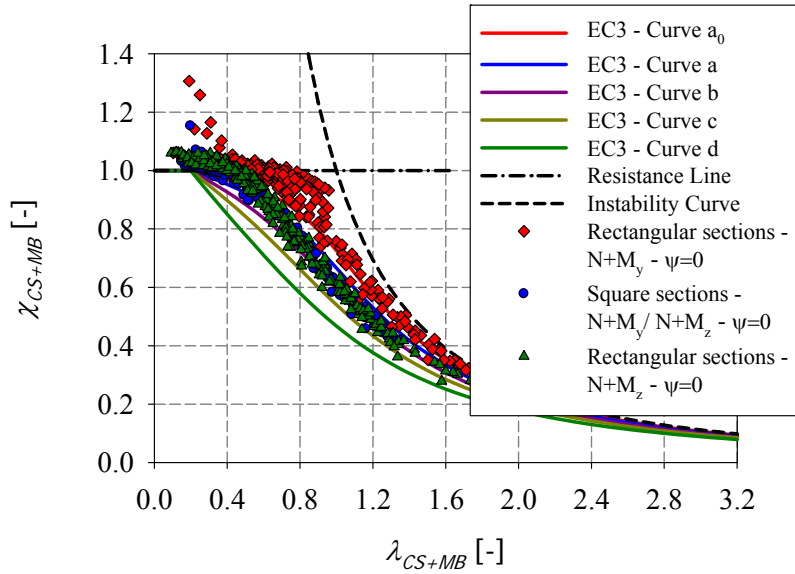
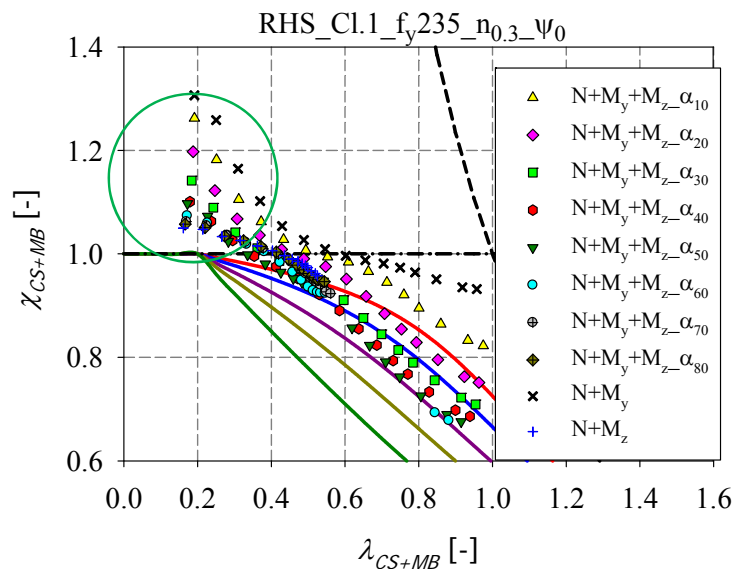


Figure 153 – Numerical results for members under combined loading $N+M_y$ and $N+M_z$ for square and rectangular sections – a) constant bending moment distribution – b) triangular bending moment distribution

Clear tendencies are observed in Figure 154 that represents the particular case of class 1 rectangular and square sections of nominal yield stress $f_y = 235 \text{ N/mm}^2$ and tested under combined loading. Various $M_y - M_z$ configurations are reported, through $\alpha_{\text{biaxiality}}$ values ranging from 10 to 80. The member is subjected to a level of compression $n = 0.3$ and to a triangular bending moment distribution. It is clearly seen that the strain hardening effects have a significant impact on the resistance of the stocky sections especially for small values of relative slenderness (see green circles).



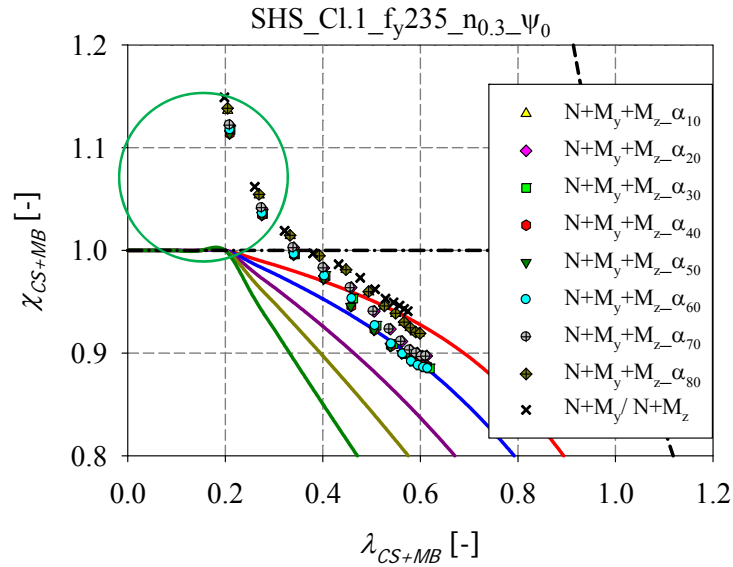


Figure 154 – Numerical results for members of class 1 sections under combined loading – a) RHS – b) SHS

4.3.3.2. Influence of yield stress

Figure 155 to Figure 157 represent the obtained results for rectangular and square hollow sections respectively under combined load cases for different steel grades: $f_y = 235 \text{ N/mm}^2$, $f_y = 355 \text{ N/mm}^2$ and $f_y = 690 \text{ N/mm}^2$.

As can be seen, an increase in yield stress f_y increases the relative slenderness λ_{CS+MB} (i.e. the instability has more influence on high strength steel products) and decreases the reduction factor χ_{CS+MB} (i.e. the section become more slender thus prone to buckling); consequently, tendencies for slightly higher χ_{CS+MB} values for high steel grades are observed. This is due to the relative level of membrane residual stresses included with a reference yield stress of 235 MPa , into the numerical model. The residual stresses – which are based on a reference yield of 235 MPa – will have a less important influence on the members having higher yield stresses than 235 MPa .

One may also notice that a relatively really small dispersion in the results is noted for $f_y = 235 \text{ N/mm}^2$ and $f_y = 355 \text{ N/mm}^2$, for all load cases. Consequently, a single interaction curve may be derived for $f_y = 235 \text{ N/mm}^2$ and $f_y = 355 \text{ N/mm}^2$ for sake of simplicity since negligible results were seen and a higher one may be derived for $f_y = 690 \text{ N/mm}^2$.

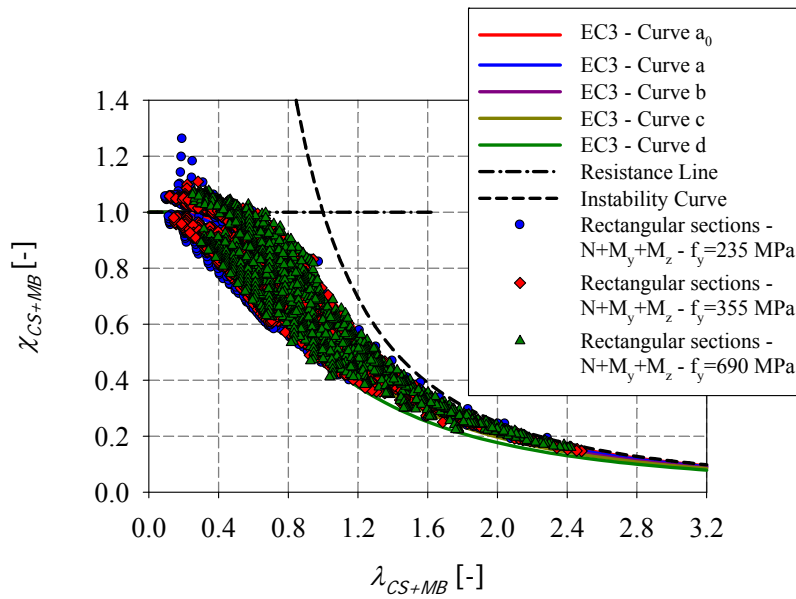


Figure 155 – Numerical results for members with rectangular sections and different steel grades under $N+M_y+M_z$

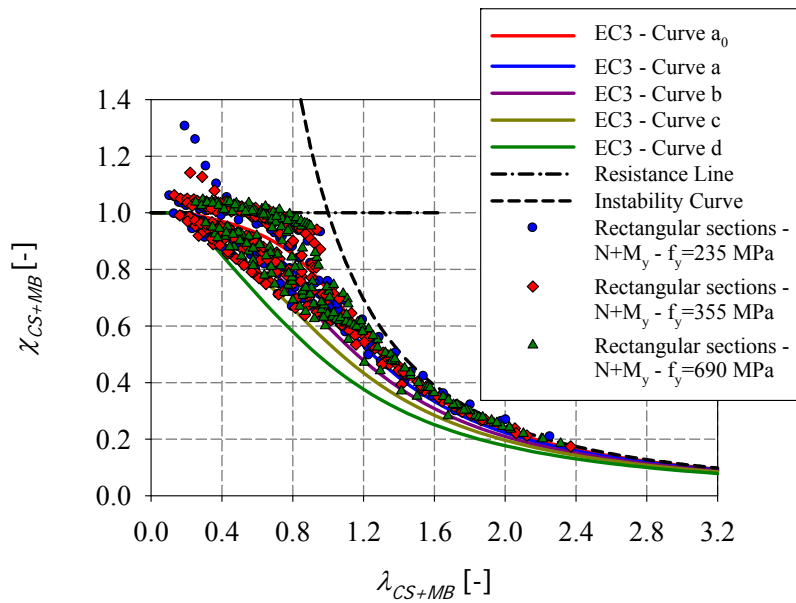


Figure 156 – Numerical results for members with rectangular sections and different steel grades under $N+M_y$

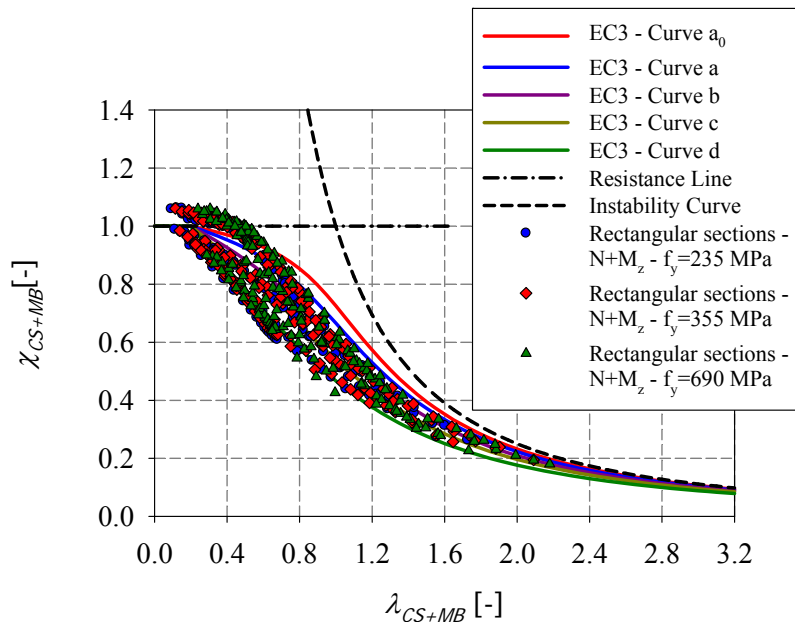


Figure 157 – Numerical results for members with rectangular sections and different steel grades under $N+M_z$

4.3.3.3. Influence of bending moment distribution

The figures below illustrate the application of the O.I.C. for tubular sections under combined loading situations: compression and mono-axial bending (Figure 159), and compression and biaxial bending (Figure 158). It is obvious that in both cases, a leading parameter identified to influence the resistance of a beam-column member is the bending moment distribution represented by the ψ factor¹⁶. This was expected since the member resistance is known to be greatly affected by the bending moment distribution. Accordingly, many existing beam-column design formulas consider the ψ factor (or the C_m factor) as a governing parameter.

No matter what the load cases are, one may notice that member subjected to a triangular bending distribution exhibit a higher resistance than member subjected to a constant moment distribution. Higher interaction curves should then be derived when considering $\psi = 0$.

Furthermore, results for hollow sections under combined loading, show that these members are less affected by instability under compression and major-axis moment $N + M_y$, than under compression and minor-axis moment $N + M_z$ or under compression and biaxial bending

¹⁶ The ψ factor represents the ratio between end moments: $-1.0 \leq \psi \leq 1.0$; $\psi = 1$ indicates constant bending moment distribution, $\psi = 0$ indicates triangular bending moment distribution.

$N + M_y + M_z$ as should be expected since (predominant) weak axis flexural buckling cumulates with weak axis bending.

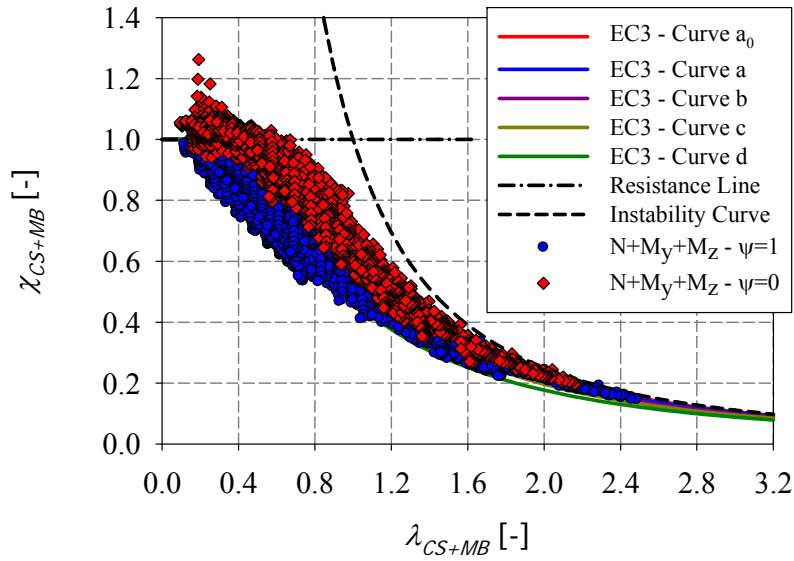
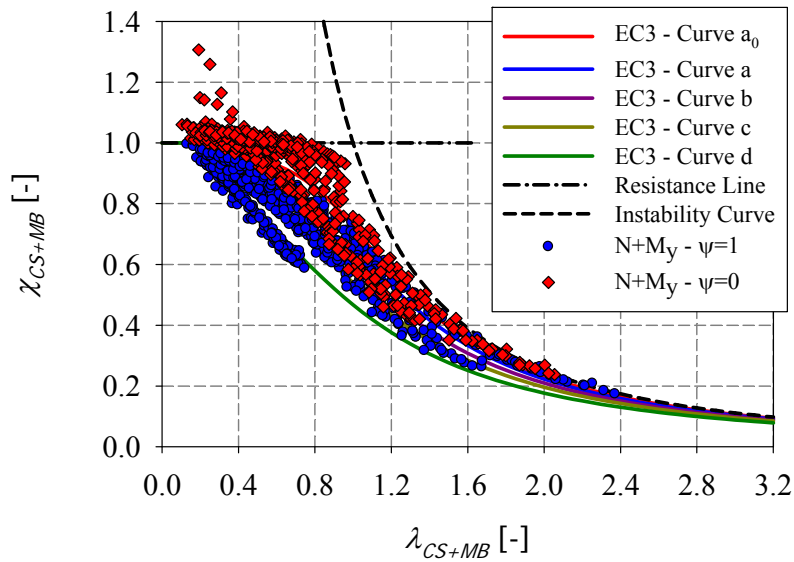


Figure 158 – Numerical results for members under compression and biaxial bending



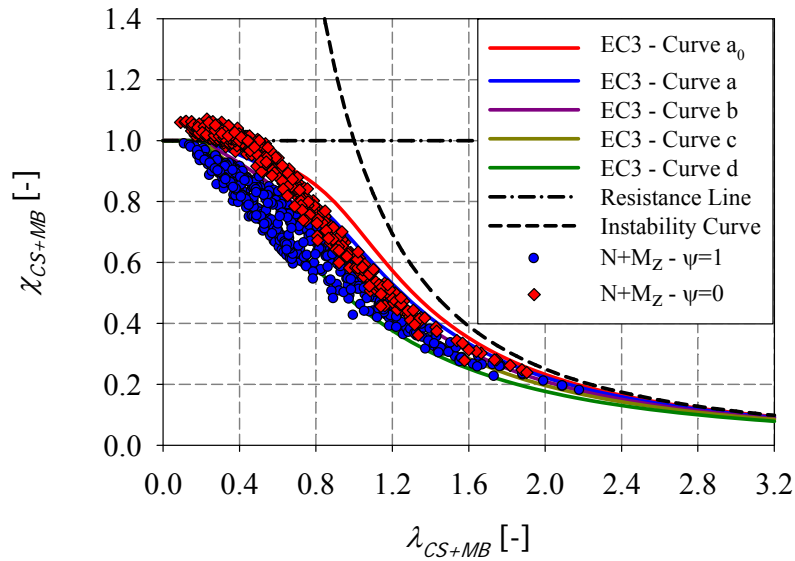


Figure 159 – Numerical results for members under compression – a) Major-axis bending – b) Minor-axis bending

Figure 160 a and b represents the particular case of class 1 rectangular section of nominal yield stress $f_y = 235 \text{ N/mm}^2$ and tested under compression with mono-axial bending $N+M_y$ and $N+M_z$ respectively. Members are subjected to a relative level of compression $n = 0.3$ and to a triangular or a constant bending moment distribution. It is clearly seen that the resistance is enhanced when members are subjected to the loading $N+M_y$ with a triangular bending moment distribution compared to the member subjected to $N+M_z$, with a constant moment distribution.

Obviously, the bending moment distribution is a key parameter that influences the member resistance and should be taken into account for the derivation of interaction curves.

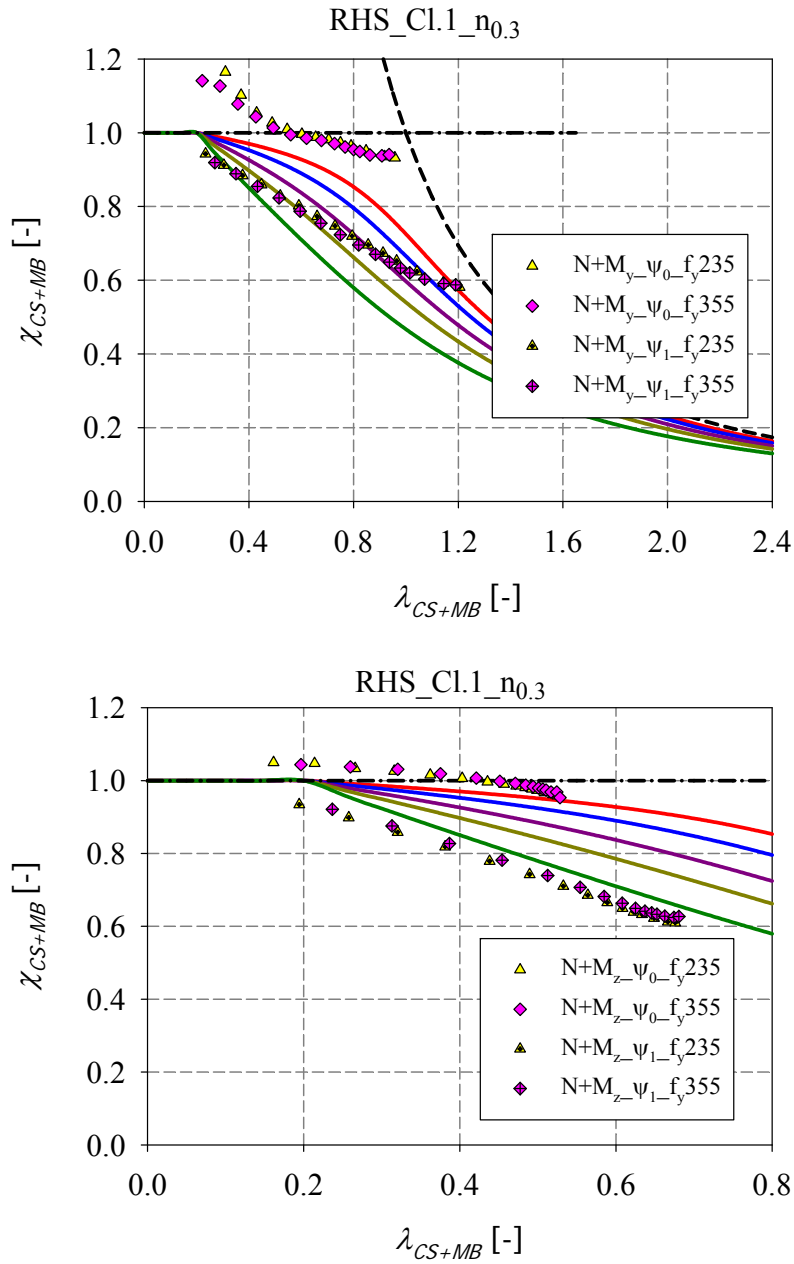


Figure 160 – Numerical results for member with class 1 rectangular sections under compression with mono-axial bending – a) $N+M_y$ – b) $N+M_z$

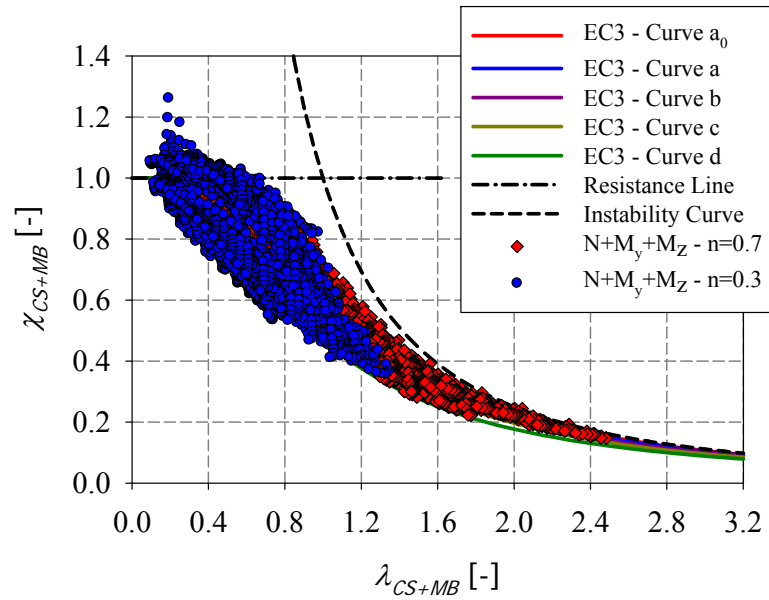
4.3.3.4. Influence of axial force level

Figure 161 clearly shows that the relative axial force ratio n defined as $n = N_{Ed} / N_{b,Rd} = (N_{Ed} / \chi \cdot N_{pl,Rd} \text{ or } N_{Ed} / \chi \cdot N_{eff,Rd})^{17}$ influences as well the member

¹⁷ $N_{pl,Rd}$ and $N_{eff,Rd}$ are calculated with $\gamma_{M1} = 1.0$

resistance. Two values of the factor n have been adopted in this numerical study ($n = 0.3$ and $n = 0.7$).

It is clearly shown that for a high level of compression ($n = 0.7$), global buckling becomes determinant, leading to a wider range of generalized relative slenderness ($\lambda_{CS+MB} > 2$). Global buckling due to the high level of compression occurs before cross-section full yielding, resulting in the failure of the element due to instability and not because of a lack of cross-sectional resistance. However, for a lower level of compression ($n = 0.3$), the curve is more restricted and reaches lower values of the generalized relative slenderness. In this case, bending is predominant. Hollow sections exhibit little influence of instability due to their high resistance towards lateral torsional buckling, and exhibit little influence of global instability due to the low level of compression.



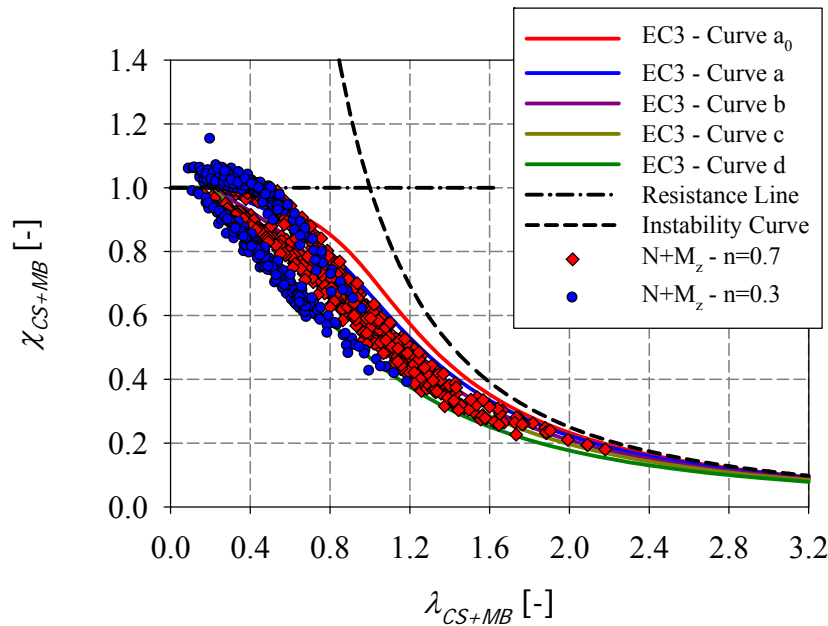
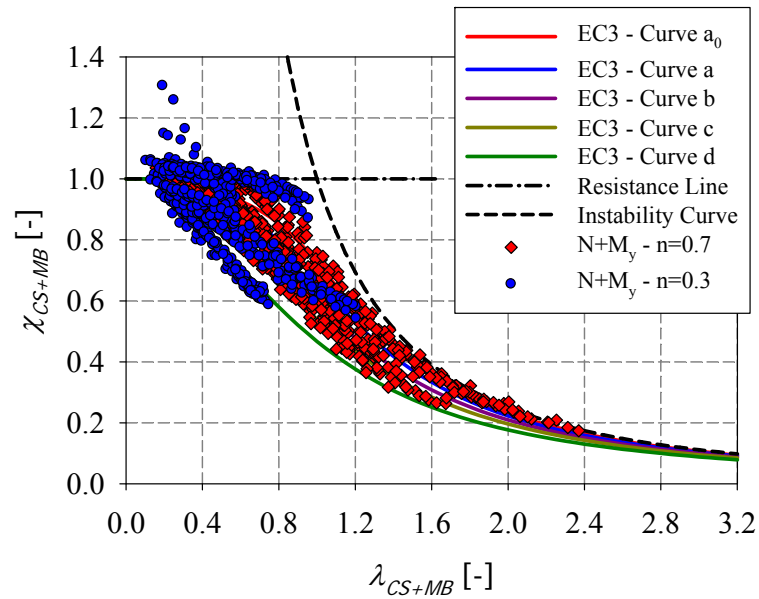


Figure 161 – Numerical results for member with different relative axial force ratios under – a) compression with biaxial bending – b) compression with major-axis bending – c) compression with minor-axis bending

Figure 162 represents the particular case of class 3 rectangular and square sections tested under compression and mono-axial bending $N+M_z$. It is clearly shown that for the case of a low level of compression $n = 0.3$, the failure of the element is mainly due to a lack of resistance and to cross-section buckling ($\lambda_{CS+MB} < 1.2$); however, for the case of high level of compression $n = 0.7$, global buckling becomes more determinant. The axial force level is obviously considered as a key parameter influencing the member resistance.

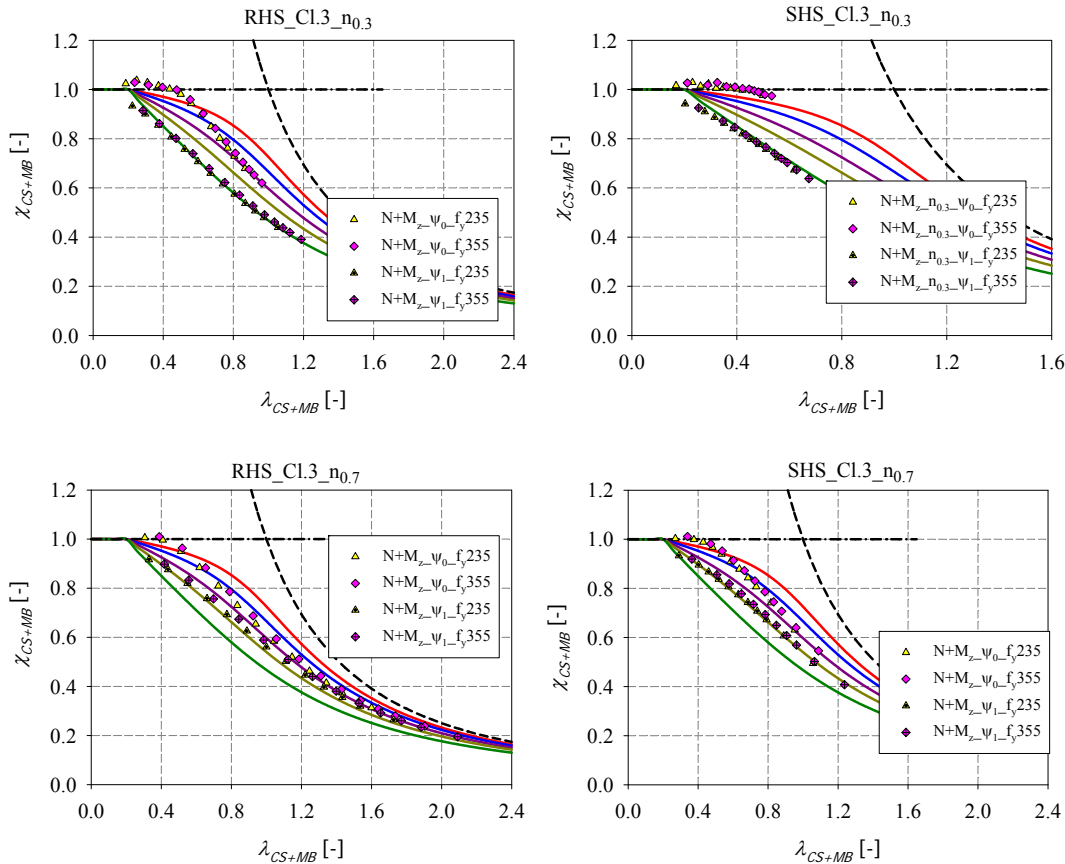


Figure 162 –F.E. results for class 3 rectangular and square sections under compression and mono-axial bending $N+M_z$

4.3.3.5. Influence of biaxial bending

The interaction between resistance and stability is greatly affected by the distribution of bending moment and by the proportions between the different loads. For sake of simplicity, only some results for combined loading situations for square and rectangular sections with the corresponding cross-sectional classes well-distributed along class 1 and class 4 are presented in Figure 164, in order to investigate the influence of the proportions of the bending moments. For each load case, 10 values of the degree of biaxial bending (i.e. representing the M_y / M_z ratio) were adopted varying from $\alpha_{biaxiality} = 0^\circ$ (i.e. the load case becoming compression with major-axis bending $N+M_y$) to $\alpha_{biaxiality} = 90^\circ$ (i.e. the load case becoming compression with minor-axis bending $N+M_z$) with a range of 10 degrees. The M_y / M_z ratio is obviously a leading parameter for the derivation of appropriate interaction curves.

For what concern square sections, a degree of biaxial bending equal to 0° (i.e. indicating that only major-axis bending is present) is identical to a degree of biaxial bending equal to 90° (i.e.

indicating that only minor-axis bending is present) due to the symmetrical geometry of the sections. Similarly, the pair of α - values: $\alpha_{_biaxiality} = 10^\circ$ and $\alpha_{_biaxiality} = 80^\circ$; $\alpha_{_biaxiality} = 20^\circ$ and $\alpha_{_biaxiality} = 70^\circ$; $\alpha_{_biaxiality} = 30^\circ$ and $\alpha_{_biaxiality} = 60^\circ$; $\alpha_{_biaxiality} = 40^\circ$ and $\alpha_{_biaxiality} = 50^\circ$ are identical as illustrated in Figure 163 that allows evidencing the influence of the degree of biaxial bending in square sections.

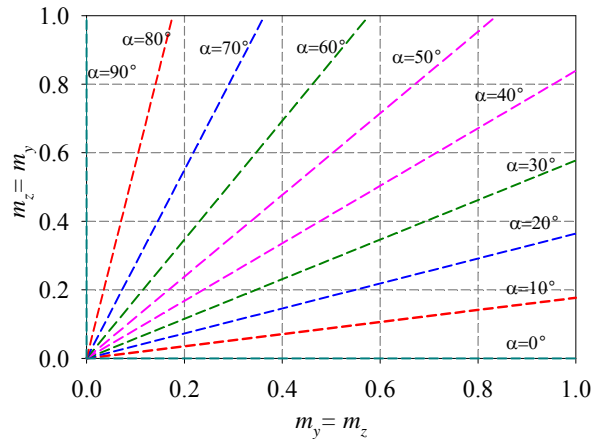
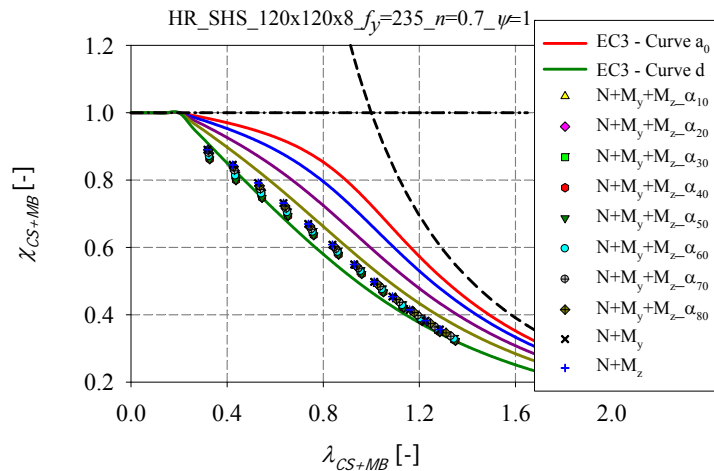
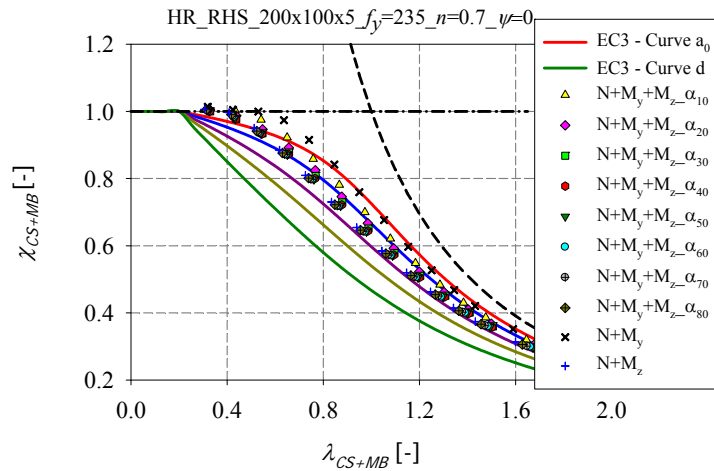
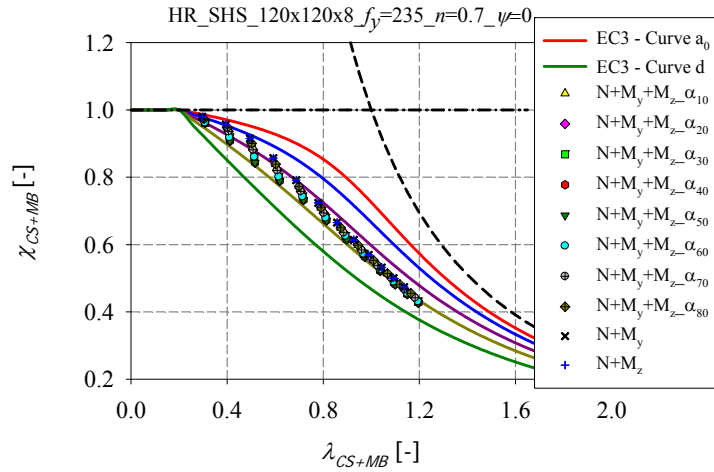


Figure 163 – Influence of the degree of biaxial bending in square sections

Ideally, very close tendencies in the obtained results should be observed for these pair of α - values. As can be seen in the figures below, quite limited scatter is observed as expected for the pair of α - values: $\alpha_{_biaxiality} = 10^\circ$ and $\alpha_{_biaxiality} = 80^\circ$; $\alpha_{_biaxiality} = 20^\circ$ and $\alpha_{_biaxiality} = 70^\circ$; $\alpha_{_biaxiality} = 30^\circ$ and $\alpha_{_biaxiality} = 60^\circ$; $\alpha_{_biaxiality} = 40^\circ$ and $\alpha_{_biaxiality} = 50^\circ$. The small differences are due to the effect of initial imperfections (i.e. inward buckles in 2 opposite plates of the element and outward buckles in the 2 other plates).

It can also be seen that for cases where weak-axis bending takes over strong-axis bending ($\alpha_{_biaxiality} > 45^\circ$), the O.I.C. resistance curves begin to increase again after a progressive drop starting from the combined loading $N+M_y$ alone. When M_z is applied to an $N+M_y$ loading with a small proportion ($\alpha_{_biaxiality} < 45^\circ$), instability is increased if compared to the $N+M_y$ loading; nevertheless when M_z becomes dominant, the section becomes more stable [1]. Consequently, the degree of biaxial bending is considered as a key parameter influencing the member resistance.



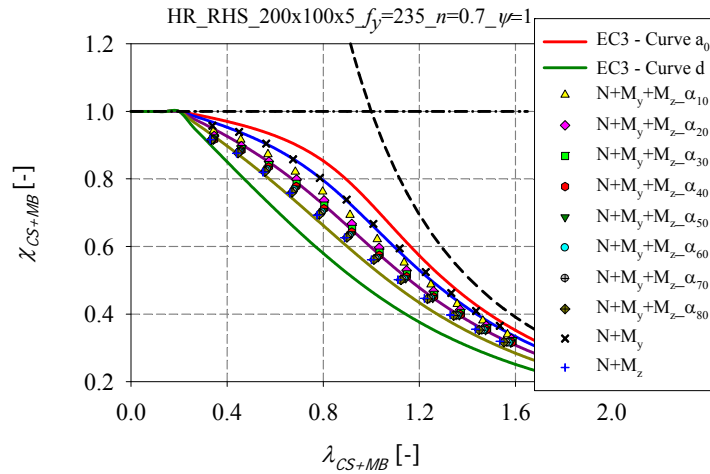
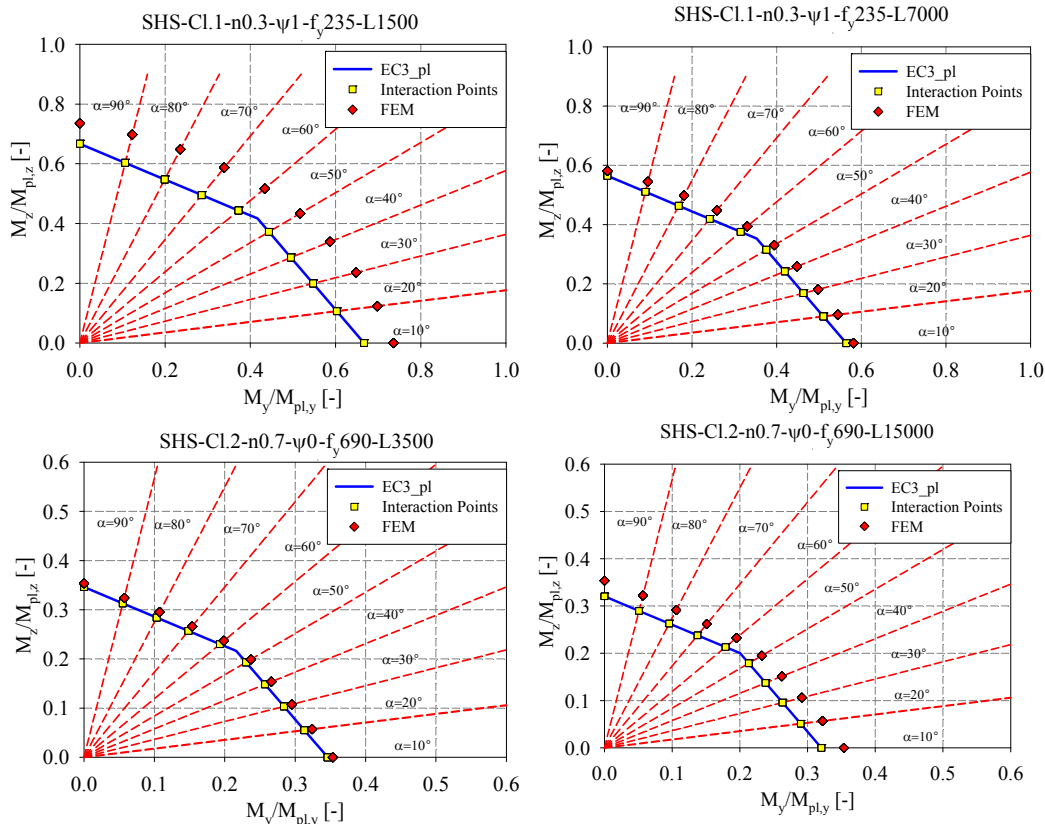
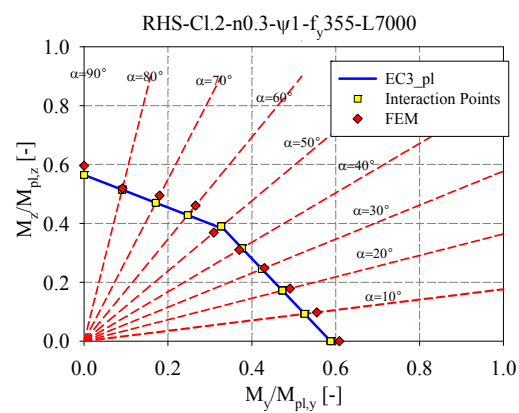
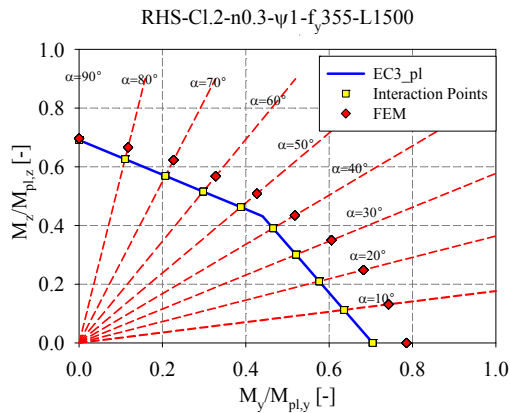
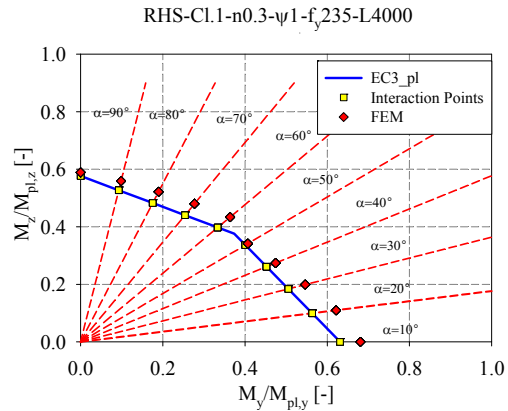
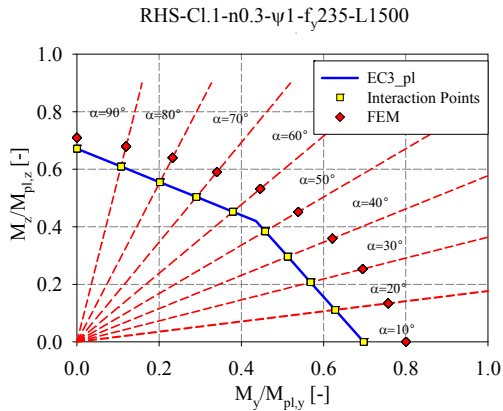
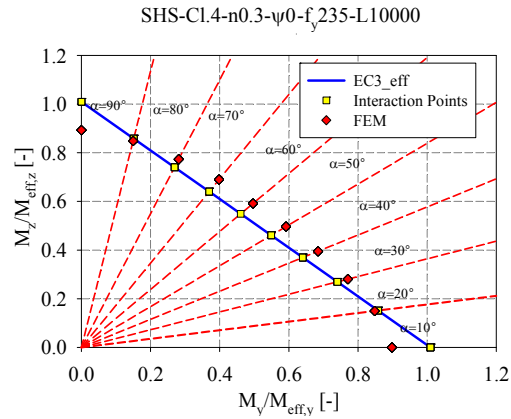
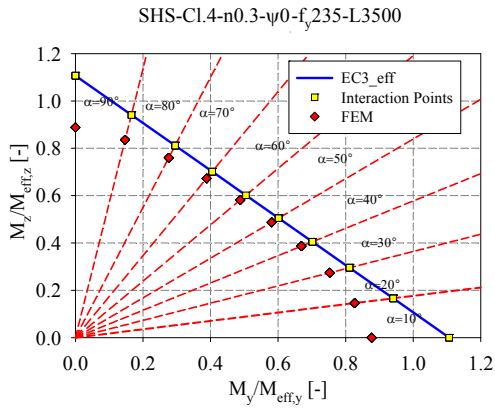
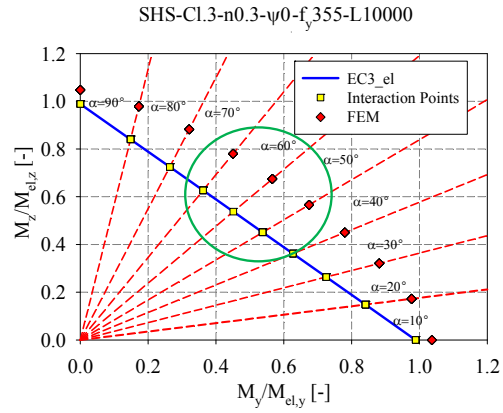
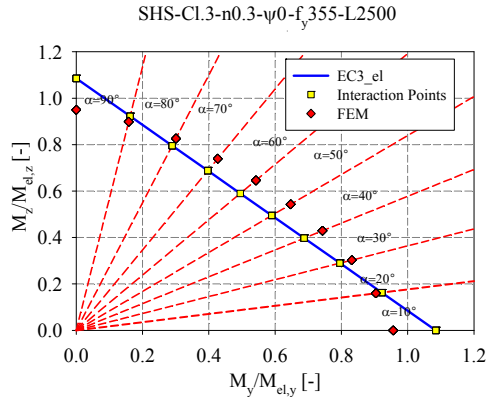


Figure 164 – Numerical results for members under different load cases by varying the degrees of biaxial bending

4.4. Comparison of F.E. results with Eurocode 3 predictions

The figures below present a comparison between Eurocode 3 and F.E. obtained simulation results. For sake of simplicity, only one loading combination was chosen for each cross-section type and presented. Two different lengths for each loading are illustrated as well. The red squares represent the F.E. results for the corresponding load case, while the yellow ones show the obtained results according to Eurocode 3 predictions.





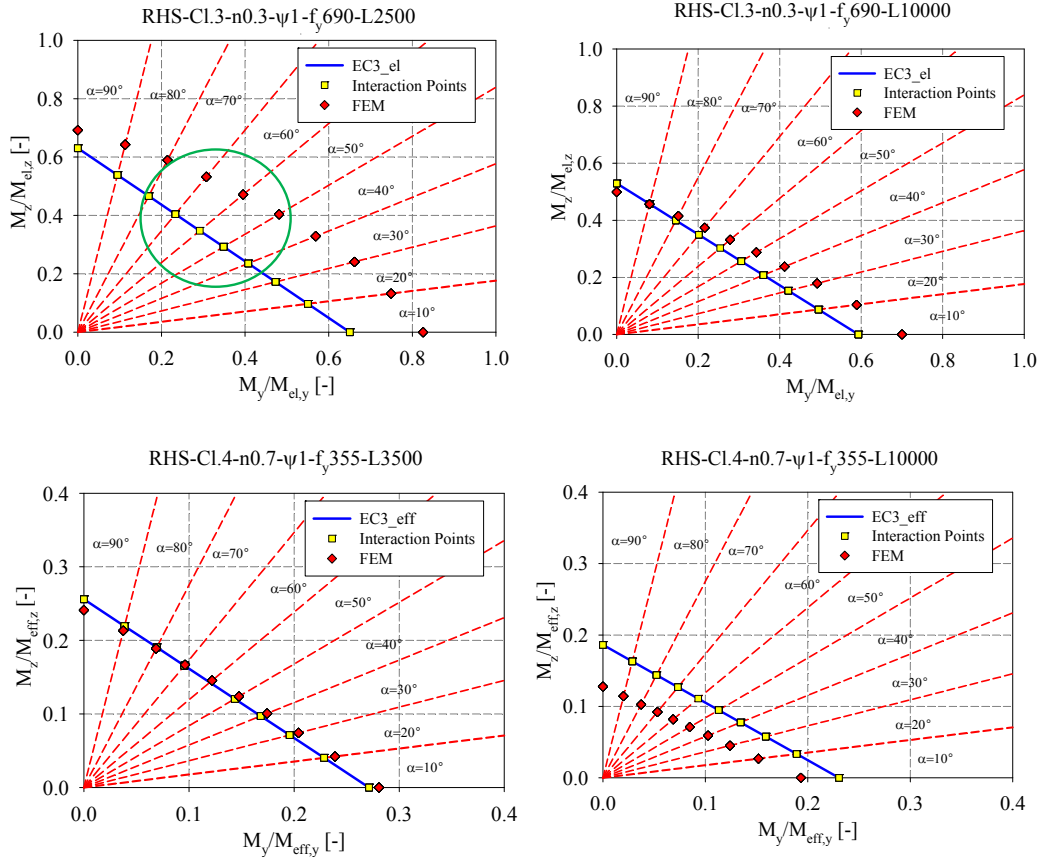


Figure 165 – Comparison of numerical capacity with Eurocode 3 resistances

It is clearly shown that the Eurocode 3 calculations can lead to conservative estimates (i.e. the F.E. predicted resistances are significantly higher) and sometimes overestimate the member's resistance.

Concerning class 3 sections, actual codes limit the cross-section resistance to its elastic value. The results obtained in using the F.E. models clearly illustrate the plastic capacities of the given cross-sections (see green circles).

4.5. Conclusions

The present chapter presented and discussed numerical results on hot-rolled square and rectangular members. The main objective was to investigate beam-column's resistance tested under different loading combinations with the use of the calibrated model. The numerical specimens were chosen in a way to cover all cross-sections classes; they were relative to different steel grades, different element lengths... Results were computed by means of beam and shell analyses in order to investigate the influence of local and global buckling on the

member's behaviour and were plotted in O.I.C. format that was shown to be suitable to characterize the behaviour and response of steel hollow section beam-columns. In addition, key parameters such as the bending moment distribution, axial force ratio, degree of biaxial bending and steel grade were identified.

Preliminary studies were performed before conducting the extensive parametric study and were described in detail. They consisted in:

- a mesh refinement study investigating the most appropriate mesh density able to provide an accurate numerical prediction of the member's behaviour;
- a sensitivity study investigating the influence of different shapes and amplitudes of initial local and global geometric imperfections on the member capacity;
- a load-path sensitivity study characterizing the differences that arise in the structural response of members if the load is applied in different sequences for a given combination;
- a study investigating the most appropriate way to calculate the R-factors (R_{RESIST} , $R_{STAB,MB}$, $R_{STAB,CS}$) involved in the O.I.C. approach.

Finally a comparison between the F.E. and Eurocode 3 calculations for different load cases were presented.

In the next chapter a second numerical parametric study on cold-formed hollow section elements will be presented to complement the one exposed in the present chapter. These data will serve as a set of reference results for the derivation of adequate interaction curves.

5. Numerical parametric study on cold-formed members

5.1. Introduction

Cold-formed tubes are mainly manufactured through two different processes: press-braking and roll-forming [65]. The press-braking route (Figure 166a) forms bending sheets by clamping the work piece between the top and bottom tools, and the cold-forming effect is limited to the corners of the section [66]. Besides, roll-forming (Figure 166b) consists in feeding a long strip of steel through sets of rolls mounted on consecutive stands to form the desired shapes by either direct or indirect forming methods.

The direct forming process consists in roll-forming the strip directly into the desired rectangular shape and then assembling the four plates by welding the corners. The associated cold-forming effect is confined to the area of corners containing the welds whereas the flat faces keep the same properties as the feed material. The continuous-forming process consists in roll-forming the strip into a circular shape, welding the edges of the tube, and then reworking it into the desired rectangular or square shape [67]. In the latter case, the flat face undergoes high cold-work effects, unlike in the direct roll-forming and press-braking methods.

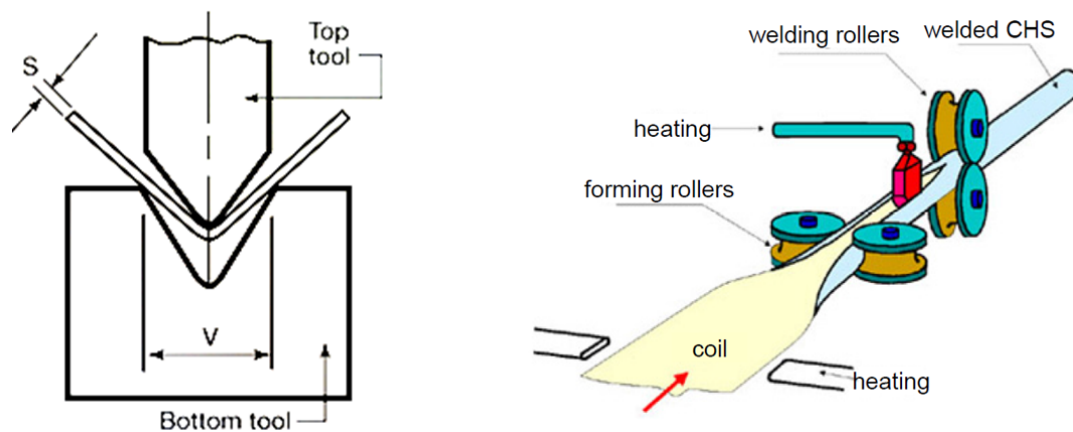


Figure 166 – Manufacturing processes – a) press-braking – b) roll-forming

The present chapter concerns the practical design of cold-formed tubular members, where both local and global instabilities play a significant role. An extensive parametric study on cold-formed hollow section members was launched and more than 39 500 non-linear F.E. simulations have been performed and the results were plotted in an O.I.C. format, i.e. with specific $\lambda - \chi$ axes.

Following section 5.2 first describes the modelling assumptions adopted for the F.E. model of cold-formed tubes (meshing, loading and support conditions, material and geometrical imperfections, adopted material law...). Section 5.3 then describes the parameters adopted in the numerical simulations and section 5.4 provides results for member behaviour in analysing the influence of various parameters on the member's response and resistance (yield stress, cross-section shape and load case). Eventually, summary and conclusions are addressed in section 5.5.

5.2. Description of F.E. models

Numerical computations have been led with the use of non-linear F.E. software FINELg [50], continuously developed at the University of Liège and Greisch Engineering Office since 1970. This software offers almost all types of F.E. analyses, and present investigations have made use of so-called G.M.N.I.A. analyses (Geometrically and Materially Non-linear with Imperfections) to determine the ultimate resistance of sections or members [52].

The F.E. models have been developed in a manner to best fit the properties of a real member. To be able to quantify the interaction between local and global buckling, members have been modelled in shell elements where potential interactions between local and global instabilities are considered. Moreover, to determine the ultimate resistance of a cross-section, shell modelling has also been used to witness local buckling of the cross-section; in such cases, the length of the specimens was chosen equal to three times the largest cross-sectional dimension in order to avoid global buckling.

5.2.1. Material behaviour and residual stresses

Unlike for hot-rolled tubes, for which the typical stress-strain curve exhibits a classic behaviour with distinct yield plateau and strain-hardening effects, the material response of cold-formed tubes shows a pronounced non-linear behaviour and thus has no identifiable yield plateau caused by cold-working of the material, and strain-hardening immediately follows first yield. Increases in yield and ultimate strengths are usually observed in the corner regions of cold-formed sections, and the amount of cold-working can be shown to be associated with an increase in yield stress and a lower level of ductility at fracture. Typically, the 0.2% proof stress is used as a convenient equivalent yield stress. Figure 167a and Figure 167b represent typical stress-strain curves obtained for corners and flat regions of cold-formed sections made of S355 and S460 steel, respectively. It can be seen that the corner

portions exhibit a higher yield stress and a lower ultimate-to-yield stress ratio $\sigma_u / \sigma_{0.2}$ than the flat portions, and that the ductility of the corners is very limited compared to that of the flat faces.

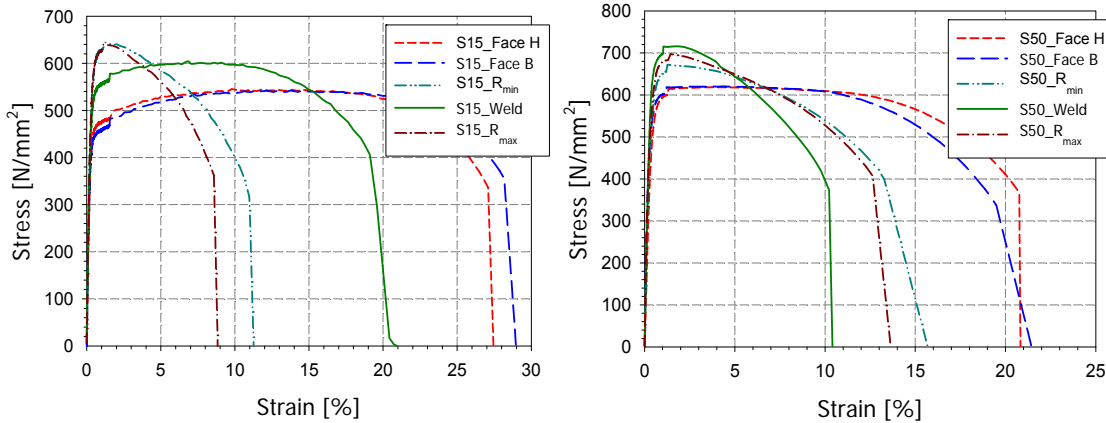


Figure 167 – Typical stress-strain curves – a) S355 – b) S460

In order to characterize the specific mechanical behaviour of cold-formed square and rectangular hollow sections of normal steel grades, experimental results on tensile coupon tests from flat faces, corner areas and welded faces were collected, both from own tensile tests and from literature; they are relative to different sizes of tubular cross-sections, different steel grades and different manufacturers across Europe. All tests and measurements were performed in the Laboratories of the University of Applied Sciences of Western Switzerland in Fribourg [57], the Technical University of Graz [68], the University of Sydney [69], and Lappeenranta University of Technology [70], RWTH Aachen University [71]. For each of the collected test result, the experimental data was plotted and compared to so-called “Ramberg-Osgood equations” – described by Rasmussen [72] – (both simple R.-O. and double R.-O. formulations), where exponent coefficients were deduced from the test by fitting the experimental data. On the basis of these results, coupled with the experimental observations, a simple Ramberg-Osgood formulation was adopted in the numerical model for the base material according to Equation (175):

$$\varepsilon = \frac{\sigma}{E_0} + 0.002 \left(\frac{\sigma}{\sigma_{0.2}} \right)^n \quad (175)$$

where E_0 is the initial Young's modulus, $\sigma_{0.2}$ the equivalent yield stress and n a strain-hardening coefficient chosen equal to 21 for normal steel grades and equal to 40 for high steel grades based on obtained tensile test results and gathered data from literature; more details

concerning the choice of the choice of the appropriate material law for cold-formed tubes can be found in Annex 2.

A multi-linear law was adopted for the corners region where a simple Ramberg-Osgood law was shown to be not suitable [3], since this material law is characterized by a small ductility and a maximum strain of 2.5 %. Therefore, once the section reached that level of strain, the corners would find themselves ineffective leading to the failure of the entire section and no more strains could be achieved beyond this value of 2.5% strain. The adopted material laws are illustrated in Figure 168.

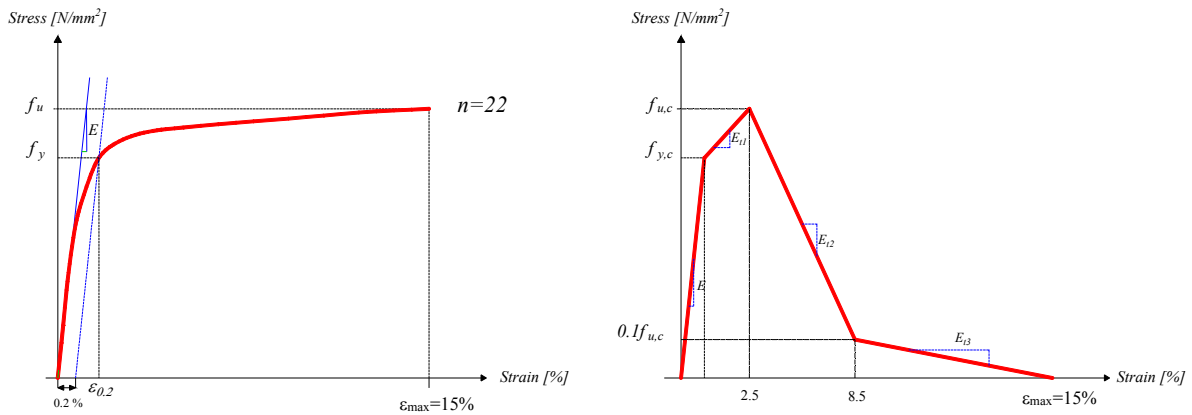


Figure 168 – Adopted material laws for – a) flat faces – b) corner regions

The multi-linear law was considered with the following parameters:

$$f_{y_corner} = 1.15 f_{y_flat} \quad (176)$$

$$f_{u_corner} = 1.15 f_{u_flat} \quad (177)$$

The factor 1.15 was adopted on the basis of statistical study on material laws from literature, and shown to be convenient.

As for material imperfections, flexural residual stresses with a maximum amplitude of 300 N/mm^2 were introduced in the numerical model, as suggested by Key [73]. As for the corner regions in which the longitudinal stresses are less important than the flat regions, a value of 235 N/mm^2 was adopted.

5.2.2. Modelling assumptions adopted for the F.E. model

The support conditions and the introduction of applied loads received particular attention, and use of so-called kinematic linear constraints has been made to ensure a “plane-sections-remain-plane” behaviour of the end sections. Following ideal simply-supported “fork” support conditions, the end cross-section can only exhibit a maximum of three degrees of freedom: axial global displacement, rotation about the strong axis and rotation about the weak axis. Only three different nodes are then necessary to describe the displacement of any point in the cross-section once the linear relationships for axial displacements are established. In other words, a maximum of three nodes may experience a “free” longitudinal displacement; all other nodes’ x-displacements linearly depend on the longitudinal displacements of the “x-free” nodes to respect a global cross-sectional displaced configuration. The three nodes were chosen at the plate edges (near different corners) of the cross-section, and all the nodes in between were constrained to the three main nodes with linear relationships. Additional fictitious nodes have been defined at the centroids of the end-cross-sections for the definition of the support conditions, and transverse supports preventing from local buckling have also been implemented in each plate. External loading was applied through four concentrated forces at the member’s ends (i.e. strong, weak axis bending moments and axial forces) and has been implemented at the flanges’ plates as shown in Figure 169.

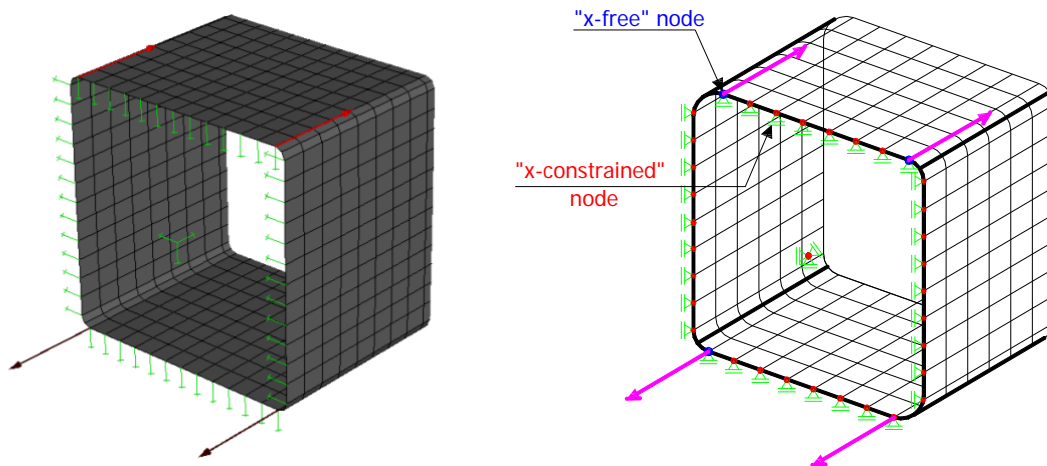


Figure 169 – Loading and support conditions

As for the hot-rolled sections, *Type II* mesh was selected on the basis of the case studies detailed in chapter 4 (see Figure 170), where it was seen to provide accurate numerical prediction of the member’s behaviour at reasonable computation costs. Specimens have been modelled with a regular mesh all over the length of the section, with corners modelled with 2

shell elements per corner. Local geometrical imperfections have been defined as square half-wave patterns in both directions of the flanges and webs, with an amplitude of $a / 200$, where a stands for the length of the considered square panel. Global initial geometrical imperfections have been introduced through adequate modifications of node coordinates following sine shapes in both major and minor-axes with the realistic average value of global imperfection amplitude equal to $L / 1000$.

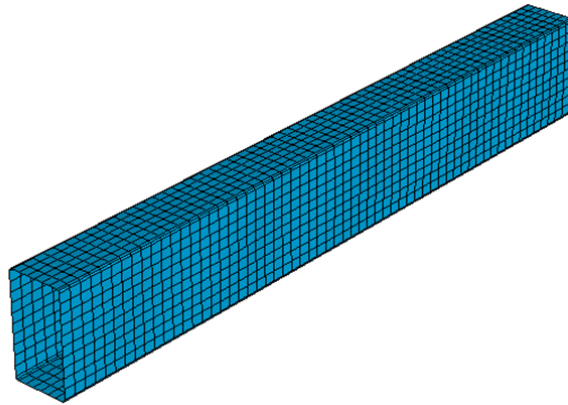


Figure 170 – Mesh *Type II* selected for G.M.N.I.A. calculations

5.3. Cases and parameters considered

Parametric calculations have been carried out for the member resistance of cold-formed sections by considering the same parameters taken for the hot-rolled sections and detailed in chapter 4, with the difference of adjusting the corner radius (taken as $1.5 t$ for hot-formed sections and $2 t$ for cold-formed section). Accordingly the following parameters were covered:

- 13 different element lengths varying from 1500 mm to 15000 mm in order to represent the whole practical range of member slenderness;
- 3 different steel grades: S235, S355, S690;
- 8 cross-section shapes: rectangular and square hollow sections covering all cross-section classes according to EN 1993-1-1;
- different loading conditions:
 - o pure compression N ;

- compression with major-axis bending $N+M_y$;
- compression with minor-axis bending $N+M_z$;
- compression with biaxial bending $N+M_y+M_z$.

A distinction has been made between the different loading situations, namely with respect to:

- linear bending moments distributions defined as the ratio between applied end moments: 2 coefficients were adopted $\psi_y = \psi_z = 1$ and $\psi_y = \psi_z = 0$ to consider constant and triangular distributions, respectively;
- the relative axial force ratio defined according to EN 1993-1-1 as $n = N / N_{b,Rd}$ ¹⁸ where:

$$N_{b,Rd} = \chi N_{pl} \text{ for class 1, 2 and 3 cross-sections;}$$

$$N_{b,Rd} = \chi N_{eff} \text{ for class 4 cross-sections;}$$

$N_{b,Rd}$, N_{pl} and N_{eff} represent respectively the buckling, plastic and effective resistance of the member; χ represents the reduction factor for instability; 3 values of the relative axial force ratio n were adopted going from 0.3 (i.e. the load case becoming thus a compression of 30% $N_{b,Rd}$ with monoaxial or biaxial bending), to 0.7 (i.e. the load case becoming thus a compression of 70% $N_{b,Rd}$ with monoaxial or biaxial bending) to 1.0 (i.e. the load case becoming thus 100% $N_{b,Rd}$, a pure compression one);

- the degree of biaxial bending defined for combined load cases as the ratio M_y / M_z . This ratio was varied on the basis of an angle $\alpha_{\text{biaxiality}}$ in order to investigate the influence of the proportion of the major and minor-axis bending on the member resistance. For each load case, 10 values of the degree of biaxial bending were adopted varying from $\alpha_{\text{biaxiality}} = 0^\circ$ (i.e. the load case becoming compression with major-axis bending $N+M_y$) to $\alpha_{\text{biaxiality}} = 90^\circ$ (i.e. the load case becoming compression with minor-axis bending $N+M_z$), as shown in Figure 171 for different types of cross-section classification.

¹⁸ $\gamma_{M1} = 1.0$ for this study.

Additional calculations were performed with the same parameters mentioned before with a length equal to three times the height of the section in order to determine the cross-section resistance.

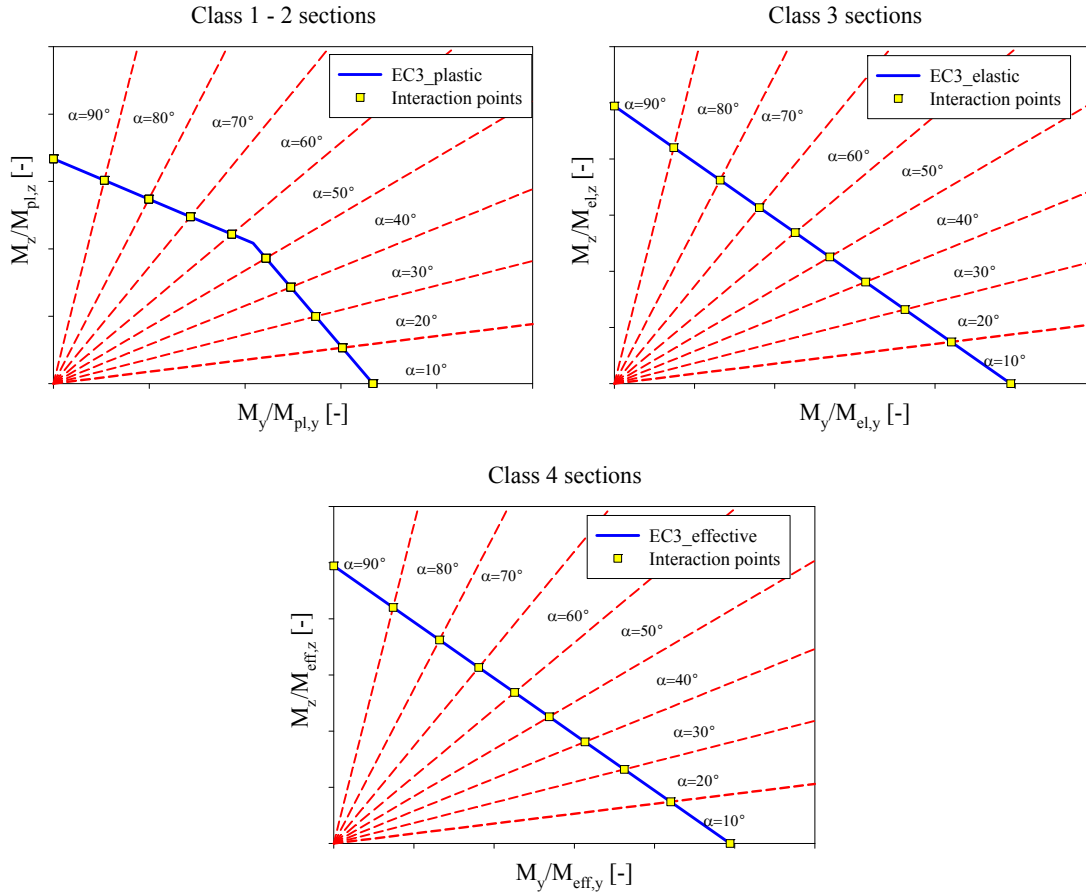


Figure 171 – Selection of load cases for $N+M_y+M_z$ combined situations – a) class 1-2 – b) class 3 – c) class 4

Case 1 loading (one-stage loading: applying N and M_y and M_z simultaneously) was again adopted for the complete F.E. parametric study since it leads to safe but realistic results for all load cases.

In total, some 31 200 non-linear G.M.N.I.A. F.E. computations have been performed for cold-formed tubular sections. In order to get the ultimate load multiplier R_{REAL} factor of cold-formed sections, 15 600 shell calculations for members were performed as well as 15 600 shell calculations for cross-sections. In addition, 15 600 simulations were performed to get the critical load multiplier for cross-sections $R_{STAB,CS}$; another 15 600 were performed to get the critical load multiplier for members $R_{STAB,MB}$ and 15 600 to get the plastic load multiplier R_{RESIST} .

Figure 172 represents the numerical results obtained for the hot-rolled and cold-formed SHS and Figure 173 represents the results for the hot-rolled and cold-formed RHS. The horizontal axis of the figures presented hereafter represents the generalized slenderness λ_{CS+MB} while the vertical axis reports the reduction factor χ_{CS+MB} defined in Equation (178) and Equation (179) respectively:

$$\lambda_{CS+MB} = \sqrt{\frac{\chi_{CS} \cdot R_{RESIST}}{R_{STAB,MB}}} \quad (178)$$

$$\chi_{CS+MB} = \frac{R_{ult,FE,SHELL}}{\chi_{CS} \cdot R_{RESIST}} \quad (179)$$

In Equations (178) and (179), χ_{CS} represents the cross-section reduction factor calculated numerically. Analytical expressions were developed to get χ_{CS} and can be found in [3]. The final resistance factor $R_{ult,FE,SHELL}$ is computed using shell elements in this case so that local and global instabilities interact; $R_{ult,FE,SHELL}$ is affected by resistance and instability as well as by initial imperfections (i.e. residual stresses, geometrical imperfections), by the material law, load cases, section geometries, boundary conditions...). R_{RESIST} is computed using a dedicated Matlab tool developed to compute the exact ratio of the section [61]. $R_{STAB,CS}$ is computed using FINELg shell models for cross-sections and software Abaqus with beam modelling for members was used to calculate $R_{STAB,MB}$.

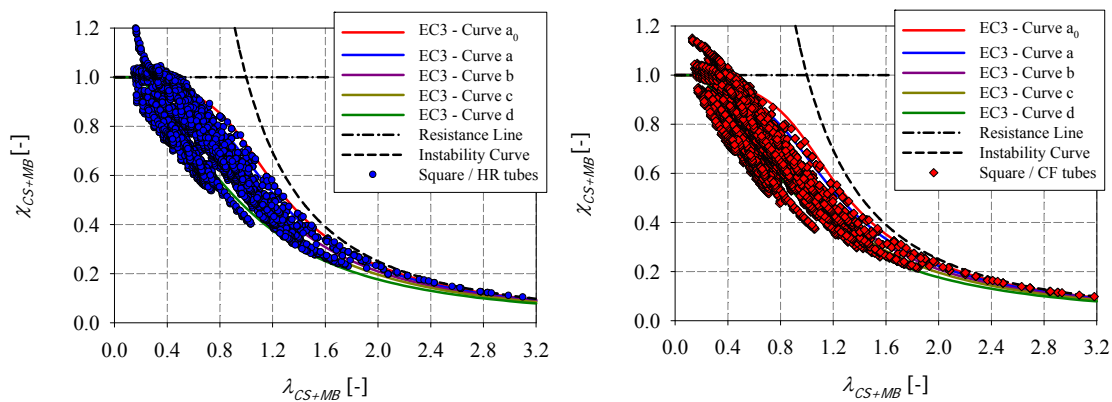


Figure 172 – Numerical results for members obtained for – a) hot-rolled SHS– b) cold-formed SHS

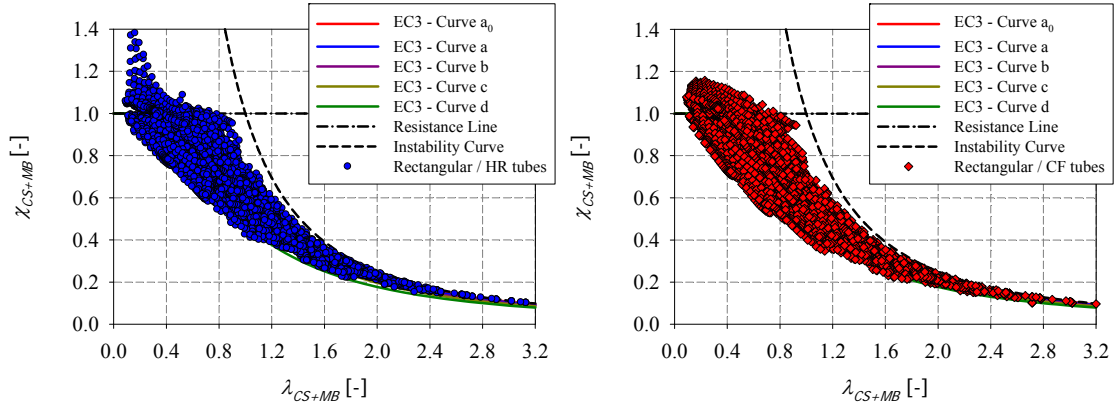


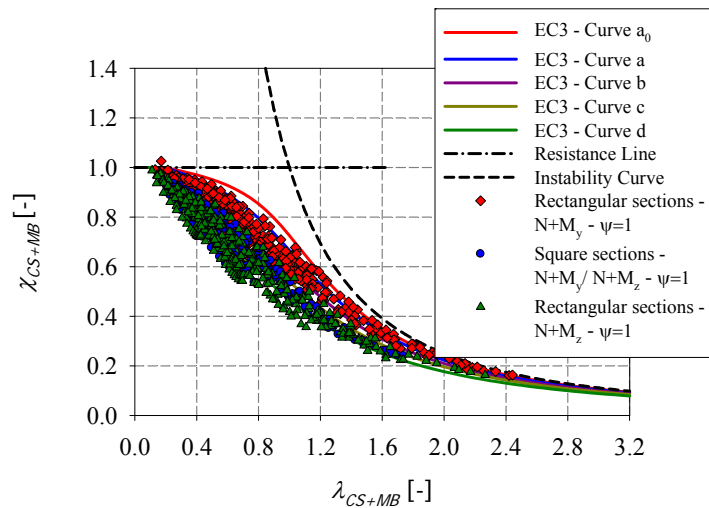
Figure 173 – Numerical results for members obtained for – a) hot-rolled RHS– b) cold-formed RHS

5.4. Analyses of results

The present paragraph identifies the key parameters that should be accounted for in the design proposal of cold-formed members and analyses the influence of these parameters on the member resistance.

5.4.1. Influence of cross-section shape and slenderness

The cross-section geometry is a key parameter that influences the cold-formed member resistance. Similarly to hot-rolled sections, rectangular sections under combined loading behave better than square ones and the members are less affected by instability and have higher resistance under compression with major-axis bending than under compression with minor-axis bending (see Figure 174).



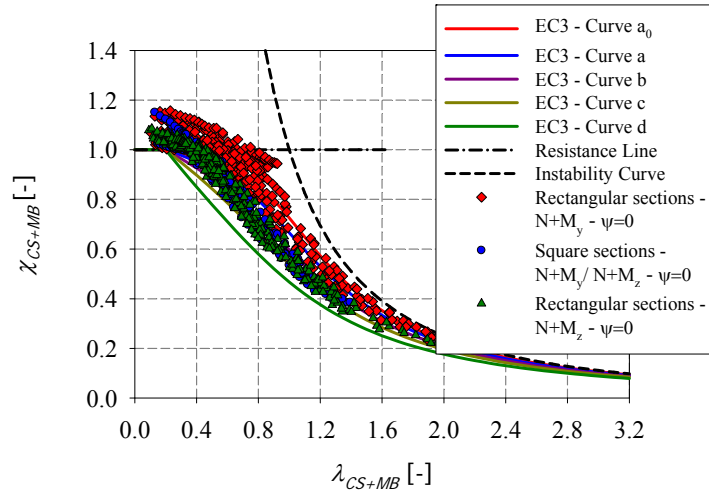


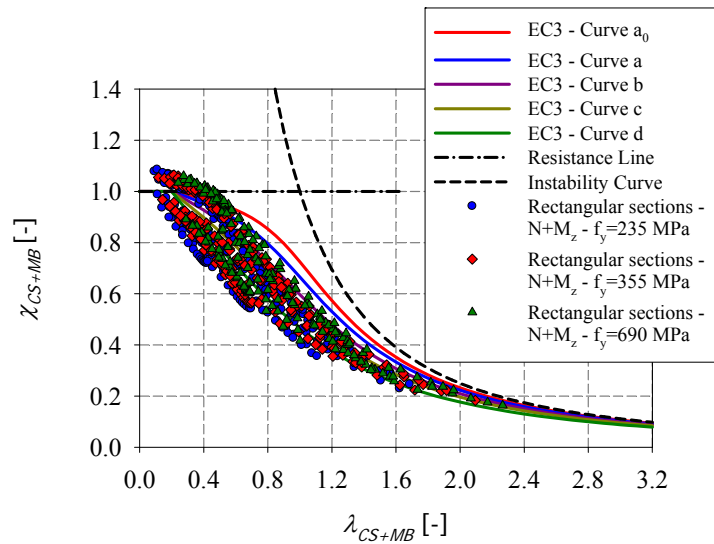
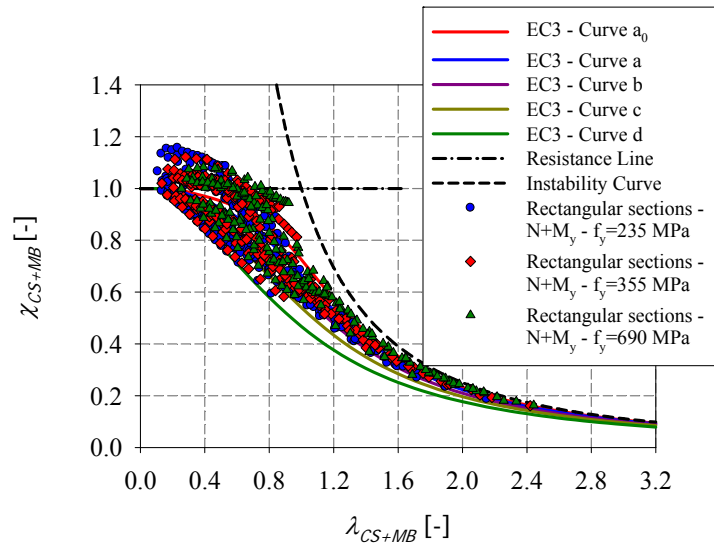
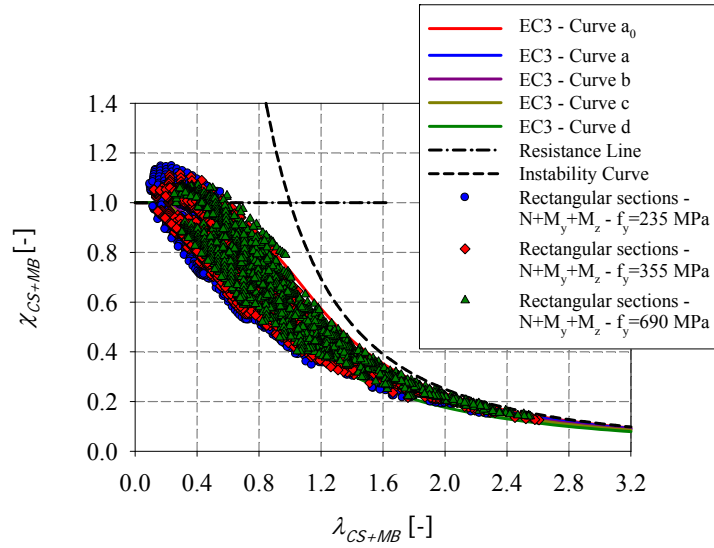
Figure 174 – Numerical results for members under combined loading $N+M_y$ and $N+M_z$ for square and rectangular sections – a) constant bending moment distribution – b) triangular bending moment distribution

5.4.2. Influence of yield stress

Figure 175 represents the obtained results for rectangular and square hollow sections respectively under combined load cases for different steel grades: $f_y = 235 \text{ N/mm}^2$, $f_y = 355 \text{ N/mm}^2$ and $f_y = 690 \text{ N/mm}^2$.

As can be seen, an increase in the yield stress f_y increases the relative slenderness λ_{CS+MB} (i.e. the instability has more influence on high strength steel products) and decreases the reduction factor χ_{CS+MB} (i.e. the section become more slender thus prone to buckling); consequently, tendencies for slightly higher χ_{CS+MB} values for high steel grades are observed (see Figure 175).

One may also notice that a relatively really small dispersion in the results is noted for $f_y = 235 \text{ N/mm}^2$ and $f_y = 355 \text{ N/mm}^2$, for all load cases. Consequently, a single interaction curve may be derived for $f_y = 235 \text{ N/mm}^2$ and $f_y = 355 \text{ N/mm}^2$ for sake of simplicity since negligible results were seen and a higher one may be derived for $f_y = 690 \text{ N/mm}^2$.



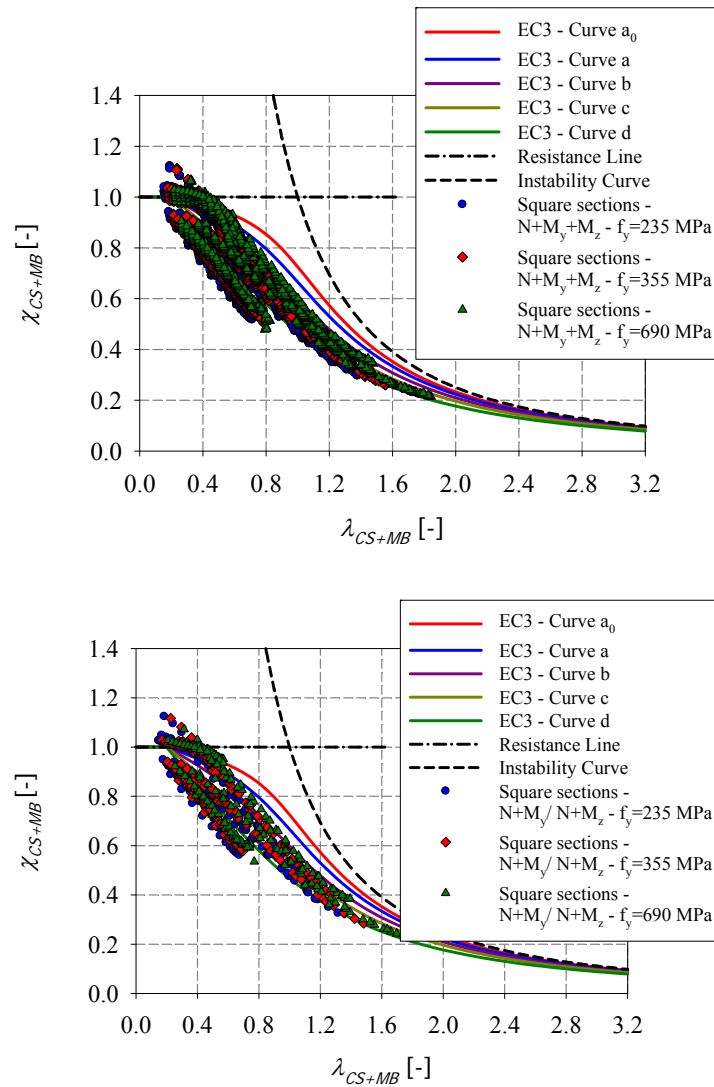


Figure 175 – Numerical results for cold-formed members tested under different steel grades

5.4.3. Influence of bending moment distribution

A leading parameter identified to influence the resistance of a beam-column member is the bending moment distribution represented by the ψ factor¹⁹ as illustrated in Figure 176 and in Figure 177. This was expected since the member resistance is known to be greatly affected by the distribution of bending moment. Accordingly, many existing beam-column design formulas consider the ψ factor (or the C_m factor) as a governing parameter.

¹⁹ The ψ factor represents the ratio between end moments: $-1.0 \leq \psi \leq 1.0$; $\psi = 1$ indicates constant bending moment distribution, $\psi = 0$ indicates triangular bending moment distribution.

No matter what the load cases are, one may notice that members subjected to a triangular bending distribution exhibit a higher resistance than members subjected to a constant moment distribution. Higher interaction curves should then be derived when considering $\psi = 0$.

Furthermore, results for hollow sections under combined loading, show that these members are less affected by instability under compression and major-axis moment $N + M_y$ than under compression and minor-axis moment $N + M_z$ or under compression and biaxial bending $N + M_y + M_z$ as should be expected since (predominant) weak axis flexural buckling cumulates with weak axis bending.

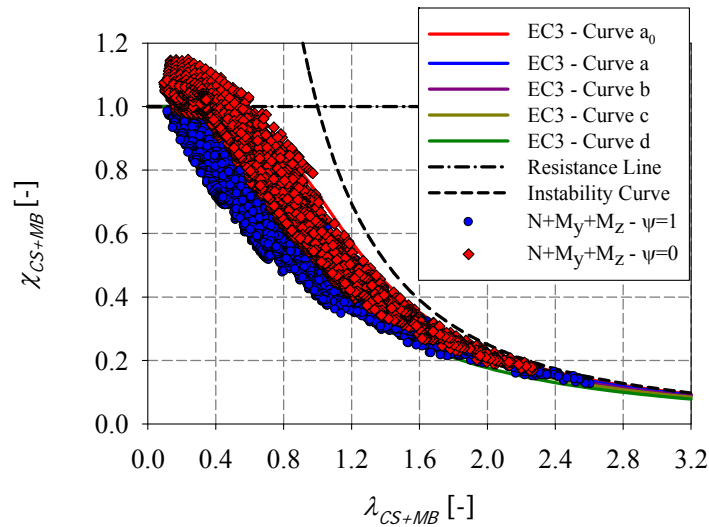
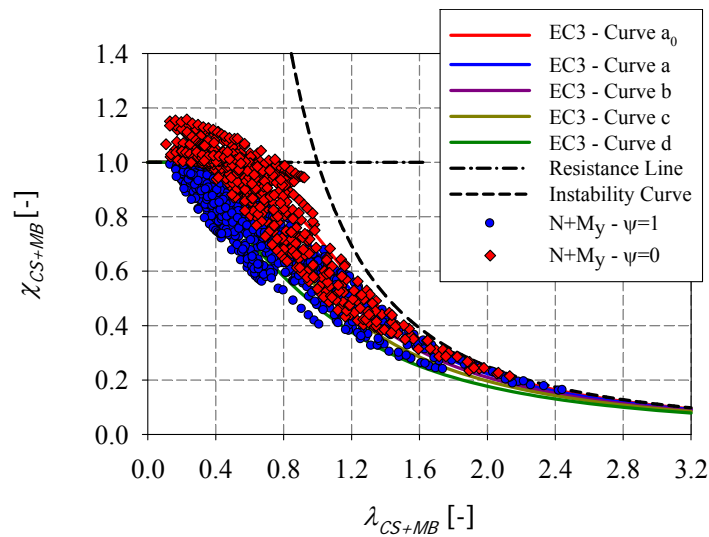


Figure 176 – Numerical results for members under compression and biaxial bending



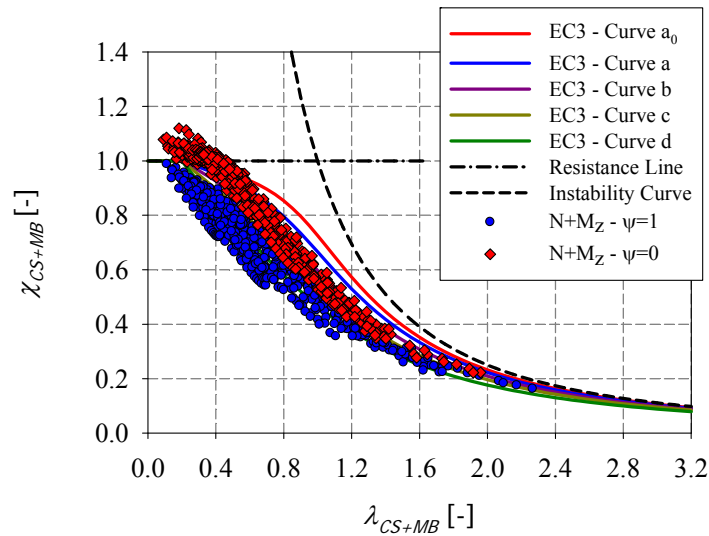


Figure 177 – Numerical results for member under compression – a) Major-axis bending – b) Minor-axis bending

5.4.4. Influence of axial force level

Figure 178 clearly shows that the relative axial force ratio n defined as $n = N_{Ed} / N_{b,Rd} = (N_{Ed} / \chi \cdot N_{pl,Rd} \text{ or } N_{Ed} / \chi \cdot N_{eff,Rd})^{20}$ influences as well the member resistance. Two values of the factor n have been adopted in this numerical study ($n = 0.3$ and $n = 0.7$).

It is clearly shown that for a high level of compression ($n = 0.7$), global buckling becomes determinant, leading to a wider range of generalized relative slenderness ($\lambda_{CS+MB} > 2$). Global buckling due to the high level of compression occurs before cross-section full yielding, resulting in the failure of the element due to instability and not because of a lack of cross-sectional resistance. However, for a lower level of compression ($n = 0.3$), the curve is more restricted and reaches lower values of the generalized relative slenderness. In this case, bending is predominant. Hollow sections exhibit little influence of instability due to their high resistance towards lateral torsional buckling, and exhibit little influence of global instability due to the low level of compression.

²⁰ $N_{pl,Rd}$ and $N_{eff,Rd}$ are calculated with $\gamma_{M1} = 1.0$.

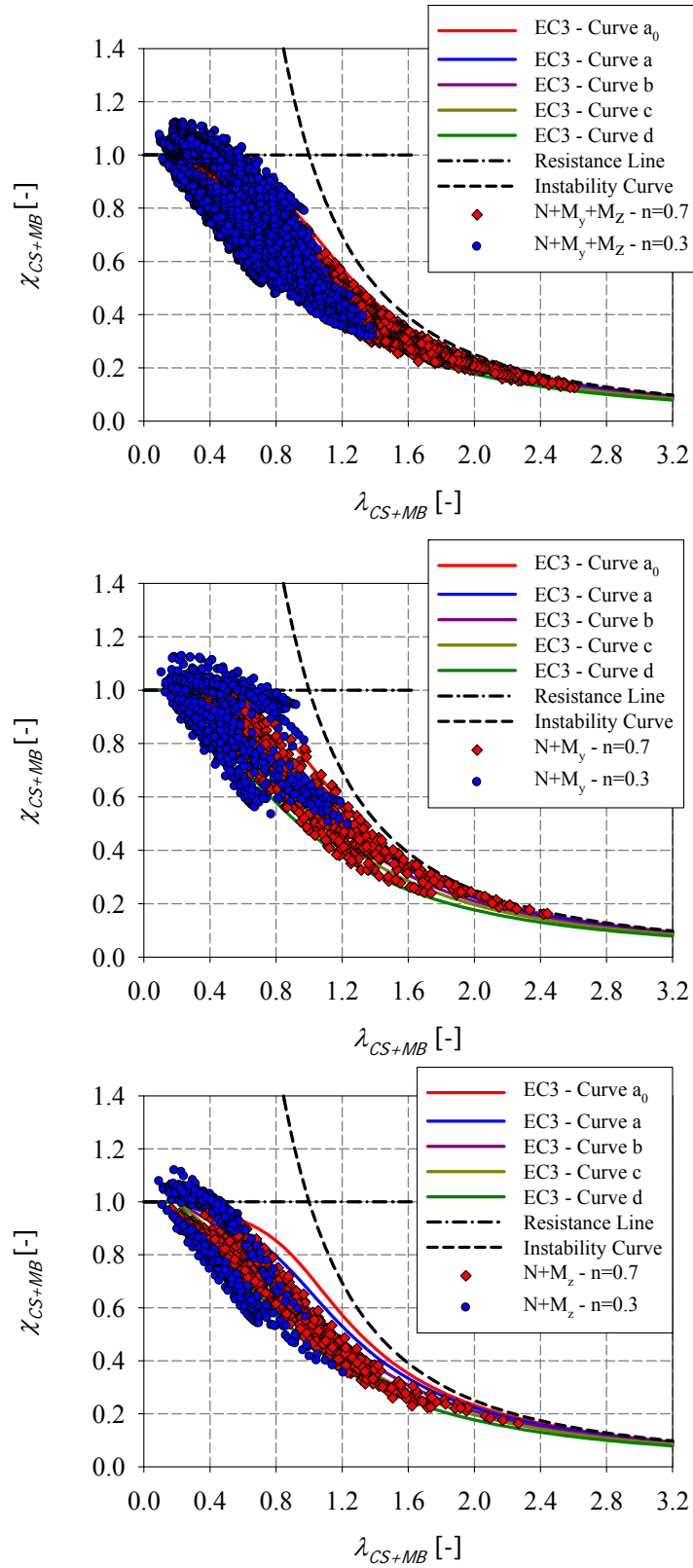


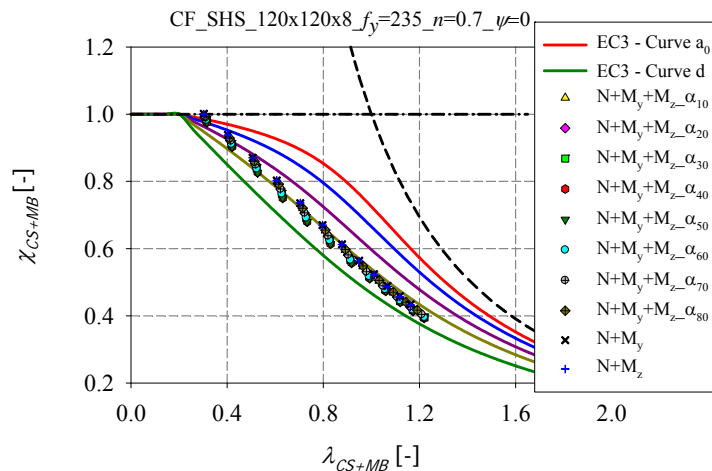
Figure 178 – Numerical results for members with different relative axial force ratios under – a) compression with biaxial bending – b) compression with major-axis bending – c) compression with minor-axis bending

5.4.5. Influence of biaxial bending

Figure 179 presents some results for combined loading situations for square and rectangular sections. One may notice that similarly to the hot-rolled sections, the proportions of the bending moments is a key parameter influencing the resistance of cold-formed hollow sections. For each load case, 10 values of the degree of biaxial bending (i.e. representing the M_y / M_z ratio) were adopted varying from $\alpha_{biaxiality} = 0^\circ$ (i.e. the load case becoming compression with major-axis bending $N+M_y$) to $\alpha_{biaxiality} = 90^\circ$ (i.e. the load case becoming compression with minor-axis bending $N+M_z$) with a range of 10 degrees.

For what concern square sections, very close tendencies in the obtained results are observed for different $\alpha_{biaxiality}$ - values. This is due to the symmetrical geometry of the sections. A degree of biaxial bending equal to 0° (i.e. indicating that only major-axis bending is present) is identical to a degree of biaxial bending equal to 90° (i.e. indicating that only minor-axis bending is present). Similarly, the pair of α - values: $\alpha_{biaxiality} = 10^\circ$ and $\alpha_{biaxiality} = 80^\circ$; $\alpha_{biaxiality} = 20^\circ$ and $\alpha_{biaxiality} = 70^\circ$; $\alpha_{biaxiality} = 30^\circ$ and $\alpha_{biaxiality} = 60^\circ$; $\alpha_{biaxiality} = 40^\circ$ and $\alpha_{biaxiality} = 50^\circ$ are identical.

However, for what concern rectangular sections, it can also be seen that for cases where weak-axis bending takes over strong-axis bending ($\alpha_{biaxiality} > 45^\circ$), the O.I.C. resistance curves begin to increase again after a progressive drop starting from the combined loading $N+M_y$ alone. When M_z is applied to an $N+M_y$ loading with a small proportion ($\alpha_{biaxiality} < 45^\circ$), instability is increased if compared to the $N+M_y$ loading; nevertheless when M_z becomes dominant, the section becomes more stable [1].



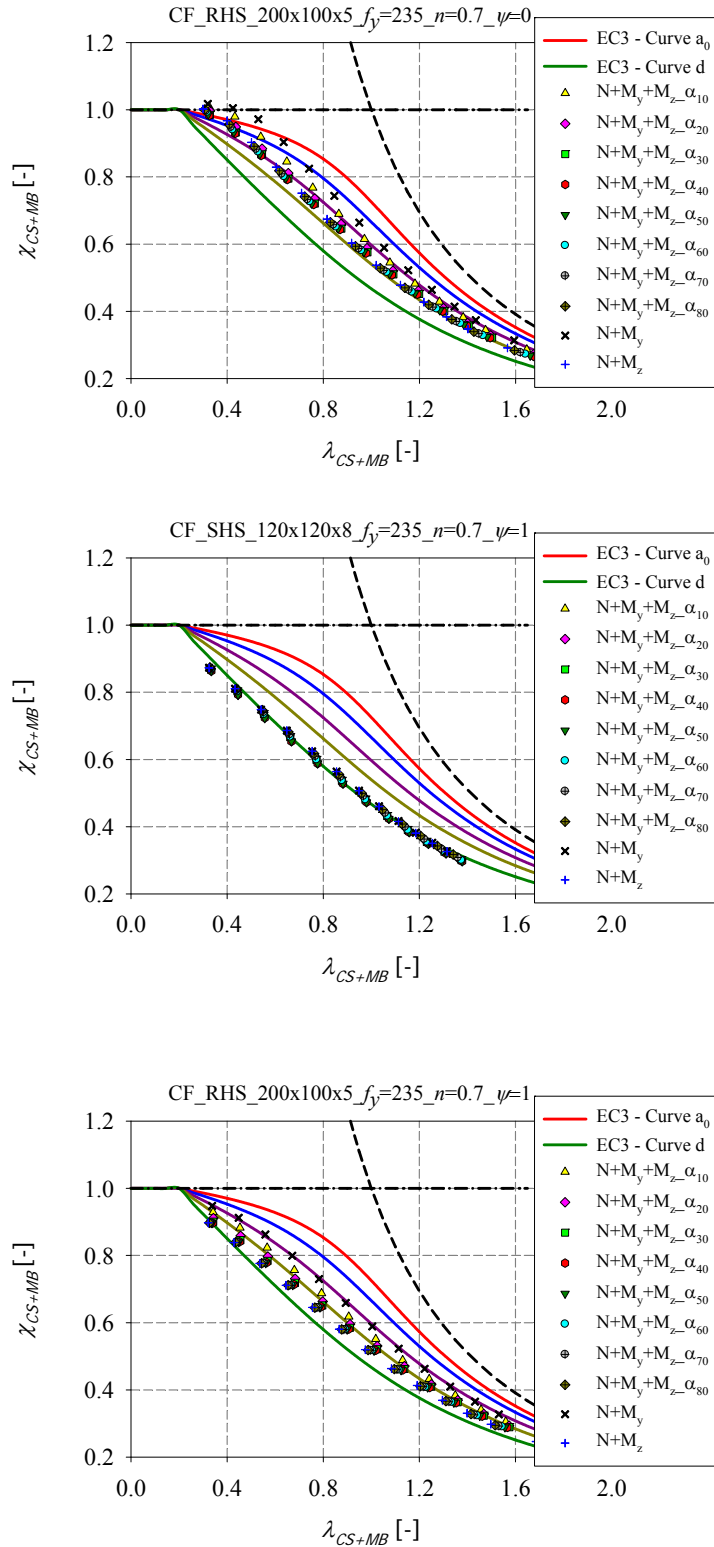


Figure 179 – Numerical results for members under different load cases by varying the degrees of biaxial bending

5.5. Conclusions

This chapter presented and discussed numerical results on cold-formed square and rectangular members. The main objective was to investigate beam-column's resistance tested under different loading combinations with the use of the calibrated model.

The numerical specimens were chosen in a way to cover all cross-sections classes; they were relative to different steel grades, different element lengths... Appropriate material laws for cold-formed tubes were determined through the collection of existing tensile test from literature and by fitting the Ramberg-Osgood analytical curves to the experimental ones in order to get the most appropriate R.O.-coefficients. On the basis of these results, coupled with the experimental observations, a value of the exponent $n = 21$ was adopted to launch the parametric study on cold-formed tubes of normal steel grades, and $n = 40$ was adopted for cold-formed tubes of high steel grades.

Results were computed by means of shell analyses in order to investigate the influence of local and global buckling on the member's behaviour and were plotted in O.I.C. format that was shown to be suitable to characterize the behaviour and response of steel hollow section beam-columns.

In addition, key parameters such as the bending moment distribution, axial force ratio, degree of biaxial bending and steel grade were identified.

The numerical parametric study on cold-formed hollow section elements exposed in the present chapter will complement the one performed on hot-rolled members. These data will serve as a set of reference results to derive accurate and continuous interaction curves along the slenderness range, by considering all the identified governing parameters.

6. O.I.C. – based design proposal

6.1. Introduction

This chapter presents the development of a design proposal for hollow sections; more precisely, it focuses on the derivation of interaction curves for the design of hot-rolled and cold-formed steel beam-column members.

In a first part (section 6.2), the assumptions accounted for to derive the proposed design curves of hot-rolled and cold-formed members are described and detailed. Section 6.3 then presents and illustrates in an O.I.C. format the experimental buckling strengths of the 12 tests performed at the Structural Engineering Laboratory of the University Of Applied Sciences Of Western Switzerland – Fribourg. These tests were complemented with extensive experimental data collected from the literature. The data comprised various load cases, fabrication processes, yield strengths, cross-section shapes, elements' lengths... The collected experimental results were used herein and presented along with the extensive numerical computed results. These data subsequently serves as a set of reference results for the derivation of adequate interaction curves, needed for the practical prediction of beam-column resistance, where both local and global instabilities play a significant role. Then, section 6.4 proposes a practical design model and the related interaction curves for hot-rolled and cold-formed square and rectangular hollow members. With the adoption of the Ayrton-Perry extended format, locally-fitted factors were defined; the proposed design curves for simple load cases are presented, followed by proposed design curves relative to combined load cases²¹. Section 6.5 illustrates the accuracy of the proposed design formulae. Statistical results of the comparison between F.E., Eurocode 3 and proposal calculations are presented. Section 6.6 gives a summary of the proposed design formulae and recommendations for practical design. Section 6.7 then proposes a simplified alternative to the complete design model suggested and section 6.8 proposes worked examples of the newly-developed O.I.C. design approach. Eventually, summary and conclusions are addressed in section 6.9.

²¹ One model was finally proposed, which can be re-formatted to a more simple expression for simple load cases. Special attention has been given so that the proposed formulae exhibit no discontinuities. Consequently, continuity was provided between the proposed curves for simple and combined load cases, for different cross-section shapes, different element lengths, different bending moment distributions...

6.2. Influence of strain-hardening on a beam-column member

Figure 180 presents examples of experimental material stress-strain curves and stub-strain responses, compared to numerical results of member tested under pure compression. The goal is to study the influence of the strain-hardening on a beam-column member. Thus, in order to provide accurate representations in terms of deviation from the stress-strain curves and stub responses, the beam-column tests were modeled numerically under pure compression, since the numerical simulations can represent the real behaviour of such members and may safely be substituted to physical testing.

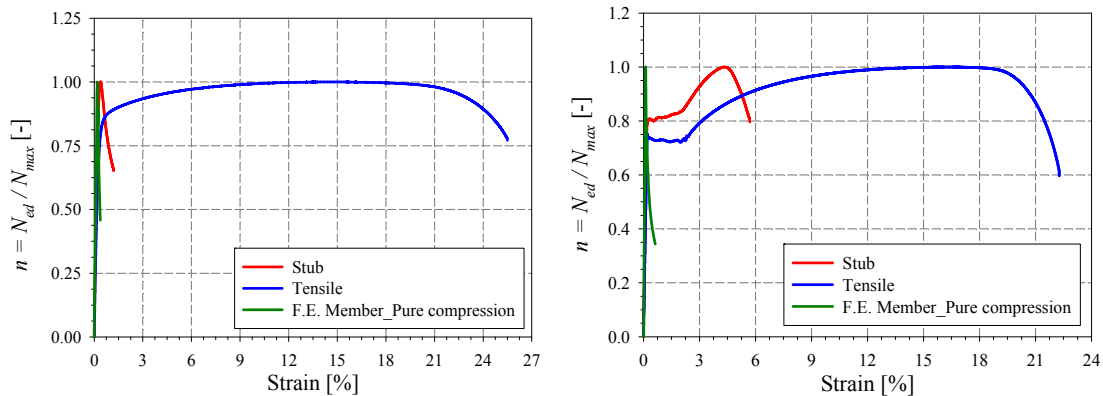


Figure 180 – Comparison of tensile, stub and member tests under pure compression for specimens – a) RHS CF 220x120x6 T4 – b) CHS HR 159x6.3 T10

The curves correspond to the specimens RHS CF 220x120x6 T4 and CHS HR 159x6.3 T10 respectively, where $n = N_{Ed} / N_{max}$. Zoomed graphs for small strains are presented in Figure 181.

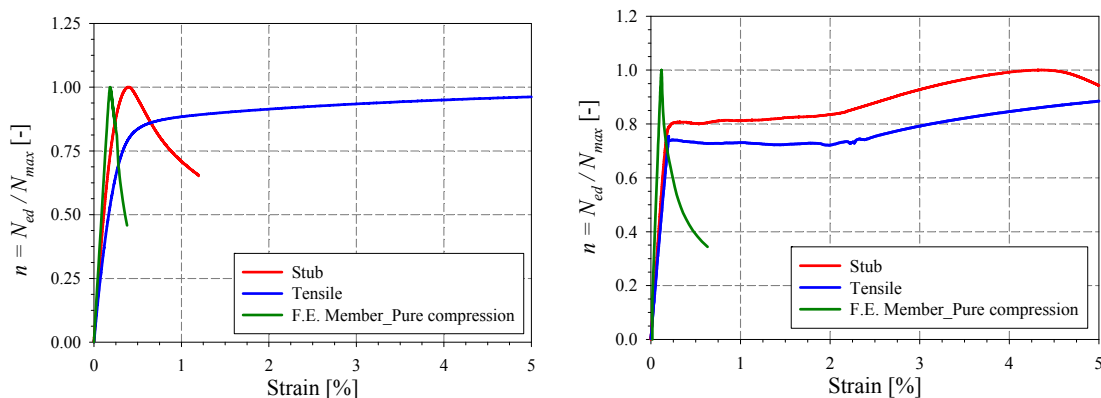


Figure 181 – Zoomed graphs for small strains for specimens – a) RHS CF 220x120x6 T4 – b) CHS HR 159x6.3 T10

The deviations of the curves are due to geometrical imperfections, the mode of failure of the element (i.e. local buckling for the case of stub column tests and local-global interaction for

the case of beam-columns tests), residual stresses, post-buckling response and inelastic material behaviour.

The values of the fracture elongations ϵ_{max} were determined from the stress-strain, stub column and buckling test curves, under pure compression and presented in Table 37, along with the $\epsilon_{max} / \epsilon_y$ ratio, where ϵ_y represents the material yield strain.

Table 37 – Values of the fracture elongations ϵ_{max} determined from the stress-strain, stub column and buckling tests curves

Test	RHS_S355_CF_220x120x6		CHS_S355_HR_159x6.3	
	ϵ_{max} [%]	$\epsilon_{max} / \epsilon_y$ [-]	ϵ_{max} [%]	$\epsilon_{max} / \epsilon_y$ [-]
Tensile	25.50	104.09	22.27	111.89
Stub	1.20	4.89	5.69	28.61
Member	0.38	1.55	0.63	3.17

The following conclusions can be drawn from this table:

- the ratio $\epsilon_{max} / \epsilon_y$ naturally reaches its maximum value for both hot-rolled and cold-formed sections for the case of tensile tests coupons ($\epsilon_{max} / \epsilon_y > 110$). The corresponding structural materials go from the elastic state to their fully plastic one and all the fibers enter the strain-hardening stage under an increasing of load: yielding first occurs when the loading reaches the yield stress, followed by the strain-hardening stage until an ultimate stress f_u is reached (see Figure 182);

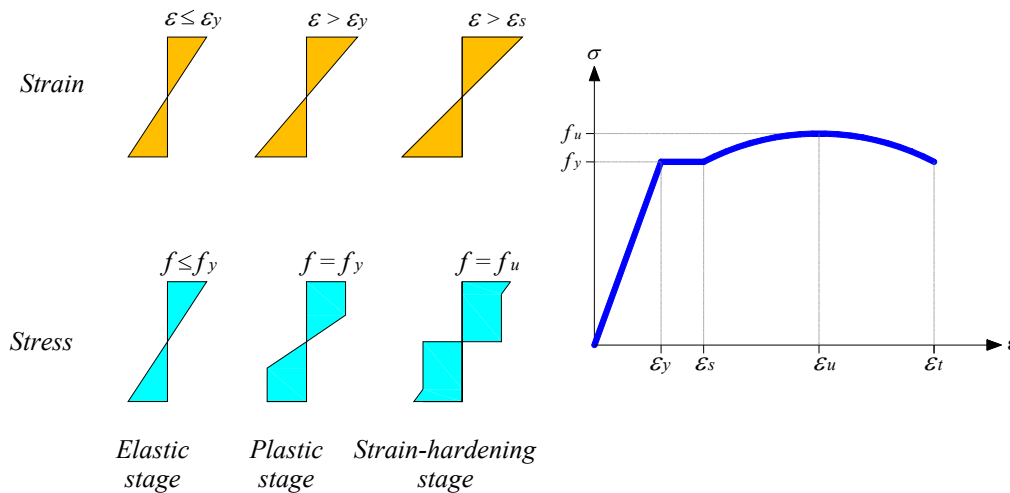


Figure 182 – Stress-strain behaviour of corresponding coupon fibers

- the ratio $\varepsilon_{\max} / \varepsilon_y$ reaches smaller values for the case of the stub column tests ($\varepsilon_{\max} / \varepsilon_y < 30$) compared to the values obtained from the material stress-strain curves. In this case, a smaller percentage of fibers reach the strain hardening stage (where $f_y \leq f \leq f_u$) as illustrated in Figure 183. This is mostly due to the presence of residual stresses in the cross-section implying that some fibers are in a state of residual compression reaching the first the yield limit under load. Residual stresses are thus a major factor affecting the strength of axially loaded columns. Stub columns fails by local buckling either prior to or subsequent to the onset of yielding. For stocky cases, deviation from the material curve occurs approximately at ultimate load where there is the onset of local buckling. For the slender cases, local buckling occurs in the elastic range, and deviation from the stress-strain curve may be followed by considerable post-buckling deformation. Deviations for the material stress-strain are obviously also due to other several effects including geometric imperfections, inelastic material behaviour...;

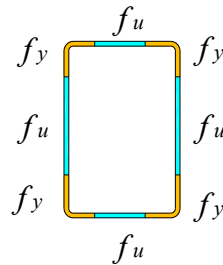


Figure 183 – Fibers reaching the strain-hardening stage for a “cross-section” case

- the ratio $\varepsilon_{\max} / \varepsilon_y$ reaches the smallest values for the case of beam-column tests, ($\varepsilon_{\max} / \varepsilon_y < 5$). Columns typically fail by global buckling in the inelastic or elastic range, and the fibers can hardly reach the strain hardening effects.

Figure 184 and Figure 185 illustrate examples of yield patterns at failure obtained numerically for a hot-rolled section RHS 220x120x10 of nominal yield stress $f_y = 235 \text{ N/mm}^2$ and ultimate stress $f_u = 360 \text{ N/mm}^2$. The section was tested under compression and constant / triangular bending moment distribution ($N+M_y$) with a level of compression $n = 0.3$ (i.e. $n = N_{Ed} / N_{b,Rd}$).

Figure 184 illustrates the cross-section results and Figure 185 presents the results obtained for a member of 4000 mm length.

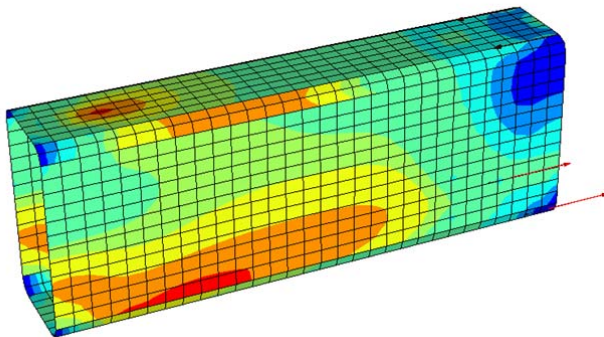
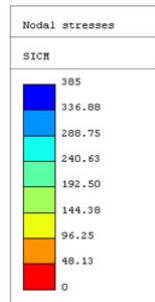
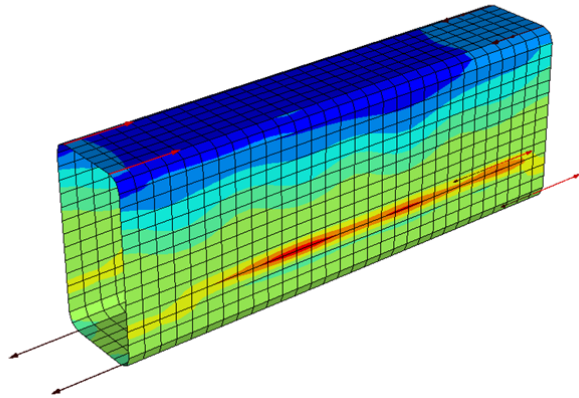
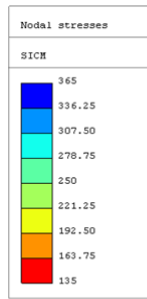
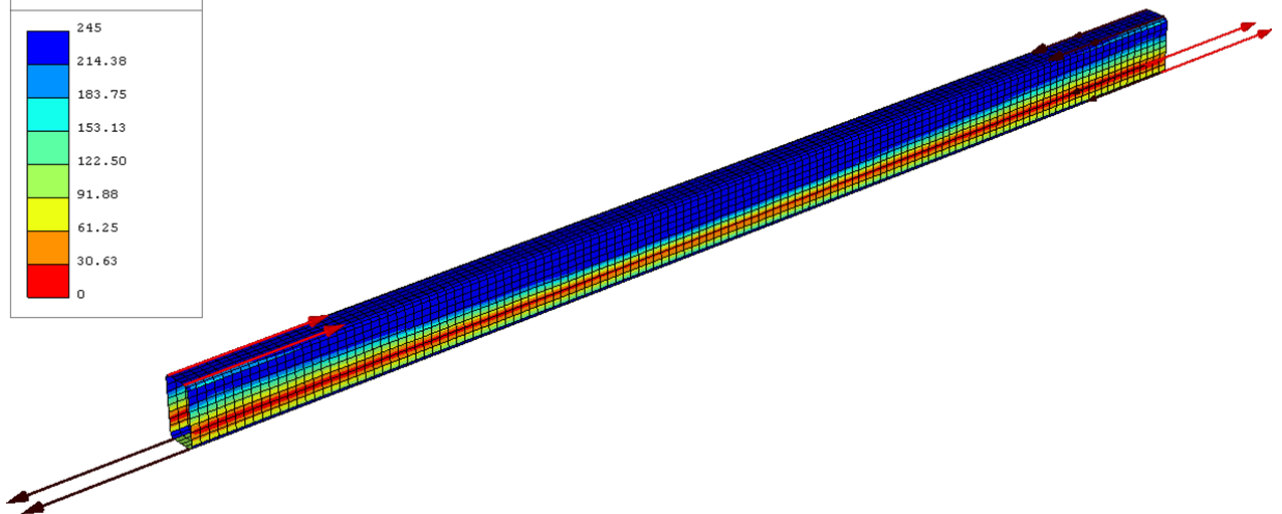
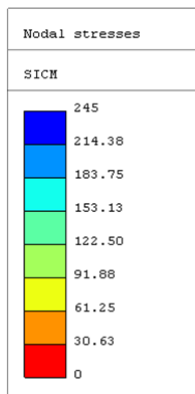


Figure 184 – Von Mises stresses at failure for the case of RHS 220x120x10 cross-section tested under compression and – a) constant bending moment distribution – b) triangular bending moment distribution



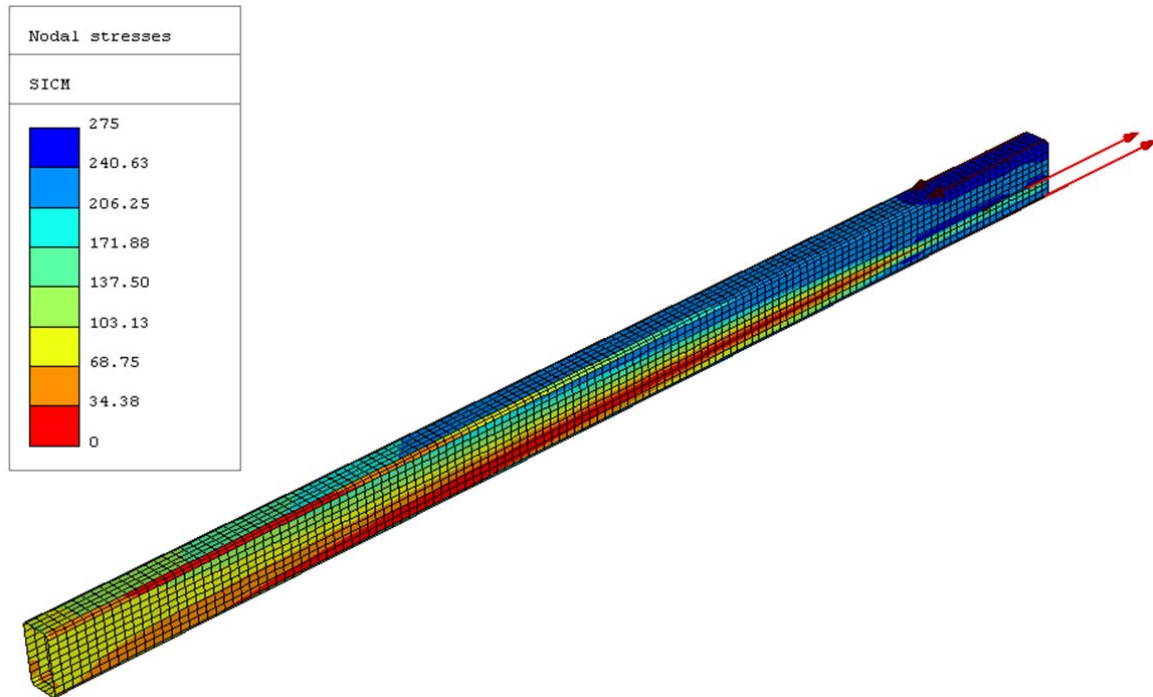


Figure 185 – Von Mises stresses at failure for the case of RHS 220x120x10 member tested under compression and – a) constant bending moment distribution – b) triangular bending moment distribution

The following conclusions can be drawn from the figures:

- the cross-sections reach higher values of stresses and can benefit more easily from strain-hardening effects (i.e. $f \geq f_y$) compared to members tested under the same load cases;
- the maximum values of Von Mises stresses are reached along all the fibers of the upper flange when the section is loaded under compression and constant bending moment distribution; and mainly on the loaded extremity of the beam-column when tested under compression and triangular bending moment distribution. The Von Mises stresses then decrease along the member length. Thus, a part of the section is less loaded in bending and provides a level of elastic restraint to the entire member.

Accordingly, the following assumptions were accounted for in the forthcoming proposed design curves:

- for the case of hot-rolled and cold-formed members, the resistance limit of the cross-sections was kept to $\chi_{CS} = 1$, since, as explained previously, the level of deformation for the case of beam-column reaches very low overall “member” strain level

($\varepsilon_{\max} / \varepsilon_y < 5$). Columns fail by global buckling in the inelastic and elastic range, and the fibers can hardly reach the strain hardening effects;

- for the case of hot-rolled and cold-formed members tested under compression and under compression with a constant bending moment distribution, the strain-hardening of the member reserve was not accounted for in the proposed design curves of the members and the resistance limit was kept to $\chi_{CS+MB} = 1$. The results in which the peak loads are in excess of the traditional plastic capacities due to strain-hardening were deemed unrealistic and were therefore disregarded;
- for the case of hot-rolled and cold-formed members subjected to a triangular bending moment distribution, strain hardening can be accounted for (i.e. $\chi_{CS+MB} > 1$) since the bending moment reaches its highest value on the extremity of the beam-column and decreases along the member length. The less loaded parts of the beam provide a level of restraint to the entire member. However, in the following the strain hardening effect was disregarded for sake of simplicity and because the extra strength provided by strain hardening does not exceed 10% of the member total resistance. Figure 186 represents the particular case of hot-rolled RHS tested under compression and triangular bending moment where $n = N_{Ed} / N_{b,Rd} = 0.3$. The ideal resistance limit was modified to allow for a potential 10% of strain-hardening. One may notice that obtained numerical results can hardly reach the defined limit specially for low values of generalized relative slenderness λ_{CS+MB} .

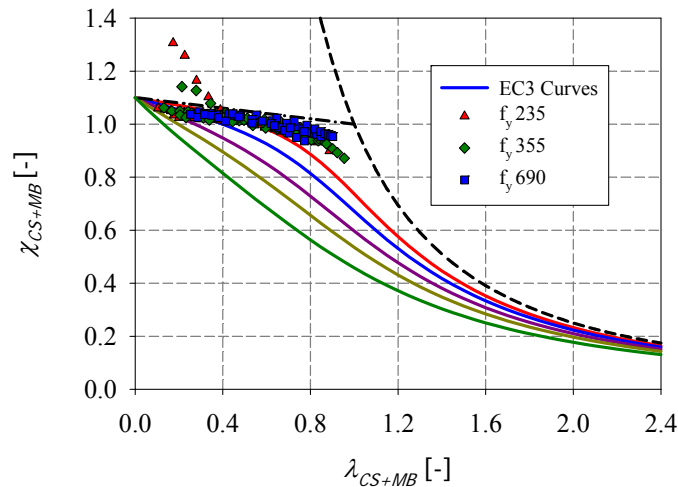


Figure 186 – Allowance of 10% strain-hardening for the particular case of hot-rolled RHS tested under compression and triangular bending moment where $n = N_{Ed} / N_{b,Rd} = 0.3$

6.3. Additional tests collected from literature

6.3.1. Characterization by means of the O.I.C.

An extensive experimental data set was found in many sources and gathered. Around 802 test results for members were collected from Grimault [29], Rondal [10], Greiner [4], Yeomans [74], Guiaux [75], Salvarinas [76], Braham [77], Sedlacek [78], Kuhn [79] and Pavlovic [80]²². The experimental beam-column tests conducted in the present work were also considered. This experimental database comprises different element lengths tested under simple and combined loading with different shapes of bending moment distribution along the member, and hollow sections covering all section classes (i.e. from stocky to slender).

All collected data along with the corresponding references can be found in Annex 1; the shape, fabrication process, number of tests, load cases and measured yield strengths are also provided.

6.3.2. Use of O.I.C. plotting – Analyses and conclusions

All collected test results, previously stated in section 6.3.1, are presented in the O.I.C. format in Figure 187 to Figure 193, where the horizontal axis relates to the generalized member slenderness λ_{CS+MB} while the vertical axis reports on the member reduction factor χ_{CS+MB} as presented in Equation (180) and Equation (181).

$$\bar{\lambda}_{CS+MB} = \sqrt{\frac{\chi_{CS} \cdot R_{RESIST}}{R_{STAB,MB}}} \quad (180)$$

$$\chi_{CS+MB} = \frac{R_{TEST}}{\chi_{CS} \cdot R_{RESIST}} \quad (181)$$

R_{RESIST} represents the load ratio to reach the resistance limit, $R_{STAB,MB}$ represents the load ratio to reach the instability limit, R_{TEST} is the ultimate load multiplier calculated from experimental peak loads and χ_{CS} represents the cross-section reduction factor deduced from the real behaviour. In all subsequent results, χ_{CS} values have been evaluated numerically (suitable

²² It shall perhaps be mentioned here that the data extracted from Braham consisted in cold-formed rectangular hollow sections for which an annealing process was performed for some of these sections.

shell non-linear F.E. simulations) so as to provide a fair estimation of the influence of local buckling on the members' overall responses.

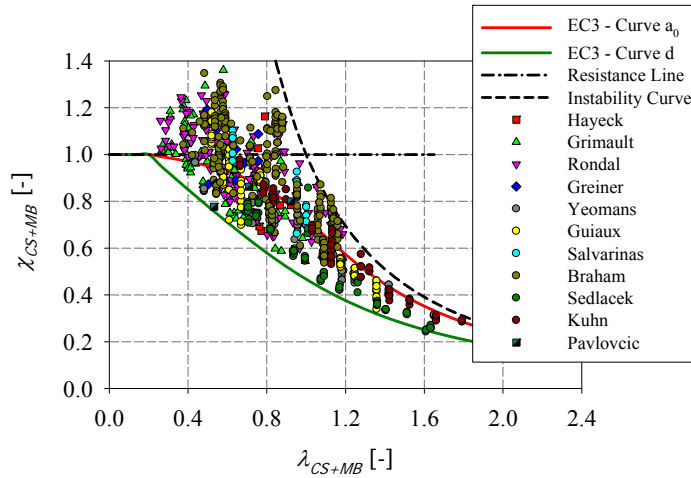


Figure 187: Collected test results and comparison with Eurocode buckling curves

Figure 187 displays all results obtained for the various tests gathered. The large scatter noticed is explained by different loading conditions, section shapes and slenderness, steel grades, production routes, member slenderness... Also, the scatter can be seen to cover the complete range between Eurocode 3 buckling curves a_0 and d and even well outside, reflecting the complex behaviour and response of beam-columns.

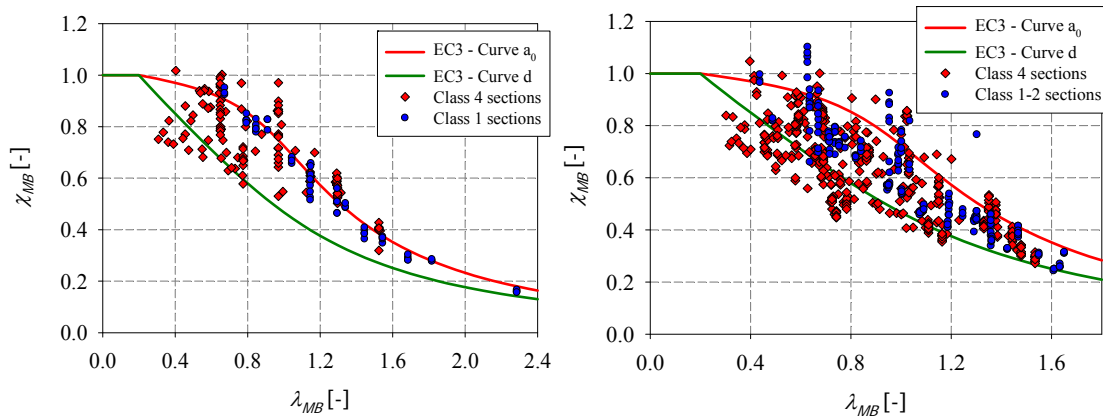


Figure 188: Experimental results relative to section classes obtained by omitting χ_{CS} for – a) hot-rolled SHS and RHS – b) cold-formed SHS and RHS

The influence of the cross-section resistance on the member response is highlighted in Figure 188, where the cross-section instabilities were omitted and not deduced from the overall behaviour, unlike in the general flowchart of the O.I.C. The horizontal axis represents

the generalized slenderness λ_{MB} while the vertical axis reports the reduction factor χ_{MB} defined in Equation (182) and Equation (183) respectively.

$$\lambda_{MB} = \sqrt{\frac{R_{RESIST}}{R_{STAB,MB}}} \quad (182)$$

$$\chi_{MB} = \frac{R_{REAL}}{R_{RESIST}} \quad (183)$$

Test results are then seen to correspond to SHS and RHS sections with cross-sectional classes well-distributed along class 1 (plastic) and class 4 (slender). Obviously, stocky sections (i.e. class 1 sections) exhibit a higher resistance than slender ones exhibiting an important influence of local buckling (i.e. class 4 sections). It is clearly seen that the influence of the section sensitivity to local buckling is important for low values of member relative slenderness λ_{MB} where different values of resistance are reached: plastic, elastic or effective depending on cross-section classification. The vertical scatter observed can be shown to be mostly due to different section classes. For low values of the member (“MB”) relative slenderness ($\lambda_{MB} < 0.8$), the failure of the elements typically is in large parts driven by cross-sectional resistance, so that the omission of $\chi_{CS} < 1.0$ factors in Equation (180) explains χ_{MB} values below Eurocode 3 curve *d*. For higher values of relative slenderness ($0.8 < \lambda_{MB} < 1.6$), the elements fail in inelastic to elastic flexural buckling. Both local (i.e. cross-section instabilities) and global (i.e. member instabilities) buckling modes are likely to occur and interact (so-called coupled instabilities); the vertical scatter is reduced accordingly. For higher values of relative slenderness, elastic global buckling becomes solely determinant, regardless of the section slenderness and local buckling that may occur. The vertical scatter is seen to be more reduced in this case.

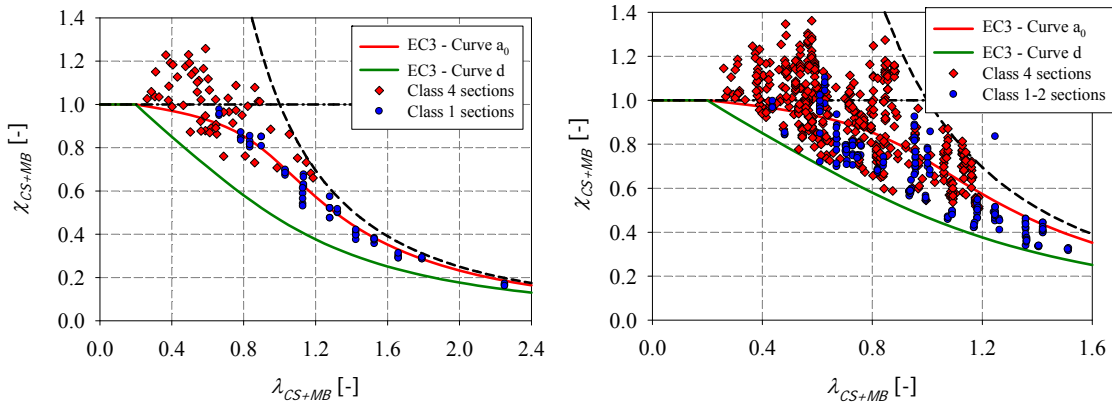


Figure 189: Experimental results relative to section classes obtained by considering χ_{CS} for – a) hot-rolled SHS and RHS – b) cold-formed SHS and RHS

Figure 189 presents results obtained for SHS and RHS sections by deducing the cross-section instabilities from the overall behaviour. As expected, the resistance of slender sections, exhibiting an important influence of local buckling, is enhanced when considering the effect of the cross-section instabilities, especially for low values of the relative slenderness.

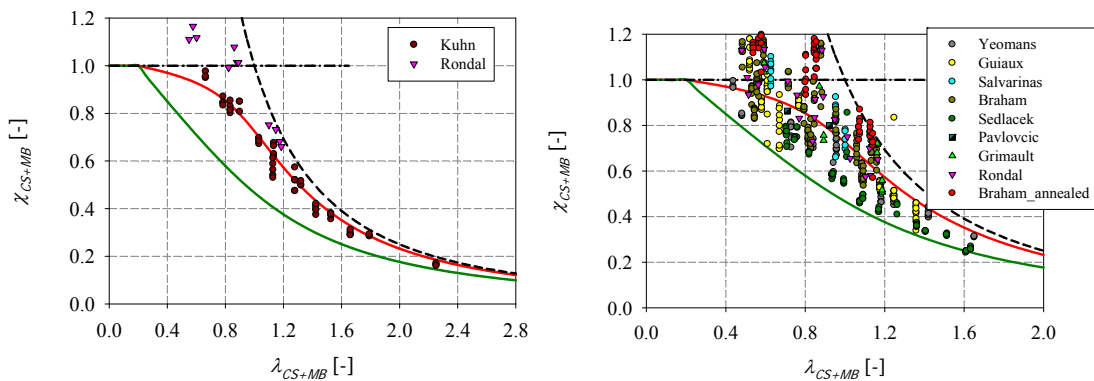


Figure 190: Experimental results relative to pure compression load cases – a) hot-rolled SHS and RHS – b) cold-formed SHS and RHS

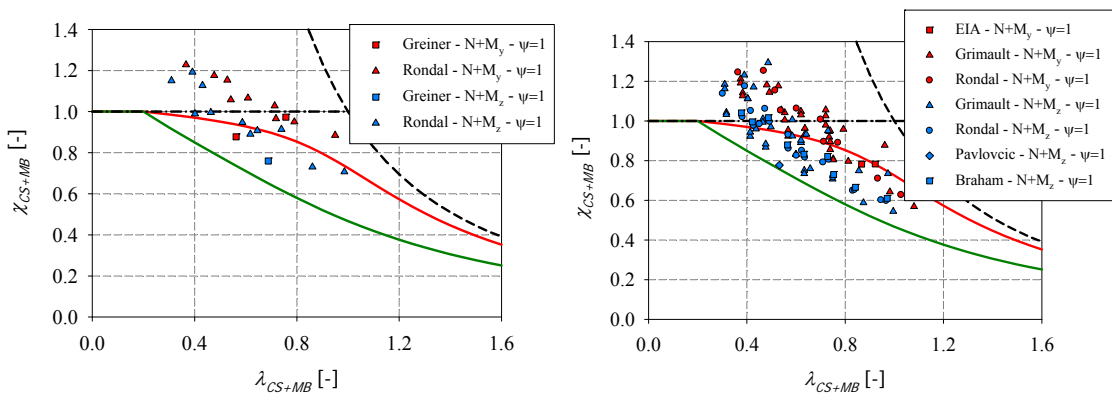


Figure 191: Experimental results relative to compression with mono-axial bending load cases for – a) hot-rolled SHS and RHS – b) cold-formed SHS and RHS

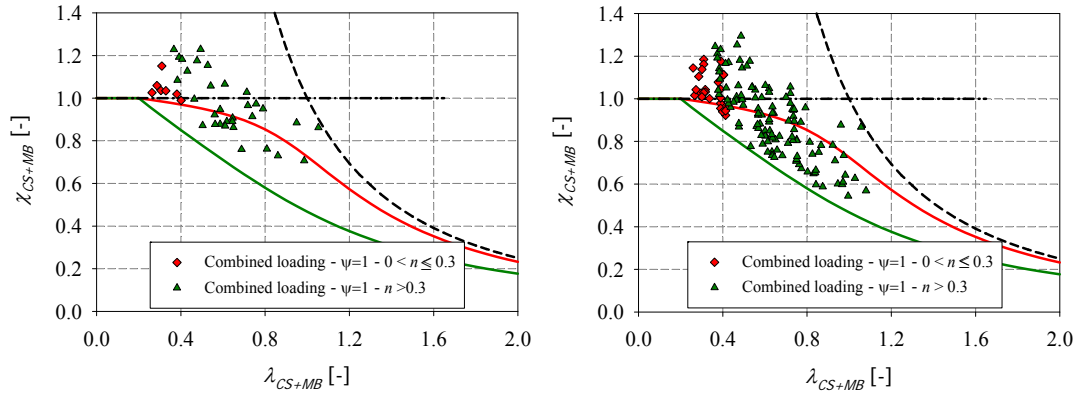


Figure 192: Experimental results under combined loading for – a) hot-rolled SHS and RHS – b) cold-formed SHS and RHS

Figure 190 and Figure 191 first filter results for pure compression and for compression with mono-axial bending load cases, respectively. For each load case, cold-formed test results were separated from hot-rolled test results. One may notice that hot-rolled sections systematically exhibit higher resistance than cold-formed ones, no matter the load case considered; this can be attributed to the material law relative to each production route and their associated material imperfections (higher influence of residual stresses for cold-formed sections). Consequently, higher interaction curves should be derived when considering buckling curves for hot-rolled hollow sections – this is typically accounted for in Eurocode 3 through higher column buckling curves for hot-rolled tubes. Moreover, results for hollow sections under compression with mono-axial bending with a constant bending moment distribution show that these members are less affected by instability under compression and major-axis moment ($N + M_y$) than under compression and minor-axis moment ($N + M_z$), as should be expected since (predominant) weak axis flexural buckling cumulates with weak axis bending.

Figure 192 highlights the influence of the axial force level n defined as $n = N_{Ed} / N_{b,Rd} = (N_{Ed} / \chi N_{pl,Rd} \text{ or } N_{Ed} / \chi N_{eff,Rd})^{23}$. A careful analysis of the results indicates that the factor n influences as well the member resistance and should be considered too as leading parameter for the derivation of appropriate interaction curves. It is clearly shown that for a high level of compression ($n > 0.3$), global buckling becomes determinant, leading to

²³ Note that $N_{b,Rd}$, N_{pl} and N_{eff} represent respectively the buckling, plastic and effective resistance of the member; χ and γ_{M1} represent respectively the flexural buckling reduction factor and the partial factors for resistance of members to instability ($\gamma_{M1} = 1.0$ assumed here), so as to remain focused on accuracy without any “interference” of safety / reliability effects.

more scattered results ($\lambda_{CS+MB} > 0.6$). Global buckling stemming from the high level of compression occurs before cross-section full yielding, resulting in the failure of the element owing to instability and not because of a lack of cross-sectional resistance. However, for a lower level of compression ($n \leq 0.3$), the results are closer and reach lower values of the generalized relative slenderness λ_{CS+MB} . In the latter cases, bending is predominant.

$$\Omega_{y/z} = \arctan\left(\frac{m_z}{m_y}\right) = \arctan\left(\frac{M_z / M_{pl,z}}{M_y / M_{pl,y}}\right) \quad (184)$$

The degree of biaxiality $\Omega_{y/z}$ (see Equation (184) – where $M_{pl,y}$, $M_{pl,z}$ are the plastic cross-section resistances and M_y , M_z are the ultimate bending moments about strong and weak axis respectively) plays as well a significant role and further studies are presented in the following paragraphs (see section 6.4) to sort the results accordingly.

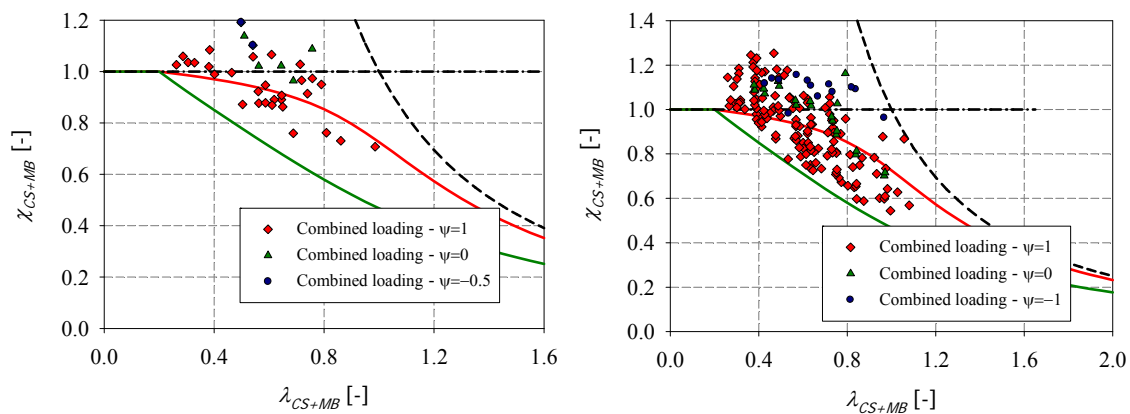


Figure 193: Experimental results under combined loading for – a) hot-rolled SHS and RHS – b) cold-formed SHS and RHS

Figure 193 illustrates the application of the O.I.C. under different (linear) bending moment distributions, represented by the ψ factor (i.e. which stands as the ratio between applied end moments: $\psi = 1$ indicates constant bending moment distribution, $\psi = 0$ triangular distribution, and $\psi = -1$ or $\psi = -0.5$ a bi-triangular pattern). All results are relative to beam-column members tested under combined loading situations (either compression with mono-axial bending or compression with bi-axial bending). Again, it is obvious that the bending moment distribution is a leading parameter influencing the resistance; no matter the load cases, one may obviously notice that members subjected to a triangular bending distribution exhibit a higher resistance than member subjected to a constant moment distribution.

All these results evidence the ability of the O.I.C. direct approach to capture the behaviour of beam-columns in a straightforward manner, i.e. without resorting to section or member interaction formulae actually used in current design codes, nor to the calculation of effective properties. All types of experimental results presented with the various load cases also clearly show the potential for accurate and safe $\chi = f(\lambda)$ equations to be derived; such developments are presently being presented within the present chapter.

6.3.3. Gathered experimental data vs. F.E. results

Following the present experimental series, extensive numerical investigations were addressed, with the intention of derivation of adequate interaction curves needed for the practical application to beam-column resistance. The collected experimental results were used herein and presented with the numerical computed results. The goal is here to confirm the adequacy and correct tendencies of the numerical results. Figure 194 shows the experimental and numerical results of cold-formed and hot-rolled beam-columns subjected to compression. Figure 195 presents the numerical and experimental tests of only cold-formed members subjected to compression and triangular minor-axis bending ($N+M_z$) since the number of hot-rolled members was seen to be insufficient to be represented fairly. Finally, Figure 196 to Figure 198 represent the cold-formed and hot-rolled results relative to experimental and numerical beam-column tests subjected to combined load cases: compression with constant major-axis bending, compression with constant minor-axis bending and compression with constant biaxial bending, respectively.

Based on these figures, it can be stated that:

- in all figures, a reasonably correct alignment of the experimental results with the numerical ones is observed;
- numerical results are showing conservative tendencies especially for cold-formed members subjected to compression with triangular minor-axis bending moment (see Figure 195). In other words, numerical computed results are showing a quite safe-sided lower bound compared to experimental results, especially for the mentioned case. Even though, general imperfections introduced in numerical computations were conservative, many experimental results would fall within the studied numerical test range, indicating that reasonably appropriate adopted imperfections was made;

- for combined load cases, results were represented in a general way, i.e. no distinction has been made according to the degree of biaxiality, the axial force ratio... A more detailed analysis will be made in the following sections to separate the various combined load cases. However, the one thing that could be stated based on the figures below is that experimental results are lying within the numerical computed range and are following the same tendencies.

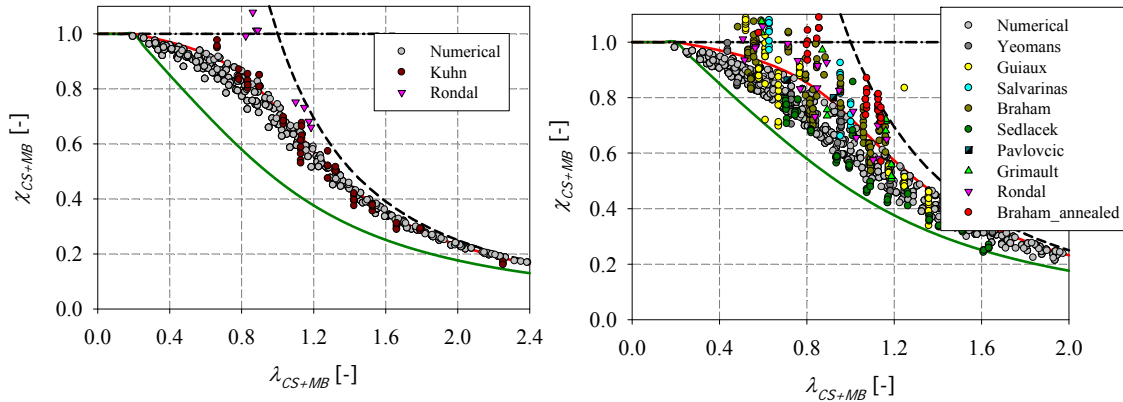


Figure 194: Experimental and numerical test results relative to pure compression load cases for – a) hot-rolled sections – b) cold-formed sections

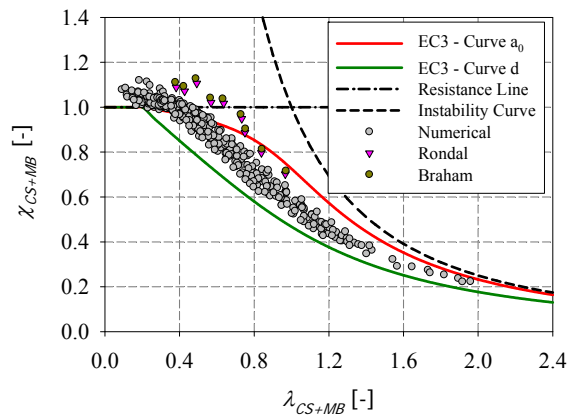


Figure 195: Experimental and numerical test results relative to cold-formed sections tested under compression and triangular bending moment $N+M_z$

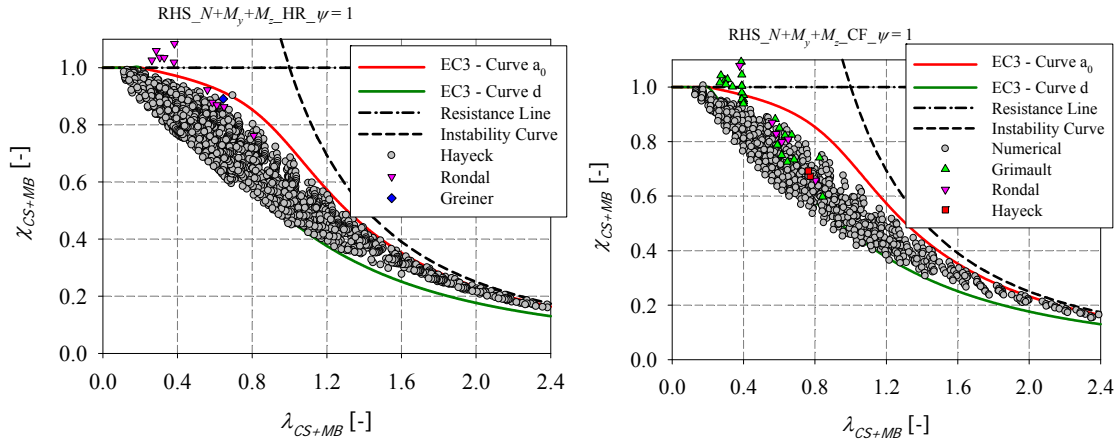


Figure 196: Experimental and numerical test results relative to members subjected to compression and constant biaxial bending moment ($N+M_y+M_z$) for– a) hot-rolled sections – b) cold-formed sections

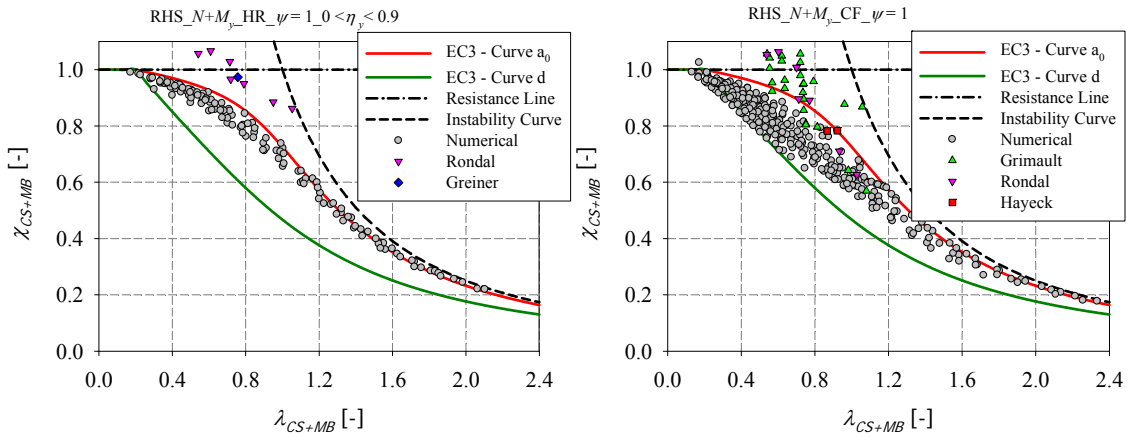


Figure 197: Experimental and numerical test results relative to members subjected to compression and constant major-axis bending moment ($N+M_y$) for– a) hot-rolled sections – b) cold-formed sections

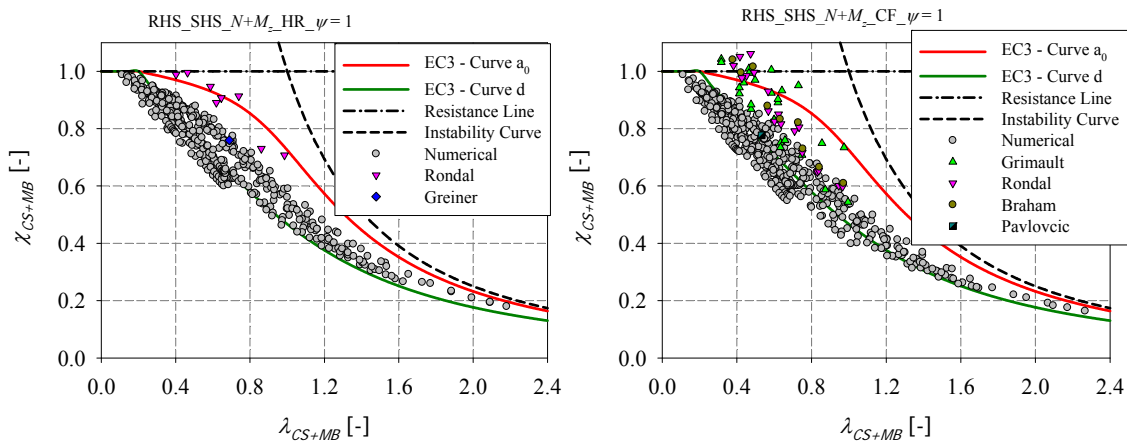


Figure 198: Experimental and numerical test results relative to members subjected to compression and constant minor-axis bending moment ($N+M_z$) for– a) hot-rolled sections – b) cold-formed sections

6.4. Proposal of design “interaction” curves – parametric studies

With the adoption the Ayrton-Perry format detailed in Equation (185), fitted factors were defined based on the numerical results.

In total, more than 70 thousand non-linear G.M.N.I.A. F.E. computations have been performed for tubular members. In order to get the R_{REAL} factors, 8 500 non-linear F.E. computations for members were obtained by using beam models; 31 200 shell calculations for members were performed as well as 31 200 shell calculations for cross-sections. In addition, 31 200 simulations were performed to get $R_{STAB,CS}$; another 31 200 were performed to get $R_{STAB,MB}$ and 31 200 to get R_{RESIST} .

All the reference F.E. results were analysed and sorted to identify the key parameters to be kept for the derivation of design curves.

The following factors defined below were locally determined through a best-fit procedure for simple and combined loading, for hot-rolled and cold-formed sections:

- the end of plateau λ_0 value;
- the imperfection factor α .

$$\chi_{CS+MB} = \frac{1}{\phi_{CS+MB} + \sqrt{\phi_{CS+MB}^2 - \lambda_{CS+MB}^2}} \quad (185)$$

$$\text{where } \phi_{CS+MB} = 0.5(1 + \alpha(\lambda_{CS+MB} - \lambda_0) + \lambda_{CS+MB}^2) \quad (186)$$

The following sections detail the design curves proposed for the practical design of tubular members.

6.4.1. Simple case of pure compression

6.4.1.1. Hot-rolled sections

Figure 199 and Figure 200 illustrate the application of the O.I.C. for hot-rolled square and rectangular sections under pure compression, for different steel grades: $f_y = 235 \text{ N/mm}^2$, $f_y = 355 \text{ N/mm}^2$ and $f_y = 690 \text{ N/mm}^2$. The results are obtained by using both shell and beam models and by adopting sections with the corresponding cross-sectional classes well-

distributed along class 1 and class 4 owing to a strong local-global buckling coupling. Results for very slender sections, of nominal yield stress $f_y = 690 \text{ N/mm}^2$ are excluded from Figure 200, and are treated separately in section 6.4.1.3.

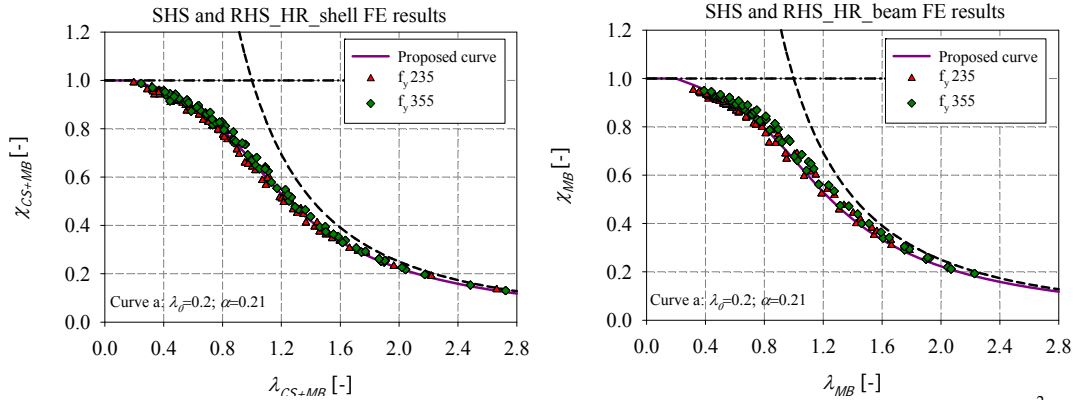


Figure 199 – Numerical member results of hot-rolled SHS and RHS of steel grades $f_y = 235 \text{ N/mm}^2$ and $f_y = 355 \text{ N/mm}^2$, tested under N – a) shell results – b) beam results

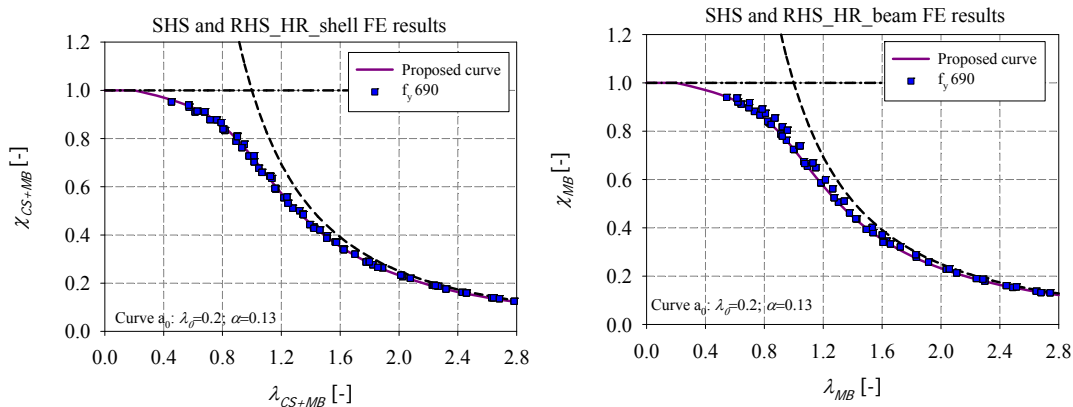


Figure 200 – Numerical member results of hot-rolled SHS and RHS of steel grade $f_y = 690 \text{ N/mm}^2$ tested under N – a) shell results – b) beam results

Close tendencies of member results computed using beam and shell models are observed. For sake of simplicity, a single interaction curve was derived for $f_y = 235 \text{ N/mm}^2$ and $f_y = 355 \text{ N/mm}^2$, since a small dispersion in the results is noticed. The imperfection factor α and the end of plateau factor λ_0 corresponding to the buckling *Curve a* defined by Eurocode 3, were proposed based on the numerical results: λ_0 was set to 0.2 and α was set to 0.21. One may notice that some numerical results lie below the proposed *Curve a*. This is due to the conservative general imperfections introduced in the numerical models. A higher resistance is observed for $f_y = 690 \text{ N/mm}^2$ and a higher curve is derived. The imperfection factor α and the end of plateau factor λ_0 corresponding to the buckling *Curve a₀* defined by

Eurocode 3, were proposed based on the numerical results: λ_0 was set to 0.2 and α was set to 0.13.

An additional sub study has been undertaken including sections having high values of yield stresses ($f_y = 460 \text{ N/mm}^2$, $f_y = 770 \text{ N/mm}^2$, $f_y = 960 \text{ N/mm}^2$) in an attempt to characterize more precisely the influence of the yield stress on the member resistance. The study covered the following parameters:

- 13 different element lengths varying from 1500 mm to 15000 mm in order to visualize well-distributed results along the relative slenderness axis;
- 3 steel grades: S460, S770, S960;
- 2 cross-section shapes: RHS 220x120x10 and SHS 120x120x8.

Additional calculations were simulated with the same parameters mentioned before with a length equal to three times the height of the section in order to determine the cross-section resistance. The results were added to the full set of numerical calculations for the simple loading cases.

Based on the observations of Figure 201, two curves can be derived for hot-rolled members tested under pure compression depending on the corresponding yield stresses:

- *Curve a* defined by Eurocode 3, for $f_y = 235 \text{ N/mm}^2$, $f_y = 355 \text{ N/mm}^2$ and $f_y = 460 \text{ N/mm}^2$: λ_0 can be set to 0.2 and α to 0.21;
- *Curve a₀* defined by Eurocode 3, for $f_y = 690 \text{ N/mm}^2$, $f_y = 770 \text{ N/mm}^2$ and $f_y = 960 \text{ N/mm}^2$: λ_0 can be set to 0.2 and α to 0.13.

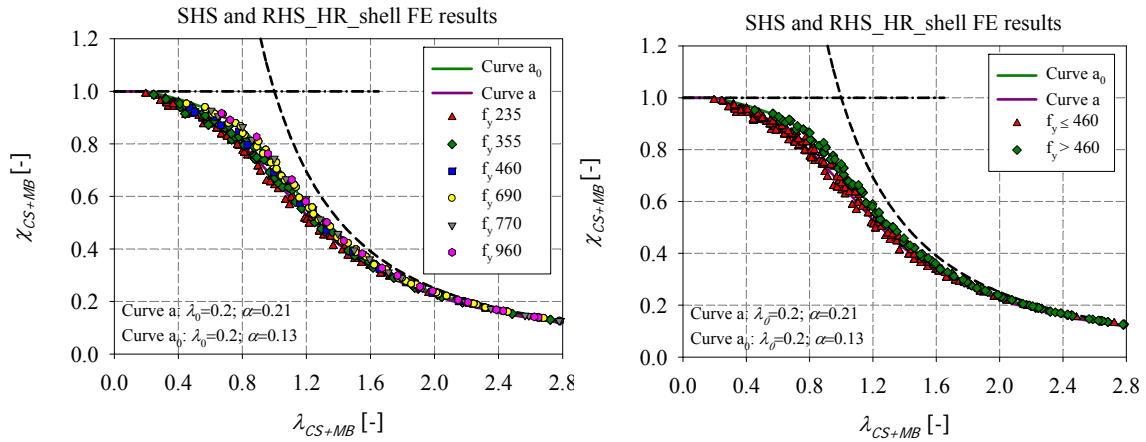
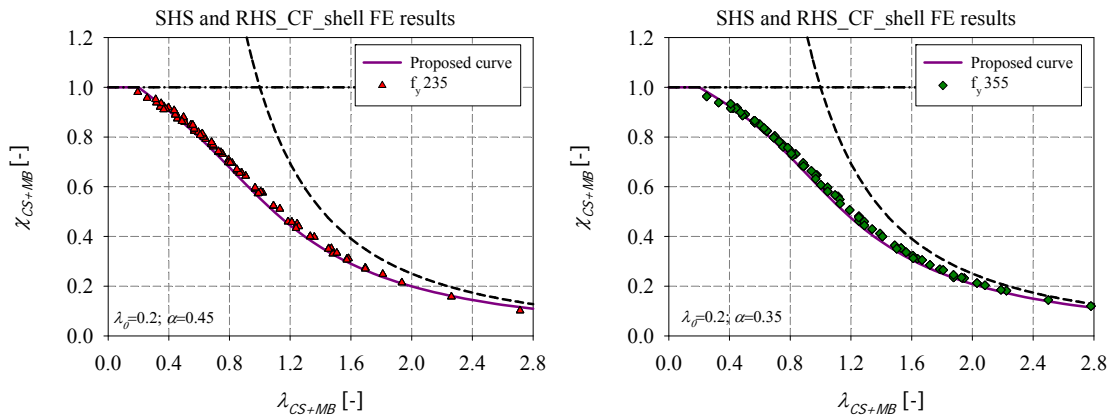


Figure 201 – Additional shell numerical member results of hot-rolled SHS and RHS of different steel grades under compression

6.4.1.2. Cold-formed sections

As for the hot-rolled sections, numerical simulations were performed on rectangular and square cold-formed sections tested under pure compression (see Figure 202). The calculations were obtained by using shell model and by adopting sections of different steel grades ($f_y = 235 \text{ N/mm}^2$, $f_y = 355 \text{ N/mm}^2$, $f_y = 690 \text{ N/mm}^2$) with the corresponding cross-sectional classes well-distributed along class 1 and class 4. Results for very slender sections, of nominal yield stress $f_y = 690 \text{ N/mm}^2$ are excluded and are treated separately in section 6.4.1.3.



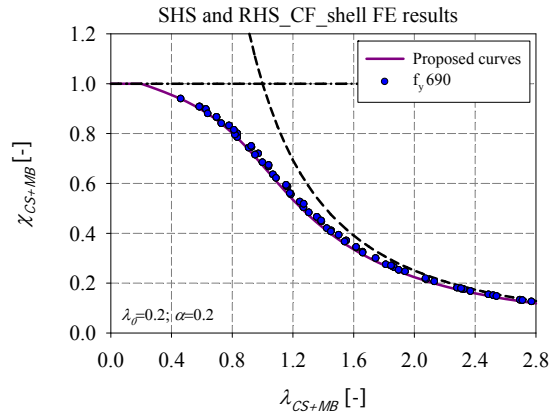


Figure 202 – Shell numerical member results of cold-formed SHS and RHS of different steel grades under compression

An identical sub study undertaken for hot-rolled sections has been performed for cold-formed sections having high values of yield stresses ($f_y = 460 \text{ N/mm}^2$, $f_y = 770 \text{ N/mm}^2$, $f_y = 960 \text{ N/mm}^2$) in an attempt to characterize more precisely the influence of the yield stress on the member resistance. Obtained results are illustrated in Figure 203.

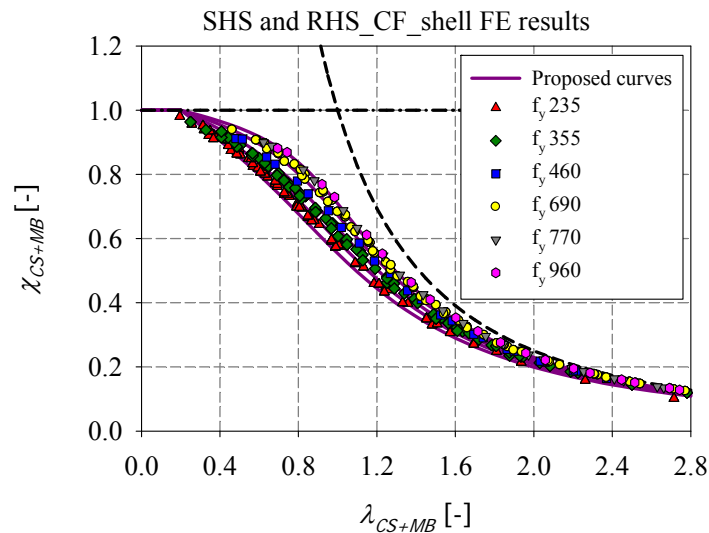


Figure 203 – Additional shell numerical member results of cold-formed SHS and RHS of different steel grades under compression

According to Eurocode 3, buckling *Curve c* is adopted for cold-formed sections of nominal yield stresses: $f_y = 235 \text{ N/mm}^2$, $f_y = 275 \text{ N/mm}^2$, $f_y = 355 \text{ N/mm}^2$, $f_y = 420 \text{ N/mm}^2$ and $f_y = 460 \text{ N/mm}^2$. However, it is clearly seen from the numerical results that an increased yield stress leads to higher design curves. Accordingly, multiple interaction curves were derived for

each cold-formed column depending on the corresponding steel grade and finally a relation was established between the imperfection factor α and the corresponding yield stress f_y (see Figure 204):

- for $f_y = 235 \text{ N/mm}^2$: λ_0 can safely be set to 0.2 and α to 0.45;
- for $f_y = 355 \text{ N/mm}^2$: λ_0 can safely be set to 0.2 and α to 0.35;
- for $f_y = 460 \text{ N/mm}^2$: λ_0 can safely be set to 0.2 and α to 0.27;
- for $f_y = 690 \text{ N/mm}^2$ and $f_y = 770 \text{ N/mm}^2$: λ_0 can safely be set to 0.2 and α to 0.20;
- for $f_y = 960 \text{ N/mm}^2$: λ_0 can safely be set to 0.2 and α to 0.15.

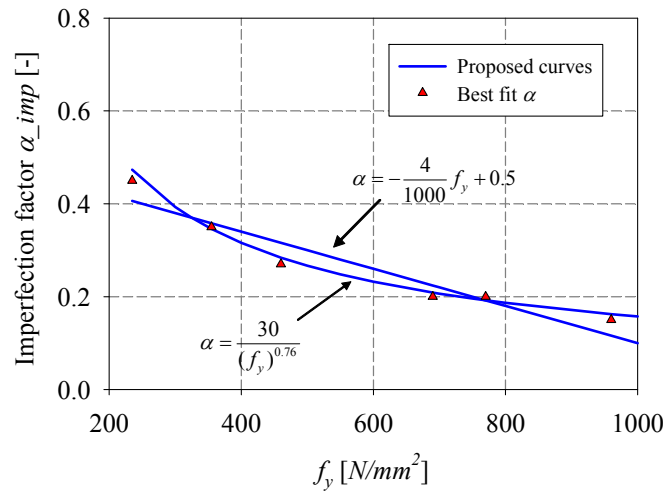


Figure 204 – Variation of α factors based on the yield stress f_y of cold-formed sections, tested under compression

According to Figure 204, a relationship between the α factors and the yield stresses f_y can be established by using one of the following equations:

$$\alpha = -\frac{4}{1000} f_y + 0.5 \text{ for } f_y \geq 235 \text{ N/mm}^2 \quad (187)$$

Or alternatively (more accurate)

$$\alpha = \frac{30}{f_y^{0.76}} \text{ for } f_y \geq 235 \text{ N/mm}^2 \quad (188)$$

Table 38 summarizes the adopted parameters for the design curves of hot-rolled and cold-formed members of different steel grades subjected to pure compression.

Table 38 –Design curves for the case of hot-rolled and cold-formed members subjected to pure compression

Simple load case: N								
$\chi_{CS+MB} = \frac{1}{\phi_{CS+MB} + \sqrt{\phi_{CS+MB}^2 - \lambda_{CS+MB}^2}}$ <p style="text-align: center;">for $\lambda_{CS+MB} \geq \lambda_0$</p> $\phi_{CS+MB} = 0.5 \left(1 + \alpha (\lambda_{CS+MB} - \lambda_0) + \lambda_{CS+MB}^2 \right)$								
Cross-section	Fabrication process	λ_0	α					
			$f_y = 235$ N/mm^2	$f_y = 355$ N/mm^2	$f_y = 460$ N/mm^2	$f_y = 690$ N/mm^2	$f_y = 770$ N/mm^2	$f_y = 960$ N/mm^2
RHS and SHS	Hot-rolled	0.2	0.21	0.21	0.21	0.13	0.13	0.13
	Cold-formed	0.2	0.45	0.35	0.27	0.20	0.20	0.15

6.4.1.3. Coupled instabilities in highly slender sections

This section is focused on the buckling behaviour of very slender members subjected to an axial compression force. A special care has to be taken in designing these members that represent a special group of elements. With respect to their static performance, they can demonstrate some kind of special phenomena which are poorly addressed in literature and not so obvious to treat in traditional ways [81]. Figure 205 represents numerical results obtained by using shell models and by adopting class 4 sections of different steel grades. Two cross-section shapes were considered: RHS 450x250x8 and SHS 300x300x6.3. One may notice that the O.I.C. resistance curves begin to decrease when slender sections of high and ultra-high yield strength are used. For the case of cold-formed sections, numerical results corresponding to very high steel grades tend to the curve defined for $f_y = 235 N/mm^2$ ($\lambda_0 = 0.2$ and $\alpha = 0.45$). For the case of hot-rolled sections, numerical results corresponding to very high strength steel tend to a curve ($\lambda_0 = 0.2$ and $\alpha = 0.45$) lower than the one defined for $f_y = 235 N/mm^2$ ($\lambda_0 = 0.2$ and $\alpha = 0.21$). When ultra-high yield strength steel is used, the handling of local buckling becomes crucial since the profiles made of such steel grades fall into the slender range (class 4 sections).

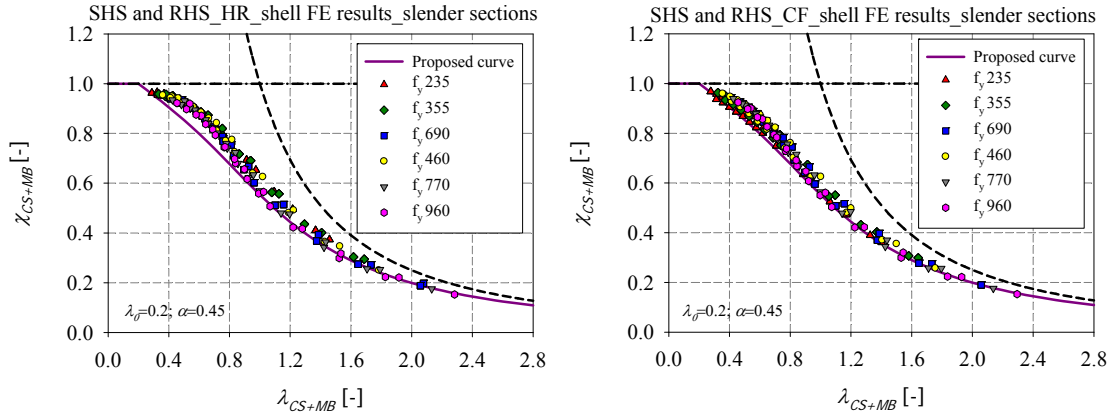


Figure 205 – Numerical member results of very slender SHS and RHS of different steel grades under compression– a) hot-rolled – b) cold-formed

Figure 206 illustrates the deformed shape / yield pattern at failure of a slender section RHS 450x250x8 of high steel grade $f_y = 690 \text{ N/mm}^2$ obtained by using a shell model. Multiple buckling modes interact and give rise to a localization of the buckling patterns and yield extent. The maximum values of yielding are mainly reached at the middle length of the member, when the section is loaded under compression. The stresses then decrease along the member length. Thus, a part of the member – less loaded under compression – is considered to be fully effective and provides a level of restraint to the entire member. When considering the O.I.C. approach (see equations (189) and (190)), or the Eurocode 3 procedure, the global interaction curves are computed by deducting the most loaded cross-section instabilities (see red circles in the equations below), located at mid-length (for the case of pure compression), from the real behaviour. This procedure does not produce realistic load carrying capacities for very slender sections, (as shown in Figure 205), where the resistance is greatly affected by the interaction between local and global buckling. Thus, deducting the most loaded cross-section from the real behaviour of the beam leads to inaccurate results, because only the most-loaded portion of the beam becomes ineffective.

$$\lambda_{CS+MB} = \sqrt{\frac{\chi_{CS} \cdot R_{RESIST}}{R_{STAB}}} \quad (189)$$

$$\chi_{CS+MB} = \frac{R_{SHELL}}{\chi_{CS} \cdot R_{RESIST}} \quad (190)$$

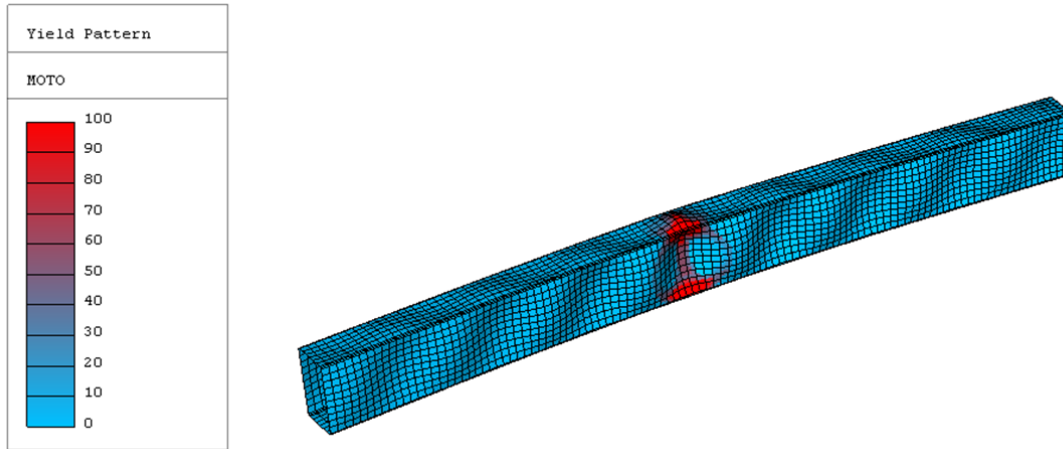


Figure 206 – Deformed shape / yield pattern at failure of RHS_450x250x8 of steel grade $f_y = 690 \text{ N/mm}^2$ obtained by using shell models

6.4.1.3.1. Influence of second-order effects

A study was undertaken to rule the local-global interaction by considering a second-order cross-sectional check of the most heavily loaded section on the member (located at mid-span). Second-order effects were first calculated by considering Figure 207 and the following equation:

$$M'' = N_{Ed} v_{\max} \quad (191)$$

where v_{\max} represents the maximum deflexion reached at peak load and was obtained numerically with the use of FINELg shell model. Hot-rolled and cold-formed sections were considered with the corresponding yield stresses varying from $f_y = 235 \text{ N/mm}^2$ to $f_y = 960 \text{ N/mm}^2$. The study was performed on two rectangular (RHS 220x120x10 and RHS 450x250x8) and two square (SHS 120x120x8 and SHS 300x300x6.3) profiles covering class 1 and class 4 sections (i.e. stocky and slender sections).

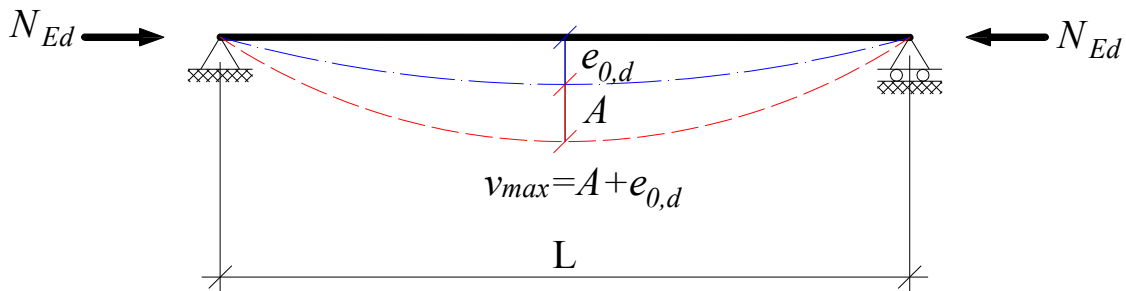


Figure 207 – Simply supported member with initial imperfection

The initial deflection at mid-span $e_{0,d}$ was then deduced from v_{max} according to the following equation:

$$e_{0,d} = v_{max} (1 - N_{Ed} / N_{cr}) \quad (192)$$

where N_{cr} is the critical flexural buckling load:

$$N_{cr} = \frac{\pi^2 EI}{L^2} \quad (193)$$

Results corresponding to hot-rolled and cold-formed sections are illustrated in Figure 208 and Figure 209 respectively. Clear tendencies are observed depending on the cross-sectional shape. Thus, several corrections should be performed to remove the influence of the cross-section shape. It should be noted that, lost points on scatter (illustrated with the red circles) mark the influence a stronger local-global interaction.

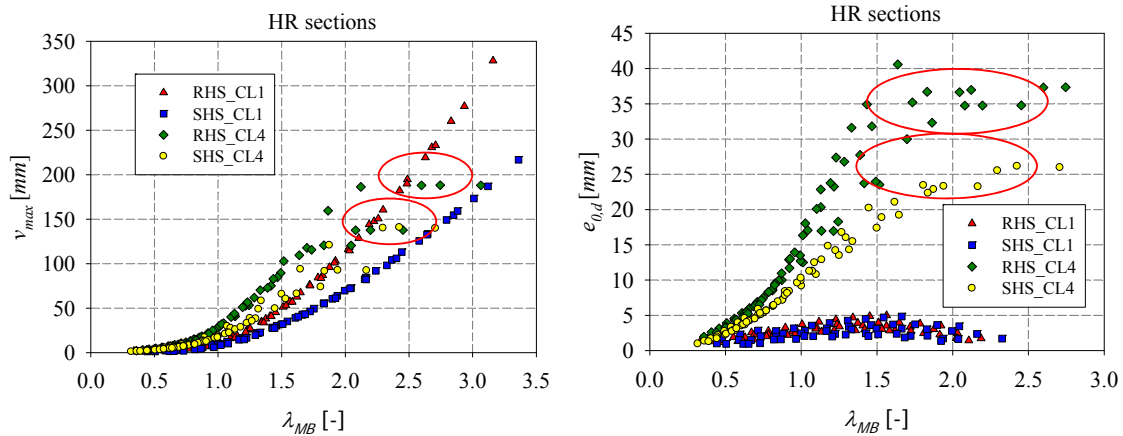


Figure 208 – Maximum and initial deflexions reached at mid-span for hot-rolled sections

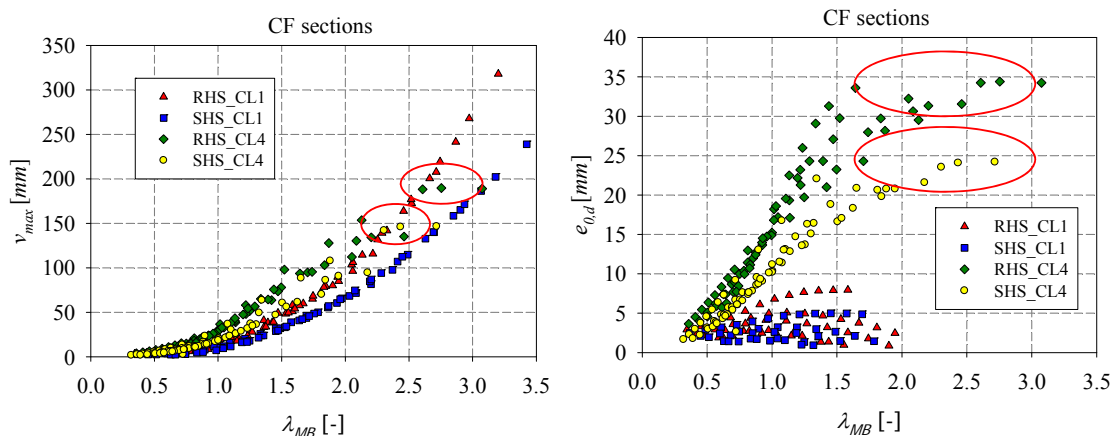


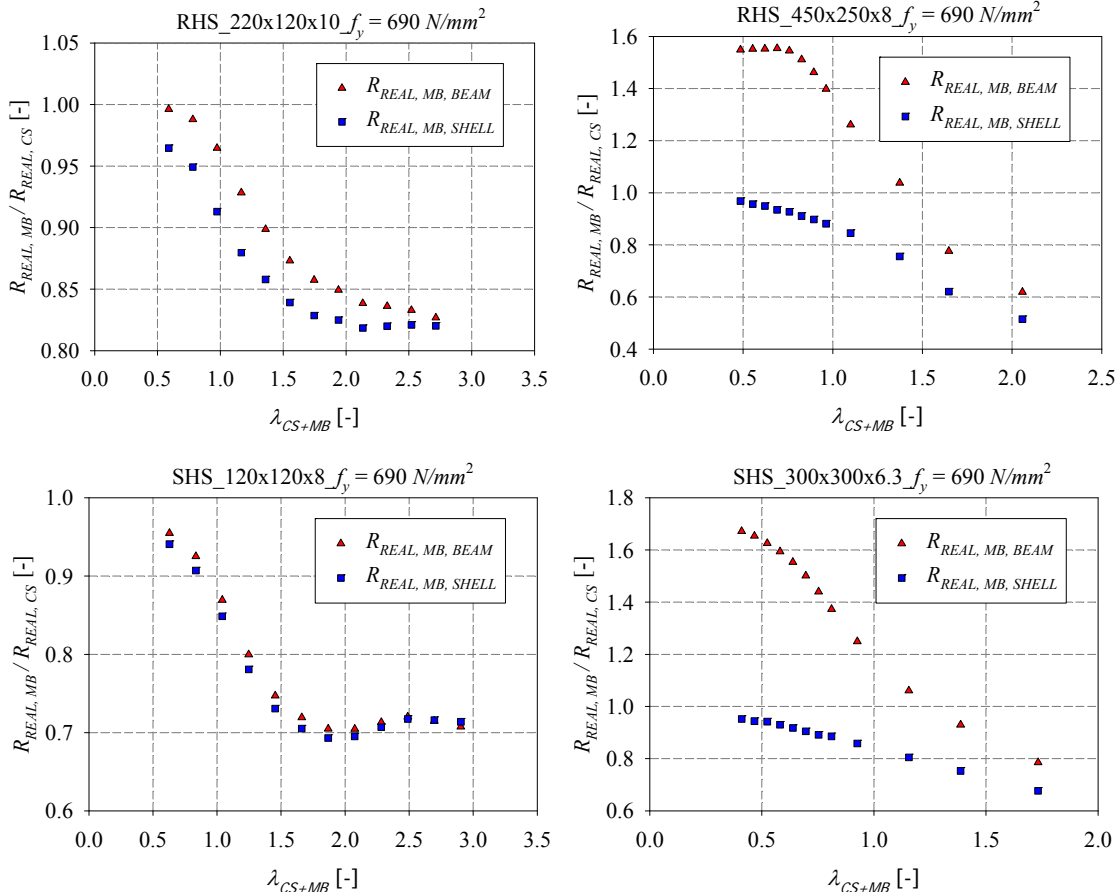
Figure 209 – Maximum and initial deflexions reached at mid-span for cold-formed sections

A verification of the most heavily cross-section (located around the mid-span of the beam, where the buckling phenomenon is more likely to occur) under the compressive load N applied and the second-order bending moments M^{II} , induced by the first order axial compression, was performed. The local-global interaction is taken into account with the inclusion of the second-order bending moment. Figure 210 compares $R_{REAL, MB, BEAM}$ and $R_{REAL, MB, SHELL}$ (representing the ultimate load multiplier of the column tested under pure compression, computed using shell and beam models respectively.) to $R_{REAL, CS}$ (representing the ultimate load multiplier of the most heavily cross-section tested under $N+M^{II}$, computed using shell model). Results corresponding to four cross-section shapes (RHS 220x120x10, RHS 450x250x8, SHS 120x120x8 and SHS 300x300x6.3) of nominal steel grades $f_y = 235 \text{ N/mm}^2$ and $f_y = 960 \text{ N/mm}^2$ are presented in Figure 210.

The following conclusions can be drawn from these figures:

- negligible differences are obtained by using both beam ($R_{REAL, MB, BEAM}$) and shell models ($R_{REAL, MB, SHELL}$) to compute the member resistance of stocky sections (RHS 220x120x10 and SHS 120x120x8); although, beam model gives always slightly higher results. Cross-section instabilities are not likely to occur for compact sections;
- beam models reach higher resistance (i.e. all the sections reach their plastic resistance) than shell ones (i.e. different values of resistance are reached: plastic or effective depending on the cross-section classification). Slender sections (RHS 450x250x8 and SHS 300x300x6.3) exhibiting an important influence of local buckling, have significantly lower resistance when modelled in shell elements than in beam elements;
- acceptable differences are obtained by comparing $R_{REAL, MB, SHELL}$ (member resistance obtained by using shell model) and $R_{REAL, CS, SHELL}$ (cross-section resistance obtained by using shell model, including the global buckling) for low values of relative slenderness. Member verification is showing safe results compared to the cross-section verification. A bigger disparity is seen with the increase of λ_{CS+MB} . For high values of relative slenderness, the highest difference between member and cross-section verification is about 48% and is reached for the class 4 section (RHS 450x250x8) of high steel grade $f_y = 690 \text{ N/mm}^2$. The difference reaches 23% for sections of steel grade $f_y = 235 \text{ N/mm}^2$.

- for low values of relative slenderness, it is clearly seen that significant difference arises when comparing $R_{REAL, MB, BEAM}$ to $R_{REAL, CS, SHELL}$. The highest deviation is about 40% and is reached for class 4 sections (SHS 300x300x6.3) of high steel grade $f_y = 690 \text{ N/mm}^2$. Beam models only able to witness global buckling regardless of the local buckling that may occur, are showing unsafe results for low values of relative slenderness. Indeed, the effect of local buckling is mainly highlighted for low values of relative slenderness where the failure of the element is due to a lack of resistance and to cross-section buckling and not because of member instability. For high values of relative slenderness, global buckling becomes determinant, thus closer tendencies are observed by comparing $R_{REAL, MB, BEAM}$ to $R_{REAL, CS, SHELL}$.



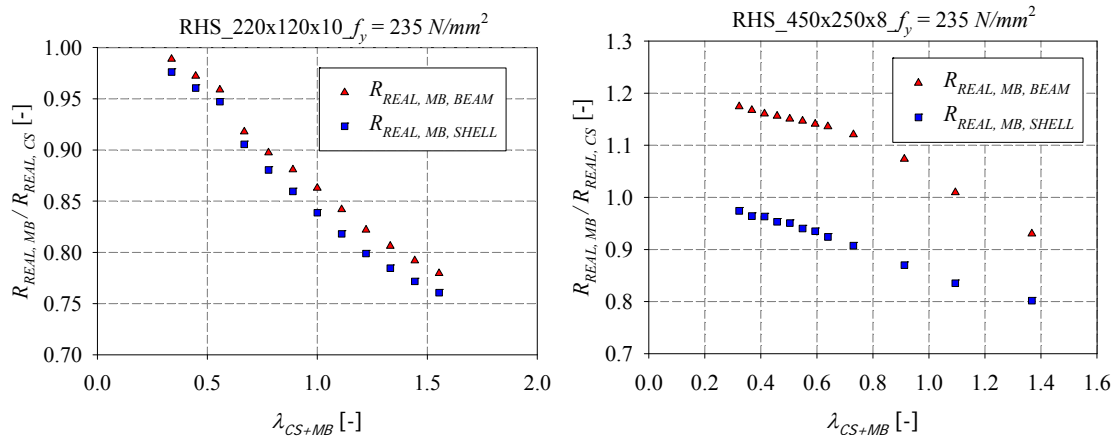


Figure 210 – $R_{REAL, MB} / R_{REAL, CS}$ graphical representation as a function of λ_{CS+MB}

6.4.1.3.2. Case of exaggeratedly slender sections

Secondly, an additional set of invented sections was analyzed, in an attempt to examine the O.I.C. approach under the most complex circumstances: when the interaction between local and global instabilities becomes crucial and deserves a special attention. Invented sections, having highly slender components are used in order to better visualize more distributed results along higher slenderness, since the European sections covers only a limited range of cross-section slenderness. The proposed sections have been derived with respect to the h/b and h/t ratios, where h/b was chosen equal to 2.5 and the h/t values spanned from 15 to 115 with a step of 2. FE results computed for “exaggerated” slender hot-rolled (see Figure 211) and cold-formed (see Figure 212) sections, of steel grades ranging from S235 to S960, tested under pure compression, are drawn in the O.I.C. format. One may notice that instability is greater with an increase of the cross-section slenderness λ_{CS} ; the sections exhibit an important influence of local buckling effects in this case. Lower curves than Eurocode 3 should be derived for this type of sections. Derived curves are drawn by using the Ayrton-Perry approach and the imperfection factors α were locally determined through a best-fit procedure: different values of α were selected for each steel grade depending on the corresponding cross-section slenderness (see Figure 211 and Figure 212). The local-global interaction is thus taken into account with the inclusion of the α factor. The adopted values of α (obtained through the best-fit) are represented with blue square dots in Figure 213 and Figure 214 for hot-rolled and cold-formed sections respectively. A comparison of the proposed calibrated expression of α to the analytical one has been done. Analytical values of

α were calculated according to Equation (194), where η was derived according to Equation (195), and are represented with green triangular in Figure 213 and Figure 214.

$$\eta = \alpha(\lambda - 0.2) \quad (194)$$

$$(1 - \chi)(1 - \chi\lambda^2) = \eta\chi \quad (195)$$

The different analytical values of α obtained for the same cross-sectional slenderness λ_{CS} , correspond to different member lengths: According to Equation (196), η represents the generalised initial imperfection that can be used to estimate the effects on the buckling phenomenon of initial imperfections such as residual stresses, initial out of straightness or eccentrically applied forces. Because the influence of some of these initial imperfections is linked with the length of the member, different value of α were accordingly obtained depending on the member length.

$$\eta = e_{0,d} \frac{A}{W_{el}} \quad (196)$$

where W_{el} is the elastic modulus and A is the gross cross-section area.

It is to be noted that according to Equation (196), the imperfection factor α accounts for the cross-section shape. One may also notice that the adopted values of α are showing in general safe sided approximations of the analytical values (see Figure 213 and Figure 214). A relation was then derived between the proposed α and λ_{CS} , represented by the red curves in Figure 213 and Figure 214. It can be clearly seen that the proposed equations are describing well enough the beam-column resistance. For low values of relative slenderness ($\lambda_{CS} < 0.8$), where global buckling is dominant, constant values of α are proposed. For higher values of relative slenderness ($0.8 < \lambda_{CS} < 2$), local buckling becomes more relevant: the O.I.C. resistance curves decrease and the values of the imperfection factor α increase with the increase of λ_{CS} . Finally, for high values of relative slenderness ($\lambda_{CS} > 2$), the O.I.C. buckling curves become more stable after a progressive drop starting from $\lambda_{CS} > 0.8$ and a constant value of α is proposed again. It should be noted that the drop of resistance was noticed only for very slender sections (class 4) of high steel grades, when the European sections were examined, since the latter covers only a limited range of cross-section slenderness. Based on the previous interpretations, Figure 213 and Figure 214 represent the design curves for the

case of hot-rolled and cold-formed sections, covering a wide range of cross-section slenderness, tested in pure compression.

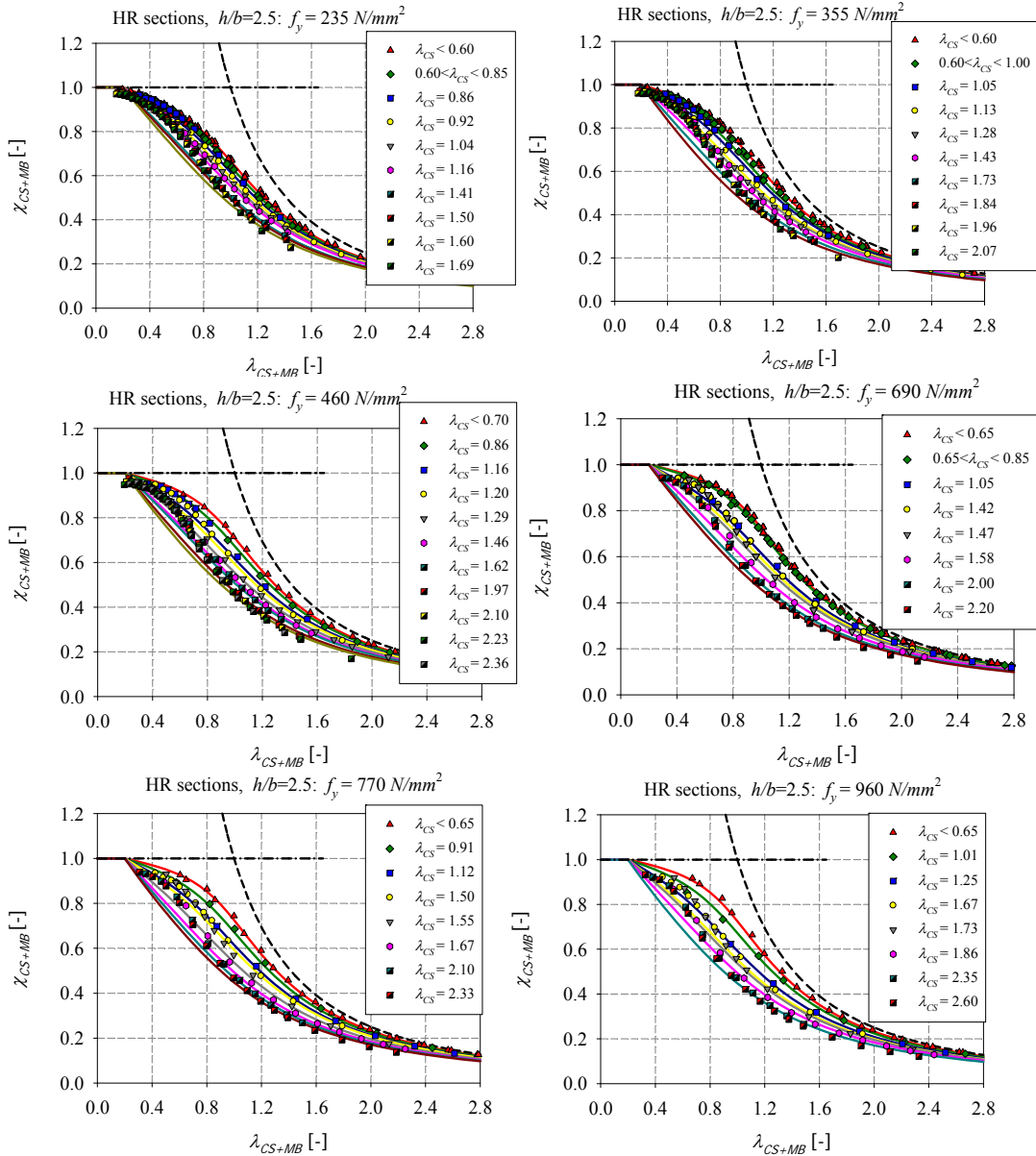
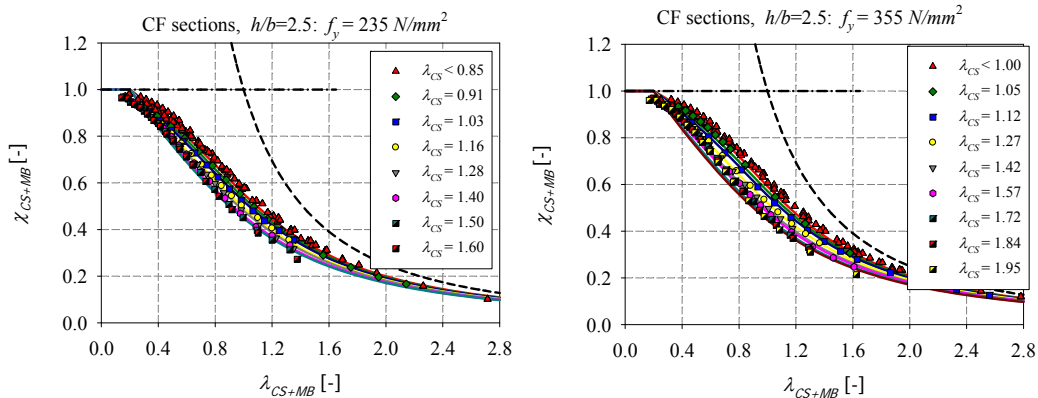


Figure 211 – Numerical member results for hot-rolled “exaggerated” slender sections under compression



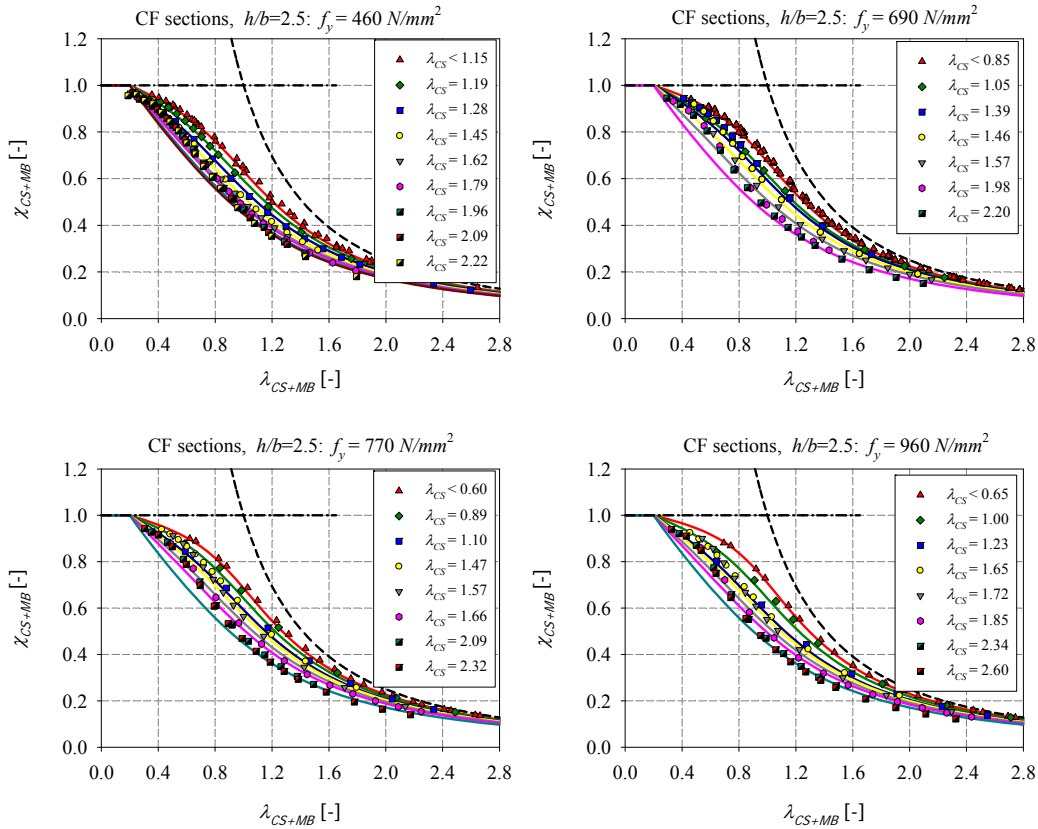


Figure 212 – Numerical member results for cold-formed “exaggerated” slender sections under compression

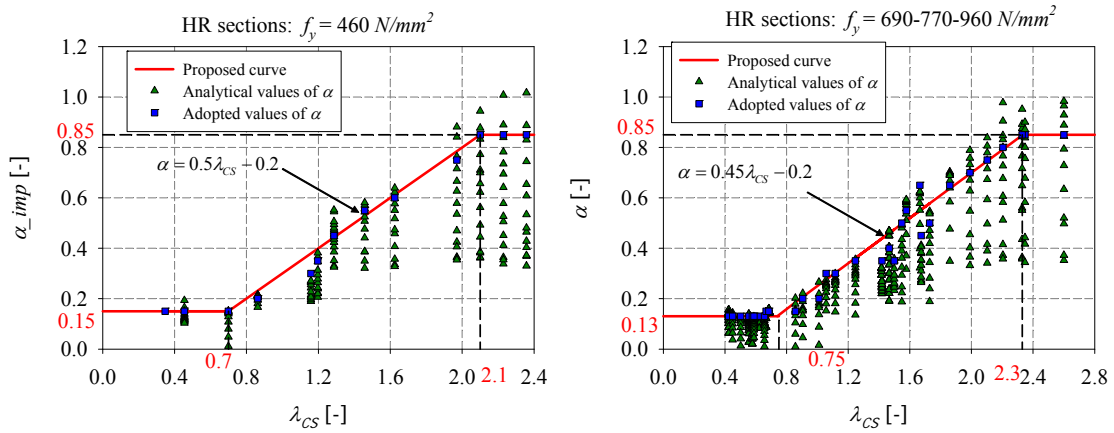


Figure 213 – Comparison of the analytical factors α with the adopted ones (obtained through the best-fit procedure) of hot-rolled sections in compression

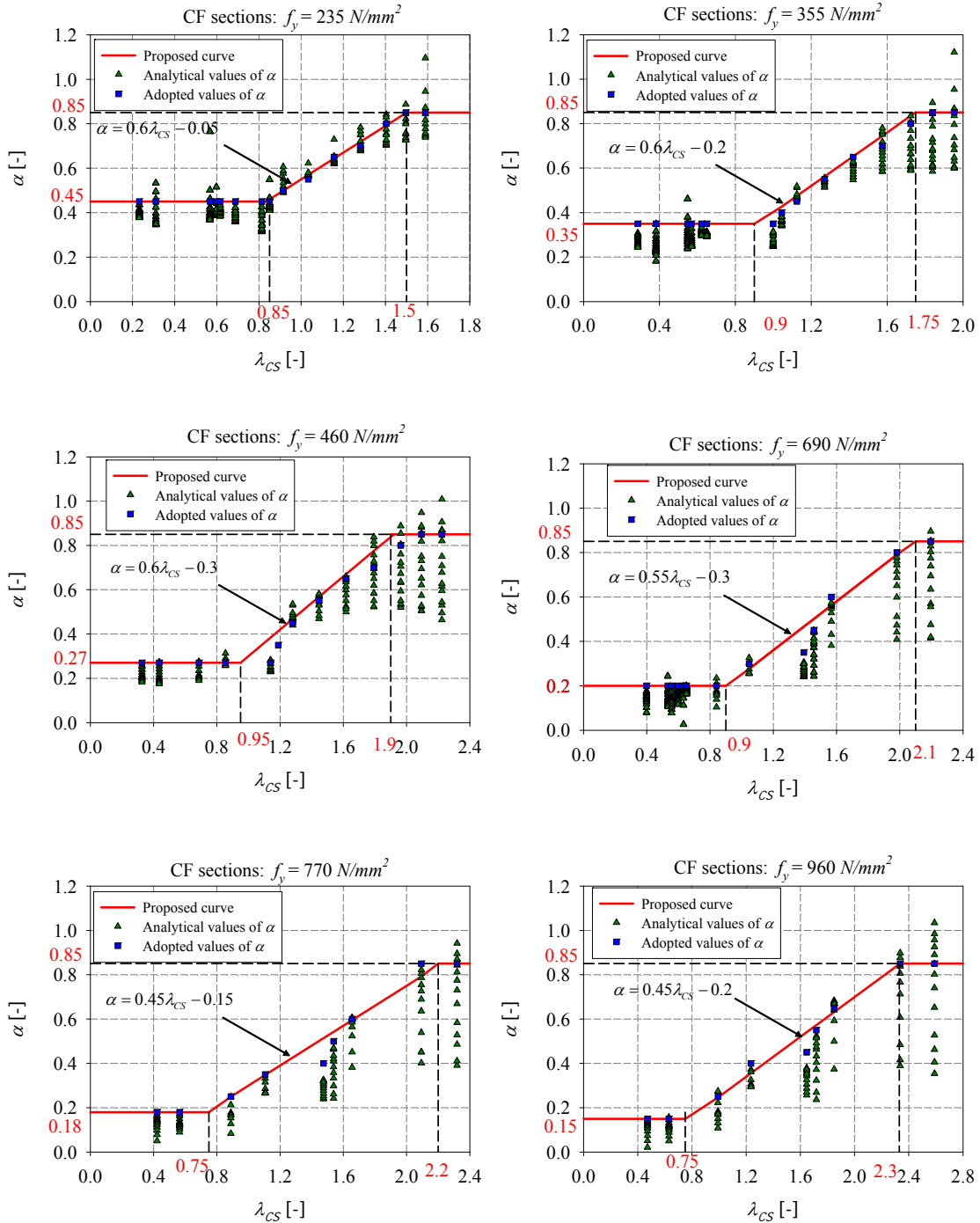


Figure 214 – Comparison of the analytical factors α with the adopted ones (obtained through the best-fit procedure) of cold-formed sections in compression

Figure 215 shows comparisons between the FE model results and the analytical results obtained by using the proposed α , for hot-rolled and cold-formed members subjected to compression. The horizontal axis represents the generalized slenderness λ_{CS+MB} while the

vertical axis reports the ratio $\chi_{FE} / \chi_{Proposal}$. It can be seen that the majority of the results computed with the proposed design curves are showing conservative tendencies. The highest difference between FE and analytical results do not exceed 15% and is reached for sections of high steel grades and for $0.4 \leq \lambda_{CS+MB} \leq 0.8$ ranges. The proposed Ayrton-Perry curves in this cases lie below the FE results (see Figure 211 and Figure 212) leading to conservative results. Eventhough, this conservatism remains acceptable.

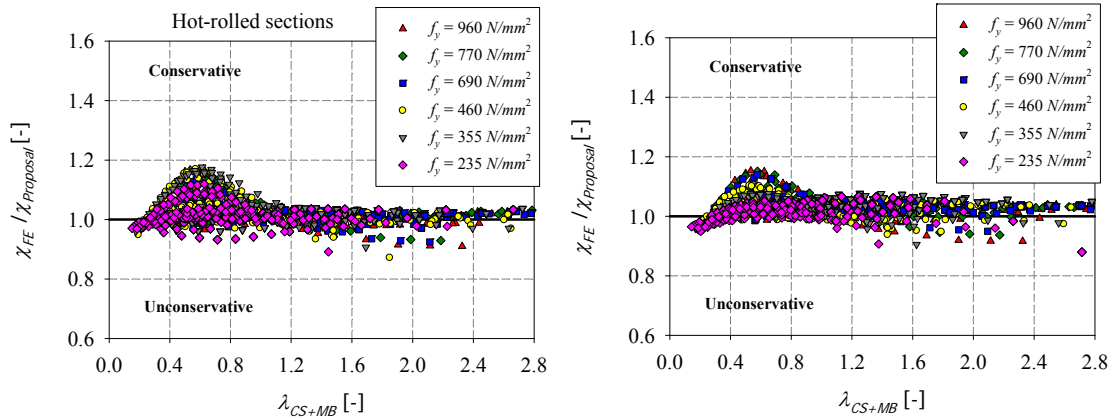


Figure 215 – Comparison of the analytical results to the FEM results – a) hot-rolled sections – b) cold-formed sections

A new parameter β could be added to the Ayrton-Perry approach in order to reduce the differences between the proposed curves and the FE results in the slenderness range of $0.4 \leq \lambda_{CS+MB} \leq 0.8$. The factor β was added to the proposed curves according to equations (197) and (198).

$$\chi_{CS+MB} = \frac{1}{\phi_{CS+MB} + \sqrt{\phi_{CS+MB}^2 - \beta \lambda_{CS+MB}^2}} \leq 1 \quad (197)$$

$$\text{where } \phi_{CS+MB} = 0.5 \left(1 + \alpha (\beta \lambda_{CS+MB} - \lambda_0) + \lambda_{CS+MB}^2 \right) \quad (198)$$

Figure 216a illustrates the derived curves drawn by using the Ayrton-Perry approach, for hot-rolled sections of yield stress $f_y = 235 \text{ N/mm}^2$, where the imperfection factor α and the β factor were locally determined through a best-fit procedure. Different values of α and β factors were chosen depending on the corresponding cross-section slenderness. The adopted values are represented in Figure 216b. A relation was then derived between the proposed α

(represented by the blue dots on the figure), β (represented by the green dots) and λ_{CS} . Finally, the β factor was not accounted for in the proposed design curves of very slender sections tested under pure compression, for sake of simplicity and since conservative results were obtained by proposing the α factor only.

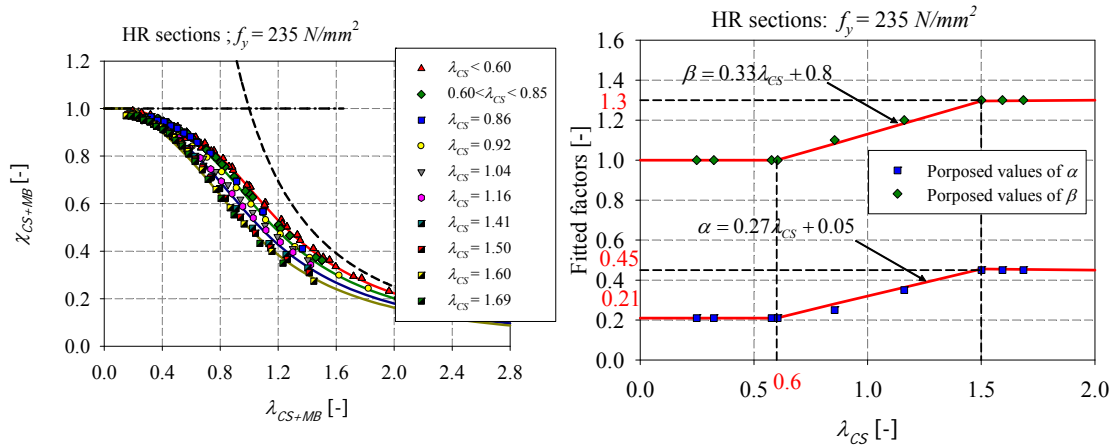


Figure 216 – Numerical member results for hot-rolled “exaggerated” slender sections of steel grade $f_y = 235 \text{ N/mm}^2$ tested under compression – a) proposed O.I.C. curves – b) fitted factors

6.4.2. Members under compression and triangular bending moment distribution

Numerical results relative to all treated hot-rolled and cold-formed members under combined loading are presented in this section.

First, a sub study has been undertaken including more values of the factor n in an attempt to characterize more precisely the influence of this factor on the member resistance. The study covered the following parameters:

- 13 different element lengths varying from 1500 mm to 15000 mm in order to visualize well-distributed results along the relative slenderness axis;
- 1 steel grade: S235;
- 2 cross-section shapes: RHS 220x120x10 and SHS 120x120x8;
- different loading conditions:
 - o compression with major-axis bending;
 - o compression with minor-axis bending;

- compression with biaxial bending.

A distinction has been made between the different loading situations, namely with respect to:

- the bending moments distributions ψ ;
- the relative axial force ratio. Two additional values of the parameter n were added ($n = 0.15$ and $n = 0.5$);
- the degree of biaxial bending defined for combined load cases as the ratio M_y / M_z . This ratio was varied on the basis of an α *biaxiality* angle (see Figure 217) in order to investigate the influence of the proportion of the major and minor-axis bending on the member resistance. For each load case, 10 values of the degree of biaxial bending were adopted varying from α *biaxiality* = 0° (i.e. the load case becoming compression with major-axis bending $N+M_y$) to α *biaxiality* = 90° (i.e. the load case becoming compression with minor-axis bending $N+M_z$).

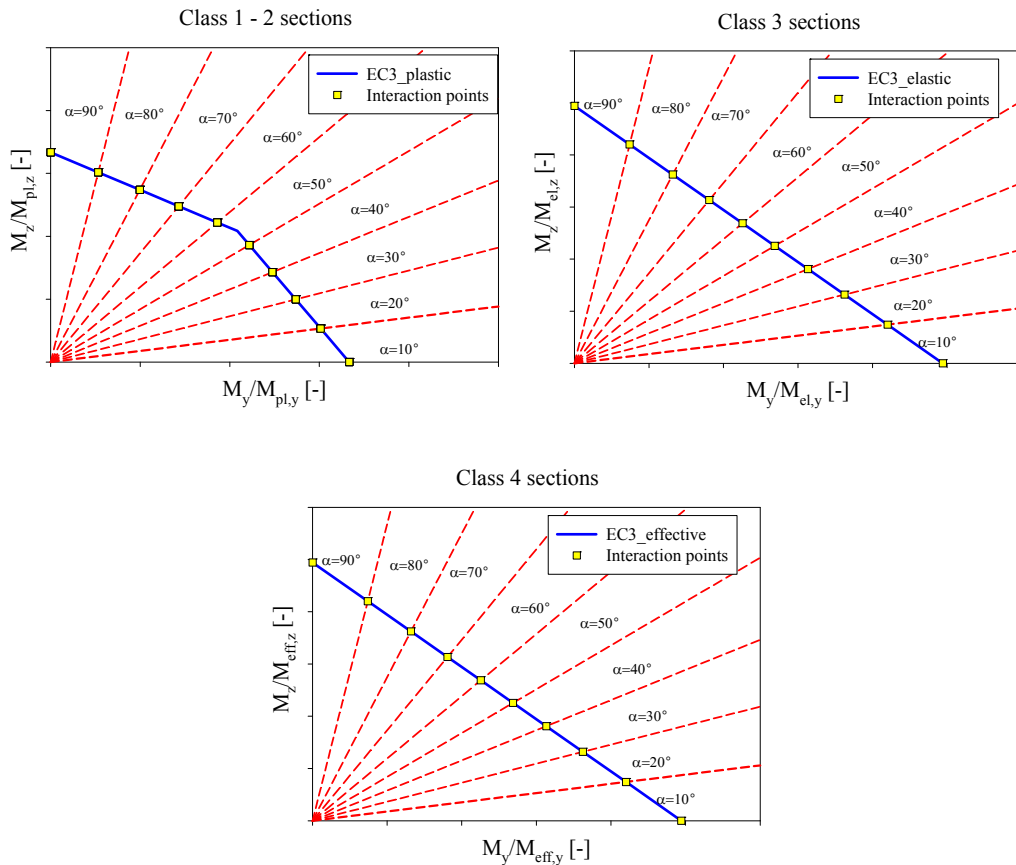


Figure 217 – Selection of load cases for $N+M_y+M_z$ combined situations – a) class 1-2 – b) class 3 – c) class 4

Additional calculations were simulated with the same parameters mentioned before with a length equal to three times the height of the section in order to determine the cross-section resistance. The results were added to the full set numerical calculations for the combined loading cases.

A leading parameter identified to influence the resistance of a beam-column member is the bending moment distribution represented by the ψ factor²⁴. In this section, the results displayed correspond to hot-rolled and cold-formed members tested under compression and triangular bending moment (i.e. $\psi = 0$).

6.4.2.1. Compression and minor-axis bending cases

6.4.2.1.1. Hot-rolled square sections

Figure 218 and Figure 219 below illustrate the application of the O.I.C. to hot-rolled square sections tested under combined loading situations: compression and triangular minor-axial bending, for different steel grades: $f_y = 235 \text{ N/mm}^2$, $f_y = 355 \text{ N/mm}^2$ and $f_y = 690 \text{ N/mm}^2$. The results are obtained by using both shell and beam models and by adopting two values for factor n ($n = 0.3$ and $n = 0.7$).

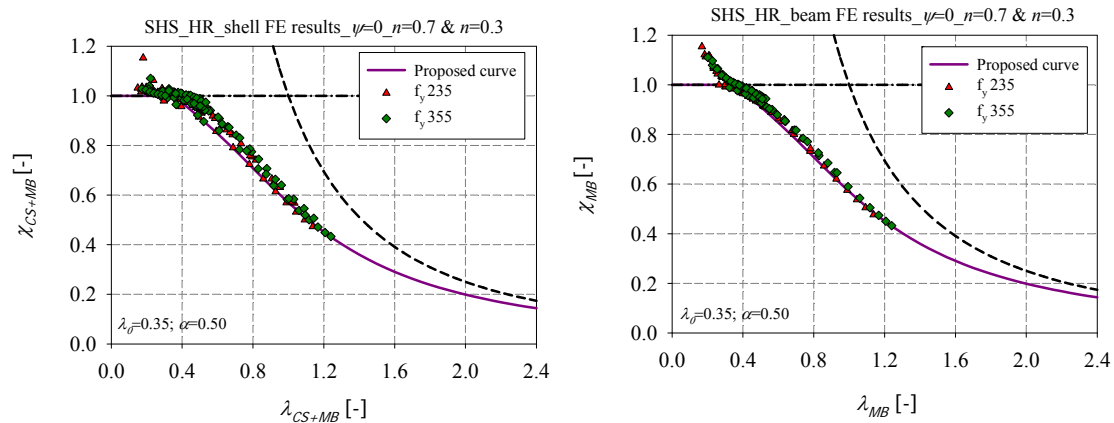


Figure 218 – Numerical member results of hot-rolled SHS of steel grades $f_y = 235 \text{ N/mm}^2$ and $f_y = 355 \text{ N/mm}^2$ under $N+M_z$ and $\psi = 0$ – a) shell results – b) beam results

²⁴ The ψ factor represents the ratio between end moments: $-1.0 \leq \psi \leq 1.0$; $\psi = 1$ indicates constant bending moment distribution, $\psi = 0$ indicates triangular bending moment distribution.

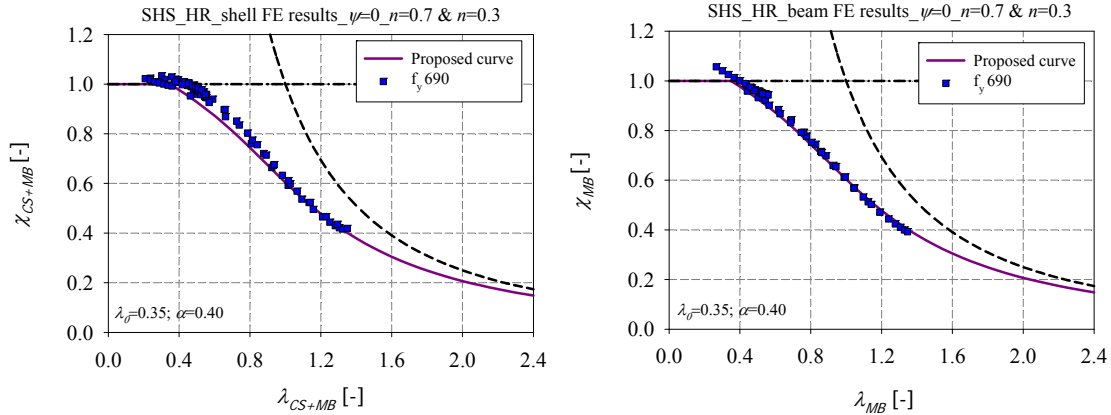


Figure 219 – Numerical member results of hot-rolled SHS of steel grade $f_y = 690 \text{ N/mm}^2$ under $N+M_z$ and $\psi = 0$
– a) shell results – b) beam results

Close tendencies of member results computed using beam and shell models are observed. Nevertheless, and even if same tendencies are shown for both cases, it can be noticed that beam results attain higher values especially for low values of slenderness. This is due to the fact that, in the beam model, no local instabilities occur whereas, in the shell approach, the global interaction curve is computed by deducing the cross-section instabilities from the real behaviour. Hence, shell results includes the non-linear effect of geometrical and material imperfections and also for some cases the occurrence of distortional buckling modes. This non-linearity at the cross-section level is neglected in the beam model which causes the shell and beam results to diverge.

For sake of simplicity, a single interaction curve was derived for $f_y = 235 \text{ N/mm}^2$ and $f_y = 355 \text{ N/mm}^2$, since a small dispersion in the results is noted. Based on the observations of Figure 218, the end of plateau factor λ_0 can be set to 0.35 and the imperfection factor α can be safely set to 0.50. However, a higher resistance is observed for $f_y = 690 \text{ N/mm}^2$ and a higher curve is derived. The imperfection factor α can safely be set to 0.40.

One may also notice that the relative axial force ratio n defined as $n = N_{Ed} / N_{b,Rd} = (N_{Ed} / \chi N_{pl,Rd} \text{ or } N_{Ed} / \chi N_{eff,Rd})$ induces a small influence on the member resistance when a triangular bending moment is applied. Results are presented in Figure 220 for the particular case of $f_y = 235 \text{ N/mm}^2$.

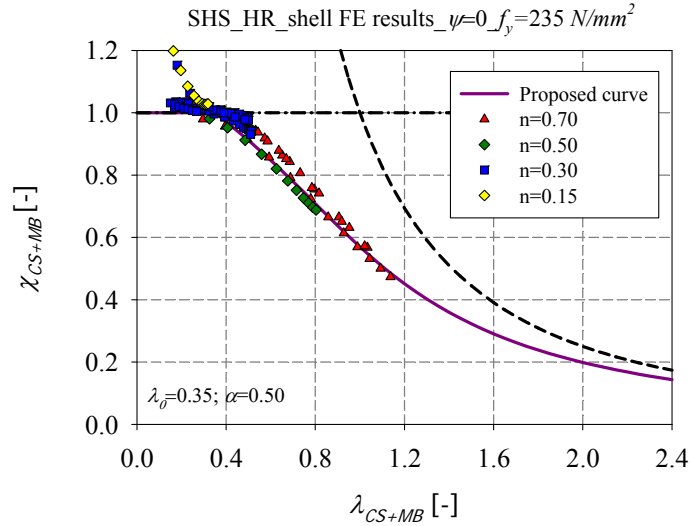


Figure 220 – Numerical member results of hot-rolled SHS of steel grade $f_y = 235 \text{ N/mm}^2$ tested under different values of axial force ratio n

With the inclusion of α_{comp} factor which represents the imperfection factor derived for members tested under pure compression load case, the imperfection factor defined for members tested under compression and minor-axis bending can be expressed according to the following equations:

$$\alpha = \alpha_{comp} + 0.25\eta_z^{0.2} \leq 0.5 \text{ for } f_y = 235 \text{ N/mm}^2 \text{ and } f_y = 355 \text{ N/mm}^2 \quad (199)$$

$$\alpha = \alpha_{comp} + 0.25\eta_z^{0.2} \leq 0.4 \text{ for } f_y = 690 \text{ N/mm}^2 \quad (200)$$

That way, for $\eta_z = 0$, Equations (199) and (200) are restored with the limiting curve being relative to the pure compression load case and for $\eta_z > 0$ the equations tend to the limiting curves relative to compression and minor-axis bending.

In addition, the end of plateau factor can be written as follows, in order to provide smooth continuities with the pure compression load case:

$$\lambda_0 = 0.2 + 0.2\eta_z^{0.2} \leq 0.35 \quad (201)$$

6.4.2.1.2. Hot-rolled rectangular sections

Displayed results show that similar tendencies to square hollow sections are obtained for the rectangular ones. Figure 221 and Figure 222 below illustrate the application of the O.I.C. for hot-rolled rectangular sections of different steel grades ($f_y = 235 \text{ N/mm}^2$, $f_y = 355 \text{ N/mm}^2$ and

$f_y = 690 \text{ N/mm}^2$), tested under compression and triangular minor-axis bending, by using both shell and beam models. The same curves adopted for the square sections were again adopted for the rectangular ones. A single interaction curve was derived for $f_y = 235 \text{ N/mm}^2$ and $f_y = 355 \text{ N/mm}^2$ since a small dispersion in the results is noted. A higher resistance is observed for $f_y = 690 \text{ N/mm}^2$ and a higher curve is derived accordingly.

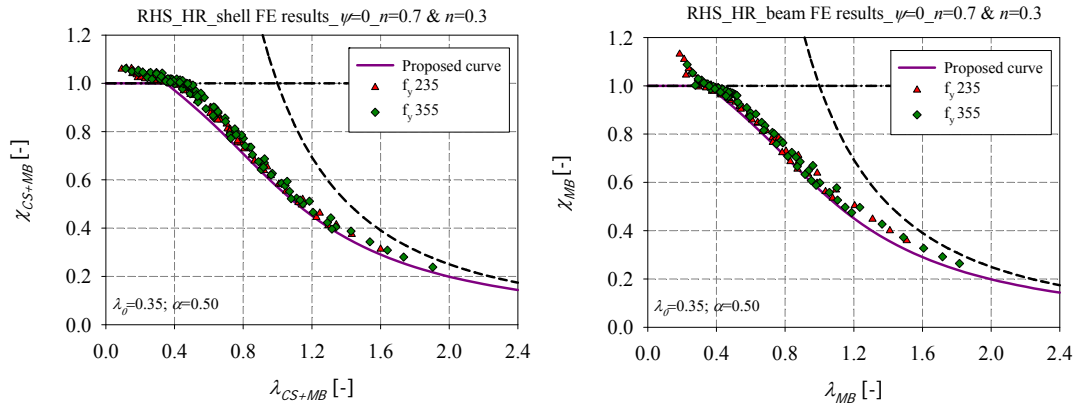


Figure 221 – Numerical member results of hot-rolled RHS of steel grades $f_y = 235 \text{ N/mm}^2$ and $f_y = 355 \text{ N/mm}^2$ under $N+M_z$ and $\psi = 0$ – a) shell results – b) beam results

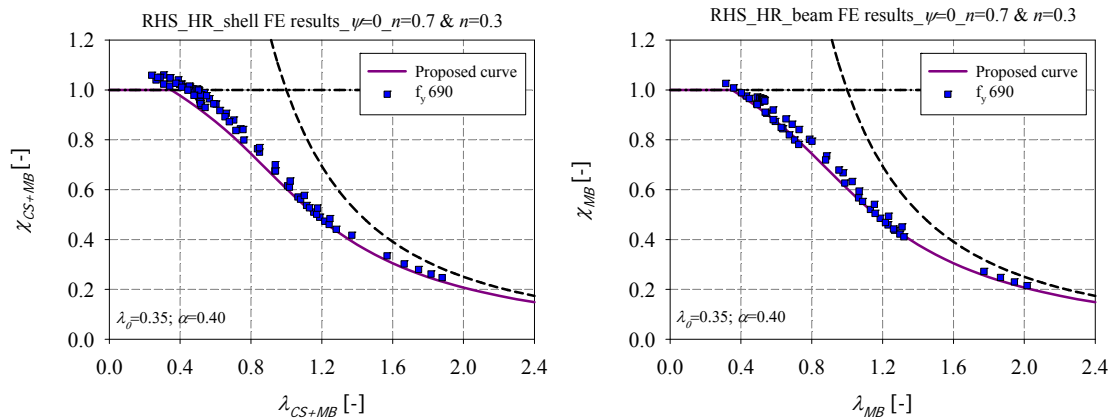


Figure 222 – Numerical member results of hot-rolled RHS of steel grade $f_y = 690 \text{ N/mm}^2$ under $N+M_z$ and $\psi = 0$ – a) shell results – b) beam results

Figure 223 represents the application of pure major or pure minor-axis bending at the cross-section level, where a comparison of the relative slenderness of the different cross-sections with various aspect ratios subjected to a weak and a strong axis bending moment are presented. One may notice that, for the case of cross-sections subjected to a pure weak axis, the O.I.C. curve corresponding to pure strong axis bending relative to an aspect ratio of $h/b = 1$ can be safely adopted as the only curve for all cross-sections subjected to such load case. This is due to the fact that with rectangular sections subjected to a pure weak axis

bending, the relative inertia I_z would not increase with an increased h/b ratio as much as the inertia I_y of similar sections subjected to a strong axis bending. Therefore, the relative slenderness finds itself almost stable with cross-sections subjected to a weak axis bending, while it decreases considerably in the case of strong axis bending (due to an increase in the R_{STAB} factor). This is clearly shown in Figure 223 in which three cross-sections, with varying h/b ratios, were adopted and their corresponding relative slenderness was compared in function of their h/b ratios for both load cases of a strong and weak axis bending moment [3]. Thus, when applying compression and weak-axis bending on beam-column members, one single curve can be adopted regardless of the section types (rectangular and square). In this case, the global buckling becomes determinant due to the compressive load applied. The failure is not affected by the cross-section shape of the member because the relative slenderness is almost stable with cross-sections (i.e. rectangular and square) subjected to a weak axis bending (see Figure 223).

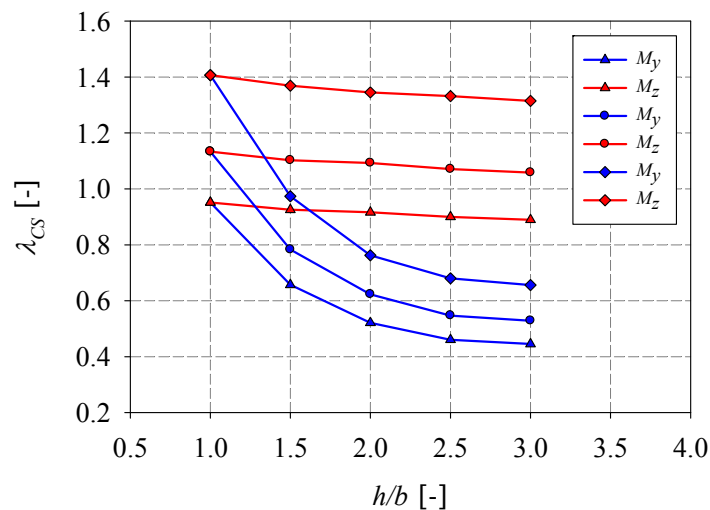


Figure 223 – Comparison of the relative slenderness of different cross-section with various aspect ratios subjected to a weak and a strong axis bending moment [3]

Results are presented in Figure 224 for the particular case of $f_y = 235 \text{ N/mm}^2$ for hot-rolled RHS highlighting the influence of the axial force ratio n . One may also notice that the factor n induces a small influence on the member resistance when a triangular bending moment is applied.

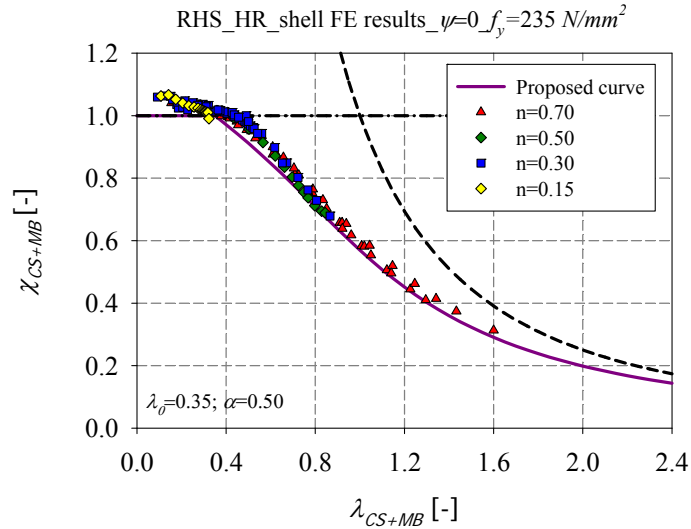


Figure 224 – Numerical member results of hot-rolled RHS of steel grade $f_y = 235 \text{ N/mm}^2$ tested under different values of axial force ratio n

6.4.2.1.3. Cold-formed square sections

Figure 225 presents results for cold-formed square members of different steel grades ($f_y = 235 \text{ N/mm}^2$, $f_y = 355 \text{ N/mm}^2$ and $f_y = 690 \text{ N/mm}^2$), tested under compression and triangular minor-axis bending moment, by adopting two values of factor n ($n = 0.3$ and $n = 0.7$). Based on the observations of Figure 225, a single interaction curve was derived for $f_y = 235 \text{ N/mm}^2$ and $f_y = 355 \text{ N/mm}^2$. The end of plateau factor λ_0 was chosen equal to 0.35 and the imperfection factor α was safely set to 0.70. Higher resistance is observed for the particular case of high strength steel ($f_y = 690 \text{ N/mm}^2$), thus the imperfection factor α was safely set to 0.45. Figure 226 highlights the influence of factor n for the particular case $f_y = 235 \text{ N/mm}^2$. It is clearly shown that for a high level of compression ($n = 0.7$), global buckling becomes determinant, leading to a widespread curve along the λ_{CS+MB} axis (many $\lambda_{CS+MB} > 1$ cases). The global buckling due to the high level of compression occurs before cross-section full yielding, resulting in the failure of the element due to instability and not because of a lack of cross-sectional resistance. However, for a lower level of compression ($n = 0.15$ and $n = 0.3$), the curve is more restricted and reaches lower values of the generalized relative slenderness λ_{CS+MB} . In this case, the bending moment is predominant. The hollow sections exhibit little influence of instability due to their high resistance towards lateral torsional buckling, and exhibit little influence of global instability due to the low level

of compression. The failure of the element is mainly due to a lack of resistance and to cross-section buckling in this case.

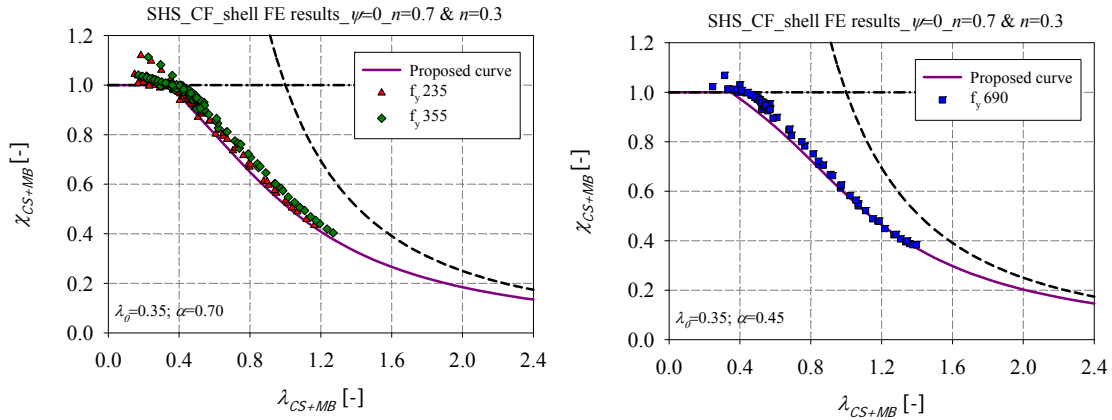


Figure 225 – Numerical member results of cold-formed SHS of different steel grades – a) $f_y = 235 \text{ N/mm}^2$ and $f_y = 355 \text{ N/mm}^2$ – b) $f_y = 690 \text{ N/mm}^2$

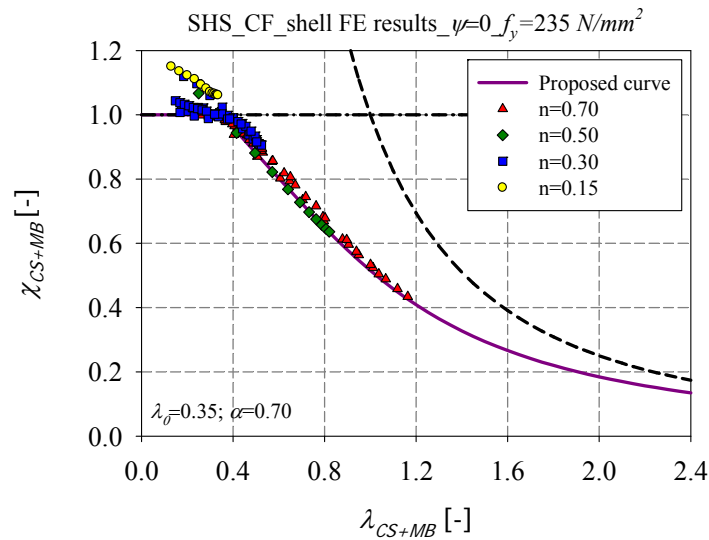


Figure 226 – Numerical member results of cold-formed SHS of steel grade $f_y = 235 \text{ N/mm}^2$ under different values of axial force ratio n

With the inclusion of α_{comp} factor which represents the imperfection factor derived for members tested under pure compression load case, the imperfection factor can be expressed according to the following equations:

$$\alpha = \alpha_{comp} + 0.25\eta_z^{0.2} \leq 0.7 \text{ for } f_y = 235 \text{ N/mm}^2 \text{ and } f_y = 355 \text{ N/mm}^2 \quad (202)$$

$$\alpha = \alpha_{comp} + 0.25\eta_z^{0.2} \leq 0.45 \text{ for } f_y = 690 \text{ N/mm}^2 \quad (203)$$

That way, for $\eta_z = 0$, Equations (202) and (203) are restored with the limiting curve being relative to the pure compression load case and for $\eta_z > 0$ the equations tend to the limiting curves relative to compression and minor-axis bending.

In addition, the end of plateau factor can be written as follows, in order to provide smooth continuities with the pure compression load case:

$$\lambda_0 = 0.2 + 0.2\eta_z^{0.2} \leq 0.35 \quad (204)$$

6.4.2.1.4. Cold-formed rectangular sections

Figure 227 illustrates the application of the O.I.C. for cold-formed rectangular members of different steel grades ($f_y = 235 \text{ N/mm}^2$, $f_y = 355 \text{ N/mm}^2$ and $f_y = 690 \text{ N/mm}^2$) tested under compression and triangular minor-axial bending. The same curves adopted for the cold-formed square sections were again adopted for the rectangular ones. Figure 228 highlights the influence of factor n for the particular case of $f_y = 235 \text{ N/mm}^2$. Based on the observations of Figure 227 and Figure 228, a single interaction curve was derived for $f_y = 235 \text{ N/mm}^2$ and $f_y = 355 \text{ N/mm}^2$. The end of plateau factor λ_0 was chosen equal to 0.35 and the imperfection factor α was safely set to 0.70. Higher resistance is observed for the particular case of high strength steel ($f_y = 690 \text{ N/mm}^2$), thus the imperfection factor α was safely set to 0.45.

Table 39 summarizes the adopted parameters for the design curves of hot-rolled and cold-formed hollow sections subjected to compression and triangular minor-axis bending moment distribution.

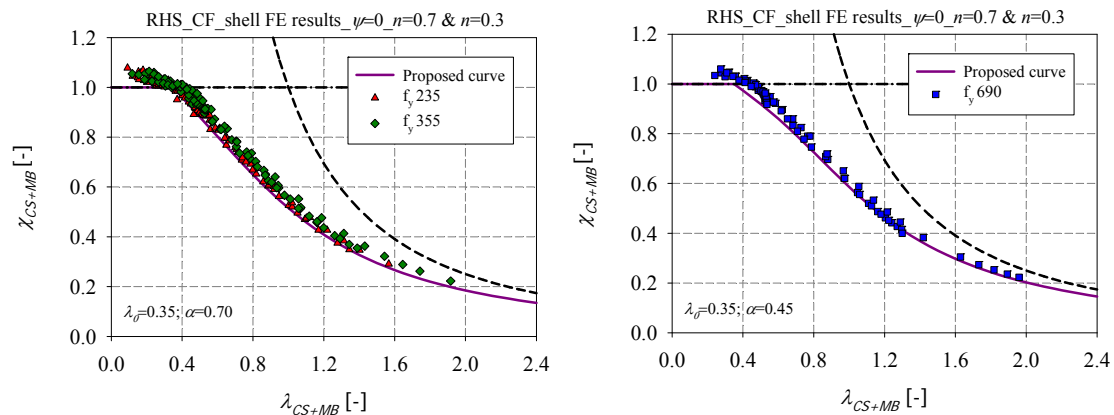


Figure 227 – Numerical member results of cold-formed RHS of different steel grades – a) $f_y = 235 \text{ N/mm}^2$ and $f_y = 355 \text{ N/mm}^2$ – b) $f_y = 690 \text{ N/mm}^2$

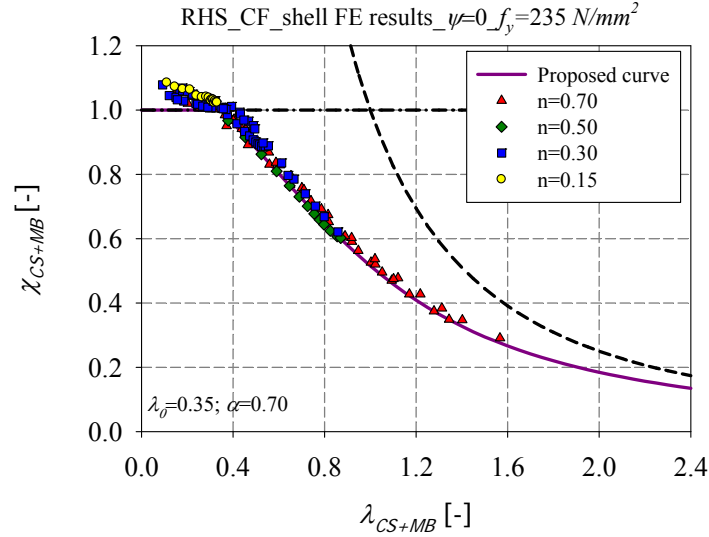


Figure 228 – Numerical member results of cold-formed RHS of steel grade $f_y = 235 \text{ N/mm}^2$ under different values of axial force ratio n .

Table 39 – Design curves for the case of hot-rolled and cold-formed members subjected to compression with triangular minor-axis bending.

Combined load cases: $N+M_z$				
Triangular bending moment distribution: $\psi = 0$				
$\chi_{CS+MB} = \frac{1}{\phi_{CS+MB} + \sqrt{\phi_{CS+MB}^2 - \lambda_{CS+MB}^2}}$ for $\lambda_{CS+MB} \geq \lambda_0$ $\phi_{CS+MB} = 0.5(1 + \alpha(\lambda_{CS+MB} - \lambda_0) + \lambda_{CS+MB}^2)$				
Cross-section	Fabrication process	λ_0	α	
			$f_y = 235 \text{ N/mm}^2$ $f_y = 355 \text{ N/mm}^2$	$f_y = 690 \text{ N/mm}^2$
RHS and SHS	Hot-rolled	$0.2 + 0.2\eta_z^{0.2} \leq 0.35$	$\alpha = \alpha_{comp} + 0.25\eta_z^{0.2} \leq 0.5$	$\alpha = \alpha_{comp} + 0.25\eta_z^{0.2} \leq 0.4$
	Cold-formed		$\alpha = \alpha_{comp} + 0.25\eta_z^{0.2} \leq 0.7$	$\alpha = \alpha_{comp} + 0.25\eta_z^{0.2} \leq 0.45$

6.4.2.2. Compression and major-axis bending cases

6.4.2.2.1. Hot-rolled square sections

For what concern square sections, results of members tested under compression and major-axis bending are identical to results of members tested under compression and minor-axis bending due to the symmetrical geometry of the sections. Therefore, the same curves proposed previously for hot-rolled square sections under compression and minor-axis

bending, were again adopted for the case of hot-rolled square sections under compression and major-axis bending.

6.4.2.2.2. Hot-rolled rectangular sections

Rectangular sections are less affected by instability and have a better behaviour under compression with major-axis bending than under compression with minor-axis bending as should be expected since (predominant) weak axis flexural buckling cumulates with weak axis bending. A higher curve was derived for this type of loading. Figure 229 and Figure 230 present results of hot-rolled members tested under compression and triangular major-axis bending obtained by shell and beam models, for different steel grades: $f_y = 235 \text{ N/mm}^2$, $f_y = 355 \text{ N/mm}^2$ and $f_y = 690 \text{ N/mm}^2$.

A single interaction curve was derived for $f_y = 235 \text{ N/mm}^2$ and $f_y = 355 \text{ N/mm}^2$, since a small dispersion in the results is noted. The end of plateau factor λ_0 was set to 0.35 and the imperfection factor α was set to 0.20. A higher curve is derived for $f_y = 690 \text{ N/mm}^2$ where the imperfection factor α can safely be set to 0.10. Figure 231 presents the particular case of $f_y = 235 \text{ N/mm}^2$ for hot-rolled RHS highlighting the influence of the axial force ratio n .

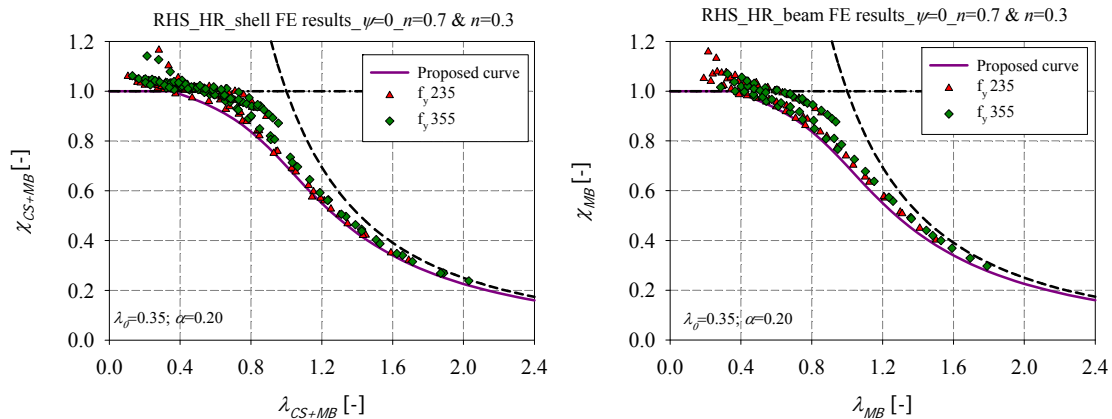


Figure 229 – Numerical member results of hot-rolled RHS of steel grades $f_y = 235 \text{ N/mm}^2$ and $f_y = 355 \text{ N/mm}^2$ under $N+M_y$ and $\psi = 0$ – a) shell results – b) beam results

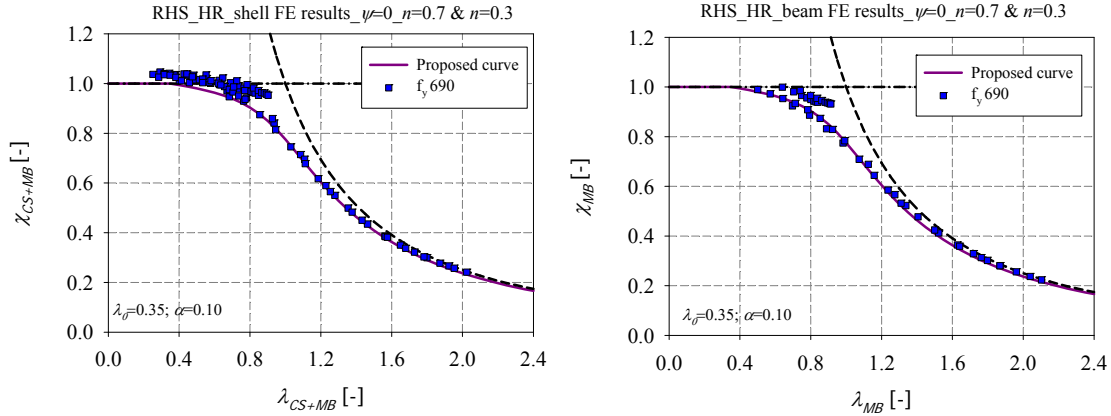


Figure 230 – Numerical member results of hot-rolled RHS of steel grade $f_y = 690 \text{ N/mm}^2$ under $N+M_y$ and $\psi = 0$ – a) shell results – b) beam results

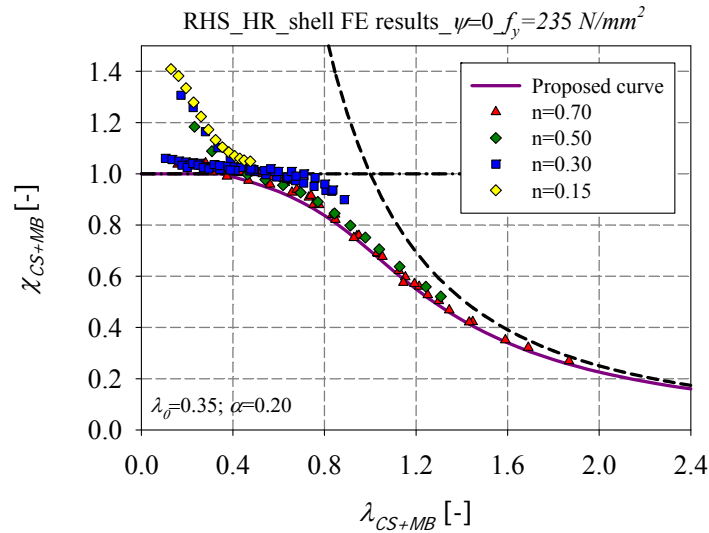


Figure 231 – Numerical member results of hot-rolled RHS of steel grade $f_y = 235 \text{ N/mm}^2$ tested under different values of axial force ratio n

With the inclusion of α_{comp} factor which represents the imperfection factor derived for members tested under pure compression load case, the imperfection factor can be written as follows, in order to provide smooth continuities with the pure compression load case.

$$\alpha = \alpha_{comp} \quad (205)$$

In addition, the end of plateau factor can be written as follows, in order to provide smooth continuities with the pure compression load case:

$$\lambda_0 = 0.2 + 0.2\eta_y^{0.2} \leq 0.35 \quad (206)$$

6.4.2.2.3. Cold-formed square sections

As for the hot-rolled case, the same curves proposed previously for cold-formed square sections under compression and minor-axis bending, were again adopted for the case of cold-formed square sections under compression and major-axis bending due to the symmetrical geometry of the square sections.

6.4.2.2.4. Cold-formed rectangular sections

Figure 232 illustrates the application of the O.I.C. for cold-formed rectangular members of different steel grades ($f_y = 235 \text{ N/mm}^2$, $f_y = 355 \text{ N/mm}^2$ and $f_y = 690 \text{ N/mm}^2$) tested under compression and triangular major-axis bending. Results are obtained by adopting two values of the factor n ($n = 0.3$ and $n = 0.7$). Figure 233 highlights the influence of factor n for the particular case $f_y = 235 \text{ N/mm}^2$.

For sake of simplicity, a single interaction curve was again derived for $f_y = 235 \text{ N/mm}^2$ and $f_y = 355 \text{ N/mm}^2$, since a small dispersion in the results is noted. Based on the observations of the figures below, the end of plateau factor λ_0 can be set to 0.35 and the imperfection factor α can be safely set to 0.40. A higher resistance is observed for $f_y = 690 \text{ N/mm}^2$ and a higher curve is derived where the imperfection factor α can safely be set to 0.15.

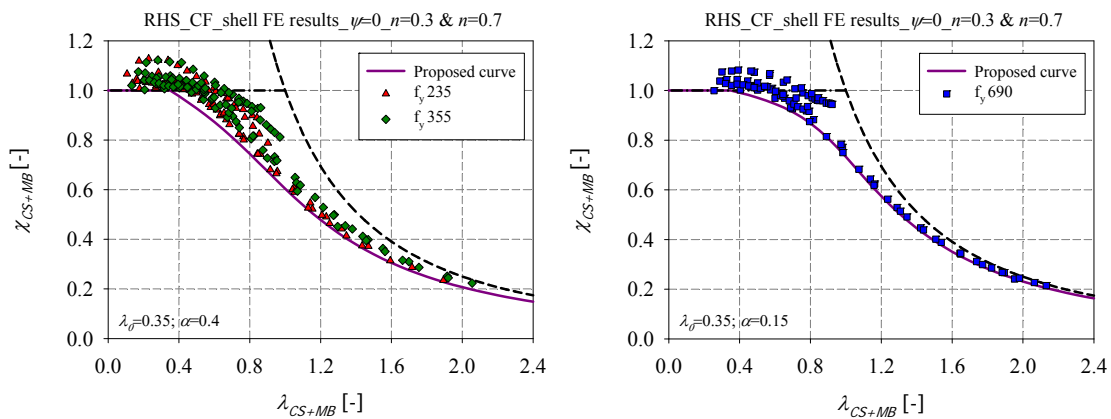


Figure 232 – Numerical member results of cold-formed RHS of different steel grades – a) $f_y = 235 \text{ N/mm}^2$ and $f_y = 355 \text{ N/mm}^2$ – b) $f_y = 690 \text{ N/mm}^2$

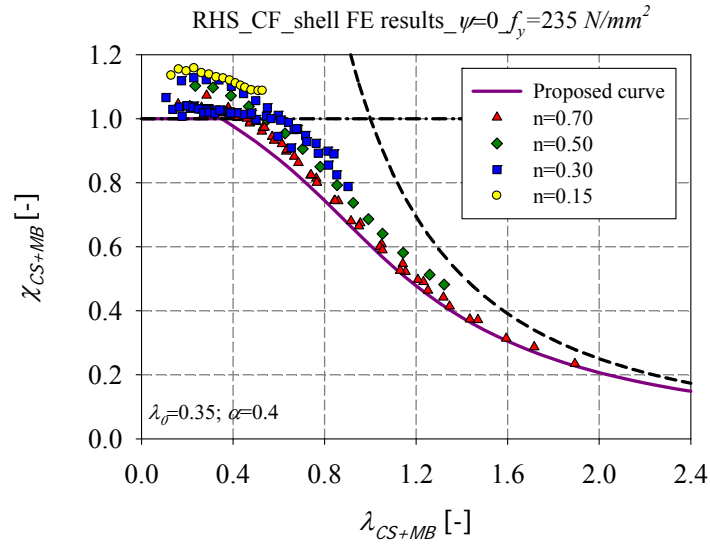


Figure 233 – Numerical member results of cold-formed RHS tested under different values of axial force ratio n for $f_y = 235 \text{ N/mm}^2$

With the inclusion of α_{comp} factor which represents the imperfection factor derived for members tested under pure compression load case, the imperfection factor can be written as follows, in order to provide smooth continuities with the pure compression load case.

$$\alpha = \alpha_{comp} \quad (207)$$

In addition, the end of plateau factor can be written as follows, in order to provide smooth continuities with the pure compression load case:

$$\lambda_0 = 0.2 + 0.2\eta_y^{0.2} \leq 0.35 \quad (208)$$

Table 40 summarizes the adopted parameters for the design curves of hot-rolled and cold-formed hollow members subjected to compression with triangular major-axis bending moment distribution.

Table 40 – Design curves for the case of hot-rolled and cold-formed members subjected to compression and triangular major-axis bending

Combined load cases: $N+M_y$				
Triangular bending moment distribution: $\psi = 0$				
$\chi_{CS+MB} = \frac{1}{\phi_{CS+MB} + \sqrt{\phi_{CS+MB}^2 - \lambda_{CS+MB}^2}}$ for $\lambda_{CS+MB} \geq \lambda_0$ $\phi_{CS+MB} = 0.5(1 + \alpha(\lambda_{CS+MB} - \lambda_0) + \lambda_{CS+MB}^2)$				
Cross-section	Fabrication process	λ_0	α	
			$f_y = 235 \text{ N/mm}^2$ $f_y = 355 \text{ N/mm}^2$	$f_y = 690 \text{ N/mm}^2$
RHS	Hot-rolled	$0.2 + 0.2\eta_y^{0.2} \leq 0.35$	$\alpha = \alpha_{comp}$	$\alpha = \alpha_{comp}$
	Cold-formed			
SHS	Hot-rolled		$\alpha = \alpha_{comp} + 0.25\eta_z^{0.2} \leq 0.5$	$\alpha = \alpha_{comp} + 0.25\eta_z^{0.2} \leq 0.4$
	Cold-formed		$\alpha = \alpha_{comp} + 0.25\eta_z^{0.2} \leq 0.7$	$\alpha = \alpha_{comp} + 0.25\eta_z^{0.2} \leq 0.45$

6.4.2.3. Compression and biaxial bending

The interaction between resistance and stability is greatly affected by the bending moment distribution and by the proportions between the different loads.

The figures hereafter present results of members tested under combined loading ($N+M_y+M_z$) with a triangular bending moment distribution. For each load case, 10 values of the degree of biaxial bending (which is called $\alpha_{\text{biaxiality}}$ to avoid confusion with the imperfection factor α) were adopted varying from $\alpha_{\text{biaxiality}} = 0^\circ$ (i.e. the load case becoming compression with major-axis bending $N+M_y$) to $\alpha_{\text{biaxiality}} = 90^\circ$ (i.e. the load case becoming compression with minor-axis bending $N+M_z$) with a range of 10 degrees. The M_y / M_z ratio is clearly considered as a leading parameter for the derivation of appropriate interaction curves. For sake of simplicity, only some results for cold-formed and hot-rolled sections tested under compression and triangular bending moment are presented in Figure 234 and Figure 235, in order to investigate the influence of the proportions of the bending moments. As can be seen in the figures, for the case of square sections, quite limited scatter is obviously observed as expected for the pair of $\alpha_{\text{biaxiality}}$ - values: $\alpha_{\text{biaxiality}} = 10^\circ$ and $\alpha_{\text{biaxiality}} = 80^\circ$;

$\alpha_{_biaxiality} = 20^\circ$ and $\alpha_{_biaxiality} = 70^\circ$; $\alpha_{_biaxiality} = 30^\circ$ and $\alpha_{_biaxiality} = 60^\circ$; $\alpha_{_biaxiality} = 40^\circ$ and $\alpha_{_biaxiality} = 50^\circ$, due to the symmetrical geometry of the sections. However, larger scatters are observed for the case of rectangular sections. The resistance of the member in this case is largely influenced by the degree of biaxial bending: for cases where weak-axis bending takes over strong-axis bending ($\alpha_{_biaxiality} > 45^\circ$), the O.I.C. resistance curves begin to increase again after a progressive drop starting from the combined loading $N+M_y$ alone. When M_z is applied to an $N+M_y$ loading with a small proportion ($\alpha_{_biaxiality} < 45^\circ$), instability is increased if compared to the $N+M_y$ loading; nevertheless when M_z becomes dominant, the section becomes more stable.

One curve was proposed for the case of square sections and this regardless of the degree of biaxial bending for sake of simplicity. The adopted curve was derived lower than the curve adopted for the case of $N+M_y$ and $N+M_z$. However, different curves were proposed for the case of rectangular sections depending on the $\alpha_{_biaxiality}$ -factor, since it has a significant impact on the resistance of rectangular sections. Accordingly, for each load case, four different design curves²⁵ were proposed based on the $\alpha_{_biaxiality}$ -factor for the case of rectangular sections and one curve was adopted for the case of square sections.

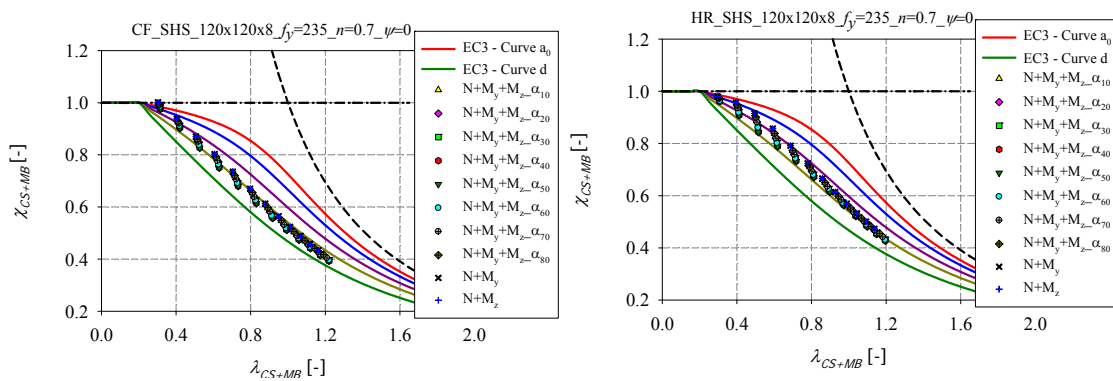


Figure 234 – Numerical member results obtained for different degrees of biaxial bending values and $\psi = 0$ for
 – a) cold-formed SHS – b) hot-rolled SHS

²⁵ The proposed curves for the case of rectangular sections correspond to lower bounds of the numerical results obtained for $\alpha_{_biaxiality} = 10^\circ$, $\alpha_{_biaxiality} = 20^\circ$, $\alpha_{_biaxiality} = 30^\circ$ and $\alpha_{_biaxiality} \geq 40^\circ$ from which the O.I.C. resistance curves begin to increase.

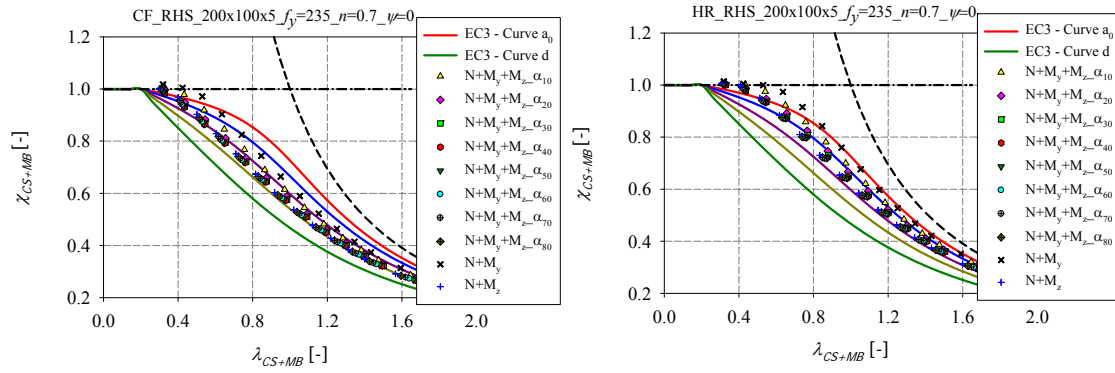


Figure 235 – Numerical member results obtained for different degrees of biaxial bending values and $\psi = 0$ for
 – a) cold-formed RHS – b) hot-rolled RHS

It should be noted that the factor $\alpha_{\text{biaxiality}}$ is equivalent to the derived factor²⁶ $\Omega_{y/z}$ and can be calculated using the following Equation (209).

$$\Omega_{y/z} = \arctan\left(\frac{m_z}{m_y}\right) = \arctan\left(\frac{M_z / M_{pl,z}}{M_y / M_{pl,y}}\right) \quad (209)$$

6.4.2.3.1. Hot-rolled square sections

Figure 236 and Figure 237 present results for hot-rolled square members of different steel grades ($f_y = 235 \text{ N/mm}^2$, $f_y = 355 \text{ N/mm}^2$ and $f_y = 690 \text{ N/mm}^2$), tested under compression and triangular biaxial bending, obtained by shell and beam models. For sake of simplicity, a single interaction curve was derived for $f_y = 235 \text{ N/mm}^2$ and $f_y = 355 \text{ N/mm}^2$, since a small dispersion in the results is noted. The end of plateau factor λ_0 was set to 0.35 and the imperfection factor α was set to 0.65. However, a higher resistance is observed for $f_y = 690 \text{ N/mm}^2$ and a higher curve is derived. The imperfection factor α can safely be set to 0.55. Figure 238 presents the particular case of $f_y = 235 \text{ N/mm}^2$ for hot-rolled square sections highlighting the influence of the axial force ratio n . One curve was adopted for the case of square sections, subjected to compression and biaxial bending, and this regardless of the degree of biaxial bending for sake

²⁶ For class 3 sections $\alpha_{\text{biaxiality}}$ was calculated as the angle between $M_y/M_{el,y}$ and $M_z/M_{el,z}$ (M_{el} representing the elastic moment); for class 4 it was calculated as the angle between $M_y/M_{eff,y}$ and $M_z/M_{eff,z}$ (M_{eff} representing the effective moment). Thus the derived factor $\Omega_{y/z}$ slightly differ from $\alpha_{\text{biaxiality}}$ for class 3 and class 4 sections.

of simplicity. The proposed curve in this case was lower than the curve proposed when the member is subjected to compression and mono-axial bending.

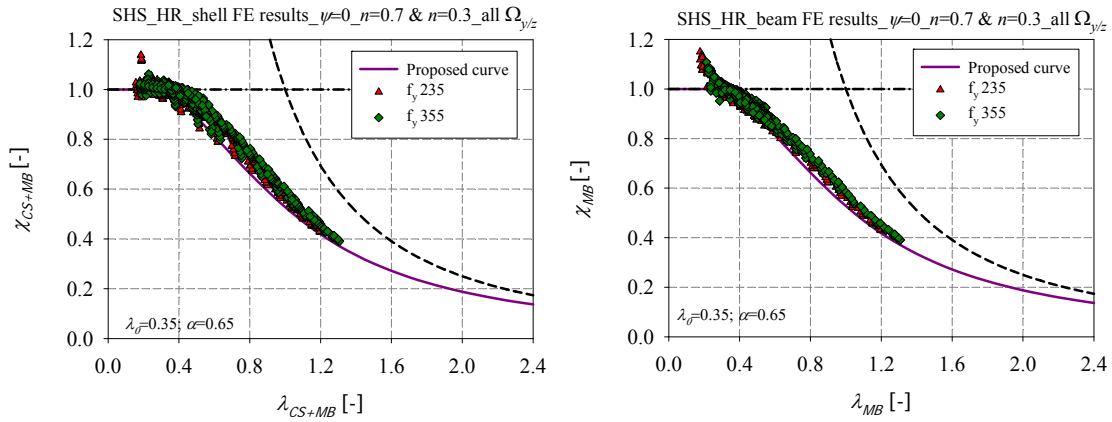


Figure 236 – Numerical member results of hot-rolled SHS of steel grades $f_y = 235 \text{ N/mm}^2$ and $f_y = 355 \text{ N/mm}^2$, under $N+M_y+M_z$ and $\psi = 0$ – a) shell results – b) beam results

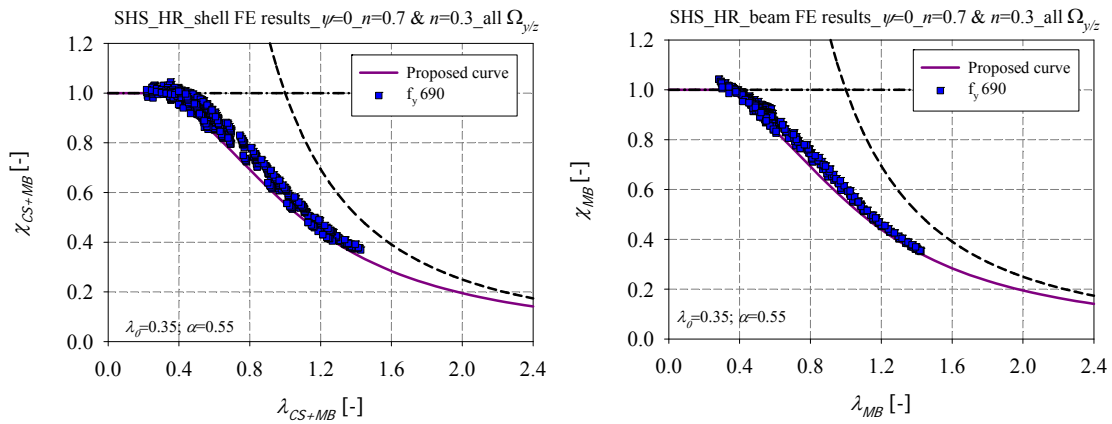


Figure 237 – Numerical member results of hot-rolled SHS of steel grade $f_y = 690 \text{ N/mm}^2$ under $N+M_y+M_z$ and $\psi = 0$ – a) shell results – b) beam results

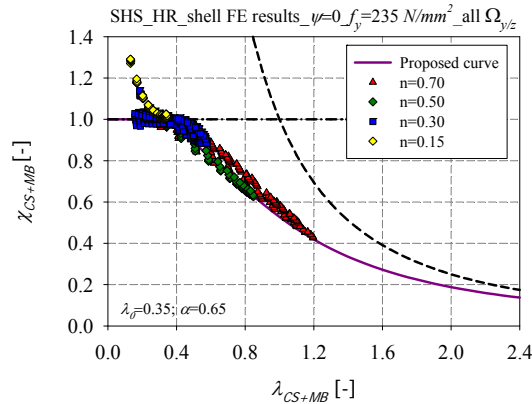


Figure 238 – Numerical member results of hot-rolled SHS of steel grade $f_y = 235 \text{ N/mm}^2$ tested under different values of axial force ratio n

Figure 239 presents a variation of the imperfection factor based on the degree of biaxial bending for the case of hot-rolled square sections, of steel grades $f_y = 235 \text{ N/mm}^2$ and $f_y = 355 \text{ N/mm}^2$, tested under compression and triangular bending moment distribution. With the inclusion of the $\Omega_{y/z}$ parameter, the proposed α formula becomes as the following:

$$\alpha = 0.015\Omega_{y/z} + 0.5 \text{ for } \Omega_{y/z} \leq 10 \quad (210)$$

$$\alpha = 0.65 \text{ for } 10 \leq \Omega_{y/z} \leq 80 \quad (211)$$

$$\alpha = -0.015\Omega_{y/z} + 1.85 \text{ for } \Omega_{y/z} \geq 80 \quad (212)$$

That way, for $\Omega_{y/z} = 0$, Equation (210) is restored with the limiting curve being relative to compression with major-axis bending load case and for $\Omega_{y/z} = 90$, Equation (212) is restored with the limiting curve being relative to compression with minor-axis bending load case.

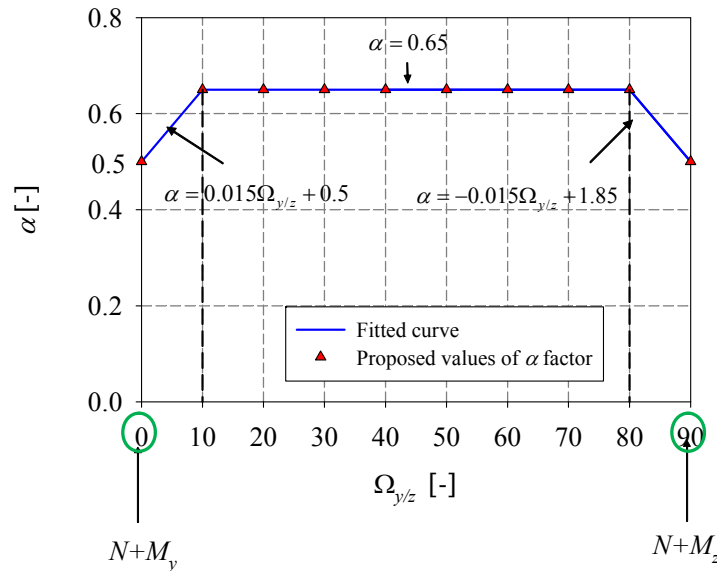


Figure 239 – Variation of α factor based on $\Omega_{y/z}$ for the case of hot-rolled SHS of steel grades $f_y = 235 \text{ N/mm}^2$ and $f_y = 355 \text{ N/mm}^2$, tested under compression and triangular bending moment

In order to provide a smooth continuity with the pure compression load case, the term 0.5 is replaced by $\alpha_{comp} + 0.25\eta^{0.2}$ as explained in section 6.4.2.1.1, and the proposed α formula becomes as the following:

$$\alpha = 0.015\Omega_{y/z} + \alpha_{comp} + 0.25\eta^{0.2} \leq 0.65 \text{ for } \Omega_{y/z} \leq 10 \quad (213)$$

$$\alpha = 0.65 \text{ for } 10 \leq \Omega_{y/z} \leq 80 \quad (214)$$

$$\alpha = -0.015\Omega_{y/z} + 1.35 + \alpha_{comp} + 0.25\eta_z^{0.2} \leq 0.65 \text{ for } \Omega_{y/z} \geq 80 \quad (215)$$

That way, for $\Omega_{y/z} = 0$ and $\eta_y = 0$, Equation (213) is restored with the limiting curve being relative to the pure compression load case and for $\Omega_{y/z} = 90$ and $\eta_z = 0$, Equation (215) is restored with the limiting curve of the pure compression as well.

The same type of relationships can be found between α and $\Omega_{y/z}$ for high strength steel hollow section, (i.e. $f_y = 690 \text{ N/mm}^2$) according to the equations below:

$$\alpha = 0.015\Omega_{y/z} + 0.4 \text{ for } \Omega_{y/z} \leq 10 \quad (216)$$

$$\alpha = 0.55 \text{ for } 10 \leq \Omega_{y/z} \leq 80 \quad (217)$$

$$\alpha = -0.015\Omega_{y/z} + 1.75 \text{ for } \Omega_{y/z} \geq 80 \quad (218)$$

These equations can be written as follows, by replacing the term 0.4 by $\alpha_{comp} + 0.25\eta^{0.2}$ in order to provide smooth continuities with the pure compression load case:

$$\alpha = 0.015\Omega_{y/z} + \alpha_{comp} + 0.25\eta_y^{0.2} \leq 0.55 \text{ for } \Omega_{y/z} \leq 10 \quad (219)$$

$$\alpha = 0.55 \text{ for } 10 \leq \Omega_{y/z} \leq 80 \quad (220)$$

$$\alpha = -0.015\Omega_{y/z} + 1.35 + \alpha_{comp} + 0.25\eta_z^{0.2} \leq 0.55 \text{ for } \Omega_{y/z} \geq 80 \quad (221)$$

6.4.2.3.2. Hot-rolled rectangular hollow sections

Figure 240 and Figure 241 present results for hot-rolled rectangular members of different steel grades ($f_y = 235 \text{ N/mm}^2$, $f_y = 355 \text{ N/mm}^2$ and $f_y = 690 \text{ N/mm}^2$) tested under compression and triangular biaxial bending obtained by using shell and beam models. The figures illustrate the influence of the degree of biaxial bending on the member response. A single curve was derived for $f_y = 235 \text{ N/mm}^2$ and $f_y = 355 \text{ N/mm}^2$ depending on the $\Omega_{y/z}$ value (see Figure 240). Higher resistances are observed for $f_y = 690 \text{ N/mm}^2$ and higher curves were derived accordingly. Figure 242 presents the particular case of $f_y = 235 \text{ N/mm}^2$ for hot-rolled RHS highlighting the influence of the axial force ratio n .

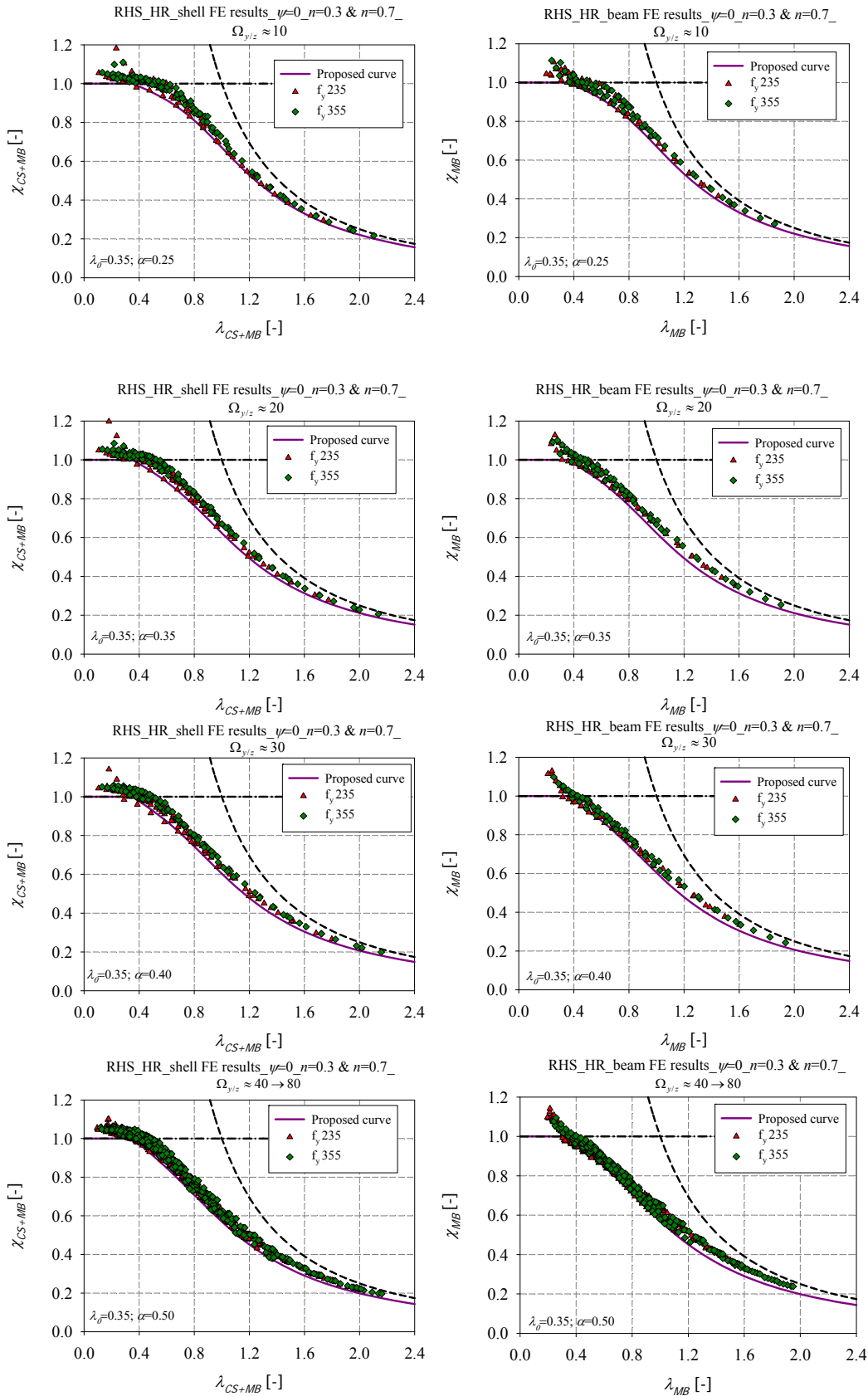


Figure 240 – Numerical shell and beam member results for hot-rolled RHS of steel grades $f_y = 235 \text{ N/mm}^2$ and $f_y = 355 \text{ N/mm}^2$ under $N+M_y+M_z$

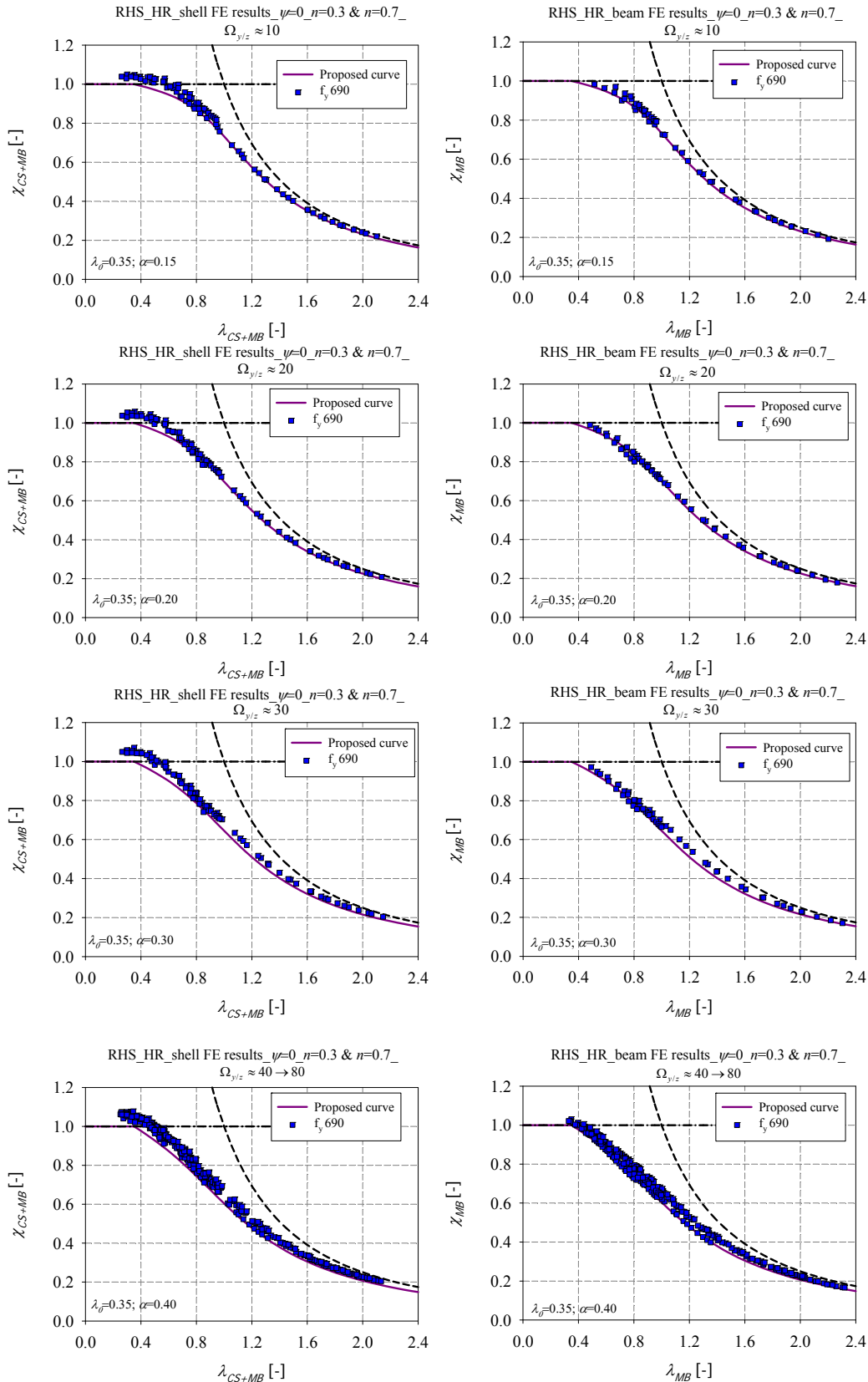


Figure 241 – Numerical shell and beam member results of hot-rolled RHS of steel grade $f_y = 690 \text{ N/mm}^2$ under $N+M_y+M_z$

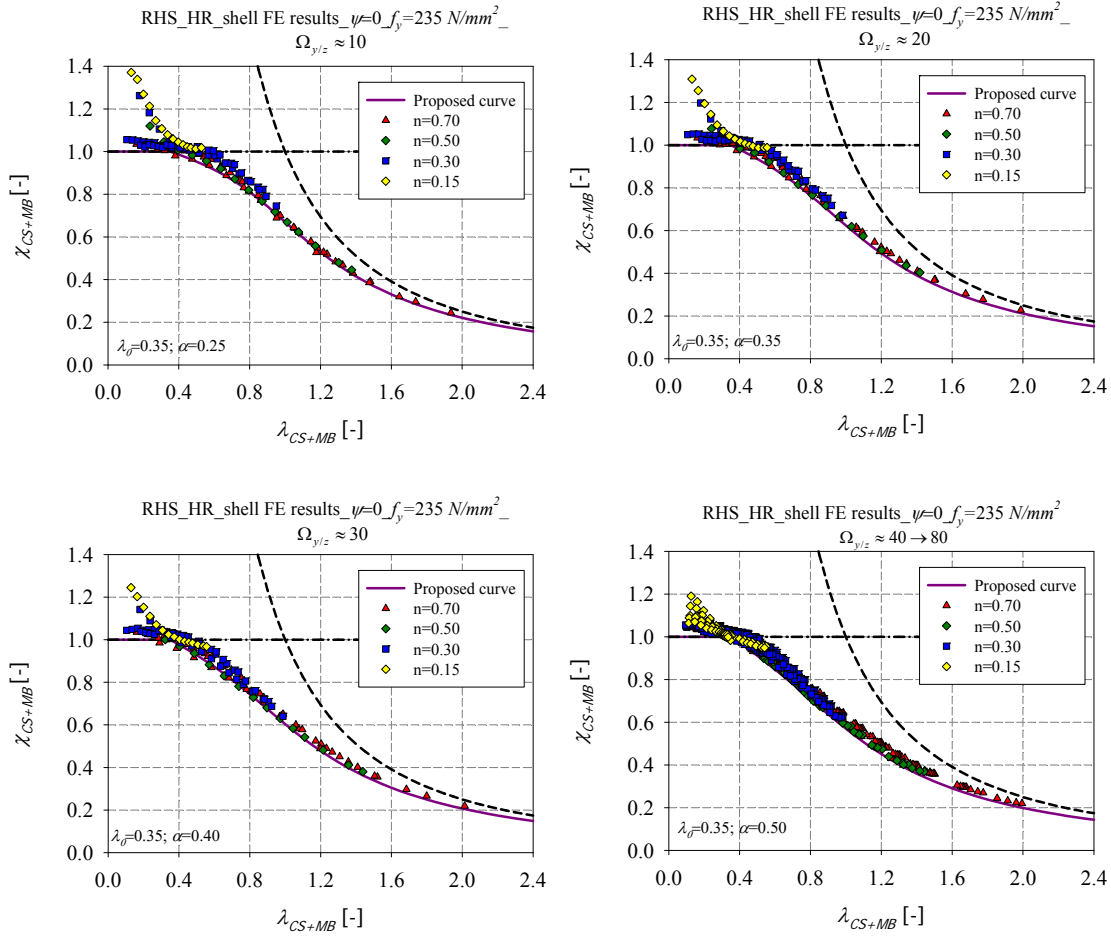


Figure 242 – Numerical member results for hot-rolled rectangular sections of steel grade $f_y = 235 \text{ N/mm}^2$ tested under different values of axial force ratio n

Figure 243 presents a variation of the imperfection factor based on the degree of biaxial bending for the case of hot-rolled rectangular sections, of steel grades $f_y = 235 \text{ N/mm}^2$ and $f_y = 355 \text{ N/mm}^2$, tested under compression and triangular bending moment distribution. With the inclusion of the $\Omega_{y/z}$ parameter, the proposed α formula becomes as follows:

$$\alpha = 0.50 \text{ for } \Omega_{y/z} \geq 40 \quad (222)$$

$$\alpha = 0.0075\Omega_{y/z} + 0.2 \text{ for } \Omega_{y/z} < 40 \quad (223)$$

That way, for $\Omega_{y/z} = 0$, Equation (223) is restored with the limiting curve being relative to compression with major-axis bending load case and for $\Omega_{y/z} = 90$, Equation (222) is restored with the limiting curve being relative to compression with minor-axis bending load case.

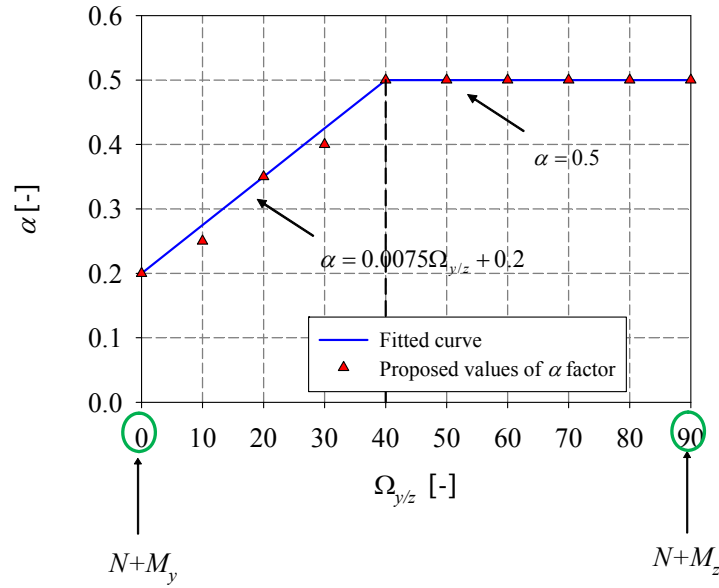


Figure 243 – Variation of α factor based on $\Omega_{y/z}$ for the case of hot-rolled RHS of steel grades $f_y = 235 \text{ N/mm}^2$ and $f_y = 355 \text{ N/mm}^2$, tested under compression and triangular bending moment

These equations can be written as follows, in order to provide smooth continuities with the pure compression load case:

$$\alpha = \alpha_{comp} + 0.25\eta_z^{0.2} \leq 0.5 \text{ for } \Omega_{y/z} \geq 40 \quad (224)$$

$$\alpha = 0.0075\Omega_{y/z} + \alpha_{comp} \leq 0.5 \text{ for } \Omega_{y/z} < 40 \quad (225)$$

That way, for $\Omega_{y/z} = 0$, Equation (225) is restored with the limiting curve being relative to the pure compression load case and for $\Omega_{y/z} = 90$ and $\eta_z = 0$, Equation (224) is restored with the limiting curve of the pure compression as well.

The same type of relationships can be found between α and $\Omega_{y/z}$ for high strength steel hollow sections, (i.e. $f_y = 690 \text{ N/mm}^2$) according to Equation (226) and Equation (227).

$$\alpha = 0.40 \text{ for } \Omega_{y/z} \geq 40 \quad (226)$$

$$\alpha = 0.0075\Omega_{y/z} + 0.1 \text{ for } \Omega_{y/z} < 40 \quad (227)$$

These equations can be written as follows, in order to provide smooth continuities with the pure compression load case:

$$\alpha = \alpha_{comp} + 0.25\eta_z^{0.2} \leq 0.40 \text{ for } \Omega_{y/z} \geq 40 \quad (228)$$

$$\alpha = 0.0075\Omega_{y/z} + \alpha_{comp} \leq 0.40 \text{ for } \Omega_{y/z} < 40 \quad (229)$$

6.4.2.3.3. Cold-formed square sections

Figure 244 illustrates the application of the O.I.C. for cold-formed square members tested under compression and triangular biaxial bending, for different steel grades: $f_y = 235 \text{ N/mm}^2$, $f_y = 355 \text{ N/mm}^2$ and $f_y = 690 \text{ N/mm}^2$. Results are obtained by adopting two values of the factor n ($n = 0.3$ and $n = 0.7$). Figure 245 highlights the influence of factor n for the particular case $f_y = 235 \text{ N/mm}^2$. One curve was adopted for the case of square sections, subjected to compression and biaxial bending, and this regardless of the degree of biaxial bending for sake of simplicity. The proposed curve in this case was lower than the curve proposed when the member is subjected to compression and mono-axial bending. A single interaction curve was again derived for $f_y = 235 \text{ N/mm}^2$ and $f_y = 355 \text{ N/mm}^2$, since a small dispersion in the results is noted. The end of plateau factor λ_0 was set to 0.35 and the imperfection factor α was set to 0.80. A higher resistance was observed for $f_y = 690 \text{ N/mm}^2$ and a higher curve was derived accordingly. The imperfection factor α can safely be set to 0.60.

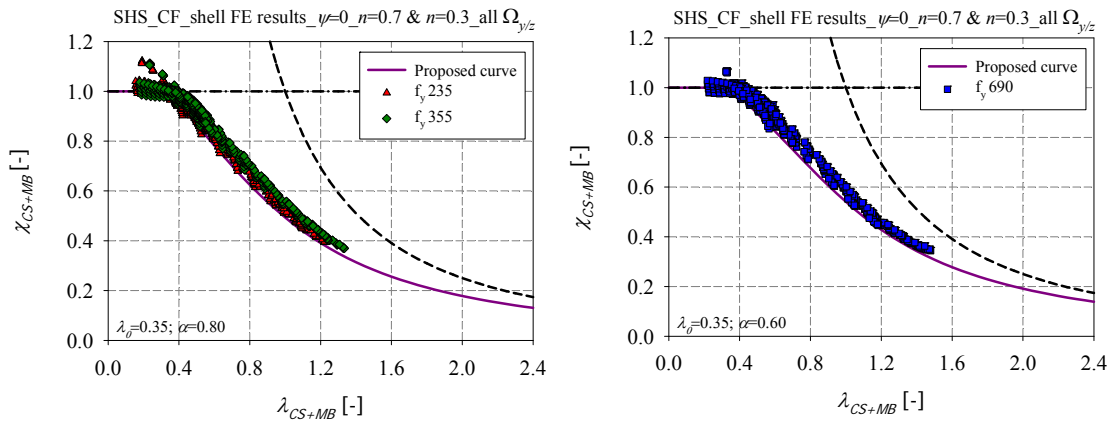


Figure 244 – Numerical member results of cold-formed SHS under different steel grades – a) $f_y = 235 \text{ N/mm}^2$ and $f_y = 355 \text{ N/mm}^2$ – b) $f_y = 690 \text{ N/mm}^2$

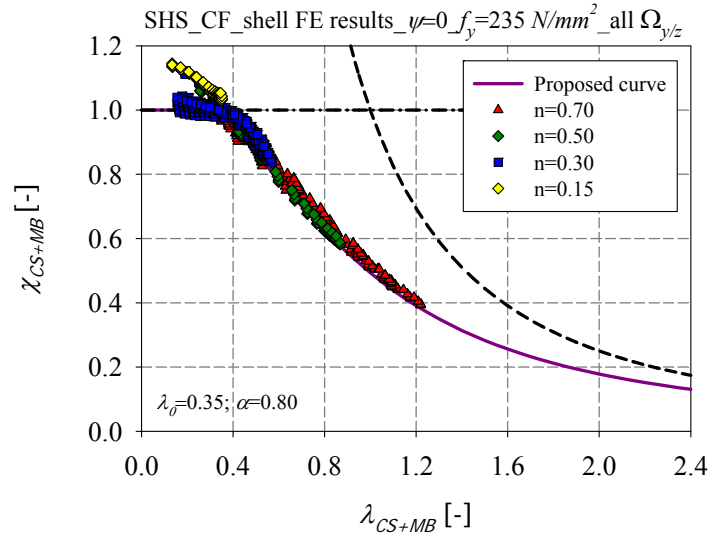


Figure 245 – Numerical member results of cold-formed SHS tested under different values of axial force ratio n for $f_y = 235 \text{ N/mm}^2$

With the inclusion of the $\Omega_{y/z}$ parameter, for cold-formed square sections of steel grades $f_y = 235 \text{ N/mm}^2$ and $f_y = 355 \text{ N/mm}^2$, the proposed α formula becomes as the following:

$$\alpha = 0.01\Omega_{y/z} + 0.7 \text{ for } \Omega_{y/z} \leq 10 \quad (230)$$

$$\alpha = 0.8 \text{ for } 10 \leq \Omega_{y/z} \leq 80 \quad (231)$$

$$\alpha = -0.01\Omega_{y/z} + 1.6 \text{ for } \Omega_{y/z} \geq 80 \quad (232)$$

That way, for $\Omega_{y/z} = 0$, Equation (230) is restored with the limiting curve being relative to compression with major-axis bending load case and for $\Omega_{y/z} = 90$, Equation (232) is restored with the limiting curve being relative to compression with minor-axis bending load case.

In order to provide a smooth continuity with the pure compression load case, the term 0.7 is replaced by $\alpha_{comp} + 0.25\eta^{0.2}$ as explained in section 6.4.2.1.3, and the proposed α formula becomes as the following:

$$\alpha = 0.01\Omega_{y/z} + \alpha_{comp} + 0.25\eta_y^{0.2} \leq 0.8 \text{ for } \Omega_{y/z} \leq 10 \quad (233)$$

$$\alpha = 0.8 \text{ for } 10 \leq \Omega_{y/z} \leq 80 \quad (234)$$

$$\alpha = -0.01\Omega_{y/z} + 0.9 + \alpha_{comp} + 0.25\eta_z^{0.2} \leq 0.8 \text{ for } \Omega_{y/z} \geq 80 \quad (235)$$

That way, for $\Omega_{y/z} = 0$ and $\eta_y = 0$, Equation (233) is restored with the limiting curve being relative to the pure compression load case and for $\Omega_{y/z} = 90$ and $\eta_z = 0$, Equation (235) is restored with the limiting curve of the pure compression as well.

The same type of relationships can be found between α and $\Omega_{y/z}$ for high strength steel hollow section, (i.e. $f_y = 690 \text{ N/mm}^2$) according to equations below:

$$\alpha = 0.015\Omega_{y/z} + 0.45 \text{ for } \Omega_{y/z} \leq 10 \quad (236)$$

$$\alpha = 0.6 \text{ for } 10 \leq \Omega_{y/z} \leq 80 \quad (237)$$

$$\alpha = -0.015\Omega_{y/z} + 1.8 \text{ for } \Omega_{y/z} \geq 80 \quad (238)$$

These equations can be written as follows, in order to provide smooth continuities with the pure compression load case:

$$\alpha = 0.015\Omega_{y/z} + \alpha_{comp} + 0.25\eta_y^{0.2} \leq 0.6 \text{ for } \Omega_{y/z} \leq 10 \quad (239)$$

$$\alpha = 0.60 \text{ for } 10 \leq \Omega_{y/z} \leq 80 \quad (240)$$

$$\alpha = -0.015\Omega_{y/z} + 1.35 + \alpha_{comp} + 0.25\eta_z^{0.2} \leq 0.6 \text{ for } \Omega_{y/z} \geq 80 \quad (241)$$

6.4.2.3.4. Cold-formed rectangular sections

Figure 246 and Figure 247 present results obtained for cold-formed rectangular members tested under compression and triangular biaxial bending moment, for different steel grades: $f_y = 235 \text{ N/mm}^2$, $f_y = 355 \text{ N/mm}^2$ and $f_y = 690 \text{ N/mm}^2$. The figures illustrate the influence of the degree of biaxial bending on the member response. A single curve was derived for $f_y = 235 \text{ N/mm}^2$ and $f_y = 355 \text{ N/mm}^2$ depending on the $\Omega_{y/z}$ value. Higher resistances are observed for $f_y = 690 \text{ N/mm}^2$ and higher curves were derived accordingly.

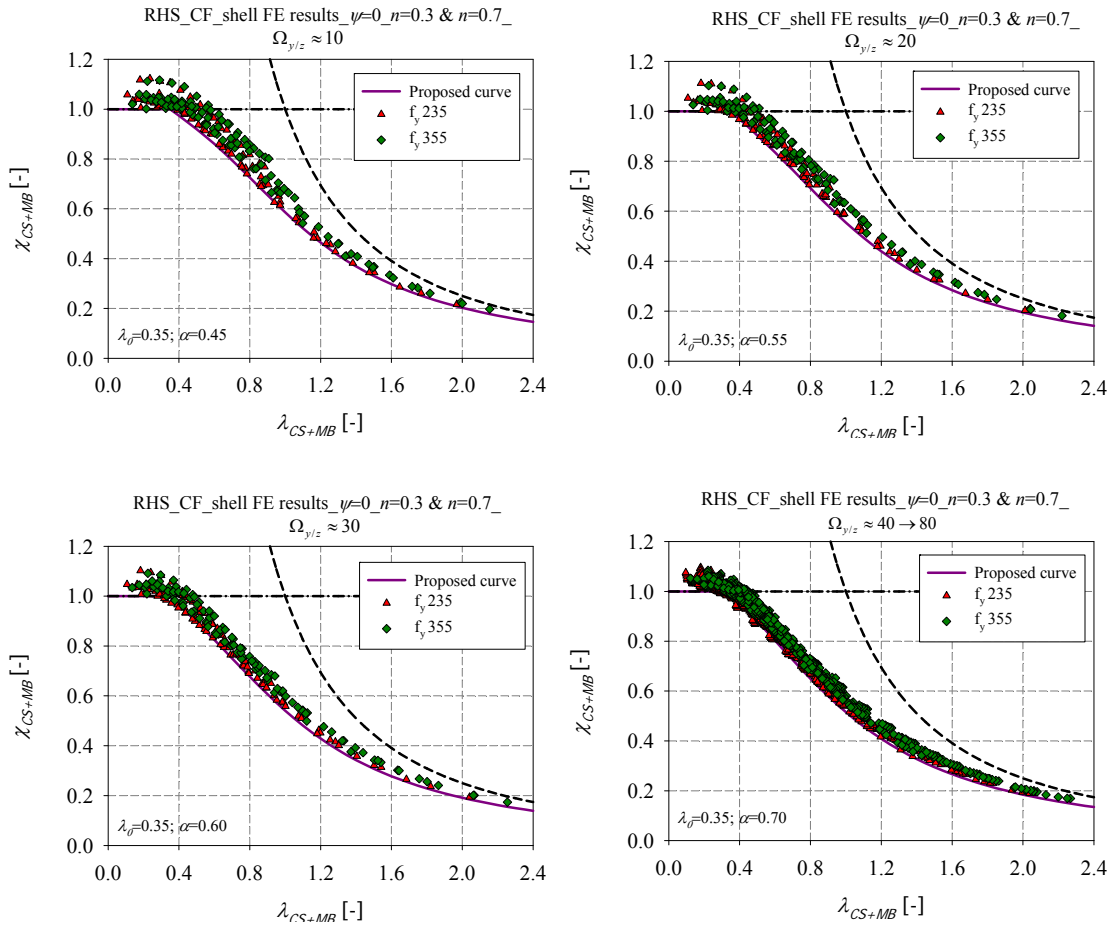
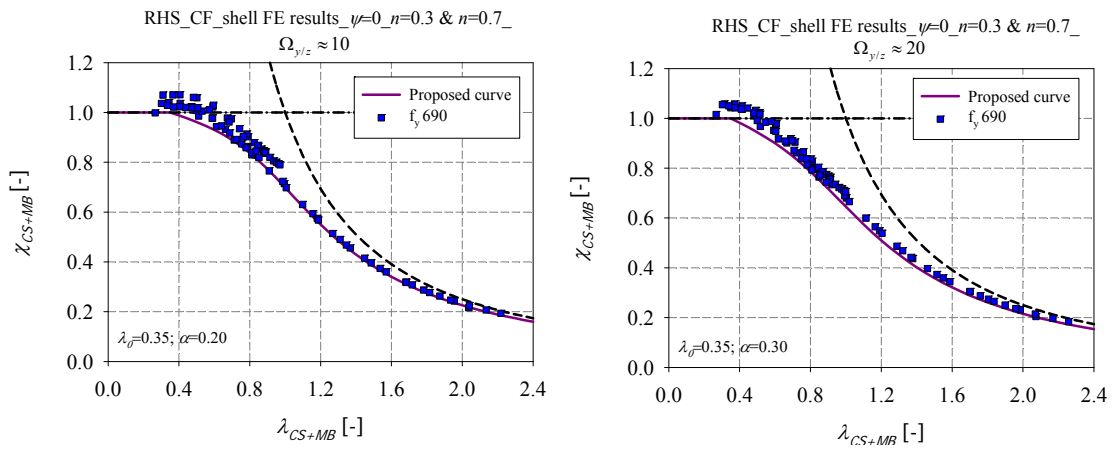


Figure 246 – Numerical member results of cold-formed RHS of steel grades $f_y = 235 \text{ N/mm}^2$ and $f_y = 355 \text{ N/mm}^2$, under $N+M_y+M_z$



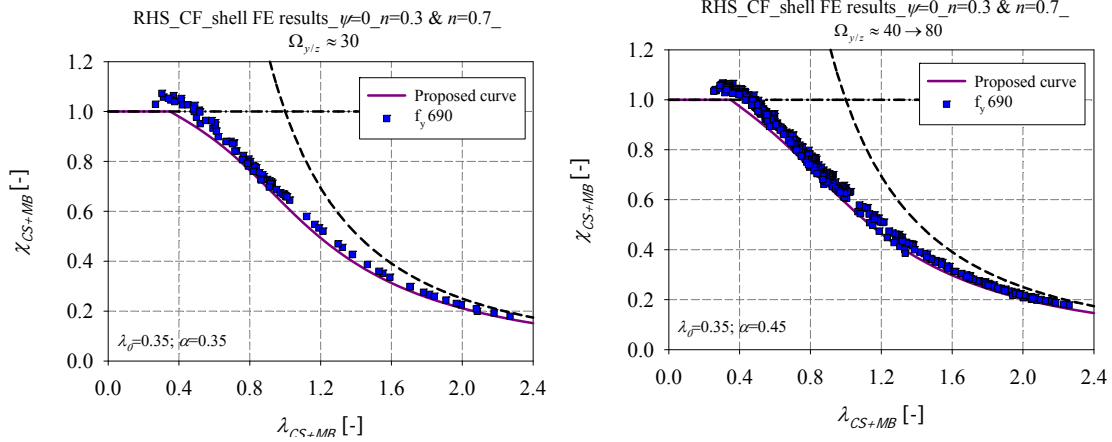


Figure 247 – Numerical member results of cold-formed RHS of steel grade $f_y = 690 \text{ N/mm}^2$ under $N+M_y+M_z$

Figure 248 presents the particular case of $f_y = 235 \text{ N/mm}^2$ for cold-formed RHS highlighting the influence of the axial force ratio n .

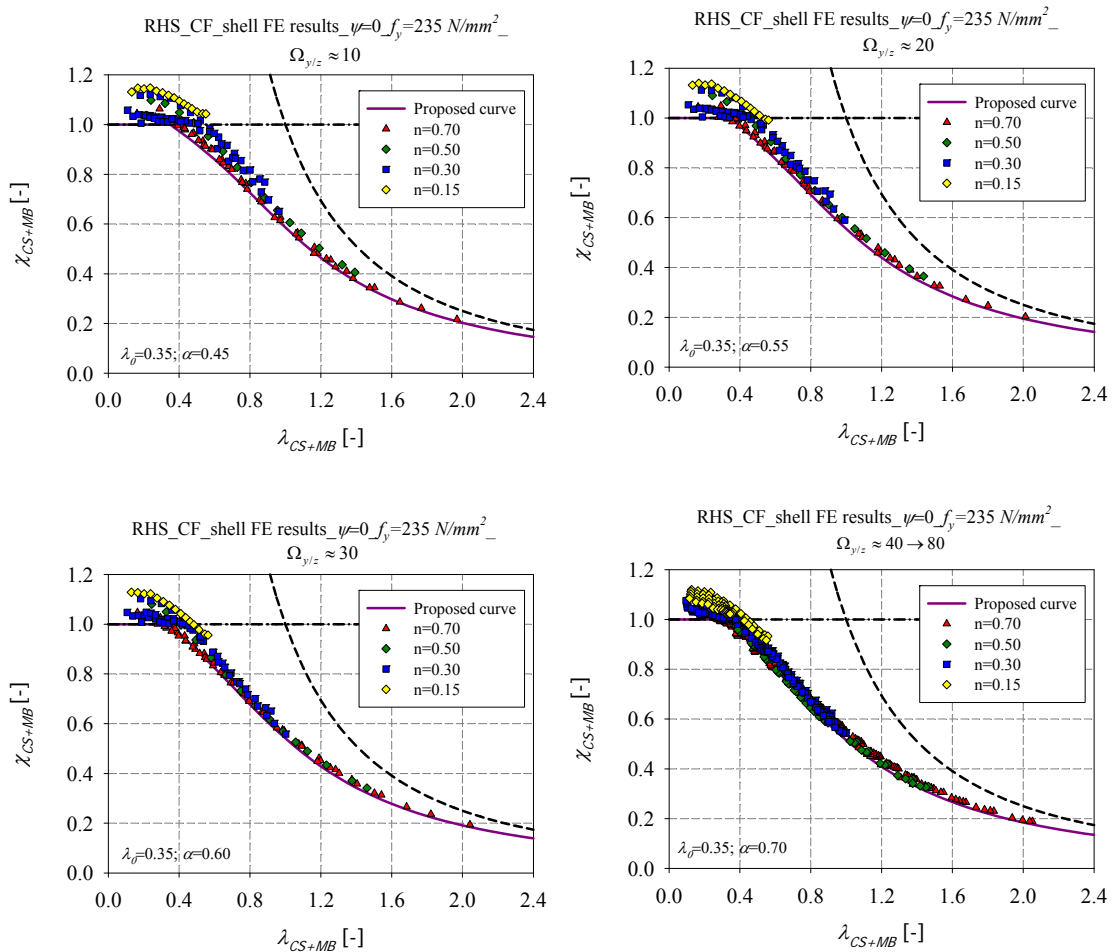


Figure 248 – Numerical member results of cold-formed RHS of steel grade $f_y = 235 \text{ N/mm}^2$ tested under different values of axial force ratio n

With the inclusion of the $\Omega_{y/z}$ parameter for cold-formed rectangular sections, of steel grades $f_y = 235 \text{ N/mm}^2$ and $f_y = 355 \text{ N/mm}^2$, the proposed α formula becomes as follows:

$$\alpha = 0.7 \text{ for } \Omega_{y/z} \geq 40 \quad (242)$$

$$\alpha = 0.0075\Omega_{y/z} + 0.4 \text{ for } \Omega_{y/z} < 40 \quad (243)$$

That way, for $\Omega_{y/z} = 0$, Equation (243) is restored with the limiting curve being relative to compression with major-axis bending load case and for $\Omega_{y/z} = 90$, Equation (242) is restored with the limiting curve being relative to compression with minor-axis bending load case.

These equations can be written as follows, in order to provide smooth continuities with the pure compression load case:

$$\alpha = \alpha_{comp} + 0.25\eta_z^{0.2} \leq 0.7 \text{ for } \Omega_{y/z} \geq 40 \quad (244)$$

$$\alpha = 0.0075\Omega_{y/z} + \alpha_{comp} \leq 0.7 \text{ for } \Omega_{y/z} < 40 \quad (245)$$

That way, for $\Omega_{y/z} = 0$ and $\eta_y = 0$, Equation (245) is restored with the limiting curve being relative to the pure compression load case and for $\Omega_{y/z} = 90$ and $\eta_z = 0$, Equation (244) is restored with the limiting curve of the pure compression as well.

The same type of relationships can be found between α and $\Omega_{y/z}$ for high strength steel rectangular hollow sections, (i.e. $f_y = 690 \text{ N/mm}^2$) according to Equation (246) and Equation (247).

$$\alpha = 0.45 \text{ for } \Omega_{y/z} \geq 40 \quad (246)$$

$$\alpha = 0.0075\Omega_{y/z} + 0.15 \text{ for } \Omega_{y/z} < 40 \quad (247)$$

These equations can be written as follows, in order to provide smooth continuities with the pure compression load case:

$$\alpha = \alpha_{comp} + 0.25\eta_z^{0.2} \leq 0.45 \text{ for } \Omega_{y/z} \geq 40 \quad (248)$$

$$\alpha = 0.0075\Omega_{y/z} + \alpha_{comp} \leq 0.45 \text{ for } \Omega_{y/z} < 40 \quad (249)$$

Table 41 summarizes the adopted parameters for the design curves of hot-rolled and cold-formed hollow members subjected to compression with triangular biaxial bending moment distribution.

Table 41 – Design curves for the case of hot-rolled and cold-formed members subjected to compression with triangular biaxial bending

Combined load cases: $N+M_y+M_z$			
Triangular bending moment distribution: $\psi = 0$			
$\chi_{CS+MB} = \frac{1}{\phi_{CS+MB} + \sqrt{\phi_{CS+MB}^2 - \lambda_{CS+MB}^2}} \text{ for } \lambda_{CS+MB} \geq \lambda_0$ $\text{With } \phi_{CS+MB} = 0.5(1 + \alpha(\lambda_{CS+MB} - \lambda_0) + \lambda_{CS+MB}^2)$ $\Omega_{y/z} = \arctan\left(\frac{m_z}{m_y}\right) = \arctan\left(\frac{M_z / M_{pl,z}}{M_y / M_{pl,y}}\right)$			
Yield stress			
$f_y = 235 \text{ N/mm}^2$ $f_y = 355 \text{ N/mm}^2$			
Cross-section	Fabrication process	λ_0	α
RHS	HR	$\lambda_0 = 0.2 + 0.2\eta_z^{0.2} \leq 0.35$ for $\Omega_{y/z} \geq 40$;	$\alpha = \alpha_{comp} + 0.25\eta_z^{0.2} \leq 0.5$ for $\Omega_{y/z} \geq 40$; $\alpha = 0.0075\Omega_{y/z} + \alpha_{comp} \leq 0.5$ for $\Omega_{y/z} < 40$.
	CF	$\lambda_0 = 0.2 + 0.2\eta_y^{0.2} \leq 0.35$ for $\Omega_{y/z} < 40$.	$\alpha = \alpha_{comp} + 0.25\eta_z^{0.2} \leq 0.7$ for $\Omega_{y/z} \geq 40$; $\alpha = 0.0075\Omega_{y/z} + \alpha_{comp} \leq 0.7$ for $\Omega_{y/z} < 40$.
SHS	HR	$\lambda_0 = 0.2 + 0.2\eta_y^{0.2} \leq 0.35$ for $\Omega_{y/z} \leq 10$; $\lambda_0 = 0.35$ for $10 \leq \Omega_{y/z} \leq 80$; $\lambda_0 = 0.2 + 0.2\eta_z^{0.2} \leq 0.35$ for $\Omega_{y/z} \geq 80$.	$\alpha = 0.015\Omega_{y/z} + \alpha_{comp} + 0.25\eta_y^{0.2} \leq 0.65$ for $\Omega_{y/z} \leq 10$; $\alpha = 0.65$ for $10 \leq \Omega_{y/z} \leq 80$; $\alpha = -0.015\Omega_{y/z} + 1.35 + \alpha_{comp} + 0.25\eta_z^{0.2} \leq 0.65$ for $\Omega_{y/z} \geq 80$.
	CF	$\lambda_0 = 0.2 + 0.2\eta_z^{0.2} \leq 0.35$ for $\Omega_{y/z} \geq 80$.	$\alpha = 0.01\Omega_{y/z} + \alpha_{comp} + 0.25\eta_y^{0.2} \leq 0.8$ for $\Omega_{y/z} \leq 10$; $\alpha = 0.8$ for $10 \leq \Omega_{y/z} \leq 80$; $\alpha = -0.01\Omega_{y/z} + 0.9 + \alpha_{comp} + 0.25\eta_z^{0.2} \leq 0.8$ for $\Omega_{y/z} \geq 80$.
Yield stress			
$f_y = 690 \text{ N/mm}^2$			
Cross-section	Fabrication process	λ_0	α

RHS	HR	$\lambda_0 = 0.2 + 0.2\eta_z^{0.2} \leq 0.35$ for $\Omega_{y/z} \geq 40$;	$\alpha = \alpha_{comp} + 0.25\eta_z^{0.2} \leq 0.4$ for $\Omega_{y/z} \geq 40$; $\alpha = 0.0075\Omega_{y/z} + \alpha_{comp} \leq 0.4$ for $\Omega_{y/z} < 40$.
	CF	$\lambda_0 = 0.2 + 0.2\eta_y^{0.2} \leq 0.35$ for $\Omega_{y/z} < 40$.	$\alpha = \alpha_{comp} + 0.25\eta_z^{0.2} \leq 0.45$ for $\Omega_{y/z} \geq 40$; $\alpha = 0.0075\Omega_{y/z} + \alpha_{comp} \leq 0.45$ for $\Omega_{y/z} < 40$.
SHS	HR	$\lambda_0 = 0.2 + 0.2\eta_y^{0.2} \leq 0.35$ for $\Omega_{y/z} \leq 10$; $\lambda_0 = 0.35$ for $10 \leq \Omega_{y/z} \leq 80$; $\lambda_0 = 0.2 + 0.2\eta_z^{0.2} \leq 0.35$ for $\Omega_{y/z} \geq 80$.	$\alpha = 0.015\Omega_{y/z} + \alpha_{comp} + 0.25\eta_y^{0.2} \leq 0.55$ for $\Omega_{y/z} \leq 10$; $\alpha = 0.55$ for $10 \leq \Omega_{y/z} \leq 80$; $\alpha = -0.015\Omega_{y/z} + 1.35 + \alpha_{comp} + 0.25\eta_z^{0.2} \leq 0.55$ for $\Omega_{y/z} \geq 80$.
	CF	$\lambda_0 = 0.2 + 0.2\eta_z^{0.2} \leq 0.35$ for $\Omega_{y/z} \geq 80$.	$\alpha = 0.015\Omega_{y/z} + \alpha_{comp} + 0.25\eta_y^{0.2} \leq 0.6$ for $\Omega_{y/z} \leq 10$; $\alpha = 0.6$ for $10 \leq \Omega_{y/z} \leq 80$; $\alpha = -0.015\Omega_{y/z} + 1.35 + \alpha_{comp} + 0.25\eta_z^{0.2} \leq 0.6$ for $\Omega_{y/z} \geq 80$.

6.4.3. Members under compression and constant bending moment distribution

In this section, the results displayed correspond to hot-rolled and cold-formed members tested under compression and constant bending moment. (i.e. $\psi = 1$).

The same sub study was undertaken including more values of the factor n , as for the case of members subjected to triangular bending moments (see section 6.4.2.), in an attempt to characterize more precisely the influence of this factor on the member resistance.

6.4.3.1. Compression and minor-axis bending cases

6.4.3.1.1. Hot-rolled square sections

Figure 249 and Figure 250 illustrate the application of the O.I.C. for hot-rolled square sections of different steel grades ($f_y = 235 \text{ N/mm}^2$, $f_y = 355 \text{ N/mm}^2$ and $f_y = 690 \text{ N/mm}^2$), tested under compression and constant minor-axis bending ($\psi = 1$). In these figures, the relative axial force ratio n defined as $n = N_{Ed} / N_{b,Rd}$ was chosen equal to 0.7. Close tendencies of member results computed using beam and shell models are observed.

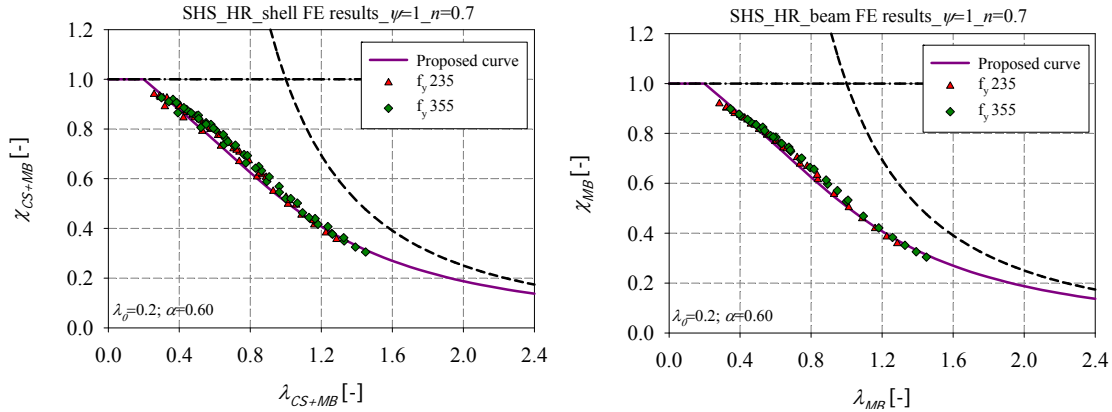


Figure 249 – Numerical member results of hot-rolled SHS of steel grades $f_y = 235 \text{ N/mm}^2$ and $f_y = 355 \text{ N/mm}^2$ under $N+M_z$ with $\psi = 1$ and $n = 0.7$ – a) shell results – b) beam results

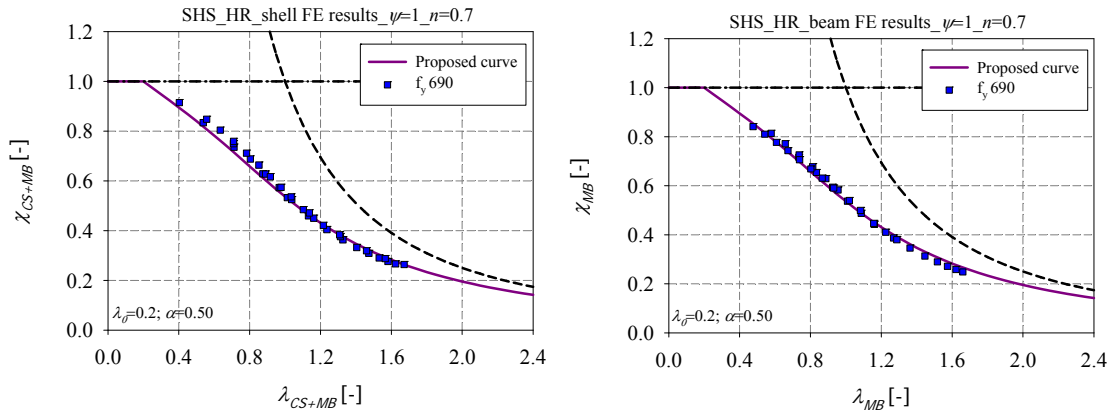


Figure 250 – Numerical member results of hot-rolled SHS of steel grade $f_y = 690 \text{ N/mm}^2$ under $N+M_z$ with $\psi = 1$ and $n = 0.7$ – a) shell results – b) beam results

Figure 251 and Figure 252 illustrate the results corresponding to hot-rolled square sections under compression and constant minor-axial bending with the relative axial force ratio n set equal to 0.3.

For each load case, a single interaction curve was derived for $f_y = 235 \text{ N/mm}^2$ and $f_y = 355 \text{ N/mm}^2$, since a small dispersion in the results is noticed. Higher resistances are observed for $f_y = 690 \text{ N/mm}^2$ and higher curves were derived accordingly. Figure 253 presents the particular case of $f_y = 235 \text{ N/mm}^2$ for hot-rolled square sections highlighting the influence of the axial force ratio n .

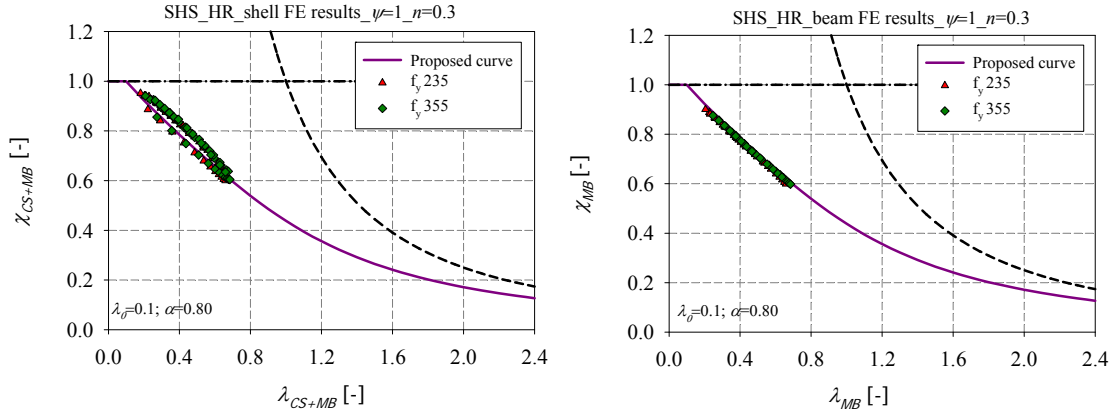


Figure 251 – Numerical member results of hot-rolled SHS of steel grades $f_y = 235 \text{ N/mm}^2$ and $f_y = 355 \text{ N/mm}^2$, under $N+M_z$ with $\psi = 1$ and $n = 0.3$ – a) shell results – b) beam results

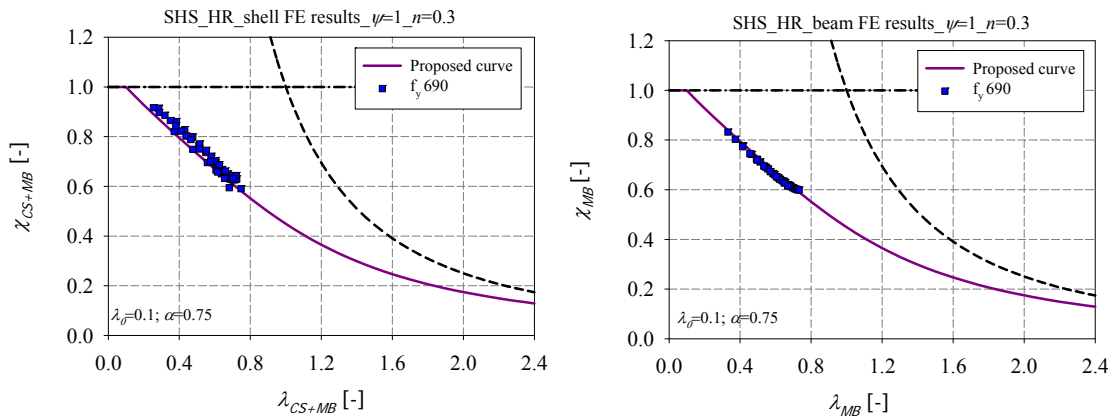


Figure 252 – Numerical member results of hot-rolled SHS of steel grade $f_y = 690 \text{ N/mm}^2$ under $N+M_z$ with $\psi = 1$ and $n = 0.3$ – a) shell – b) beam results

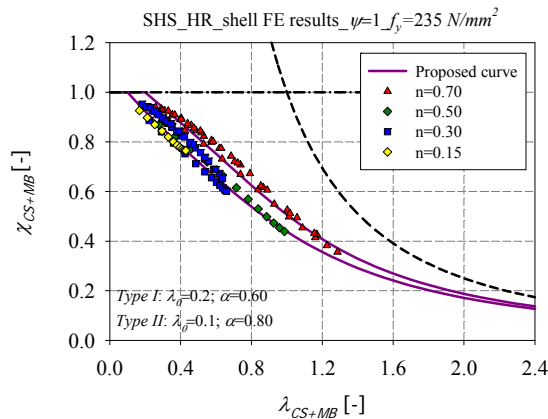


Figure 253 – Numerical member results of hot-rolled SHS of steel grade $f_y = 235 \text{ N/mm}^2$ tested under different values of axial force ratio n

One may notice that the relative axial force ratio n has a bigger influence on the member resistance if it is loaded under compression with constant bending moment than under compression with triangular bending moment. In the latter case, a part of the section is less loaded in bending and provides a level of restraint to the entire member, thus the influence of the bending moment is reduced along the member length. Accordingly, the deflection induced by the bending moment is bigger when a constant moment is applied and thus leads to a higher second-order effect and to a premature column buckling.

Accordingly, a leading parameter was defined according to Equation (250) and was used to sort the results regardless of the axial force ratio n .

$$\eta_z = \frac{m_z}{n_z} = \frac{M_z / M_{pl,z}}{N / N_{pl}} \quad (250)$$

In Equation (250), N_{pl} and $M_{pl,z}$ are the plastic cross-section resistance for pure axial force, and for pure bending moment about the weak axis respectively; N and M_z are the ultimate axial force, and ultimate bending moment about the weak axis, respectively.

The factor η was proposed by Taras [82].

It should be mentioned that dispersion is noticed in results, when the member is subjected to axial force ratios $n = 0.3$ and $n = 0.7$, where different cross-section shapes were tested; whereas for $n = 0.15$ and $n = 0.5$, only one section shape was tested since negligible differences in results were observed for different cross-section shapes.

Two curves were first derived according to the parameter η_z (see Figure 254). The limits of the parameter η_z ($0 < \eta_z \leq 0.9$ and $\eta_z > 0.9$) were chosen according to the results of steel grade $f_y = 235 \text{ N/mm}^2$. For higher steel grades, one may notice that the upper limit of the parameter η_z should be increased. However, the same limits of the parameter η_z derived for $f_y = 235 \text{ N/mm}^2$ were kept for higher steel grades, for sake of simplicity and consistency, since they lead to conservative results (see green circles for high values of λ_{CS+MB}).

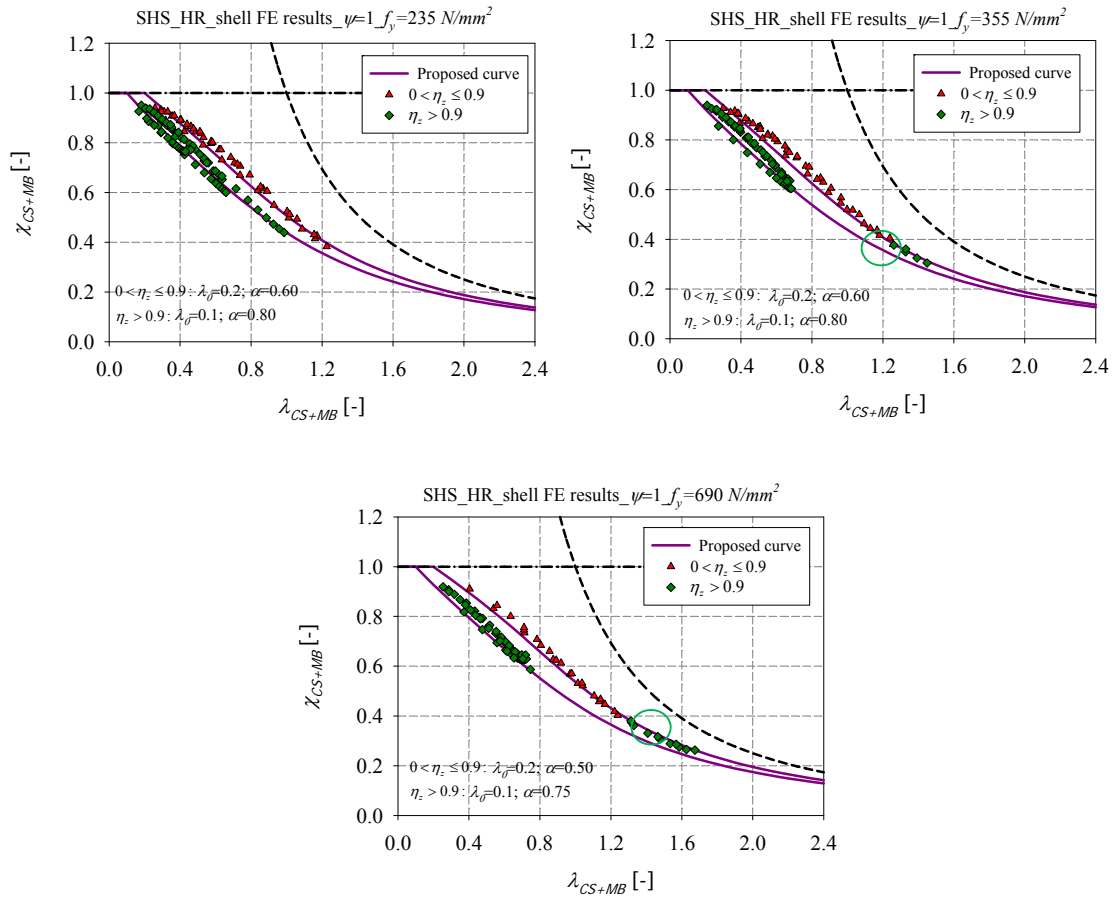


Figure 254 – Numerical member results of hot-rolled SHS derived according to the parameter η_z under different steel grades – a) $f_y = 235$ N/mm² – b) $f_y = 355$ N/mm² – c) $f_y = 690$ N/mm²

One may notice that, the proposed curves present a discontinuity in the transition between $0 < \eta_z \leq 0.9$ and $\eta_z > 0.9$. Such discontinuity has no physical meaning and could lead to conservative or to unconservative results and to uneconomical beam-column capacities. In order to overcome this shortcoming, a linear interpolation is defined for the transition of the beam-column resistance from one curve to the other. Thus a smooth conservative continuity is provided with the new proposed design curves.

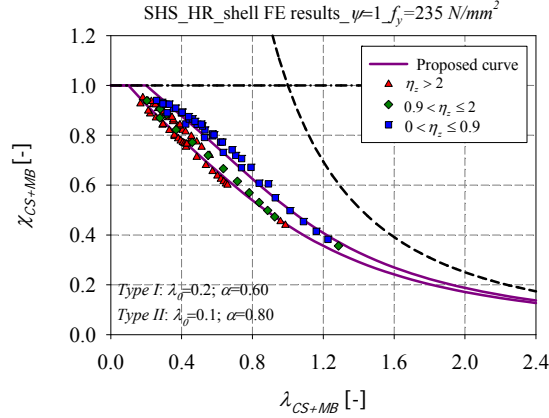


Figure 255 – Numerical member results for hot-rolled SHS of steel grade $f_y = 235 \text{ N/mm}^2$ derived according to the parameter η_z

With the inclusion of the η_z parameter, the proposed α formula becomes as the following for hot-rolled square sections of steel grades $f_y = 235 \text{ N/mm}^2$ and $f_y = 355 \text{ N/mm}^2$:

$$\alpha = \alpha_1 = 0.6 \text{ for } 0 < \eta_z \leq \eta_{z,1} = 0.9 \quad (251)$$

$$\alpha = \left(\frac{\alpha_2 - \alpha_1}{\eta_{z,2} - \eta_{z,1}} \right) (\eta_z - \eta_{z,2}) + \alpha_2 \text{ for } 0.9 < \eta_z \leq 2 \quad (252)$$

$$\alpha = \alpha_2 = 0.90 \text{ for } \eta_z > \eta_{z,2} = 2 \quad (253)$$

With the inclusion of α_{comp} factor which represents the imperfection factor derived for members tested under pure compression load case, Equation (251) can be written as follows:

$$\alpha = \alpha_1 = \alpha_{comp} + 0.4\eta_z^{0.2} \text{ for } 0 \leq \eta_z \leq \eta_{z,1} = 0.9 \quad (254)$$

That way, for $\eta_z = 0$, Equation (254) is restored with the limiting curve being relative to the pure compression load case.

The proposed λ_0 formula becomes as the following:

$$\lambda_0 = 0.2 \text{ for } 0 \leq \eta_z \leq \eta_{z,1} = 0.9 \quad (255)$$

$$\lambda_0 = \left(-\frac{0.1}{\eta_{z,2} - \eta_{z,1}} \right) (\eta_z - \eta_{z,2}) + 0.1 \text{ for } 0.9 < \eta_z \leq 2 \quad (256)$$

$$\lambda_0 = 0.1 \text{ for } \eta_z > \eta_{z,2} = 2 \quad (257)$$

The same type of relationships can be found between η_z and α for high strength steel hollow section, (i.e. $f_y = 690 \text{ N/mm}^2$) according to equations below:

$$\alpha = \alpha_1 = 0.5 \text{ for } 0 < \eta_z \leq \eta_{z,1} = 0.9 \quad (258)$$

$$\alpha = \left(\frac{\alpha_2 - \alpha_1}{\eta_{z,2} - \eta_{z,1}} \right) (\eta_z - \eta_{z,1}) + \alpha_1 \text{ for } 0.9 < \eta_z \leq 2 \quad (259)$$

$$\alpha = \alpha_2 = 0.75 \text{ for } \eta_z > \eta_{z,2} = 2 \quad (260)$$

Equation (258) can be written as follows, in order to provide smooth continuities with the pure compression load case:

$$\alpha = \alpha_1 = \alpha_{comp} + 0.4\eta_z^{0.2} \text{ for } 0 \leq \eta_z \leq \eta_{z,1} = 0.9 \quad (261)$$

That way, for $\eta_z = 0$, Equation (261) is restored with the limiting curve being relative to the pure compression load case.

The proposed λ_0 formula becomes as the following:

$$\lambda_0 = 0.2 \text{ for } 0 \leq \eta_z \leq \eta_{z,1} = 0.9 \quad (262)$$

$$\lambda_0 = \left(-\frac{0.1}{\eta_{z,2} - \eta_{z,1}} \right) (\eta_z - \eta_{z,1}) + 0.2 \text{ for } 0.9 < \eta_z \leq 2 \quad (263)$$

$$\lambda_0 = 0.1 \text{ for } \eta_z > \eta_{z,2} = 2 \quad (264)$$

6.4.3.1.2. Hot-rolled rectangular sections

The same curves adopted for the square sections were again adopted for the rectangular ones. Figure 256 and Figure 257 present results obtained for hot-rolled rectangular members tested under compression and constant minor-axis bending, modelled numerically by shell and beam elements, for different steel grades: $f_y = 235 \text{ N/mm}^2$, $f_y = 355 \text{ N/mm}^2$ and $f_y = 690 \text{ N/mm}^2$. In these figures, the relative axial force ratio n was chosen equal to 0.7. The dispersion in results noticed for sections having the same yield stress is due to the influence of the cross-section shape. Figure 258 and Figure 259 illustrate the same set of results with a relative axial force n set equal to 0.3.

For each load case, a single interaction curve was derived for $f_y = 235 \text{ N/mm}^2$ and $f_y = 355 \text{ N/mm}^2$, since a small dispersion in the results is noted. Higher resistances are observed for $f_y = 690 \text{ N/mm}^2$ and higher curves were derived accordingly. Figure 260 presents the particular case of $f_y = 235 \text{ N/mm}^2$ for hot-rolled RHS highlighting the influence of the axial force n . One may notice that the results may be derived into two interaction curves depending on the relative axial force n .

In Figure 261, the defined leading parameter η_z was used to sort the results regardless of the axial force ratio n . It is clearly shown that the ratio η_z can rule the differences in scatter for a given ψ value. The limits of the parameter η_z were again chosen according to the results of steel grade $f_y = 235 \text{ N/mm}^2$. For higher steel grades, one may notice that the upper limit of the parameter η_z should be increased. However, the same limits of the parameter η_z derived for $f_y = 235 \text{ N/mm}^2$ were kept for higher steel grades, for sake of simplicity and consistency.

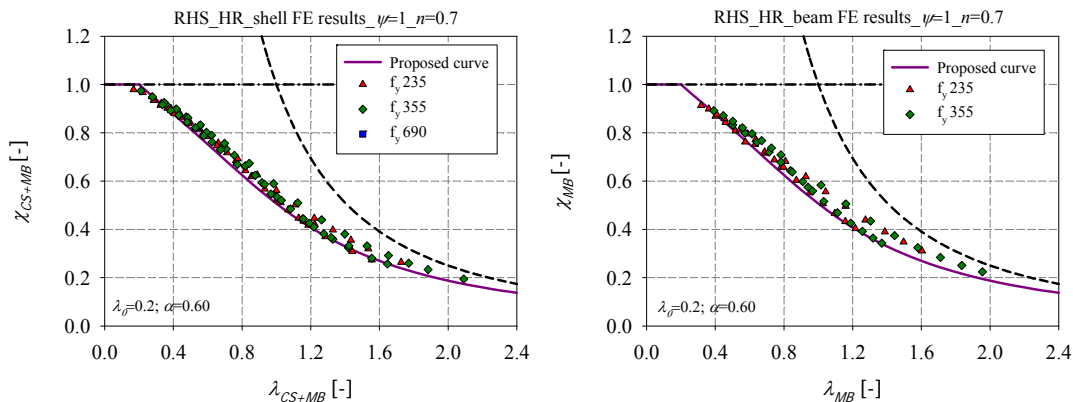


Figure 256 – Numerical member results of hot-rolled RHS of steel grades $f_y = 235 \text{ N/mm}^2$ and $f_y = 355 \text{ N/mm}^2$ under $N+M_z$ with $\psi = 1$ and $n = 0.7$ – a) shell results – b) beam results

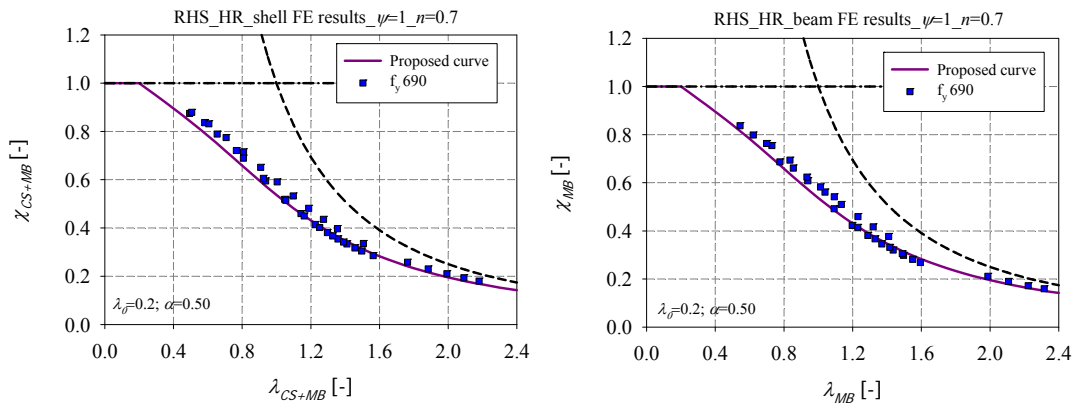


Figure 257 – Numerical member results of hot-rolled RHS of steel grade $f_y = 690 \text{ N/mm}^2$ under $N+M_z$ with $\psi = 1$ and $n = 0.7$ – a) shell results – b) beam results

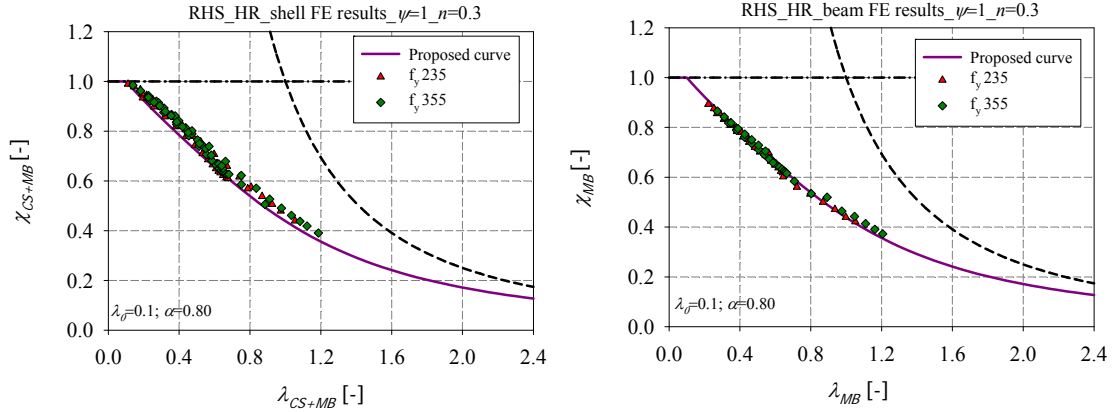


Figure 258 – Numerical member results for hot-rolled RHS of grades $f_y = 235 \text{ N/mm}^2$ and $f_y = 355 \text{ N/mm}^2$ under $N+M_z$ with $\psi = 1$ and $n = 0.3$ – a) shell results – b) beam results

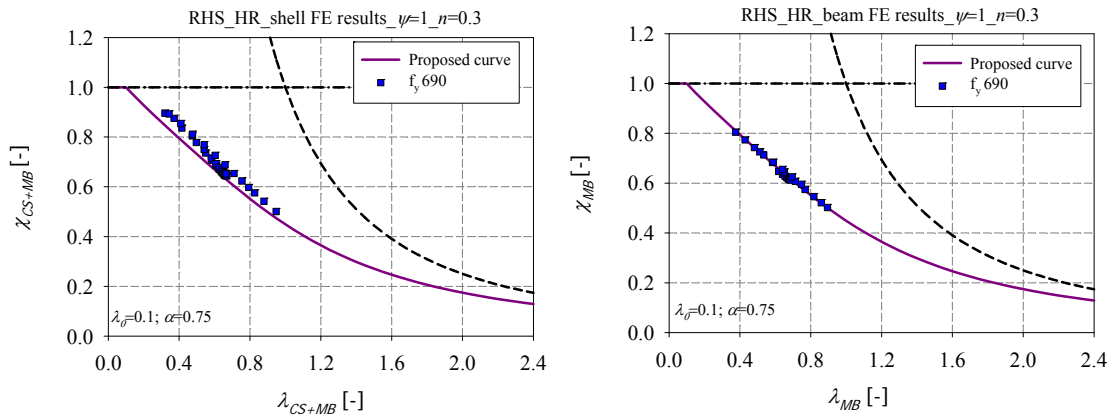


Figure 259 – Numerical member results for hot-rolled RHS of steel grade $f_y = 690 \text{ N/mm}^2$ under $N+M_z$ with $\psi = 1$ and $n = 0.3$ – a) shell results – b) beam results

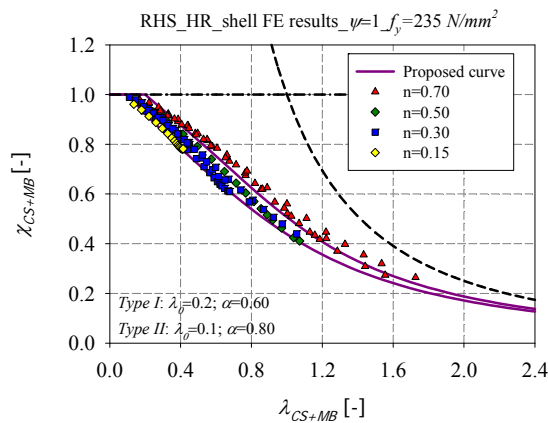


Figure 260 – Numerical member results for hot-rolled RHS of steel grade $f_y = 235 \text{ N/mm}^2$ tested under different values of axial force ratio n

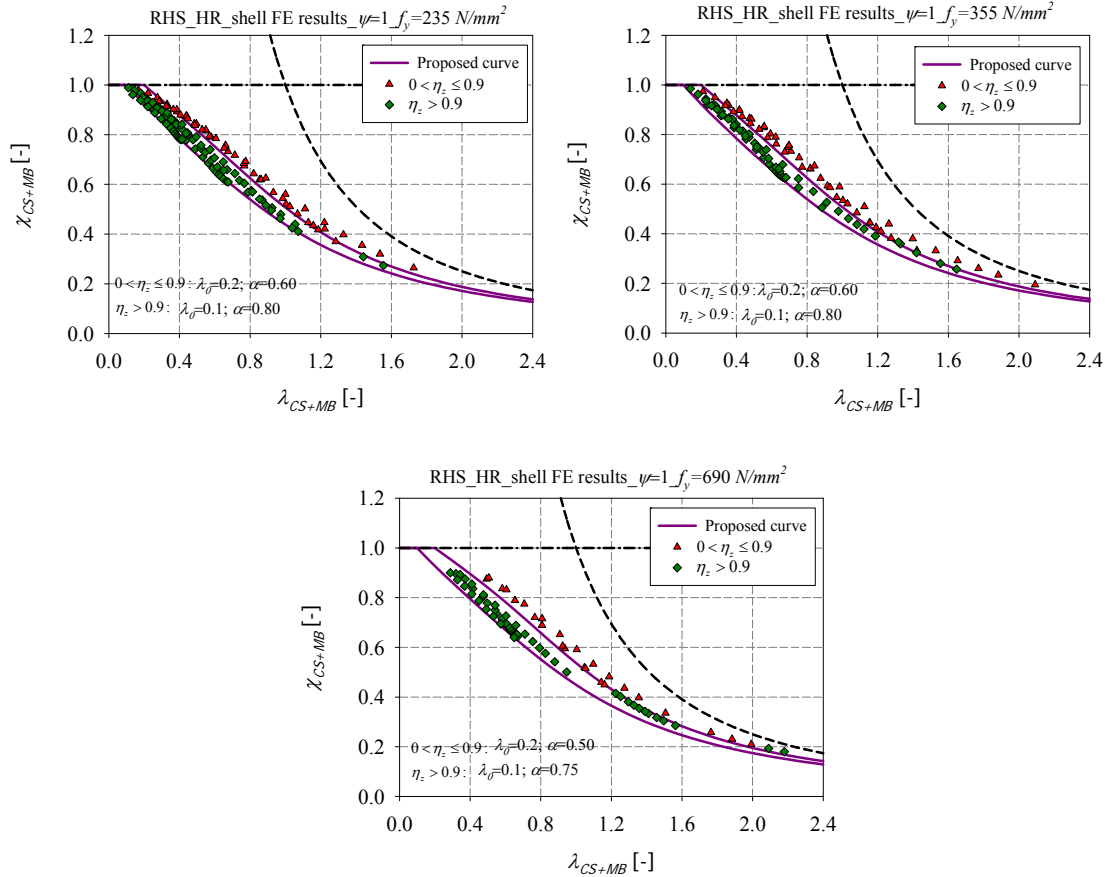


Figure 261 – Numerical member results for hot-rolled RHS derived according to the parameter η_z under different steel grades – a) $f_y = 235$ N/mm² – b) $f_y = 355$ N/mm² – c) $f_y = 690$ N/mm²

In order to overcome the discontinuity noticed with the proposed design curves, a linear interpolation is defined for the transition between the curves corresponding to $0 < \eta_z \leq 0.9$ and $\eta_z > 0.9$. The same relations adopted for the square sections between η_z and α on one hand, and between η_z and λ_0 on the other, were again adopted for the rectangular one.

Figure 262 illustrates numerical results for hot-rolled RHS of nominal steel grade $f_y = 235$ N/mm² subjected to compression and minor-axis bending, where a smooth conservative continuity is provided with the new proposed design curves.

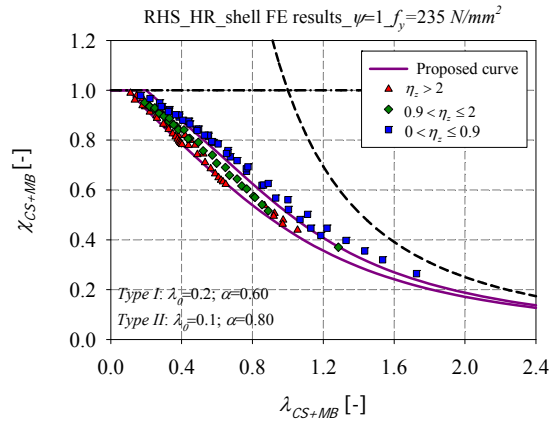


Figure 262 – Numerical member results of hot-rolled RHS of steel grade $f_y = 235 \text{ N/mm}^2$ derived according to the parameter η_z

6.4.3.1.3. Cold-formed square sections

Figure 263 and Figure 264 illustrate the application of the O.I.C. for cold-formed square sections of different steel grades ($f_y = 235 \text{ N/mm}^2$, $f_y = 355 \text{ N/mm}^2$ and $f_y = 690 \text{ N/mm}^2$) under compression and constant minor-axial bending. In these figures, the relative axial force ratio n defined as $n = N_{Ed} / N_{b,Rd}$ was chosen equal to 0.7 and 0.3. For each load case, a single interaction curve was derived for $f_y = 235 \text{ N/mm}^2$ and $f_y = 355 \text{ N/mm}^2$, since a small dispersion in the results is noted. Higher resistances are observed for $f_y = 690 \text{ N/mm}^2$ and higher curves were derived accordingly. Figure 265 presents the particular case of $f_y = 235 \text{ N/mm}^2$ for cold-formed square sections highlighting the influence of the axial force ratio n . One may notice that the results may be derived into two independent interaction curves depending on the relative axial force n . In Figure 266, the defined leading parameter η_z was used to sort the results regardless of the axial force ratio n . It is clearly shown that the ratio η_z can rule the differences in scatter for a given ψ value. The limits of the parameter η_z were again chosen according to the results of steel grade $f_y = 235 \text{ N/mm}^2$. For higher steel grades, one may notice that the upper limit of the parameter η_z should be increased. However, the same limits of the parameter η_z derived for $f_y = 235 \text{ N/mm}^2$ were kept for higher steel grades, for sake of simplicity and consistency.

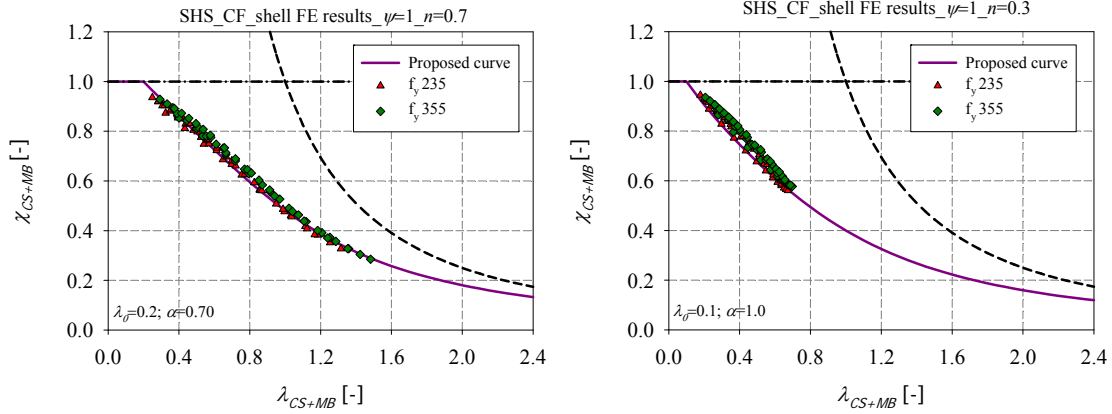


Figure 263 – Numerical member results of cold-formed SHS of steel grades $f_y = 235 \text{ N/mm}^2$ and $f_y = 355 \text{ N/mm}^2$ under $N+M_z$ with $\psi = 1$ with – a) $n = 0.7$ – b) $n = 0.3$

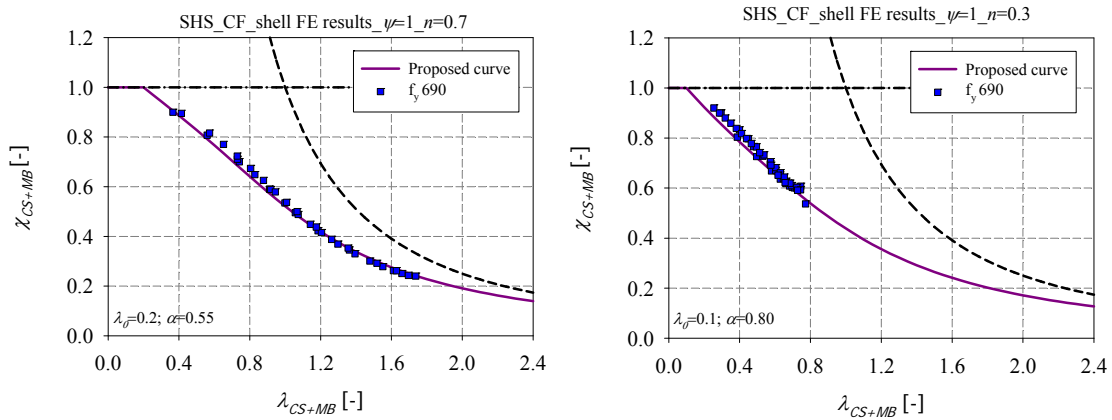


Figure 264 – Numerical member results for cold-formed SHS of steel grade $f_y = 690 \text{ N/mm}^2$ under $N+M_z$ with $\psi = 1$ with – a) $n = 0.7$ – b) $n = 0.3$

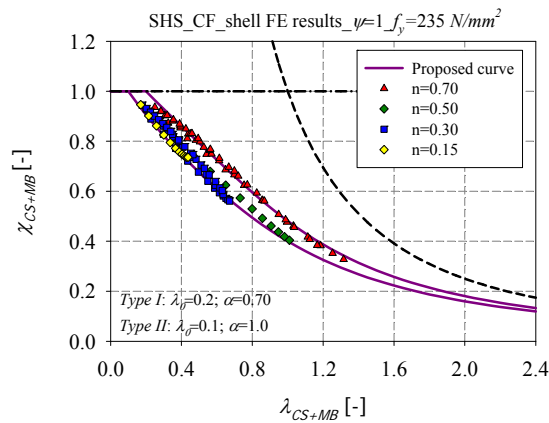


Figure 265 – Numerical member results for cold-formed SHS of steel grade $f_y = 235 \text{ N/mm}^2$ tested under different values of axial force ratio n

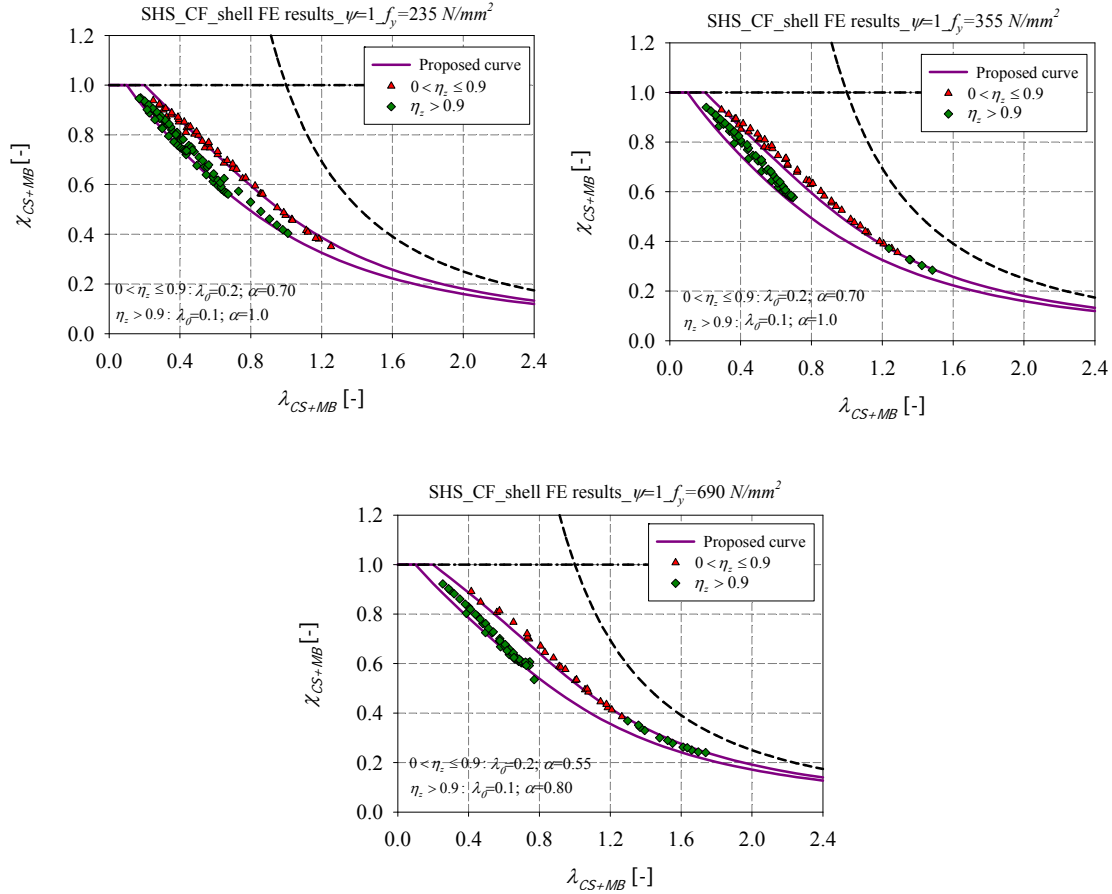


Figure 266 – Numerical member results of cold-formed SHS derived according to the parameter η_z under different steel grades – a) $f_y = 235 \text{ N/mm}^2$ – b) $f_y = 355 \text{ N/mm}^2$ – c) $f_y = 690 \text{ N/mm}^2$

In order to overcome the discontinuity noticed with the proposed design curves, a linear interpolation is defined for the transition between the curves corresponding to $0 < \eta_z \leq 0.9$ and $\eta_z > 0.9$. The proposed α formula becomes as the following for cold-formed square sections of steel grade $f_y = 235 \text{ N/mm}^2$ and $f_y = 355 \text{ N/mm}^2$:

$$\alpha = \alpha_1 = 0.70 \text{ for } 0 \leq \eta_z \leq \eta_{z,1} = 0.9 \quad (265)$$

$$\alpha = \left(\frac{\alpha_2 - \alpha_1}{\eta_{z,2} - \eta_{z,1}} \right) (\eta_z - \eta_{z,1}) + \alpha_1 \text{ for } \eta_{z,1} < \eta_z \leq \eta_{z,2} \quad (266)$$

$$\alpha = \alpha_2 = 1.0 \text{ for } \eta_z > \eta_{z,2} = 2 \quad (267)$$

Equation (265) can be written as follows, in order to provide smooth continuities with the pure compression load case:

$$\alpha = \alpha_1 = \alpha_{comp} + 0.4\eta_z^{0.2} \text{ for } 0 \leq \eta_z \leq \eta_{z,1} = 0.9 \quad (268)$$

The proposed λ_0 formula becomes as the following:

$$\lambda_0 = 0.2 \text{ for } 0 < \eta_z \leq \eta_{z,1} = 0.9 \quad (269)$$

$$\lambda_0 = \left(-\frac{0.1}{\eta_{z,2} - \eta_{z,1}} \right) (\eta_z - \eta_{z,2}) + 0.1 \text{ for } 0.9 < \eta_z \leq 2 \quad (270)$$

$$\lambda_0 = 0.1 \text{ for } \eta_z > \eta_{z,2} = 2 \quad (271)$$

The same type of relationships can be found between η_z and α for high strength steel hollow section, (i.e. $f_y = 690 \text{ N/mm}^2$) according to the equations below:

$$\alpha = \alpha_1 = 0.55 \text{ for } 0 < \eta_z \leq \eta_{z,1} = 0.9 \quad (272)$$

$$\alpha = \left(\frac{\alpha_2 - \alpha_1}{\eta_{z,2} - \eta_{z,1}} \right) (\eta_z - \eta_{z,2}) + \alpha_2 \text{ for } 0.9 < \eta_z \leq 2 \quad (273)$$

$$\alpha = \alpha_2 = 0.80 \text{ for } \eta_z > \eta_{z,2} = 2 \quad (274)$$

Equation (272) can be written as follows, in order to provide smooth continuities with the pure compression load case:

$$\alpha = \alpha_1 = \alpha_{comp} + 0.4\eta_z^{0.2} \text{ for } 0 \leq \eta_z \leq \eta_{z,1} = 0.9 \quad (275)$$

The proposed λ_0 formula becomes as the following:

$$\lambda_0 = 0.2 \text{ for } 0 < \eta_z \leq \eta_{z,1} = 0.9 \quad (276)$$

$$\lambda_0 = \left(-\frac{0.1}{\eta_{z,2} - \eta_{z,1}} \right) (\eta_z - \eta_{z,2}) + 0.1 \text{ for } 0.9 < \eta_z \leq 2 \quad (277)$$

$$\lambda_0 = 0.1 \text{ for } \eta_z > \eta_{z,2} = 2 \quad (278)$$

The numerical results are derived according to the defined limits of the parameter η_z (see Figure 267).

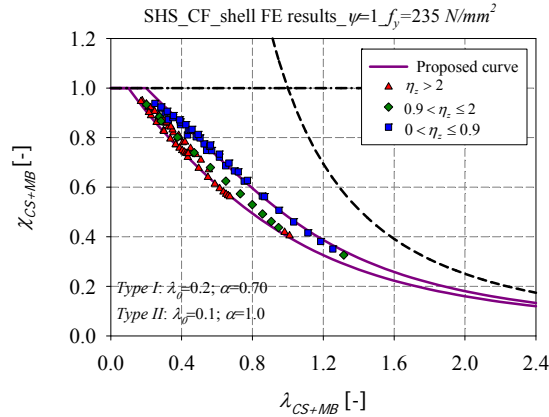


Figure 267 – Numerical member results of cold-formed SHS of steel grade $f_y = 235 \text{ N/mm}^2$ derived according to the parameter η_z

6.4.3.1.4. Cold-formed rectangular hollow sections

Figure 268 and Figure 269 illustrates the application of the O.I.C. for cold-formed rectangular sections of different steel grades ($f_y = 235 \text{ N/mm}^2$, $f_y = 355 \text{ N/mm}^2$ and $f_y = 690 \text{ N/mm}^2$), tested under compression and constant minor-axial bending. In these figures, the relative axial force ratio n defined as $n = N_{Ed} / N_{b,Rd}$ was chosen equal to 0.7 and 0.3. For each load case, a single interaction curve was derived for $f_y = 235 \text{ N/mm}^2$ and $f_y = 355 \text{ N/mm}^2$, since a small dispersion in the results is noted. Higher resistances are observed for $f_y = 690 \text{ N/mm}^2$ and higher curves were derived accordingly.

Figure 270 presents the particular case of $f_y = 235 \text{ N/mm}^2$ for cold-formed rectangular sections highlighting the influence of the axial force ratio n . One may notice that the results may be derived into two independent interaction curves depending on the relative axial force n , and that similar results to square hollow sections are obtained for the rectangular hollow sections. The same curves adopted for the square sections tested under $N+M_z$, were again adopted for the rectangular ones.

In Figure 271, the defined leading parameter η_z was used to sort the results regardless of the axial force ratio n . It is clearly shown that the ratio η_z can rule the differences in scatter for a given ψ value. The limits of the parameter η_z were again chosen according to the results of steel grade $f_y = 235 \text{ N/mm}^2$ for sake of simplicity and consistency.

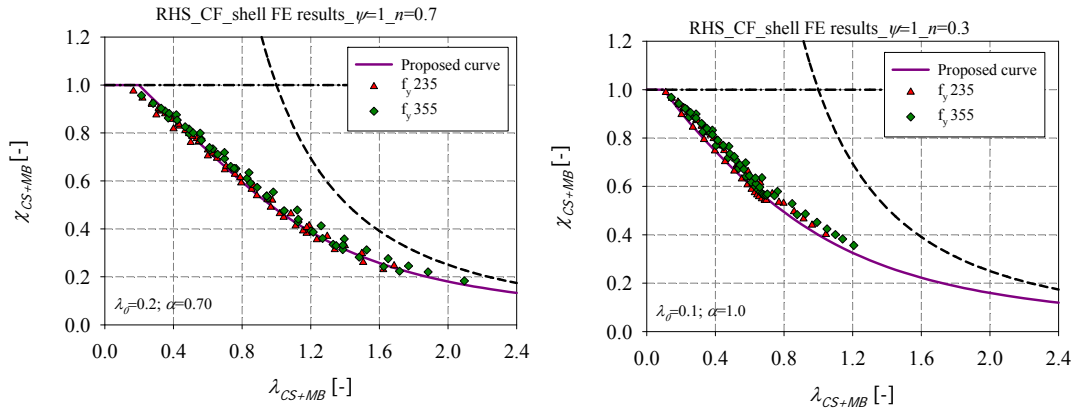


Figure 268 – Numerical member results of cold-formed RHS of steel grades $f_y = 235 \text{ N/mm}^2$ and $f_y = 355 \text{ N/mm}^2$, tested under $N+M_z$ with $\psi = 1$ and under different axial force level – a) $n = 0.7$ – b) $n = 0.3$

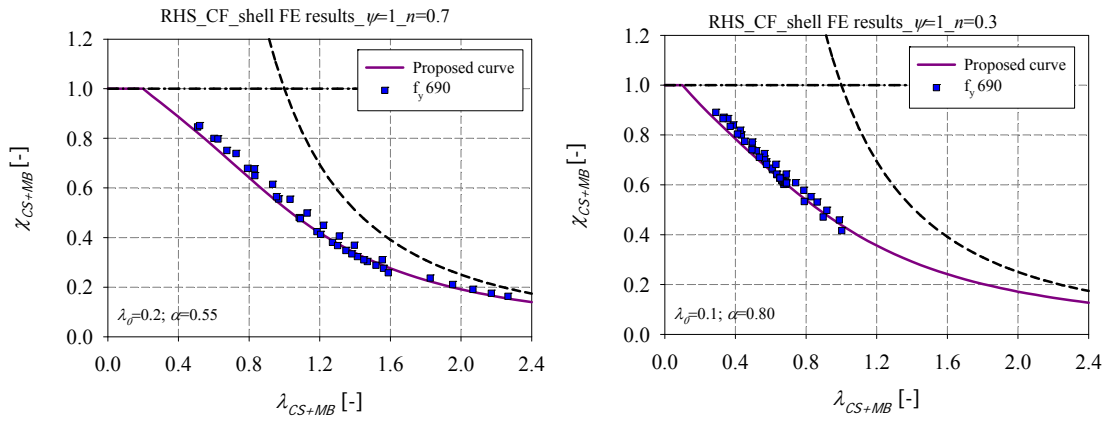


Figure 269 – Numerical member results of cold-formed RHS of steel grade $f_y = 690 \text{ N/mm}^2$ tested under $N+M_z$ with $\psi = 1$ and under different axial force level – a) $n = 0.7$ – b) $n = 0.3$

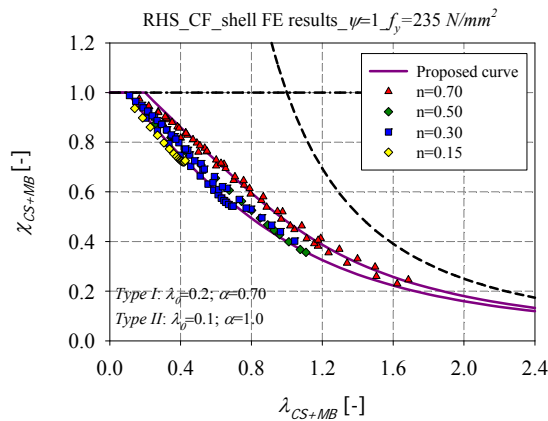


Figure 270 – Numerical member results of cold-formed RHS of steel grade $f_y = 235 \text{ N/mm}^2$ tested under different values of axial force ratio n

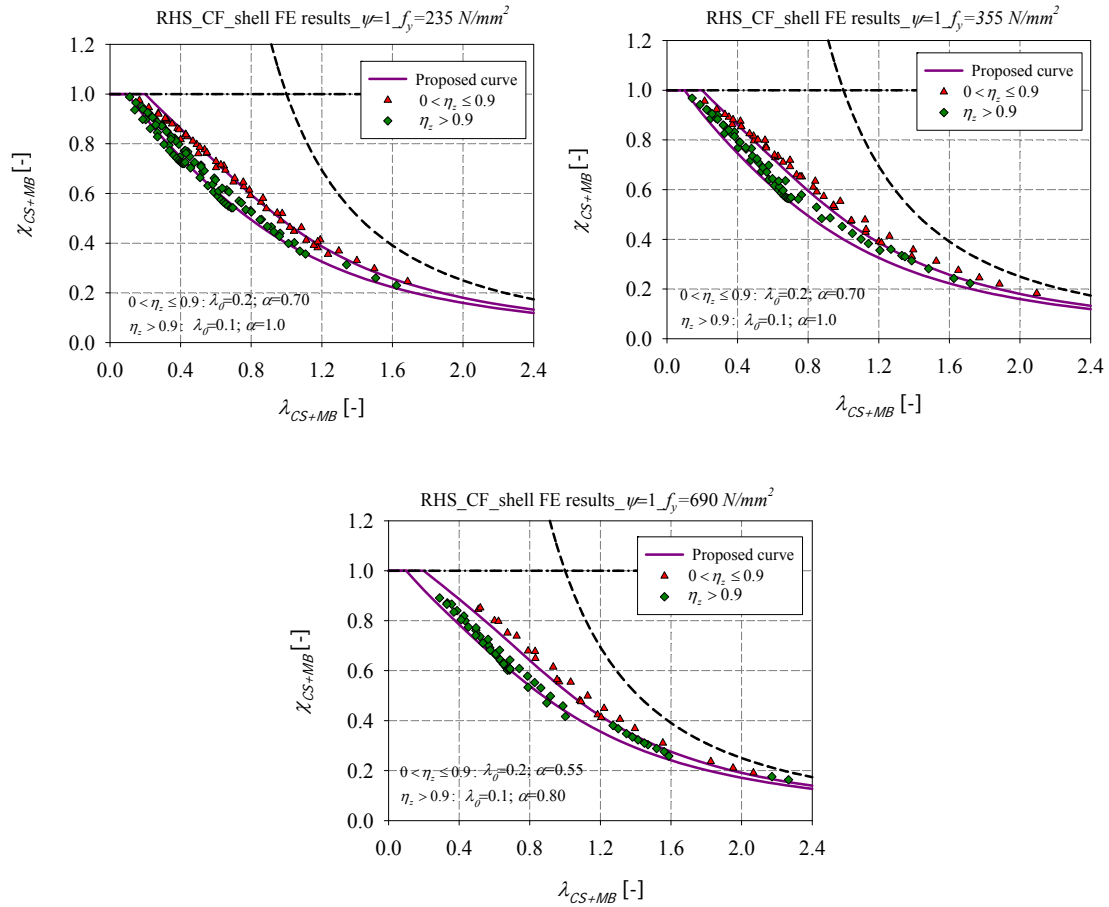


Figure 271 – Numerical member results of cold-formed RHS derived according to the parameter η_z under different steel grades – a) $f_y = 235 \text{ N/mm}^2$ – b) $f_y = 355 \text{ N/mm}^2$ – c) $f_y = 690 \text{ N/mm}^2$

In order to overcome the discontinuity noticed between the two proposed design curves, a linear interpolation is defined for the transition between $0 < \eta_z \leq 0.9$ and $\eta_z > 0.9$.

The same relations adopted for the square sections between η_z and α on one hand, and between η_z and λ_0 on the other, were again adopted for the rectangular one.

Figure 272 illustrates numerical results for cold-formed RHS of nominal steel grade $f_y = 235 \text{ N/mm}^2$ subjected to compression and minor-axis bending, where a smooth conservative continuity is provided with the new proposed design curves.

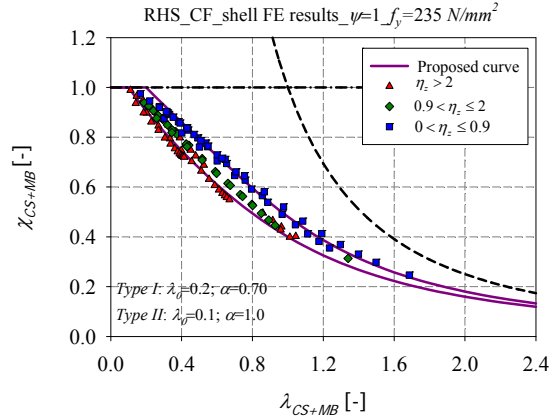


Figure 272 – Numerical member results of cold-formed RHS of steel grade $f_y = 235 \text{ N/mm}^2$ derived according to the parameter η_z

Table 42 summarizes the adopted parameters for the design curves of hot-rolled and cold-formed hollow members subjected to compression with constant minor-axis bending moment distribution.

Table 42 – Design curves for the case of hot-rolled and cold-formed members subjected to compression with constant minor-axis bending

Combined load cases: $N+M_z$
Constant bending moment distribution: $\psi = 1$

$$\chi_{CS+MB} = \frac{1}{\phi_{CS+MB} + \sqrt{\phi_{CS+MB}^2 - \lambda_{CS+MB}^2}}$$

for $\lambda_{CS+MB} \geq \lambda_0$

$$\phi_{CS+MB} = 0.5 \left(1 + \alpha (\lambda_{CS+MB} - \lambda_0) + \lambda_{CS+MB}^2 \right)$$

$$\text{With } \eta_z = \frac{m_z}{n_z} = \frac{M_z / M_{pl,z}}{N / N_{pl}}$$

Cross-section	Fabrication process	η_z	λ_0	α	
				$f_y = 235 \text{ N/mm}^2$ $f_y = 355 \text{ N/mm}^2$	$f_y = 690 \text{ N/mm}^2$
RHS and SHS	Hot-rolled	$0 < \eta_z \leq \eta_{z,1} = 0.9$	0.2	$\alpha_1 = \alpha_{comp} + 0.4\eta_z^{0.2}$	
		$0.9 < \eta_z \leq 2$	$\lambda_0 = \left(-\frac{0.1}{\eta_{z,2} - \eta_{z,1}} \right) (\eta_z - \eta_{z,2}) + 0.1$	$\alpha = \left(\frac{\alpha_2 - \alpha_1}{\eta_{z,2} - \eta_{z,1}} \right) (\eta_z - \eta_{z,2}) + \alpha_2$	
		$\eta_z > \eta_{z,2} = 2$	0.1	$\alpha_2 = 0.80$	$\alpha_2 = 0.75$

Cold- formed	$0 < \eta_z \leq \eta_{z,1} = 0.9$	0.2	$\alpha_1 = \alpha_{comp} + 0.4\eta_z^{0.2}$	
	$0.9 < \eta_z \leq 2$	$\lambda_0 = \left(-\frac{0.1}{\eta_{z,2} - \eta_{z,1}} \right) (\eta_z - \eta_{z,2}) + 0.1$	$\alpha = \left(\frac{\alpha_2 - \alpha_1}{\eta_{z,2} - \eta_{z,1}} \right) (\eta_z - \eta_{z,2}) + \alpha_2$	
	$\eta_z > \eta_{z,2} = 2$	0.1	$\alpha_2 = 1.00$	$\alpha_2 = 0.80$

6.4.3.2. Compression and major-axis bending cases

As for the case of members subjected to compression and minor-axis bending, a leading parameter was again defined according to Equation (279) for the case of compression and major-axis bending and was used to sort the results regardless of the axial force ratio n .

$$\eta_y = \frac{m_y}{n_y} = \frac{M_y / M_{pl,y}}{N / N_{pl}} \quad (279)$$

where N_{pl} and M_{ply} are the plastic cross-section resistance for pure axial force, and for pure bending moment about the strong axis respectively; N and M_y are the ultimate axial force, and ultimate bending moment about the strong axis respectively.

6.4.3.2.1. Hot-rolled square sections

For what concern square sections, results of members tested under compression and major-axis bending are identical to results of members tested under compression and minor-axis bending due to the symmetrical geometry of the sections. Therefore, the same curves proposed previously for hot-rolled square sections under compression and minor-axis bending were again adopted for the case of hot-rolled square sections under compression and major-axis bending.

6.4.3.2.2. Hot-rolled rectangular sections

Figure 273 and Figure 274 present results obtained for hot-rolled rectangular members of different steel grades ($f_y = 235 \text{ N/mm}^2$, $f_y = 355 \text{ N/mm}^2$ and $f_y = 690 \text{ N/mm}^2$), tested under compression and constant major-axis bending, modelled numerically by shell and beam elements. In these figures, the relative axial force ratio n was chosen equal to 0.7. Figure 275 and Figure 276 illustrate the same set of results with a relative axial force n set equal to 0.3. Figure 277 presents the particular case of $f_y = 235 \text{ N/mm}^2$ for hot-rolled RHS highlighting the

influence of the axial force n . One may notice that the results may be derived into two independent interaction curves depending on the relative axial force n . In Figure 278, the defined leading parameter η_y was used to sort the results regardless of the axial force ratio n . It is clearly shown that the ratio η_y can rule the differences in scatter for a given ψ value. The limits of the parameter η_y were again chosen according to the results of steel grade $f_y = 235 \text{ N/mm}^2$ for sake of simplicity and consistency.

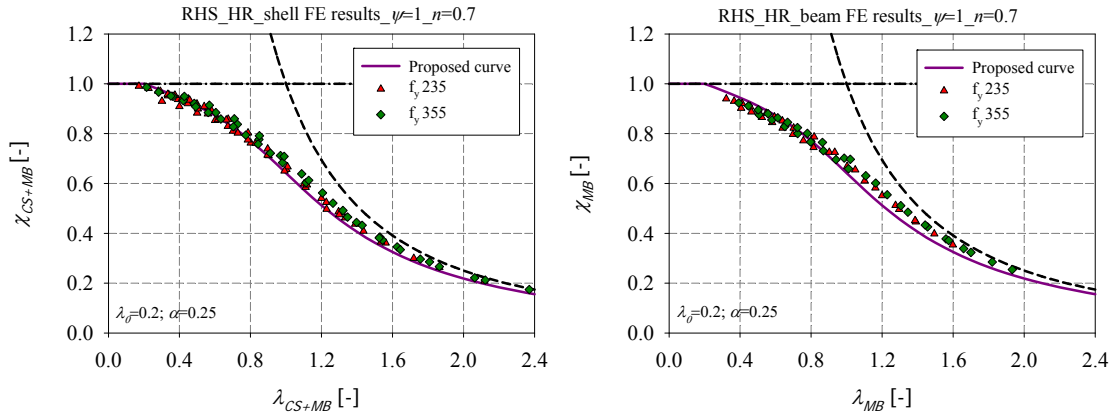


Figure 273 – Numerical member results of hot-rolled RHS of steel grades $f_y = 235 \text{ N/mm}^2$ and $f_y = 355 \text{ N/mm}^2$ tested under $N+M_y$, with $\psi = 1$ and $n = 0.7$ – a) shell results – b) beam results

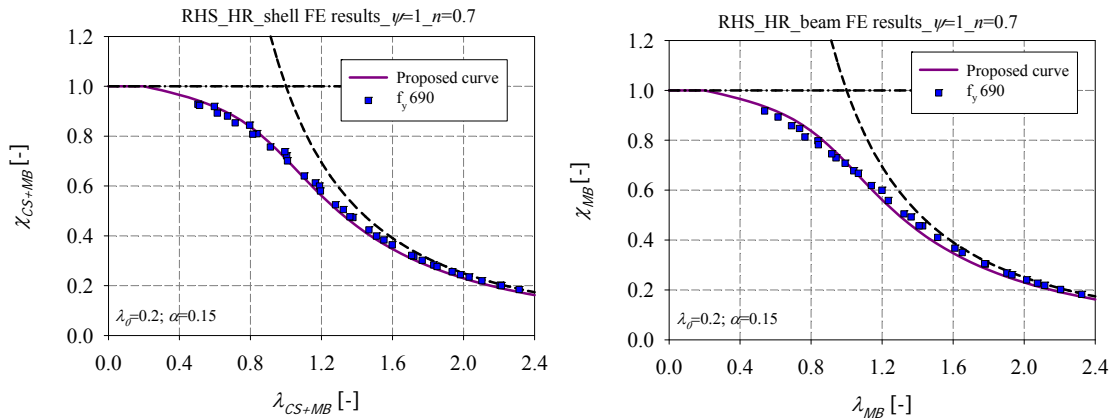


Figure 274 – Numerical member results of hot-rolled RHS of steel grade $f_y = 690 \text{ N/mm}^2$ tested under $N+M_y$, with $\psi = 1$ and $n = 0.7$ – a) shell results – b) beam results

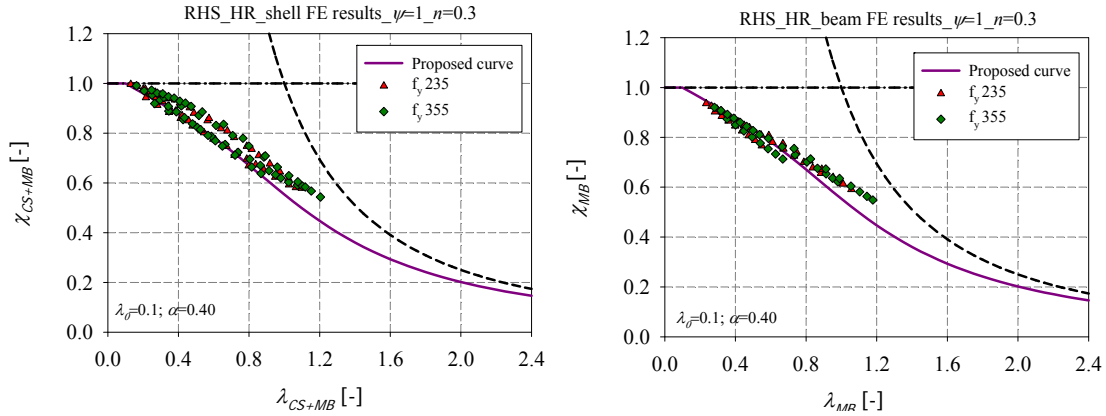


Figure 275 – Numerical member results of hot-rolled RHS of steel grades $f_y = 235 \text{ N/mm}^2$ and $f_y = 355 \text{ N/mm}^2$ tested under $N+M_y$ with $\psi = 1$ and $n = 0.3$ – a) shell results – b) beam results

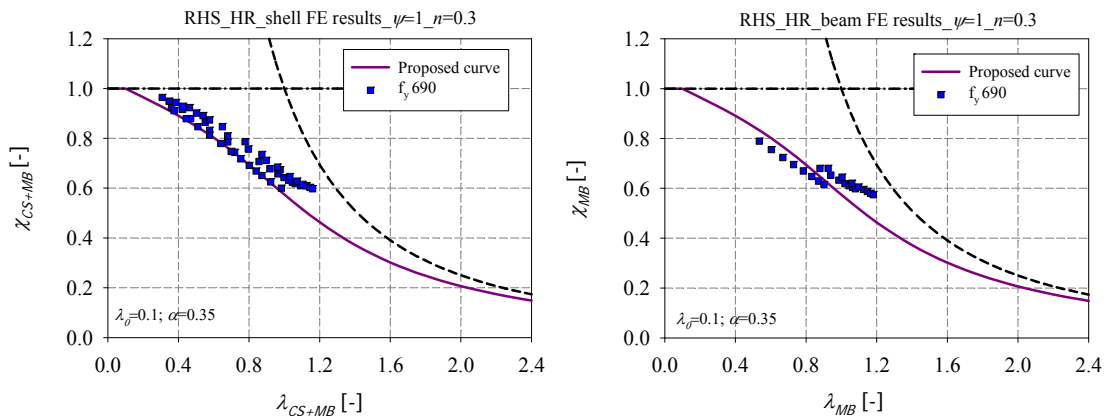


Figure 276 – Numerical member results of hot-rolled RHS of steel grade $f_y = 690 \text{ N/mm}^2$ tested under $N+M_y$ with $\psi = 1$ and $n = 0.3$ – a) shell results – b) beam results

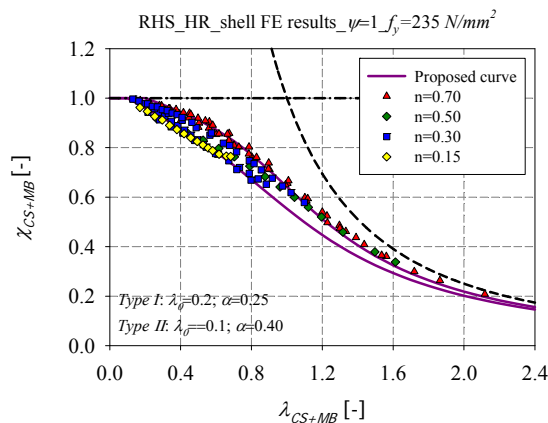


Figure 277 – Numerical member results of hot-rolled RHS of steel grade $f_y = 235 \text{ N/mm}^2$ tested under different values of axial force ratio n

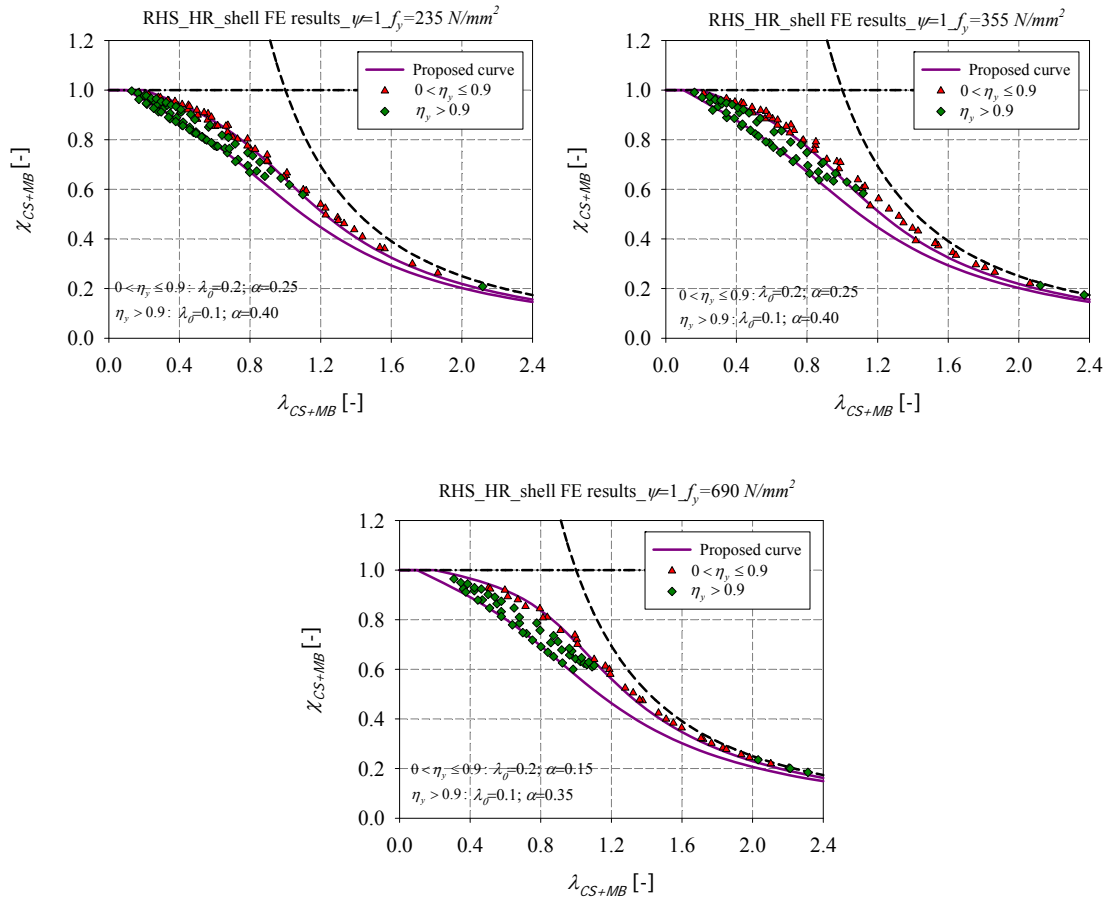


Figure 278 – Numerical member results of hot-rolled RHS derived according to the parameter η_y for different steel grades – a) $f_y = 235$ N/mm² – b) $f_y = 355$ N/mm² – c) $f_y = 690$ N/mm²

In order to overcome the discontinuity noticed with the proposed design curves, a linear interpolation is defined for the transition between the curves corresponding to $0 < \eta_y \leq 0.9$ and $\eta_y > 0.9$. With the inclusion of the η_y parameter, the proposed α formula becomes as the following for hot-rolled rectangular sections of steel grade $f_y = 235$ N/mm² and $f_y = 355$ N/mm²:

$$\alpha = \alpha_1 = 0.25 \text{ for } 0 < \eta_y \leq \eta_{y,1} = 0.9 \quad (280)$$

$$\alpha = \left(\frac{\alpha_2 - \alpha_1}{\eta_{y,2} - \eta_{y,1}} \right) (\eta_y - \eta_{y,1}) + \alpha_1 \text{ for } \eta_{y,1} < \eta_y \leq \eta_{y,2} \quad (281)$$

$$\alpha = \alpha_2 = 0.40 \text{ for } \eta_y > \eta_{y,2} = 2 \quad (282)$$

Equation (280) can be written as follows, in order to provide smooth continuities with the pure compression load case:

$$\alpha = \alpha_1 = \alpha_{comp} + 0.05\eta_y^{0.2} \text{ for } 0 < \eta_y \leq \eta_{y,1} = 0.9 \quad (283)$$

The proposed λ_0 formula becomes as the following:

$$\lambda_0 = 0.2 \text{ for } 0 < \eta_y \leq \eta_{y,1} = 0.9 \quad (284)$$

$$\lambda_0 = \left(-\frac{0.1}{\eta_{y,2} - \eta_{y,1}} \right) (\eta_y - \eta_{y,2}) + 0.1 \text{ for } 0.9 < \eta_y \leq 2 \quad (285)$$

$$\lambda_0 = 0.1 \text{ for } \eta_y > \eta_{y,2} = 2 \quad (286)$$

The same type of relationships can be found between η_y and α for high strength steel hollow section, (i.e. $f_y = 690 \text{ N/mm}^2$) according to equations below:

$$\alpha = \alpha_1 = 0.15 \text{ for } 0 < \eta_y \leq \eta_{y,1} = 0.9 \quad (287)$$

$$\alpha = \left(\frac{\alpha_2 - \alpha_1}{\eta_{y,2} - \eta_{y,1}} \right) (\eta_y - \eta_{y,2}) + \alpha_2 \text{ for } 0.9 < \eta_y \leq 2 \quad (288)$$

$$\alpha = \alpha_2 = 0.35 \text{ for } \eta_y > \eta_{y,2} = 2 \quad (289)$$

Equation (287) can be written as follows, in order to provide smooth continuities with the pure compression load case:

$$\alpha = \alpha_1 = \alpha_{comp} + 0.05\eta_y^{0.2} \text{ for } 0 \leq \eta_y \leq \eta_{y,1} = 0.9 \quad (290)$$

The proposed λ_0 formula becomes as follows:

$$\lambda_0 = 0.2 \text{ for } 0 < \eta_y \leq \eta_{y,1} = 0.9 \quad (291)$$

$$\lambda_0 = \left(-\frac{0.1}{\eta_{y,2} - \eta_{y,1}} \right) (\eta_y - \eta_{y,2}) + 0.1 \text{ for } 0.9 < \eta_y \leq 2 \quad (292)$$

$$\lambda_0 = 0.1 \text{ for } \eta_y > \eta_{y,2} = 2 \quad (293)$$

The numerical results are derived according to the defined limits of the parameter η_y (see Figure 279), where a smooth conservative continuity is provided with the proposed design curves.

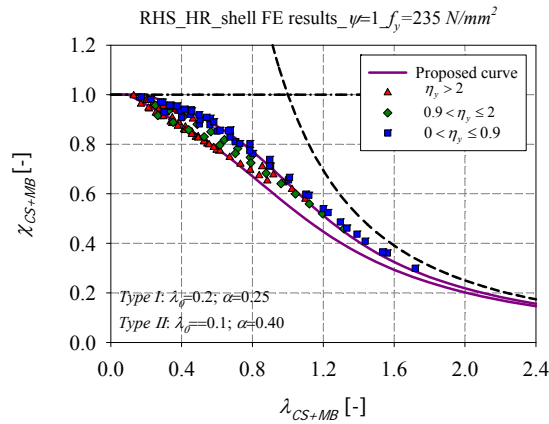


Figure 279 – Numerical member results of hot-rolled RHS of steel grade $f_y = 235 \text{ N/mm}^2$ derived according to the parameter η_y

6.4.3.2.3. Cold-formed square sections

The same curves proposed previously for cold-formed square members under compression and minor-axis bending, were again adopted for the case of cold-formed square sections under compression and major-axis bending due to the symmetrical geometry of the square sections.

6.4.3.2.4. Cold-formed rectangular sections

Figure 280 and Figure 281 illustrate the application of the O.I.C. for cold-formed rectangular sections of different steel grades ($f_y = 235 \text{ N/mm}^2$, $f_y = 355 \text{ N/mm}^2$ and $f_y = 690 \text{ N/mm}^2$), tested under compression and constant major-axial bending ($\psi = 1$). In these figures, the relative axial force ratio n defined as $n = N_{Ed} / N_{b,Rd}$ was chosen equal to 0.7 and 0.3. For each load case, a single interaction curve was derived for $f_y = 235 \text{ N/mm}^2$ and $f_y = 355 \text{ N/mm}^2$, since a small dispersion in the results is noted. Higher resistances are observed for $f_y = 690 \text{ N/mm}^2$ and higher curves were derived accordingly. Figure 282 presents the particular case of $f_y = 235 \text{ N/mm}^2$ for cold-formed rectangular sections highlighting the influence of the axial force ratio n . One may notice that the results may be derived into two independent interaction curves depending on the relative axial force n . In Figure 283, the defined leading parameter η_y was used to sort the results regardless of the axial force ratio n . It is clearly shown that the ratio η_y can rule the differences in scatter for a given ψ value. The limits of the parameter

η_y were again chosen according to the results of steel grade $f_y = 235 \text{ N/mm}^2$ for sake of simplicity and consistency.

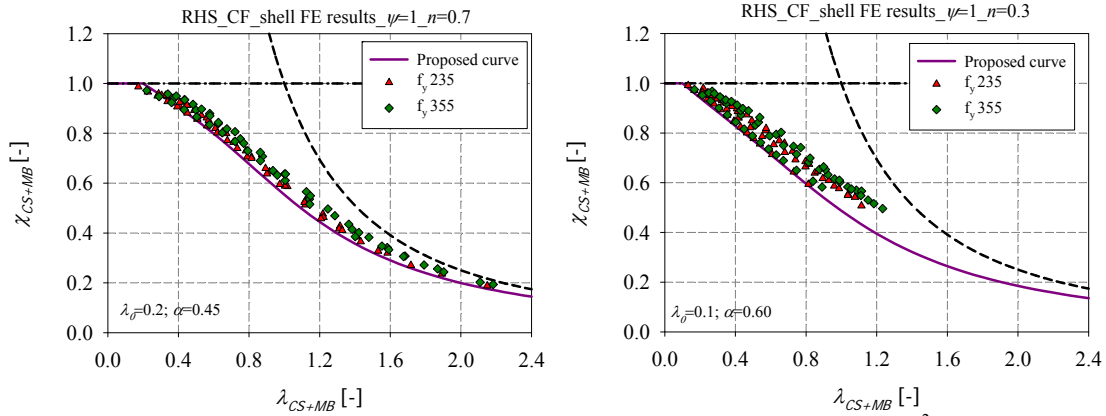


Figure 280 – Numerical member results of cold-formed RHS of steel grades $f_y = 235 \text{ N/mm}^2$ and $f_y = 355 \text{ N/mm}^2$ tested under $N+M_y$ with $\psi = 1$ and under different axial force level – a) $n = 0.7$ – b) $n = 0.3$

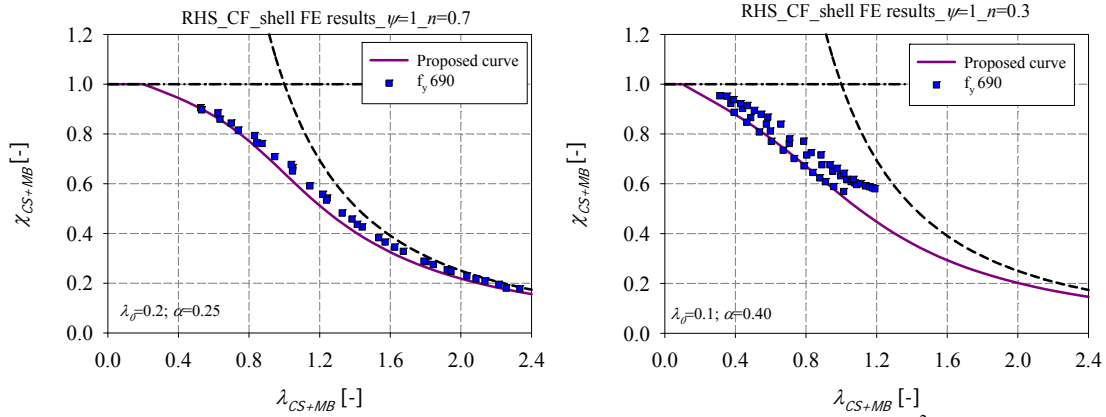


Figure 281 – Numerical member results of cold-formed RHS of steel grade $f_y = 690 \text{ N/mm}^2$ tested under $N+M_y$ with $\psi = 1$ and under different axial force level – a) $n = 0.7$ – b) $n = 0.3$

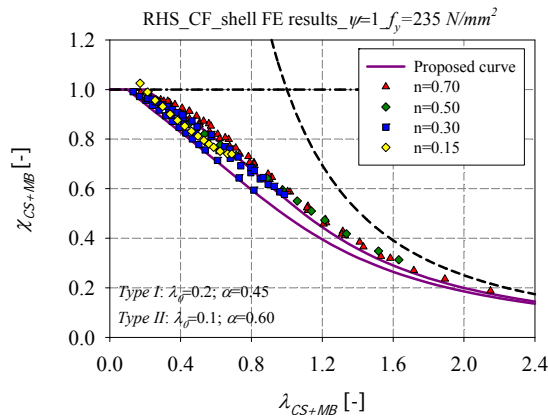


Figure 282 – Numerical member results of cold-formed RHS of steel grade $f_y = 235 \text{ N/mm}^2$ tested under different values of axial force ratio n

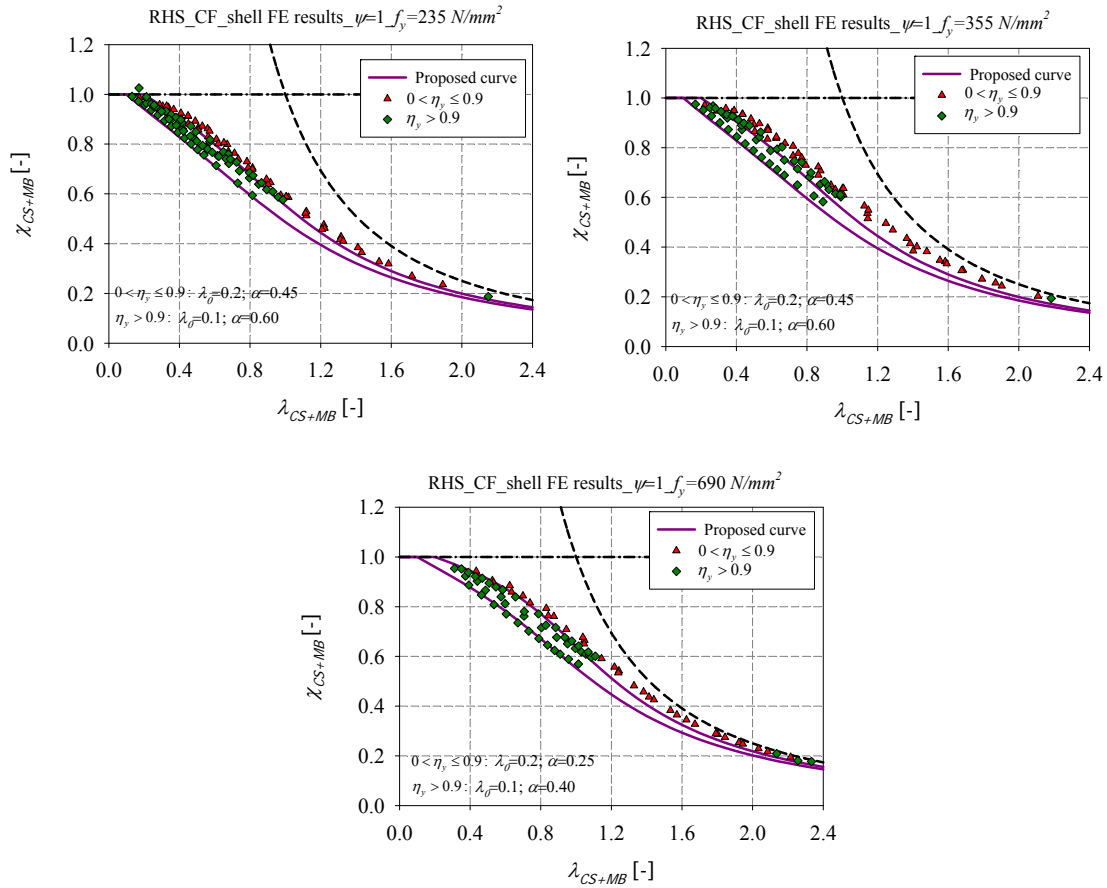


Figure 283 – Numerical member results of cold-formed RHS derived according to the parameter η_y under different steel grades – a) $f_y = 235 \text{ N/mm}^2$ – b) $f_y = 355 \text{ N/mm}^2$ – c) $f_y = 690 \text{ N/mm}^2$

In order to overcome the discontinuity noticed with the proposed design curves, a linear interpolation is defined for the transition between the curves corresponding to $0 < \eta_y \leq 0.9$ and $\eta_y > 0.9$.

With the inclusion of the η_y parameter, the proposed α formula becomes as the following for cold-formed rectangular sections of steel grade $f_y = 235 \text{ N/mm}^2$ and $f_y = 355 \text{ N/mm}^2$:

$$\alpha = \alpha_1 = 0.45 \text{ for } 0 < \eta_y \leq \eta_{y,1} = 0.9 \quad (294)$$

$$\alpha = \left(\frac{\alpha_2 - \alpha_1}{\eta_{y,2} - \eta_{y,1}} \right) (\eta_y - \eta_{y,1}) + \alpha_1 \text{ for } \eta_{y,1} < \eta_y \leq \eta_{y,2} \quad (295)$$

$$\alpha = \alpha_2 = 0.60 \text{ for } \eta_y > \eta_{y,2} = 2 \quad (296)$$

Equation (294) can be written as follows, in order to provide smooth continuities with the pure compression load case:

$$\alpha = \alpha_1 = \alpha_{comp} + 0.05\eta_y^{0.2} \text{ for } 0 \leq \eta_y \leq \eta_{y,1} = 0.9 \quad (297)$$

The proposed λ_0 formula becomes as the following:

$$\lambda_0 = 0.2 \text{ for } 0 < \eta_y \leq \eta_{y,1} = 0.9 \quad (298)$$

$$\lambda_0 = \left(-\frac{0.1}{\eta_{y,2} - \eta_{y,1}} \right) (\eta_y - \eta_{y,2}) + 0.1 \text{ for } 0.9 < \eta_y \leq 2 \quad (299)$$

$$\lambda_0 = 0.1 \text{ for } \eta_y > \eta_{y,2} = 2 \quad (300)$$

The same type of relationships can be found between η_y and α for high strength steel hollow section, (i.e. $f_y = 690 \text{ N/mm}^2$) according to equations below:

$$\alpha = \alpha_1 = 0.25 \text{ for } 0 < \eta_y \leq \eta_{y,1} = 0.9 \quad (301)$$

$$\alpha = \left(\frac{\alpha_2 - \alpha_1}{\eta_{y,2} - \eta_{y,1}} \right) (\eta_y - \eta_{y,2}) + \alpha_2 \text{ for } 0.9 < \eta_y \leq 2 \quad (302)$$

$$\alpha = \alpha_2 = 0.40 \text{ for } \eta_y > \eta_{y,2} = 2 \quad (303)$$

Equation (301) can be written as follows, in order to provide smooth continuities with the pure compression load case:

$$\alpha = \alpha_1 = \alpha_{comp} + 0.05\eta_y^{0.2} \text{ for } 0 \leq \eta_y \leq \eta_{y,1} = 0.9 \quad (304)$$

The proposed λ_0 formula becomes as the following:

$$\lambda_0 = 0.2 \text{ for } 0 < \eta_y \leq \eta_{y,1} = 0.9 \quad (305)$$

$$\lambda_0 = \left(-\frac{0.1}{\eta_{y,2} - \eta_{y,1}} \right) (\eta_y - \eta_{y,2}) + 0.1 \text{ for } 0.9 < \eta_y \leq 2 \quad (306)$$

$$\lambda_0 = 0.1 \text{ for } \eta_y > \eta_{y,2} = 2 \quad (307)$$

The numerical results are derived according to the defined limits of the parameter η_y (see Figure 284), where a smooth conservative continuity is provided with the proposed design curves.

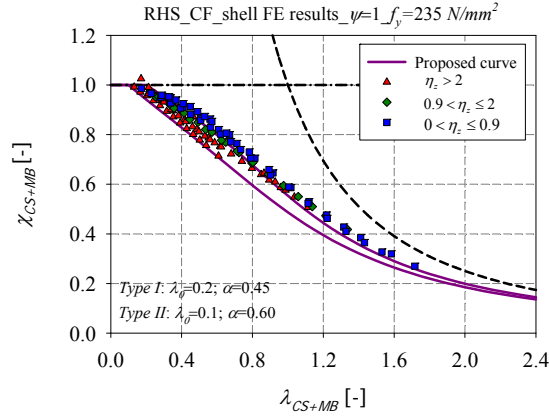


Figure 284 – Numerical member results of cold-formed RHS of steel grade $f_y = 235 \text{ N/mm}^2$ derived according to the parameter η_y

Table 43 summarizes the adopted parameters for the design curves of hot-rolled and cold-formed members subjected to compression with constant major-axis bending moment distribution.

Table 43 – Design curves for the case of hot-rolled and cold-formed members subjected to compression with constant major-axis bending

Combined load cases: $N+M_y$	
Constant bending moment distribution: $\psi = 1$	

$$\chi_{CS+MB} = \frac{1}{\phi_{CS+MB} + \sqrt{\phi_{CS+MB}^2 - \lambda_{CS+MB}^2}}$$

for $\lambda_{CS+MB} \geq \lambda_0$

$$\text{With } \phi_{CS+MB} = 0.5 \left(1 + \alpha (\lambda_{CS+MB} - \lambda_0) + \lambda_{CS+MB}^2 \right); \quad \eta_y = \frac{m_y}{n_y} = \frac{M_y / M_{pl,y}}{N / N_{pl}}$$

Cross-section	Fabrication process	η_y	λ_0	α	
				$f_y = 235 \text{ N/mm}^2$ $f_y = 355 \text{ N/mm}^2$	$f_y = 690 \text{ N/mm}^2$
RHS	Hot-rolled	$0 < \eta_y \leq \eta_{y,1} = 0.9$	0.2	$\alpha = \alpha_1 = \alpha_{comp} + 0.05\eta^{0.2}$	
		$0.9 < \eta_y \leq 2$	$\lambda_0 = \left(-\frac{0.1}{\eta_{y,2} - \eta_{y,1}} \right) (\eta_y - \eta_{y,2}) + 0.1$	$\alpha = \left(\frac{\alpha_2 - \alpha_1}{\eta_{y,2} - \eta_{y,1}} \right) (\eta_y - \eta_{y,2}) + \alpha_2$	

		$\eta_y > \eta_{y,2} = 2$	0.1	$\alpha_2 = 0.40$	$\alpha_2 = 0.35$
	Cold-formed	$0 < \eta_y \leq \eta_{y,1} = 0.9$	0.2	$\alpha = \alpha_1 = \alpha_{comp} + 0.05\eta^{0.2}$	
		$0.9 < \eta_y \leq 2$	$\lambda_0 = \left(-\frac{0.1}{\eta_{y,2} - \eta_{y,1}} \right) (\eta_y - \eta_{y,2}) + 0.1$	$\alpha = \left(\frac{\alpha_2 - \alpha_1}{\eta_{y,2} - \eta_{y,1}} \right) (\eta_y - \eta_{y,2}) + \alpha_2$	
		$\eta_y > \eta_{y,2} = 2$	0.1	$\alpha_2 = 0.60$	$\alpha_2 = 0.40$
SHS	Hot-rolled	$0 < \eta_y \leq \eta_{y,1} = 0.9$	0.2	$\alpha = \alpha_1 = \alpha_{comp} + 0.4\eta^{0.2}$	
		$0.9 < \eta_y \leq 2$	$\lambda_0 = \left(-\frac{0.1}{\eta_{y,2} - \eta_{y,1}} \right) (\eta_y - \eta_{y,2}) + 0.1$	$\alpha = \left(\frac{\alpha_2 - \alpha_1}{\eta_{y,2} - \eta_{y,1}} \right) (\eta_y - \eta_{y,2}) + \alpha_2$	
		$\eta_y > \eta_{y,2} = 2$	0.1	$\alpha_2 = 0.80$	$\alpha_2 = 0.75$
	Cold-formed	$0 < \eta_y \leq \eta_{y,1} = 0.9$	0.2	$\alpha = \alpha_1 = \alpha_{comp} + 0.4\eta^{0.2}$	
		$0.9 < \eta_y \leq 2$	$\lambda_0 = \left(-\frac{0.1}{\eta_{y,2} - \eta_{y,1}} \right) (\eta_y - \eta_{y,2}) + 0.1$	$\alpha = \left(\frac{\alpha_2 - \alpha_1}{\eta_{y,2} - \eta_{y,1}} \right) (\eta_y - \eta_{y,2}) + \alpha_2$	
		$\eta_y > \eta_{y,2} = 2$	0.1	$\alpha_2 = 1.00$	$\alpha_2 = 0.80$

6.4.3.3. Compression and biaxial bending

The figures hereafter present results of members tested under combined loading with a constant bending moment distribution. For each load case, 10 values of the degree of biaxial bending were adopted varying from $\alpha_{biaxiality} = 0^\circ$ (i.e. the load case becoming compression with major-axis bending $N+M_y$) to $\alpha_{biaxiality} = 90^\circ$ (i.e. the load case becoming compression with minor-axis bending $N+M_z$) with a range of 10 degrees. The M_y/M_z ratio is clearly considered as a leading parameter for the derivation of appropriate interaction curves.

For sake of simplicity, only some results for combined loading situations for cold-formed and hot-rolled square and rectangular sections, tested under constant bending moment, are presented in Figure 285 and Figure 286, in order to investigate the influence of the proportions of the bending moments. As can be seen in the figures, as for the case of triangular bending moment distribution, quite limited scatter is observed for square sections as expected for the pair of $\alpha_{biaxiality}$ - values: $\alpha_{biaxiality} = 10^\circ$ and $\alpha_{biaxiality} = 80^\circ$; $\alpha_{biaxiality} = 20^\circ$ and $\alpha_{biaxiality} = 70^\circ$; $\alpha_{biaxiality} = 30^\circ$ and $\alpha_{biaxiality} = 60^\circ$; $\alpha_{biaxiality} = 40^\circ$ and $\alpha_{biaxiality} = 50^\circ$, due to the symmetrical geometry of the sections. However, larger scatters are observed for the case of rectangular sections. The resistance of

the member in this case is largely influenced by the degree of biaxial bending: For cases where weak-axis bending takes over strong-axis bending ($\alpha_{biaxiality} > 45^\circ$), the O.I.C. resistance curves begin to increase again after a progressive drop starting from the combined loading $N+M_y$ alone. When M_z is applied to an $N+M_y$ loading with a small proportion ($\alpha_{biaxiality} < 45^\circ$), instability is increased if compared to the $N+M_y$ loading; nevertheless when M_z becomes dominant, the section becomes more stable.

Consequently, one curve was proposed for the case of square sections and this regardless of the degree of biaxial bending for sake of simplicity. The adopted curve was derived lower than the one adopted for the case of $N+M_y$ and $N+M_z$. However, different curves were proposed for the case of rectangular sections depending on the $\alpha_{biaxiality}$ -factor, since it has a significant impact on the resistance of rectangular sections. Accordingly, for each load case, four different design curves²⁷ were proposed based on the $\alpha_{biaxiality}$ -factor for the case of rectangular sections and one curve was adopted for the case of square sections. The factor $\alpha_{biaxiality}$ is equivalent to the derived factor $\Omega_{y/z}$ and can be calculated following Equation (209).

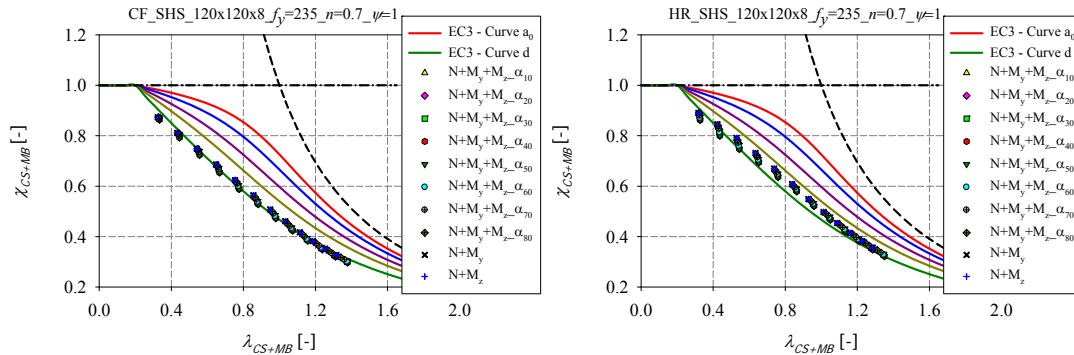


Figure 285 – Numerical member results obtained for different degrees of biaxial bending values and $\psi = 1$ for
 – a) cold-formed SHS – b) hot-rolled SHS

²⁷ The proposed curves for the case of rectangular sections correspond to lower bound of the numerical results obtained for $\alpha_{biaxiality} = 10^\circ$, $\alpha_{biaxiality} = 20^\circ$, $\alpha_{biaxiality} = 30^\circ$ and $\alpha_{biaxiality} \geq 40^\circ$ from which the O.I.C. resistance curves begin to increase.

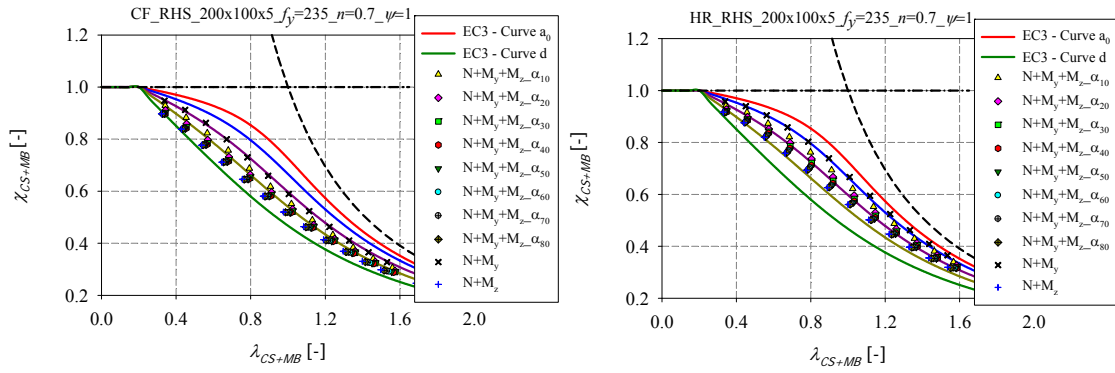


Figure 286 – Numerical member results obtained for different degrees of biaxial bending values and $\psi = 1$ for
 – a) cold-formed RHS – b) hot-rolled RHS

6.4.3.3.1. Hot-rolled square sections

Figure 287 and Figure 288 illustrate the application of the O.I.C. for hot-rolled square sections of different steel grades ($f_y = 235 \text{ N/mm}^2$, $f_y = 355 \text{ N/mm}^2$ and $f_y = 690 \text{ N/mm}^2$), tested under compression and constant biaxial bending. In these figures, the relative axial force ratio n was chosen equal to 0.7. Close tendencies of member results computed using beam and shell models are observed. Figure 289 and Figure 290 illustrate the results corresponding to hot-rolled square sections under compression and constant biaxial bending with the relative axial force ratio n set equal to 0.3. For each load case, a single interaction curve was derived for $f_y = 235 \text{ N/mm}^2$ and $f_y = 355 \text{ N/mm}^2$, since a small dispersion in the results is noticed. Higher resistances are observed for $f_y = 690 \text{ N/mm}^2$ and higher curves were derived accordingly. Figure 291 presents the particular case of $f_y = 235 \text{ N/mm}^2$ for hot-rolled square sections highlighting the influence of the axial force ratio n .

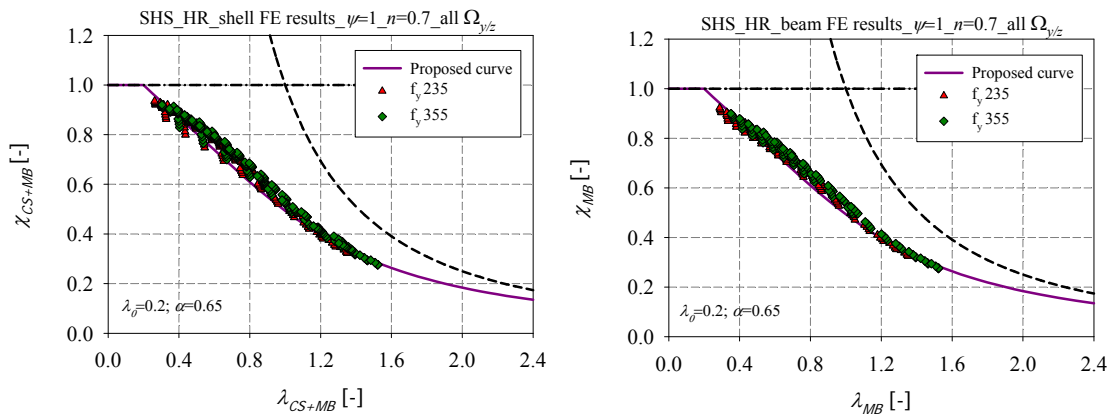


Figure 287 – Numerical member results of hot-rolled SHS of steel grades $f_y = 235 \text{ N/mm}^2$ and $f_y = 355 \text{ N/mm}^2$ tested under $N+M_y+M_z$, $\psi = 1$ and $n = 0.7$ – a) shell results – b) beam results

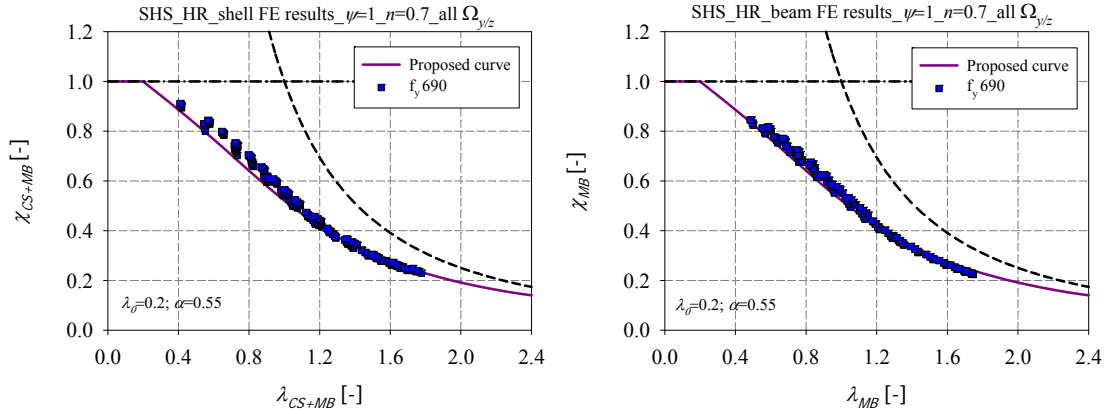


Figure 288 – Numerical member results of hot-rolled SHS of steel grade $f_y = 690 \text{ N/mm}^2$ tested under $N+M_y+M_z$, $\psi = 1$ and $n = 0.7$ – a) shell results – b) beam results

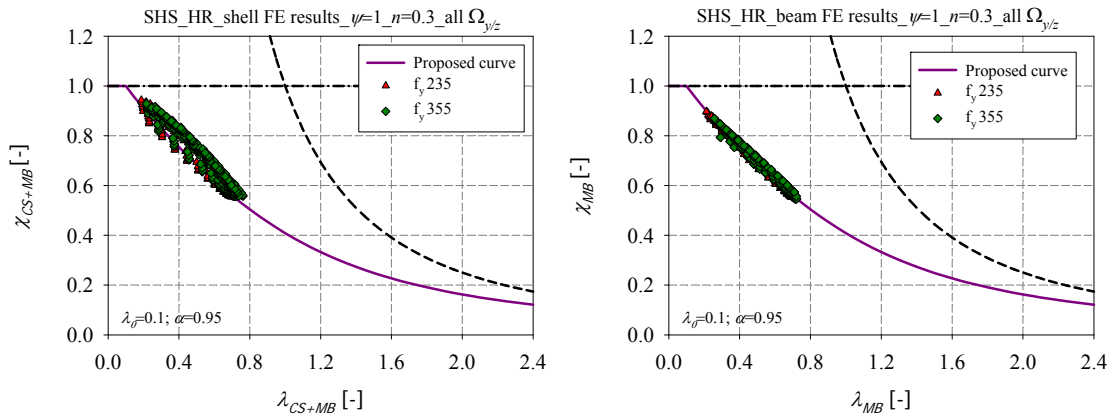


Figure 289 – Numerical member results of hot-rolled SHS of steel grades $f_y = 235 \text{ N/mm}^2$ and $f_y = 355 \text{ N/mm}^2$ tested under $N+M_y+M_z$, $\psi = 1$ and $n = 0.3$ – a) shell results – b) beam results

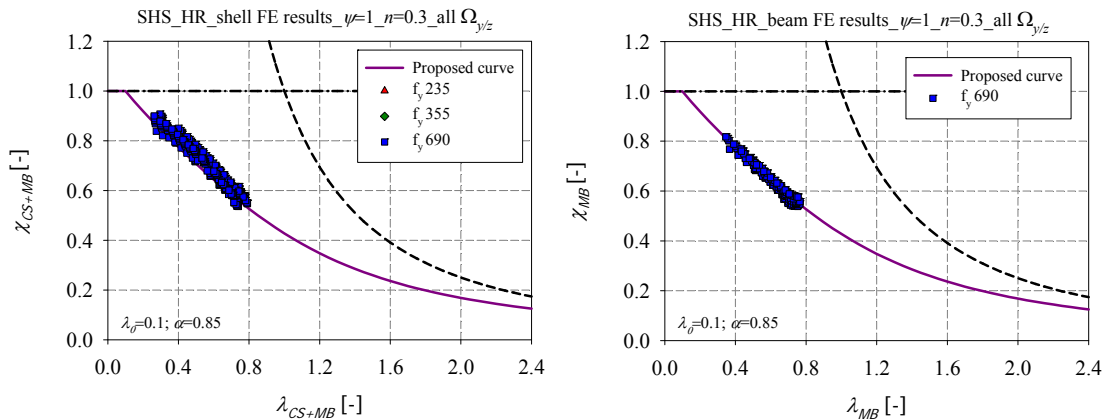


Figure 290 – Numerical member results of hot-rolled SHS of steel grade $f_y = 690 \text{ N/mm}^2$ tested under $N+M_y+M_z$, $\psi = 1$ and $n = 0.3$ – a) shell results – b) beam results

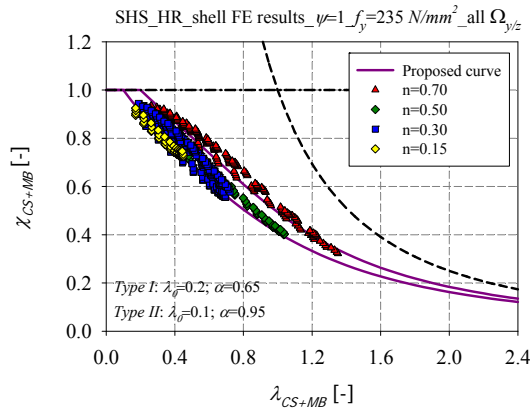
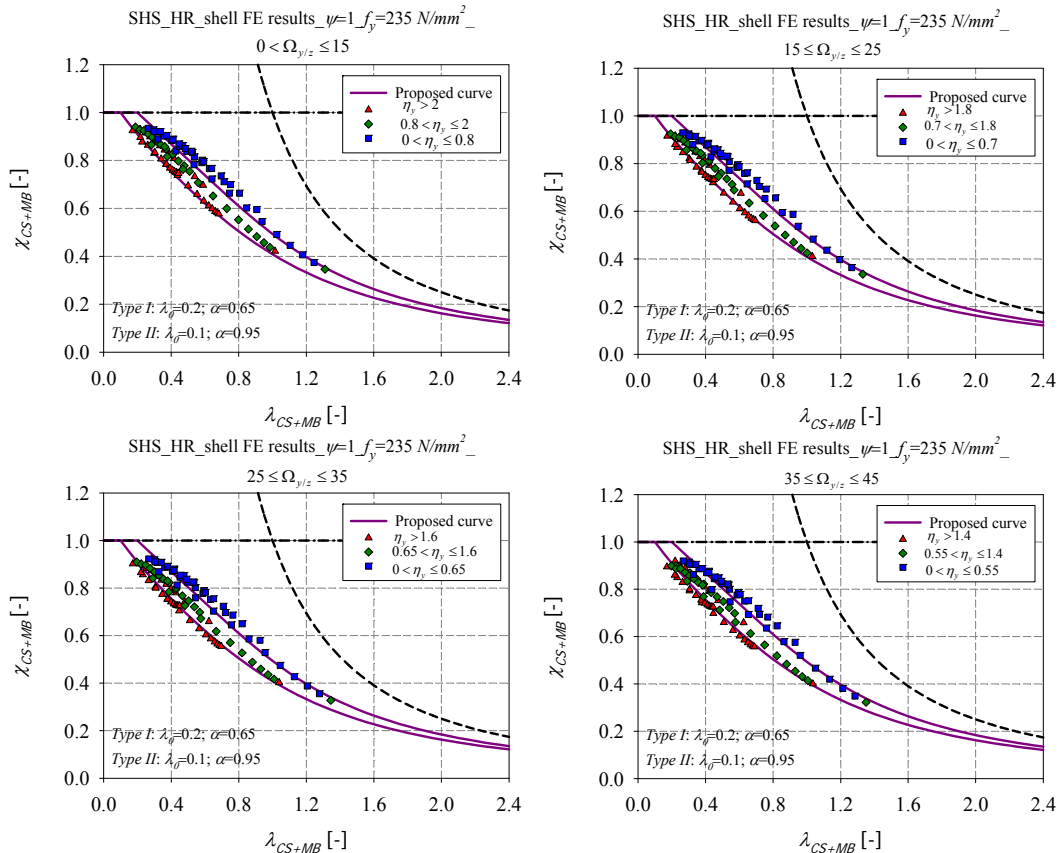


Figure 291 – Numerical member results of hot-rolled SHS of steel grade $f_y = 235 \text{ N/mm}^2$ tested under different values of axial force ratio n

The results were then sorted as a function of both parameters η_y and $\Omega_{y/z}$ regardless of the axial force ratio n . Two curves were derived accordingly (*Type I* and *Type II* curves) as illustrated in Figure 292 and a linear interpolation is defined for the transition between the two types of curves. The limits of the parameter η_y were chosen according to the results of steel grade $f_y = 235 \text{ N/mm}^2$. The same limits were derived for higher steel grades, for sake of simplicity and consistency, since they lead to conservative results.



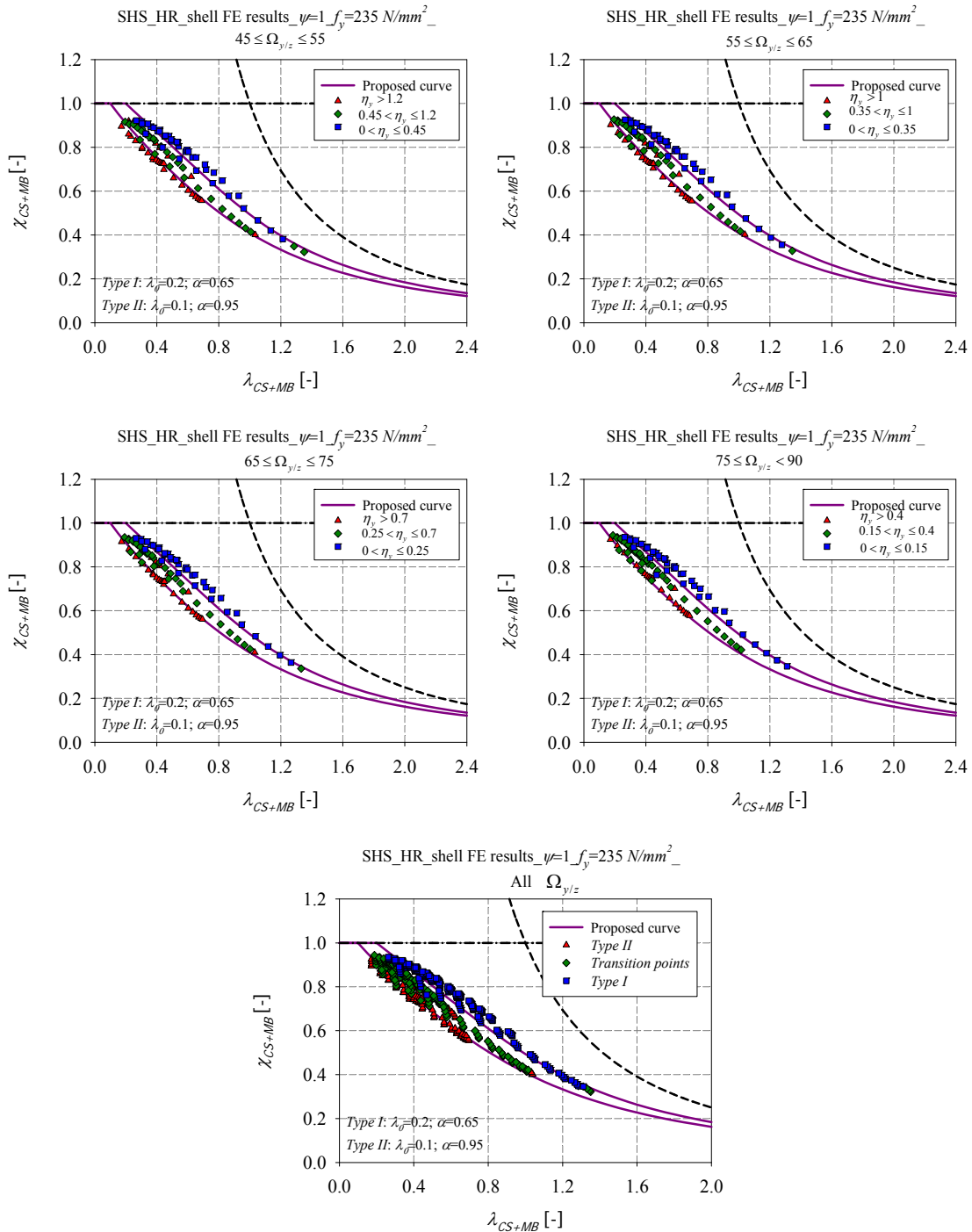


Figure 292 – Numerical member results for hot-rolled SHS of steel grade $f_y = 235 \text{ N/mm}^2$ tested under different values of axial force ratio n and derived as a function of the parameters $\Omega_{y/z}$ and η_y .

The defined limits of the parameters $\Omega_{y/z}$ and η_y between *Type I*, *Type II* and the transition curves are illustrated in Figure 293. Special attention has been given so that the borders between *Type I* curves and the transition curves on one hand (represented by the factor $\eta_{y,1}$)

and the borders between the transition curves and *Type II* curves (represented by the factor $\eta_{y,2}$) on another hand, exhibit no discontinuities. Thus, linear relations were adopted between $\Omega_{y/z}$ and $\eta_{y,1}$, and between $\Omega_{y/z}$ and $\eta_{y,2}$.

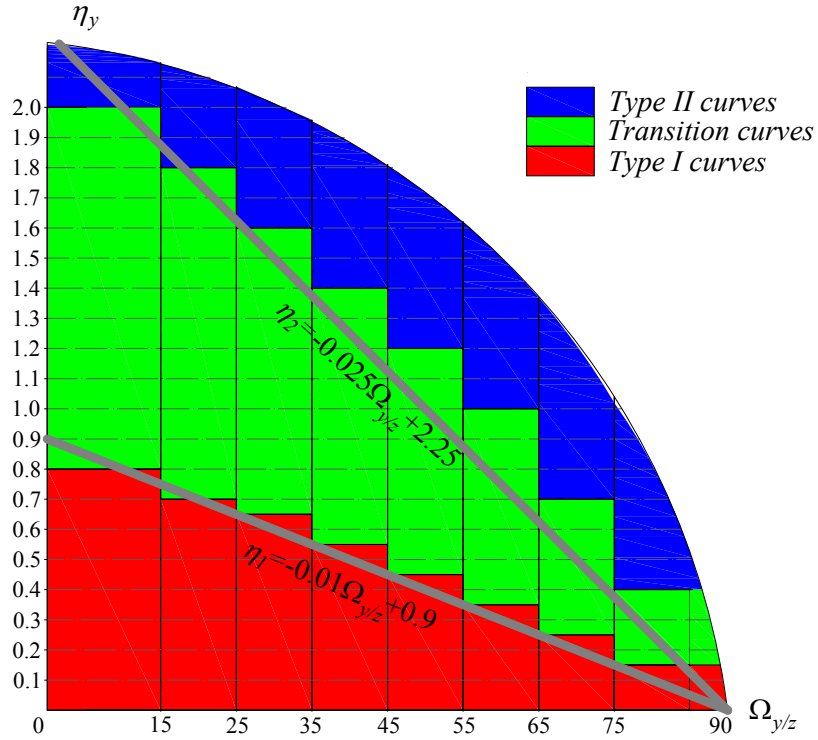


Figure 293 – Defined limits of the parameters $\Omega_{y/z}$ and η_y between *Type I*, *Type II* and the transition curves

A relation was then found between the imperfection factor and the degree of biaxial bending for the two types of curves. Figure 294 presents a variation of the imperfection factor based on the degree of biaxial bending for *Type I* curves, relative to hot-rolled square sections of normal steel grades ($f_y = 235 \text{ N/mm}^2$ and $f_y = 355 \text{ N/mm}^2$) and tested under compression and constant bending moment distribution.

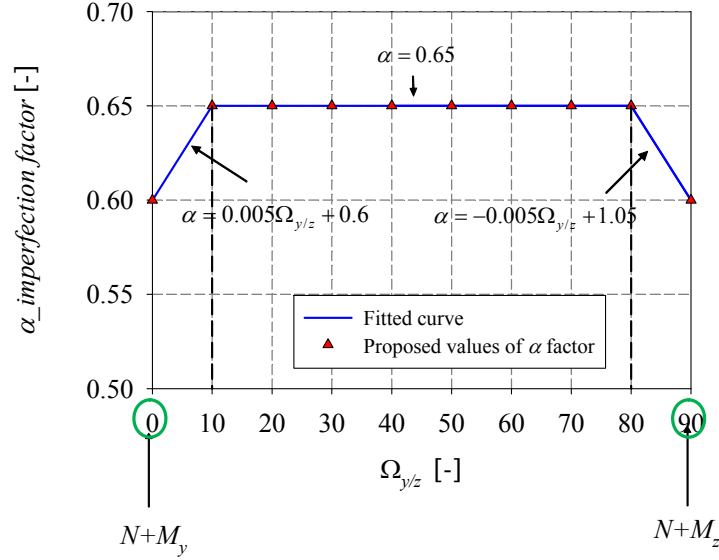


Figure 294 – Variation of α based on $\Omega_{y/z}$ for *Type I* curves, relative to HR SHS of steel grades $f_y = 235 \text{ N/mm}^2$ and $f_y = 355 \text{ N/mm}^2$, tested under compression and constant bending moment distribution.

With the inclusion of the $\Omega_{y/z}$ parameter, the proposed α formula becomes as follows:

$$\alpha = 0.005\Omega_{y/z} + 0.60 \text{ for } \Omega_{y/z} \leq 10 \quad (308)$$

$$\alpha = 0.65 \text{ for } 10 \leq \Omega_{y/z} \leq 80 \quad (309)$$

$$\alpha = -0.005\Omega_{y/z} + 1.05 \text{ for } \Omega_{y/z} \geq 80 \quad (310)$$

That way, for $\Omega_{y/z} = 0$, Equation (308) is restored with the limiting curve being relative to compression with major-axis bending load case and for $\Omega_{y/z} = 90$, Equation (310) is restored with the limiting curve being relative to compression with minor-axis bending load case.

In order to provide a smooth continuity with the pure compression load case, the term 0.6 is replaced by $\alpha_{comp} + 0.4\eta^{0.2}$ as explained in section 6.4.3.1.1, and the proposed α formula becomes as follows:

$$\alpha = 0.005\Omega_{y/z} + \alpha_{comp} + 0.4\eta_y^{0.2} \leq 0.65 \text{ for } \Omega_{y/z} \leq 10 \quad (311)$$

$$\alpha = 0.65 \text{ for } 10 \leq \Omega_{y/z} \leq 80 \quad (312)$$

$$\alpha = -0.005\Omega_{y/z} + 0.45 + \alpha_{comp} + 0.4\eta_z^{0.2} \leq 0.65 \text{ for } \Omega_{y/z} \geq 80 \quad (313)$$

That way, for $\Omega_{y/z} = 0$ and $\eta_y = 0$, Equation (311) is restored with the limiting curve being relative to the pure compression load case and for $\Omega_{y/z} = 90$ and $\eta_z = 0$, Equation (313) is restored with the limiting curve of the pure compression as well.

The same type of relationships between α and $\Omega_{y/z}$ can be found for *Type I* curves, relative to high strength steel (i.e. $f_y = 690 \text{ N/mm}^2$) hot-rolled square sections, according to the following equations:

$$\alpha = 0.005\Omega_{y/z} + 0.50 \text{ for } \Omega_{y/z} \leq 10 \quad (314)$$

$$\alpha = 0.55 \text{ for } 10 \leq \Omega_{y/z} \leq 80 \quad (315)$$

$$\alpha = -0.005\Omega_{y/z} + 0.95 \text{ for } \Omega_{y/z} \geq 80 \quad (316)$$

These equations can be written as follows, in order to provide smooth continuities with the pure compression load case:

$$\alpha = 0.005\Omega_{y/z} + \alpha_{comp} + 0.4\eta_y^{0.2} \leq 0.55 \text{ for } \Omega_{y/z} \leq 10 \quad (317)$$

$$\alpha = 0.55 \text{ for } 10 \leq \Omega_{y/z} \leq 80 \quad (318)$$

$$\alpha = -0.005\Omega_{y/z} + 0.45 + \alpha_{comp} + 0.4\eta_z^{0.2} \leq 0.55 \text{ for } \Omega_{y/z} \geq 80 \quad (319)$$

A variation of the imperfection factor based on the degree of biaxial bending was established in a similar manner for *Type II* curves, relative to hot-rolled square sections of normal steel grades ($f_y = 235 \text{ N/mm}^2$ and $f_y = 355 \text{ N/mm}^2$) and tested under compression and constant bending moment distribution. With the inclusion of the $\Omega_{y/z}$ parameter, the proposed α formula becomes as follows:

$$\alpha = 0.015\Omega_{y/z} + 0.80 \text{ for } \Omega_{y/z} \leq 10 \quad (320)$$

$$\alpha = 0.95 \text{ for } 10 \leq \Omega_{y/z} \leq 80 \quad (321)$$

$$\alpha = -0.015\Omega_{y/z} + 2.15 \text{ for } \Omega_{y/z} \geq 80 \quad (322)$$

That way, for $\Omega_{y/z} = 0$, Equation (320) is restored with the limiting curve being relative to compression with major-axis bending load case and for $\Omega_{y/z} = 90$, Equation (322) is restored with the limiting curve being relative to compression with minor-axis bending load case.

The same type of relationships can be found for *Type II* curves, relative to high strength steel (i.e. $f_y = 690 \text{ N/mm}^2$) hot-rolled square sections, according to the following equations:

$$\alpha = 0.01\Omega_{y/z} + 0.75 \text{ for } \Omega_{y/z} \leq 10 \quad (323)$$

$$\alpha = 0.85 \text{ for } 10 \leq \Omega_{y/z} \leq 80 \quad (324)$$

$$\alpha = -0.01\Omega_{y/z} + 1.65 \text{ for } \Omega_{y/z} \geq 80 \quad (325)$$

Table 44 summarizes the adopted parameters for the design curves of hot-rolled square members subjected to compression with constant bending moment distribution.

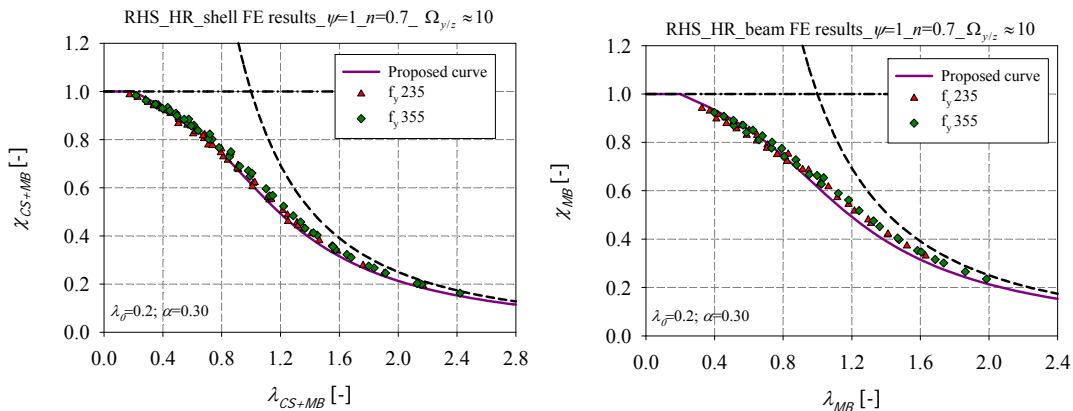
Table 44 – Design curves for the case of hot-rolled square members subjected to compression with biaxial constant bending moment

Combined load cases: $N+M_y+M_z$		
Constant bending moment distribution: $\psi = 1$		
Cross-section shape: SHS	Fabrication process: Hot-rolled	
$\chi_{CS+MB} = \frac{1}{\phi_{CS+MB} + \sqrt{\phi_{CS+MB}^2 - \lambda_{CS+MB}^2}}$ <p style="text-align: center;">for $\lambda_{CS+MB} \geq \lambda_0$</p> $\phi_{CS+MB} = 0.5(1 + \alpha(\lambda_{CS+MB} - \lambda_0) + \lambda_{CS+MB}^2)$ <p style="text-align: center;">With $\eta_y = \frac{m_y}{n_y} = \frac{M_y / M_{pl,y}}{N / N_{pl}}$; $\Omega_{y/z} = \arctan\left(\frac{m_z}{m_y}\right) = \arctan\left(\frac{M_z / M_{pl,z}}{M_y / M_{pl,y}}\right)$</p>		
Yield stress		
$f_y = 235 \text{ N/mm}^2$ $f_y = 355 \text{ N/mm}^2$		
Type I	Transition curve	Type II
$\alpha = \alpha_1 = 0.005\Omega_{y/z} + \alpha_{comp} + 0.4\eta_y^{0.2} \leq 0.65$ for $\Omega_{y/z} \leq 10$; $\alpha = \alpha_1 = 0.65$ for $10 \leq \Omega_{y/z} \leq 80$; $\alpha = -0.005\Omega_{y/z} + 0.45 + \alpha_{comp} + 0.4\eta_z^{0.2} \leq 0.65$ for $\Omega_{y/z} \geq 80$. $\lambda_0 = 0.2$	$\lambda_0 = \left(-\frac{0.1}{\eta_{y,2} - \eta_{y,1}}\right)(\eta_y - \eta_{y,2}) + 0.1$ $\alpha = \left(\frac{\alpha_2 - \alpha_1}{\eta_{y,2} - \eta_{y,1}}\right)(\eta_y - \eta_{y,2}) + \alpha_2$	$\alpha = \alpha_2 = 0.015\Omega_{y/z} + 0.80$ for $\Omega_{y/z} \leq 10$; $\alpha = \alpha_2 = 0.95$ for $10 \leq \Omega_{y/z} \leq 80$; $\alpha = \alpha_2 = -0.015\Omega_{y/z} + 2.15$ for $\Omega_{y/z} \geq 80$. $\lambda_0 = 0.1$

Yield stress $f_y = 690 \text{ N/mm}^2$		
Type I	Transition curve	Type II
$\alpha = 0.005\Omega_{y/z} + \alpha_{comp} + 0.4\eta_y^{0.2} \leq 0.55$ for $\Omega_{y/z} \leq 10$; $\alpha = \alpha_1 = 0.55$ for $10 \leq \Omega_{y/z} \leq 80$; $\alpha = -0.005\Omega_{y/z} + 0.45 + \alpha_{comp} + 0.4\eta_z^{0.2} \leq 0.55$ for $\Omega_{y/z} \geq 80$. $\lambda_0 = 0.2$	$\lambda_0 = \left(-\frac{0.1}{\eta_{y,2} - \eta_{y,1}} \right) (\eta_y - \eta_{y,2}) + 0.1$ $\alpha = \left(\frac{\alpha_2 - \alpha_1}{\eta_{y,2} - \eta_{y,1}} \right) (\eta_y - \eta_{y,2}) + \alpha_2$	$\alpha = \alpha_2 = 0.01\Omega_{y/z} + 0.75$ for $\Omega_{y/z} \leq 10$; $\alpha = \alpha_2 = 0.85$ for $10 \leq \Omega_{y/z} \leq 80$; $\alpha = \alpha_2 = -0.01\Omega_{y/z} + 1.65$ for $\Omega_{y/z} \geq 80$. $\lambda_0 = 0.1$

6.4.3.3.2. Hot-rolled rectangular sections

Figure 295 and Figure 296 illustrate the application of the O.I.C. for hot-rolled rectangular sections of different steel grades ($f_y = 235 \text{ N/mm}^2$, $f_y = 355 \text{ N/mm}^2$ and $f_y = 690 \text{ N/mm}^2$) tested under compression and constant biaxial bending. In these figures, the relative axial force ratio n was chosen equal to 0.7. Close tendencies of member results computed using beam and shell models are observed. Figure 297 and Figure 298 illustrate the results corresponding to hot-rolled rectangular sections under compression and constant biaxial bending with the relative axial force ratio n set equal to 0.3. The influence of the degree of biaxial bending on the member response is highlighted in the figures below. For each load case, a single interaction curve was derived for $f_y = 235 \text{ N/mm}^2$ and $f_y = 355 \text{ N/mm}^2$, since a small dispersion in the results is noted. Higher resistances are observed for $f_y = 690 \text{ N/mm}^2$ and higher curves were derived accordingly.



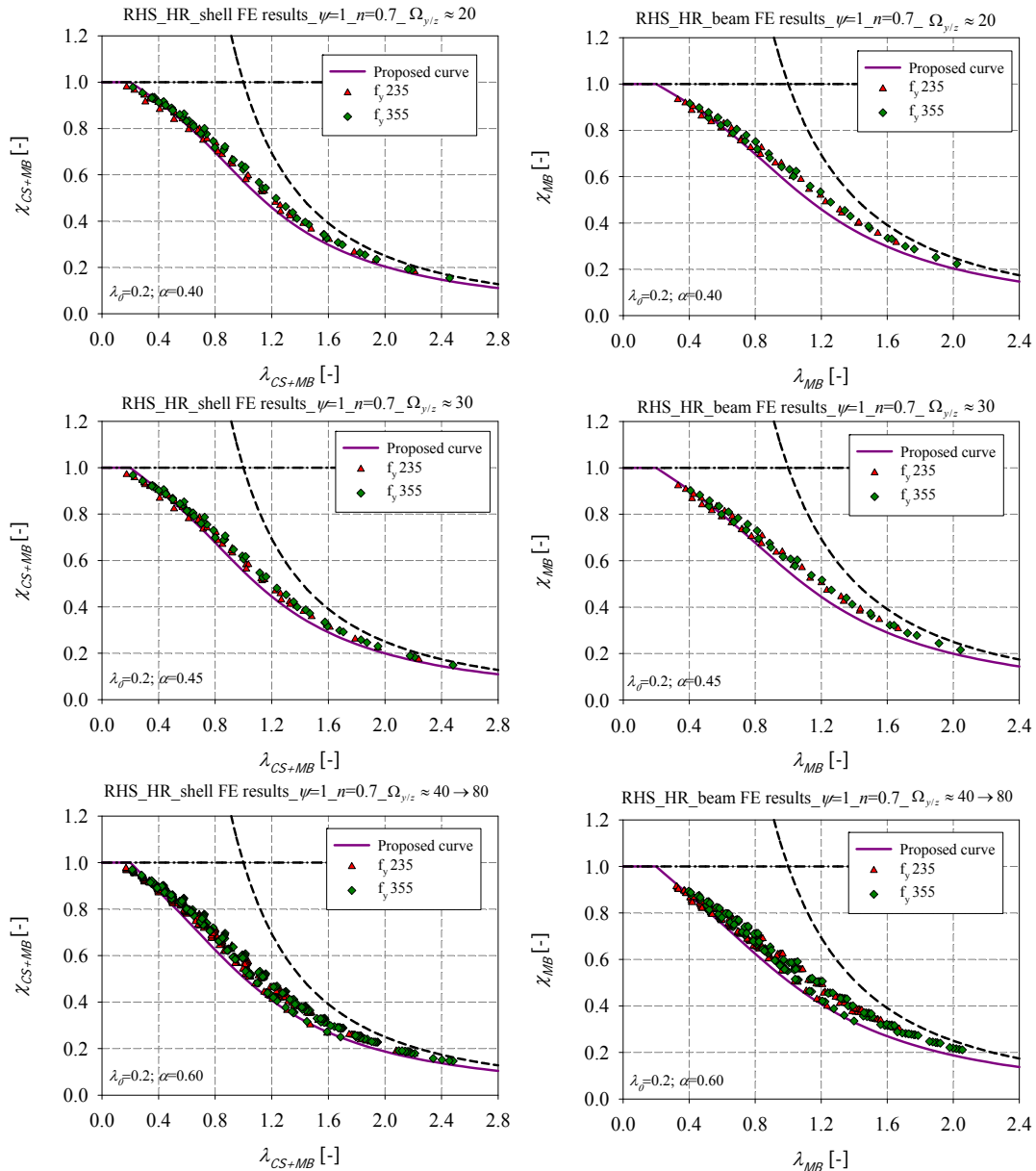
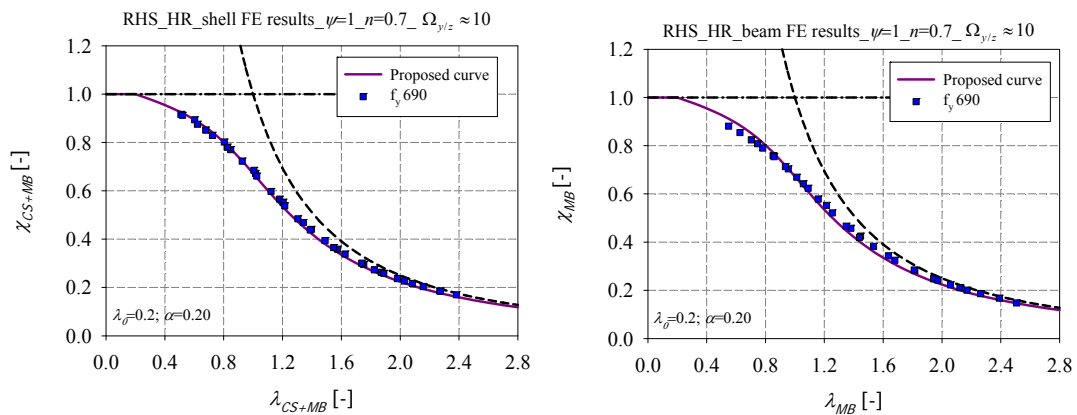


Figure 295 – Numerical member results for hot-rolled RHS of steel grades $f_y = 235 \text{ N/mm}^2$ and $f_y = 355 \text{ N/mm}^2$ tested under $N+M_y+M_z$, $\psi = 1$ and $n = 0.7$ – a) shell results – b) beam results



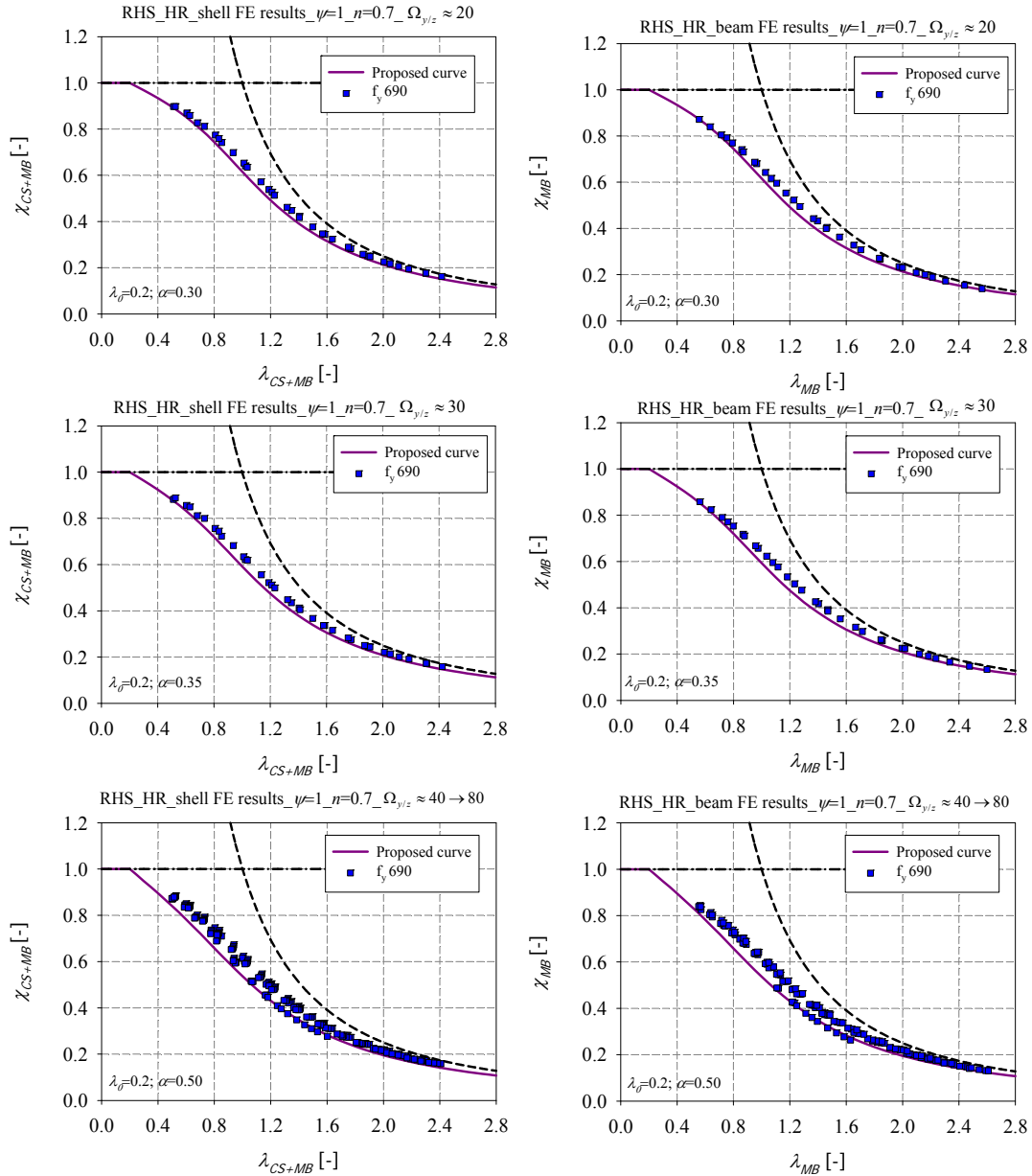
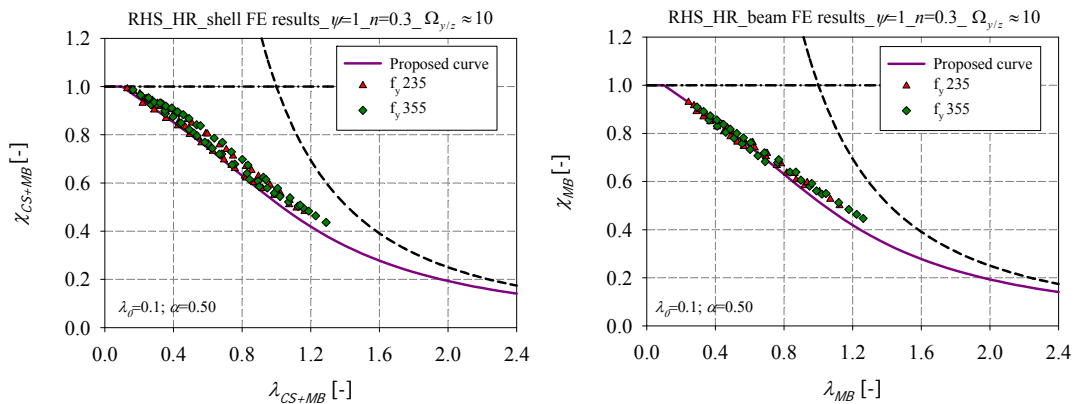


Figure 296 – Numerical member results of hot-rolled RHS of steel grade $f_y = 690 \text{ N/mm}^2$ tested under $N+M_y+M_z$,

$\psi = 1$ and $n = 0.7$ – a) shell results – b) beam results



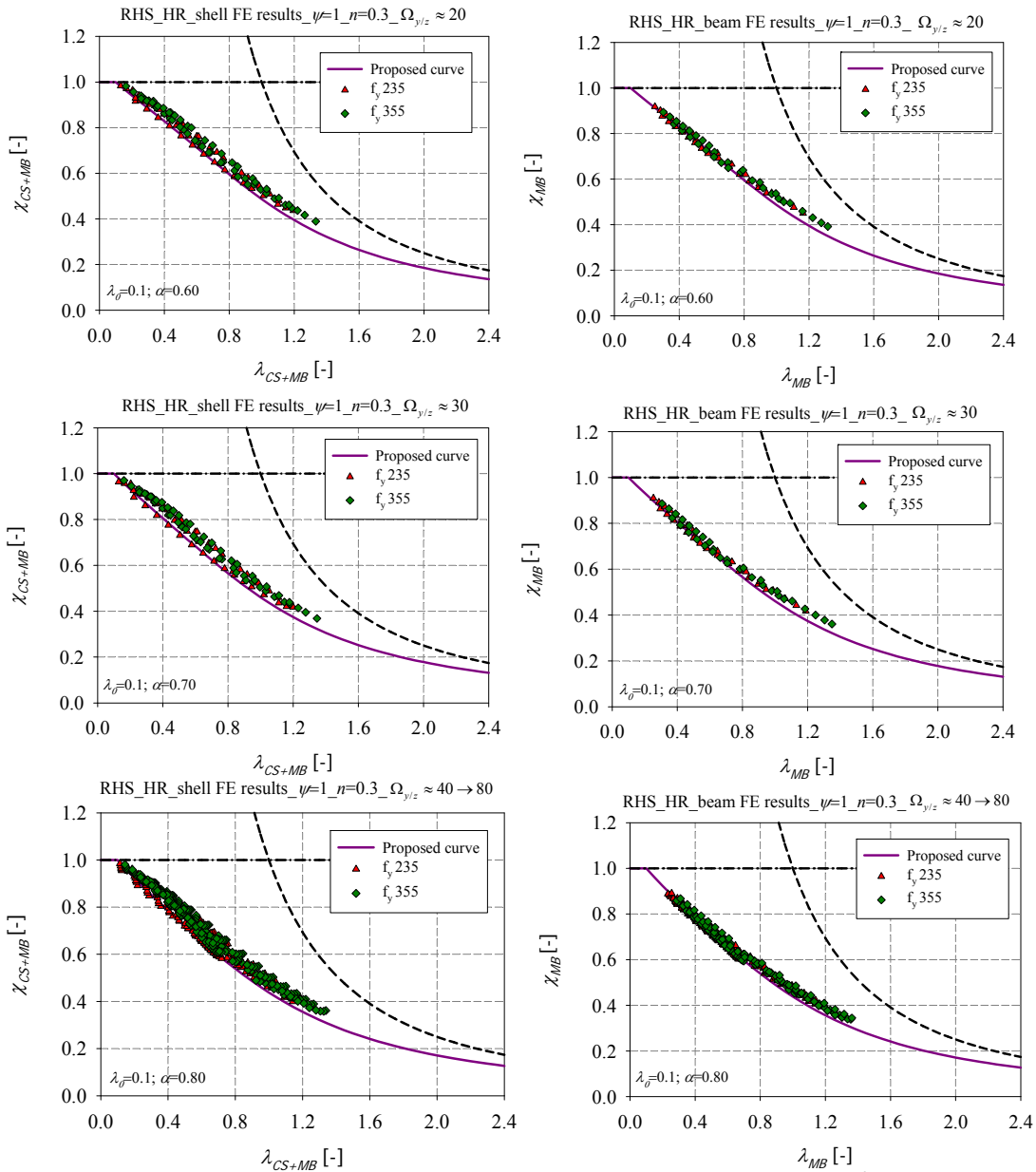
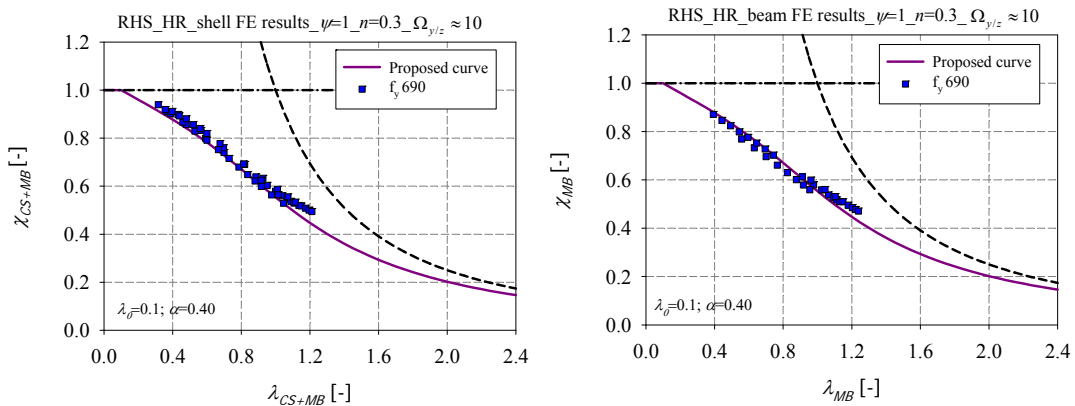


Figure 297 – Numerical member results of hot-rolled RHS of steel grades $f_y = 235 \text{ N/mm}^2$ and $f_y = 355 \text{ N/mm}^2$ tested under $N+M_y+M_z$, $\psi = 1$ and $n = 0.3$ – a) shell results – b) beam results



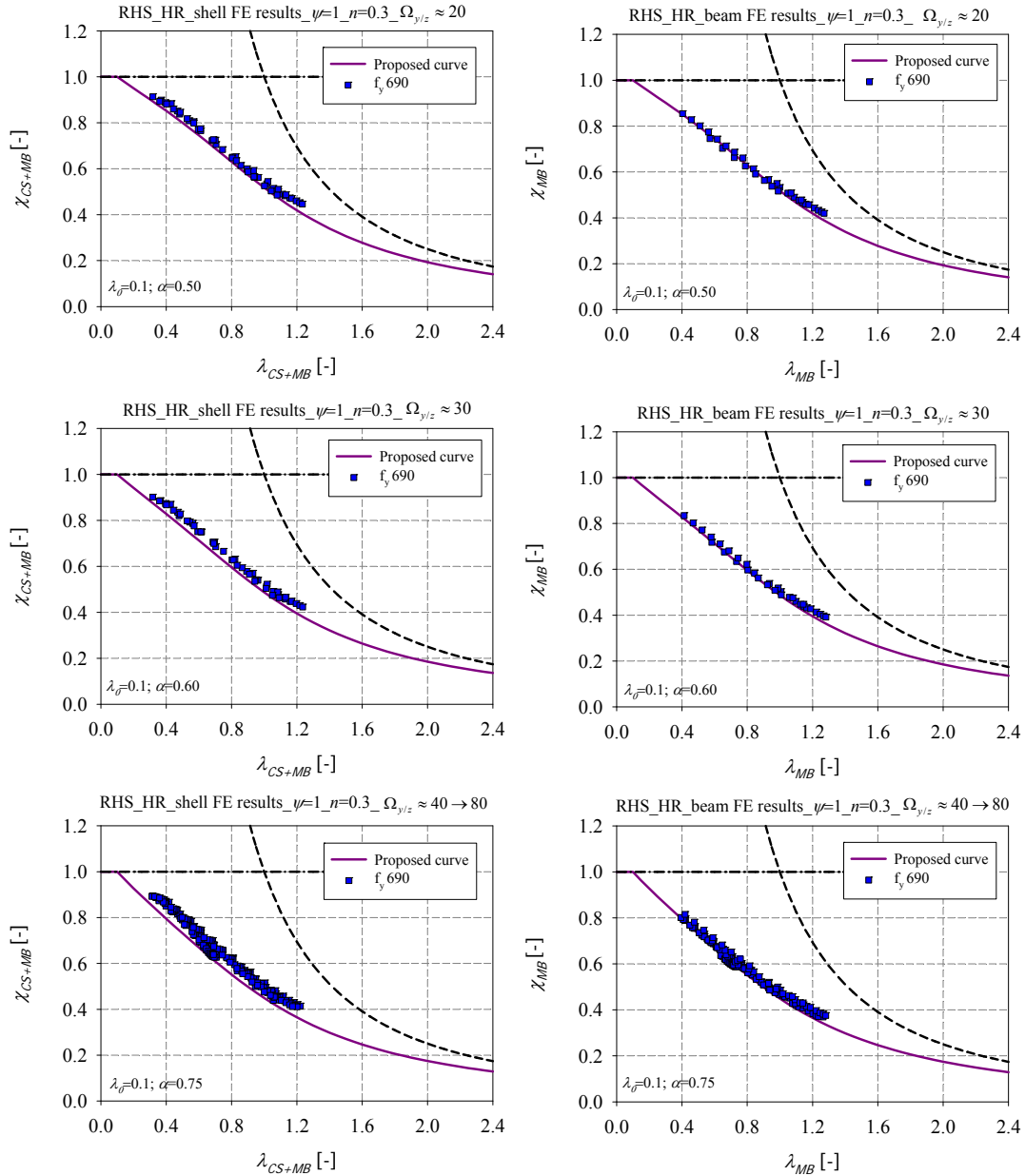


Figure 298 – Numerical member results of hot-rolled RHS of steel grade $f_y = 690 \text{ N/mm}^2$ tested under $N+M_y+M_z$, $\psi = 1$ and $n = 0.3$ – a) shell results – b) beam results

Figure 299 presents the particular case of $f_y = 235 \text{ N/mm}^2$ for hot-rolled rectangular sections tested under combined loading with $40 \leq \Omega_{y/z} \leq 80$. The results highlight the influence of the axial force ratio n . It can be clearly seen that the axial force ratio should be considered as a leading parameter for the derivation of appropriate interaction curves when the member is subjected to compression and a constant bending moment distribution.

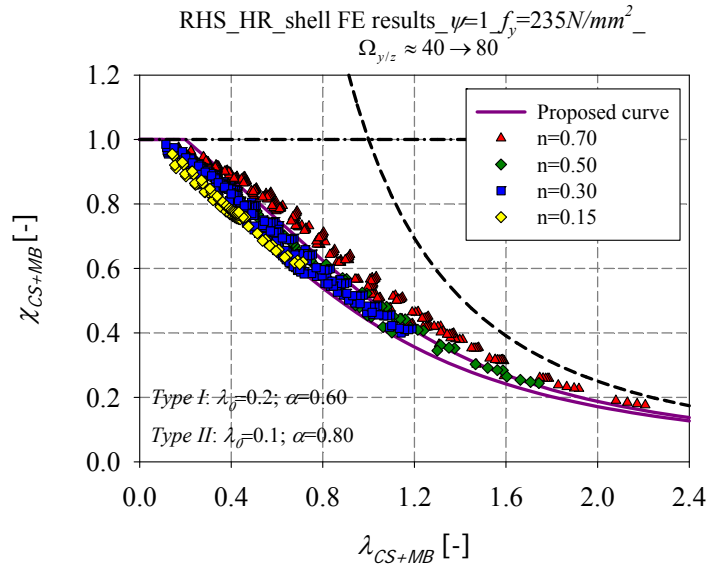
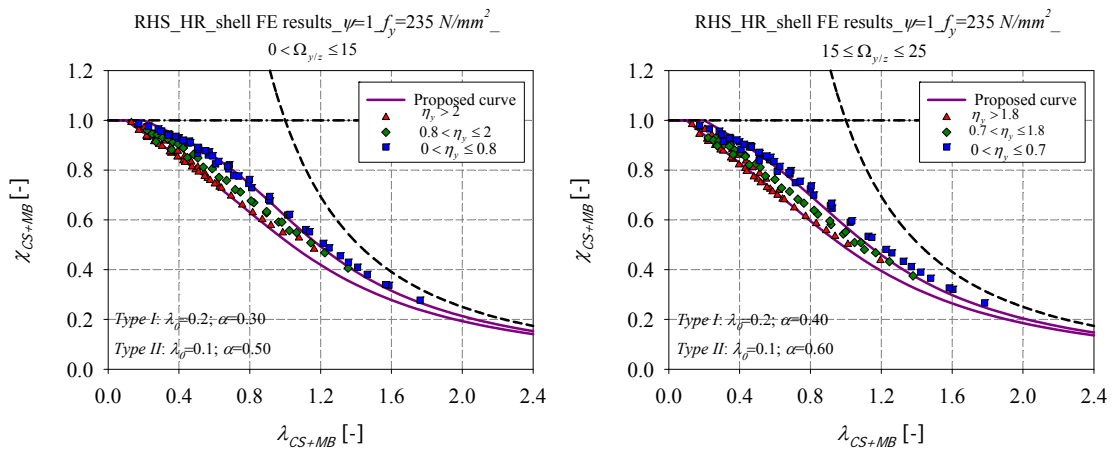


Figure 299 – Numerical member results of hot-rolled RHS of steel grade $f_y = 235 \text{ N/mm}^2$ tested under different values of axial force ratio n

The results were then sorted as a function of both parameters η_y and $\Omega_{y/z}$ regardless of the axial force ratio n . Two curves were derived accordingly (*Type I* and *Type II* curves) as illustrated in Figure 300 and a linear interpolation is defined for the transition between the two types of curves. The limits of the parameter η_y were chosen according to the results of steel grade $f_y = 235 \text{ N/mm}^2$. The same limits were derived for higher steel grades, for sake of simplicity and consistency, since they lead to conservative results.



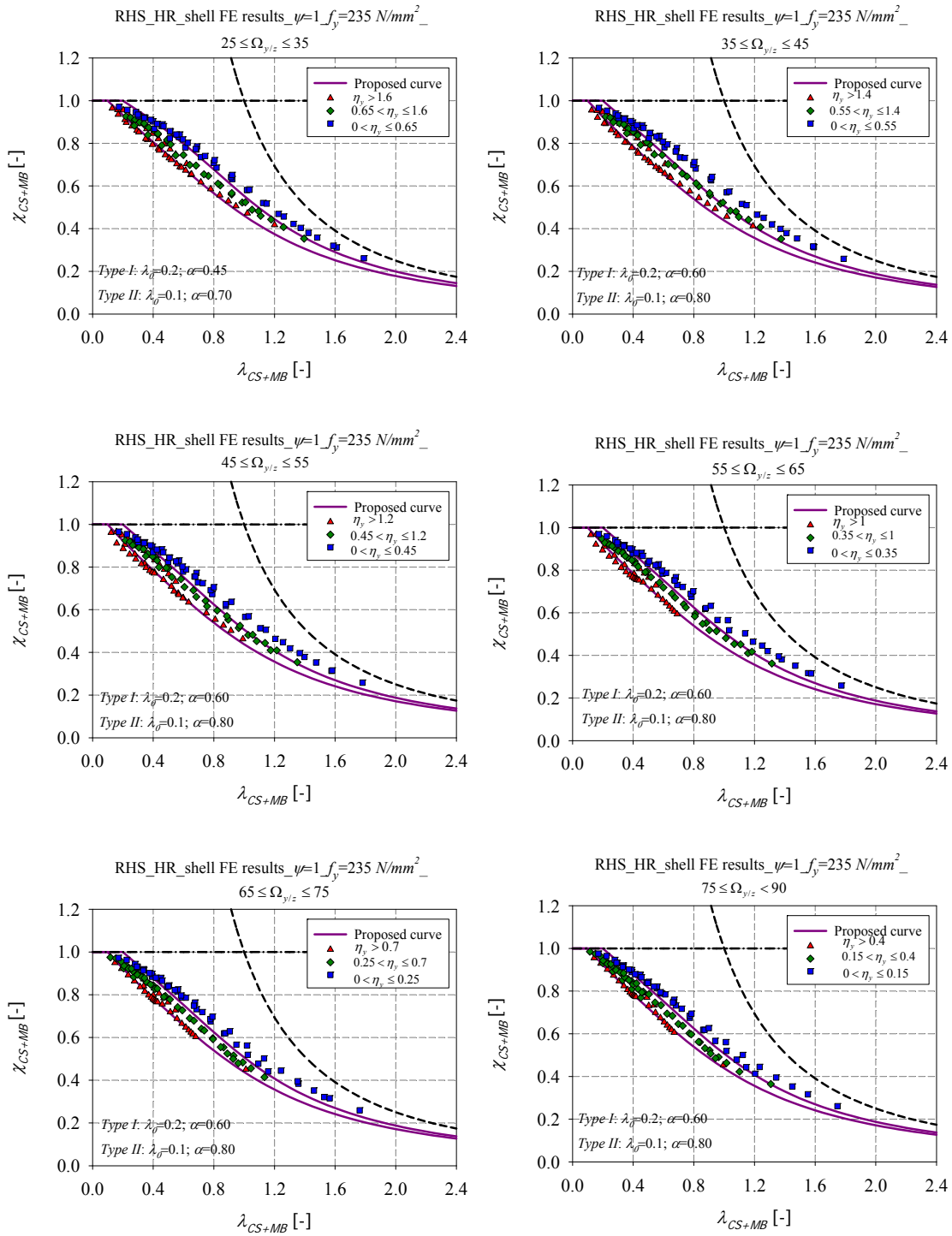


Figure 300 – Numerical member results of hot-rolled RHS of steel grade $f_y = 235 \text{ N/mm}^2$ derived as a function of the parameters $\Omega_{y/z}$ and η_y .

A relation was established between the imperfection factor and the degree of biaxial bending for the two types of curves.

Figure 301 presents a variation of the imperfection factor based on the degree of biaxial bending for *Type I* curves, relative to hot-rolled rectangular sections of normal steel grades ($f_y = 235 \text{ N/mm}^2$ and $f_y = 355 \text{ N/mm}^2$) and tested under compression and constant bending moment distribution. With the inclusion of the $\Omega_{y/z}$ parameter, the proposed α formula becomes as follows:

$$\alpha = 0.6 \text{ for } \Omega_{y/z} \geq 40 \quad (326)$$

$$\alpha = 0.0085\Omega_{y/z} + 0.25 \text{ for } \Omega_{y/z} < 40 \quad (327)$$

That way, for $\Omega_{y/z} = 0$, Equation (327) is restored with the limiting curve being relative to compression with major-axis bending load case and for $\Omega_{y/z} = 90$, Equation (326) is restored with the limiting curve being relative to compression with minor-axis bending load case.

These equations can be written as follows, in order to provide smooth continuities with the pure compression load case:

$$\alpha = \alpha_{comp} + 0.4\eta_z^{0.2} \leq 0.6 \text{ for } \Omega_{y/z} \geq 40 \quad (328)$$

$$\alpha = 0.0085\Omega_{y/z} + \alpha_{comp} + 0.05\eta_y^{0.2} \leq 0.6 \text{ for } \Omega_{y/z} < 40 \quad (329)$$

That way, for $\Omega_{y/z} = 0$ and $\eta_y = 0$, Equation (329) is restored with the limiting curve being relative to the pure compression load case and for $\Omega_{y/z} = 90$ and $\eta_z = 0$, Equation (328) is restored with the limiting curve of the pure compression as well.

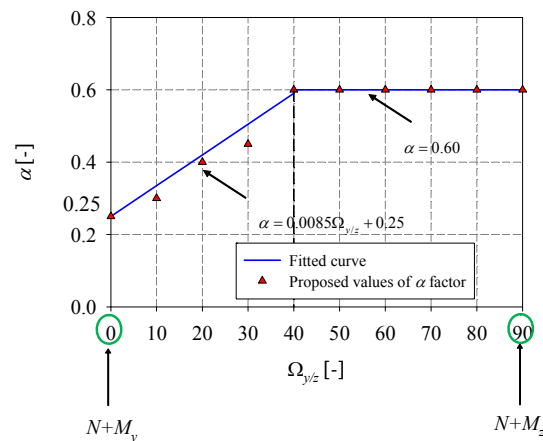


Figure 301 – Variation of α based on $\Omega_{y/z}$ for *Type I* curves, relative to HR RHS of steel grades $f_y = 235 \text{ N/mm}^2$ and $f_y = 355 \text{ N/mm}^2$, tested under compression and constant bending moment distribution.

The same type of relationships between α and $\Omega_{y/z}$ can be found for *Type I* curves relative to high strength steel (i.e. $f_y = 690 \text{ N/mm}^2$) hot-rolled rectangular sections, according to Equation (330) and Equation (331).

$$\alpha = 0.5 \text{ for } \Omega_{y/z} \geq 40 \quad (330)$$

$$\alpha = 0.0085\Omega_{y/z} + 0.15 \text{ for } \Omega_{y/z} < 40 \quad (331)$$

These equations can be written as follows, in order to provide smooth continuities with the pure compression load case:

$$\alpha = \alpha_{comp} + 0.4\eta_z^{0.2} \leq 0.5 \text{ for } \Omega_{y/z} \geq 40 \quad (332)$$

$$\alpha = 0.0085\Omega_{y/z} + \alpha_{comp} + 0.05\eta_z^{0.2} \leq 0.5 \text{ for } \Omega_{y/z} < 40 \quad (333)$$

A variation of the imperfection factor based on the degree of biaxial bending can be found in a similar manner for *Type II* curves, relative to hot-rolled rectangular sections of normal steel grades ($f_y = 235 \text{ N/mm}^2$ and $f_y = 355 \text{ N/mm}^2$) and tested under compression and constant bending moment distribution. With the inclusion of the $\Omega_{y/z}$ parameter, the proposed α formula becomes as follows:

$$\alpha = 0.8 \text{ for } \Omega_{y/z} \geq 40 \quad (334)$$

$$\alpha = 0.01\Omega_{y/z} + 0.4 \text{ for } \Omega_{y/z} < 40 \quad (335)$$

That way, for $\Omega_{y/z} = 0$, Equation (335) is restored with the limiting curve being relative to compression with major-axis bending load case and for $\Omega_{y/z} = 90$, Equation (334) is restored with the limiting curve being relative to compression with minor-axis bending load case.

The same type of relationships between α and $\Omega_{y/z}$ can be found for *Type II* curves, relative to high strength steel (i.e. $f_y = 690 \text{ N/mm}^2$) hot-rolled rectangular sections, according to Equation (336) and Equation (337).

$$\alpha = 0.75 \text{ for } \Omega_{y/z} \geq 40 \quad (336)$$

$$\alpha = 0.01\Omega_{y/z} + 0.35 \text{ for } \Omega_{y/z} < 40 \quad (337)$$

Table 45 summarizes the adopted parameters for the design curves of hot-rolled rectangular members subjected to compression with constant bending moment distribution.

Table 45 – Design curves for the case of hot-rolled RHS members subjected to compression with biaxial constant bending moment

Combined load cases: $N+M_y+M_z$		
Constant bending moment distribution: $\psi = 1$		
Cross-section shape: RHS	Fabrication process: Hot-rolled	
$\chi_{CS+MB} = \frac{1}{\phi_{CS+MB} + \sqrt{\phi_{CS+MB}^2 - \lambda_{CS+MB}^2}}$ for $\lambda_{CS+MB} \geq \lambda_0$ $\phi_{CS+MB} = 0.5(1 + \alpha(\lambda_{CS+MB} - \lambda_0) + \lambda_{CS+MB}^2)$ With $\eta_y = \frac{m_y}{n_y} = \frac{M_y / M_{pl,y}}{N / N_{pl}}$; $\Omega_{y/z} = \arctan\left(\frac{m_z}{m_y}\right) = \arctan\left(\frac{M_z / M_{pl,z}}{M_y / M_{pl,y}}\right)$		
Yield stress		
$f_y = 235 \text{ N/mm}^2$ $f_y = 355 \text{ N/mm}^2$		
Type I	Transition curve	Type II
$\alpha = \alpha_1 = \alpha_{comp} + 0.4\eta_z^{0.2} \leq 0.6$ for $\Omega_{y/z} \geq 40$; $\alpha = \alpha_1 = 0.0085\Omega_{y/z} + \alpha_{comp} + 0.05\eta_y^{0.2} \leq 0.6$ for $\Omega_{y/z} < 40$. $\lambda_0 = 0.2$	$\lambda_0 = \left(-\frac{0.1}{\eta_{y,2} - \eta_{y,1}}\right)(\eta_y - \eta_{y,2}) + 0.1$ $\alpha = \left(\frac{\alpha_2 - \alpha_1}{\eta_{y,2} - \eta_{y,1}}\right)(\eta_y - \eta_{y,2}) + \alpha_2$	$\alpha = \alpha_2 = 0.80$ for $\Omega_{y/z} \geq 40$; $\alpha = \alpha_2 = 0.01\Omega_{y/z} + 0.4$ for $\Omega_{y/z} < 40$. $\lambda_0 = 0.1$
Yield stress		
$f_y = 690 \text{ N/mm}^2$		
Type I	Transition curve	Type II
$\alpha = \alpha_1 = \alpha_{comp} + 0.4\eta_z^{0.2} \leq 0.5$ for $\Omega_{y/z} \geq 40$; $\alpha = 0.0085\Omega_{y/z} + \alpha_{comp} + 0.05\eta_z^{0.2} \leq 0.5$ for $\Omega_{y/z} < 40$. $\lambda_0 = 0.2$	$\lambda_0 = \left(-\frac{0.1}{\eta_{y,2} - \eta_{y,1}}\right)(\eta_y - \eta_{y,2}) + 0.1$ $\alpha = \left(\frac{\alpha_2 - \alpha_1}{\eta_{y,2} - \eta_{y,1}}\right)(\eta_y - \eta_{y,2}) + \alpha_2$	$\alpha = \alpha_2 = 0.75$ for $\Omega_{y/z} \geq 40$; $\alpha = \alpha_2 = 0.01\Omega_{y/z} + 0.35$ for $\Omega_{y/z} < 40$. $\lambda_0 = 0.1$

6.4.3.3. Cold-formed square sections

Figure 302 and Figure 303 illustrate the application of the O.I.C. for cold-formed square members of different steel grades ($f_y = 235 \text{ N/mm}^2$, $f_y = 355 \text{ N/mm}^2$ and $f_y = 690 \text{ N/mm}^2$), tested under combined loading situations: compression and constant biaxial bending. In these

figures, the relative axial force ratio n was chosen equal to 0.7 and to 0.3, respectively. For each load case, a single interaction curve was derived for $f_y = 235 \text{ N/mm}^2$ and $f_y = 355 \text{ N/mm}^2$, since a small dispersion in the results is noted. Higher resistances are observed for $f_y = 690 \text{ N/mm}^2$ and higher curves were derived accordingly. Figure 304 presents the particular case of $f_y = 235 \text{ N/mm}^2$ for cold-formed square sections highlighting the influence of the axial force ratio n .

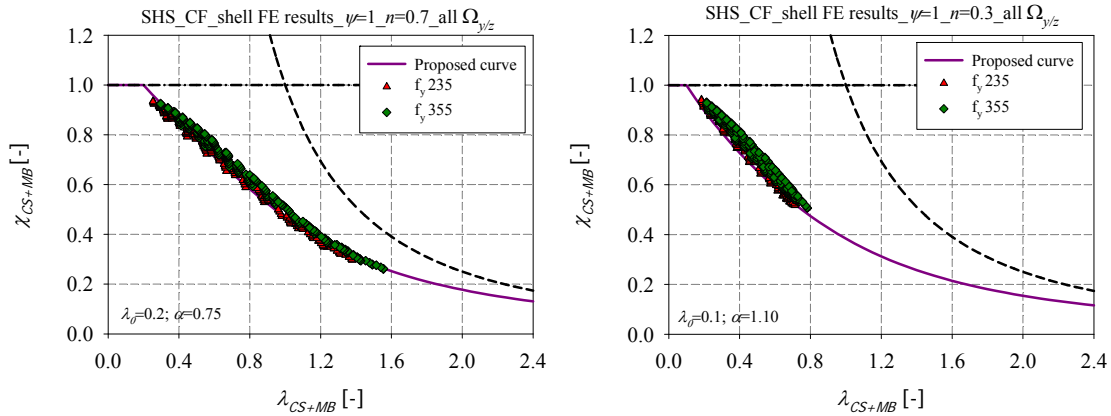


Figure 302 – Numerical member results of cold-formed SHS of steel grades $f_y = 235 \text{ N/mm}^2$ and $f_y = 355 \text{ N/mm}^2$ tested under $N + M_y + M_z$ with $\psi = 1$ and under different axial force level – a) $n = 0.7$ – b) $n = 0.3$

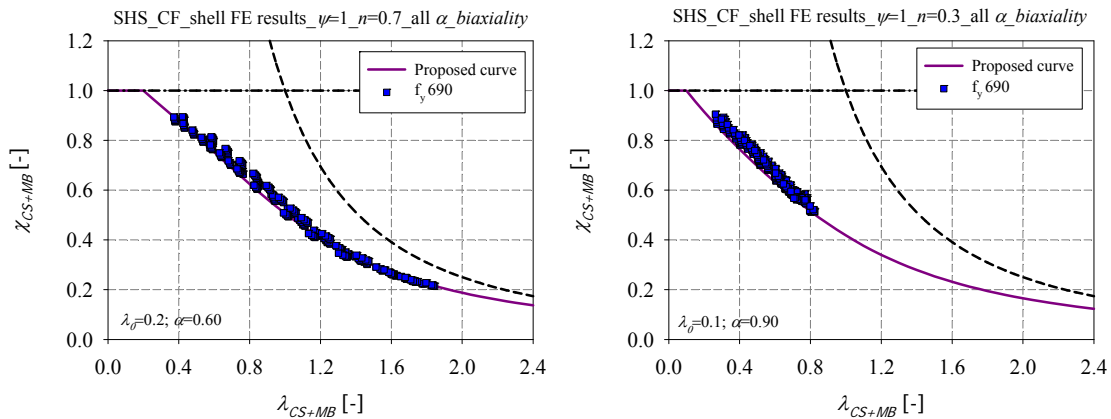


Figure 303 – Numerical member results of cold-formed SHS of steel grade $f_y = 690 \text{ N/mm}^2$ under $N + M_y + M_z$ with $\psi = 1$ and under different axial force level – a) $n = 0.7$ – b) $n = 0.3$

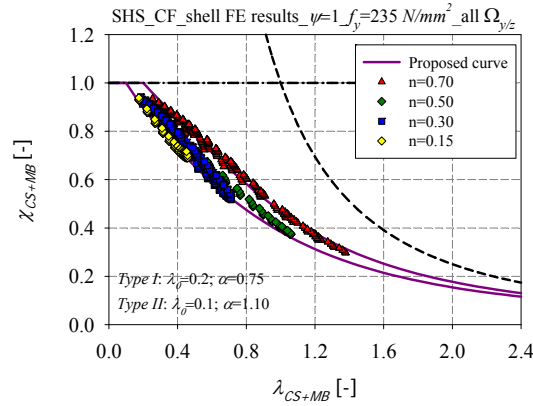
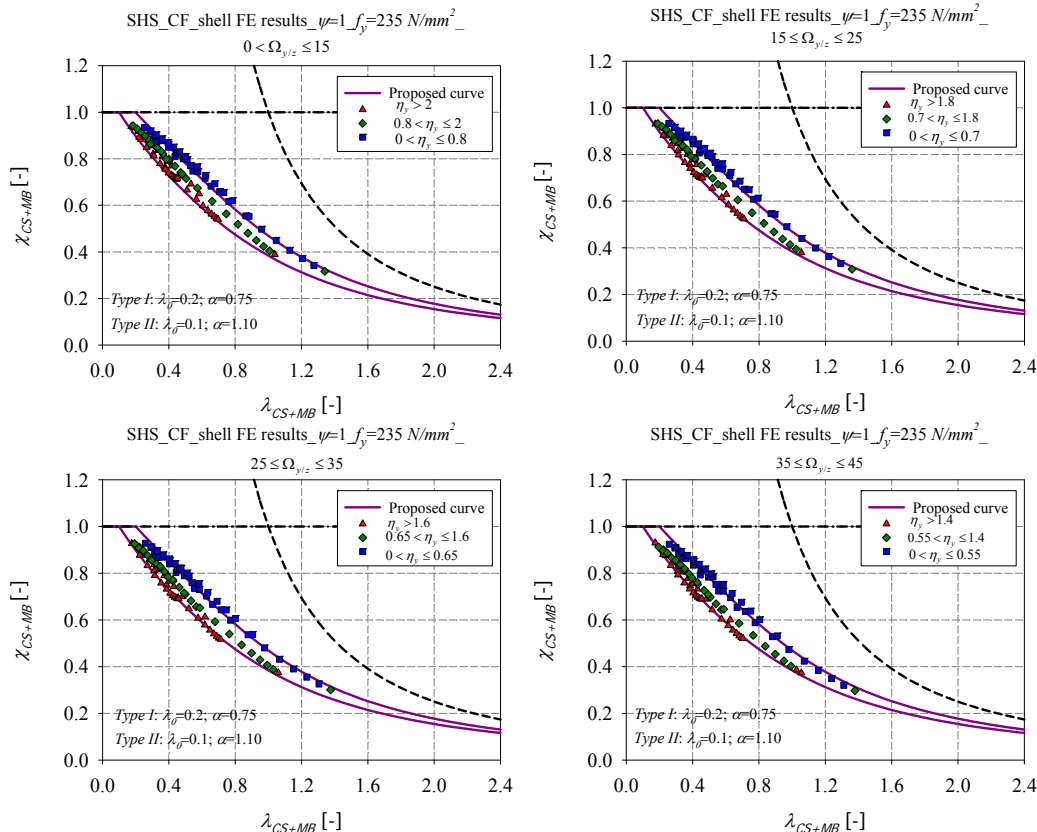


Figure 304 – Numerical member results of cold-formed SHS of steel grade $f_y = 235 \text{ N/mm}^2$ tested under different values of axial force ratio n

The results were then sorted as a function of both parameters η_y and $\Omega_{y/z}$ regardless of the axial force ratio n . Two curves were derived accordingly (*Type I* and *Type II* curves) as illustrated in Figure 305 and a linear interpolation is defined for the transition between the two types of curves. The limits of the parameter η_y were chosen according to the results of steel grade $f_y = 235 \text{ N/mm}^2$. The same limits were derived for higher steel grades, for sake of simplicity and consistency, since they lead to conservative results.



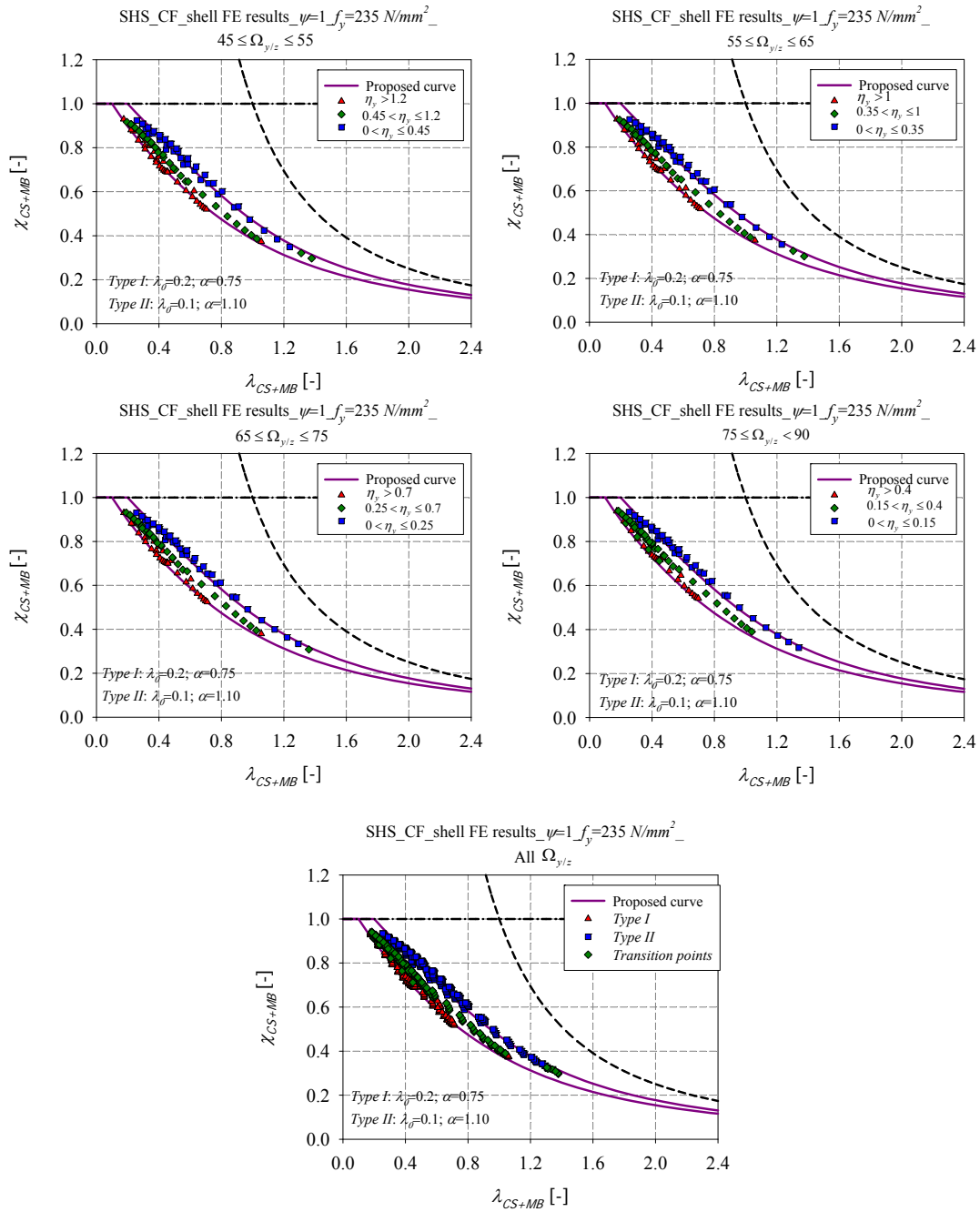


Figure 305 – Numerical member results for cold-formed SHS of steel grade $f_y = 235 \text{ N/mm}^2$ derived as a function of the parameters $\Omega_{y/z}$ and η_y .

A relation was established between the imperfection factor and the degree of biaxial bending for the two types of curves. Figure 306 presents a variation of the imperfection factor based on the degree of biaxial bending for *Type I* curves, relative to cold-formed square sections of normal steel grades ($f_y = 235 \text{ N/mm}^2$ and $f_y = 355 \text{ N/mm}^2$) and tested under compression and

constant bending moment distribution. With the inclusion of the $\Omega_{y/z}$ parameter, the proposed α formula becomes as the following:

$$\alpha = 0.005\Omega_{y/z} + 0.70 \text{ for } \Omega_{y/z} \leq 10 \quad (338)$$

$$\alpha = 0.75 \text{ for } 10 \leq \Omega_{y/z} \leq 80 \quad (339)$$

$$\alpha = -0.005\Omega_{y/z} + 1.15 \text{ for } \Omega_{y/z} \geq 80 \quad (340)$$

That way, for $\Omega_{y/z} = 0$, Equation (338) is restored with the limiting curve being relative to compression with major-axis bending load case and for $\Omega_{y/z} = 90$, Equation (340) is restored with the limiting curve being relative to compression with minor-axis bending load case.

In order to provide a smooth continuity with the pure compression load case, the term 0.7 is replaced by $\alpha_{comp} + 0.4\eta^{0.2}$ as explained in section 6.4.3.1.3, and the proposed α formula becomes as follows:

$$\alpha = 0.005\Omega_{y/z} + \alpha_{comp} + 0.4\eta_y^{0.2} \leq 0.75 \text{ for } \Omega_{y/z} \leq 10 \quad (341)$$

$$\alpha = 0.75 \text{ for } 10 \leq \Omega_{y/z} \leq 80 \quad (342)$$

$$\alpha = -0.005\Omega_{y/z} + 0.45 + \alpha_{comp} + 0.4\eta_z^{0.2} \leq 0.75 \text{ for } \Omega_{y/z} \geq 80 \quad (343)$$

That way, for $\Omega_{y/z} = 0$ and $\eta_y = 0$, Equation (341) is restored with the limiting curve being relative to the pure compression load case and for $\Omega_{y/z} = 90$ and $\eta_z = 0$, Equation (343) is restored with the limiting curve of the pure compression as well.

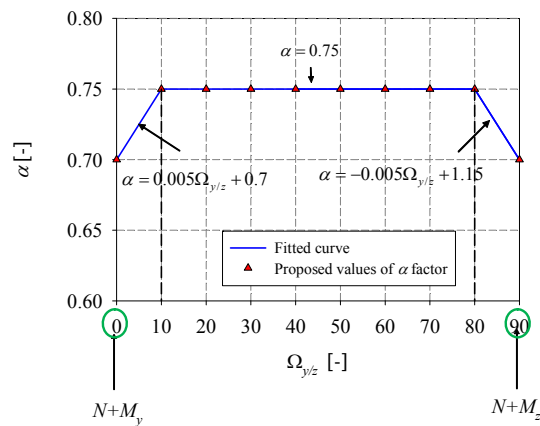


Figure 306 – Variation of α based on $\Omega_{y/z}$ for Type I curves, relative to CF SHS of steel grades

$f_y = 235 \text{ N/mm}^2$ and $f_z = 355 \text{ N/mm}^2$, tested under compression and constant bending moment distribution.

The same type of relationships between α and $\Omega_{y/z}$ can be found for high strength steel (i.e. $f_y = 690 \text{ N/mm}^2$) *Type I* curves, relative to cold-formed square sections according to the following equations:

$$\alpha = 0.005\Omega_{y/z} + 0.55 \text{ for } \Omega_{y/z} \leq 10 \quad (344)$$

$$\alpha = 0.60 \text{ for } 10 \leq \Omega_{y/z} \leq 80 \quad (345)$$

$$\alpha = -0.005\Omega_{y/z} + 1.0 \text{ for } \Omega_{y/z} \geq 80 \quad (346)$$

These equations can be written as follows, in order to provide smooth continuities with the pure compression load case:

$$\alpha = 0.005\Omega_{y/z} + \alpha_{comp} + 0.4\eta_y^{0.2} \leq 0.6 \text{ for } \Omega_{y/z} \leq 10 \quad (347)$$

$$\alpha = 0.60 \text{ for } 10 \leq \Omega_{y/z} \leq 80 \quad (348)$$

$$\alpha = -0.005\Omega_{y/z} + 0.45 + \alpha_{comp} + 0.4\eta_z^{0.2} \leq 0.6 \text{ for } \Omega_{y/z} \geq 80 \quad (349)$$

A variation of the imperfection factor based on the degree of biaxial bending can be found in a similar manner for *Type II* curves, relative to cold-formed square sections of normal steel grades ($f_y = 235 \text{ N/mm}^2$ and $f_y = 355 \text{ N/mm}^2$) and tested under compression and constant bending moment distribution. With the inclusion of the $\Omega_{y/z}$ parameter, the proposed α formula becomes as follows:

$$\alpha = 0.01\Omega_{y/z} + 1.0 \text{ for } \Omega_{y/z} \leq 10 \quad (350)$$

$$\alpha = 1.1 \text{ for } 10 \leq \Omega_{y/z} \leq 80 \quad (351)$$

$$\alpha = -0.01\Omega_{y/z} + 1.9 \text{ for } \Omega_{y/z} \geq 80 \quad (352)$$

That way, for $\Omega_{y/z} = 0$, Equation (350) is restored with the limiting curve being relative to compression with major-axis bending load case and for $\Omega_{y/z} = 90$, Equation (352) is restored with the limiting curve being relative to compression with minor-axis bending load case.

The same type of relationships between α and $\Omega_{y/z}$ can be found for *Type II* curves, relative to high strength steel (i.e. $f_y = 690 \text{ N/mm}^2$) cold-formed square sections, according to the following equations:

$$\alpha = 0.01\Omega_{y/z} + 0.80 \text{ for } \Omega_{y/z} \leq 10 \quad (353)$$

$$\alpha = 0.90 \text{ for } 10 \leq \Omega_{y/z} \leq 80 \quad (354)$$

$$\alpha = -0.01\Omega_{y/z} + 1.7 \text{ for } \Omega_{y/z} \geq 80 \quad (355)$$

Table 46 summarizes the adopted parameters for the design curves of cold-formed square hollow members subjected to compression with constant bending moment distribution.

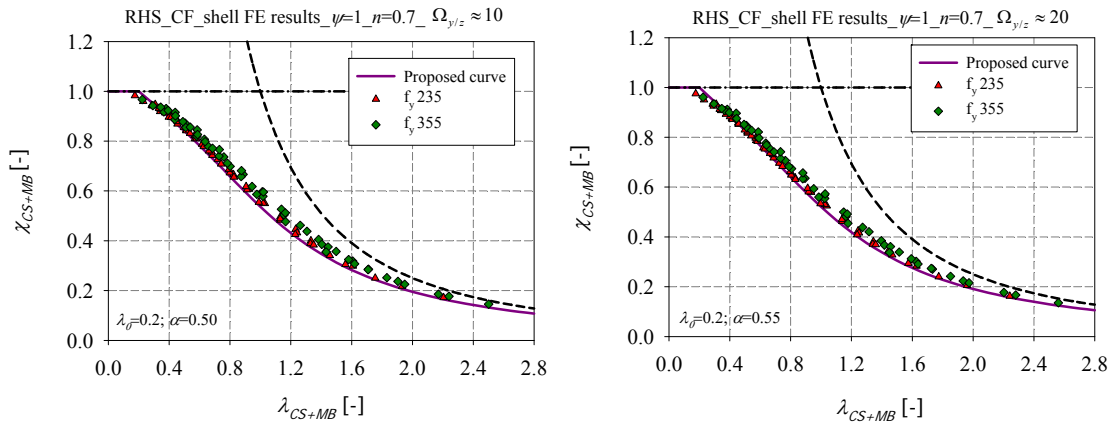
Table 46 – Design curves for the case of cold-formed SHS members subjected to compression with biaxial constant bending moment

Combined load cases: $N+M_y+M_z$		
Constant bending moment distribution: $\psi = 1$		
Cross-section shape: SHS	Fabrication process: Cold-formed	
$\chi_{CS+MB} = \frac{1}{\phi_{CS+MB} + \sqrt{\phi_{CS+MB}^2 - \lambda_{CS+MB}^2}}$ for $\lambda_{CS+MB} \geq \lambda_0$ $\phi_{CS+MB} = 0.5(1 + \alpha(\lambda_{CS+MB} - \lambda_0) + \lambda_{CS+MB}^2)$		
With $\eta_y = \frac{m_y}{n_y} = \frac{M_y / M_{pl,y}}{N / N_{pl}}$; $\Omega_{y/z} = \arctan\left(\frac{m_z}{m_y}\right) = \arctan\left(\frac{M_z / M_{pl,z}}{M_y / M_{pl,y}}\right)$		
Yield stress		
$f_y = 235 \text{ N/mm}^2$ $f_y = 355 \text{ N/mm}^2$		
Type I	Transition curve	Type II
$\alpha = \alpha_1 = 0.005\Omega_{y/z} + \alpha_{comp} + 0.4\eta_y^{0.2} \leq 0.75$ for $\Omega_{y/z} \leq 10$; $\alpha = \alpha_1 = 0.75$ for $10 \leq \Omega_{y/z} \leq 80$; $\alpha = \alpha_1 = -0.005\Omega_{y/z} + 0.45 + \alpha_{comp} + 0.4\eta_z^{0.2} \leq 0.75$ for $\Omega_{y/z} \geq 80$. $\lambda_0 = 0.2$	$\lambda_0 = \left(-\frac{0.1}{\eta_{y,2} - \eta_{y,1}}\right)(\eta_y - \eta_{y,2}) + 0.1$ $\alpha = \left(\frac{\alpha_2 - \alpha_1}{\eta_{y,2} - \eta_{y,1}}\right)(\eta_y - \eta_{y,2}) + \alpha_2$	$\alpha = \alpha_2 = 0.01\Omega_{y/z} + 1.0$ for $\Omega_{y/z} \leq 10$; $\alpha = \alpha_2 = 1.1$ for $10 \leq \Omega_{y/z} \leq 80$; $\alpha = \alpha_2 = -0.01\Omega_{y/z} + 1.9$ for $\Omega_{y/z} \geq 80$. $\lambda_0 = 0.1$
Yield stress		
$f_y = 690 \text{ N/mm}^2$		
Type I	Transition curve	Type II

$\alpha = \alpha_1 = 0.005\Omega_{y/z} + \alpha_{comp} + 0.4\eta_y^{0.2} \leq 0.6$ <p style="text-align: center;">for $\Omega_{y/z} \leq 10$;</p> $\alpha = 0.60$ <p style="text-align: center;">for $10 \leq \Omega_{y/z} \leq 80$;</p> $\alpha = \alpha_1 = -0.005\Omega_{y/z} + 0.45 + \alpha_{comp} + 0.4\eta_z^{0.2} \leq 0.6$ <p style="text-align: center;">for $\Omega_{y/z} \geq 80$.</p> $\lambda_0 = 0.2$	$\lambda_0 = \left(-\frac{0.1}{\eta_{y,2} - \eta_{y,1}} \right) (\eta_y - \eta_{y,2}) + 0.1$ $\alpha = \left(\frac{\alpha_2 - \alpha_1}{\eta_{y,2} - \eta_{y,1}} \right) (\eta_y - \eta_{y,2}) + \alpha_2$	$\alpha = \alpha_2 = 0.01\Omega_{y/z} + 0.80$ <p style="text-align: center;">for $\Omega_{y/z} \leq 10$;</p> $\alpha = \alpha_2 = 0.90$ <p style="text-align: center;">for $10 \leq \Omega_{y/z} \leq 80$;</p> $\alpha = \alpha_2 = -0.01\Omega_{y/z} + 1.7$ <p style="text-align: center;">for $\Omega_{y/z} \geq 80$.</p> $\lambda_0 = 0.1$
---	---	--

6.4.3.3.4. Cold-formed rectangular sections

Figure 307 and Figure 308 illustrate the application of the O.I.C. for cold-formed rectangular members tested under combined loading situations: compression and constant biaxial bending, for different steel grades: $f_y = 235 \text{ N/mm}^2$, $f_y = 355 \text{ N/mm}^2$ and $f_y = 690 \text{ N/mm}^2$. The ψ factor was chosen equal to 1 and the relative axial force ratio n was chosen equal to 0.7. Figure 309 and Figure 310 illustrate the same set of results with a relative axial force ratio n equal to 0.3. The influence of the degree of biaxial bending on the member response is highlighted in the figures below. For each load case, single interaction curves were derived for $f_y = 235 \text{ N/mm}^2$ and $f_y = 355 \text{ N/mm}^2$, since a small dispersion in the results is noted. Higher resistances are observed for $f_y = 690 \text{ N/mm}^2$ and higher curves were derived accordingly.



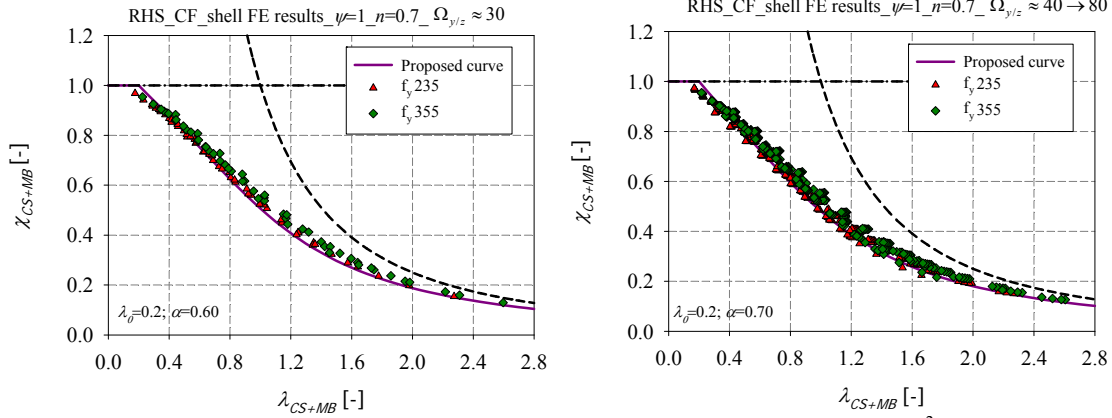


Figure 307 – Numerical member results for cold-formed RHS of steel grades $f_y = 235 \text{ N/mm}^2$ and $f_y = 355 \text{ N/mm}^2$ tested under $N+M_y+M_z$, $\psi = 1$ and $n = 0.7$

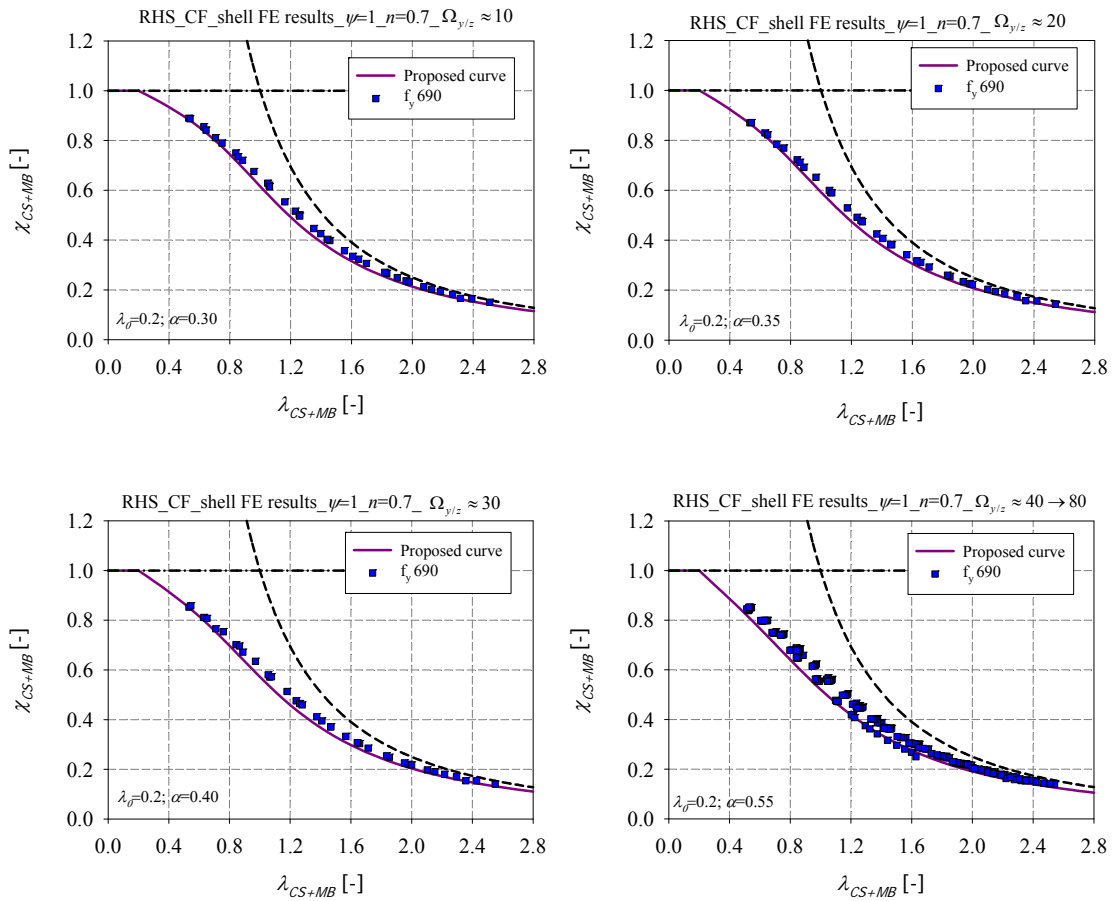


Figure 308 – Numerical member results for cold-formed RHS of steel grade $f_y = 690 \text{ N/mm}^2$, tested under $N+M_y+M_z$, $\psi = 1$ and $n = 0.7$

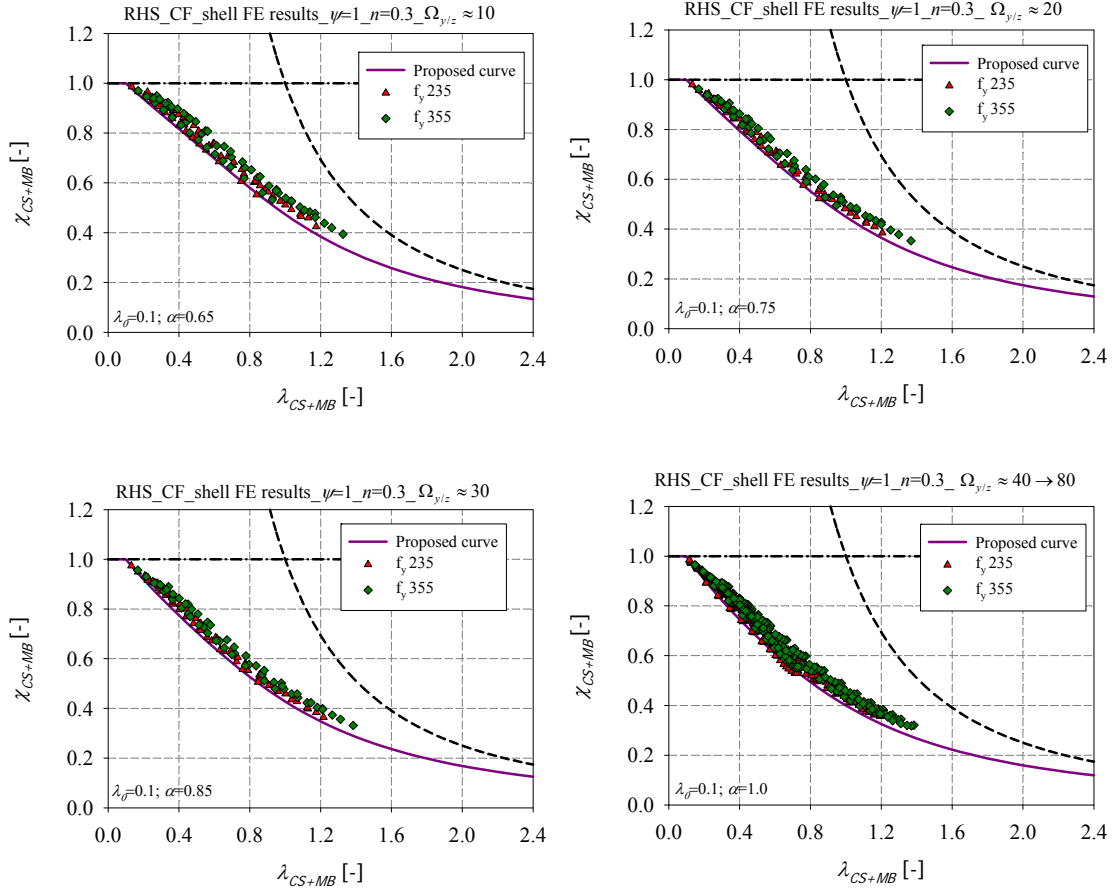
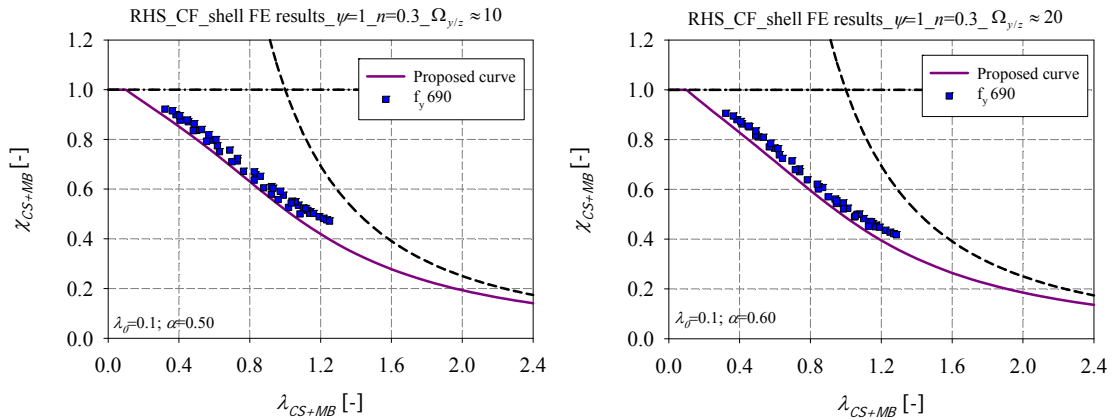


Figure 309 – Numerical member results for cold-formed RHS of steel grades $f_y = 235 \text{ N/mm}^2$ and $f_y = 355 \text{ N/mm}^2$ tested under $N+M_y+M_z$, $\psi = 1$ and $n = 0.3$



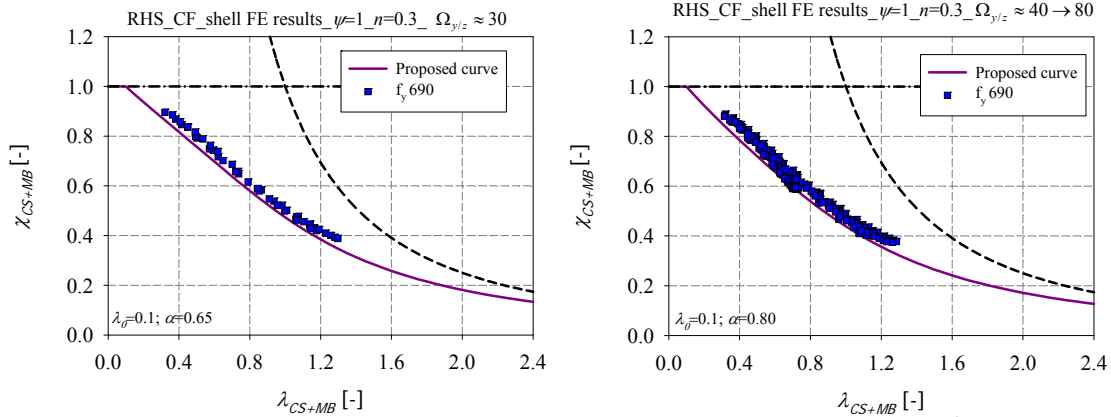


Figure 310 – Numerical member results of cold-formed RHS of steel grade $f_y = 690 \text{ N/mm}^2$ tested under $N+M_y+M_z$, $\psi = 1$ and $n = 0.3$

Figure 311 presents the particular case of $f_y = 235 \text{ N/mm}^2$ for cold-formed rectangular sections tested under combined loading with $40 \leq \Omega_{y/z} \leq 80$. The results highlight the influence of the axial force ratio n . It can be clearly seen that the axial force ratio should be considered as a leading parameter for the derivation of appropriate interaction curves.

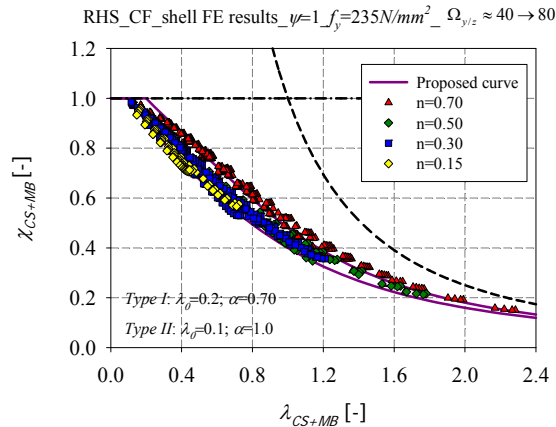
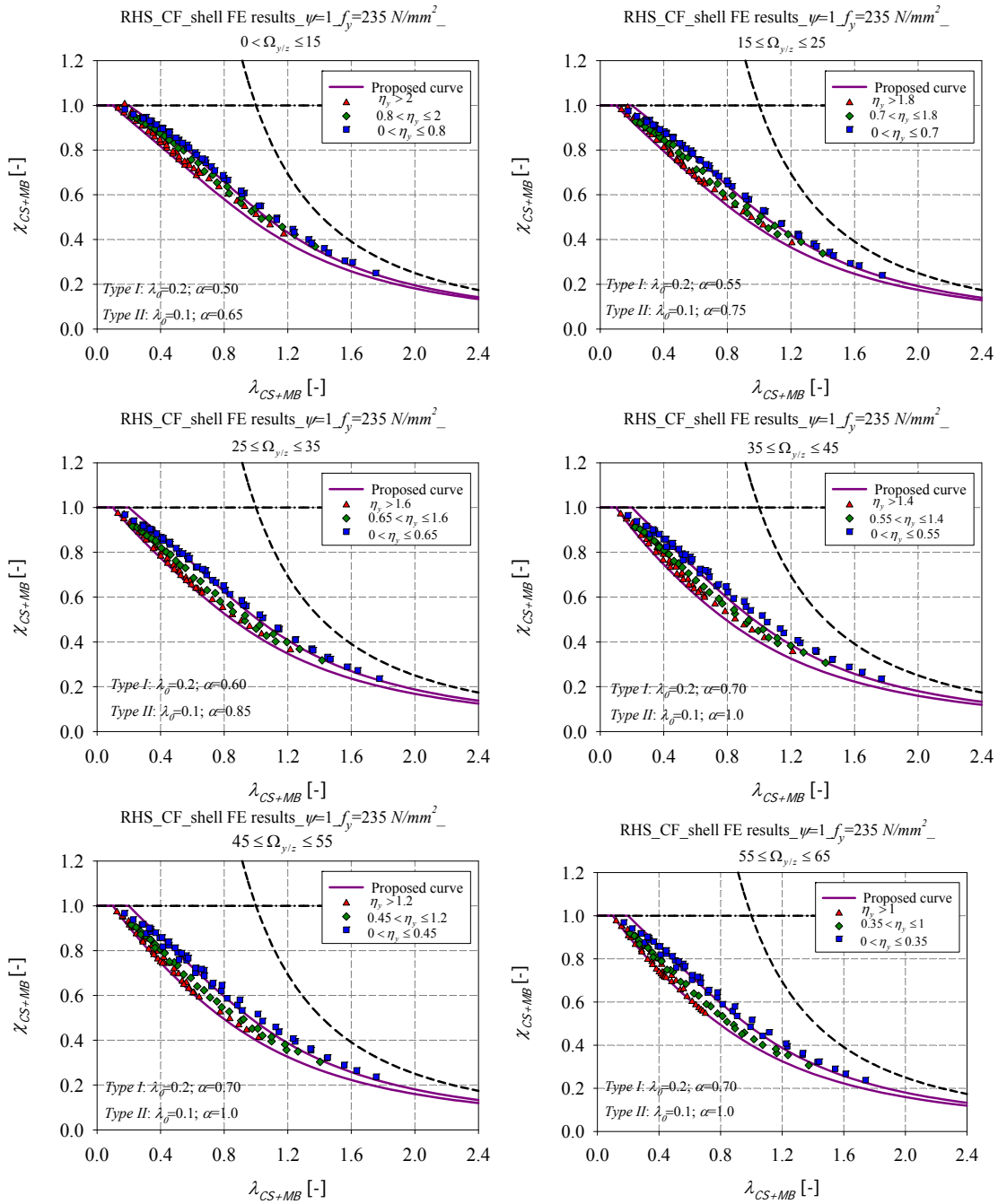


Figure 311 – Numerical member results of cold-formed RHS of steel grade $f_y = 235 \text{ N/mm}^2$ tested under different values of axial force ratio n

The results were then sorted as a function of both parameters η_y and $\Omega_{y/z}$ regardless of the axial force ratio n . Two curves were derived accordingly (*Type I* and *Type II* curves) as illustrated in Figure 312 and a linear interpolation is defined for the transition between the two types of curves. The limits of the parameter η_y were chosen according to the results of steel grade $f_y = 235 \text{ N/mm}^2$. The same limits were derived for higher steel grades, for sake of simplicity and consistency, since they lead to conservative results.



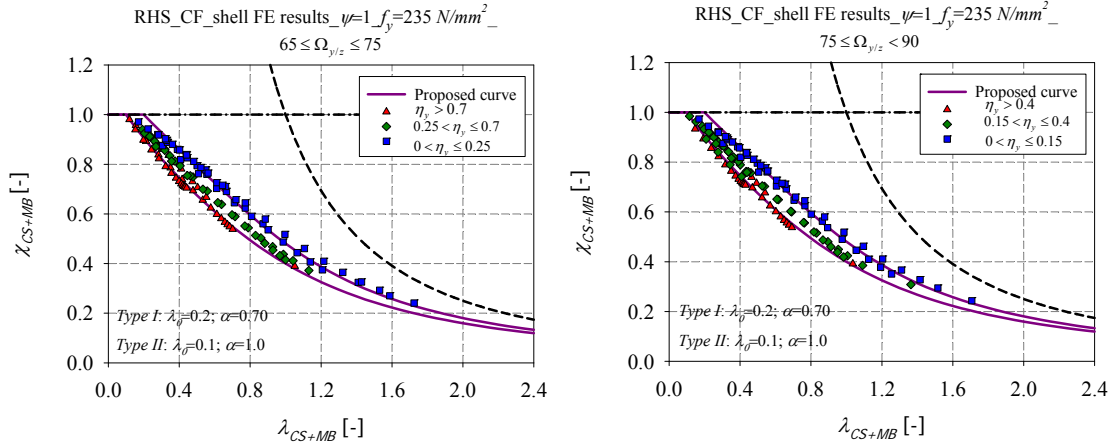


Figure 312 – Numerical member results for cold-formed RHS of steel grade $f_y = 235 \text{ N/mm}^2$ tested under different values of axial force ratio n and derived as a function of the parameters $\Omega_{y/z}$ and η_y .

Figure 313 presents a variation of the imperfection factor based on the degree of biaxial bending for *Type I* curves, relative to cold-formed rectangular sections of normal steel grades ($f_y = 235 \text{ N/mm}^2$ and $f_y = 355 \text{ N/mm}^2$) and tested under compression and constant bending moment distribution. With the inclusion of the $\Omega_{y/z}$ parameter, the proposed α formula becomes as follows:

$$\alpha = 0.7 \text{ for } \Omega_{y/z} \geq 40 \quad (356)$$

$$\alpha = 0.006\Omega_{y/z} + 0.45 \text{ for } \Omega_{y/z} < 40 \quad (357)$$

That way, for $\Omega_{y/z} = 0$, Equation (357) is restored with the limiting curve being relative to compression with major-axis bending load case and for $\Omega_{y/z} = 90$, Equation (356) is restored with the limiting curve being relative to compression with minor-axis bending load case.

These equations can be written as follows, in order to provide smooth continuities with the pure compression load case:

$$\alpha = \alpha_{comp} + 0.4\eta_z^{0.2} \leq 0.7 \text{ for } \Omega_{y/z} \geq 40 \quad (358)$$

$$\alpha = 0.006\Omega_{y/z} + \alpha_{comp} + 0.05\eta_y^{0.2} \leq 0.7 \text{ for } \Omega_{y/z} < 40 \quad (359)$$

That way, for $\Omega_{y/z} = 0$ and $\eta_y = 0$, Equation (359) is restored with the limiting curve being relative to the pure compression load case and for $\Omega_{y/z} = 90$ and $\eta_z = 0$, Equation (358) is restored with the limiting curve of the pure compression as well.

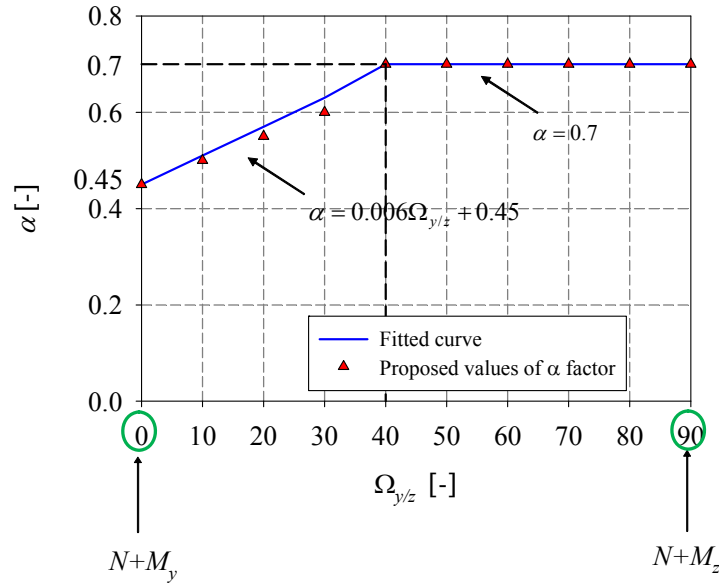


Figure 313 – Variation of α based on $\Omega_{y/z}$ for *Type I* curves, relative to CF RHS of steel grades $f_y = 235 \text{ N/mm}^2$ and $f_y = 355 \text{ N/mm}^2$, tested under compression and constant bending moment distribution.

The same type of relationships between α and $\Omega_{y/z}$ can be found for *Type I* curves, relative to high strength steel (i.e. $f_y = 690 \text{ N/mm}^2$) cold-formed rectangular sections, according to Equation (360) and Equation (361).

$$\alpha = 0.55 \text{ for } \Omega_{y/z} \geq 40 \quad (360)$$

$$\alpha = 0.007\Omega_{y/z} + 0.25 \text{ for } \Omega_{y/z} < 40 \quad (361)$$

These equations can be written as follows, in order to provide smooth continuities with the pure compression load case:

$$\alpha = \alpha_{comp} + 0.4\eta_z^{0.2} \leq 0.55 \text{ for } \Omega_{y/z} \geq 40 \quad (362)$$

$$\alpha = 0.007\Omega_{y/z} + \alpha_{comp} + 0.05\eta_y^{0.2} \leq 0.55 \text{ for } \Omega_{y/z} < 40 \quad (363)$$

A variation of the imperfection factor based on the degree of biaxial bending can be found in a similar manner for *Type II* curves, relative to cold-formed rectangular sections of normal steel grades and tested under compression and constant bending moment distribution. With the inclusion of the $\Omega_{y/z}$ parameter, the proposed α formula becomes as follows:

$$\alpha = 1 \text{ for } \Omega_{y/z} \geq 40 \quad (364)$$

$$\alpha = 0.01\Omega_{y/z} + 0.6 \text{ for } \Omega_{y/z} < 40 \quad (365)$$

That way, for $\Omega_{y/z} = 0$, Equation (365) is restored with the limiting curve being relative to compression with major-axis bending load case and for $\Omega_{y/z} = 90$, Equation (364) is restored with the limiting curve being relative to compression with minor-axis bending load case.

The same type of relationships between α and $\Omega_{y/z}$ can be found for *Type II* curves, relative to high strength steel (i.e. $f_y = 690 \text{ N/mm}^2$) cold-formed rectangular sections, according to Equation (366) and Equation (367).

$$\alpha = 0.8 \text{ for } \Omega_{y/z} \geq 40 \quad (366)$$

$$\alpha = 0.01\Omega_{y/z} + 0.4 \text{ for } \Omega_{y/z} < 40 \quad (367)$$

Table 47 summarizes the adopted parameters for the design curves of cold-formed rectangular hollow members subjected to compression with constant bending moment distribution.

Table 47 – Design curves for the case of cold-formed RHS members subjected to compression with biaxial constant bending moment

Combined load cases: $N+M_y+M_z$		
Constant bending moment distribution: $\psi = 1$		
Cross-section shape: RHS		Fabrication process: Cold-formed
$\chi_{CS+MB} = \frac{1}{\phi_{CS+MB} + \sqrt{\phi_{CS+MB}^2 - \lambda_{CS+MB}^2}}$ <p style="text-align: center;">for $\lambda_{CS+MB} \geq \lambda_0$</p> $\phi_{CS+MB} = 0.5 \left(1 + \alpha (\lambda_{CS+MB} - \lambda_0) + \lambda_{CS+MB}^2 \right)$ <p style="text-align: center;">With $\eta_y = \frac{m_y}{n_y} = \frac{M_y / M_{pl,y}}{N / N_{pl}}; \Omega_{y/z} = \arctan \left(\frac{m_z}{m_y} \right) = \arctan \left(\frac{M_z / M_{pl,z}}{M_y / M_{pl,y}} \right)$</p>		
Yield stress		
$f_y = 235 \text{ N/mm}^2$ $f_y = 355 \text{ N/mm}^2$		
Type I	Transition curve	Type II
$\alpha = \alpha_1 = \alpha_{comp} + 0.4\eta_z^{0.2} \leq 0.7$ for $\Omega_{y/z} \geq 40$; $\alpha = \alpha_1 = 0.006\Omega_{y/z} + \alpha_{comp} + 0.05\eta_y^{0.2} \leq 0.7$ for $\Omega_{y/z} < 40$. $\lambda_0 = 0.2$	$\lambda_0 = \left(-\frac{0.1}{\eta_{y,2} - \eta_{y,1}} \right) (\eta_y - \eta_{y,2}) + 0.1$ $\alpha = \left(\frac{\alpha_2 - \alpha_1}{\eta_{y,2} - \eta_{y,1}} \right) (\eta_y - \eta_{y,2}) + \alpha_2$	$\alpha = \alpha_2 = 1.0$ for $\Omega_{y/z} \geq 40$; $\alpha = \alpha_2 = 0.01\Omega_{y/z} + 0.6$ for $\Omega_{y/z} < 40$. $\lambda_0 = 0.1$

Yield stress		
$f_y = 690 \text{ N/mm}^2$		
Type I	Transition curve	Type II
$\alpha = \alpha_1 = \alpha_{comp} + 0.4\eta_z^{0.2} \leq 0.55$ for $\Omega_{y/z} \geq 40$; $\alpha = \alpha_1 = 0.007\Omega_{y/z} + \alpha_{comp} + 0.05\eta_y^{0.2} \leq 0.55$ for $\Omega_{y/z} < 40$. $\lambda_0 = 0.2$	$\lambda_0 = \left(-\frac{0.1}{\eta_{y,2} - \eta_{y,1}} \right) (\eta_y - \eta_{y,2}) + 0.1$ $\alpha = \left(\frac{\alpha_2 - \alpha_1}{\eta_{y,2} - \eta_{y,1}} \right) (\eta_y - \eta_{y,2}) + \alpha_2$	$\alpha = \alpha_2 = 0.80$ for $\Omega_{y/z} \geq 40$; $\alpha = \alpha_2 = 0.01\Omega_{y/z} + 0.4$ for $\Omega_{y/z} < 40$. $\lambda_0 = 0.1$

6.4.4. Influence of bending moment distribution

Special attention has been given so that the proposed formulae exhibit no discontinuities; indeed, a proposal that is intended to be as general as possible must be able to cover a wide range of configurations. Particular attention has been paid to characterize more precisely the influence of the bending moment distribution on the member resistance.

A sub study has been undertaken including members tested under linearly varying moment distribution with different end-moment ψ values. Shell modelling has been used and the study covered the following parameters:

- 8 different element lengths varying from 1500 mm to 15000 mm in order to visualize well-distributed results along the relative slenderness axis;
- 2 steel grades: S235, S690;
- 2 cross-section shapes: RHS 220x120x10 and SHS 120x120x8;
- 2 types of fabrication processes: hot-rolled and cold-formed sections;
- different loading conditions:
 - o compression with major-axis bending;
 - o compression with minor-axis bending;
 - o compression with biaxial bending.

A distinction has been made between the different loading situations, namely with respect to:

- the bending moments distributions ψ : 5 linear coefficients were adopted $\psi_y = \psi_z = -0.33$, $\psi_y = \psi_z = 0$, $\psi_y = \psi_z = 0.33$, $\psi_y = \psi_z = 0.67$ and $\psi_y = \psi_z = 1$;
- the relative axial force ratio n : 2 values of the relative axial force ratio n were adopted going from 0.3 (i.e. the load case becoming thus a compression of 30% $N_{b,Rd}$ with monoaxial or biaxial bending), to 0.7 (i.e. the load case becoming thus a compression of 70% $N_{b,Rd}$ with monoaxial or biaxial bending);
- the degree of biaxial bending defined for combined load cases as the ratio M_y / M_z . For each load case, 5 values of the degree of biaxial bending were adopted varying from $\alpha_{\text{biaxiality}} = 0^\circ$ (i.e. the load case becoming compression with major-axis bending $N+M_y$) to $\alpha_{\text{biaxiality}} = 90^\circ$ (i.e. the load case becoming compression with minor-axis bending $N+M_z$).

Additional calculations were simulated with the same parameters mentioned before with a length equal to three times the height of the section in order to determine the cross-section resistance. The results were added to the full set of numerical calculations.

Numerical results are presented in O.I.C. format in Figure 315 to Figure 319, along with the corresponding proposed curves. On one hand, a relation was established between the imperfection factor α_ψ and the imperfection factors $\alpha_{\psi=1}$, $\alpha_{\psi=0}$ for $\psi = 1$ and $\psi = 0$ respectively; and on the other, between the end of plateau $\lambda_{0,\psi}$ and the ends of plateau $\lambda_{0,\psi=1}$, $\lambda_{0,\psi=0}$ for $\psi = 1$ and $\psi = 0$ as well according to Figure 314 and to the equations below:

$$\alpha_\psi = (\alpha_{\psi=1} - \alpha_{\psi=0})\psi + \alpha_{\psi=0} \quad \text{with } \alpha_\psi \geq 0 \quad (368)$$

$$\lambda_{0,\psi} = (\lambda_{0,\psi=1} - \lambda_{0,\psi=0})\psi + \lambda_{0,\psi=0} \quad \text{with } \lambda_0 \geq 0 \quad (369)$$

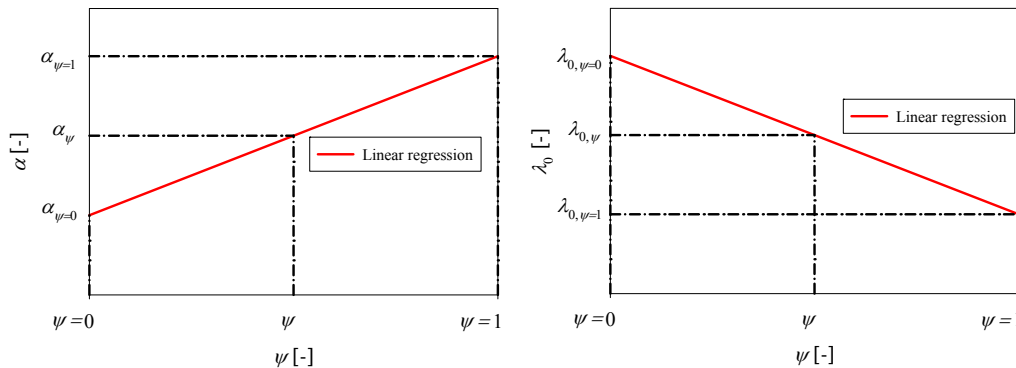
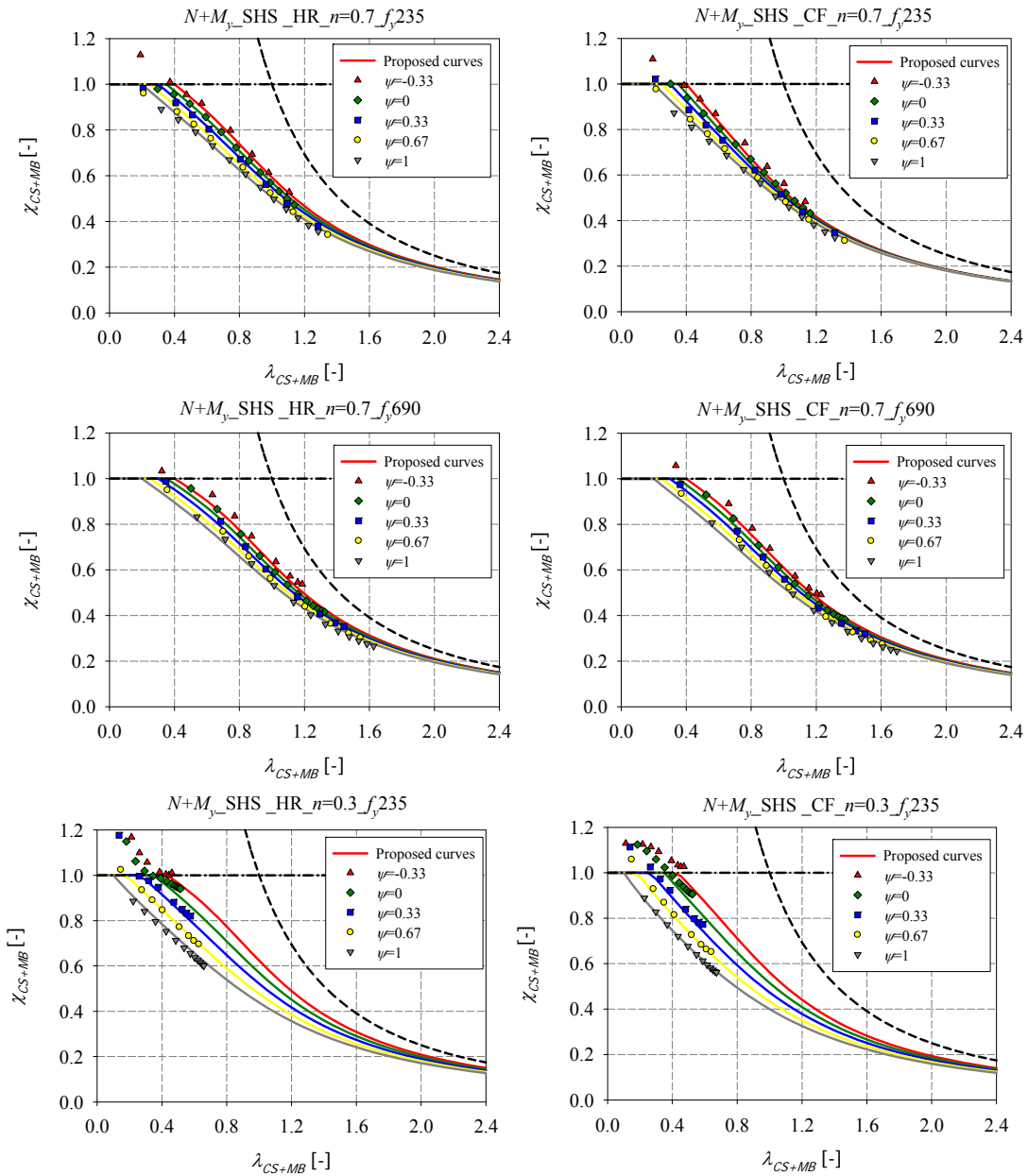


Figure 314 – Linear regression between – a) $\alpha - \psi$ – b) $\lambda_0 - \psi$

The proposed curves illustrated in the figures below are obtained by using equations (368) and (369).



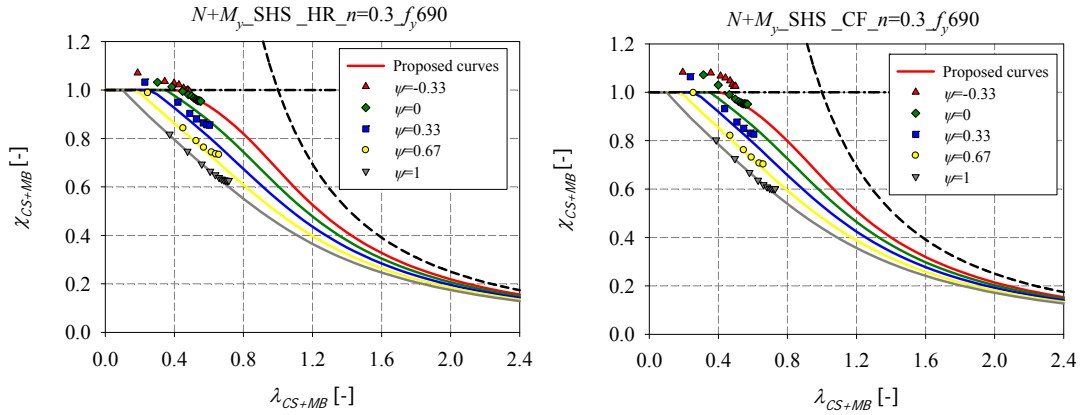
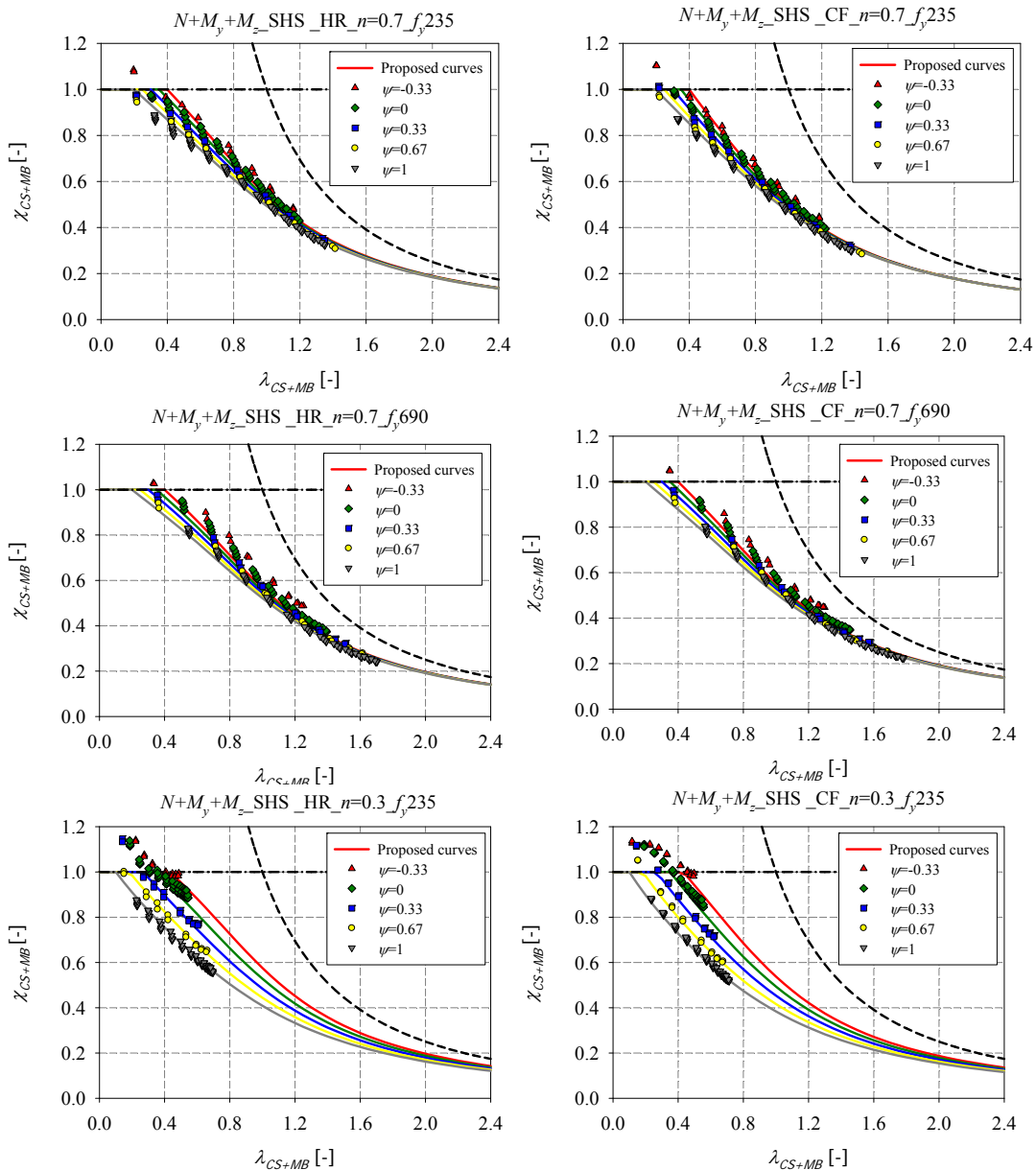


Figure 315 – Numerical member results of hot-rolled and cold-formed SHS of steel grades $f_y = 235 \text{ N/mm}^2$ and $f_y = 690 \text{ N/mm}^2$ tested under compression and mono-axial bending with different end-moment values



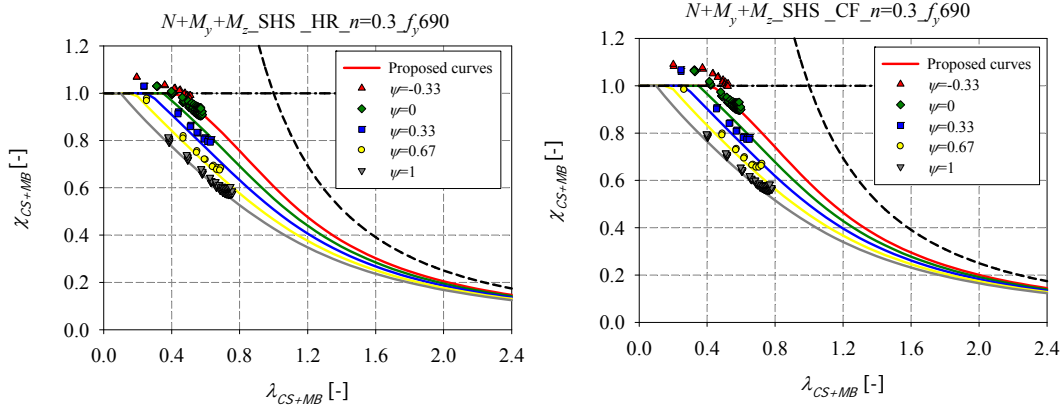
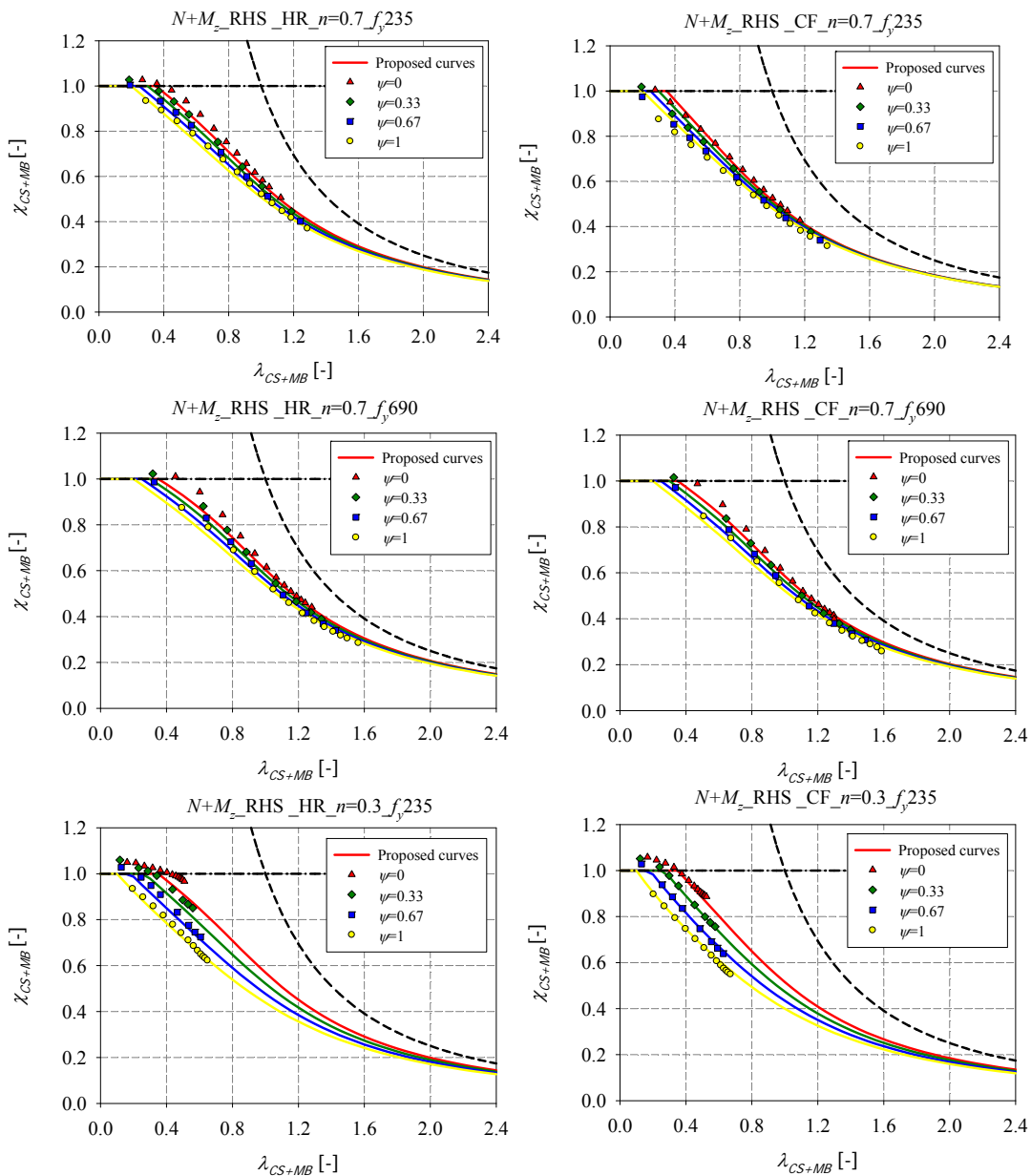


Figure 316 – Numerical member results of hot-rolled and cold-formed SHS of steel grades $f_y = 235 \text{ N/mm}^2$ and $f_y = 690 \text{ N/mm}^2$ tested under $N+M_y+M_z$



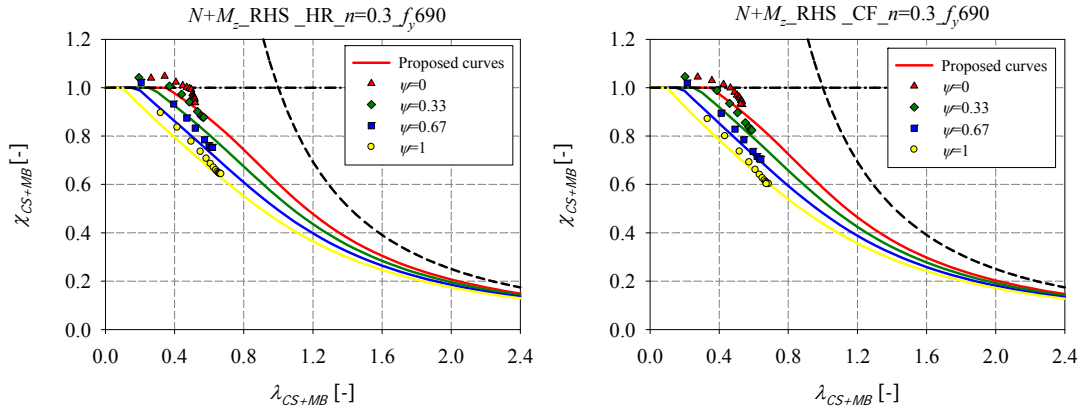
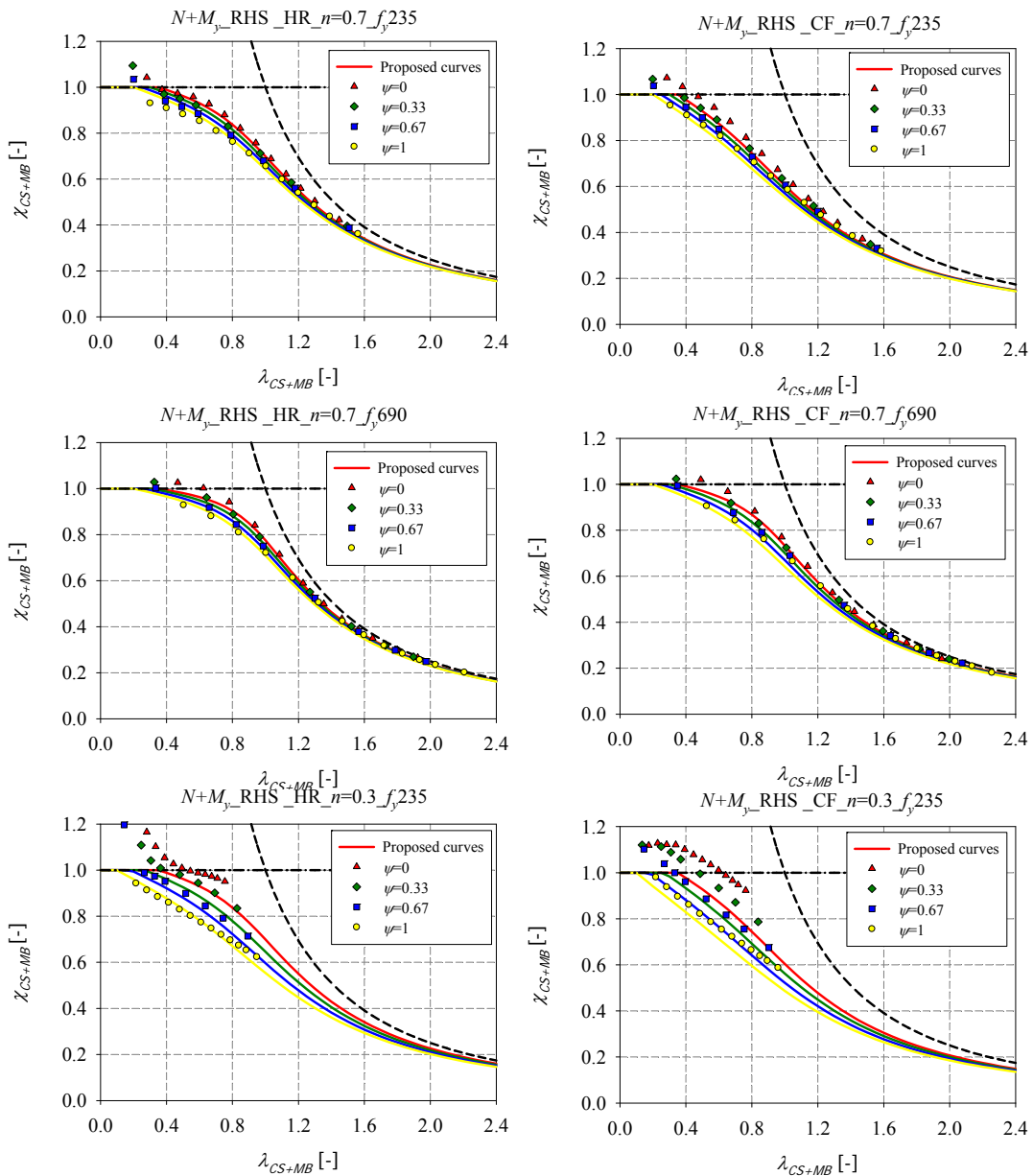


Figure 317 – Numerical member results of hot-rolled and cold-formed RHS of steel grades $f_y = 235 \text{ N/mm}^2$ and $f_y = 690 \text{ N/mm}^2$ tested under combined loading $N+M_z$



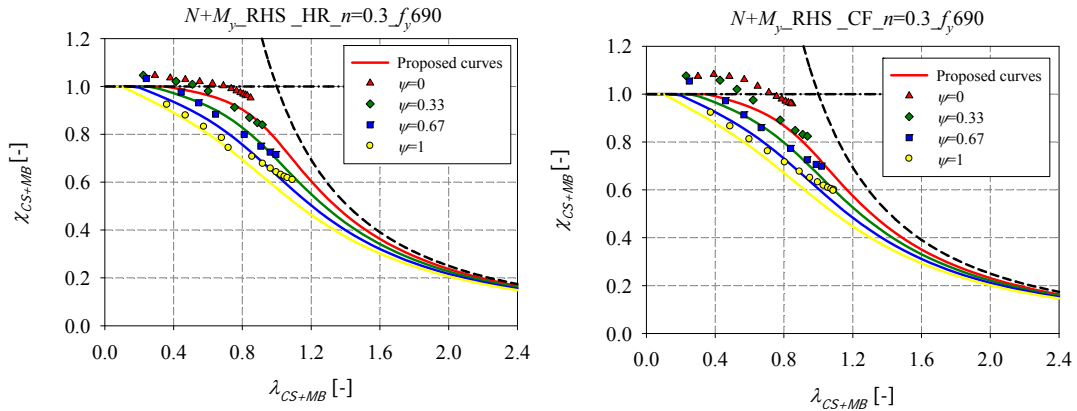
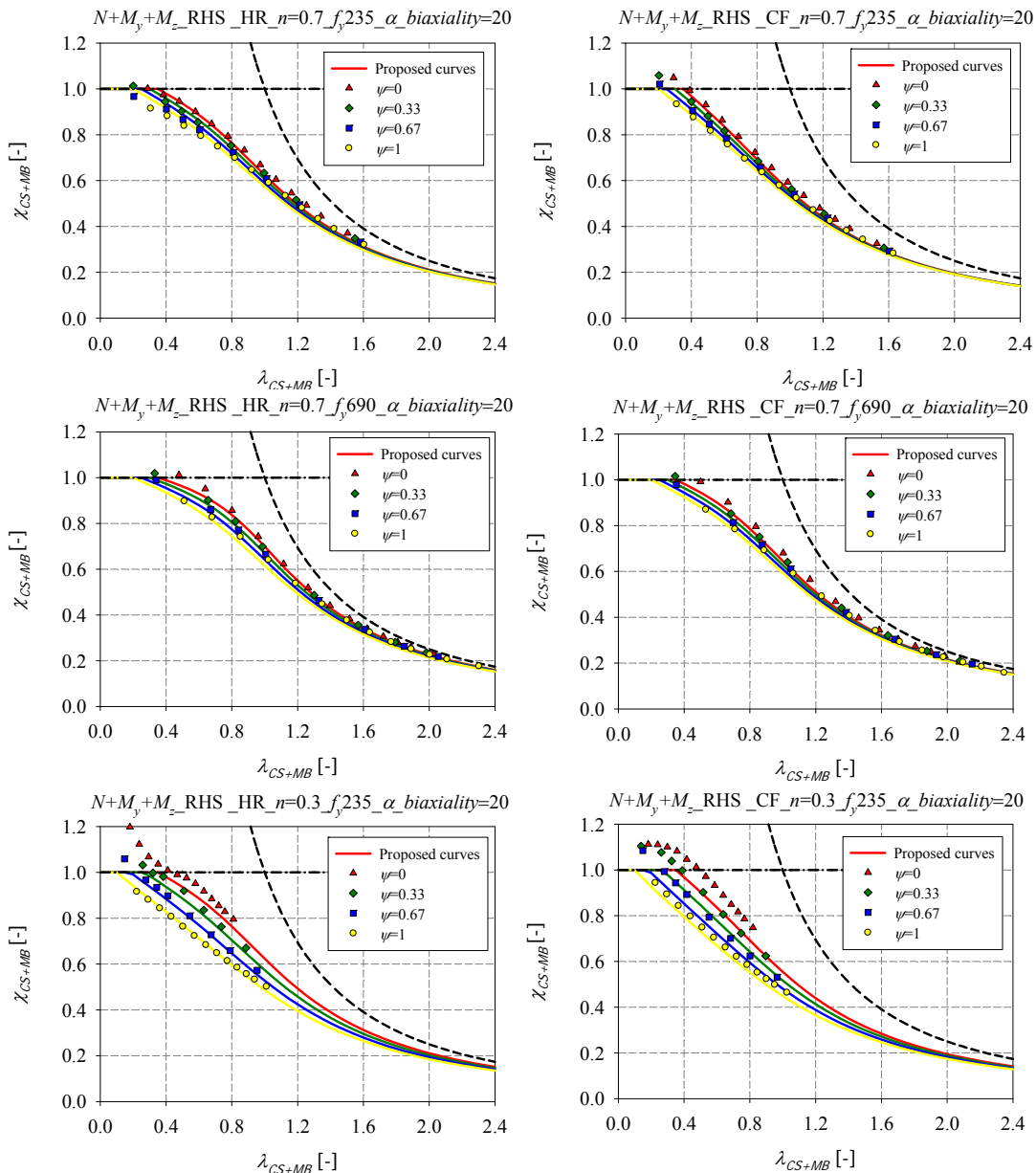
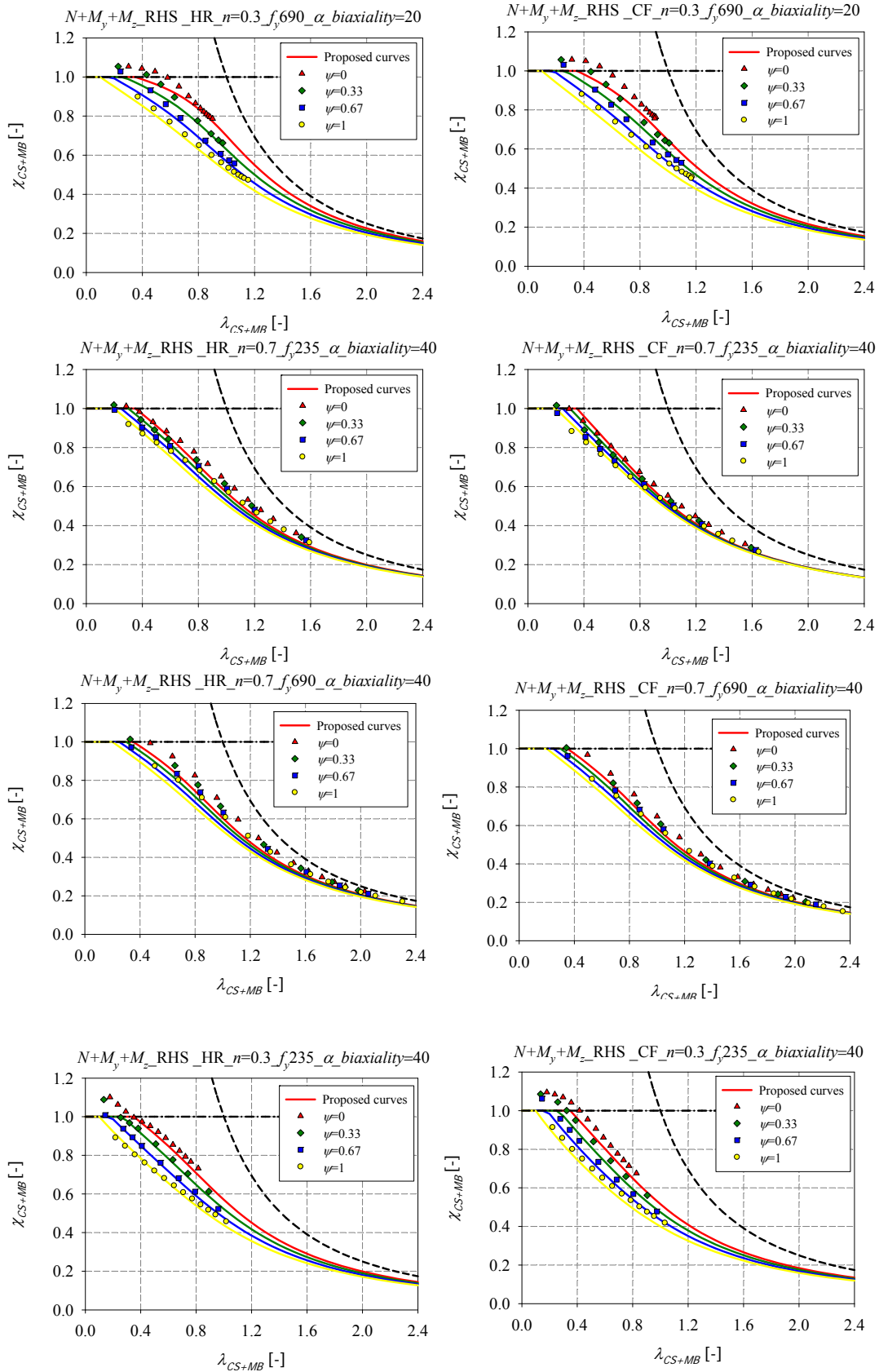
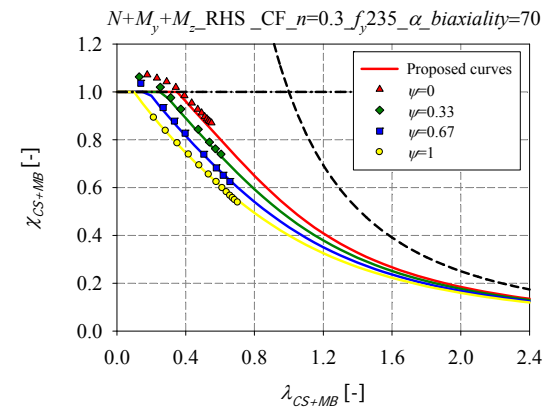
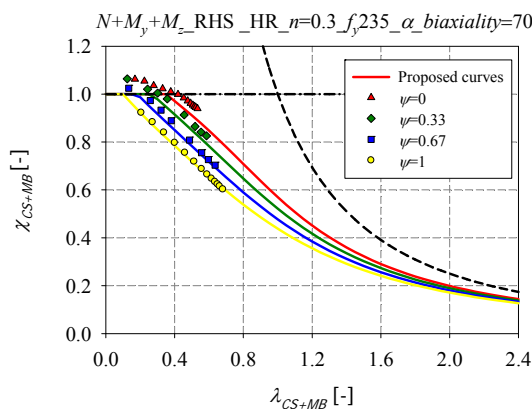
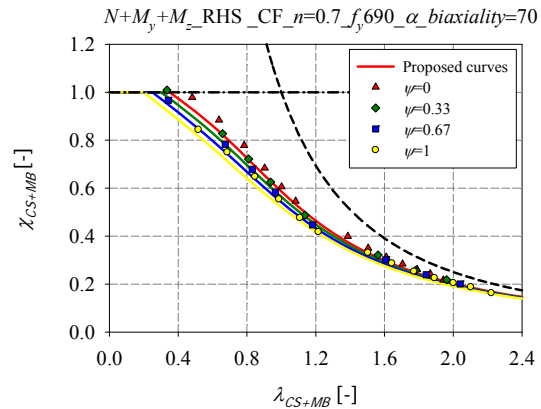
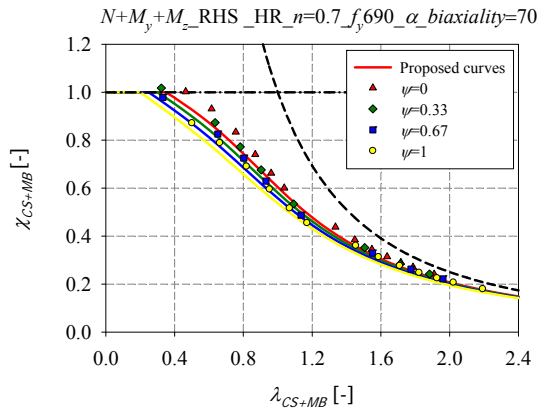
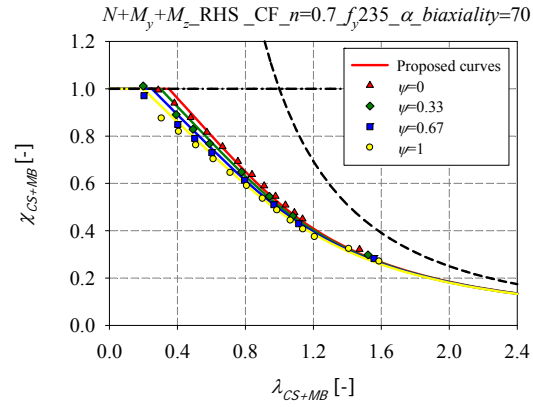
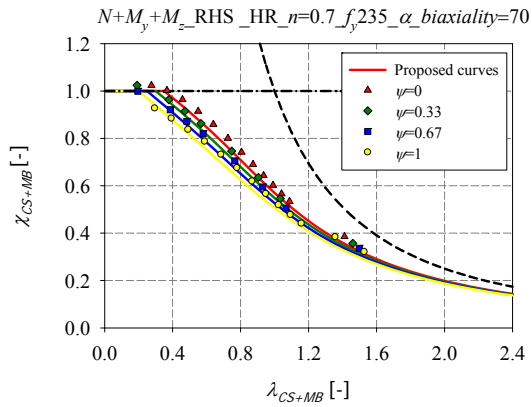
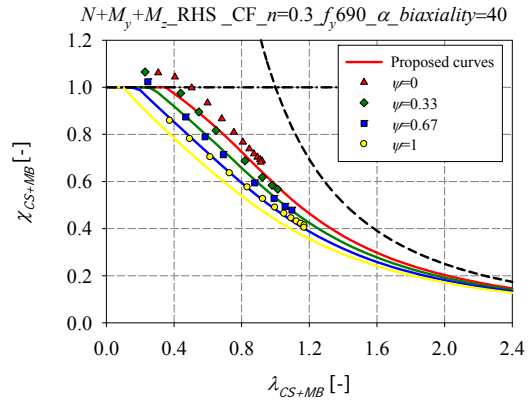
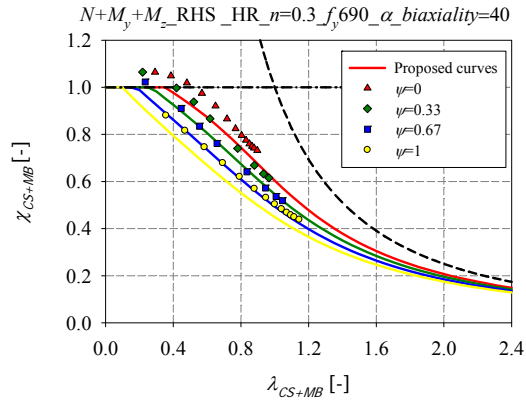


Figure 318 – Numerical member results of hot-rolled and cold-formed RHS of steel grades $f_y = 235 \text{ N/mm}^2$ and $f_y = 690 \text{ N/mm}^2$ tested under $N+M_y$







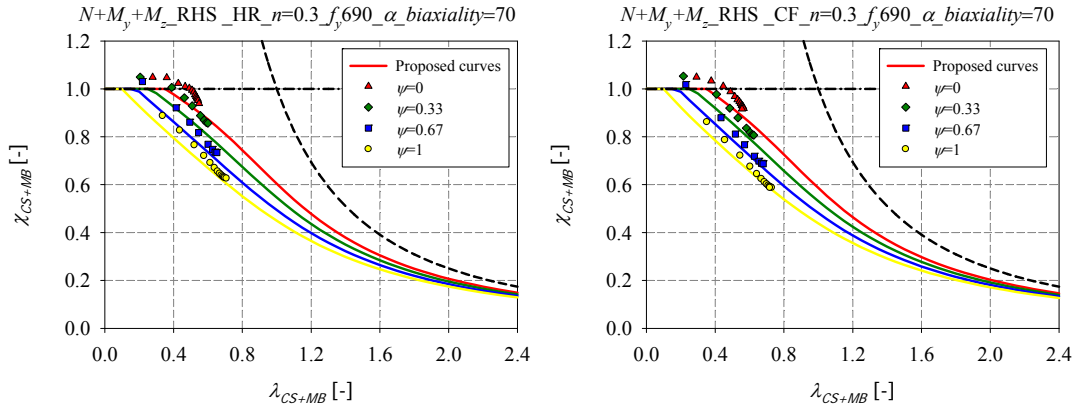


Figure 319 – Numerical member results of hot-rolled and cold-formed RHS of steel grades $f_y = 235 \text{ N/mm}^2$ and $f_y = 690 \text{ N/mm}^2$ tested under $N+M_y+M_z$

6.4.5. Influence of the section shape

As noticed in the sections above, the cross-section shape (rectangular or square) influenced the member resistance. Special attention is given so that the proposed formulae exhibit no discontinuities. Accordingly, the h/b ratio was introduced in the derived formulae for beam-column resistance as illustrated in Figure 320, where $\alpha_{h/b=1}$ represent the imperfection factors proposed for the case of square sections, $\alpha_{h/b \geq 1.3}$ correspond to the imperfection factors proposed for the rectangular European sections²⁸ and $\alpha_{1 < h/b < 1.3}$ correspond to the imperfection factors of invented sections having aspect ratios ranging from 1 to 1.3.

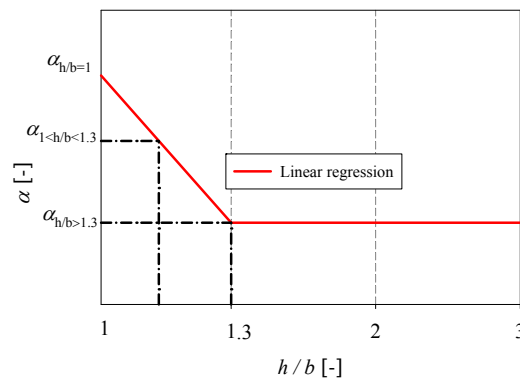


Figure 320 – Linear transition between $\alpha - h/b$

²⁸ The sections used to derive the design curves for members tested under combined loading, were taken from the European catalogue which defines rectangular sections with the corresponding aspect ratios ranging from 1.3 to 3.

6.5. Accuracy of proposed models – Comparison with actual Eurocode 3 rules

Table 48 proposes statistical results of the comparison between FEM, EC3 and proposal calculations for all the computed results. As can be seen, the resistance estimates are significantly improved by the new proposal, and the mean and standard deviation values also indicate a better level of consistency compared to EC3 calculations. With the adoption of the EC3 procedure, the calculations can sometimes lead to unconservative results and sometimes to overly conservative results.

Table 48 – Comparison between FEM, EC3 and proposal results for all treated load cases²⁹

Load case	Fabrication process	Number of results	χ_{FEM} / χ_{EC3}				$\chi_{FEM} / \chi_{proposal}$			
			Average	Min	Max	St.Dev	Average	Min	Max	St.Dev
N	HR	1056	1.00	0.89	1.11	0.05	1.01	0.93	1.09	0.03
N	CF	1056	1.22	0.98	1.56	0.11	1.04	0.95	1.14	0.03
$N+M_z$	HR	1160	0.98	0.72	1.19	0.08	1.03	0.96	1.15	0.03
$N+M_z$	CF	1160	1.08	0.73	1.35	0.13	1.03	0.91	1.13	0.03
$N+M_y$	HR	1304	0.98	0.70	1.29	0.08	1.04	0.92	1.41	0.05
$N+M_y$	CF	1304	1.08	0.75	1.36	0.12	1.06	0.91	1.30	0.06
$N+M_y+M_z$ $\psi = -0.33$	HR	64	0.97	0.76	1.20	0.11	1.05	0.95	1.36	0.07
$N+M_y+M_z$ $\psi = -0.33$	CF	64	1.13	0.83	1.39	0.15	1.06	0.97	1.14	0.03
$N+M_y+M_z$ $\psi = 0$	HR	4207	1.00	0.77	1.28	0.09	1.05	0.95	1.37	0.04
$N+M_y+M_z$ $\psi = 0$	CF	4207	1.12	0.78	1.46	0.14	1.05	0.96	1.18	0.04
$N+M_y+M_z$ $\psi = 0.33$	HR	160	1.08	0.97	1.23	0.05	1.04	0.95	1.21	0.04
$N+M_y+M_z$ $\psi = 0.33$	CF	160	1.24	1.08	1.42	0.09	1.05	0.96	1.12	0.04
$N+M_y+M_z$ $\psi = 0.67$	HR	160	1.09	0.98	1.26	0.06	1.03	0.94	1.13	0.04
$N+M_y+M_z$ $\psi = 0.67$	CF	160	1.24	1.08	1.42	0.08	1.04	0.95	1.12	0.04
$N+M_y+M_z$ $\psi = 1$	HR	4576	1.06	0.93	1.23	0.06	1.05	0.89	1.19	0.05
$N+M_y+M_z$ $\psi = 1$	CF	4576	1.16	0.90	1.44	0.10	1.05	0.93	1.20	0.04

²⁹ χ_{FEM} / χ_{EC3} and $\chi_{FEM} / \chi_{proposal}$ are determined for the combined loading by comparing the load ratios

R_{FEM} to R_{EC3} and R_{FEM} to $R_{proposal}$ respectively.

The figures below show comparisons between FEM, EC3 and ‘proposal’ results for hot-rolled and cold-formed members subjected to compression and to combined loading situations with the three considered steel grades in this work. It should be mentioned that only the European (catalogue) cross-sections are considered.

On the left column, plots illustrating comparisons between χ_{FEM} / χ_{EC3} and $\chi_{FEM} / \chi_{proposal}$ ratios are presented, while the right column shows these same results in the form of histograms in an attempt to better illustrate and translate the observations of the left column plots. Both columns allow to distinguish between conservative and unconservative approaches, and to detect their accuracy as well as their consistency. For a given value of χ_{FEM} / χ_{EC3} or $\chi_{proposal}$, it is possible to identify the frequency using the diagram on the right which is not deemed possible by reading the diagram on the left, as most of the values are hidden. The left diagram allows detecting the accuracy of the corresponding approaches depending on the member relative slenderness.

Figure 321 and Figure 322 illustrate the results for all hot-rolled and cold-formed members subjected to pure compression load case. Figure 323 and Figure 324 show results for members subjected to compression with minor-axis bending ($N+M_z$), while Figure 325 and Figure 326 present results relative to member subjected to compression with major-axis bending ($N+M_y$). Figure 327 to Figure 332 illustrate the results of members tested under different (linear) bending moment distributions, represented by the ψ factor (i.e. which stands as the ratio between applied end moments); these results are relative to beam-column members tested under combined loading situations ($N+M_y+M_z$). Figure 333 to Figure 334 show results for members subjected to combined load cases ($N+M_y+M_z$) with 30% of $N_{b,Rd}$, while Figure 335 to Figure 336 present results relative to 70% of $N_{b,Rd}$. These two cases were selected since results with $n = 0.3$ are supposed to represent the least satisfactory proposed outcome and results with $n = 0.7$ would represent one of the best proposed outcome.

The following remarks can be stated based on these figures:

- for the case of hot-rolled and cold-formed members subjected to compression and triangular bending moment distribution, the bending moment reaches its highest value on the extremity of the beam-column and decreases along the member length. The less loaded part of the beam provides a level of restraint to the entire member. In the proposed design curves the resistance limit was kept to $\chi_{CS+MB} = 1$, for sake of

simplicity and consistency and because the extra strength provided does not exceed 10% of the member total resistance for almost all considered load cases. Therefore, both results, computed with EC3 specifications and the new design proposal, would lead to similar overlapped results illustrated at the small slenderness range. This would explain why overconservative results appear in the right histogram plot (see red circles);

- the results computed according to the proposed design curves are showing much better distributions for all considered load cases, both in terms of mean and standard deviation; O.I.C. predictions are showing way better continuous results with smaller standard deviations compared to EC3 predictions;
- the comparisons between histograms clearly demonstrate the improved accuracy features of the proposed new rules (since a bigger number of $\chi_{FEM} / \chi_{proposal}$ ratios are close to 1) which are then seen to be much more accurate than the actual ones;
- with cold-formed sections, and with EC3 calculations, histograms plots are illustrating somewhat equivalent conservative and unconservative results, while the majority of the results seem conservative on the left plot. This is due to EC3 computations that propose a conservative and unique formulation for cold-formed sections no matter what the yield stresses are. Numerical results showed that an increased yield stress lead to higher design curves. Accordingly, multiple curves were derived for cold-formed section depending on the corresponding steel grade;
- the results computed according to EC3 calculations under combined loadings, are showing unconservative results for small values of relative slenderness, where the failure of the element is due to both local (i.e. cross-section instabilities) and global (i.e. member instabilities) buckling modes. These unconservative results are more visible for small relative axial force ratio ($n = 0.3$) where the bending moment is predominant and the sections exhibit little influence of global instability due to the low level of compression; the failure of the elements in this case is mainly due to a lack of resistance and to cross-section buckling. These unconservative results for low values of relative slenderness are due to the influence of the cross-sections, mainly to class 2 sections. Eurocode 3 approach considers class 2 sections as plastic ones capable of reaching their full plastic capacity. It has been shown [4] that several values of the b / t

limit ratios of Eurocode 3 are often misleading (in particular the b/t limit ratios at the class 2-3 border), and some sections considered as class 2 are not able to reach their full plastic capacity, leading to unconservative capacities.

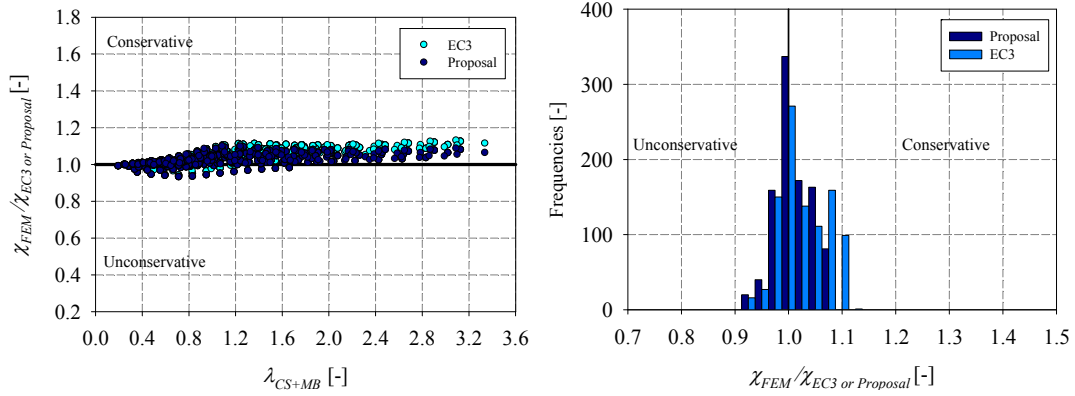


Figure 321 – Hot-rolled, pure compression – a) Comparison of proposal and EC3 results with FEM results – b) Frequency distributions (total number of results: 1056)

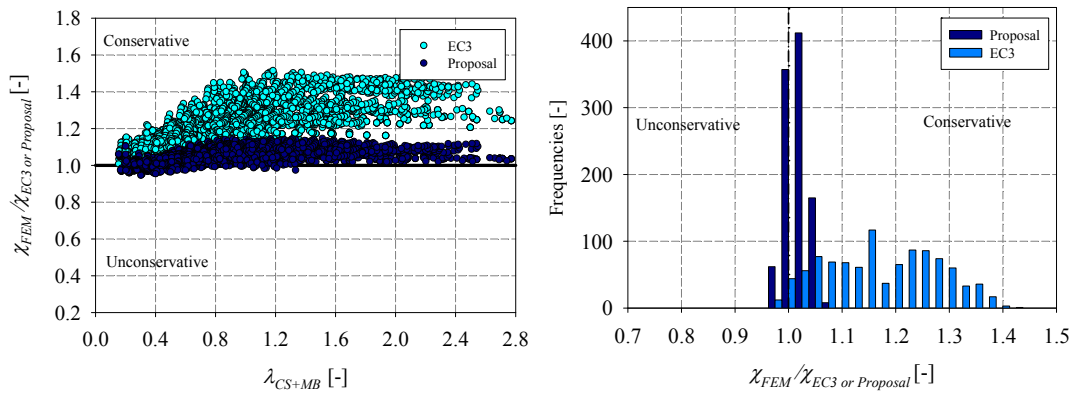


Figure 322 – Cold-formed, pure compression – a) Comparison of Proposal and EC3 results with FEM results – b) Frequency distributions (total number of results: 1056).

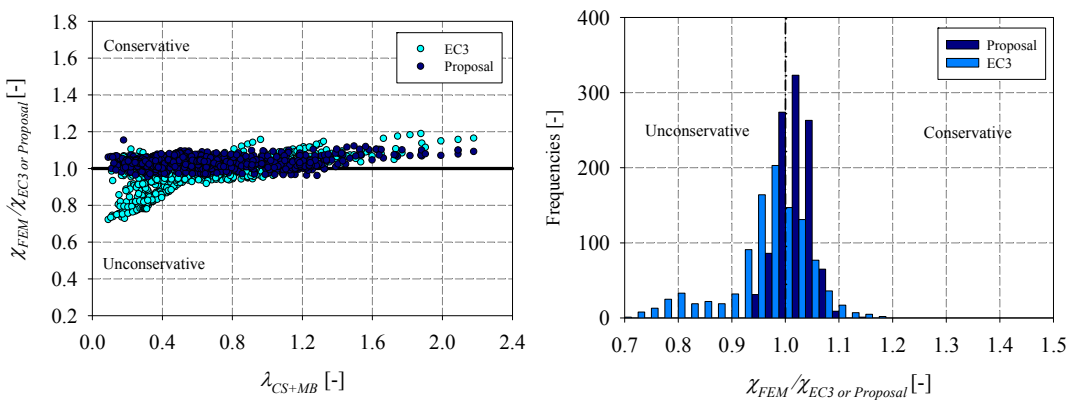


Figure 323 – Hot-rolled, $N+M_z$ – a) Comparison of Proposal and EC3 results with FEM results – b) Frequency distributions (total number of results: 1160).

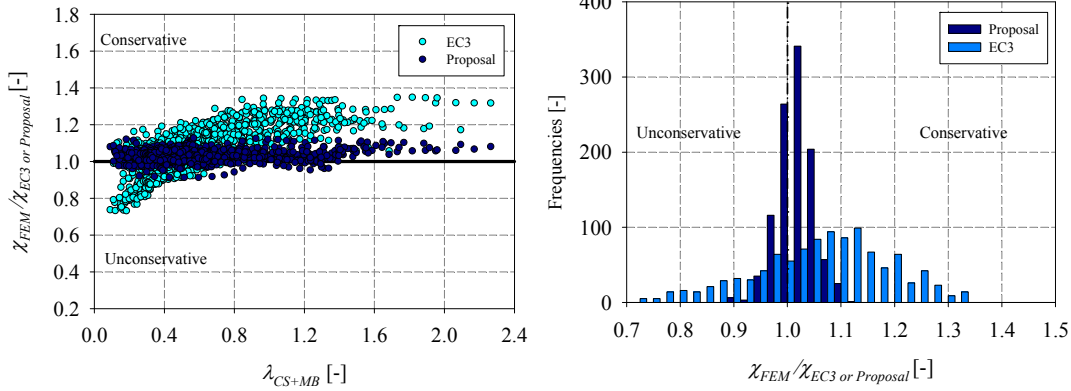


Figure 324 – Cold-formed, $N+M_z$ – a) Comparison of Proposal and EC3 results with FEM results – b) Frequency distributions (total number of results: 1160).

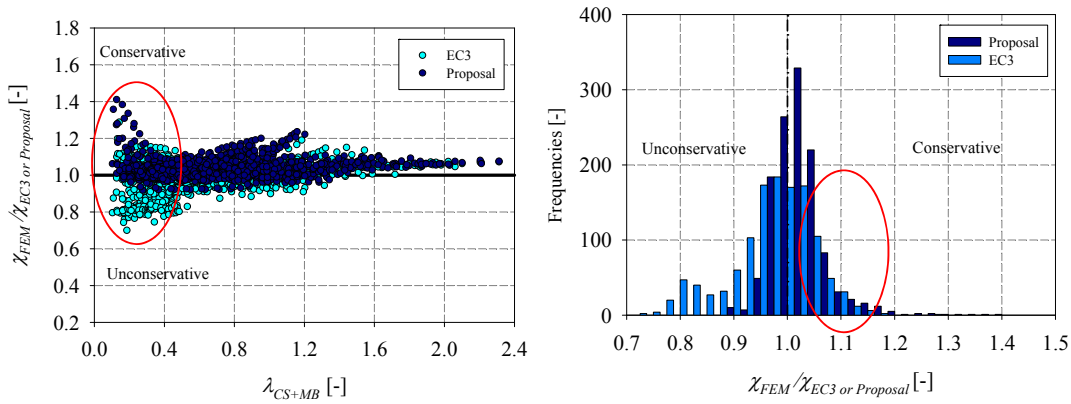


Figure 325 – Hot-rolled, $N+M_y$ – a) Comparison of Proposal and EC3 results with FEM results – b) Frequency distributions (total number of results: 1304).

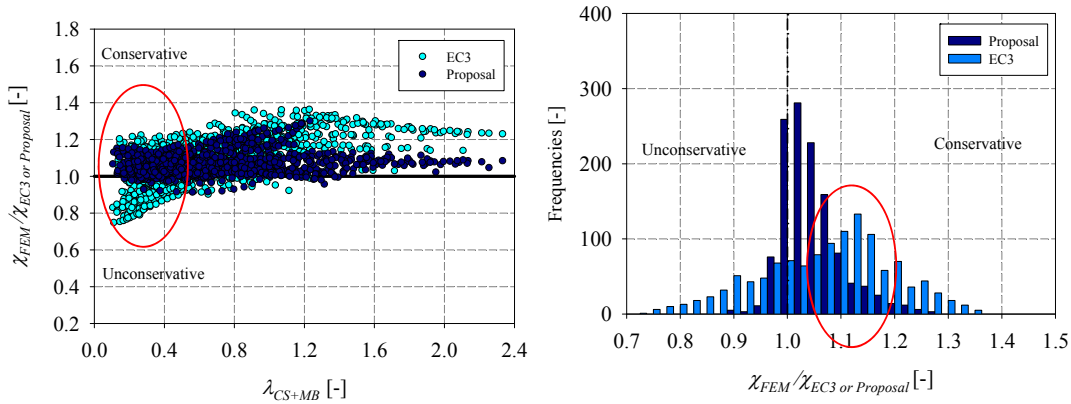


Figure 326 – Cold-formed, $N+M_y$ – a) Comparison of Proposal and EC3 results with FEM results – b) Frequency distributions (total number of results: 1304).

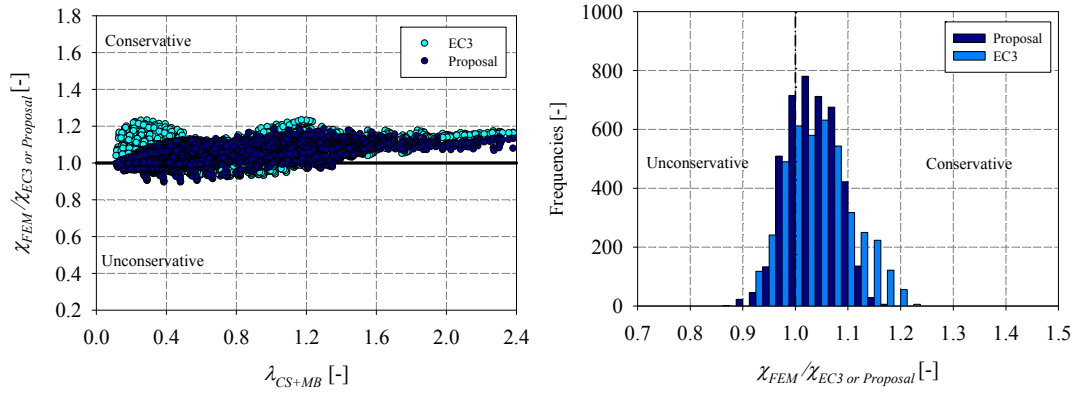


Figure 327 – Hot-rolled, $N+M_y+M_z$, $\psi = 1$ – a) Comparison of Proposal and EC3 results with FEM results – b) Frequency distributions (total number of results: 4576).

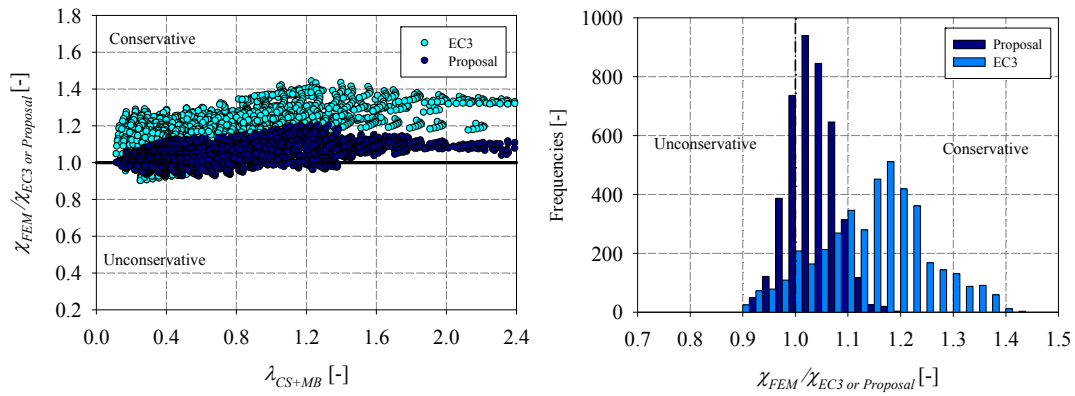


Figure 328 – Cold-formed, $N+M_y+M_z$, $\psi = 1$ – a) Comparison of Proposal and EC3 results with FEM results – b) Frequency distributions (total number of results: 4576).

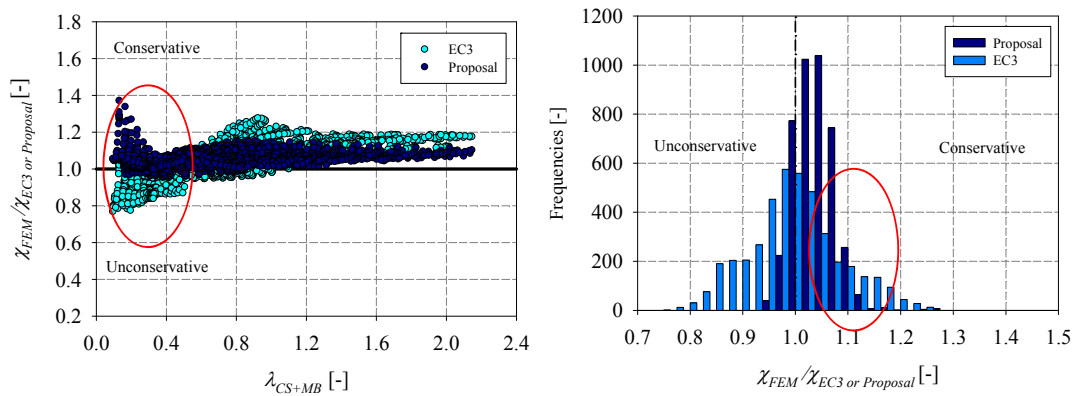


Figure 329 – Hot-rolled, $N+M_y+M_z$, $\psi = 0$ – a) Comparison of Proposal and EC3 results with FEM results – b) Frequency distributions (total number of results: 4207).

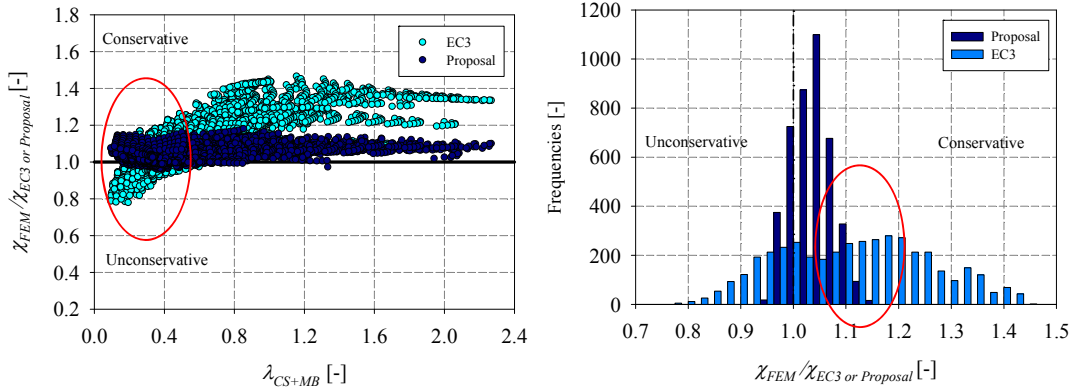


Figure 330 – Cold-formed, $N+M_y+M_z$, $\psi = 0$ – a) Comparison of Proposal and EC3 results with FEM results – b) Frequency distributions (total number of results: 4207).

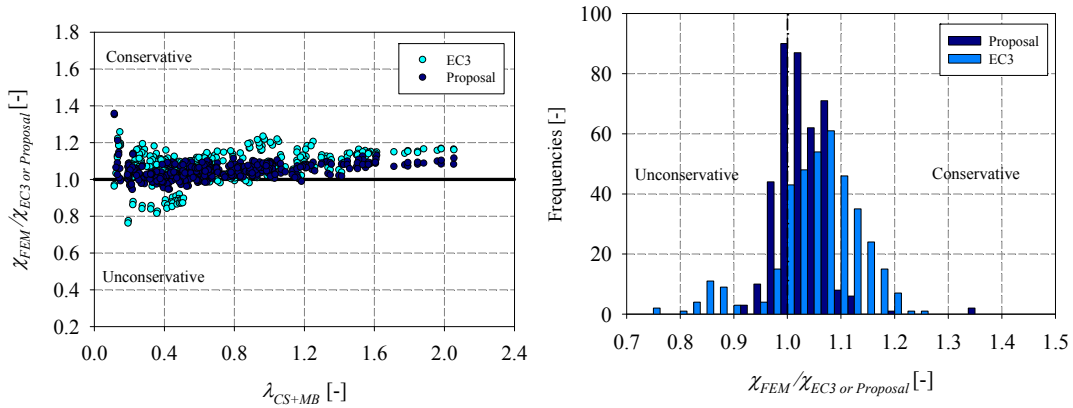


Figure 331 – Hot-rolled, $N+M_y+M_z$, $\psi = -0.33/0.33/0.67$ – a) Comparison of Proposal and EC3 results with FEM results – b) Frequency distributions (total number of results: 384).

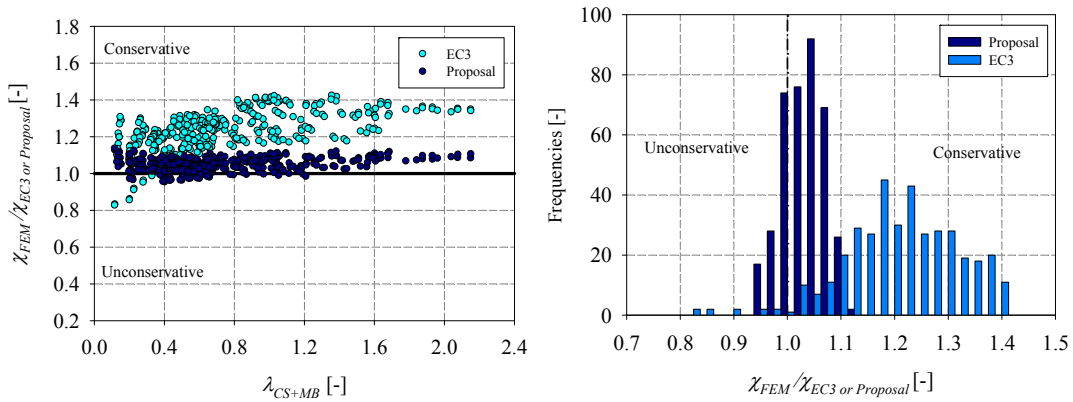


Figure 332 – Cold-formed, $N+M_y+M_z$, $\psi = -0.33/0.33/0.67$ – a) Comparison of Proposal and EC3 results with FEM results – b) Frequency distributions (total number of results: 384).

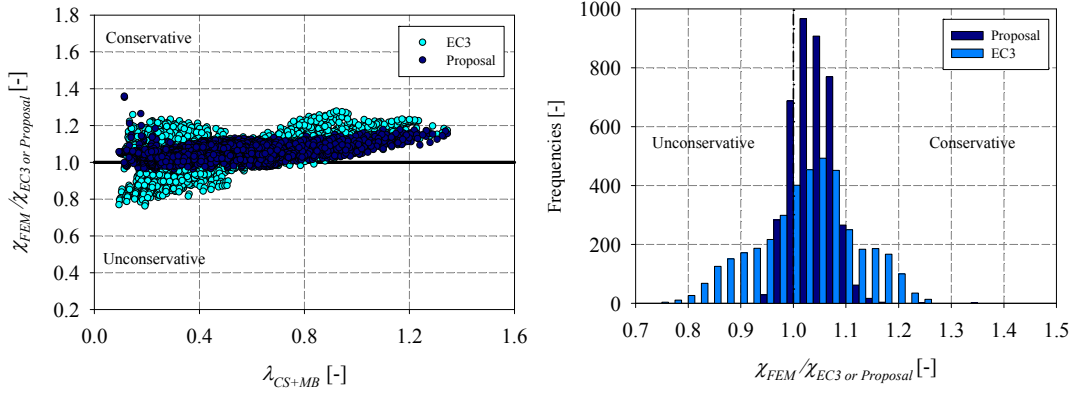


Figure 333 – Hot-rolled, $N+M_y+M_z$, $n = 0.3$ – a) Comparison of Proposal and EC3 results with FEM results – b) Frequency distributions (total number of results: 4368).

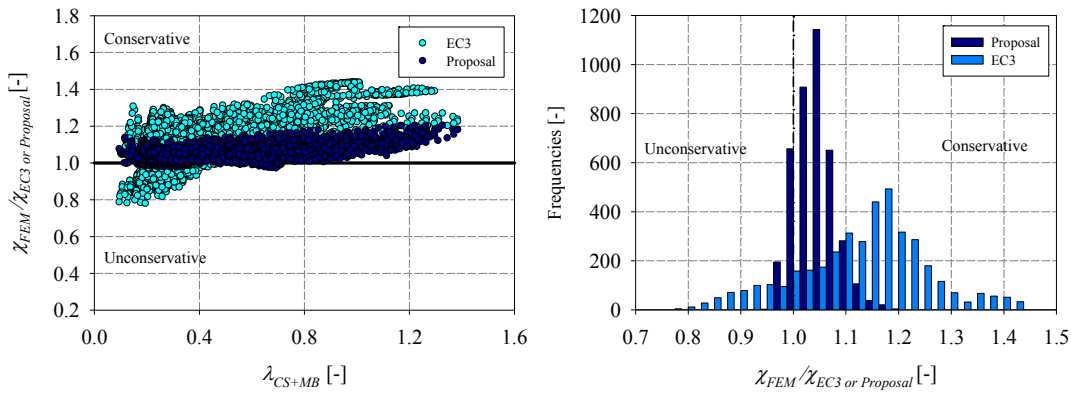


Figure 334 – Cold-formed, $N+M_y+M_z$, $n = 0.3$ – a) Comparison of Proposal and EC3 results with FEM results – b) Frequency distributions (total number of results: 4368).

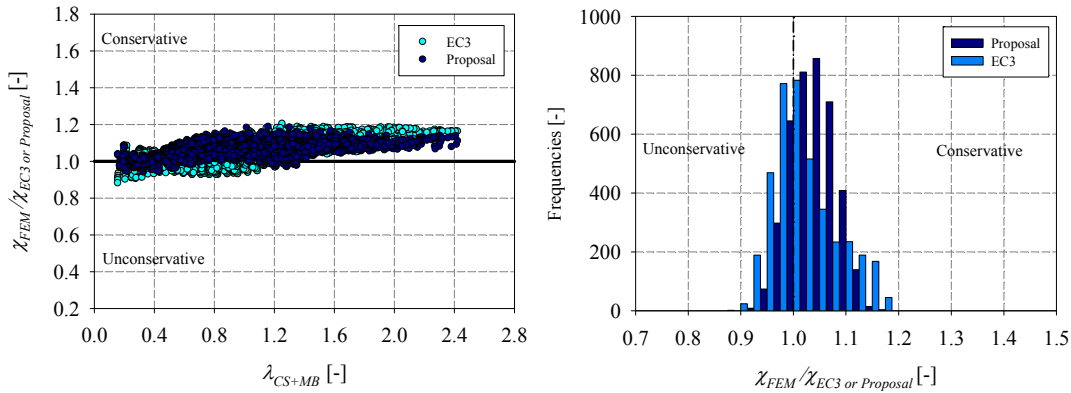


Figure 335 – Hot-rolled, $N+M_y+M_z$, $n = 0.7$ – a) Comparison of Proposal and EC3 results with FEM results – b) Frequency distributions (total number of results: 3988).

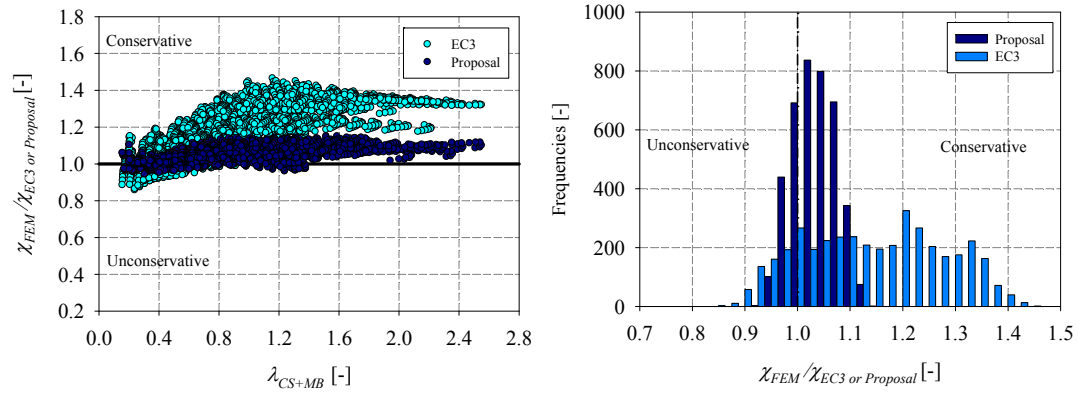


Figure 336 – Cold-formed, $N+M_y+M_z$, $n = 0.7$ – a) Comparison of Proposal and EC3 results with FEM results –
 b) Frequency distributions (total number of results: 3988).

6.6. Summary of proposal

The proposed O.I.C. interaction design curves for tubular beam-column members are summarized and presented in this section. The followings steps and remarks are recommended for the design of steel hollow members:

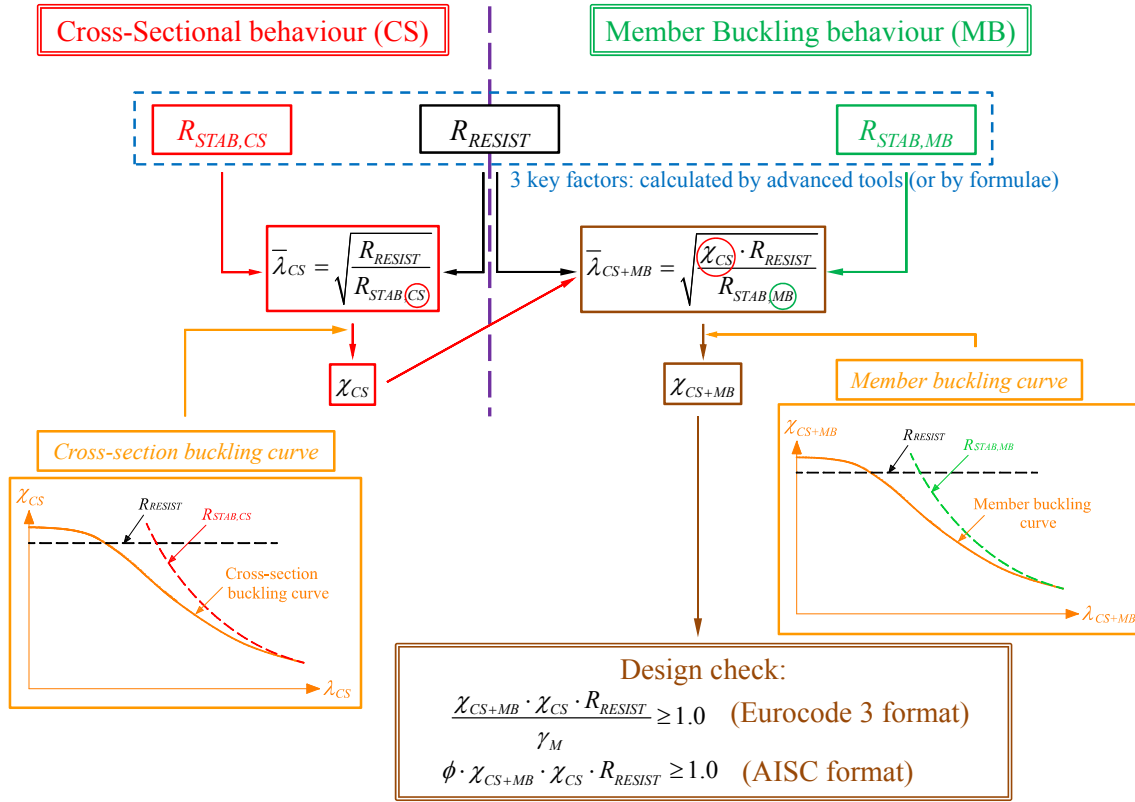


Figure 337 – Principles and application steps of the Overall Interaction Concept

Step 1: determination of the R -factors involved in the O.I.C. approach by advanced tools (or by formulae):

- the plastic load multiplier R_{RESIST} ;
- the critical load multiplier for cross-sections $R_{STAB,CS}$;
- the critical load multiplier for members $R_{STAB,MB}$.

Step 2: calculation of the cross-section slenderness $\lambda_{CS} = \sqrt{\frac{R_{RESIST}}{R_{STAB,CS}}}$;

Step 3: calculation of the cross-section penalty factor χ_{CS} according to the O.I.C. approach for cross-sections [3];

Step 4: calculation of the member slenderness $\lambda_{CS+MB} = \sqrt{\frac{\chi_{CS} R_{RESIST}}{R_{STAB,MB}}}$;

Step 5: calculation of the beam-column penalty χ_{CS+MB} as follows:

$$\chi_{CS+MB} = \frac{1}{\phi_{CS+MB} + \sqrt{\phi_{CS+MB}^2 - \lambda_{CS+MB}^2}} \text{ for } \lambda_{CS+MB} \geq \lambda_0$$

$$\text{With } \phi_{CS+MB} = 0.5(1 + \alpha(\lambda_{CS+MB} - \lambda_0) + \lambda_{CS+MB}^2)$$

In order to get the Ayrton-Perry parameters (end of plateau λ_0 and imperfection factor α), the load ratios are calculated and the curves are determined as follows:

Step 5a: calculation of the load ratios:

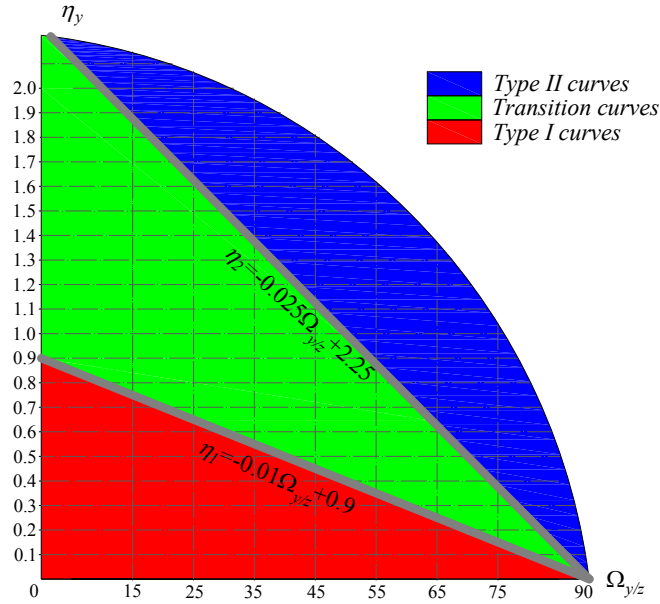
$$- \Omega_{y/z} = \arctan\left(\frac{m_z}{m_y}\right) = \arctan\left(\frac{M_z / M_{pl,z}}{M_y / M_{pl,y}}\right);$$

$$- \eta_y = \frac{m_y}{n_y} = \frac{M_y / M_{pl,y}}{N / N_{pl}};$$

$$- \eta_z = \frac{m_z}{n_z} = \frac{M_z / M_{pl,z}}{N / N_{pl}};$$

Step 5b: for the case of members subjected to constant bending moment, determination of the type of curve and to the defined limits η_2 and η_1 according to Figure 338. When the member is subjected to compression and minor-axis bending $N+M_z$, the degree of biaxial bending is equal to $\Omega_{y/z} = 90$ and the degree of major-axis bending is equal to $\eta_y = 0$. In this case the defined limits are as follows:

- *Type I* curve: $0 < \eta_z \leq 0.9$;
- *Type II* curve: $\eta_z > 2$;
- *Transition* curve: $\eta_1 = 0.9 < \eta_z \leq \eta_2 = 2$.


 Figure 338 – Defined limits for *Type I*, *Type II* and *Transition curves*

Step 5c: choice of adequate parameters according to Table 49 and Table 50 depending on the studied case (fabrication process, cross-section dimensions, load type...).

Step 6: calculation of the ultimate load multiplier $R_{REAL,MB} = \chi_{CS+MB} \cdot \chi_{CS} \cdot R_{RESIST}$.

The following remarks can be drawn from the tables below:

- the proposed curves corresponding to members subjected to combined loadings are presented, with the particular case of constant $\psi = 1$ and triangular bending moments $\psi = 0$. The proposed formulae can account correctly for the linearly varying moment diagrams with different end-moment values by considering the following equations:

$$\alpha_{\psi} = (\alpha_{\psi=1} - \alpha_{\psi=0})\psi + \alpha_{\psi=0} \quad \text{with } \alpha_{\psi} \geq 0 \quad (370)$$

$$\lambda_{0,\psi} = (\lambda_{0,\psi=1} - \lambda_{0,\psi=0})\psi + \lambda_{0,\psi=0} \quad \text{with } \lambda_0 \geq 0 \quad (371)$$

where, on one hand, a relation was established between the imperfection factor α_{ψ} and the imperfection factors $\alpha_{\psi=1}$, $\alpha_{\psi=0}$ for $\psi = 1$ and $\psi = 0$ respectively; and on the other, between the end of plateau $\lambda_{0,\psi}$ and the ends of plateau $\lambda_{0,\psi=1}$, $\lambda_{0,\psi=0}$ for $\psi = 1$ and $\psi = 0$;

- the curves corresponding to compression and mono-axial bending can be derived from the tables, by considering $\Omega_{y/z} = 0$ (i.e. the load case becoming compression with major-axis bending $N+M_y$) and $\Omega_{y/z} = 90$ (i.e. the load case becoming compression with minor-axis bending $N+M_z$). In a similar manner, the curves corresponding to pure compression load case can be derived from the tables of combined loading by considering $\Omega_{y/z} = 0$ with $\eta_y = 0$, or $\Omega_{y/z} = 90$ with $\eta_z = 0$. In the proposed formulae α_{comp} represents the imperfection factor for the pure compression load case;
- for the case of sections having an aspect ratio ranging from 1 to 1.3, $\alpha_{h/b=1}$ and $\alpha_{h/b \geq 1.3}$ should be determined in order to get $\alpha_{1 < h/b < 1.3}$ using the following equation:

$$\alpha = \left(\frac{\alpha_{h/b \geq 1.3} - \alpha_{h/b=1}}{0.3} \right) \left(\frac{h}{b} - 1.3 \right) + \alpha_{h/b \geq 1.3} \quad (372)$$

Table 49 – Proposed O.I.C. design curves for hot-rolled members tested under combined loadings with the corresponding bending moment – a) $\psi = 0$ – b) $\psi = 1$

Combined load cases for hot-rolled sections	
Triangular bending moment distribution: $\psi = 0$	
Yield stress	
$f_y = 235 \text{ N/mm}^2$	
$f_y = 355 \text{ N/mm}^2$	
Parameters for $h/b = 1$	
If $\Omega_{y/z} \leq 10$: $\lambda_0 = 0.2 + 0.2\eta_y^{0.2} \leq 0.35$, $\alpha = 0.015\Omega_{y/z} + \alpha_{comp} + 0.25\eta_y^{0.2} \leq 0.65$;	
If $10 \leq \Omega_{y/z} \leq 80$: $\lambda_0 = 0.35$, $\alpha = 0.65$;	
If $\Omega_{y/z} \geq 80$: $\lambda_0 = 0.2 + 0.2\eta_z^{0.2} \leq 0.35$, $\alpha = -0.015\Omega_{y/z} + 1.35 + \alpha_{comp} + 0.25\eta_z^{0.2} \leq 0.65$.	
Parameters for $h/b \geq 1.3$	
If $\Omega_{y/z} < 40$: $\lambda_0 = 0.2 + 0.2\eta_y^{0.2} \leq 0.35$, $\alpha = 0.0075\Omega_{y/z} + \alpha_{comp} \leq 0.5$;	
If $\Omega_{y/z} \geq 40$: $\lambda_0 = 0.2 + 0.2\eta_z^{0.2} \leq 0.35$, $\alpha = \alpha_{comp} + 0.25\eta_z^{0.2} \leq 0.5$.	
Parameters for $1 < h/b < 1.3$	
$\lambda_0 = \left(\frac{\lambda_{0h/b \geq 1.3} - \lambda_{0h/b=1}}{0.3} \right) \left(\frac{h}{b} - 1.3 \right) + \lambda_{0h/b \geq 1.3}, \alpha = \left(\frac{\alpha_{h/b \geq 1.3} - \alpha_{h/b=1}}{0.3} \right) \left(\frac{h}{b} - 1.3 \right) + \alpha_{h/b \geq 1.3}$	
Yield stress	
$f_y = 690 \text{ N/mm}^2$	
Parameters for $h/b = 1$	
If $\Omega_{y/z} \leq 10$: $\lambda_0 = 0.2 + 0.2\eta_y^{0.2} \leq 0.35$, $\alpha = 0.015\Omega_{y/z} + \alpha_{comp} + 0.25\eta_y^{0.2} \leq 0.55$;	
If $10 \leq \Omega_{y/z} \leq 80$: $\lambda_0 = 0.35$, $\alpha = 0.55$;	
If $\Omega_{y/z} \geq 80$: $\lambda_0 = 0.2 + 0.2\eta_z^{0.2} \leq 0.35$, $\alpha = -0.015\Omega_{y/z} + 1.35 + \alpha_{comp} + 0.25\eta_z^{0.2} \leq 0.55$.	
Parameters for $h/b \geq 1.3$	
If $\Omega_{y/z} < 40$: $\lambda_0 = 0.2 + 0.2\eta_y^{0.2} \leq 0.35$, $\alpha = 0.0075\Omega_{y/z} + \alpha_{comp} \leq 0.4$;	
If $\Omega_{y/z} \geq 40$: $\lambda_0 = 0.2 + 0.2\eta_z^{0.2} \leq 0.35$, $\alpha = \alpha_{comp} + 0.25\eta_z^{0.2} \leq 0.4$.	
Parameters for $1 < h/b < 1.3$ ⁽²⁾	
$\lambda_0 = \left(\frac{\lambda_{0h/b \geq 1.3} - \lambda_{0h/b=1}}{0.3} \right) \left(\frac{h}{b} - 1.3 \right) + \lambda_{0h/b \geq 1.3}, \alpha = \left(\frac{\alpha_{h/b \geq 1.3} - \alpha_{h/b=1}}{0.3} \right) \left(\frac{h}{b} - 1.3 \right) + \alpha_{h/b \geq 1.3}$	
Constant bending moment distribution: $\psi = 1$	
Yield stress	
$f_y = 235 \text{ N/mm}^2$	
$f_y = 355 \text{ N/mm}^2$	
Parameters for $h/b = 1$	
Type I curve:	If $\Omega_{y/z} \leq 10$: $\lambda_0 = 0.2$, $\alpha = \alpha_1 = 0.005\Omega_{y/z} + \alpha_{comp} + 0.4\eta_y^{0.2} \leq 0.65$; If $10 \leq \Omega_{y/z} \leq 80$: $\lambda_0 = 0.2$, $\alpha = \alpha_1 = 0.65$; If $\Omega_{y/z} \geq 80$: $\lambda_0 = 0.2$, $\alpha = \alpha_1 = -0.005\Omega_{y/z} + 0.45 + \alpha_{comp} + 0.4\eta_z^{0.2} \leq 0.65$.
	If $\Omega_{y/z} \leq 10$: $\lambda_0 = 0.1$, $\alpha = \alpha_2 = 0.015\Omega_{y/z} + 0.80$; If $10 \leq \Omega_{y/z} \leq 80$: $\lambda_0 = 0.1$, $\alpha = \alpha_2 = 0.95$; If $\Omega_{y/z} \geq 80$: $\lambda_0 = 0.1$, $\alpha = \alpha_2 = -0.015\Omega_{y/z} + 2.15$.
	$\lambda_0 = \left(-\frac{0.1}{\eta_2 - \eta_1} \right) (\eta_y - \eta_2) + 0.1, \alpha = \left(\frac{\alpha_2 - \alpha_1}{\eta_2 - \eta_1} \right) (\eta_y - \eta_2) + \alpha_2$
Transition curve ⁽¹⁾ :	

Parameters for $h/b \geq 1.3$	
Type I curve:	If $\Omega_{y/z} < 40$: $\lambda_0 = 0.2$, $\alpha = \alpha_1 = 0.0085\Omega_{y/z} + \alpha_{comp} + 0.05\eta_y^{0.2} \leq 0.6$; If $\Omega_{y/z} \geq 40$: $\lambda_0 = 0.2$, $\alpha = \alpha_1 = \alpha_{comp} + 0.4\eta_z^{0.2} \leq 0.6$.
Type II curve:	If $\Omega_{y/z} < 40$: $\lambda_0 = 0.1$, $\alpha = \alpha_2 = 0.01\Omega_{y/z} + 0.4$; If $\Omega_{y/z} \geq 40$: $\lambda_0 = 0.1$, $\alpha = \alpha_2 = 0.80$.
Transition curve ⁽¹⁾ :	$\lambda_0 = \left(-\frac{0.1}{\eta_2 - \eta_1} \right) (\eta_y - \eta_2) + 0.1, \alpha = \left(\frac{\alpha_2 - \alpha_1}{\eta_2 - \eta_1} \right) (\eta_y - \eta_2) + \alpha_2$
Parameters for $1 < h/b < 1.3$	
Type I curve:	$\lambda_0 = 0.2, \alpha = \left(\frac{\alpha_{h/b \geq 1.3} - \alpha_{h/b=1}}{0.3} \right) \left(\frac{h}{b} - 1.3 \right) + \alpha_{h/b \geq 1.3}$
Type II curve:	$\lambda_0 = 0.1, \alpha = \left(\frac{\alpha_{h/b \geq 1.3} - \alpha_{h/b=1}}{0.3} \right) \left(\frac{h}{b} - 1.3 \right) + \alpha_{h/b \geq 1.3}$
Transition curve ⁽¹⁾ :	$\lambda_0 = \left(-\frac{0.1}{\eta_2 - \eta_1} \right) (\eta_y - \eta_2) + 0.1, \alpha = \left(\frac{\alpha_{h/b \geq 1.3} - \alpha_{h/b=1}}{0.3} \right) \left(\frac{h}{b} - 1.3 \right) + \alpha_{h/b \geq 1.3}$
Yield stress	
$f_y = 690 \text{ N/mm}^2$	
Parameters for $h/b = 1$	
Type I curve:	If $\Omega_{y/z} \leq 10$: $\lambda_0 = 0.2$, $\alpha = \alpha_1 = 0.005\Omega_{y/z} + \alpha_{comp} + 0.4\eta_y^{0.2} \leq 0.55$; If $10 \leq \Omega_{y/z} \leq 80$: $\lambda_0 = 0.2$, $\alpha = \alpha_1 = 0.55$; If $\Omega_{y/z} \geq 80$: $\lambda_0 = 0.2$, $\alpha = \alpha_1 = -0.005\Omega_{y/z} + 0.45 + \alpha_{comp} + 0.4\eta_z^{0.2} \leq 0.55$.
Type II curve:	If $\Omega_{y/z} \leq 10$: $\lambda_0 = 0.1$, $\alpha = \alpha_2 = 0.01\Omega_{y/z} + 0.75$; If $10 \leq \Omega_{y/z} \leq 80$: $\lambda_0 = 0.1$, $\alpha = \alpha_2 = 0.85$; If $\Omega_{y/z} \geq 80$: $\lambda_0 = 0.1$, $\alpha = \alpha_2 = -0.01\Omega_{y/z} + 1.65$.
Transition curve ⁽¹⁾ :	$\lambda_0 = \left(-\frac{0.1}{\eta_2 - \eta_1} \right) (\eta_y - \eta_2) + 0.1, \alpha = \left(\frac{\alpha_2 - \alpha_1}{\eta_2 - \eta_1} \right) (\eta_y - \eta_2) + \alpha_2$
Parameters for $h/b \geq 1.3$	
Type I curve:	If $\Omega_{y/z} < 40$: $\lambda_0 = 0.2$, $\alpha = \alpha_1 = 0.0085\Omega_{y/z} + \alpha_{comp} + 0.05\eta_z^{0.2} \leq 0.5$; If $\Omega_{y/z} \geq 40$: $\lambda_0 = 0.2$, $\alpha = \alpha_1 = \alpha_{comp} + 0.4\eta_z^{0.2} \leq 0.5$.
Type II curve:	If $\Omega_{y/z} < 40$: $\lambda_0 = 0.1$, $\alpha = \alpha_2 = 0.01\Omega_{y/z} + 0.35$; If $\Omega_{y/z} \geq 40$: $\lambda_0 = 0.1$, $\alpha = \alpha_2 = 0.75$.
Transition curve ⁽¹⁾ :	$\lambda_0 = \left(-\frac{0.1}{\eta_2 - \eta_1} \right) (\eta_y - \eta_2) + 0.1, \alpha = \left(\frac{\alpha_2 - \alpha_1}{\eta_2 - \eta_1} \right) (\eta_y - \eta_2) + \alpha_2$
Parameters for $1 < h/b < 1.3$	
Type I curve:	$\lambda_0 = 0.2, \alpha = \left(\frac{\alpha_{h/b \geq 1.3} - \alpha_{h/b=1}}{0.3} \right) \left(\frac{h}{b} - 1.3 \right) + \alpha_{h/b \geq 1.3}$
Type II curve:	$\lambda_0 = 0.1, \alpha = \left(\frac{\alpha_{h/b \geq 1.3} - \alpha_{h/b=1}}{0.3} \right) \left(\frac{h}{b} - 1.3 \right) + \alpha_{h/b \geq 1.3}$
Transition curve ⁽¹⁾ :	$\lambda_0 = \left(-\frac{0.1}{\eta_2 - \eta_1} \right) (\eta_y - \eta_2) + 0.1, \alpha = \left(\frac{\alpha_{h/b \geq 1.3} - \alpha_{h/b=1}}{0.3} \right) \left(\frac{h}{b} - 1.3 \right) + \alpha_{h/b \geq 1.3}$

⁽¹⁾ η_y is replaced by η_z for the particular case $\Omega_{y/z} = 90$ where the load case becomes compression with minor-axis $N+M_z$ and $\eta_y = 0$

Table 50 – Proposed O.I.C. design curves for cold-formed members tested under combined loadings with the corresponding bending moment – a) $\psi = 0$ – b) $\psi = 1$

Combined load cases for cold-formed sections	
Triangular bending moment distribution: $\psi = 0$	
Yield stress	
$f_y = 235 \text{ N/mm}^2$	
$f_y = 355 \text{ N/mm}^2$	
Parameters for $h/b = 1$	
If $\Omega_{y/z} \leq 10$: $\lambda_0 = 0.2 + 0.2\eta_y^{0.2} \leq 0.35$, $\alpha = 0.01\Omega_{y/z} + \alpha_{comp} + 0.25\eta_y^{0.2} \leq 0.8$;	
If $10 \leq \Omega_{y/z} \leq 80$: $\lambda_0 = 0.35$, $\alpha = 0.8$;	
If $\Omega_{y/z} \geq 80$: $\lambda_0 = 0.2 + 0.2\eta_z^{0.2} \leq 0.35$, $\alpha = -0.01\Omega_{y/z} + 0.9 + \alpha_{comp} + 0.25\eta_z^{0.2} \leq 0.8$.	
Parameters for $h/b \geq 1.3$	
If $\Omega_{y/z} < 40$: $\lambda_0 = 0.2 + 0.2\eta_y^{0.2} \leq 0.35$, $\alpha = 0.0075\Omega_{y/z} + \alpha_{comp} \leq 0.7$;	
If $\Omega_{y/z} \geq 40$: $\lambda_0 = 0.2 + 0.2\eta_z^{0.2} \leq 0.35$, $\alpha = \alpha_{comp} + 0.25\eta_z^{0.2} \leq 0.7$.	
Parameters for $1 < h/b < 1.3$	
$\lambda_0 = \left(\frac{\lambda_{0h/b \geq 1.3} - \lambda_{0h/b=1}}{0.3} \right) \left(\frac{h}{b} - 1.3 \right) + \lambda_{0h/b \geq 1.3}$, $\alpha = \left(\frac{\alpha_{h/b \geq 1.3} - \alpha_{h/b=1}}{0.3} \right) \left(\frac{h}{b} - 1.3 \right) + \alpha_{h/b \geq 1.3}$	
Yield stress	
$f_y = 690 \text{ N/mm}^2$	
Parameters for $h/b = 1$	
If $\Omega_{y/z} \leq 10$: $\lambda_0 = 0.2 + 0.2\eta_y^{0.2} \leq 0.35$, $\alpha = 0.015\Omega_{y/z} + \alpha_{comp} + 0.25\eta_y^{0.2} \leq 0.6$;	
If $10 \leq \Omega_{y/z} \leq 80$: $\lambda_0 = 0.35$, $\alpha = 0.6$;	
If $\Omega_{y/z} \geq 80$: $\lambda_0 = 0.2 + 0.2\eta_z^{0.2} \leq 0.35$, $\alpha = -0.015\Omega_{y/z} + 1.35 + \alpha_{comp} + 0.25\eta_z^{0.2} \leq 0.6$.	
Parameters for $h/b \geq 1.3$	
If $\Omega_{y/z} < 40$: $\lambda_0 = 0.2 + 0.2\eta_y^{0.2} \leq 0.35$, $\alpha = 0.0075\Omega_{y/z} + \alpha_{comp} \leq 0.45$;	
If $\Omega_{y/z} \geq 40$: $\lambda_0 = 0.2 + 0.2\eta_z^{0.2} \leq 0.35$, $\alpha = \alpha_{comp} + 0.25\eta_z^{0.2} \leq 0.45$.	
Parameters for $1 < h/b < 1.3$	
$\lambda_0 = \left(\frac{\lambda_{0h/b \geq 1.3} - \lambda_{0h/b=1}}{0.3} \right) \left(\frac{h}{b} - 1.3 \right) + \lambda_{0h/b \geq 1.3}$, $\alpha = \left(\frac{\alpha_{h/b \geq 1.3} - \alpha_{h/b=1}}{0.3} \right) \left(\frac{h}{b} - 1.3 \right) + \alpha_{h/b \geq 1.3}$	
Constant bending moment distribution: $\psi = 1$	
Yield stress	
$f_y = 235 \text{ N/mm}^2$	
$f_y = 355 \text{ N/mm}^2$	
Parameters for $h/b = 1$	
<i>Type I curve:</i>	If $\Omega_{y/z} \leq 10$: $\lambda_0 = 0.2$, $\alpha = \alpha_1 = 0.005\Omega_{y/z} + \alpha_{comp} + 0.4\eta_y^{0.2} \leq 0.75$;
	If $10 \leq \Omega_{y/z} \leq 80$: $\lambda_0 = 0.2$, $\alpha = \alpha_1 = 0.75$;
	If $\Omega_{y/z} \geq 80$: $\lambda_0 = 0.2$,
$\alpha = \alpha_1 = -0.005\Omega_{y/z} + 0.45 + \alpha_{comp} + 0.4\eta_z^{0.2} \leq 0.75$.	
<i>Type II curve:</i>	If $\Omega_{y/z} \leq 10$: $\lambda_0 = 0.1$, $\alpha = \alpha_2 = 0.01\Omega_{y/z} + 1.0$;
	If $10 \leq \Omega_{y/z} \leq 80$: $\lambda_0 = 0.1$, $\alpha = \alpha_2 = 1.1$;
	If $\Omega_{y/z} \geq 80$: $\lambda_0 = 0.1$, $\alpha = \alpha_2 = -0.01\Omega_{y/z} + 1.9$.

<i>Transition curve</i> ⁽¹⁾ :	$\lambda_0 = \left(-\frac{0.1}{\eta_2 - \eta_1} \right) (\eta_y - \eta_2) + 0.1, \alpha = \left(\frac{\alpha_2 - \alpha_1}{\eta_2 - \eta_1} \right) (\eta_y - \eta_2) + \alpha_2$
Parameters for $h/b \geq 1.3$	
<i>Type I curve</i> :	If $\Omega_{y/z} < 40$: $\lambda_0 = 0.2, \alpha = \alpha_1 = 0.006\Omega_{y/z} + \alpha_{comp} + 0.05\eta_y^{0.2} \leq 0.7$; If $\Omega_{y/z} \geq 40$: $\lambda_0 = 0.2, \alpha = \alpha_1 = \alpha_{comp} + 0.4\eta_z^{0.2} \leq 0.7$.
<i>Type II curve</i> :	If $\Omega_{y/z} < 40$: $\lambda_0 = 0.1, \alpha = \alpha_2 = 0.01\Omega_{y/z} + 0.6$; If $\Omega_{y/z} \geq 40$: $\lambda_0 = 0.1, \alpha = \alpha_2 = 1.0$.
<i>Transition curve</i> ⁽¹⁾ :	$\lambda_0 = \left(-\frac{0.1}{\eta_2 - \eta_1} \right) (\eta_y - \eta_2) + 0.1, \alpha = \left(\frac{\alpha_2 - \alpha_1}{\eta_2 - \eta_1} \right) (\eta_y - \eta_2) + \alpha_2$
Parameters for $1 < h/b < 1.3$	
<i>Type I curve</i> :	$\lambda_0 = 0.2, \alpha = \left(\frac{\alpha_{h/b \geq 1.3} - \alpha_{h/b=1}}{0.3} \right) \left(\frac{h}{b} - 1.3 \right) + \alpha_{h/b \geq 1.3}$
<i>Type II curve</i> :	$\lambda_0 = 0.1, \alpha = \left(\frac{\alpha_{h/b \geq 1.3} - \alpha_{h/b=1}}{0.3} \right) \left(\frac{h}{b} - 1.3 \right) + \alpha_{h/b \geq 1.3}$
<i>Transition curve</i> ⁽¹⁾ :	$\lambda_0 = \left(-\frac{0.1}{\eta_2 - \eta_1} \right) (\eta_y - \eta_2) + 0.1, \alpha = \left(\frac{\alpha_{h/b \geq 1.3} - \alpha_{h/b=1}}{0.3} \right) \left(\frac{h}{b} - 1.3 \right) + \alpha_{h/b \geq 1.3}$
Yield stress	
$f_y = 690 \text{ N/mm}^2$	
Parameters for $h/b = 1$	
<i>Type I curve</i> :	If $\Omega_{y/z} \leq 10$: $\lambda_0 = 0.2, \alpha = \alpha_1 = 0.005\Omega_{y/z} + \alpha_{comp} + 0.4\eta_y^{0.2} \leq 0.6$; If $10 \leq \Omega_{y/z} \leq 80$: $\lambda_0 = 0.2, \alpha = \alpha_1 = 0.60$; If $\Omega_{y/z} \geq 80$: $\lambda_0 = 0.2, \alpha = \alpha_1 = -0.005\Omega_{y/z} + 0.45 + \alpha_{comp} + 0.4\eta_z^{0.2} \leq 0.6$.
<i>Type II curve</i> :	If $\Omega_{y/z} \leq 10$: $\lambda_0 = 0.1, \alpha = \alpha_2 = 0.01\Omega_{y/z} + 0.80$; If $10 \leq \Omega_{y/z} \leq 80$: $\lambda_0 = 0.1, \alpha = \alpha_2 = 0.90$; If $\Omega_{y/z} \geq 80$: $\lambda_0 = 0.1, \alpha = \alpha_2 = -0.01\Omega_{y/z} + 1.7$.
<i>Transition curve</i> ⁽¹⁾ :	$\lambda_0 = \left(-\frac{0.1}{\eta_2 - \eta_1} \right) (\eta_y - \eta_2) + 0.1, \alpha = \left(\frac{\alpha_2 - \alpha_1}{\eta_2 - \eta_1} \right) (\eta_y - \eta_2) + \alpha_2$
Parameters for $h/b \geq 1.3$	
<i>Type I curve</i> :	If $\Omega_{y/z} < 40$: $\lambda_0 = 0.2, \alpha = \alpha_1 = 0.007\Omega_{y/z} + \alpha_{comp} + 0.05\eta_y^{0.2} \leq 0.55$; If $\Omega_{y/z} \geq 40$: $\lambda_0 = 0.2, \alpha = \alpha_1 = \alpha_{comp} + 0.4\eta_z^{0.2} \leq 0.55$.
<i>Type II curve</i> :	If $\Omega_{y/z} < 40$: $\lambda_0 = 0.1, \alpha = \alpha_2 = 0.01\Omega_{y/z} + 0.4$; If $\Omega_{y/z} \geq 40$: $\lambda_0 = 0.1, \alpha = \alpha_2 = 0.80$.
<i>Transition curve</i> ⁽¹⁾ :	$\lambda_0 = \left(-\frac{0.1}{\eta_2 - \eta_1} \right) (\eta_y - \eta_2) + 0.1, \alpha = \left(\frac{\alpha_2 - \alpha_1}{\eta_2 - \eta_1} \right) (\eta_y - \eta_2) + \alpha_2$
Parameters for $1 < h/b < 1.3$	
<i>Type I curve</i> :	$\lambda_0 = 0.2, \alpha = \left(\frac{\alpha_{h/b \geq 1.3} - \alpha_{h/b=1}}{0.3} \right) \left(\frac{h}{b} - 1.3 \right) + \alpha_{h/b \geq 1.3}$
<i>Type II curve</i> :	$\lambda_0 = 0.1, \alpha = \left(\frac{\alpha_{h/b \geq 1.3} - \alpha_{h/b=1}}{0.3} \right) \left(\frac{h}{b} - 1.3 \right) + \alpha_{h/b \geq 1.3}$
<i>Transition curve</i> ⁽¹⁾ :	$\lambda_0 = \left(-\frac{0.1}{\eta_2 - \eta_1} \right) (\eta_y - \eta_2) + 0.1, \alpha = \left(\frac{\alpha_{h/b \geq 1.3} - \alpha_{h/b=1}}{0.3} \right) \left(\frac{h}{b} - 1.3 \right) + \alpha_{h/b \geq 1.3}$

⁽¹⁾ η_y is replaced by η_z for the particular case $\Omega_{y/z} = 90$

6.7. Simplified proposal

As discussed in section 6.5, the resistance estimates are significantly improved by the new proposal, and the mean and standard deviation values also indicate a better level of consistency compared to EC3 calculations. As an alternative to this proposed model, a second one was derived, able to provide sufficient compromise between satisfactory accuracy and minimum computational time.

The interaction curves based on the numerical results relative to an aspect ratio equal to 1.0, can be safely adopted to determine the resistance of members having higher aspect ratios, since they lead to conservative results;

Accordingly, the simplified proposed models are summarized in the tables below:

Table 51 – Proposed O.I.C. design curves for hot-rolled members tested under combined loadings with the corresponding bending moment – a) $\psi = 0$ – b) $\psi = 1$

Combined load cases for hot-rolled sections	
Triangular bending moment distribution: $\psi = 0$	
Yield stress	
$f_y = 235 \text{ N/mm}^2$ $f_y = 355 \text{ N/mm}^2$	
Parameters	
If $\Omega_{y/z} \leq 10$: $\lambda_0 = 0.2 + 0.2\eta_y^{0.2} \leq 0.35$, $\alpha = 0.015\Omega_{y/z} + \alpha_{comp} + 0.25\eta_y^{0.2} \leq 0.65$; If $10 \leq \Omega_{y/z} \leq 80$: $\lambda_0 = 0.35$, $\alpha = 0.65$; If $\Omega_{y/z} \geq 80$: $\lambda_0 = 0.2 + 0.2\eta_z^{0.2} \leq 0.35$, $\alpha = -0.015\Omega_{y/z} + 1.35 + \alpha_{comp} + 0.25\eta_z^{0.2} \leq 0.65$.	
Yield stress	
$f_y = 690 \text{ N/mm}^2$	
Parameters	
If $\Omega_{y/z} \leq 10$: $\lambda_0 = 0.2 + 0.2\eta_y^{0.2} \leq 0.35$, $\alpha = 0.015\Omega_{y/z} + \alpha_{comp} + 0.25\eta_y^{0.2} \leq 0.55$; If $10 \leq \Omega_{y/z} \leq 80$: $\lambda_0 = 0.35$, $\alpha = 0.55$; If $\Omega_{y/z} \geq 80$: $\lambda_0 = 0.2 + 0.2\eta_z^{0.2} \leq 0.35$, $\alpha = -0.015\Omega_{y/z} + 1.35 + \alpha_{comp} + 0.25\eta_z^{0.2} \leq 0.55$.	
Constant bending moment distribution: $\psi = 1$	
Yield stress	
$f_y = 235 \text{ N/mm}^2$ $f_y = 355 \text{ N/mm}^2$	
Parameters	
Type I curve:	If $\Omega_{y/z} \leq 10$: $\lambda_0 = 0.2$, $\alpha = \alpha_1 = 0.005\Omega_{y/z} + \alpha_{comp} + 0.4\eta_y^{0.2} \leq 0.65$; If $10 \leq \Omega_{y/z} \leq 80$: $\lambda_0 = 0.2$, $\alpha = \alpha_1 = 0.65$; If $\Omega_{y/z} \geq 80$: $\lambda_0 = 0.2$, $\alpha = \alpha_1 = -0.005\Omega_{y/z} + 0.45 + \alpha_{comp} + 0.4\eta_z^{0.2} \leq 0.65$.
Type II curve:	If $\Omega_{y/z} \leq 10$: $\lambda_0 = 0.1$, $\alpha = \alpha_2 = 0.015\Omega_{y/z} + 0.80$; If $10 \leq \Omega_{y/z} \leq 80$: $\lambda_0 = 0.1$, $\alpha = \alpha_2 = 0.95$; If $\Omega_{y/z} \geq 80$: $\lambda_0 = 0.1$, $\alpha = \alpha_2 = -0.015\Omega_{y/z} + 2.15$.
Transition curve ⁽¹⁾ :	$\lambda_0 = \left(-\frac{0.1}{\eta_2 - \eta_1} \right) (\eta_y - \eta_2) + 0.1$, $\alpha = \left(\frac{\alpha_2 - \alpha_1}{\eta_2 - \eta_1} \right) (\eta_y - \eta_2) + \alpha_2$
Yield stress	
$f_y = 690 \text{ N/mm}^2$	
Parameters	
Type I curve:	If $\Omega_{y/z} \leq 10$: $\lambda_0 = 0.2$, $\alpha = \alpha_1 = 0.005\Omega_{y/z} + \alpha_{comp} + 0.4\eta_y^{0.2} \leq 0.55$; If $10 \leq \Omega_{y/z} \leq 80$: $\lambda_0 = 0.2$, $\alpha = \alpha_1 = 0.55$; If $\Omega_{y/z} \geq 80$: $\lambda_0 = 0.2$, $\alpha = \alpha_1 = -0.005\Omega_{y/z} + 0.45 + \alpha_{comp} + 0.4\eta_z^{0.2} \leq 0.55$.
Type II curve:	If $\Omega_{y/z} \leq 10$: $\lambda_0 = 0.1$, $\alpha = \alpha_2 = 0.01\Omega_{y/z} + 0.75$; If $10 \leq \Omega_{y/z} \leq 80$: $\lambda_0 = 0.1$, $\alpha = \alpha_2 = 0.85$; If $\Omega_{y/z} \geq 80$: $\lambda_0 = 0.1$, $\alpha = \alpha_2 = -0.01\Omega_{y/z} + 1.65$.
Transition curve ⁽¹⁾ :	$\lambda_0 = \left(-\frac{0.1}{\eta_2 - \eta_1} \right) (\eta_y - \eta_2) + 0.1$, $\alpha = \left(\frac{\alpha_2 - \alpha_1}{\eta_2 - \eta_1} \right) (\eta_y - \eta_2) + \alpha_2$

⁽¹⁾ η_y is replaced by η_z for the particular case $\Omega_{y/z} = 90$

Table 52 – Proposed O.I.C. design curves for cold-formed members tested under combined loadings with the corresponding bending moment – a) $\psi = 0$ – b) $\psi = 1$

Combined load cases for cold-formed sections	
Triangular bending moment distribution: $\psi = 0$	
Yield stress	
$f_y = 235 \text{ N/mm}^2$	
$f_y = 355 \text{ N/mm}^2$	
Parameters	
If $\Omega_{y/z} \leq 10$: $\lambda_0 = 0.2 + 0.2\eta_y^{0.2} \leq 0.35$, $\alpha = 0.01\Omega_{y/z} + \alpha_{comp} + 0.25\eta_y^{0.2} \leq 0.8$;	
If $10 \leq \Omega_{y/z} \leq 80$: $\lambda_0 = 0.35$, $\alpha = 0.8$;	
If $\Omega_{y/z} \geq 80$: $\lambda_0 = 0.2 + 0.2\eta_z^{0.2} \leq 0.35$, $\alpha = -0.01\Omega_{y/z} + 0.9 + \alpha_{comp} + 0.25\eta_z^{0.2} \leq 0.8$.	
Yield stress	
$f_y = 690 \text{ N/mm}^2$	
Parameters	
If $\Omega_{y/z} \leq 10$: $\lambda_0 = 0.2 + 0.2\eta_y^{0.2} \leq 0.35$, $\alpha = 0.015\Omega_{y/z} + \alpha_{comp} + 0.25\eta_y^{0.2} \leq 0.6$;	
If $10 \leq \Omega_{y/z} \leq 80$: $\lambda_0 = 0.35$, $\alpha = 0.6$;	
If $\Omega_{y/z} \geq 80$: $\lambda_0 = 0.2 + 0.2\eta_z^{0.2} \leq 0.35$, $\alpha = -0.015\Omega_{y/z} + 1.35 + \alpha_{comp} + 0.25\eta_z^{0.2} \leq 0.6$.	
Constant bending moment distribution: $\psi = 1$	
Yield stress	
$f_y = 235 \text{ N/mm}^2$	
$f_y = 355 \text{ N/mm}^2$	
Parameters	
Type I curve:	If $\Omega_{y/z} \leq 10$: $\lambda_0 = 0.2$, $\alpha = \alpha_1 = 0.005\Omega_{y/z} + \alpha_{comp} + 0.4\eta_y^{0.2} \leq 0.75$; If $10 \leq \Omega_{y/z} \leq 80$: $\lambda_0 = 0.2$, $\alpha = \alpha_1 = 0.75$; If $\Omega_{y/z} \geq 80$: $\lambda_0 = 0.2$, $\alpha = \alpha_1 = -0.005\Omega_{y/z} + 0.45 + \alpha_{comp} + 0.4\eta_z^{0.2} \leq 0.75$.
Type II curve:	If $\Omega_{y/z} \leq 10$: $\lambda_0 = 0.1$, $\alpha = \alpha_2 = 0.01\Omega_{y/z} + 1.0$; If $10 \leq \Omega_{y/z} \leq 80$: $\lambda_0 = 0.1$, $\alpha = \alpha_2 = 1.1$; If $\Omega_{y/z} \geq 80$: $\lambda_0 = 0.1$, $\alpha = \alpha_2 = -0.01\Omega_{y/z} + 1.9$.
Transition curve ⁽¹⁾ :	$\lambda_0 = \left(-\frac{0.1}{\eta_2 - \eta_1} \right) (\eta_y - \eta_2) + 0.1$, $\alpha = \left(\frac{\alpha_2 - \alpha_1}{\eta_2 - \eta_1} \right) (\eta_y - \eta_2) + \alpha_2$
Yield stress	
$f_y = 690 \text{ N/mm}^2$	
Parameters	
Type I curve:	If $\Omega_{y/z} \leq 10$: $\lambda_0 = 0.2$, $\alpha = \alpha_1 = 0.005\Omega_{y/z} + \alpha_{comp} + 0.4\eta_y^{0.2} \leq 0.6$; If $10 \leq \Omega_{y/z} \leq 80$: $\lambda_0 = 0.2$, $\alpha = \alpha_1 = 0.60$; If $\Omega_{y/z} \geq 80$: $\lambda_0 = 0.2$, $\alpha = \alpha_1 = -0.005\Omega_{y/z} + 0.45 + \alpha_{comp} + 0.4\eta_z^{0.2} \leq 0.6$.
Type II curve:	If $\Omega_{y/z} \leq 10$: $\lambda_0 = 0.1$, $\alpha = \alpha_2 = 0.01\Omega_{y/z} + 0.80$; If $10 \leq \Omega_{y/z} \leq 80$: $\lambda_0 = 0.1$, $\alpha = \alpha_2 = 0.90$; If $\Omega_{y/z} \geq 80$: $\lambda_0 = 0.1$, $\alpha = \alpha_2 = -0.01\Omega_{y/z} + 1.7$.
Transition curve ⁽¹⁾ :	$\lambda_0 = \left(-\frac{0.1}{\eta_2 - \eta_1} \right) (\eta_y - \eta_2) + 0.1$, $\alpha = \left(\frac{\alpha_2 - \alpha_1}{\eta_2 - \eta_1} \right) (\eta_y - \eta_2) + \alpha_2$

⁽¹⁾ η_y is replaced by η_z for the particular case $\Omega_{y/z} = 90$

Table 53 and the figures below propose statistical results of the comparison between FEM, EC3 and proposal calculations obtained by using the simplified proposed models, for hot-rolled and cold-formed members subjected to combined loading situations with the three considered steel grades in this work.

On the left column, plots illustrating comparisons between χ_{FEM} / χ_{EC3} and $\chi_{FEM} / \chi_{proposal}$ ratios are presented, while the right column shows these same results in the form of histograms in an attempt to better illustrate and translate the observations of the left column plots.

Table 53 – Comparison between FEM, EC3 and proposal results for all treated load cases.

Load case	Fabrication process	Number of results	χ_{FEM} / χ_{EC3}				$\chi_{FEM} / \chi_{proposal}$			
			Average	Min	Max	St.Dev	Average	Min	Max	St.Dev
$N+M_y+M_z$	Hot-rolled	8796	1.03	0.76	1.28	0.08	1.09	0.90	1.44	0.08
$N+M_z$	Hot-rolled	1052	0.98	0.72	1.19	0.08	1.04	0.95	1.15	0.03
$N+M_y$	Hot-rolled	1241	0.98	0.70	1.29	0.08	1.11	0.92	1.57	0.12
$N+M_y+M_z$	Cold-formed	8796	1.15	0.78	1.46	0.13	1.08	0.93	1.46	0.07
$N+M_z$	Cold-formed	1052	1.08	0.73	1.35	0.12	1.03	0.91	1.13	0.03
$N+M_y$	Cold-formed	1241	1.08	0.75	1.36	0.12	1.13	0.91	1.61	0.13

With the adoption of the simplified proposed models, the calculations can sometimes lead to unconservative results and sometimes to overly conservative results, while the majority of the results seem conservative on the left plot.

The first proposed approach for hot-rolled and cold-formed members is seen to present better results since a bigger number of $\chi_{FEM} / \chi_{proposal}$ ratios are close to 1.0, as expected, since all the defined leading parameters were considered in the derivation of the interaction formulae.

However, even though the second proposed model provides more conservative results (expect for the $N+M_z$ load case, where the failure of the element is not affected by the cross-section shape of the member), it can be safely used to determine the resistance of beam-column members since it leads to satisfactory results with minimal computational effort.

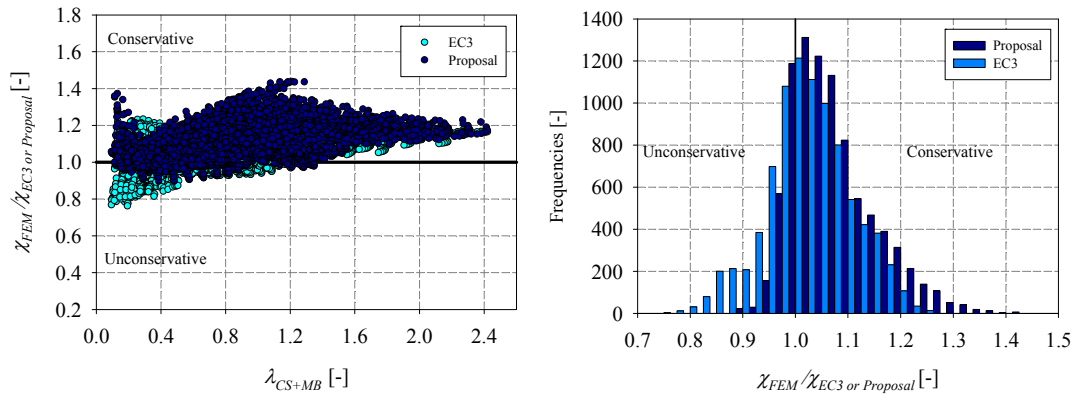


Figure 339 – Hot-rolled, $N+M_y+M_z$ – a) Comparison of proposal and EC3 results with FEM results – b) Frequency distributions (total number of results: 8796)

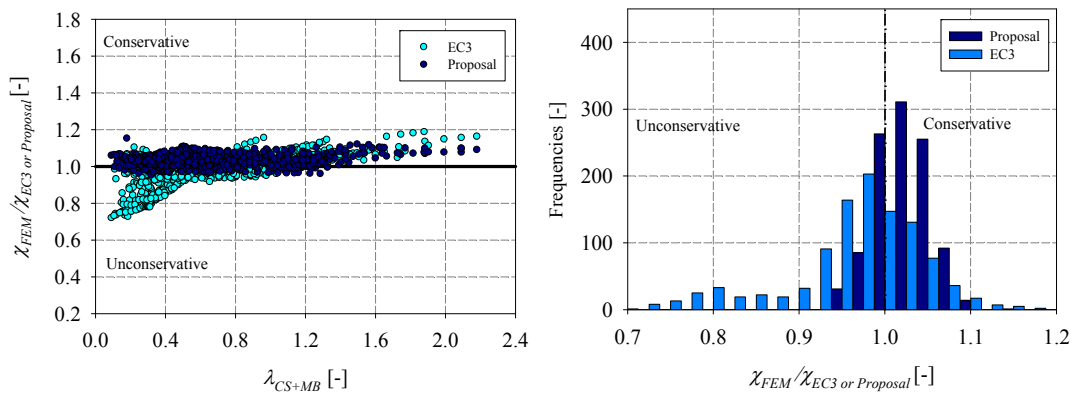


Figure 340 – Hot-rolled, $N+M_z$ – a) Comparison of proposal and EC3 results with FEM results – b) Frequency distributions (total number of results: 1052)

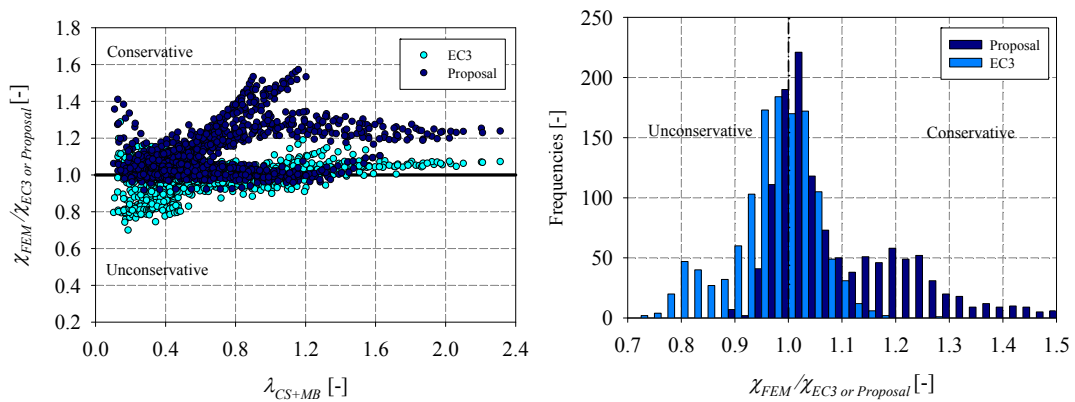


Figure 341 – Hot-rolled, $N+M_y$ – a) Comparison of proposal and EC3 results with FEM results – b) Frequency distributions (total number of results: 1241)

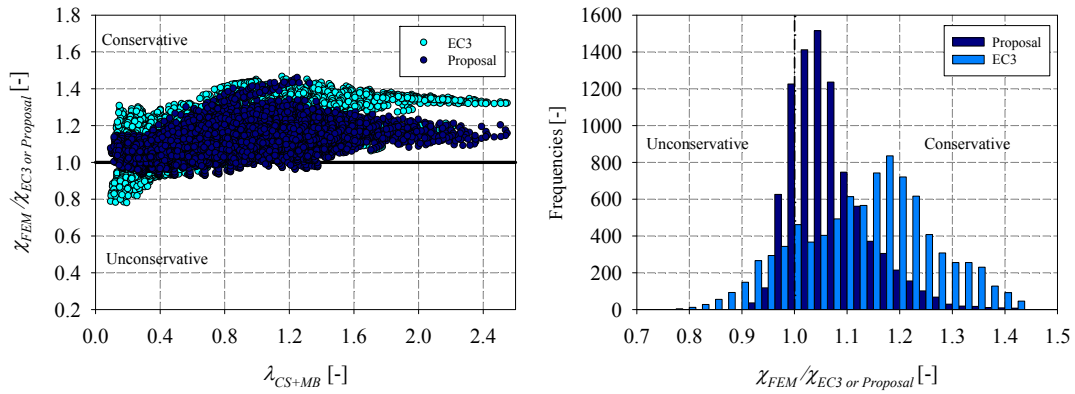


Figure 342 – Cold-formed, $N+M_y+M_z$ – a) Comparison of proposal and EC3 results with FEM results – b) Frequency distributions (total number of results: 8796)

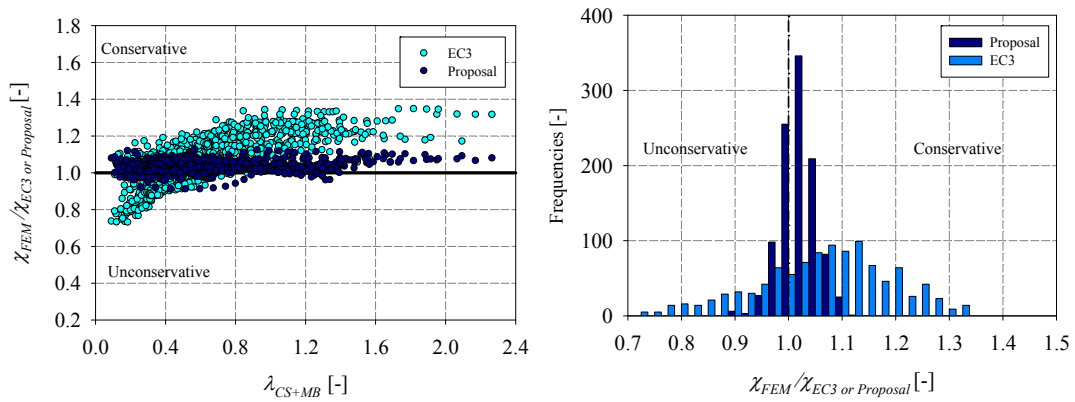


Figure 343 – Cold-formed, $N+M_z$ – a) Comparison of proposal and EC3 results with FEM results – b) Frequency distributions (total number of results: 1052)

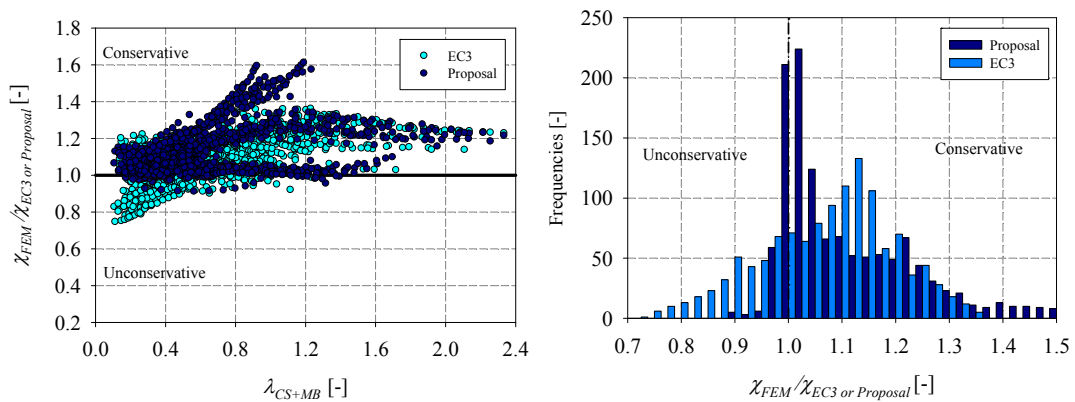


Figure 344 – Cold-formed, $N+M_y$ – a) Comparison of proposal and EC3 results with FEM results – b) Frequency distributions (total number of results: 1241)

6.8. Worked examples

6.8.1. Cold-formed rectangular hollow section: RHS 200x100x5

6.8.1.1. Member geometry and loading

This worked example deals with spatial behaviour. The beam-column is subjected to compression and triangular biaxial bending moment distribution as illustrated in Figure 345. Lateral torsional buckling is not a potential mode of failure because of the shape of the cross-section. Cold-formed rectangular section RHS 200x100x5 of steel grade $f_y = 355 \text{ N/mm}^2$ is considered.

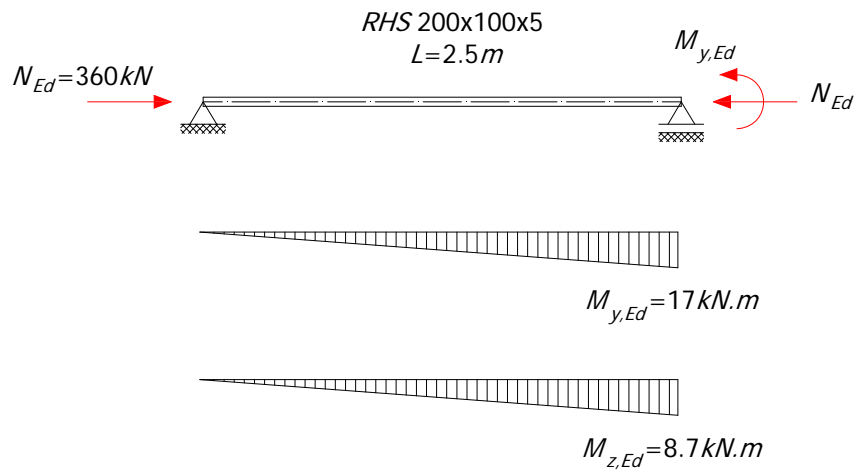


Figure 345 – Member tested under compression and biaxial bending moment

Table 54 – Cross-section characteristics

Flexural buckling length	$L = 2.5 \text{ m}$	
Flange and web dimensions	$b = 100 \text{ mm}$	$h = 200 \text{ mm}$
	$t_f = 5 \text{ mm}$	$t_w = 5 \text{ mm}$
Radius	$r = 7.5 \text{ mm}$	
Cross-section area	$A = 2835 \text{ mm}^2$	
Inertia	$I_y = 14382547 \text{ mm}^4$	
	$I_z = 4876020 \text{ mm}^4$	
Section plastic modulus	$W_{pl,y} = 181372 \text{ mm}^3$	
	$W_{pl,z} = 112091 \text{ mm}^3$	
Section elastic modulus	$W_{el,y} = 143825 \text{ mm}^3$	
	$W_{el,z} = 97520 \text{ mm}^3$	

Table 55 – Loading

Compression force	$N_{Ed} = 360 \text{ kN}$
Bending moment distribution, strong axis	$M_{y,Ed,left} = 0 \text{ kNm}$ $M_{y,Ed,right} = 17 \text{ kNm}$
Bending moment distribution, weak axis	$M_{z,Ed,left} = 0 \text{ kNm}$ $M_{z,Ed,right} = 8.7 \text{ kNm}$

Table 56: Material properties

Elastic modulus	$E = 210000 \text{ MPa}$
Characteristic yield strength	$f_y = 355 \text{ MPa}$
Partial safety factors	$\gamma_{M0} = 1.0$ $\gamma_{M1} = 1.0$

6.8.1.2. Cross-section classification

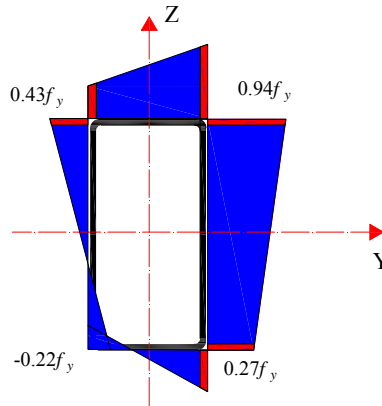


Figure 346 – Stress distribution

-Stress distribution in the right web:

$$\sigma_{\text{sup}} = \frac{N_{ED}}{A} + \frac{M_{y,Ed} \cdot v}{I_y} + \frac{M_{z,Ed} \cdot v'}{I_z} = \frac{360 \times 10^3}{2835} + \frac{17.10^6 \times \frac{200}{2}}{14382547} + \frac{8.7 \times 10^6 \times \frac{100}{2}}{4876020} = 334.4 \text{ MPa} = 0.94 f_y$$

$$\sigma_{\text{inf}} = \frac{N_{ED}}{A} - \frac{M_{y,Ed} \cdot v}{I_y} + \frac{M_{z,Ed} \cdot v'}{I_z} = \frac{360 \times 10^3}{2835} - \frac{17.10^6 \times \frac{200}{2}}{14382547} + \frac{8.7 \times 10^6 \times \frac{100}{2}}{4876020} = 98 \text{ MPa} = 0.27 f_y$$

At the plates extremities:

$$\sigma_1 = \frac{334(h - 2r - t)}{h} = \frac{334(200 - 2 \times 7.5 - 5)}{200} = 300.6 \text{ MPa};$$

$$\sigma_2 = \frac{98(h-2r-t)}{h} = \frac{98(200-2 \times 7.5-5)}{200} = 88.2 \text{ MPa};$$

$$\frac{c_{web}}{t} = \frac{h-t-2r}{t} = \frac{180}{5} = 36;$$

$$\psi = \frac{\sigma_2}{\sigma_1} = \frac{88.2}{300.6} = 0.29;$$

Web in compression and flexion

$$\text{Class 3 limit with } \psi > -1: \frac{42\varepsilon}{0.67+0.33\psi} = \frac{42 \times 0.81}{0.67+0.33 \times 0.29} = 44.4 > \frac{c_{web}}{t} = 36;$$

$$\text{Class 2 limit: } 38\sqrt{\frac{235}{355}} = 30.9 < 36;$$

The web is found to be class 3.

The stress distribution at the flange is:

$$\sigma_{sup} = \frac{N_{Ed}}{A} + \frac{M_{y,Ed} \cdot v}{I_y} + \frac{M_{z,Ed} \cdot v'}{I_z} = \frac{360 \times 10^3}{2835} + \frac{17.10^6 \times \frac{200}{2}}{14382547} + \frac{8.7 \times 10^6 \times \frac{100}{2}}{4876020} = 334.4 \text{ MPa} = 0.94 f_y$$

$$\sigma_{inf} = \frac{N_{Ed}}{A} + \frac{M_{y,Ed} \cdot v}{I_y} - \frac{M_{z,Ed} \cdot v'}{I_z} = \frac{360 \times 10^3}{2835} - \frac{17.10^6 \times \frac{200}{2}}{14382547} + \frac{8.7 \times 10^6 \times \frac{100}{2}}{4876020} = 156 \text{ MPa} = 0.43 f_y$$

At the plates extremities:

$$\sigma_1 = \frac{334(h-2r-t)}{h} = \frac{334(100-2 \times 7.5-5)}{200} = 268 \text{ MPa};$$

$$\sigma_2 = \frac{156(h-2r-t)}{h} = \frac{156(100-2 \times 7.5-5)}{100} = 125 \text{ MPa};$$

$$\frac{c_{flange}}{t} = \frac{b-t-2r}{t} = \frac{80}{5} = 16;$$

$$\psi = \frac{\sigma_2}{\sigma_1} = \frac{125}{268} = 0.47 ;$$

Flange in compression and flexion:

$$\text{Class 1 limit: } 33\sqrt{\frac{235}{355}} = 27 < \frac{c_{flange}}{t} = 16 ;$$

The flange is found to be class 1;

Thus, the cross-section is found to be class 3.

6.8.1.3. Cross-section verification

$$\frac{N_{Ed}}{N_{el,Rd}} + \frac{M_{y,Ed}}{M_{el,y,Rd}} + \frac{M_{z,Ed}}{M_{el,z,Rd}} = \frac{360 \times 10^3}{2835 \times 355} + \frac{17 \times 10^6}{143825 \times 355} + \frac{8.7 \times 10^6}{97520 \times 355} = 0.94 \leq 1$$

6.8.1.4. Member verification according to Eurocode 3 Method 2

Stability verification:

– Reduction factors for compression buckling

$$N_{cr,y} = \frac{\pi^2 EI_y}{L^2} = 4769.52 kN ;$$

$$N_{cr,z} = \frac{\pi^2 EI_z}{L^2} = 1616.98 kN ;$$

$$\lambda_y = \sqrt{\frac{N_{el,Rd}}{N_{cr,y}}} = 0.46 ;$$

$$\lambda_z = \sqrt{\frac{N_{el,Rd}}{N_{cr,z}}} = 0.79 ;$$

Imperfection factor: $\alpha = 0.49$

$$\phi_y = 0.5(1 + \alpha(\lambda_y - 0.2) + \lambda_y^2) = 0.67 ;$$

$$\phi_z = 0.5(1 + \alpha(\lambda_z - 0.2) + \lambda_z^2) = 0.96 ;$$

$$\chi_y = \frac{1}{\phi_y + \sqrt{(\phi_y^2 - \lambda_y^2)}} = 0.865 \leq 1;$$

$$\chi_z = \frac{1}{\phi_z + \sqrt{(\phi_z^2 - \lambda_z^2)}} = 0.67 \leq 1;$$

- Equivalent uniform moment factors C_m

$$\psi_y = \frac{M_{y,Ed,right}}{M_{y,Ed,left}} = 0;$$

$$\psi_z = \frac{M_{z,Ed,right}}{M_{z,Ed,left}} = 0;$$

$$C_{m,y} = 0.6 + 0.4\psi_y = 0.6 \geq 0.4;$$

$$C_{m,z} = 0.6 + 0.4\psi_z = 0.6 \geq 0.4;$$

- Interaction factors for class 3 sections

$$n_y = \frac{N_{Ed}}{\chi_y N_{el,Rd}} = \frac{360 \times 10^3}{0.865 \times 2835 \times 355} = 0.41;$$

$$n_z = \frac{N_{Ed}}{\chi_z N_{el,Rd}} = \frac{360 \times 10^3}{0.67 \times 2835 \times 355} = 0.53;$$

$$k_{yy} = C_{m,y} (1 + 0.6 \times \lambda_y \times n_y) \leq C_{m,y} (1 + 0.6 \times n_y)$$

$$\Rightarrow k_{yy} = 0.6(1 + 0.6 \times 0.46 \times 0.41) = 0.67 \leq 0.6(1 + 0.6 \times 0.41) = 0.75$$

$$\Rightarrow k_{yy} = 0.67$$

$$k_{zz} = C_{m,z} (1 + 0.6 \times \lambda_z \times n_z) \leq C_{m,z} (1 + 0.6 \times n_z)$$

$$\Rightarrow k_{zz} = 0.6(1 + 0.6 \times 0.79 \times 0.53) = 0.75 \leq 0.6(1 + 0.60 \times 0.53) = 0.79$$

$$\Rightarrow k_{zz} = 0.75$$

$$k_{zy} = 0.8k_{yy} = 0.8 \times 0.67 = 0.53;$$

$$k_{yz} = k_{zz} = 0.75;$$

- Verification:

$$\frac{N_{Ed}}{\chi_y N_{el,Rd}} + k_{yy} \frac{M_{y,Ed}}{\gamma_{M1} M_{y,el,Rd}} + k_{yz} \frac{M_{z,Ed}}{\gamma_{M1} M_{z,el,Rd}} = \frac{360 \times 10^3}{0.865 \frac{355 \times 2835}{1}} + 0.67 \frac{17 \times 10^6}{143825 \times 355} + 0.75 \frac{8.7 \times 10^6}{97520 \times 355} = 0.82 < 1$$

$$\frac{N_{Ed}}{\chi_z N_{el,Rd}} + k_{zy} \frac{M_{y,Ed}}{\gamma_{M1} M_{y,el,Rd}} + k_{zz} \frac{M_{z,Ed}}{\gamma_{M1} M_{z,el,Rd}} = \frac{360 \times 10^3}{0.67 \frac{355 \times 2835}{1}} + 0.53 \frac{17 \times 10^6}{143825 \times 355} + 0.75 \frac{8.7 \times 10^6}{97520 \times 355} = 0.90 < 1$$

Satisfactory according to Eurocode.

6.8.1.5. Member verification according to the O.I.C. approach

Figure 347 illustrates the application of the O.I.C. for the corresponding tested beam-column member.

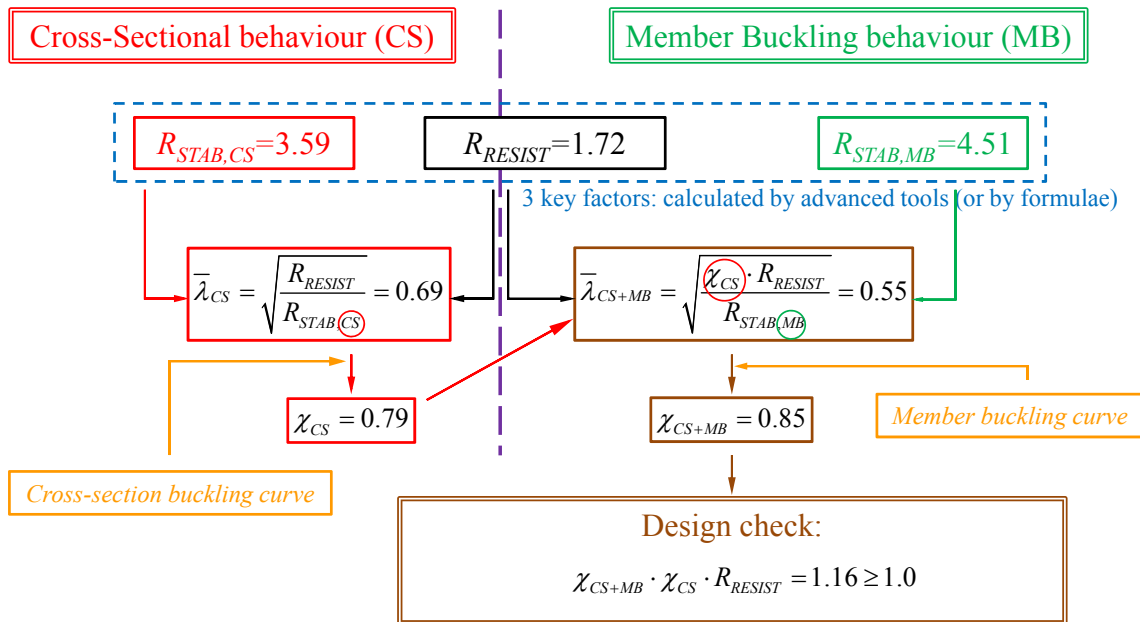


Figure 347: Application steps of the Overall Interaction Concept

Step 1: The *R-factors* involved in the O.I.C. approach, were determined as follows:

$R_{RESIST} = 1.72$ – computed using a specially developed Matlab tool which is capable to take into account the effect of the cross-section corners, unlike Eurocode 3 formulae;

$R_{STAB,CS} = 3.59$ – from numerical tool (CUFSM in the present case – shall be replaced by a dedicated software in the near future);

$R_{STAB,MB} = 4.51$ – computed using ABAQUS for members;

$$\text{Step 2: } \lambda_{CS} = \sqrt{\frac{R_{RESIST}}{R_{STAB,CS}}} = \sqrt{\frac{1.719}{3.59}} = 0.69;$$

Step 3: $\chi_{CS} = 0.79$ according to O.I.C. 1st approach for cross-sections [3].

Where:

$$\gamma = \left(\frac{h/b}{5}\right) - \frac{1}{10} = 0.3;$$

$$\delta = -0.4h/b + 1.45 = 0.65;$$

$$\alpha_{CS} = \frac{1}{10}\delta + \frac{3}{40} = 0.14;$$

$$\beta = -0.15\lambda_{CS} + 1.15 = 1.04; \lambda_0 = 0;$$

$$\begin{aligned} \phi_{CS} &= 0.5(1 + \alpha_{CS} + \alpha_{CS}(1 - n^\gamma))(\lambda_{CS} - (\lambda_0 - \lambda_0(1 - n^\gamma))) + \lambda_{CS}^\delta \beta \\ &= 0.5(1 + (0.14 + 0.14(1 - 0.357^{0.3})))(0.69 - (0 - 0(1 - 0.357^{0.3}))) + 0.69^{0.65}1.04 = 0.97; \end{aligned}$$

$$\chi_{CS} = \frac{\beta}{\phi + \sqrt{\phi^2 - \lambda_{CS}^\delta \beta}} = \frac{1.04}{0.97 + \sqrt{0.97^2 - 0.69^{0.65}1.04}} = 0.79;$$

$$\text{Step 4: } \lambda_{CS+MB} = \sqrt{\frac{\chi_{CS} R_{RESIST}}{R_{STAB,MB}}} = \sqrt{\frac{0.79 \times 1.719}{4.51}} = 0.55;$$

$$\text{Step 5: } \Omega_{y/z} = \arctan\left(\frac{m_z}{m_y}\right) = \arctan\left(\frac{M_z / M_{pl,z}}{M_y / M_{pl,y}}\right) = 39.6; \eta_y = \frac{m_y}{n_y} = \frac{M_y / M_{pl,y}}{N / N_{pl}} = 0.75;$$

$$\alpha = 0.0075\Omega_{y/z} + \alpha_{comp} = 0.65 \leq 0.7; \lambda_0 = 0.2 + 0.2\eta_y^{0.2} = 0.39 > 0.35 \Rightarrow \lambda_0 = 0.35;$$

$$\phi_{CS+MB} = 0.5(1 + \alpha(\lambda_{CS+MB} - \lambda_0) + \lambda_{CS+MB}^2) = 0.5(1 + 0.65(0.55 - 0.35) + 0.55^2) = 0.72;$$

$$\chi_{CS+MB} = \frac{1}{\phi_{CS+MB} + \sqrt{\phi_{CS+MB}^2 - \lambda_{CS+MB}^2}} = \frac{1}{0.72 + \sqrt{0.72^2 - 0.55^2}} = 0.85.$$

$$\text{Step 6: } R_{REAL,MB} = \chi_{CS+MB} \cdot \chi_{CS} \cdot R_{RESIST} = 0.85 \times 0.79 \times 1.72 = 1.16 > 1;$$

Satisfactory according to O.I.C. approach (values of $R_{REAL,MB} > 1$ indicates that the actual loadings needs to be increased to reach failure).

The criterion for member resistance is fulfilled for the given profile according to the O.I.C. approach, however $R_{ULT,EC3}$ is equal to 1.11 ($1 / 0.90 = 1.11$) leading to overconservative EC3 results with a benefit brought by O.I.C. approach equal to 4.5% ($1.16 / 1.11 = 4.5\%$).

6.8.2. Cold-formed square hollow section: SHS 120x120x8

6.8.2.1. Member geometry and loading

The beam-column is subjected to compression and constant biaxial bending moment distribution. Cold-formed square section SHS 120x120x8 of steel grade $f_y = 355 \text{ N/mm}^2$ is considered.

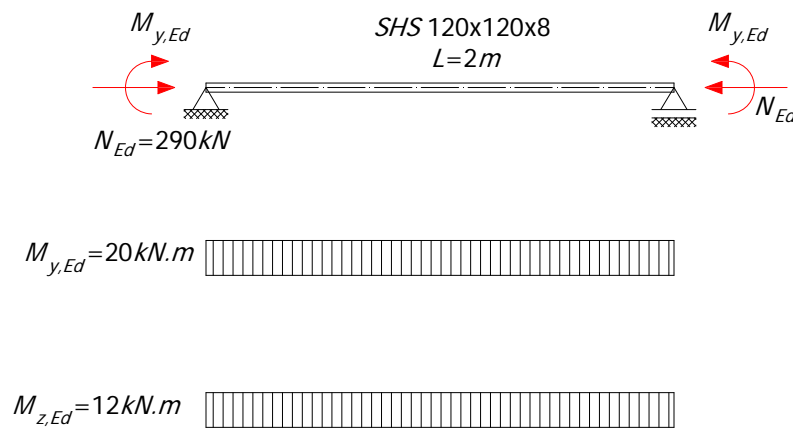


Figure 348 – Member tested under compression and biaxial bending moment

Table 57 – Cross-section characteristics

Flexural buckling length	$L = 2m$	
Flange and web dimensions	$b = 120 \text{ mm}$	$h = 120 \text{ mm}$
	$t_f = 8 \text{ mm}$	$t_w = 8 \text{ mm}$
Radius	$r = 12 \text{ mm}$	
Cross-section area	$A = 3419 \text{ mm}^2$	
Inertia	$I_y = 6547649 \text{ mm}^4$	
	$I_z = 6547649 \text{ mm}^4$	
Section plastic modulus	$W_{pl,y} = 141143 \text{ mm}^3$	
	$W_{pl,z} = 141143 \text{ mm}^3$	
Section elastic modulus	$W_{el,y} = 109127 \text{ mm}^3$	
	$W_{el,z} = 109127 \text{ mm}^3$	

Table 58 – Loading

Compression force	$N_{Ed} = 290 \text{ kN}$
Bending moment distribution, strong axis	$M_{y,Ed,left} = 20 \text{ kNm}$ $M_{y,Ed,right} = 20 \text{ kNm}$
Bending moment distribution, weak axis	$M_{z,Ed,left} = 12 \text{ kNm}$ $M_{z,Ed,right} = 12 \text{ kNm}$

Table 59: Material properties

Elastic modulus	$E = 210000 \text{ MPa}$
Characteristic yield strength	$f_y = 355 \text{ MPa}$
Partial safety factors	$\gamma_{M0} = 1.0$ $\gamma_{M1} = 1.0$

6.8.2.2. Cross-section classification

-Stress distribution in the right web:

$$\sigma_{\text{sup}} = \frac{N_{ED}}{A} + \frac{M_{y,Ed} \cdot v}{I_y} + \frac{M_{z,Ed} \cdot v'}{I_z} = \frac{290 \times 10^3}{3419} + \frac{20 \cdot 10^6 \times \frac{120}{2}}{6547649} + \frac{12 \times 10^6 \times \frac{120}{2}}{6547649} = 378 \text{ MPa}$$

$$\sigma_{\text{inf}} = \frac{N_{ED}}{A} - \frac{M_{y,Ed} \cdot v}{I_y} + \frac{M_{z,Ed} \cdot v'}{I_z} = \frac{290 \times 10^3}{3419} - \frac{20 \cdot 10^6 \times \frac{120}{2}}{6547649} + \frac{12 \times 10^6 \times \frac{120}{2}}{6547649} = 11.5 \text{ MPa}$$

At the plates extremities:

$$\sigma_1 = \frac{378(h-2r-t)}{h} = \frac{378(120-2 \times 12-8)}{120} = 277 \text{ MPa};$$

$$\sigma_2 = \frac{11.5(h-2r-t)}{h} = \frac{11.5(120-2 \times 12-8)}{200} = 8.5 \text{ MPa};$$

$$\frac{c_{\text{web}}}{t} = \frac{h-t-2r}{t} = \frac{88}{8} = 11;$$

Web in compression and flexion

$$\text{Class 1 limit: } 33 \sqrt{\frac{235}{355}} = 27 > 11;$$

The web is found to be class 1.

The stress distribution at the flange is:

$$\sigma_{\text{sup}} = \frac{N_{ED}}{A} + \frac{M_{y,Ed} \cdot v}{I_y} + \frac{M_{z,Ed} \cdot v'}{I_z} = \frac{290 \times 10^3}{3419} + \frac{20.10^6 \times \frac{120}{2}}{6547649} + \frac{12 \times 10^6 \times \frac{120}{2}}{6547649} = 378 \text{ MPa}$$

$$\sigma_{\text{inf}} = \frac{N_{ED}}{A} + \frac{M_{y,Ed} \cdot v}{I_y} - \frac{M_{z,Ed} \cdot v'}{I_z} = \frac{290 \times 10^3}{3419} + \frac{20.10^6 \times \frac{120}{2}}{6547649} - \frac{12 \times 10^6 \times \frac{120}{2}}{6547649} = 158 \text{ MPa}$$

At the plates extremities:

$$\sigma_1 = \frac{378(h-2r-t)}{h} = \frac{378(120-2 \times 12-8)}{120} = 277 \text{ MPa};$$

$$\sigma_2 = \frac{158(h-2r-t)}{h} = \frac{158(120-2 \times 12-8)}{120} = 116 \text{ MPa};$$

$$\frac{c_{\text{flange}}}{t} = \frac{b-t-2r}{t} = \frac{88}{8} = 11;$$

Flange in compression and flexion:

$$\text{Class 1 limit: } 33 \sqrt{\frac{235}{355}} = 27 > \frac{c_{\text{flange}}}{t} = 11;$$

The flange is found to be class 1;

Thus, the cross-section is found to be class 1.

6.8.2.3. Cross-section verification

$$\frac{N_{Ed}}{N_{pl,Rd}} + \frac{M_{y,Ed}}{M_{pl,y,Rd}} + \frac{M_{z,Ed}}{M_{pl,z,Rd}} = \frac{290 \times 10^3}{3419 \times 355} + \frac{20 \times 10^6}{141143 \times 355} + \frac{12 \times 10^6}{141143 \times 355} = 0.88 \leq 1$$

6.8.2.4. Member verification according to Eurocode 3 Method 2

Stability verification:

– Reduction factors for compression buckling

$$N_{cr,z} = N_{cr,y} = \frac{\pi^2 EI_y}{L^2} = 3392.7 \text{ kN};$$

$$\lambda_z = \lambda_y = \sqrt{\frac{N_{pl,Rd}}{N_{cr,y}}} = 0.60 ;$$

Imperfection factor: $\alpha = 0.49$

$$\phi_z = \phi_y = 0.5(1 + \alpha(\lambda_y - 0.2) + \lambda_y^2) = 0.78 ;$$

$$\chi_z = \chi_y = \frac{1}{\phi_y + \sqrt{(\phi_y^2 - \lambda_y^2)}} = 0.79 \leq 1 ;$$

- Equivalent uniform moment factors C_m

$$\psi_y = \frac{M_{y,Ed,right}}{M_{y,Ed,left}} = 1 ;$$

$$\psi_z = \frac{M_{z,Ed,right}}{M_{z,Ed,left}} = 1 ;$$

$$C_{m,y} = 0.6 + 0.4\psi_y = 1 \geq 0.4 ;$$

$$C_{m,z} = 0.6 + 0.4\psi_z = 1 \geq 0.4 ;$$

- Interaction factors for class 1 sections

$$n_z = n_y = \frac{N_{Ed}}{\chi_y N_{pl,Rd}} = \frac{290 \times 10^3}{0.79 \times 3419 \times 355} = 0.30 ;$$

$$k_{yy} = C_{m,y}(1 + (\lambda_y - 0.2) \times n_y) \leq C_{m,y}(1 + 0.8 \times n_y)$$

$$\Rightarrow k_{yy} = 1(1 + (0.6 - 0.2) \times 0.3) = 1.12 \leq 1(1 + 0.8 \times 0.3) = 1.24$$

$$\Rightarrow k_{yy} = 1.12$$

$$k_{zz} = 1.12 ;$$

$$k_{zy} = 0.6k_{yy} = 0.6 \times 1.12 = 0.67 ;$$

$$k_{yz} = 0.67 ;$$

- Verification:

$$\frac{N_{Ed}}{\chi_y N_{pl,Rd}} + k_{yy} \frac{M_{y,Ed}}{M_{y,pl,Rd}} + k_{yz} \frac{M_{z,Ed}}{M_{z,pl,Rd}} = \frac{290 \times 10^3}{0.79 \times 355 \times 3419} + 1.12 \frac{20 \times 10^6}{141143 \times 355} + 0.67 \frac{12 \times 10^6}{141143 \times 355} = 0.91 < 1$$

$$\frac{N_{Ed}}{\chi_z N_{pl,Rd}} + k_{zy} \frac{M_{y,Ed}}{M_{y,pl,Rd}} + k_{zz} \frac{M_{z,Ed}}{M_{z,pl,Rd}} = \frac{290 \times 10^3}{0.79 \times 355 \times 3419} + 0.67 \frac{20 \times 10^6}{141143 \times 355} + 1.12 \frac{12 \times 10^6}{141143 \times 355} = 0.84 < 1$$

Satisfactory according to Eurocode.

6.8.2.5. Member verification according to the O.I.C. approach

Step 1: The *R*-factors involved in the O.I.C. approach, were determined as follows:

$R_{RESIST} = 1.72$ – computed using a specially developed Matlab tool.

$R_{STAB,CS} = 19.2$ – from numerical tool (FINELg);

$R_{STAB,MB} = 11.83$ – computed using ABAQUS for members;

Step 2: $\lambda_{CS} = \sqrt{\frac{R_{RESIST}}{R_{STAB,CS}}} = \sqrt{\frac{1.72}{19.2}} = 0.30$;

Step 3: $\chi_{CS} = 1.0$ according to O.I.C. 1st approach for cross-sections [3].

Step 4: $\lambda_{CS+MB} = \sqrt{\frac{\chi_{CS} R_{RESIST}}{R_{STAB,MB}}} = \sqrt{\frac{1.0 \times 1.72}{11.83}} = 0.38$;

Step 5: $\Omega_{y/z} = \arctan\left(\frac{m_z}{m_y}\right) = \arctan\left(\frac{M_z / M_{pl,z}}{M_y / M_{pl,y}}\right) = 31$; $\eta_y = \frac{m_y}{n_y} = \frac{M_y / M_{pl,y}}{N / N_{pl}} = 1.67 \Rightarrow$ curve

Type II.

$10 \leq \Omega_{y/z} = 31 \leq 80 \Rightarrow \alpha = 1.1$ and $\lambda_0 = 0.1$

$\phi_{CS+MB} = 0.5 \left(1 + \alpha (\lambda_{CS+MB} - \lambda_0) + \lambda_{CS+MB}^2 \right) = 0.5 (1 + 1.1 (0.38 - 0.1) + 0.38^2) = 0.73$;

$\chi_{CS+MB} = \frac{1}{\phi_{CS+MB} + \sqrt{\phi_{CS+MB}^2 - \lambda_{CS+MB}^2}} = \frac{1}{0.73 + \sqrt{0.73^2 - 0.38^2}} = 0.74$.

Step 6: $R_{REAL,MB} = \chi_{CS+MB} \cdot \chi_{CS} \cdot R_{RESIST} = 0.74 \times 1.0 \times 1.72 = 1.28 > 1$;

Satisfactory according to O.I.C. approach (values of $R_{REAL,MB} > 1$ indicates that the actual loadings needs to be increased to reach failure).

The criterion for member resistance is fulfilled for the given profile according to the O.I.C. approach, however $R_{ULT,EC3}$ is equal to 1.10 ($1 / 0.91 = 1.10$) leading to overconservative EC3 results with a benefit brought by O.I.C. approach equal to 16.5% ($1.28 / 1.10 = 16.5\%$).

6.8.3. Hot-rolled square hollow section: SHS 120x120x8

6.8.3.1. Member geometry and loading

The beam-column is subjected to compression and constant biaxial bending moment distribution. Hot-rolled section SHS 120x120x8 of steel grade $f_y = 355 \text{ N/mm}^2$ is considered. (The same example detailed in section 6.8.2 is considered in this section, by replacing the cold-formed member tested previously by a hot-rolled one).

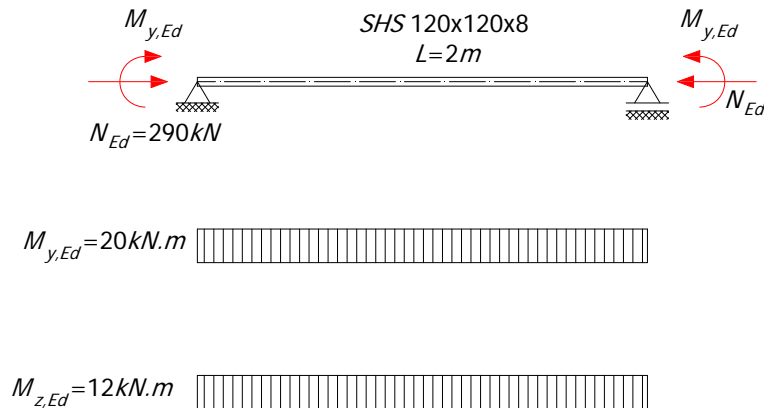


Figure 349 – Member tested under compression and biaxial bending moment

Table 60 – Cross-section characteristics

Flexural buckling length	$L = 2m$	
Flange and web dimensions	$b = 120 \text{ mm}$	$h = 120 \text{ mm}$
	$t_f = 8 \text{ mm}$	$t_w = 8 \text{ mm}$
Radius	$r = 12 \text{ mm}$	
Cross-section area	$A = 3419 \text{ mm}^2$	
Inertia	$I_y = 6547649 \text{ mm}^4$	
	$I_z = 6547649 \text{ mm}^4$	
Section plastic modulus	$W_{pl,y} = 141143 \text{ mm}^3$	
	$W_{pl,z} = 141143 \text{ mm}^3$	
Section elastic modulus	$W_{el,y} = 109127 \text{ mm}^3$	
	$W_{el,z} = 109127 \text{ mm}^3$	

Table 61 – Loading

Compression force	$N_{Ed} = 290 \text{ kN}$
Bending moment distribution, strong axis	$M_{y,Ed,left} = 20 \text{ kNm}$
	$M_{y,Ed,right} = 20 \text{ kNm}$
Bending moment distribution, weak axis	$M_{z,Ed,left} = 12 \text{ kNm}$
	$M_{z,Ed,right} = 12 \text{ kNm}$

Table 62: Material properties

Elastic modulus	$E = 210000 \text{ MPa}$
Characteristic yield strength	$f_y = 355 \text{ MPa}$
Partial safety factors	$\gamma_{M0} = 1.0$
	$\gamma_{M1} = 1.0$

6.8.3.2. Cross-section classification

The cross-section is found to be class 1 (see section 6.8.2.2.).

6.8.3.3. Cross-section verification

$$\frac{N_{Ed}}{N_{pl,Rd}} + \frac{M_{y,Ed}}{M_{pl,y,Rd}} + \frac{M_{z,Ed}}{M_{pl,z,Rd}} = \frac{290 \times 10^3}{3419 \times 355} + \frac{20 \times 10^6}{141143 \times 355} + \frac{12 \times 10^6}{141143 \times 355} = 0.88 \leq 1$$

6.8.3.4. Member verification according to Eurocode 3 Method 2

Stability verification:

– Reduction factors for compression buckling

$$N_{cr,z} = N_{cr,y} = \frac{\pi^2 EI_y}{L^2} = 3392.7 \text{ kN} ;$$

$$\lambda_z = \lambda_y = \sqrt{\frac{N_{pl,Rd}}{N_{cr,y}}} = 0.60 ;$$

Imperfection factor: $\alpha = 0.21$

$$\phi_z = \phi_y = 0.5(1 + \alpha(\lambda_y - 0.2) + \lambda_y^2) = 0.72 ;$$

$$\chi_z = \chi_y = \frac{1}{\phi_y + \sqrt{(\phi_y^2 - \lambda_y^2)}} = 0.89 \leq 1;$$

- Equivalent uniform moment factors C_m

$$\psi_y = \frac{M_{y,Ed,right}}{M_{y,Ed,left}} = 1;$$

$$\psi_z = \frac{M_{z,Ed,right}}{M_{z,Ed,left}} = 1;$$

$$C_{m,y} = 0.6 + 0.4\psi_y = 1 \geq 0.4;$$

$$C_{m,z} = 0.6 + 0.4\psi_z = 1 \geq 0.4;$$

- Interaction factors for class 1 sections

$$n_z = n_y = \frac{N_{Ed}}{\chi_y N_{pl,Rd}} = \frac{290 \times 10^3}{0.89 \times 3419 \times 355} = 0.27;$$

$$\begin{aligned} k_{yy} &= C_{m,y} (1 + (\lambda_y - 0.2) \times n_y) \leq C_{m,y} (1 + 0.8 \times n_y) \\ \Rightarrow k_{yy} &= 1(1 + (0.6 - 0.2) \times 0.27) = 1.11 \leq 1(1 + 0.8 \times 0.27) = 1.22 \\ \Rightarrow k_{yy} &= 1.11 \end{aligned}$$

$$k_{zz} = 1.11;$$

$$k_{zy} = 0.6k_{yy} = 0.6 \times 1.11 = 0.67;$$

$$k_{yz} = 0.67;$$

- Verification:

$$\frac{N_{Ed}}{\chi_y N_{pl,Rd}} + k_{yy} \frac{M_{y,Ed}}{M_{y,pl,Rd}} + k_{yz} \frac{M_{z,Ed}}{M_{z,pl,Rd}} = \frac{290 \times 10^3}{0.89 \frac{355 \times 3419}{1}} + 1.11 \frac{20 \times 10^6}{141143 \times 355} + 0.67 \frac{12 \times 10^6}{141143 \times 355} = 0.87 < 1$$

$$\frac{N_{Ed}}{\chi_z N_{pl,Rd}} + k_{zy} \frac{M_{y,Ed}}{M_{y,pl,Rd}} + k_{zz} \frac{M_{z,Ed}}{M_{z,pl,Rd}} = \frac{290 \times 10^3}{0.89 \frac{355 \times 3419}{1}} + 0.67 \frac{20 \times 10^6}{141143 \times 355} + 1.11 \frac{12 \times 10^6}{141143 \times 355} = 0.80 < 1$$

Satisfactory according to Eurocode.

6.8.3.5. Member verification according to the O.I.C. approach

Step 1: The R -factors involved in the O.I.C. approach, were determined as follows:

$R_{RESIST} = 1.72$ – computed using a specially developed Matlab tool.

$R_{STAB,CS} = 19.2$ – from numerical tool (FINELg);

$R_{STAB,MB} = 11.83$ – computed using ABAQUS for members;

Step 2: $\lambda_{CS} = \sqrt{\frac{R_{RESIST}}{R_{STAB,CS}}} = \sqrt{\frac{1.72}{19.2}} = 0.30$;

Step 3: $\chi_{CS} = 0.93$ according to O.I.C. approach for cross-sections [3].

Step 4: $\lambda_{CS+MB} = \sqrt{\frac{\chi_{CS} R_{RESIST}}{R_{STAB,MB}}} = \sqrt{\frac{0.93 \times 1.72}{11.83}} = 0.37$;

Step 5: $\Omega_{y/z} = \arctan\left(\frac{m_z}{m_y}\right) = \arctan\left(\frac{M_z / M_{pl,z}}{M_y / M_{pl,y}}\right) = 31$; $\eta_y = \frac{m_y}{n_y} = \frac{M_y / M_{pl,y}}{N / N_{pl}} = 1.67 \Rightarrow$ curve

Type II.

$10 \leq \Omega_{y/z} = 31 \leq 80 \Rightarrow \alpha = 0.95$ and $\lambda_0 = 0.1$

$\phi_{CS+MB} = 0.5 \left(1 + \alpha (\lambda_{CS+MB} - \lambda_0) + \lambda_{CS+MB}^2 \right) = 0.5 (1 + 0.95 (0.37 - 0.1) + 0.37^2) = 0.7$;

$\chi_{CS+MB} = \frac{1}{\phi_{CS+MB} + \sqrt{\phi_{CS+MB}^2 - \lambda_{CS+MB}^2}} = \frac{1}{0.7 + \sqrt{0.7^2 - 0.37^2}} = 0.78$.

Step 6: $R_{REAL,MB} = \chi_{CS+MB} \cdot \chi_{CS} \cdot R_{RESIST} = 0.78 \times 0.93 \times 1.72 = 1.25 > 1$;

Satisfactory according to O.I.C. approach (values of $R_{REAL,MB} > 1$ indicates that the actual loadings needs to be increased to reach failure).

The criterion for member resistance is fulfilled for the given profile according to the O.I.C. approach, however $R_{ULT,EC3}$ is equal to 1.15 ($1 / 0.87 = 1.15$) leading to overconservative EC3 results with a benefit brought by O.I.C. approach equal to 9% ($1.25 / 1.15 = 9\%$).

6.8.4. Cold-formed square hollow section: SHS 300x300x6.3

6.8.4.1. Member geometry and loading

The beam-column is subjected to compression and constant biaxial bending moment distribution. Cold-formed square section SHS 120x120x8 of steel grade $f_y = 355 \text{ N/mm}^2$ is considered.

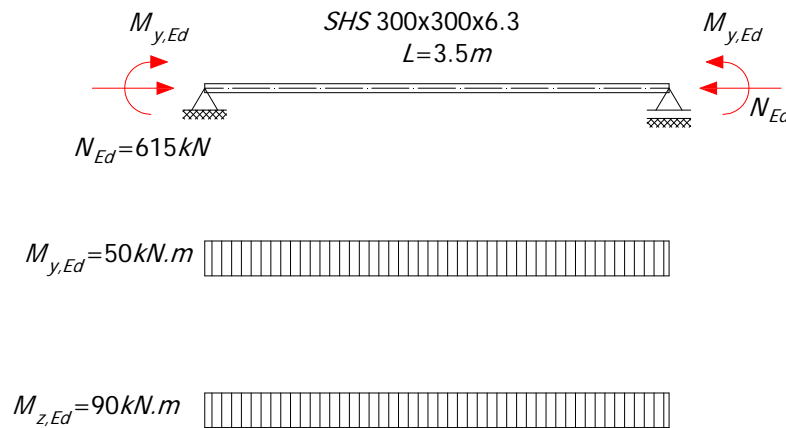


Figure 350 – Member tested under compression and biaxial bending moment

Table 63 – Cross-section characteristics

Flexural buckling length	$L = 3.5\text{m}$	
Flange and web dimensions	$b = 300 \text{ mm}$	$h = 300 \text{ mm}$
	$t_f = 6.3 \text{ mm}$	$t_w = 6.3 \text{ mm}$
Radius	$r = 9.5 \text{ mm}$	
Cross-section area	$A = 7298 \text{ mm}^2$	
Inertia	$I_y = 103530721 \text{ mm}^4$	
	$I_z = 103530721 \text{ mm}^4$	
Section plastic modulus	$W_{pl,y} = 799987 \text{ mm}^3$	
	$W_{pl,z} = 799987 \text{ mm}^3$	
Section elastic modulus	$W_{el,y} = 690205 \text{ mm}^3$	
	$W_{el,z} = 690205 \text{ mm}^3$	

Table 64 – Loading

Compression force	$N_{Ed} = 615 \text{ kN}$
Bending moment distribution, strong axis	$M_{y,Ed,left} = 50 \text{ kNm}$ $M_{y,Ed,right} = 50 \text{ kNm}$
Bending moment distribution, weak axis	$M_{z,Ed,left} = 90 \text{ kNm}$ $M_{z,Ed,right} = 90 \text{ kNm}$

Table 65: Material properties

Elastic modulus	$E = 210000 \text{ MPa}$
Characteristic yield strength	$f_y = 355 \text{ MPa}$
Partial safety factors	$\gamma_{M0} = 1.0$ $\gamma_{M1} = 1.0$

6.8.4.2. Cross-section classification

Stress distribution in the right web:

$$\sigma_{\text{sup}} = \frac{N_{ED}}{A} + \frac{M_{y,Ed} \cdot v}{I_y} + \frac{M_{z,Ed} \cdot v'}{I_z} = \frac{615 \times 10^3}{7298} + \frac{50 \cdot 10^6 \times \frac{300}{2}}{103530721} + \frac{90 \times 10^6 \times \frac{300}{2}}{103530721} = 287.1 \text{ MPa}$$

$$\sigma_{\text{inf}} = \frac{N_{ED}}{A} - \frac{M_{y,Ed} \cdot v}{I_y} + \frac{M_{z,Ed} \cdot v'}{I_z} = \frac{615 \times 10^3}{7298} - \frac{50 \cdot 10^6 \times \frac{300}{2}}{103530721} + \frac{90 \times 10^6 \times \frac{300}{2}}{103530721} = 142.2 \text{ MPa}$$

At the plates extremities:

$$\sigma_1 = \frac{287.1(h - 2r - t)}{h} = \frac{287.1(300 - 2 \times 9.5 - 6.3)}{300} = 262.9 \text{ MPa};$$

$$\sigma_2 = \frac{142.2(h - 2r - t)}{h} = \frac{142.2(300 - 2 \times 9.5 - 6.3)}{300} = 130.2 \text{ MPa};$$

$$\frac{c_{\text{web}}}{t} = \frac{h - t - 2r}{t} = \frac{274.7}{6.3} = 43.6;$$

$$\psi = \frac{\sigma_2}{\sigma_1} = \frac{130.2}{262.9} = 0.495$$

Web in compression and flexion:

Class 3 limit with $\psi > -1$:

$$\frac{42\varepsilon}{0.67+0.33\psi} = \frac{42 \cdot 0.81}{0.67+0.33(0.495)} = 40.82 < \frac{c_{web}}{t} = 43.6$$

The web is found to be class 4.

Thus, the cross-section is found to be class 4.

6.8.4.3. Cross-section verification

Effective cross-section calculation:

$$k_{\sigma} = 4;$$

$$\bar{b} = b - 2 \cdot r - t = 250 - 2 \cdot 7.5 - 5 = 230;$$

$$\bar{\lambda}_p = \sqrt{\frac{f_y}{\sigma_{cr}}} = \frac{\bar{b}/t}{28,4 \cdot \varepsilon \cdot \sqrt{k_{\sigma}}} = \frac{300/6.3}{28,4 \cdot 0.81 \cdot \sqrt{4}} = 1.04;$$

$$\rho_f = \frac{\bar{\lambda}_p - 0.055(3 + \psi)}{\bar{\lambda}_p^2} = \frac{1.04 - 0.055(3 + 1)}{1.04^2} = 0.76;$$

$$b_{eff} = \rho_f \cdot \bar{b} = 0.76 \cdot 300 = 228 \text{ mm};$$

$$b_{e1} = b_{e2} = 0.5 b_{eff} = 0.5 \cdot 228 = 114 \text{ mm}$$

With respect to Figure 351.

Stress distribution (compression positive)			Effective ^p width b_{eff}			
			$\psi = 1:$ $b_{eff} = \rho \bar{b}$ $b_{e1} = 0,5 b_{eff} \quad b_{e2} = 0,5 b_{eff}$			
			$1 > \psi \geq 0:$ $b_{eff} = \rho \bar{b}$ $b_{e1} = \frac{2}{5 - \psi} b_{eff} \quad b_{e2} = b_{eff} - b_{e1}$			
			$\psi < 0:$ $b_{eff} = \rho b_c = \rho \bar{b} / (1 - \psi)$ $b_{e1} = 0,4 b_{eff} \quad b_{e2} = 0,6 b_{eff}$			
$\psi = \sigma_2 / \sigma_1$	1	$1 > \psi > 0$	0	$0 > \psi > -1$	-1	$-1 > \psi > -3$
Buckling factor k_{σ}	4,0	$8,2 / (1,05 + \psi)$	7,81	$7,81 - 6,29\psi + 9,78\psi^2$	23,9	$5,98 (1 - \psi)^2$

Figure 351 – Internal compressed elements

The effective cross-section properties are thus calculated as follows:

- Effective area:

$$A_{eff} = \pi (r + 0,5t)^2 - \pi (r - 0,5t)^2 + 2(h - 2r - t) + 2\rho_f (b - 2r - t) = 6005 \text{ mm}^2$$

- Effective inertia about the strong axis:

$$\begin{aligned}
 I_{y,eff} &= \frac{(b - 2r - t) \cdot t^3}{12} + (b - 2r - t)t \left(v' - \frac{t}{2} \right)^2 + 2 \cdot \left[\frac{(h - 2r - t)^3 t}{12} \right] + (h - 2r - t) \cdot t \cdot \left(v - \frac{h}{2} \right)^2 \\
 &+ (b - 2r - t) \cdot t \cdot \rho \cdot \left[\left(v - \frac{t}{2} \right)^2 (b - 2r - t) \cdot t \cdot \rho \right] \\
 &+ 2 \left[\left(\frac{(r + t/2)^4}{16} + \frac{\pi (r + t/2)^2}{4} \left(v' - \frac{t}{2} - r \right)^2 \right) - \left(\frac{(r - t/2)^4}{16} + \frac{\pi (r - t/2)^2}{4} \left(v' - \frac{t}{2} - r \right)^2 \right) \right] \\
 &+ 2 \left[\left(\frac{(r + t/2)^4}{16} + \frac{\pi (r + t/2)^2}{4} \left(v - \frac{t}{2} - r \right)^2 \right) - \left(\frac{(r - t/2)^4}{16} + \frac{\pi (r - t/2)^2}{4} \left(v - \frac{t}{2} - r \right)^2 \right) \right] \\
 &= 96933025 \text{ mm}^4
 \end{aligned}$$

- Effective inertia about the weak axis:

$$I_{z,eff} = I_z - \frac{(\bar{b} - \rho\bar{b})^3 t}{12} = 96933025 \text{ mm}^4$$

- Effective loads:

$$N_{eff,Rd} = A_{eff} \cdot f_y = 6005 \cdot 355 \cdot 10^{-3} = 2132 \text{ kN}$$

$$W_{y,eff} = \frac{I_{y,eff}}{v} = \frac{96933025}{155.7} = 622597 \text{ mm}^3$$

$$W_{z,eff} = \frac{I_{z,eff}}{v'} = \frac{96933025}{155.7} = 622597 \text{ mm}^3$$

$$M_{y,eff,Rd} = M_{z,eff,Rd} = W_{y,eff} \cdot f_y = 338752 \cdot 355 \cdot 10^{-6} = 120.3 \text{ kNm}$$

Cross-section verification:

$$\frac{N_{Ed}}{N_{eff,Rd}} + \frac{M_{y,Ed}}{M_{eff,y,Rd}} + \frac{M_{z,Ed}}{M_{eff,z,Rd}} = \frac{615}{2132} + \frac{50}{221} + \frac{90}{221} = 0.92 \leq 1$$

6.8.4.4. Member verification according to Eurocode 3 Method 2

Stability verification:

– Reduction factors for compression buckling

$$N_{cr,z} = N_{cr,y} = \frac{\pi^2 EI_y}{L^2} = 17517 \text{ kN};$$

$$\lambda_z = \lambda_y = \sqrt{\frac{N_{eff,Rd}}{N_{cr,y}}} = 0.35;$$

Imperfection factor: $\alpha = 0.49$

$$\phi_z = \phi_y = 0.5(1 + \alpha(\lambda_y - 0.2) + \lambda_y^2) = 0.60;$$

$$\chi_z = \chi_y = \frac{1}{\phi_y + \sqrt{(\phi_y^2 - \lambda_y^2)}} = 0.924 \leq 1;$$

- Equivalent uniform moment factors C_m

$$\psi_y = \frac{M_{y,Ed,right}}{M_{y,Ed,left}} = 1;$$

$$\psi_z = \frac{M_{z,Ed,right}}{M_{z,Ed,left}} = 1;$$

$$C_{m,y} = 0.6 + 0.4\psi_y = 1 \geq 0.4;$$

$$C_{m,z} = 0.6 + 0.4\psi_z = 1 \geq 0.4;$$

- Interaction factors for class 4 sections

$$n_z = n_y = \frac{N_{Ed}}{\chi_y N_{eff,Rd}} = \frac{615}{0.924 \times 2132} = 0.31;$$

$$\begin{aligned} k_{yy} &= C_{m,y} (1 + 0.6 \times \lambda_y \times n_y) \leq C_{m,y} (1 + 0.6 \times n_y) \\ \Rightarrow k_{yy} &= 1(1 + 0.6 \times 0.35 \times 0.31) = 1.065 \leq 1(1 + 0.6 \times 0.31) = 1.19 \\ \Rightarrow k_{yy} &= 1.065 \end{aligned}$$

$$k_{zz} = 1.065;$$

$$k_{yz} = k_{zz} = 1.065;$$

$$k_{zy} = 0.8k_{yy} = 0.852;$$

- Verification:

$$\begin{aligned} \frac{N_{Ed}}{\chi_y N_{eff,Rd}} + k_{yy} \frac{M_{y,Ed}}{\gamma_{M1} M_{y,eff,Rd}} + k_{yz} \frac{M_{z,Ed}}{\gamma_{M1} M_{z,eff,Rd}} &= \frac{615}{0.924 \frac{2132}{1}} + 1.065 \frac{50}{\frac{221}{1}} + 1.065 \frac{90}{\frac{221}{1}} = 0.99 < 1 \\ \frac{N_{Ed}}{\chi_z N_{eff,Rd}} + k_{zy} \frac{M_{y,Ed}}{\gamma_{M1} M_{y,eff,Rd}} + k_{zz} \frac{M_{z,Ed}}{\gamma_{M1} M_{z,eff,Rd}} &= \frac{615}{0.924 \frac{2132}{1}} + 0.852 \frac{50}{\frac{221}{1}} + 1.065 \frac{90}{\frac{221}{1}} = 0.94 < 1 \end{aligned}$$

Satisfactory according to Eurocode.

6.8.4.5. Member verification according to the O.I.C. approach

Step 1: The *R-factors* involved in the O.I.C. approach, were determined as follows:

$R_{RESIST} = 1.99$ – computed using a specially developed Matlab tool.

$R_{STAB,CS} = 2.07$ – from numerical tool (FINELg);

$R_{STAB,MB} = 26.75$ – computed using ABAQUS for members;

$$\text{Step 2: } \lambda_{CS} = \sqrt{\frac{R_{RESIST}}{R_{STAB,CS}}} = \sqrt{\frac{1.99}{2.07}} = 0.98;$$

Step 3: $\chi_{CS} = 0.65$ according to O.I.C. 1st approach for cross-sections [3].

$$\text{Step 4: } \lambda_{CS+MB} = \sqrt{\frac{\chi_{CS} R_{RESIST}}{R_{STAB,MB}}} = \sqrt{\frac{0.67 \times 1.99}{26.75}} = 0.22;$$

$$\text{Step 5: } \Omega_{y/z} = \arctan\left(\frac{m_z}{m_y}\right) = \arctan\left(\frac{M_z / M_{pl,z}}{M_y / M_{pl,y}}\right) = 61; \eta_y = \frac{m_y}{n_y} = \frac{M_y / M_{pl,y}}{N / N_{pl}} = 0.74 \Rightarrow \text{curve}$$

Type II.

$$10 \leq \Omega_{y/z} = 61 \leq 80 \Rightarrow \alpha = 1.1 \text{ and } \lambda_0 = 0.1$$

$$\phi_{CS+MB} = 0.5 \left(1 + \alpha (\lambda_{CS+MB} - \lambda_0) + \lambda_{CS+MB}^2 \right) = 0.5 (1 + 1.1 (0.22 - 0.1) + 0.22^2) = 0.59;$$

$$\chi_{CS+MB} = \frac{1}{\phi_{CS+MB} + \sqrt{\phi_{CS+MB}^2 - \lambda_{CS+MB}^2}} = \frac{1}{0.59 + \sqrt{0.59^2 - 0.22^2}} = 0.88.$$

$$\text{Step 6: } R_{REAL,MB} = \chi_{CS+MB} \cdot \chi_{CS} \cdot R_{RESIST} = 0.88 \times 0.65 \times 1.99 = 1.14 > 1;$$

Satisfactory according to O.I.C. approach (values of $R_{REAL,MB} > 1$ indicates that the actual loadings needs to be increased to reach failure).

The criterion for member resistance is fulfilled for the given profile according to the O.I.C. approach, however $R_{ULT,EC3}$ is equal to 1.01 ($1 / 0.99 = 1.01$) leading to overconservative EC3 results with a benefit brought by O.I.C. approach equal to 13% ($1.14/1.01 = 13\%$).

6.9. Conclusions

This chapter presented the development of a design proposal for hollow section members; more precisely, it focused on the derivation of interaction curves for the design of hot-rolled and cold-formed steel beam-column members.

The results on members showed that the O.I.C., although being based on simple principles with straightforward application steps, may appear as an accurate and consistent approach, and serve as a basis for the next generation of standards and practical tools. This approach has been shown to be a fully appropriate alternative to the current well-known design rules. It allows combined loading conditions to be treated as easily as simple ones and therefore avoids resorting to long and tedious calculations "beam-columns" formula such as in Eurocode 3.

In section 6.2, the assumptions accounted for to derive the proposed design curves of hot-rolled and cold-formed members have been described and detailed.

In section 6.3, an experimental database comprising more than 800 results was assembled from literature. It comprises various load cases, fabrication processes and yield strengths, cross-sections shapes, elements lengths... Obtained results were plotted along with the 12 tests performed at the University Of Applied Sciences Of Western Switzerland – Fribourg, and along with the performed extensive numerical study, in an O.I.C. format that was shown to be suitable to characterize the behaviour and response of steel hollow section beam-columns; in addition, key parameters such as the fabrication processes, bending moment distribution ψ factor, axial force ratio, degree of biaxial bending $\Omega_{y/z}$ and steel grade were identified.

Section 6.4 detailed the derivation of several adequate interaction curves, which were proposed based on the numerical results with the use of an extended Ayrton-Perry approach covering simple and combined load cases for both hot-rolled and cold-formed sections.

In section 6.5, the accuracy of the proposed design formulae was examined. Statistical results of the comparison between F.E., EC3 and proposal calculations for all the computed results were presented. The resistance estimates were significantly improved by the new proposal, with mean and standard deviation values indicating a far better level of accuracy and consistency.

A summary of all proposed formulae and recommendations for practical design were then presented in section 6.6, and section 6.7 consisted in proposing a simplified alternative to the proposed design model followed (in section 6.8) by a description of worked examples presented to illustrate the effectiveness, the simplicity and the economic benefit of the newly developed design proposal.

7. Conclusion and future developments

This thesis set out to investigate the behaviour, resistance and design of steel hollow section members. The main objective was to propose an original design approach for beam-column hollow members based on the Overall Interaction Concept (O.I.C.) which addresses the inelastic beam-column response, and includes possible local-global interaction under simple and combined loading situations - one of the most complex element's responses.

A comprehensive survey concerning the field of the beam-column resistance was conducted in chapter 2. A detailed history of the buckling handling and development was made, along with an actual description of the methods used in nowadays standards.

A total of 12 beam-column tests, consisting of hot-rolled and cold-formed RHS and CHS members under eccentrically-applied compression has been carried out and detailed in chapter 3. Results relative to material response, residual stresses measurements and careful determination of initial geometrical imperfections were reported. The (imperfect) initial geometry was measured along the whole column by means of two different procedures. The first method relied on the use of a set of equally spaced LVDTs displaced on each specimen's plates; the second method consisted in scanning the specimen's plates by means of a laser Tracker *AT401*. Residual stresses were examined by mean of the sectioning technique and compared to the stresses obtained by the electrical strain gauges.

Besides, numerical shell models simulating the test conditions as closely as possible were developed. For both the present test series and another one from the literature, it was found that the FE models were capable of replicating accurately the response and resistance of the experiments.

Accordingly, the validated FE models have been further used in extensive numerical studies, and a database comprising more than seventy thousand results was built consecutively, for hot-rolled and cold-formed members, as detailed in chapter 4 and chapter 5 respectively. The numerical specimens were chosen in a way to cover all cross-sections classes; they are relative to different steel grades, different element lengths, different fabrication processes... Results were computed by means of beam and shell analyses in order to investigate the influence of local and global buckling on the member's behaviour. These results have served to assess the application of the O.I.C. to hollow section resistance.

Chapter 6 reports on the results of the extensive numerical parametric studies that have been further used to assess the merits of the proposed new design approach. Accurate and continuous interaction curves were derived, for hot-rolled and cold-formed steel hollow beam-column members along the slenderness range, by considering all the identified governing parameters. With the adoption of the Ayrton-Perry extended format, locally fitted factors were defined; the proposed design curves for simple and combined load cases are presented. Chapter 6 then illustrates the accuracy of the proposed design formulae. Statistical results of the comparison between F.E., Eurocode 3 and proposal calculations are presented. The resistance estimates were significantly improved by the new proposal, with mean and standard deviation values indicating a far better level of accuracy and consistency. A summary of the proposed design formulae and recommendations for practical design are presented followed by a description of worked examples illustrating the effectiveness, the simplicity and the economic benefit of the newly developed design proposals.

The personal contributions made in this thesis include the following listed points:

- the determination of the load-carrying capacity of 12 beam-column tests with various loading conditions, cross-section shapes and fabrication modes;
- besides the present experimental series, an experimental database comprising more than 800 results was assembled from literature. These data, together with the extensive performed numerical parametric study, served as a set of reference results for the derivation of adequate interaction curves;
- a mesh refinement study was performed in the purpose to adopt the most appropriate meshing density, able to provide an accurate numerical prediction of the member's behaviour;
- a sensitivity study on the influence of different shapes and amplitudes of initial local and global geometric imperfections on the member capacity was performed;
- a load-path sensitivity study to characterize the differences that arise in the structural response of members if the load is applied in different sequences for a given combination was performed;

-
- a study has been undertaken to investigate the most appropriate way to calculate the R-factors (R_{RESIST} , $R_{STAB,MB}$, $R_{STAB,CS}$) involved in the O.I.C. approach. R_{RESIST} determined by means of empirical formulae proposed by Eurocode 3 and by Lescouarch were compared to R_{RESIST} computed using a specially developed Matlab tool. $R_{STAB,CS}$ determined by L.B.A. calculations using the non-linear numerical software FINELg and the semi-analytical finite strip method CUFSM were compared to the theoretical differential equation for elastic buckling of a plate. $R_{STAB,MB}$ computed using ABAQUS and FINELg beam modelling were also compared;
 - the determination of appropriate material law for cold-formed tubes through the collection of existing tensile tests from literature and by fitting the simple and double Ramberg-osgood analytical curves to the experimental ones in order to get the most appropriate R.O.-coefficients. Additional parametric study was performed to analyse the influence of various parameters on the resistance of cold-formed tubes;
 - the determination of appropriate material law for hot-rolled high strength steel through the review of the current design codes and the performance of a parametric study where three types of material law were investigated;
 - the development of a new design formula based on the Ayrton-Perry approach, capable of describing the buckling behaviour of members subjected to pure compression load case (N), compression with mono-axial bending ($N+N_y / N+M_z$) and compression with bi-axial bending ($N+M_y+M_z$). Hot-rolled and cold-formed square and rectangular hollow sections of nominal steel grades $f_y = 235 \text{ N/mm}^2$, $f_y = 355 \text{ N/mm}^2$ and $f_y = 690 \text{ N/mm}^2$ with the corresponding cross-sectional classes well-distributed along class 1 and class 4 (i.e. stocky to slender) were investigated;
 - key parameters were taken into account for the derivation of buckling curves such as the fabrication processes, bending moment distribution ψ factor, the ratio between normalized major/minor bending moment to normalized axial force ratio η , degree of biaxial bending $\Omega_{y/z}$, the steel grade and the cross-section shape (rectangular / square);
 - particular attention has been paid to the influence of the bending moment distribution on the member resistance. The numerical simulation results showed that the behaviour of members subjected to a constant moment was quite different then the behaviour of

members subjected to triangular bending moment. Accordingly, different derived curves were proposed for $\psi = 1$ and $\psi = 0$, then extended to consider any value of ψ by allowing for a linear transition between the imperfection factors $\alpha_{\psi=1}$, $\alpha_{\psi=0}$ for $\psi = 1$ and $\psi = 0$ on one hand, and between the ends of plateau $\lambda_{0,\psi=1}$, $\lambda_{0,\psi=0}$ for $\psi = 1$ and $\psi = 0$ on the other;

- for the case of members subjected to combined loading, the presence of axial forces (by means of the parameter n) was seen to have the most important effect on the structural behaviour of members subjected to constant bending moment and a minor influence on the behaviour of members subjected to triangular bending moment. Thus this effect was included in the proposed formula for $\psi = 1$ through the parameters η_y and η_z and not included for $\psi = 0$.

The investigations carried out in the scope of this thesis identified several areas where further research is required. They consisted in the following:

- the application of the O.I.C. for other materials, in situations where instability is of prime importance. This concerns for example members made of composite sections, stainless steel, aluminum, ultra-high performance concrete with fibers, structural glass...;
- a deeper analysis of coupled instabilities of highly slender sections will become necessary, as a consequence of the development of new slender cross-sectional shapes and the development of the new generation of high strength steel. As already discussed, a special care has to be taken in designing these members that represent a special group of structures;
- investigations within fire and earthquake steel design will become necessary, as a consequence of calling off the classification concept;
- improvement of the design of specific members where coupled instabilities and/or complex solutions to implement require (partial) numerical solutions and the associated conceptual framework (e.g. tapered members, cellular beams...);
- development of shear stresses on cross-sectional resistance;

- for now, the O.I.C. proposed interaction formulae are calibrated for RHS and SHS cross-sections and members subjected to simple and combined loads. Many other contributions need to be developed to have a complete 'package', i.e. extending the O.I.C. to circular and open (I and H-shaped) sections...

8. References

- [1] Boissonnade N., Nseir J., and Saloumi E., “The Overall Interaction Concept: an alternative approach to the stability and resistance of steel sections and members”, Proceedings of the Annual Stability Conference, Structural Stability Research Council, St. Louis, Missouri, 2013.
- [2] Ayrton W.E. and Perry J., “On struts”, *The engineer*, Vol.62, 1886.
- [3] Nseir J., “Development of a new design method for the cross-section capacity of steel hollow sections”, PhD thesis, Université de Liège, 2015.
- [4] Greiner R., Kettler M., Lechner A., Jaspart J-P., Boissonnade N., Bortolotti E., Weynand K., Ziller C., Freytag B., Linder J., and Oerder R., “SEMI-COMP: Plastic member capacity of semi-compact steel sections – A more economic design”, Research Fund for Coal and Steel, European Commission, ISBN 978-92-79-11113-6, 2009.
- [5] EN 1993-1-1, “Eurocode 3: Design of steel structures, Part 1-1: General rules and rules for buildings”, 2005.
- [6] NAVIER L., “Résumé des leçons données à l’école des ponts et chaussées sur l’application de la mécanique”, Carillan-Goeury, Paris, 1833.
- [7] Engesser F., “Über die knickfestigkeit gerader stabe”, *Zeitschr. des arch. u. Ing. vereins*, Vol. 35, Hannover, 1889.
- [8] Considere A., “Résistance des pièces comprimées”, *Congrès international de procédés de construction*, Paris, 1889.
- [9] Jasinski F., “Recherches sur la flexion des pièces comprimées”, *Annales des Pons et Chaussées*, 7ème série, Vol.8, 1894.
- [10] Rondal J., “Contribution à l’étude de la stabilité des profils creux à parois minces”, Université de Liège, 1984.
- [11] Young T., “A course of lectures on natural philosophy and the mechanical arts”, J. Johnson, London, 1807.
- [12] Boissonnade N., Greiner R., Jaspart J-P., and Lindner J., “Rules for Member Stability in EN 1993–1–1 Background documentation and design guidelines”, ECCS Technical Committee 8 – Stability, N 119, 2006.
- [13] Mouty J. and Braham M., “Recent progress in the study of the column buckling of hollow sections and its interaction with the possible local buckling of the walls”, 1984.

-
- [14] Robertson A., "The strength of struts", Institute of civil engineering, selected Engineering Paper N 28, London, 1925.
- [15] Godfrey G.B., "The allowable stresses in axially loaded steel struts", The Structural Engineer, Vol.40, N 3, 1962.
- [16] Duthail J., "Le flambement des parois comprimées dans les ossatures en acier", Institut technique du Batiment et des travaux publics, Circulaire série I, N 35, Paris, Sep-1947.
- [17] Duthail J., "Théorie de l'instabilité par divergence d'équilibre", Association internationale des ponts et charpentes, Quatrième congrès, publication préliminaire, Cambridge et Londres, 1952.
- [18] Sfantesco D., "Fondement expérimental des courbes européennes de flambements", Construction Métallique, n°3, 1970.
- [19] Baar S., "CECM buckling curves: Search for a simple equation giving the best fit to the available data", Report of CECM Committee 8. Sercom., No.5B/1 W st.26, Liège, 1970.
- [20] "Recommendations for the plastic design of steel structures", Journal "Construction Métallique, No.4, 1975.
- [21] "Design Code for thin-walled steel construction", Journal "Construction Métallique, No.4, 1978.
- [22] "European convention on metal structures", European recommendations for steel construction, Mar-1978.
- [23] R. Bjorhovde, "Deterministic and probabilistic approaches to the strength of steel columns", Ph.D. Dissertation, Lehigh University, 1972.
- [24] J. Lindner, "Näherungen für die Europäischen Knickspannungskurven, Die bautechnik", heft 10, pp. 344-347, 1978.
- [25] B. Unger, "Ein Konzept zur Berechnung der Traglast von Biegedrillknickgefährdeten Stäben unter Berücksichtigung des einflusses geometrischer und Werkstofflicher Imperfektionen", Heft 11, pp.329-338, 1977.
- [26] DIN 4114, Teil 1, "DIN. Stabilitätsfälle im Stahlbau, knicken von Stäben und Stabwerken", Deutsches Institut für Normung, Berlin, Entwurf, 1978.
- [27] J. B. Dwight, "Use of Perry formula to represent the new European strut curves", Cambridge University, engineering department, report n CUED/C-struct/TR.30, 1972.
- [28] Maquoi R. and Rondal J., "Mise en equation des nouvelles courbes européennes de flambement", Construction métallique, n 1, pp. 17-30, 1978.

-
- [29] Rondal J., Grimault J.P., and Plumier A., “Flambement des profils creux a parois minces, cas des profils rectangulaires charges excentriquement”, Commission des communautés européennes, 2002.
- [30] F. Bleich, “Buckling strength of metal structures”, McGraw-Hill, New York, 1952.
- [31] Chilver A.H., “The stability and strength of thin-walled steel struts”, *The engineer*, pp.180, Aug-1955.
- [32] Dwight J.B., “Structural design with ho rolled hollow sections subject to local buckling”, CUED, C-Struc. TR 49, 1975.
- [33] Gilson S., “La mesure de contraintes résiduelles dans les profils creux à parois minces et leur influence sur la sabilité des parois”, Université de Liege, 1980.
- [34] Jaspart J.P., Ly L., Weynand K., and Josa O., “Resistance and stability of structural members with hollow sections under sombined compression and bending”, Cidect report 2X-1/10.
- [35] Boissonnade N. and Muzeau J.P., “Development of New Interaction Formulae for Beam-Columns”, Proceedings of the International Conference on Steel Structures of the 2000’s, Istanbul Technical University, pp. 233-238., 2000.
- [36] Boissonnade N., Jaspart J.P., Muzeau J.P., and Villette M., “A Proposal for Beam-Column Interaction Formulae”, Proceedings of the 3rd International Conference on Coupled Instabilities in Metal Structures, CIMS’2000, Imperial College Press, London, pp. 697-704, 2000.
- [37] Boissonnade N., Jaspart J.P., Muzeau J.P., and Villette M., “Improvement of the interaction formulae for beam-columns in Eurocode 3”, *Computers & Structures*, Vol. 80, pp. 2375- 2385., 2002.
- [38] Boissonnade N., Jaspart J.P., Muzeau J.P., and Villette M., “New interaction formulae for beam-columns in Eurocode 3: the French-Belgian approach”, *Journal of Constructional Steel Research*, N°60, 2004, pp. 421-431.
- [39] Villette M., Boissonnade N., Muzeau J.P., and Jaspart J.P., “Development of a comprehensive formula for the design of beam-columns”, Internal report, Baudin-Châteauneuf, LERMESCUST, University of Liege, 2000.
- [40] Villette M., “Analyse critique du traitement de la barre comprimée et fléchie et propositions de nouvelles formulations.” .
- [41] Austin W.J., “Strength and design of steel beam-columns”, Proceedings of ASCE, *Journal of the Structural Division*, Vol. 87, N° ST4, Apr-1981.
-

-
- [42] Sneddon I.N., "Encyclopaedie dictionary of mathematics for engineers and applied scientists", Pergamon Press, Oxford, 1976.
- [43] EN 10210-2, "Hot finished structural hollow sections of non-alloy and fine grain steels", 2006.
- [44] EN 10219-1, "Cold-formed welded structural hollow sections of non-alloy and fine grain steels", 2006.
- [45] Cruise R. and Gardner L., "Residual stress analysis of structural stainless steel sections", *Journal of Constructional Steel Research* 64: 352-366, 2008.
- [46] SSRC, Structural Stability Research Council, "S.S.R.C. guide to stability criteria for metal structures", Third edition, B.G. Johnson editor, Wiley, New-york, 1976.
- [47] Rasmussen K.J.R. and Hancock, "Design of cold-formed stainless steel tubular members I:columns", *Journal of Structural Engineering, American Society of Civil Engineers*, Vol. 119, pp 2349-2367, 1993.
- [48] Rasmussen K.J.R. and Hancock, "Design of cold-formed stainless steel tubular members II:Beams", *Journal of Structural Engineering, American Society of Civil Engineers*, Vol. 119, pp 2368-2386, 1993.
- [49] Rasmussen K.J.R., "Recent research on stainless steel tubular structures", *Journal of structural engineering*, Vol 54, No. 1, pp. 75-88, 2000.
- [50] Greish and Ulg, Finelg, "Non linear finite element analysis software", University of Liege- Greisch engineering office, 1999.
- [51] Huang Y. and Young B., "The art of cold-formed steel and aluminium alloy coupon tests", EUROSTEEL, 2014.
- [52] Boissonnade N. and Somja H., "Influence of Imperfections in FEM Modelling of Lateral Torsional Buckling", *Proceedings of the Annual Stability Conference, Structural Stability Research Council, Grapevine, Texas, April 18-21, 2012.*
- [53] ECCS, "Ultimate limit state calculation of sway frames with rigid joints", ECCS publications, n 33-1987.
- [54] DIN 18800, "DIN 18800 Stahlbauten", Beuth Verlag GmbH, Berlin, 1990.
- [55] "Eurocode 3 - Design of steel structures - Part 1-12: Additional rules for the extension of EN1993 up to steel grades S700", 2007.
- [56] Sedlacek G. and Müller C., "High strength steels in steel construction", Institute of Steel Construction, RWTH Aachen, Germany.

-
- [57] Nseir J., Boissonade N., “Cross-sectional resistance – Experimental tests and validation of FE models”, HOLLOPOC report, Part B, research report, University of Applied Sciences of Western Switzerland – Fribourg, Switzerland, 2014.
- [58] Nseir J., Hayeck M., Saloumi E., and Boissonade N., “Influence of imperfections on the local buckling response of hollow structural shapes”, Structural Stability Research Council, Apr-2016.
- [59] Nseir J., Saloumi E., and Boissonade N., “A new design methodology for steel hollow sections: the Overall Interaction Concept”, University of Applied Sciences of Western Switzerland, Fribourg, Switzerland, 2013.
- [60] Shayan S., Rasmussen K.J.R., and Zhang H., “On the modelling of initial geometric imperfections of steel frames in advanced analysis”, School of Civil Engineering, The University of Sydney, NSW, Australia, 2006.
- [61] Epiney V., “Resistance et stabilité des éléments en acier fléchis et tendus”, Msc thesis, HES-SO Ingénierie du Territoire MIT, 2015.
- [62] Lescouarc’h Y., “Capacité de résistance d’une section soumise à divers types de sollicitations”, Construction Métallique, n°2, 1997.
- [63] M. Seif and B. W. Schafer, “Local buckling of structural steel shapes”, Journal of Constructional Steel Research, 2010.
- [64] Kato B., “Rotation capacity of H-section members as determined by local buckling”, Department of Architecture, University of Tokyo, 7-3-1, Hongo, Bunkyo-ku, Tokyo, 113 Japan, 1989.
- [65] Zhao W., “Behaviour and design of cold-formed steel hollow flange section under axial compression”, Queensland University of Technology, 2005.
- [66] Akiyama H., Kuwamura H., Yamada S., Chiu J.C., “Influences of manufacturing processes on the ultimate behaviour of box section members”, Tokyo, 1992.
- [67] Sun M. and Packer J., “Direct formed and continuous formed rectangular hollow sections”, University of Toronto, 2013.
- [68] Kettler M., “Elastic-Plastic Cross-Sectional Resistance Of Semi-Compact H- And Hollow Sections”, 2008.
- [69] Wilkinson T., “The Plastic Behaviour of Cold-Formed Rectangular Hollow Sections”, Ph.D. thesis, University of Sydney, Australia, 1999.
- [70] Pekka S., “Design Rules for Cold-formed Hollow Sections”, Lappeeranta University of Technology, 2004.
-

-
- [71] Schillo N., Theofanous M., Gardner L., Feldmann M., “Material properties and local buckling behaviour of high strength steel hollow sections”, RWTH Aachen University, Institute of Steel Construction, Germany - Dept. of Civil and Environmental Engineering, Imperial College London, UK, 2014.
- [72] Rasmussen K.J.R., “Full-range stress-strain curves for stainless steel alloys”, *Journal of Constructional Steel Research*, 59, 47-61, 2003.
- [73] Key P.W., “The Behaviour of Cold-Formed Square Hollow Section Columns”, University of Sydney, Australia, 1988.
- [74] Yeomans N., “Commentary on buckling tests on square and circular structural hollow sections”, *comite international pour le developpement et l’etude de la construction tubulaire*, programme 2B.
- [75] Guiaux P., “Essais de flambement sur profils creux formes a froid, carres et circulaires”, *Comite international pour le developpement et l’etude de la construction tubulaire*, 2002.
- [76] Salvarinas J.J., “An experimental investigation of the column behaviour of cold-formed stress-relieved hollow structural steel sections”, University of Toronto, 1978.
- [77] Braham M., “Flambement des profils creux a parois minces cas des profils rectangulaires charges axialement”, *Universite de Liege*, 1979.
- [78] Sedlacek G., “Buckling behaviour of a new generation of cold-formed hollow sections”, *Research project No 2R, Cidect*, 1996.
- [79] Sedlacek G., “Buckling behaviour of hot-formed SHS in high strength steel grade E-460”, *Comite international pour le developpement et l’etude de la construction tubulaire*, *Cidect report 2T-2/99*, 1999.
- [80] Pavlovic L., “Finite element simulation of slender thin-walled box columns by implementing real initial conditions”, *Faculty of Civil and Geodetic Engineering, University of Ljubljana, Slovenia*, 2011.
- [81] Kotorman I., “Interaction of different phenomena in the behaviour of box girders”, *Departement of steel structures, Budapest University of Technology and Economics*, 2000.
- [82] Taras A., “Contribution to the development of consistent stability design rules for steel members”, *Graz University of Technology, Faculty of Civil Engineering*, 2011.

9. Annexes

9.1. Annex 1: Collection of existing buckling beam-column test results

Around 802 test results for members were collected from many sources, comprising hollow sections covering all section classes, different element lengths tested under simple and combined loading with different shapes of bending moment distribution along the member. Table 66 presents all collected data along with the corresponding references, the shape, fabrication process, the number of tests, load cases and measured yield strengths.

Table 66 – Summary of the gathered test data

Source	Shape	Fabrication process	Number of tests	Load case	ψ_y	ψ_z	Length [m]	f_y [N/mm ²] (measured)
Hayeck	RHS 200x100x4	Cold-formed	1	$N+M_y$	1	-	4.0	475
			1	$N+M_y+M_z$	1	1	4.0	450
			1	$N+M_y$	0	-	4.0	480
	RHS 220x120x6	Cold-formed	1	$N+M_y$	1	-	4.0	450
			1	$N+M_y+M_z$	1	1	4.0	462
			1	$N+M_y$	0	-	4.0	448
	CHS 159x5	Hot-rolled	1	$N+M_y$	1	-	4.0	399
			1	$N+M_y$	1	-	4.9	393
			1	$N+M_y$	0	-	4.0	405
	CHS 159x6.3	Hot-rolled	1	$N+M_y$	1	-	4.9	396
			1	$N+M_y+M_z$	1	1	4.0	389
			1	$N+M_y$	0	-	4.0	394

Source	Shape	Fabrication process	Number of tests	Load case	ψ_y	ψ_z	Length [m]	f_y [N/mm ²] (measured)
Grimault	RHS 200*100*4	Cold-formed	2	N	-	-	2.11	395
			2		-	-	2.11	376
			2		-	-	3.17	395
			2		-	-	3.17	376
			3		-	-	4.23	395
			3		-	-	4.23	376
			4	$N+M_y$	1	-	2.11	395
			4		1	-	2.11	376
			8		1	-	3.17	395
			8		1	-	3.17	376
			4		1	-	4.23	395
			4		1	-	4.23	376
			4	$N+M_z$	-	1	2.11	395
			5		-	1	2.11	376
			8		-	1	3.17	395
			8		-	1	3.17	376
			4		-	1	4.23	395
			4		-	1	4.23	376
			6	$N+M_y+M_z$	1	1	2.11	376
			2		1	1	2.11	395
			4		1	1	3.17	395
			5		1	1	3.17	376
			5		1	1	4.23	395
			5		1	1	4.23	376

Source	Shape	Fabrication process	Number of tests	Load case	ψ_y	ψ_z	Length [m]	f_y [N/mm ²] (measured)
Rondal	RHS 300*100*5	Hot-rolled	1	N	-	-	2.17	342
			1		-	-	3.25	342
			1		-	-	4.35	342
	RHS 200*200*3.8	Hot-rolled	1	N	-	-	4.05	480
			1		-	-	6	480
			1		-	-	8	480
	RHS 330*200*4	Cold-formed	1	N	-	-	4.25	416
			1		-	-	6.37	416
			1		-	-	8.5	416
	RHS 265*265*4	Cold-formed	1	N	-	-	5.335	436
			1		-	-	8	436
			1		-	-	10.67	436
	RHS 300*100*5	Cold-formed	1	N	-	-	2.17	386
			1		-	-	3.25	386
			1		-	-	4.35	386
	RHS 300*200*5	Cold-formed	1	N	-	-	4.21	270
			1		-	-	6.25	270
			1		-	-	8.33	270
	RHS 220*140*3	Cold-formed	1	N	-	-	3	481
			1		-	-	4.47	481
			1		-	-	5.9	481
	RHS 250*150*5	Cold-formed	1	N	-	-	3.18	374
			1		-	-	4.75	374
			1		-	-	6.27	374
	RHS 200*100*4	Hot-rolled	3	$N+M_y$	1	-	2.11	354
			4	$N+M_z$	1	1	2.11	354
			6	$N+M_y+M_z$	1	1	2.11	354
			4	$N+M_y$	1	-	3.17	354
			5	$N+M_z$	-	1	3.17	354
			1	$N+M_y+M_z$	1	1	3.17	354
			3	$N+M_y$	1	-	4.23	354
			3	$N+M_z$	-	1	4.23	354
			5	$N+M_y+M_z$	1	1	4.23	354
			1	N	-	-	2.11	354
			1		-	-	3.17	354
			1		-	-	4.23	354
		Cold-formed	3	$N+M_y$	1	-	2.11	343
			3	$N+M_z$	-	1	2.11	343
			2	$N+M_y+M_z$	1	1	2.11	343
			4	$N+M_y$	1	-	3.17	343
			5	$N+M_z$	-	1	3.17	343
			1	$N+M_y+M_z$	1	1	3.17	343
3			$N+M_y$	1	-	4.23	343	
3			$N+M_z$	-	1	4.23	343	
5			$N+M_y+M_z$	1	1	4.23	343	
1	N		-	-	2.11	343		
1		-	-	3.17	343			
1		-	-	4.23	343			
RHS 250*150*5	Cold-formed	2	$N+M_z$	-	-1	3.18	381	
		3		-	0	3.18	381	
		3		-	1	3.18	381	
		2		-	-1	4.75	381	
		3		-	0	4.75	381	
		3		-	1	4.75	381	
		2		-	-1	6.27	381	
		3		-	0	6.27	381	
		3		-	1	6.27	381	
	1	N	-	-	3.18	381		
	1		-	-	4.75	381		

		Hot-rolled	1	N	-	-	3.14	337	
			1			-	-	4.71	337
			1			-	-	6.28	337

Source	Shape	Fabrication process	Number of tests	Load case	ψ_y	ψ_z	Length [m]	f_y [N/mm ²] (measured)		
Greiner	RHS 200*120*4	Hot-rolled	1	$N+M_y$	1	-	4.05	378		
			1	$N+M_y$	0	-	4.05	378		
			1	$N+M_z$	-	1	4.05	378		
			1	$N+M_z$	-	0	4.05	378		
			1	$N+M_y+M_z$	1	1	4.05	378		
			1	$N+M_y+M_z$	0	0	4.05	378		
	SHS 180*5		1	$N+M_y$	1	-	4.05	413		
			1	$N+M_y$	0	-	4.05	413		
			1	$N+M_y$	-	0.455	-	4.05	413	
			1	$N+M_y+M_z$	1	1	3.99	413		
			1	$N+M_y+M_z$	0	0	4.05	413		
			1	$N+M_y+M_z$	-	-	0.455	0.455	4.02	413
								5		

Source	Shape	Fabrication process	Number of tests	Load case	ψ_y	ψ_z	Length [m]	f_y [N/mm ²] (measured)
Yeomans	SHS 127*9.5	Cold-formed	3	N	-	-	4.951	480
			3	N	-	-	3.733	480
			3	N	-	-	2.512	480
			3	N	-	-	1.294	480
	SHS 203.2*7.9	Cold-formed	3	N	-	-	4.952	469
			3	N	-	-	2.512	469
	SHS 80*2.8	Cold-formed	8	N	-	-	2.27	380
			8	N	-	-	3.37	380
	SHS 100*3.8	Cold-formed	8	N	-	-	2.212	340
			8	N	-	-	3.572	340
	CHS 141.3*6.5	Cold-formed	3	N	-	-	4.952	362
			3	N	-	-	3.732	362
			3	N	-	-	2.512	362
			3	N	-	-	1.294	362
	CHS 168.3*7.1	Cold-formed	3	N	-	-	4.951	384
			3	N	-	-	2.512	384
	CHS 273*6.3	Cold-formed	3	N	-	-	4.952	308
			3	N	-	-	2.512	308
	CHS 88.9*3.2	Cold-formed	8	N	-	-	2.801	444

Source	Shape	Fabrication process	Number of tests	Load case	ψ_y	ψ_z	Length [m]	f_y [N/mm ²] (measured)
Guiaux	SHS 125*3	Cold-formed	10	N	-	-	2.404	374
			10	N	-	-	4.884	374
	SHS 125*4		10	N	-	-	2.368	360
			10	N	-	-	4.862	360
	SHS 125*6		10	N	-	-	2.35	372
			10	N	-	-	4.776	372
	SHS 170*4		10	N	-	-	3.294	305
			10	N	-	-	4.875	305

Source	Shape	Fabrication process	Number of tests	Load case	ψ_y	ψ_z	Length [m]	f_y [N/mm ²] (measured)
Salvarinas	SHS 203.2*9.53	Cold-formed	5	N	-	-	5.486	406

	SHS 203.2*11.4	Cold-formed	5	N	-	-	3.551	365
			6	N	-	-	5.415	365
	SHS 304.8*9.53	Cold-formed	4	N	-	-	5.486	423

Source	Shape	Fabrication process	Number of tests	Load case	ψ_y	ψ_z	Length [m]	f_y [N/mm ²] (measured)
Braham	RHS 330*200*4	Cold-formed	8	N	-	-	4.25	416
			6	N	-	-	6.37	416
			8	N	-	-	8.5	416
	SHS 265*4	Cold-formed	8	N	-	-	5.335	436
			8	N	-	-	8	436
			8	N	-	-	10.67	436
	RHS 250*150*5	Cold-formed (annealed)	8	N	-	-	3.14	337
			8	N	-	-	4.71	337
			8	N	-	-	6.28	337
	RHS 300*100*5	Cold-formed	8	N	-	-	2.17	386
			8	N	-	-	3.25	386
			8	N	-	-	4.35	386
		Cold-formed (annealed)	8	N	-	-	2.17	342
			8	N	-	-	3.25	342
	RHS 300*200*5	Cold-formed	8	N	-	-	4.35	342
			8	N	-	-	4.21	270
			8	N	-	-	6.24	270
	RHS 220*140*3	Cold-formed	8	N	-	-	8.33	270
			8	N	-	-	3	481
			7	N	-	-	4.47	481
	SHS 200*3.8	Cold-formed (annealed)	8	N	-	-	5.9	481
			8	N	-	-	4.05	480
			8	N	-	-	6	480
	RHS 250*150*5	Cold-formed	8	N	-	-	8	480
			8	N	-	-	3.18	374
			8	N	-	-	4.75	374
			8	N	-	-	6.27	374
			1	N	-	-	3.14	388
			2	$N+M_z$	-	-1	3.14	388
			3	$N+M_z$	-	0	3.14	388
			3	$N+M_z$	-	1	3.14	388
			1	N	-	-	4.71	388
			2	$N+M_z$	-	-1	4.71	388
			3	$N+M_z$	-	0	4.71	388
			3	$N+M_z$	-	1	4.71	388
			3	$N+M_z$	-	-1	6.28	388
3	$N+M_z$	-	0	6.28	388			
3	$N+M_z$	-	1	6.28	388			

Source	Shape	Fabrication process	Number of tests	Load case	ψ_y	ψ_z	Length [m]	f_y [N/mm ²] (measured)
Sedlacek	SHS 100*5	Cold-formed	4	N	-	-	2.8	445
			4	N	-	-	4.2	445
	SHS 100*4	Cold-formed	3	N	-	-	2.1	429
			3	N	-	-	2.8	429
			3	N	-	-	3.5	429
	SHS 150*6.3	Cold-formed	3	N	-	-	4.2	429
			4	N	-	-	3	433
	SHS 100*5	Cold-formed	4	N	-	-	4	433
			4	N	-	-	2.1	458
			4	N	-	-	2.8	458
			4	N	-	-	3.5	458
			4	N	-	-	4.2	458

SHS 150*6	Cold-formed	4	N	-	-	3	388
		4	N	-	-	4	388
SHS 120*5	Cold-formed	4	N	-	-	2.1	507
		4	N	-	-	2.8	507
		4	N	-	-	3.5	507
		4	N	-	-	4.2	507

Source	Shape	Fabrication process	Number of tests	Load case	ψ_y	ψ_z	Length [m]	f_y [N/mm ²] (measured)
Kuhn	RHS 120*80*5	Hot-rolled	3	N	-	-	1.4	465
			3	N	-	-	1.9	465
			4	N	-	-	2.4	465
			3	N	-	-	2.8	465
			3	N	-	-	3.8	465
	SHS 120*8	Hot-rolled	4	N	-	-	2.2	538
			4	N	-	-	2.9	538
			6	N	-	-	3.6	538
	120*80*7.2	Hot-rolled	4	N	-	-	4.3	538
			5	N	-	-	1.4	693
			5	N	-	-	1.9	693
			5	N	-	-	2.4	693
			Hot-rolled	4	N	-	-	2.8
		Hot-rolled	4	N	-	-	3.8	693

Source	Shape	Fabrication process	Number of tests	Load case	ψ_y	ψ_z	Length [m]	f_y [N/mm ²] (measured)
Pavlovic	RHS 190*160*4	Cold-formed	1	N	-	-	4	373
		Cold-formed	1	N	-	-	5.2	373
		Cold-formed	1	$N+M_z$	-	1	4	373

9.2. Annex 2: Determination of appropriate material law for cold-formed tubes

9.2.1. Cold-formed sections with normal steel grades

9.2.1.1. Collection of existing experimental tensile test results

In order to characterize the specific mechanical behaviour of cold-formed square and rectangular hollow sections, experimental results on tensile coupon tests were collected, both from own tensile tests and from literature. Figure 352 illustrates the locations where the various samples were cut, and the adopted dimension labelling system.

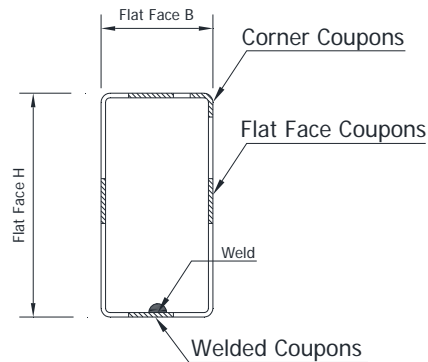


Figure 352 – Section notation and designations for cold-formed RHS and SHS

Based on the gathered data (see Table 67), a study was devoted to the determination of appropriate material coefficients for so-called Ramberg-Osgood (R.-O.) equations, through a “simple” or “double” R.-O. format.

Table 67 – Coupon tests extracted from cold-formed hollow sections of normal steel grades

Section	Source	Section	Grade	Coupon specimens types	Manufacturer
S1	1*	200x100x4	S355	Flat face, corner	
S2		220x120x6	S355	Flat face, corner	
S3		200x200x5	S355	Flat face, corner	
S4		200x200x6	S355	Flat face, corner	
S5	2*	180x180x5	S355	Opposite and adjacent to the weld, corner, weld	
S6		200x120x4	S275	Opposite and adjacent to the weld, corner, weld	
S7	3*	150x50x5	S450	Opposite to the weld, corner	
S8		75x50x2	S450	Adjacent to the weld	
S9		150x50x4	S350	Opposite to the weld	
S10		150x50x4	S450	Web and flange faces	
S11		100x50x2	S350	Opposite and adjacent to the weld	
S12	4*	100x100x3	S355	Weld, face H, face B, corner R_{max} , corner R_{min}	A
S13		100x100x5	S355	Weld, face H, face B, corner R_{max} , corner R_{min}	A
S14		100x100x6	S355	Weld, face H, face B, corner R_{max} , corner R_{min}	A
S15		100x100x8	S355	Weld, face H, face B, corner R_{max} , corner R_{min}	A
S16		100x100x10	S355	Weld, face H, face B, corner R_{max} , corner R_{min}	A

S17		150x150x8	S355	Weld, face H, face B, corner R_{max} , corner R_{min}	A
S18		200x200x10	S355	Weld, face H, face B, corner R_{max} , corner R_{min}	A
S19		300x300x6	S355	Weld, face H, face B, corner R_{max} , corner R_{min}	A
S20		300x300x12.5	S355	Weld, face H, face B, corner R_{max} , corner R_{min}	A
S21		200x100x8	S355	Weld, face H, face B, corner R_{max} , corner R_{min}	A
S22		200x100x10	S355	Weld, face H, face B, corner R_{max} , corner R_{min}	A
S23		50x50x3	S355	Weld, face H, face B, corner R_{max} , corner R_{min}	B
S24		50x50x5	S355	Weld, face H, face B, corner R_{max} , corner R_{min}	B
S25		100x100x3	S355	Weld, face H, face B, corner R_{max} , corner R_{min}	B
S26		100x100x5	S355	Weld, face H, face B, corner R_{max} , corner R_{min}	B
S27		100x100x6	S355	Weld, face H, face B, corner R_{max} , corner R_{min}	B
S28		100x100x8	S355	Weld, face H, face B, corner R_{max} , corner R_{min}	B
S29		100x100x10	S355	Weld, face H, face B, corner R_{max} , corner R_{min}	B
S30		150x150x8	S355	Weld, face H, face B, corner R_{max} , corner R_{min}	B
S31		200x200x10	S355	Weld, face H, face B, corner R_{max} , corner R_{min}	B
S32		200x100x8	S355	Weld, face H, face B, corner R_{max} , corner R_{min}	B
S33		200x100x10	S355	Weld, face H, face B, corner R_{max} , corner R_{min}	B
S34		100x100x5	S355	Weld, face H, face B, corner R_{max} , corner R_{min}	C
S35		200x100x8	S355	Weld, face H, face B, corner R_{max} , corner R_{min}	C
S36		160x160x6	S355	Weld, face H, face B, corner R_{max} , corner R_{min}	C
S37		100x100x8	S355	Weld, face H, face B, corner R_{max} , corner R_{min}	D
S38		100x100x10	S355	Weld, face H, face B, corner R_{max} , corner R_{min}	D
S39		150x150x8	S355	Weld, face H, face B, corner R_{max} , corner R_{min}	D
S40		200x100x8	S355	Weld, face H, face B, corner R_{max} , corner R_{min}	D
S41		50x50x3	S355	Weld, face H, face B, corner R_{max} , corner R_{min}	E
S42		50x50x5	S355	Weld, face H, face B, corner R_{max} , corner R_{min}	E
S43		100x100x3.2	S355	Weld, face H, face B, corner R_{max} , corner R_{min}	E
S44		100x100x6	S355	Weld, face H, face B, corner R_{max} , corner R_{min}	E
S45		100x100x10	S355	Weld, face H, face B, corner R_{max} , corner R_{min}	E
S46		160x160x6	S355	Weld, face H, face B, corner R_{max} , corner R_{min}	E
S47		100x100x3	S460	Weld, face H, face B, corner R_{max} , corner R_{min}	F
S48		100x100x5	S460	Weld, face H, face B, corner R_{max} , corner R_{min}	F
S49		100x100x6	S460	Weld, face H, face B, corner R_{max} , corner R_{min}	F
S50		100x100x8	S460	Weld, face H, face B, corner R_{max} , corner R_{min}	F

1* Results collected from the University of Applied Science of Western Switzerland – Fribourg

2* Results collected from Graz Technical University

3* Results collected from the University of Sydney

4* Results collected from Lappeenranta University of Technology

9.2.1.2. Simple Ramberg-Osgood formulation

In the design of aluminium and stainless steel structures, the stress-strain relationship is usually associated to the simple R.-O. formula and given in Equation (373):

$$\varepsilon = \frac{\sigma}{E_0} + 0.002 \left(\frac{\sigma}{\sigma_{0.2}} \right)^n \quad (373)$$

where E_0 is the initial Young's modulus, $\sigma_{0.2}$ the equivalent yield stress and n a strain-hardening coefficient. From the format of Equation (373), it can be noticed that when the value of n increases, the roundness of the stress-strain curve decreases. For high values of n (i.e. $n > 50$), the material response tends to become bi-linear, with a distinct yield plateau such as for hot-formed tubes. All tensile test results collected from different sources have been

used to back-calculate adjusted values of parameter n so as the experimental and analytical curves to fit best. Figure 353 presents typical examples of measured stress-strain compared to simple R.-O. equations. As another example, the key results from experimental tensile coupon tests reported by Kettler, with the corresponding material properties, are given in

Table 69, where σ_u and ε_u refer to the yield and ultimate strengths and strain of the material respectively. The parameter n is obtained using Equation (373) for $\varepsilon = \varepsilon_u$ and $\sigma = \sigma_u$.

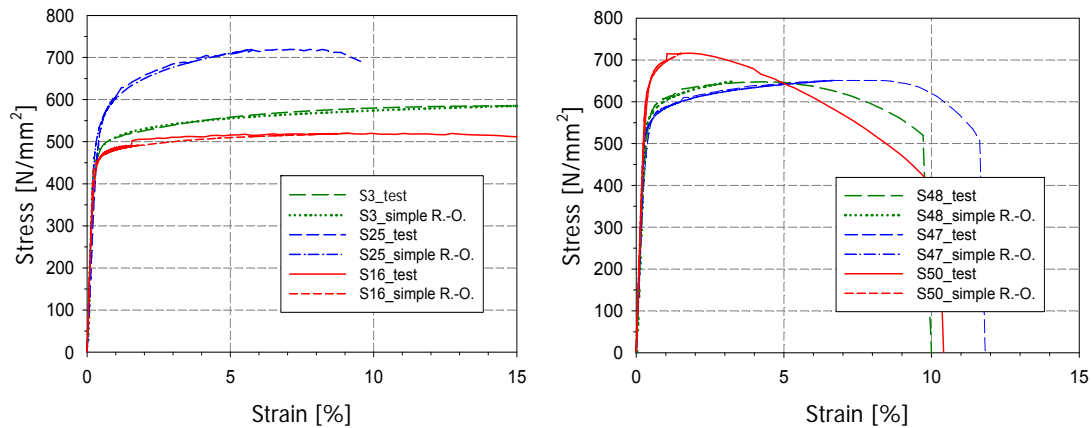


Figure 353 – Comparison of test stress-strain curves vs. simple R.-O. equation with fitted n value – a) S355 (S3, S16, S25 specimens) – b) S460 (S47, S48, S50)

All available experimental data were analysed (in total, 235 coupon tests) in order to develop the stress-strain equation. The strain-hardening coefficients obtained are shown in Figure 354 and Figure 355, where B/t is the width-to-thickness ratio for the weld, flat and corner faces. For each coupon, the obtained yield stress of the opposite face was found higher than that of the adjacent face to the weld, and the yield stress of the corner was higher than that of the opposite face. Considerable cold-forming work is reported in the corners, and on the flat faces opposite to the weld. For cold-formed sections with low values of B/t ratios, the difference in ductility between the flat faces and the corners is minor; however, for sections with high B/t ratios, such differences becomes obvious. Globally, the values of the simple R.-O. parameter n ranged from 8.5 to 33.9 with an average value of 20 as shown in Figure 354 to Figure 356 and in Table 67. Also, as Figure 356 clearly shows, no direct correlation could be drawn between the coupon's steel grade and coefficient n , in view of the rather large scatters reported.

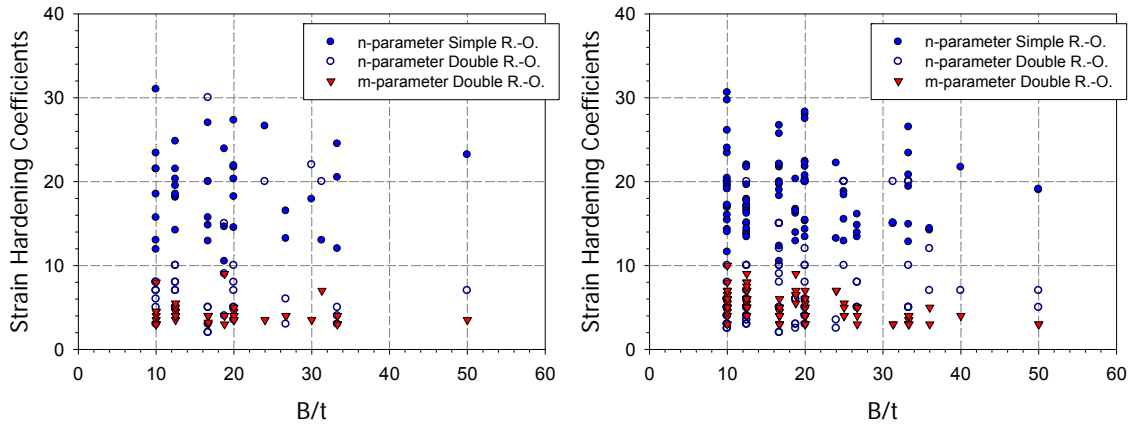


Figure 354 – Simple and double R.-O. calculated parameters – a) welded faces – b) flat faces.

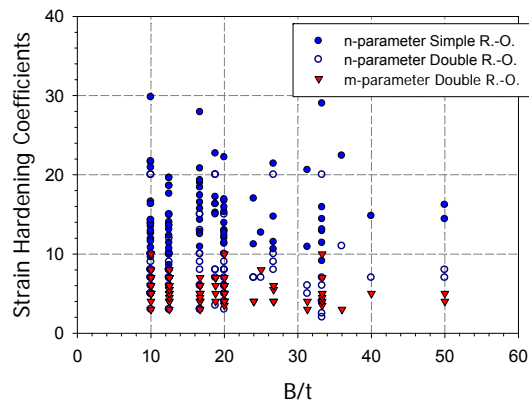


Figure 355 – Simple and double R.-O. calculated parameters for corners.

Table 68 – Calculated n values through simple R.-O. formulation.

n values	Min.	Max.	Average
Flat faces	10.5	33.9	18.6
Corners	8.5	29.7	15.4
Weld faces	10.5	31.0	19.0

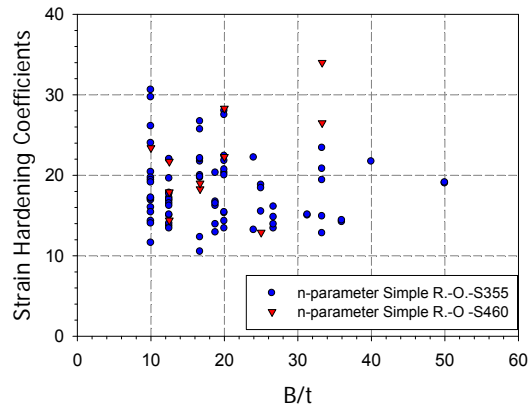


Figure 356 – Simple R.-O. n parameter for flat faces from steel grades S355 and S460.

Table 69 – Examples of fitted values for n coefficient – sections S5 and S6.

Section	Position	E[Gpa]	$\sigma_{0.2}$ [MPa]	σ_u [MPa]	ϵ_u [-]	n [-]
S5-1	a opposite	184.8	400.6	538.8	0.12	13.74
	b adjacent	179.3	386.3	520	0.13	13.96
	c adjacent	187.7	401.1	543.5	0.11	13.22
	d weld	198.3	421.2	534	0.11	16.94
	e corner	205.3	593.08	649.04	0.01	17.67
	f corner	196.0	595.56	645.66	0.01	18.35
S5-2	a opposite	182.0	399.3	537	0.12	13.65
	b adjacent	186.6	371.1	518.1	0.14	12.68
	c adjacent	188.5	400.2	543.4	0.11	13.05
	d weld	195.1	419.8	530	0.12	17.36
	e corner	182.2	610.29	644.49	0.01	25.79
	f corner	210.1	602.73	659.74	0.01	16.09
S6-1	a opposite	195.1	398.7	494.9	0.13	19.38
	b adjacent	193.8	392.2	502.3	0.13	16.71
	c adjacent	196.7	389.9	496	0.13	17.14
	d weld	201.6	411.5	506.7	0.11	19.06
	e corner	210.7	550.84	619.9	0.02	19.00
	f corner	192.5	569.58	624.51	0.01	19.05
S6-2	a opposite	198.1	411.8	500.7	0.12	20.75
	b adjacent	192.8	386.8	496	0.13	16.67
	c adjacent	199.9	384	498.7	0.13	15.89
	d weld	196.3	407.7	501.6	0.12	19.73
	e corner	205.8	558.67	631.33	0.03	20.86
	f corner	193.4	566.15	632.3	0.02	19.38

9.2.1.3. Double Ramberg-Osgood formulation

The “double Ramberg-Osgood” equation is denoted as:

$$\epsilon = \frac{\sigma - \sigma_{0.2}}{E_{0.2}} + \epsilon_u \left(\frac{\sigma - \sigma_{0.2}}{\sigma_u - \sigma_{0.2}} \right)^m + \epsilon_{0.2} \quad \text{for } \sigma > \sigma_{0.2} \quad (374)$$

$$\text{with } E_{0.2} = \frac{E_0}{1 + 0.002 \cdot n / e} \quad (375)$$

In Equation (374), $e = \sigma_{0.2} / E_0$ is the non-dimensional proof stress. For stresses up to $\sigma_{0.2}$, the stress strain curve can be determined using Equation (373). Figure 357 shows typical measured stress-strain curves compared with the double R.-O. equations for $\sigma \leq \sigma_{0.2}$ and $\sigma > \sigma_{0.2}$. Adjusted n and m values are determined so as to best fit the experimental curve with the analytical one. The results of the “best fit procedure” are shown in Figure 354 and Figure 355 as a function of the B / t ratio for the weld, flat and corner coupons, respectively.

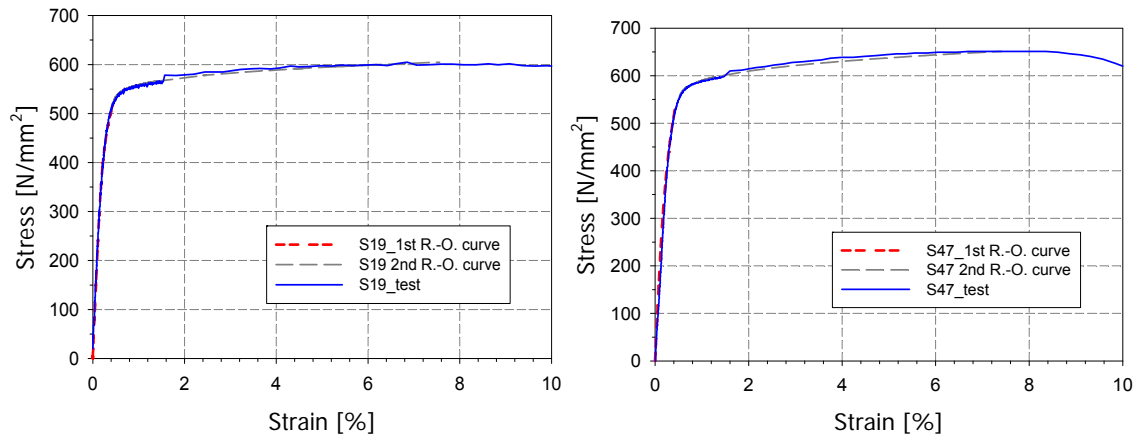


Figure 357 – Experimental vs. fitted double R.-O. material curves – a) S19 specimen – b) S47 specimen.

Generally, n values were found lower than those obtained from the simple equation, and the m coefficients had the lowest range values. The values of the double R.-O. coefficient n ranged from 2 to 30 with an average of 8.2, and the coefficient m ranged from 3 to 10 with an average of 5.1 as shown in Table 70. Double R.-O. parameters for the flat faces of steel grades S355 and S460 are presented in Figure 358. Figure 359 finally proposes representative experimental stress-strain curves compared with their associated simple and double R.-O. equations.

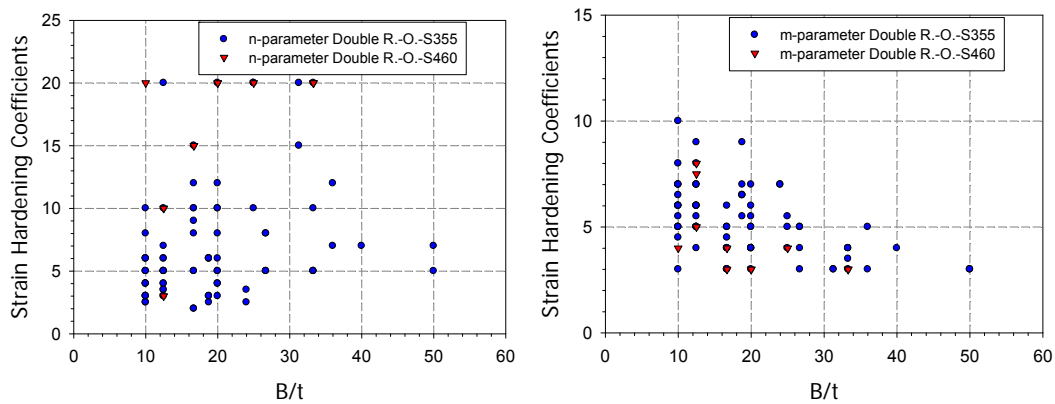


Figure 358 – Double R.-O. coefficients for flat faces S355 and S460 – a) n parameter $\sigma \leq \sigma_{0.2}$ – b) m parameter

$\sigma > \sigma_{0.2}$.

Table 70 – Calculated n and m values through double R.-O. formulation.

n values	Min.	Max.	Average
Flat	2	20	8
Corners	2	20	8
Weld	2	30	8
m values	Min.	Max.	Average
Flat	3	10	5
Corners	3	10	5.4
Weld	3	9	4

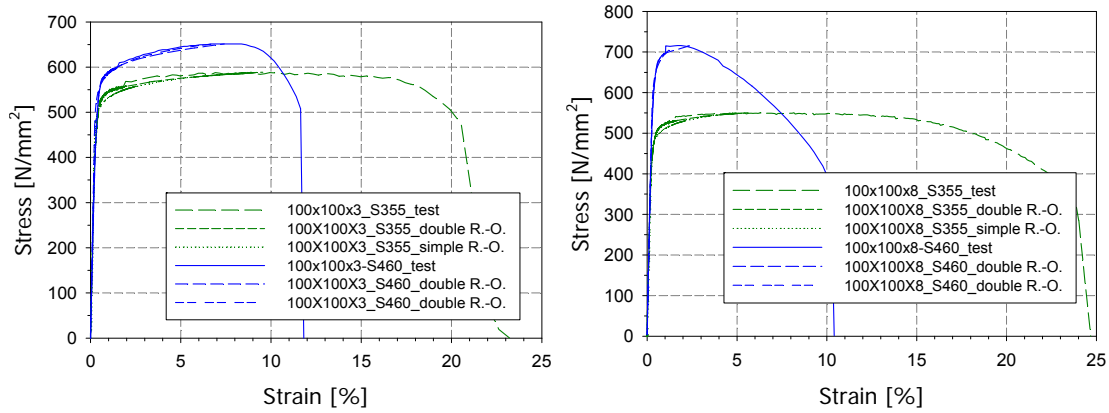


Figure 359 – Experimental and analytical stress-strain curves for different steel grades – a) SHS 100x100x3 – b) SHS100x100x8.

9.2.1.4. Influence of R.-O. coefficients on the resistance of cold-formed tubes

The present paragraph analyses the influence of various parameters on the resistance of cold-formed tubes, by means of shell F.E. numerical results. In this respect, G.M.N.I.A. parametric studies have been conducted, with the following set of parameters:

- four cross-section shapes: RHS 220x120x6 and 220x120x10, and SHS 100x5 and 200x3. These sizes have been selected so as to cover plastic to slender responses of the sections, either in compression or in bending;
- two steel grades: S235 and S460;
- two different load cases: compression N or major axis bending M_y ;
- simple R.-O. material laws with different values of R.-O. coefficients n .

Figure 360 presents examples of deformed shapes and yield patterns at failure obtained with the F.E. model, for major-axis bending moment and axial compression load cases, respectively.

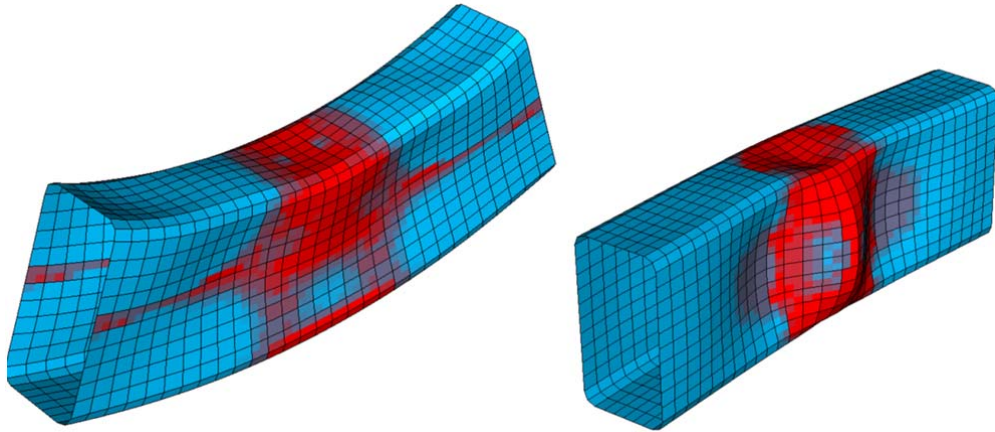


Figure 360 – Deformed shapes and yield patterns at failure – a) under major-axis bending moment – b) under axial compression

In total, 320 non-linear F.E. computations have been performed. Figure 361 presents the ultimate loads reached for each value of n used in the parametric study using a simple R.-O material model. It is observed that, in the case of a simple R.-O. material law, quite close failure loads are reached, whatever the load case considered; one may however note higher peak loads for the smallest n values, where the influence of strain-hardening effects is more pronounced

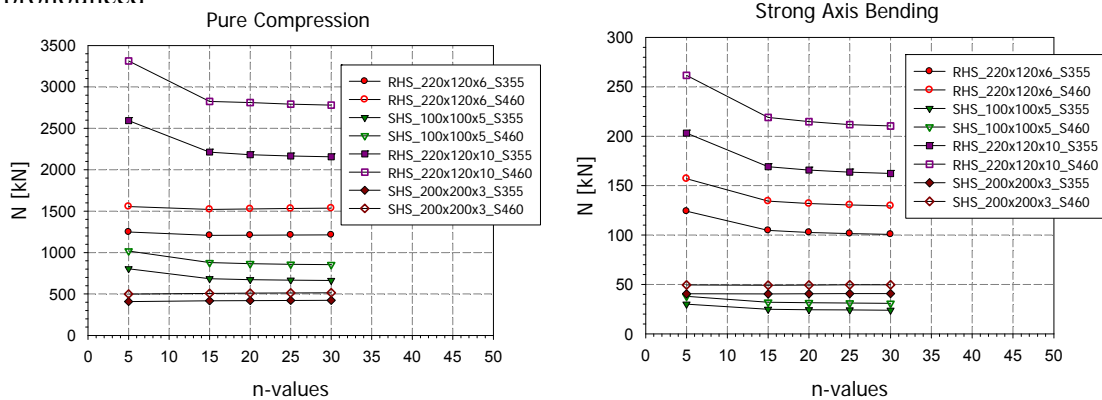


Figure 361 – F.E. results – a) sections in compression – b) sections under major-axis bending.

Figure 362a plots various moment-rotation curves obtained for a SHS100x100x5 under major-axis bending obtained through different values of strain-hardening coefficients; Figure 362b reports on the load-displacement response of the same section in compression. One may notice that the cross-section carrying capacity in both load cases is nearly constant for values of the strain-hardening coefficients ranging from 20 to 30. However, low values of

n are seen to lead to higher resistances and deformations at peak load, especially for $n = 5$

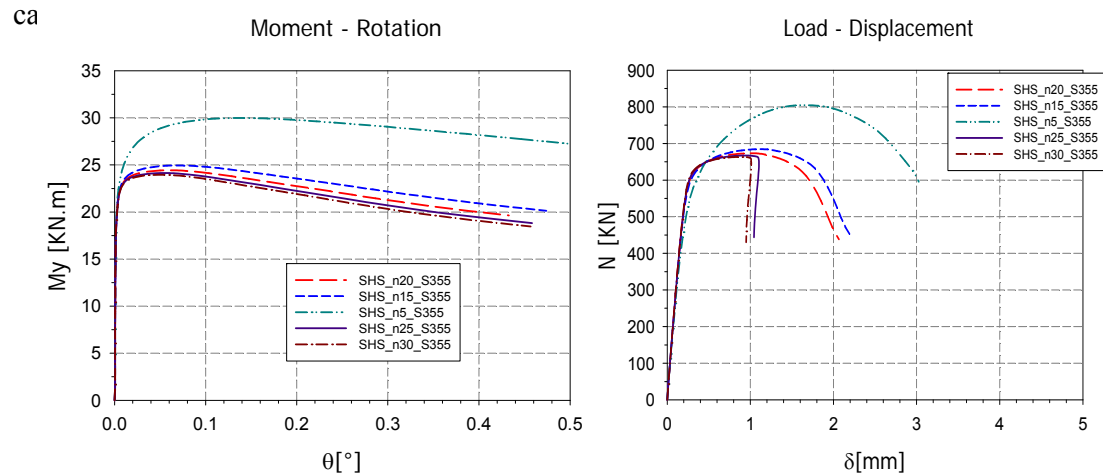


Figure 362 – SHS100x100x5 cross-section carrying capacity a) moment-rotation curves – b) load-shortening behaviour of section loaded in compression

Results show that for slender sections, the cross-section resistance to compression and major-axis bending is nearly constant for various values of the strain-hardening coefficients. However, low values of n are seen to lead to higher resistances for stockier sections.

On the basis of these results, coupled with the experimental observations, a value of the exponent $n = 22$ was adopted to launch the parametric study on cold-formed tubes of normal steel grades. Besides, when using double R.-O. equations, a pair $n = 8$ and $m = 5$ can safely be adopted in F.E. models.

9.2.2. Cold-formed sections with high steel grades

Another set of tensile coupon were collected where tensile tests were performed on cold-formed high strength steel hollow sections, covering steel grades between S460 and S960. Tensile coupons were extracted from the flat faces of the corresponding hollow sections. As for the normal steel grade, for each of the collected test result, the experimental data was plotted and compared to so-called “Ramberg-Osgood equations” (both simple R.-O. and double R.-O. formulations), where exponent coefficients were deduced from the test by fitting the experimental data.

Table 71 represents a summary of all test series containing section sizes, steel grades, and obtained values of the simple R.-O. parameter n . The strain-hardening coefficients obtained

are shown in Figure 363, where B/t is the width-to-thickness ratio for the weld, flat and corner faces.

Table 71 – Coupon test results used within present study.

Tensile test	b [mm]	t [mm]	Steel grade [N/mm ²]	$\sigma_{0.2}$ [N/mm ²]	σ_u [N/mm ²]	ϵ_y [%]	ϵ_u [%]	n [-]
T1	110	4	700	676.3	763.3	0.65	11.18	32.96
T2	110	4	700	744.4	805.2	3.37	12.65	52.39
T3	110	4	700	741.3	803.9	3.14	11.88	49.90
T4	110	4	700	728.1	802.4	3.40	12.97	42.64
T5	150	4	700	807.4	878.6	0.68	6.57	40.55
T6	150	4	700	783.2	832.8	0.58	4.38	48.67
T7	150	4	700	813.5	869.9	0.68	6.90	51.92
T8	130	4	500	580.4	651.8	0.59	9.23	32.77
T9	130	4	500	564.2	644.0	0.51	13.93	31.91
T10	130	4	500	597.8	654.2	0.54	8.37	40.96
T11	130	4	500	592.7	658.2	0.54	10.32	37.34
T12	200	5	500	534.4	604.7	0.56	11.89	32.86
T13	200	5	500	558.1	613.8	0.46	9.59	40.31
T14	200	5	500	514.0	609.1	0.52	10.90	23.39
T15	200	5	500	472.2	589.4	0.40	12.78	18.65
T16	200	4	500	546.0	603.4	0.49	10.27	39.13
T17	200	4	500	537.0	600.1	0.55	10.57	35.45
T18	200	4	500	515.2	585.3	0.55	12.91	32.50
T19	200	4	500	529.2	607.9	0.51	12.08	29.40
							Average	37.56

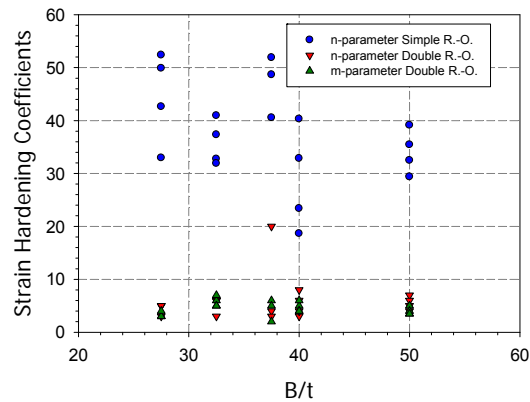


Figure 363 – Simple and double R.-O. calculated parameters for high strength steel tensile tests

G.M.N.I.A. parametric studies have been conducted on high strength steel cross-sections in order to analyse the influence of various parameters on the resistance of cold-formed tubes, by means of shell F.E. numerical results. The following set of parameters was adopted:

- eight cross-section shapes either in compression or in bending;
- steel grades: S690;
- two different load cases: compression N or major axis bending M_y ;

- simple R.-O. material law, with different values of R.-O. coefficients n .

Figure 364 presents the ultimate loads reached for each value of n used in the parametric study with a simple R.-O material model. It is observed that, in the case of a simple R.-O. material law, quite close failure loads are reached, whatever the load case considered; one may however note higher peak loads for the smallest n values, where the influence of strain-hardening effects is more pronounced.

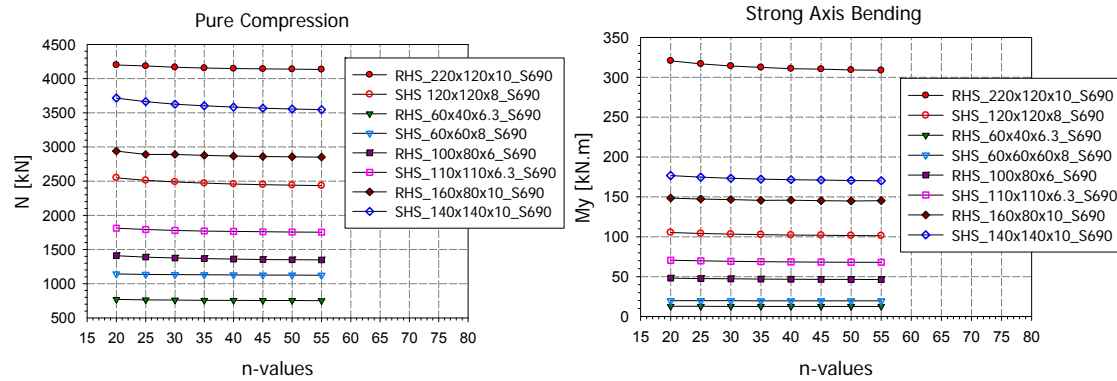


Figure 364 – F.E. results – a) sections in compression – b) sections under major-axis bending.

On the basis of these results, coupled with the experimental observations, a value of the exponent $n = 40$ was adopted in the numerical parametric study for cold-formed members of steel grade $f_y = 690 \text{ N/mm}^2$.

9.3. Annex 3: Selection of the loading combinations adopted in the experimental main buckling tests

A sub-study was conducted in an attempt to choose adequately the loading combinations and element lengths. In total 45 combinations were considered and are presented in Table 72.

Table 72 – Load combination launched numerically – a) rectangular sections – b) circular sections

Comb.#	Cross-section shape	Load case	Bending moment distribution	Length [mm]	e_z [mm]	e_y [mm]	F [kN] Eurocode
1	RHS_S355CF_220x120x6	70%N+30% M_y	Constant	4700	57.5	0.0	496.2
2	RHS_S355CF_220x120x6	60%N+40% M_y	Constant	4700	91.7	0.0	425.3
3	RHS_S355CF_220x120x6	40%N+30% M_y +30% M_z	Constant	4700	108.6	55.7	283.5
4	RHS_S355CF_200x100x4	70%N+30% M_y	Constant	4700	69.7	0.0	227.0
5	RHS_S355CF_200x100x4	60%N+40% M_y	Constant	4700	110.8	0.0	194.6
6	RHS_S355CF_220x120x6	60%N+40% M_y	Constant	3500	61.5	0.0	637.1
7	RHS_S355CF_220x120x6	40%N+30% M_y +30% M_z	Constant	3500	72.7	37.2	424.7
8	RHS_S355CF_200x100x4	60%N+40% M_y	Constant	3500	69.1	0.0	312.1
9	RHS_S355CF_200x100x4	70%N+30% M_y	Triangular	3500	72.4	0.0	364.1
10	RHS_S355CF_200x100x4	60%N+40% M_y	Triangular	3500	115.1	0.0	312.1
11	RHS_S355CF_220x120x6	60%N+40% M_y	Constant	4000	72.2	0.0	541.0
12	RHS_S355CF_220x120x6	40%N+30% M_y +30% M_z	Constant	4000	85.4	43.8	360.7
13	RHS_S355CF_200x100x4	60%N+40% M_y	Constant	4000	84.6	0.0	255.1
14	RHS_S355CF_220x120x6	70%N+30% M_y	Triangular	4000	75.5	0.0	631.2
15	RHS_S355CF_220x120x6	60%N+40% M_y	Triangular	4000	120.3	0.0	541.0
16	RHS_S355CF_200x100x4	70%N+30% M_y	Triangular	4000	88.6	0.0	297.6
17	RHS_S355CF_200x100x4	60%N+40% M_y	Triangular	4000	141.0	0.0	255.1
18	RHS_S355CF_200x100x4	50%N+25% M_y +25% M_z	Constant	4700	87.4	34.2	157.8
19	RHS_S355CF_200x100x4	50%N+25% M_y +25% M_z	Constant	4000	67.7	26.5	203.7
20	RHS_S355CF_200x100x4	40%N+30% M_y +30% M_z	Constant	4000	104.0	41.7	163.0
21	RHS_S355CF_200x100x4	50%N+25% M_y +25% M_z	Triangular	4000	112.8	44.2	203.7

Comb.#	Cross-section shape	Load case	Bending moment distribution	Length [mm]	e_z [mm]	e_y [mm]	F [kN] Eurocode
22	CHS_S355HR_159x6.3	50%N+50% M_y	Constant	4900	78.8	0.0	301.8
23	CHS_S355HR_159x6.3	33%N+33% M_y +33% M_z	Constant	4900	107.9	75.3	201.2
24	CHS_S355HR_159x6.3	50%N+50% M_y	Triangular	4900	169.6	0.0	301.8
25	CHS_S355HR_159x6.3	33%N+33% M_y +33% M_z	Triangular	4900	183.4	117.6	201.2
26	CHS_S355HR_159x6.3	50%N+50% M_y	Constant	4000	69.5	0.0	398.5
27	CHS_S355HR_159x6.3	33%N+33% M_y +33% M_z	Constant	4000	88.4	58.7	265.7
28	CHS_S355HR_159x6.3	50%N+50% M_y	Triangular	4000	132.8	0.0	398.5
29	CHS_S355HR_159x6.3	33%N+33% M_y +33% M_z	Triangular	4000	142.4	89.6	265.7
30	CHS_S355HR_159x6.3	50%N+50% M_y	Constant	4500	73.6	0.0	342.2
31	CHS_S355HR_159x6.3	33%N+33% M_y +33% M_z	Constant	4500	97.9	66.9	228.1
32	CHS_S355HR_159x6.3	50%N+50% M_y	Triangular	4500	151.0	0.0	342.2
33	CHS_S355HR_159x6.3	33%N+33% M_y +33% M_z	Triangular	4500	163.0	103.7	228.1
34	CHS_S355HR_159x5	50%N+50% M_y	Constant	4900	77.8	0.0	244.6
35	CHS_S355HR_159x5	33%N+33% M_y +33% M_z	Constant	4900	106.9	75.1	163.0
36	CHS_S355HR_159x5	50%N+50% M_y	Triangular	4900	167.7	0.0	244.6
37	CHS_S355HR_159x5	33%N+33% M_y +33% M_z	Triangular	4900	181.8	117.0	163.0
38	CHS_S355HR_159x5	50%N+50% M_y	Constant	4000	68.9	0.0	322.0
39	CHS_S355HR_159x5	33%N+33% M_y +33% M_z	Constant	4000	88.0	58.8	214.7
40	CHS_S355HR_159x5	50%N+50% M_y	Triangular	4000	131.8	0.0	322.0
41	CHS_S355HR_159x5	33%N+33% M_y +33% M_z	Triangular	4000	141.7	87.7	214.7
42	CHS_S355HR_159x5	50%N+50% M_y	Constant	4500	72.8	0.0	277.1
43	CHS_S355HR_159x5	33%N+33% M_y +33% M_z	Constant	4500	97.1	66.9	184.7
44	CHS_S355HR_159x5	50%N+50% M_y	Triangular	4500	149.5	0.0	277.1
45	CHS_S355HR_159x5	33%N+33% M_y +33% M_z	Triangular	4500	161.8	103.2	184.7

9.4. Annex 4: Load path sensitivity – $L = 5500 \text{ mm}$

In order to examine the influence of the loading introduction on the member resistance, 4 different loading sequences were examined, based on different combinations described as follows:

- case 1: one-stage loading: applying N and M_y and M_z simultaneously;
- case 2: two-stages loading: applying N in a first stage, then continue with M_y+M_z simultaneously in the second stage;
- case 3: two-stages loading: applying M_y in a first stage then continue with $N+M_z$ simultaneously in the second stage;
- case 4: applying M_z in a first stage, then continue with $N+M_y$ simultaneously in the second stage.

A series of F.E. calculations were carried out on rectangular and square hollow sections by considering the load sequences described above.

Obtained G.M.N.I.A. results for rectangular members of $L = 5500 \text{ mm}$ are compared with Eurocode 3 predictions and presented in Figure 365 to Figure 368 and results obtained for square one of $L = 5500 \text{ mm}$ are shown in Figure 369 to Figure 372.

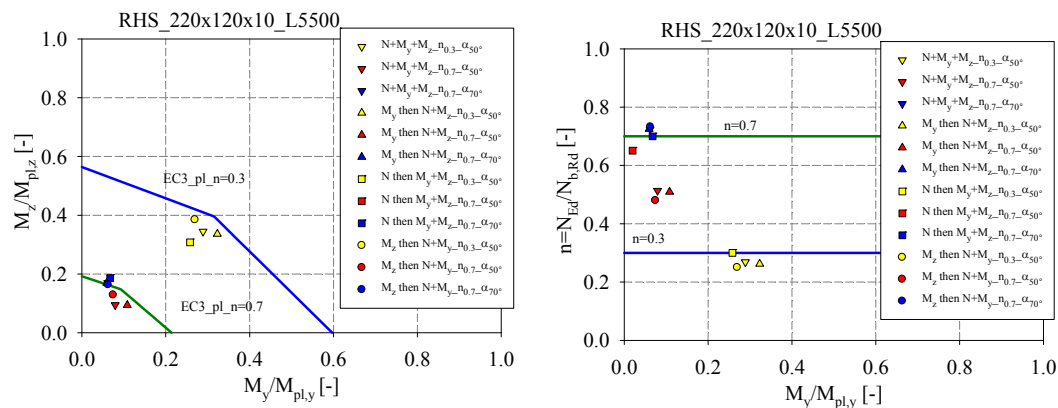


Figure 365 – Comparison of G.M.N.I.A. results for the RHS_220x120x10 of $L = 5500$ – a) m_z vs. m_y diagram – b) n vs. m_y diagram

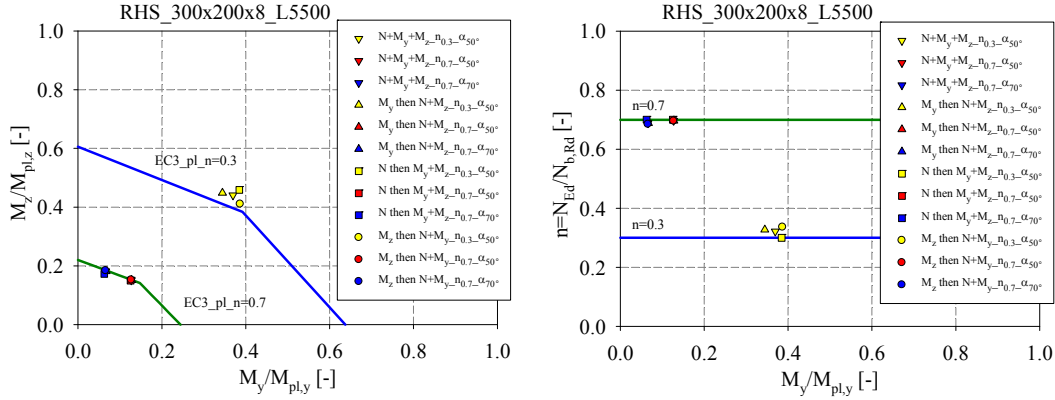


Figure 366 – Comparison of G.M.N.I.A. results for the RHS_300x200x8 of $L = 5500$ – a) m_z vs. m_y diagram – b) n vs. m_y diagram

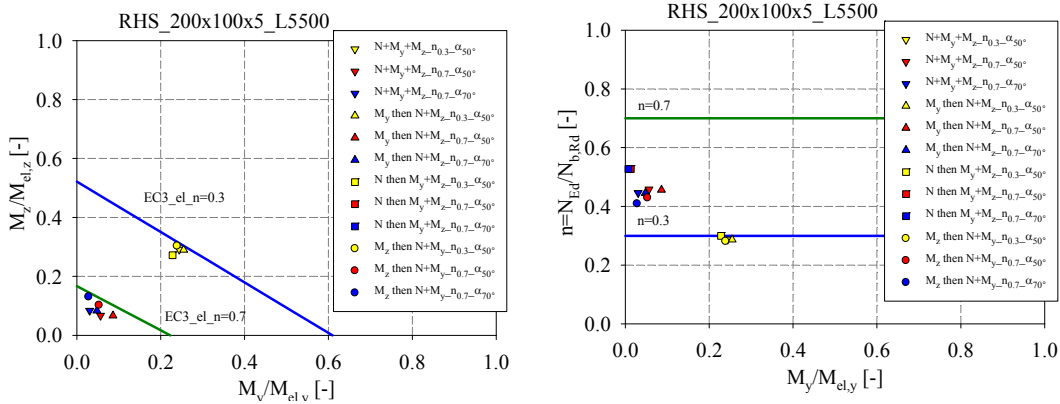


Figure 367 – Comparison of G.M.N.I.A. results for the RHS_200x100x5 of $L = 5500$ – a) m_z vs. m_y diagram – b) n vs. m_y diagram

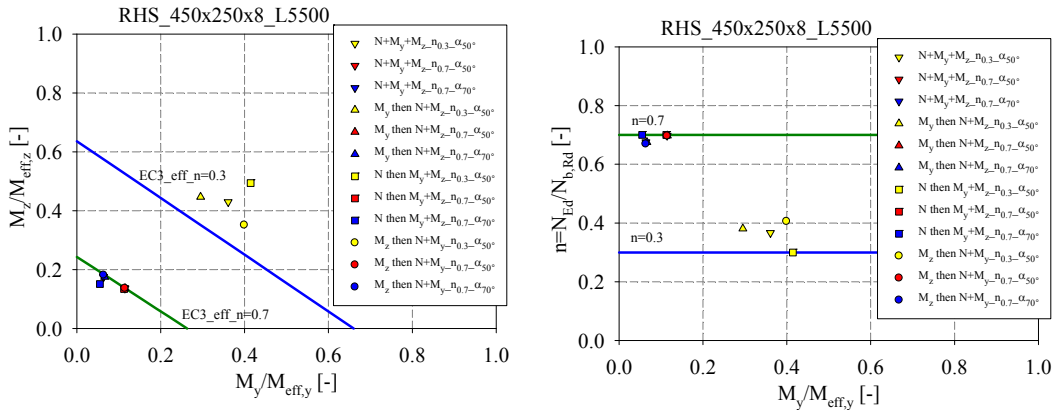


Figure 368 – Comparison of G.M.N.I.A. results for the RHS_450x250x8 of $L = 5500$ – a) m_z vs. m_y diagram – b) n vs. m_y diagram

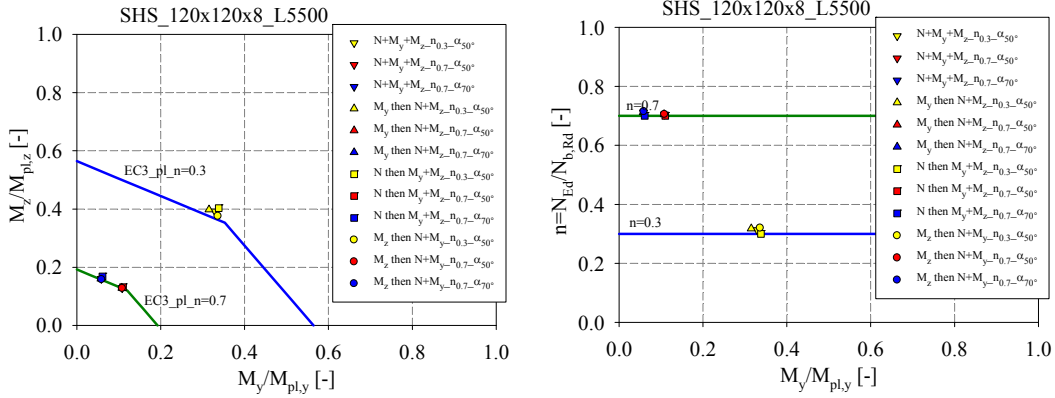


Figure 369 – Comparison of G.M.N.I.A. results for the SHS_120x120x8 of $L = 5500$ – a) m_z vs. m_y diagram – b) n vs. m_y diagram

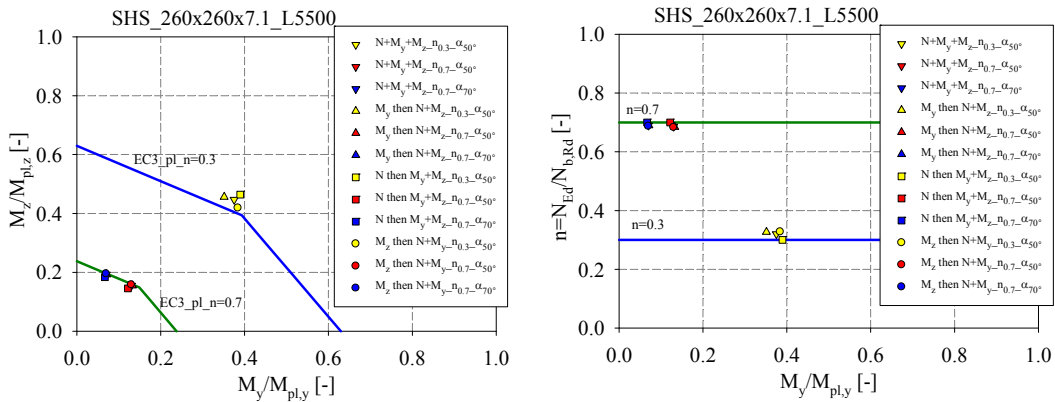


Figure 370 – Comparison of G.M.N.I.A. results for the SHS_260x260x7.1 of $L = 5500$ – a) m_z vs. m_y diagram – b) n vs. m_y diagram

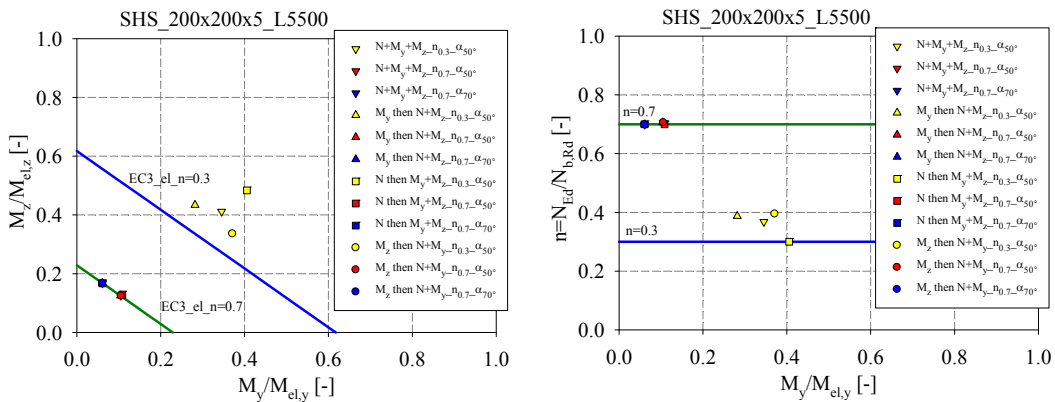


Figure 371 – Comparison of G.M.N.I.A. results for the SHS_200x200x5 of $L = 5500$ – a) m_z vs. m_y diagram – b) n vs. m_y diagram

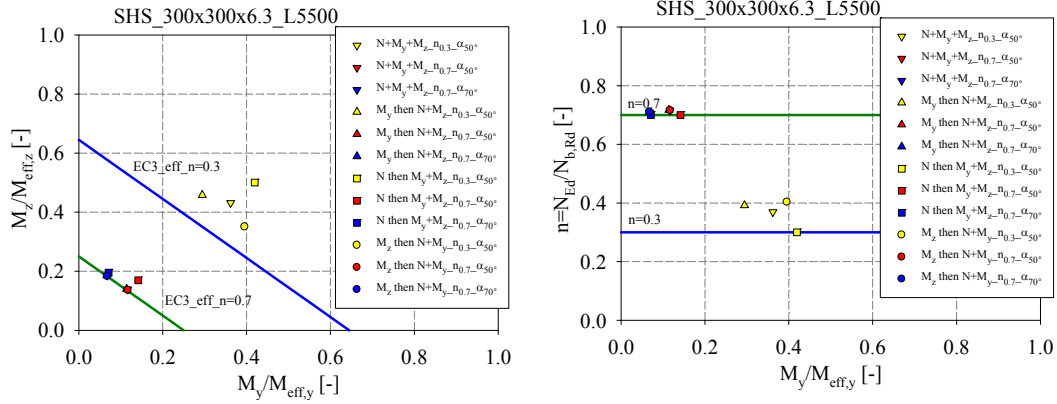


Figure 372 – Comparison of G.M.N.I.A. results for the SHS_300x300x6.3 of $L = 5500$ – a) m_z vs. m_y diagram –
 b) n vs. m_y diagram

9.5. Annex 5: Application steps of the Overall Interaction Concept for members

The followings steps are recommended for the design of steel hollow members using the proposed O.I.C. approach.

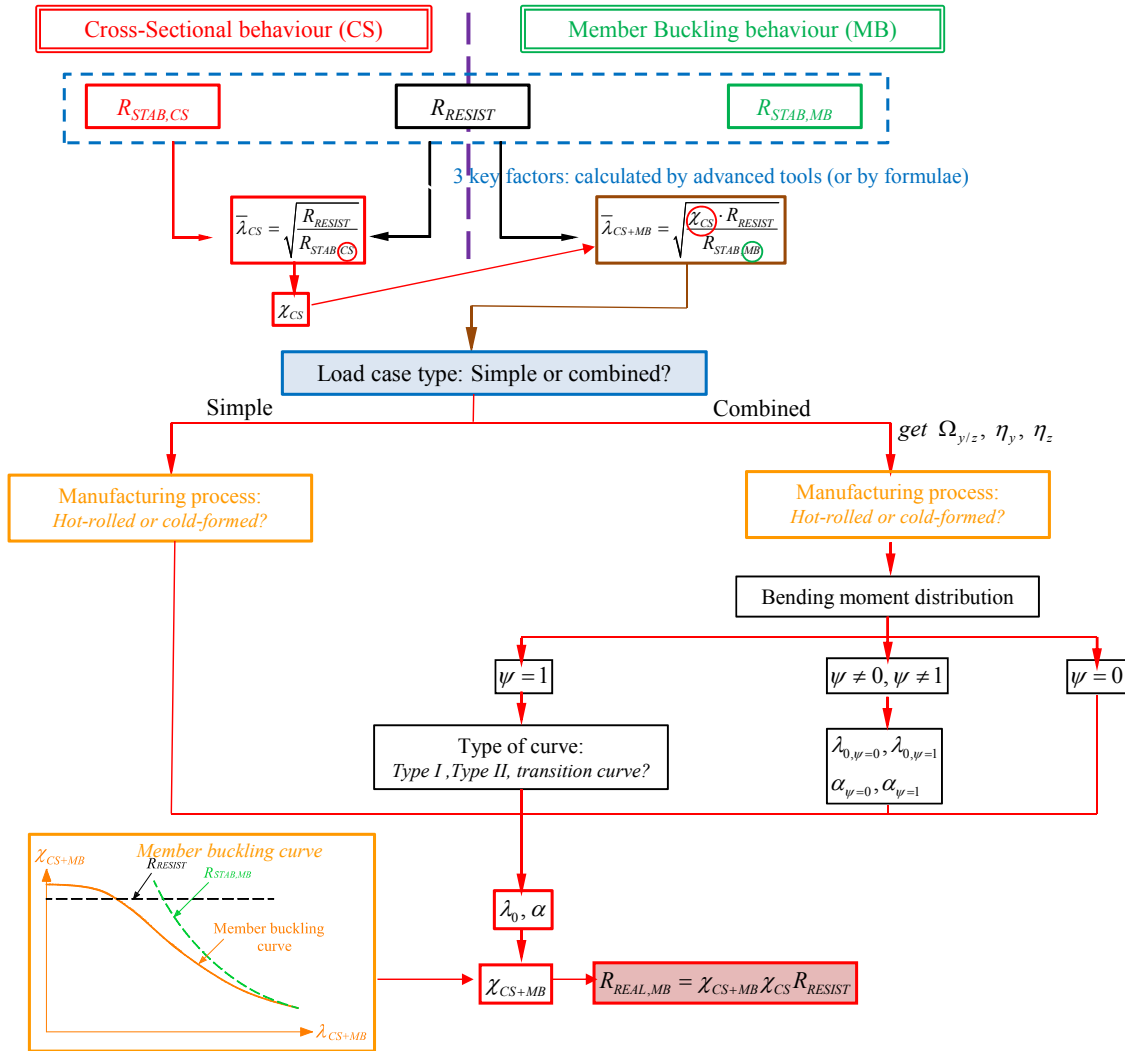


Figure 373 – Principles and application steps of the Overall Interaction Concept

9.6. Annex 6: Detailed results of beam-column tests

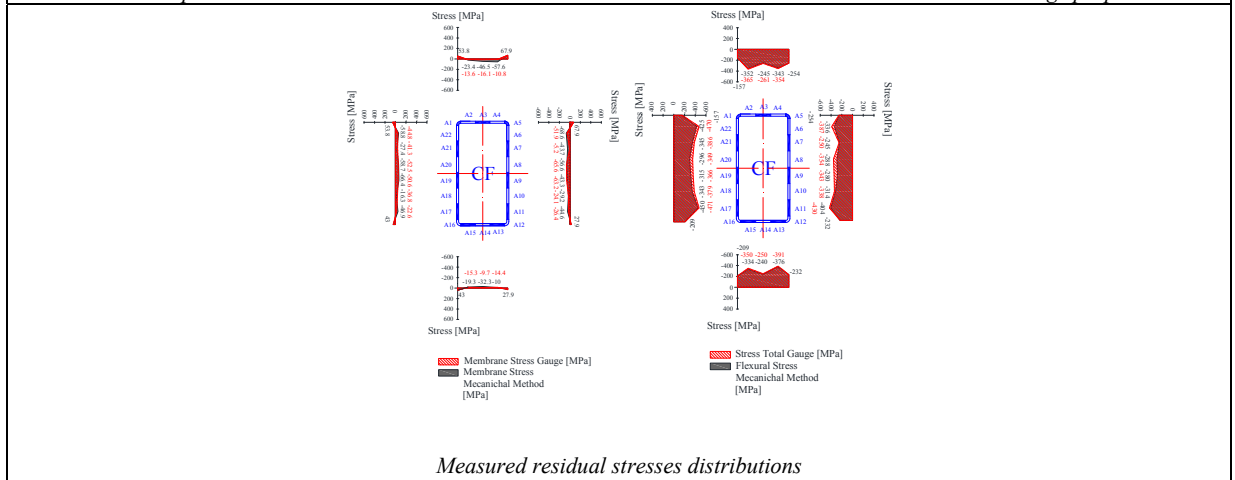
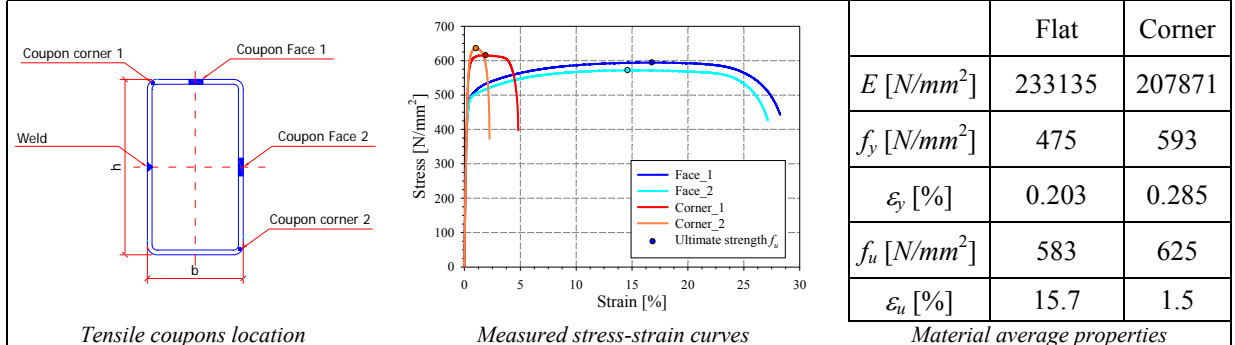
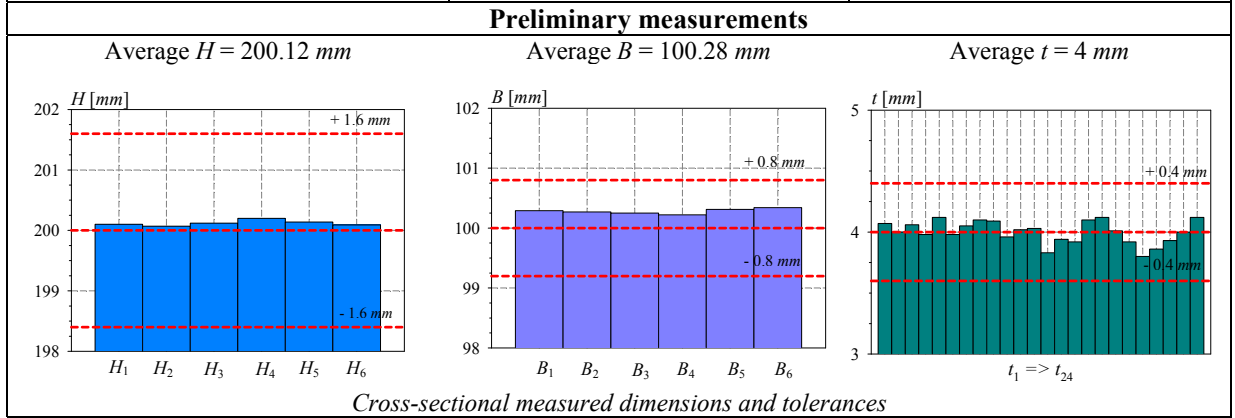
This annex presents the full sets of results associated with the main buckling tests, including the corresponding preliminary measurements performed before each test. It also provides comparisons between experimental results and their numerical counterparts.

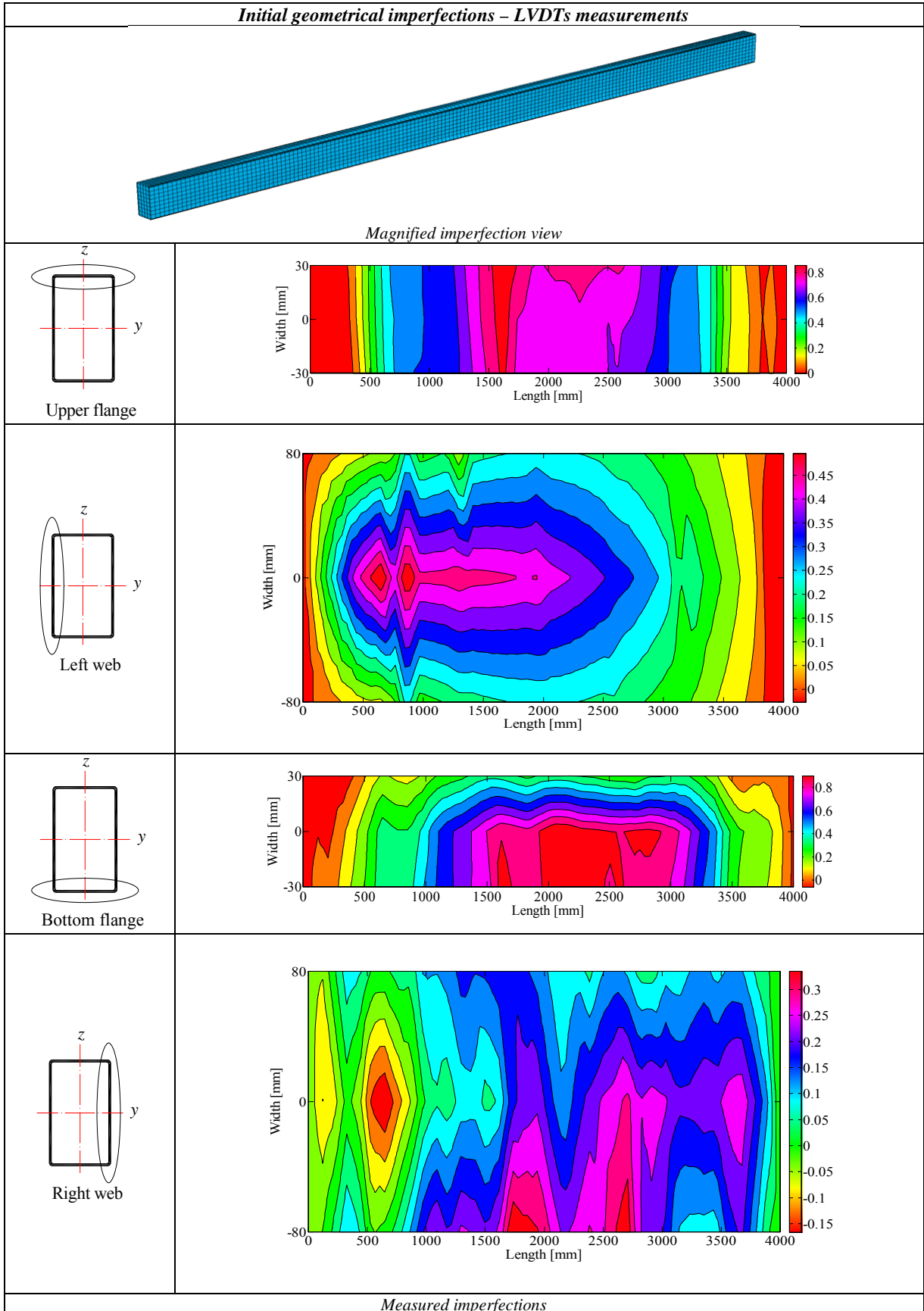
For each test, all measurements and results are summarized by mean of 4 pages standard format as follow:

- The first page provides:
 - o specimen name, shape and details;
 - o cross-sectional measured dimensions with the corresponding tolerances;
 - o measured material properties (tensile tests results);
 - o measured membrane and flexural stresses obtained by means of the electrical strain readings and of the mechanical procedure for cross-sections shapes RHS_200x100x4_CF and RHS_220x120x6_CF.
- The second and third pages provide initial geometrical imperfections obtained by means of equally-spaced linear variable displacement displayed on each specimen's plates (LVDTs measurements) and by scanning the specimen's plates by means of a laser Tracker AT401 (topometric method). The contour plots of each plate's out-of-flatness imperfections as well as a picture of the imperfection mesh fitted in the non-linear finite element model.
- The fourth page provides results obtained for stub columns tests (pure compression). It provides:
 - o relative axial force vs. strain ratio $\varepsilon / \varepsilon_y$ recordings;
 - o stub column load-shortening curves from the experimental sources before and after correction;
 - o comparison between numerical and experimental stub column load- displacement curves;

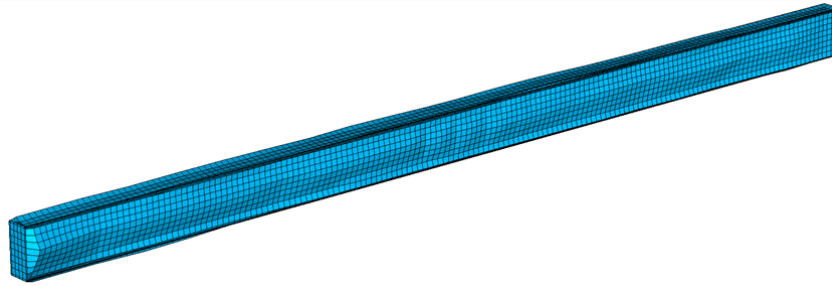
- comparison between material and stub column stress-strain curves;
- experimental failure shape after test for each specimen.
- The fifth, sixth and seventh pages provide the main buckling test results and include:
 - info on the positioning of each column between the 2 spherical supports (i.e. hinges) and the corresponding eccentricities applied at both end of the specimen;
 - LVDTs recordings on the mid-span cross-section (both lateral and transversal displacements are presented) compared to their numerical counterparts;
 - LVDTs recordings of axial shortening on the bottom endplate of the specimens;
 - column end rotations in both principal planes measured by the inclinometers fixed at both ends of the columns compared to the rotations obtained by means of the LVDTs, and to the numerical rotations obtained with the F.E. model;
 - comparison between the numerical and experimental load-displacement curves. Numerical curves are obtained by using the laser tracker AT401 and the LVDTs initial imperfections for the cold-formed RHS;
 - numerical and experimental deformed shapes for each specimen.

Test #: 1		
Specimen name	Shape	Details
RHS_S355CF_200x100x4		<p>Shape: Rectangular Hollow Section</p> <p>Nominal yield limit: 355 N/mm^2</p> <p>Length = 4000 mm</p> <p>$H = 200 \text{ mm}$ $B = 100 \text{ mm}$ $t = 4 \text{ mm}$</p> <p>Fabrication process: Cold-Formed</p> <p>Load case: $60\%N + 40\%M_y$</p> <p>Moment distribution: Constant</p>

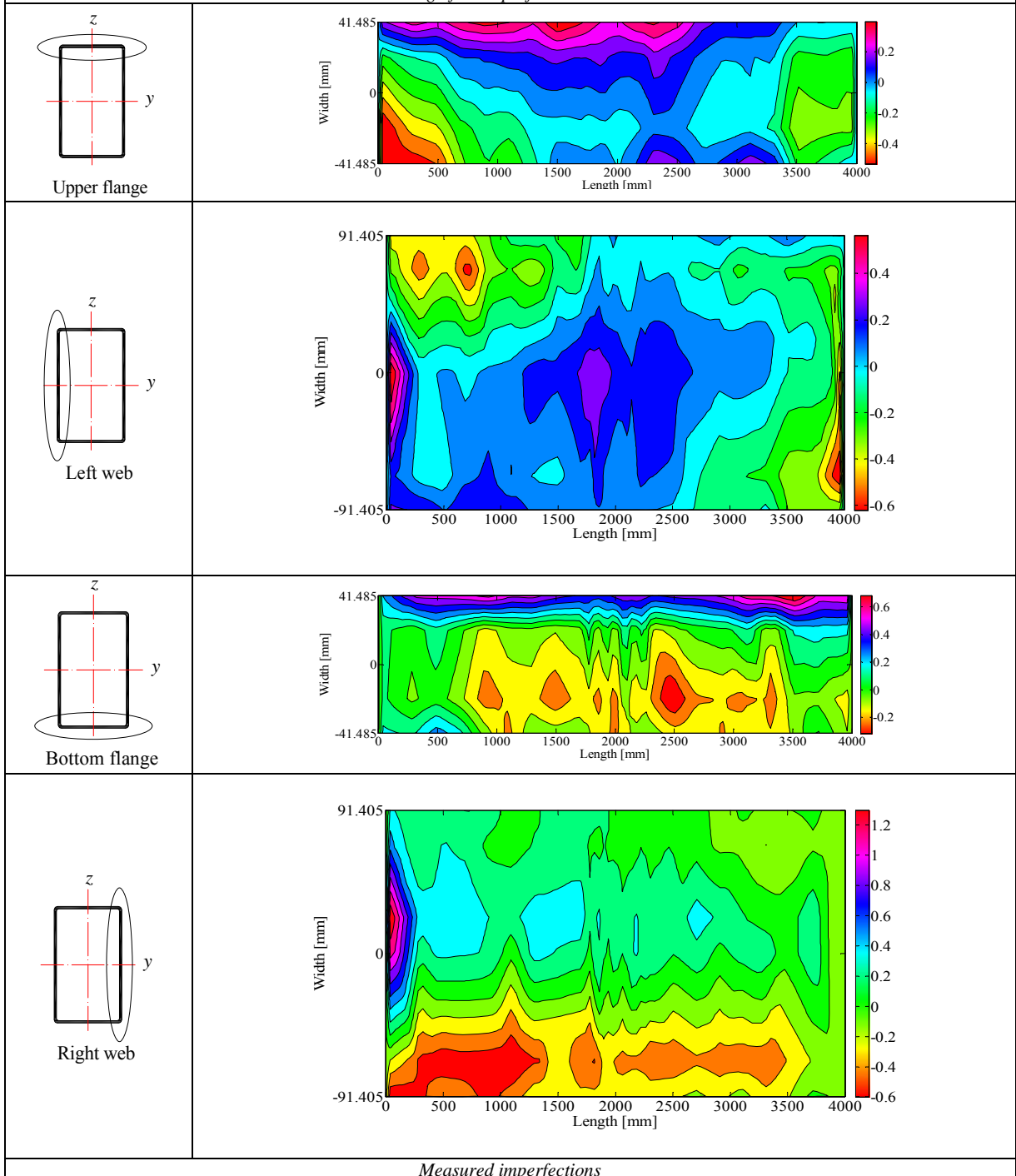




Initial geometrical imperfections – Topometric measurements

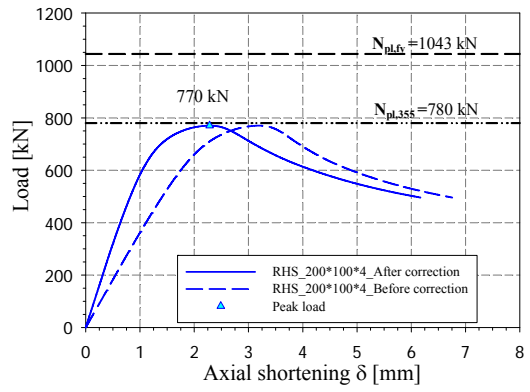
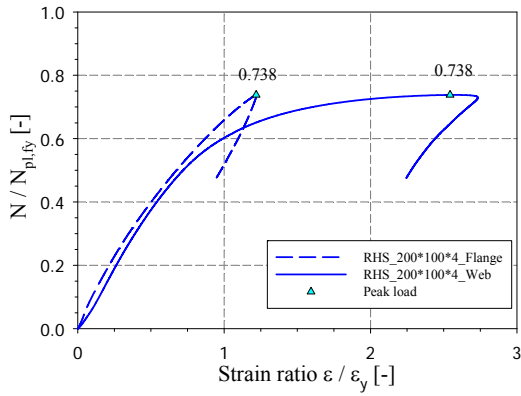


Magnified imperfection view

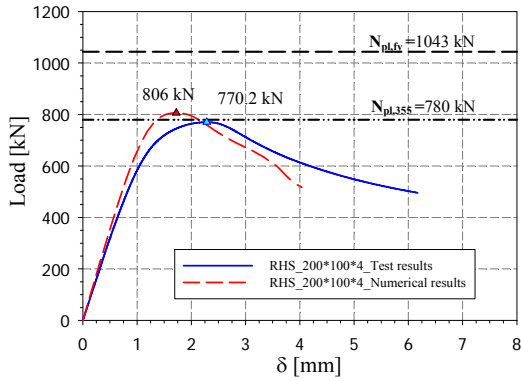


Measured imperfections

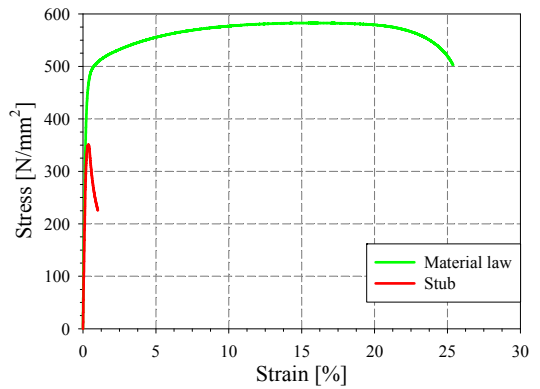
Stub column tests



Strain gauges recordings

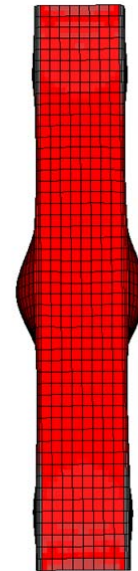


Load displacement curves before and after correction



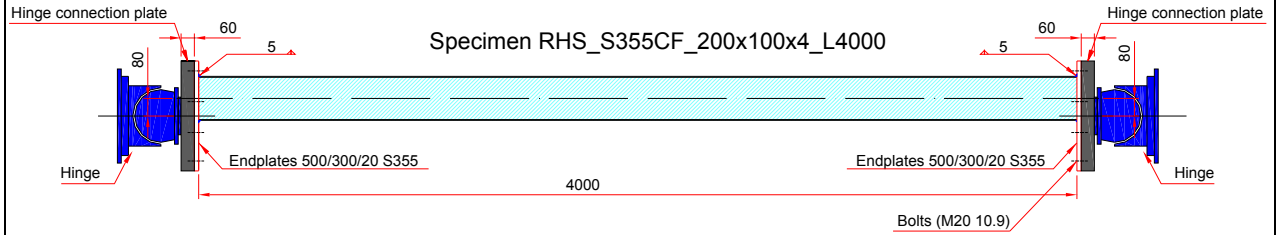
Numerical vs. experimental load displacement curves

Material stress-strain curve vs. stub stress-strain curve

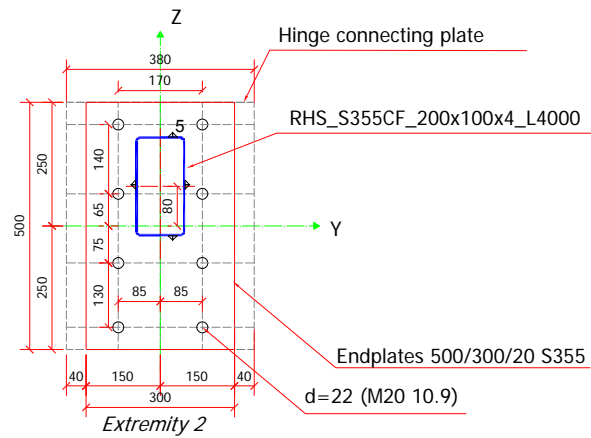
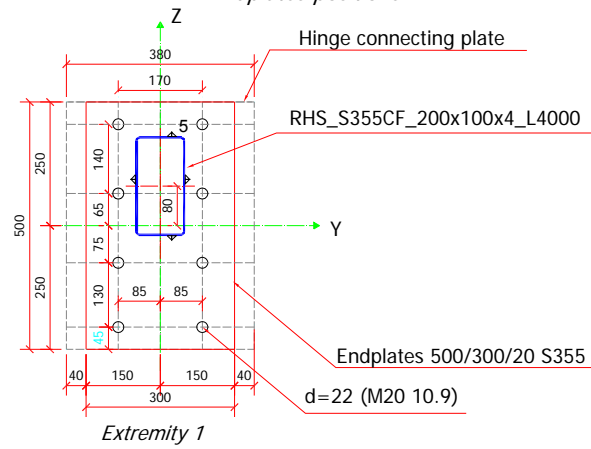


Stub column specimen after test

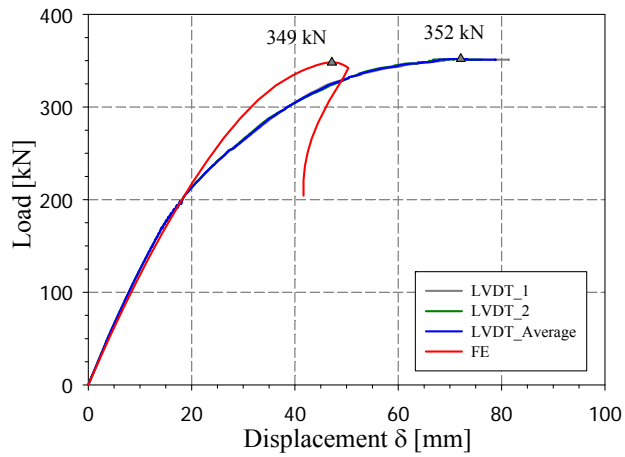
Column positioning



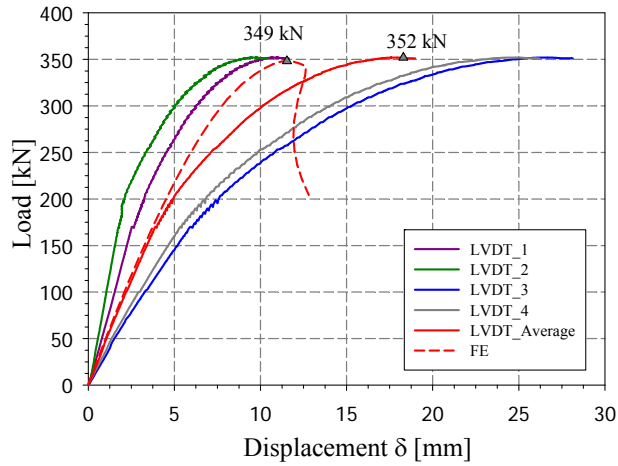
Endplates positions



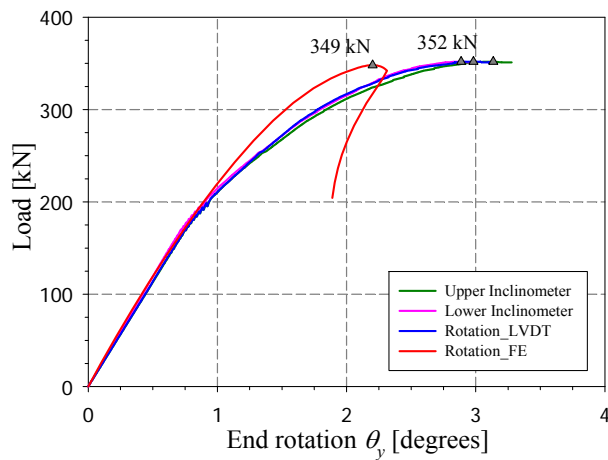
Main buckling tests



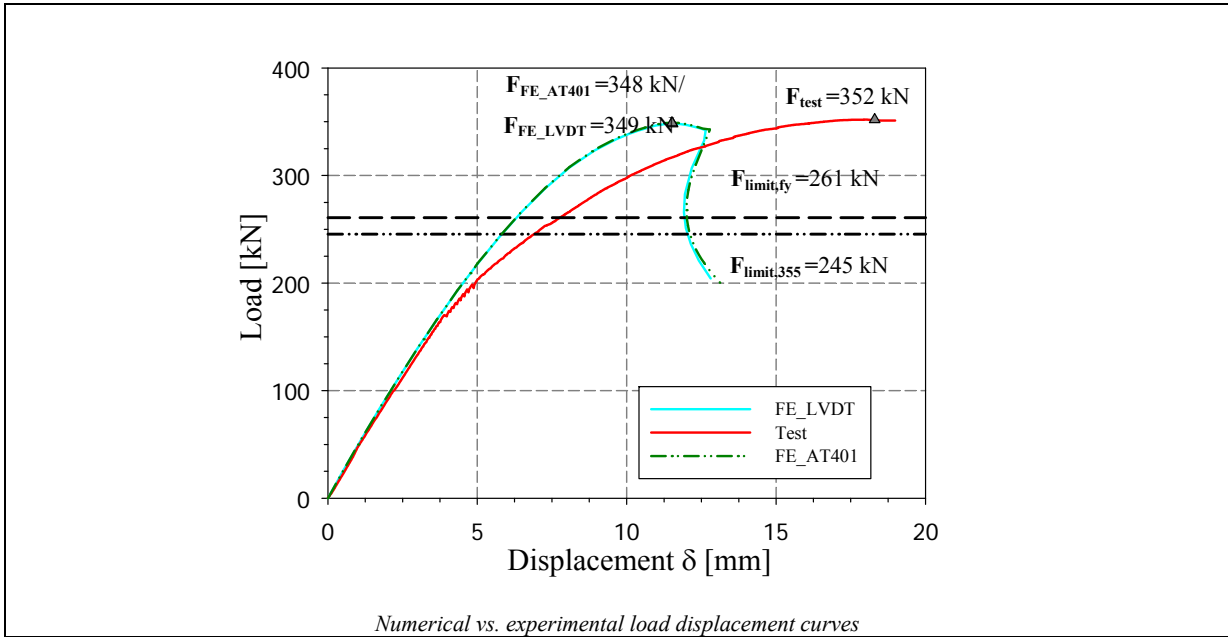
*Lateral displacement
LVDT recording mid-span displacements*

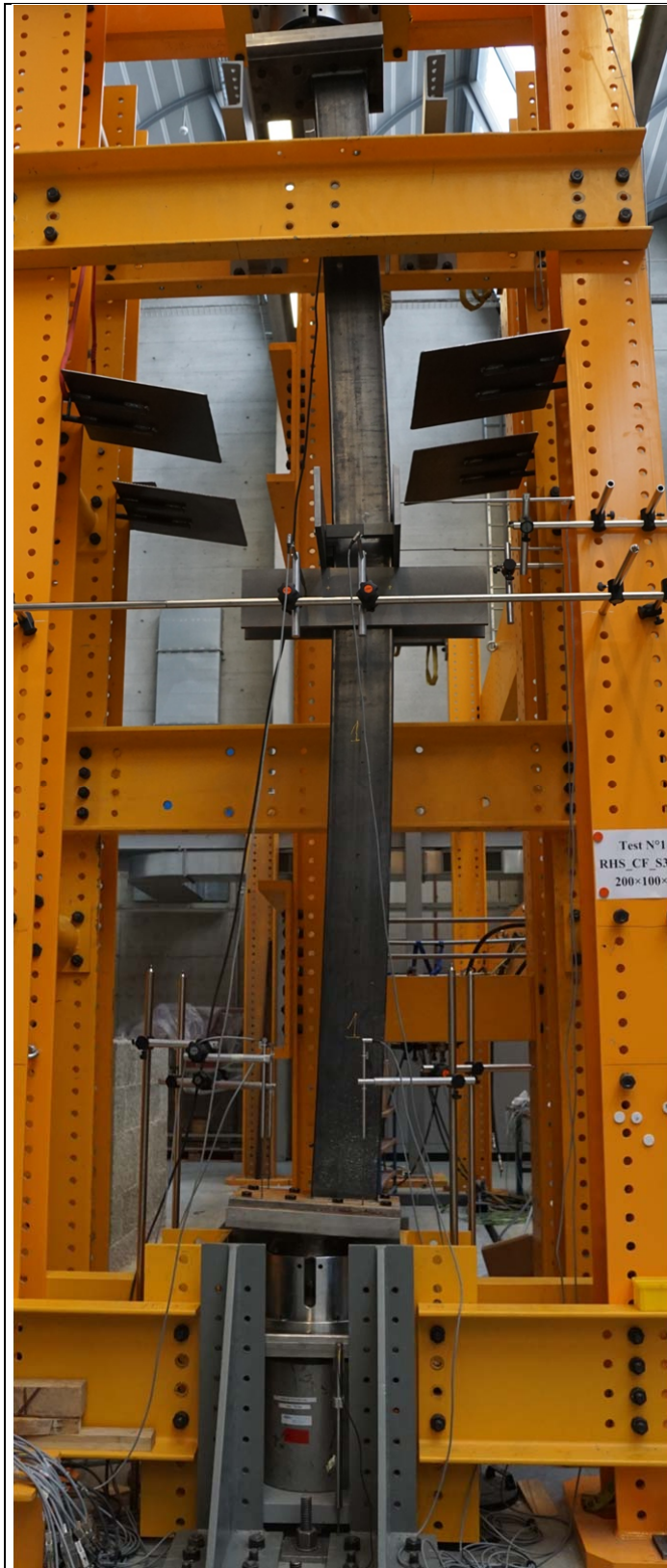


LVDTs recording axial shortening

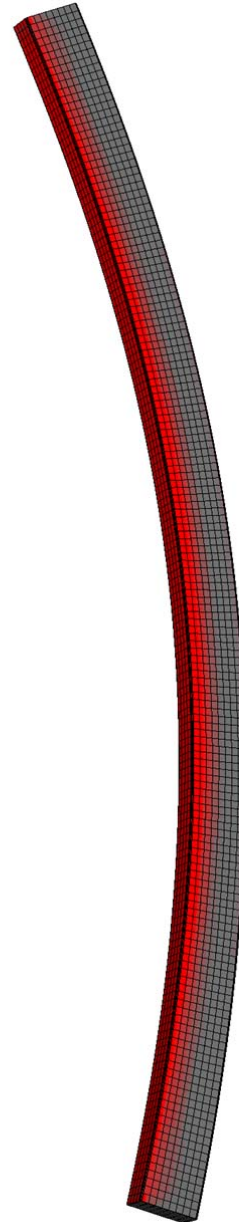


*Rotation along major axis
Column end rotations*



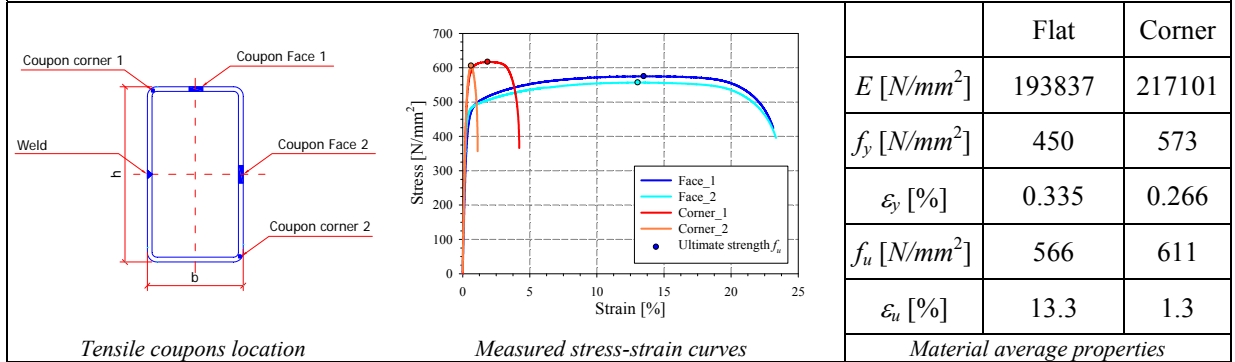
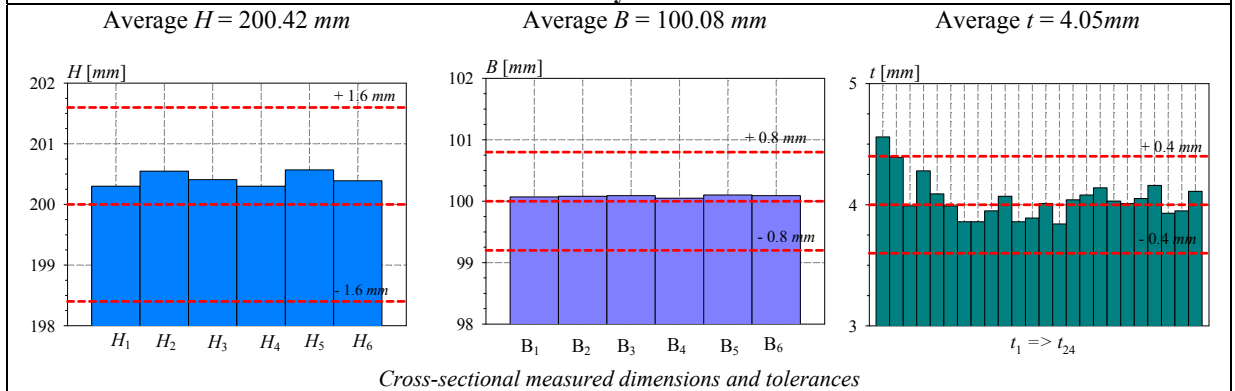


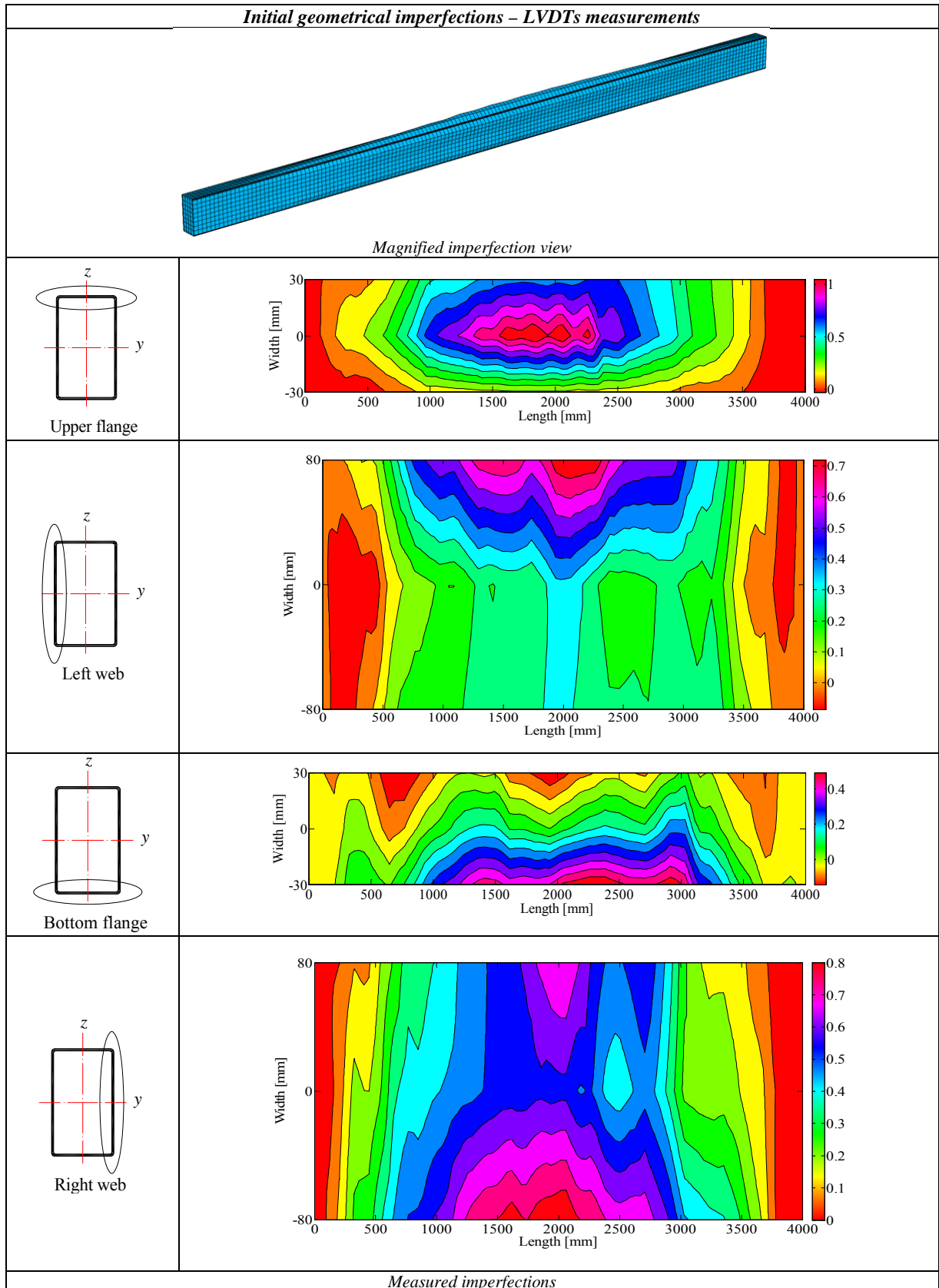
Buckling specimen after test



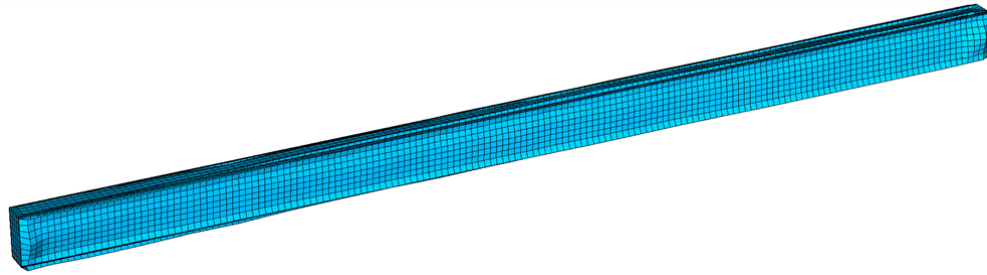
Test #: 2		
Specimen name	Shape	Details
RHS_S355CF_200x100x4		<p>Shape: Rectangular Hollow Section</p> <p>Nominal yield limit: 355 N/mm^2</p> <p>Length = 4000 mm</p> <p>$H = 200 \text{ mm}$ $B = 100 \text{ mm}$ $t = 4 \text{ mm}$</p> <p>Fabrication process: Cold-Formed</p> <p>Load case: $40\%N + 30\% M_y + 30\% M_z$</p> <p>Moment distribution: Constant</p>

Preliminary measurements

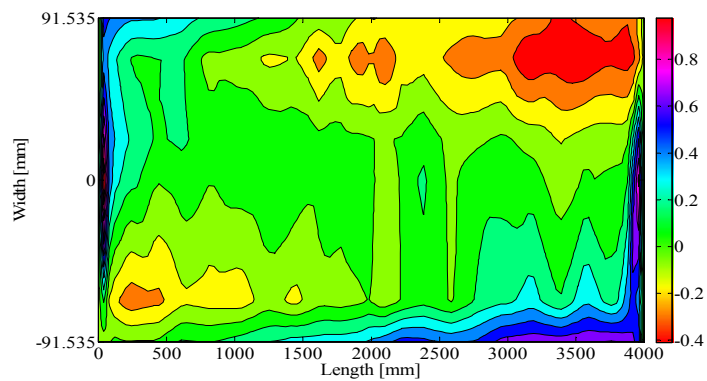
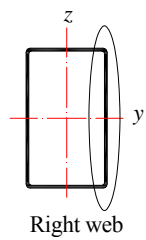
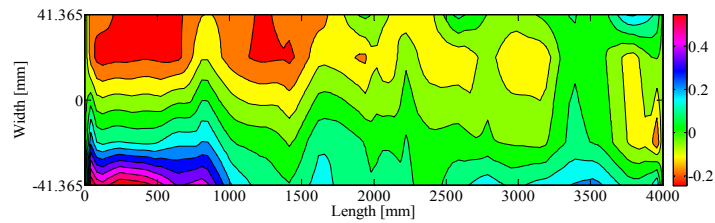
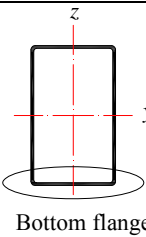
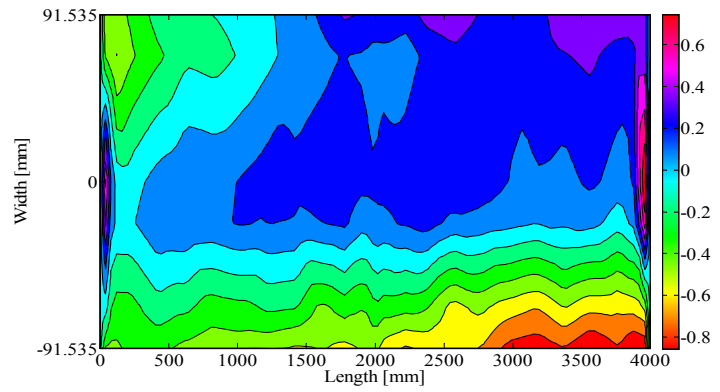
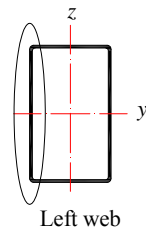
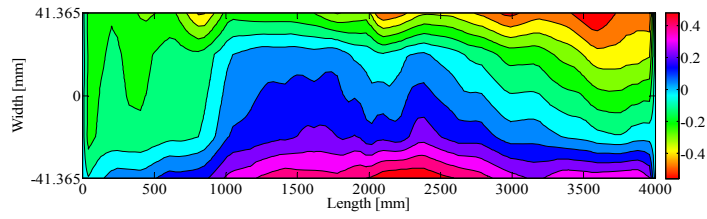
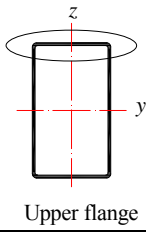




Initial geometrical imperfections – Topometric measurements

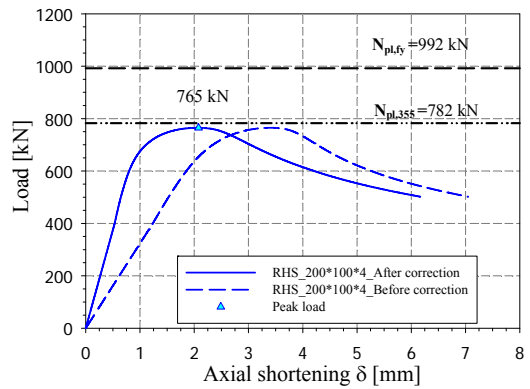
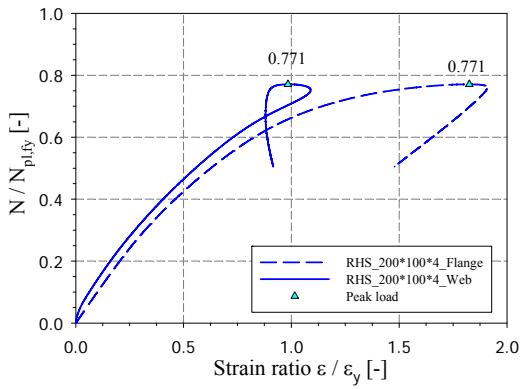


Magnified imperfection view



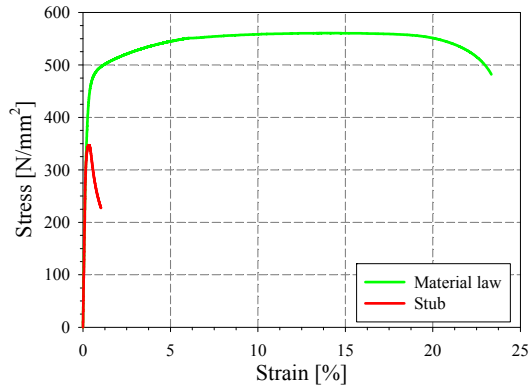
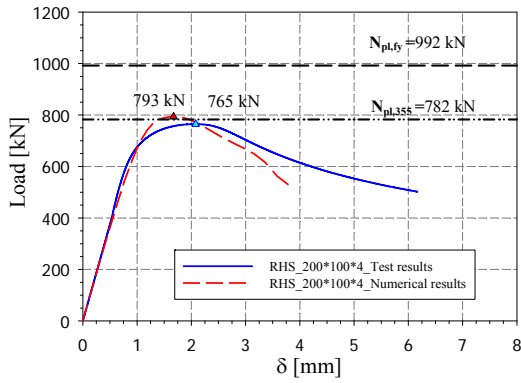
Measured imperfections

Stub column tests



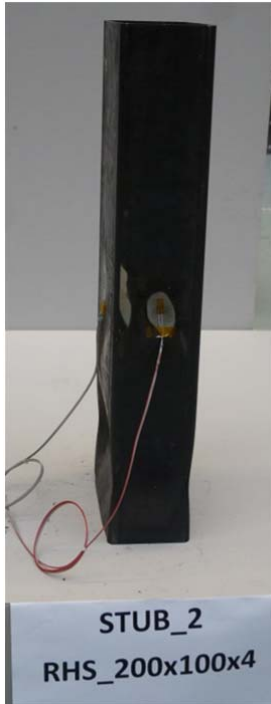
Strain gauges recordings

Load displacement curves before and after correction



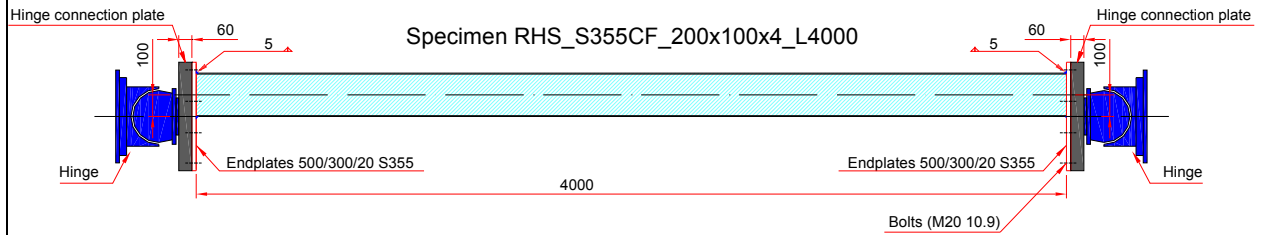
Numerical vs. experimental load displacement curves

Material stress-strain curve vs. stub stress-strain curve

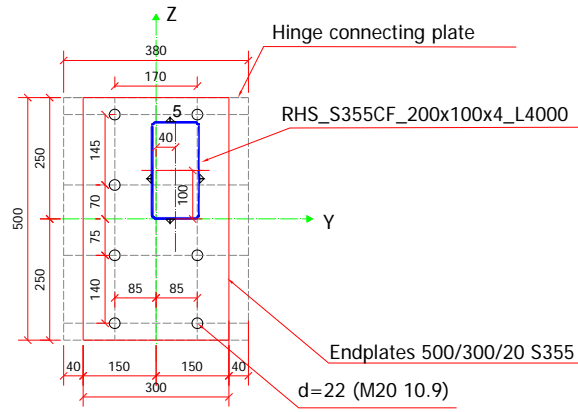


Stub column specimen after test

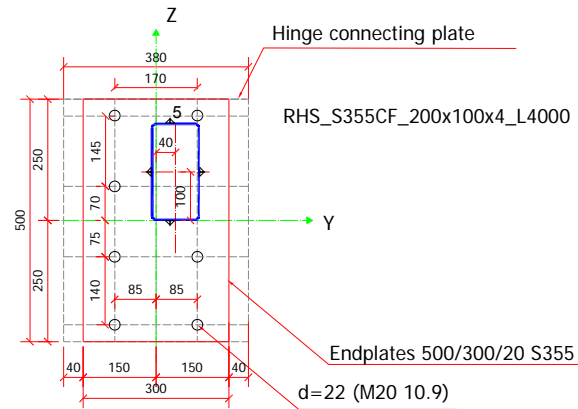
Column positioning



Endplates positions

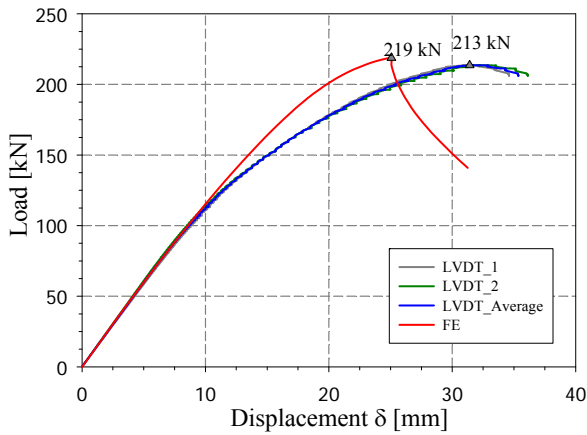


Extremity 1

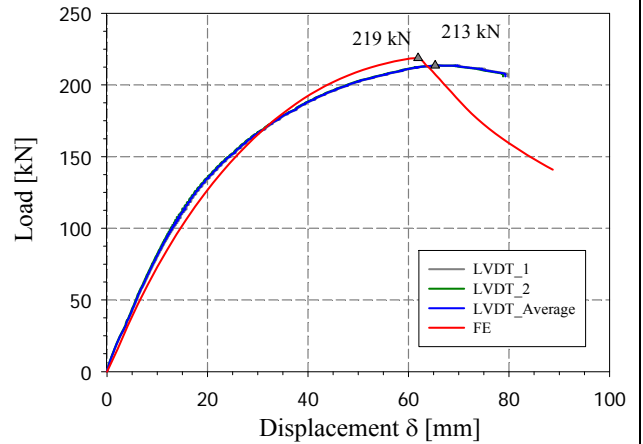


Extremity 2

Main buckling tests

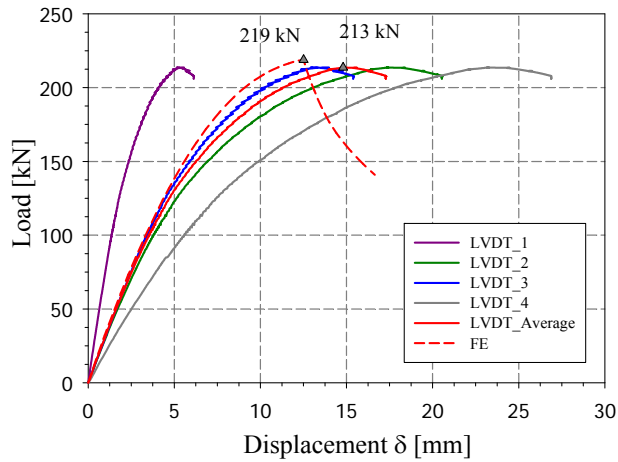


Lateral displacement

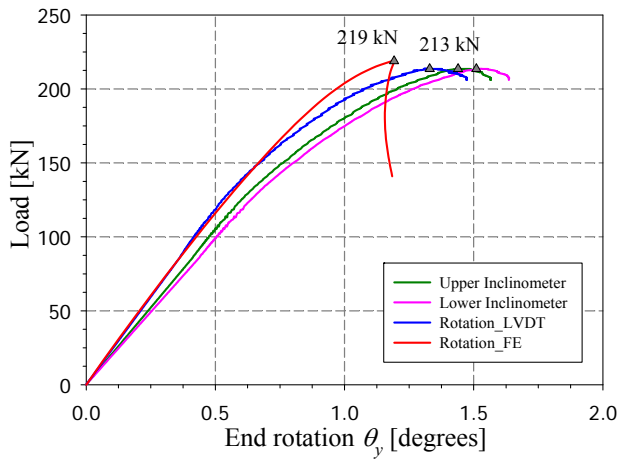


Transversal displacement

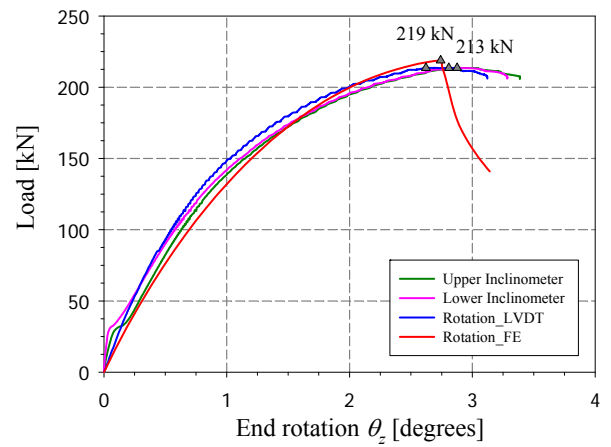
LVDT recording mid-span displacement



LVDTs recording axial shortening

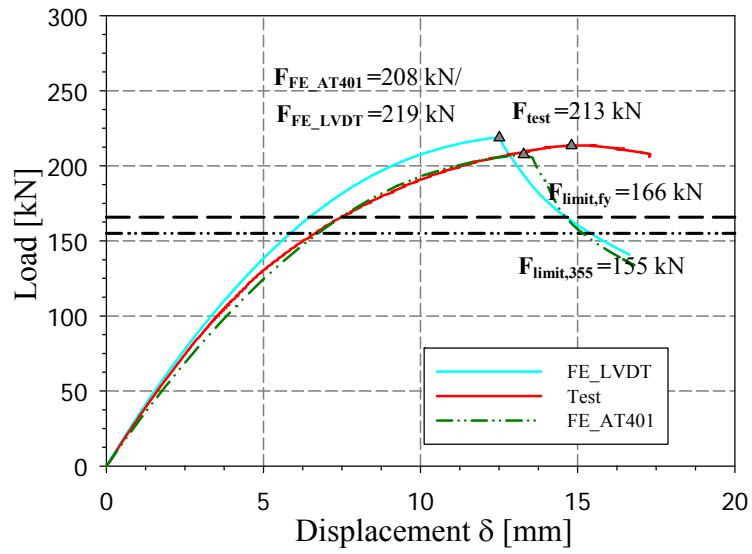


Rotation along major axis

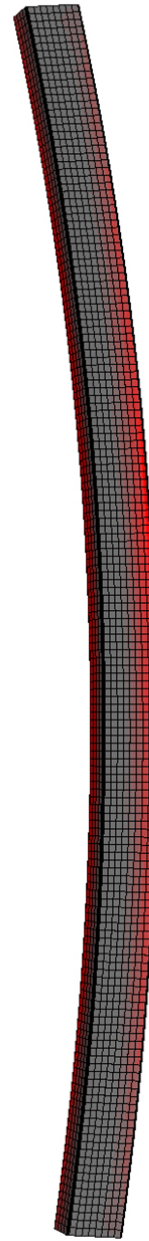


Rotation along minor axis

Column end rotations

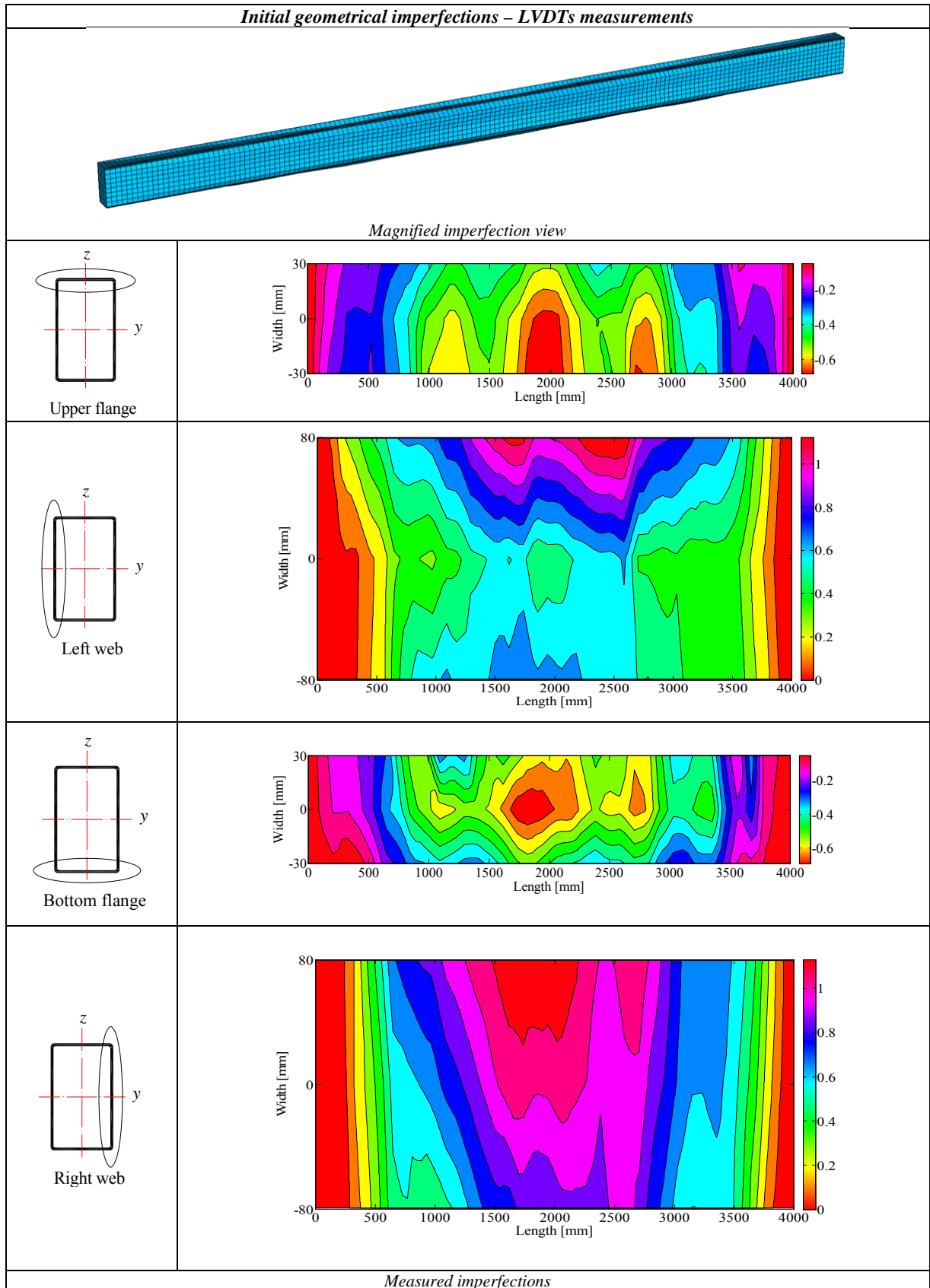


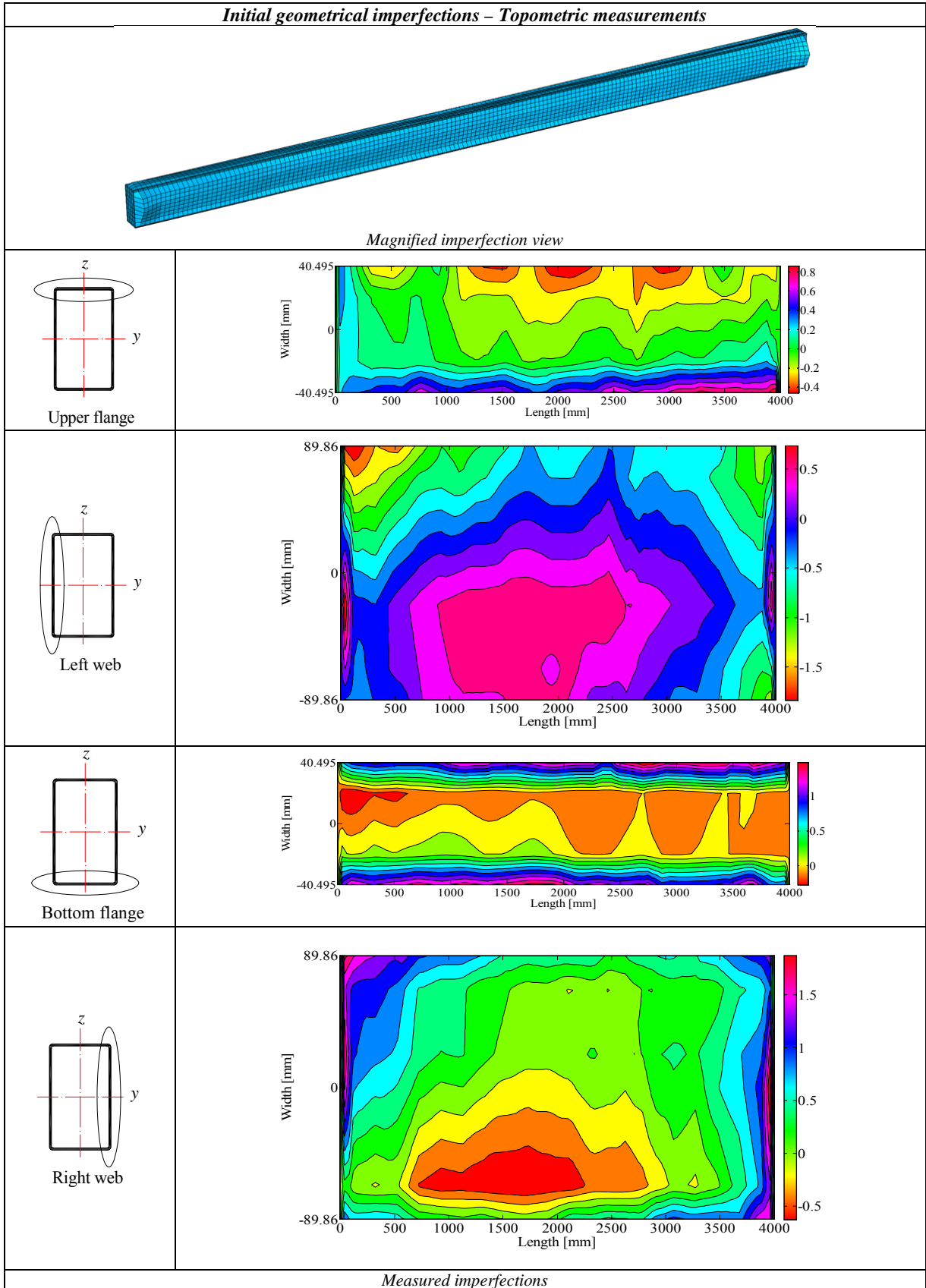
Numerical vs. experimental load displacement curves



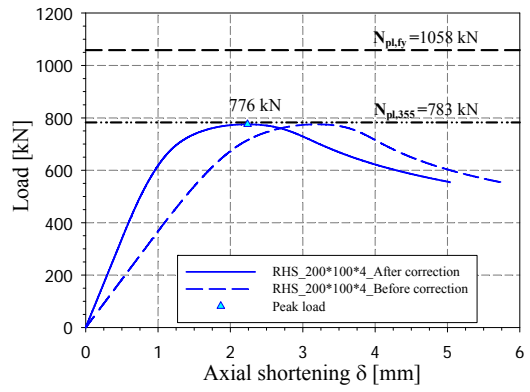
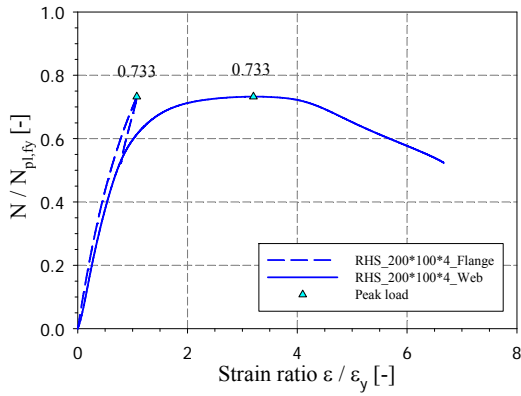
Buckling specimen after test

Test #: 3																				
Specimen name	Shape	Details																		
RHS_S355CF_200x100x4		<p>Shape: Rectangular Hollow Section</p> <p>Nominal yield limit: 355 N/mm^2</p> <p>Length = 4000 mm</p> <p>$H = 200 \text{ mm}$ $B = 100 \text{ mm}$ $t = 4 \text{ mm}$</p> <p>Fabrication process: Cold-Formed</p> <p>Load case: $60\%N + 40\%M_y$</p> <p>Moment distribution: Triangular</p>																		
Preliminary measurements																				
Average $H = 198.66 \text{ mm}$	Average $B = 99.93 \text{ mm}$	Average $t = 3.85 \text{ mm}$																		
<i>Cross-sectional measured dimensions and tolerances</i>																				
		<table border="1" style="width: 100%; border-collapse: collapse;"> <thead> <tr> <th></th> <th style="text-align: center;">Flat</th> <th style="text-align: center;">Corner</th> </tr> </thead> <tbody> <tr> <td>$E \text{ [N/mm}^2\text{]}$</td> <td style="text-align: center;">206437</td> <td style="text-align: center;">180307</td> </tr> <tr> <td>$f_y \text{ [N/mm}^2\text{]}$</td> <td style="text-align: center;">480</td> <td style="text-align: center;">588</td> </tr> <tr> <td>$\epsilon_y \text{ [%]}$</td> <td style="text-align: center;">0.234</td> <td style="text-align: center;">0.329</td> </tr> <tr> <td>$f_u \text{ [N/mm}^2\text{]}$</td> <td style="text-align: center;">589</td> <td style="text-align: center;">618</td> </tr> <tr> <td>$\epsilon_u \text{ [%]}$</td> <td style="text-align: center;">12.0</td> <td style="text-align: center;">2.4</td> </tr> </tbody> </table>		Flat	Corner	$E \text{ [N/mm}^2\text{]}$	206437	180307	$f_y \text{ [N/mm}^2\text{]}$	480	588	$\epsilon_y \text{ [%]}$	0.234	0.329	$f_u \text{ [N/mm}^2\text{]}$	589	618	$\epsilon_u \text{ [%]}$	12.0	2.4
	Flat	Corner																		
$E \text{ [N/mm}^2\text{]}$	206437	180307																		
$f_y \text{ [N/mm}^2\text{]}$	480	588																		
$\epsilon_y \text{ [%]}$	0.234	0.329																		
$f_u \text{ [N/mm}^2\text{]}$	589	618																		
$\epsilon_u \text{ [%]}$	12.0	2.4																		
<i>Tensile coupons location</i>	<i>Measured stress-strain curves</i>	<i>Material average properties</i>																		

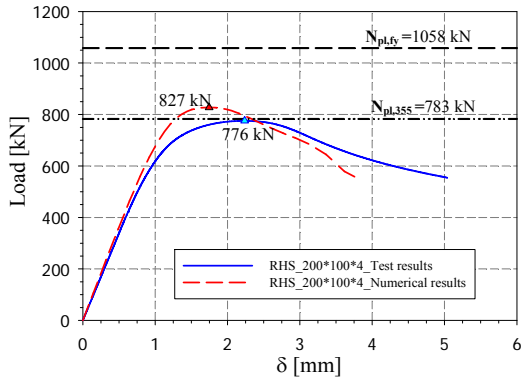




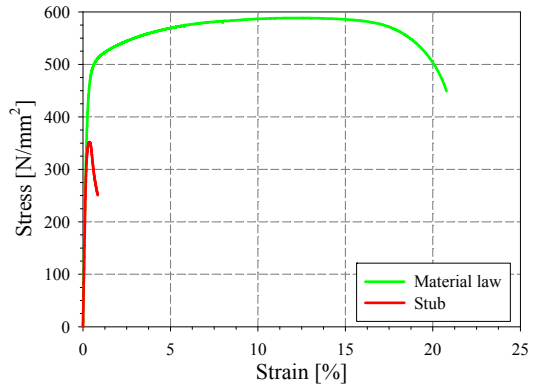
Stub column tests



Strain gauges recordings

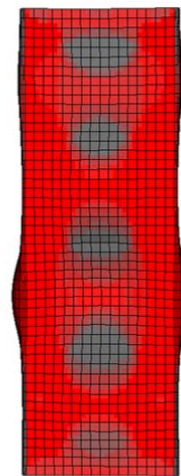
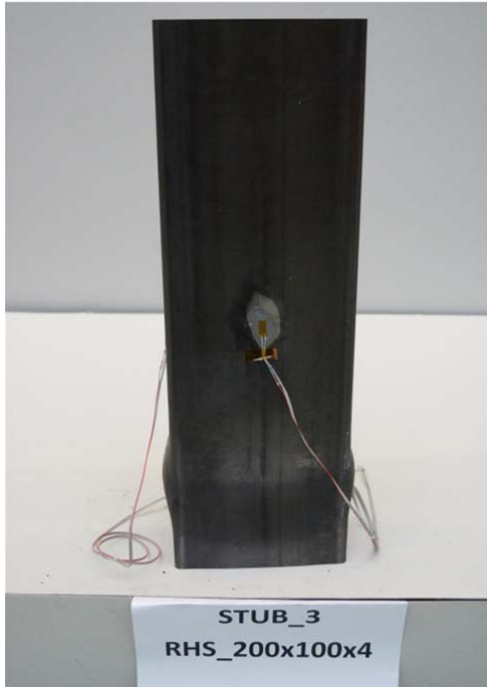


Load displacement curves before and after correction



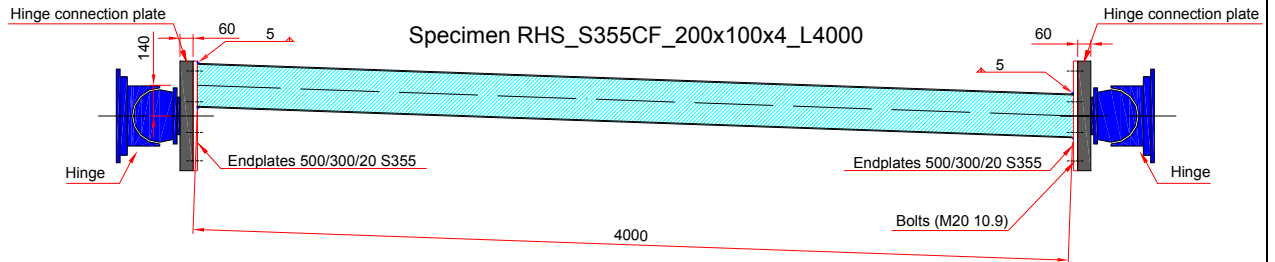
Numerical vs. experimental load displacement curves

Material stress-strain curve vs. stub stress-strain curve

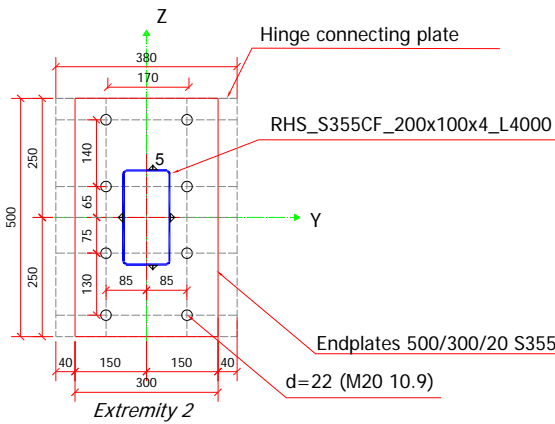
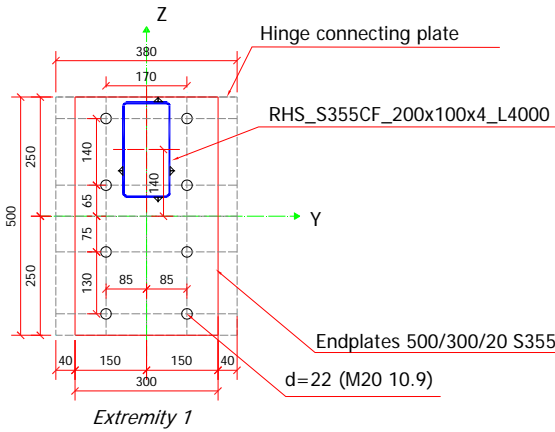


Stub column specimen after test

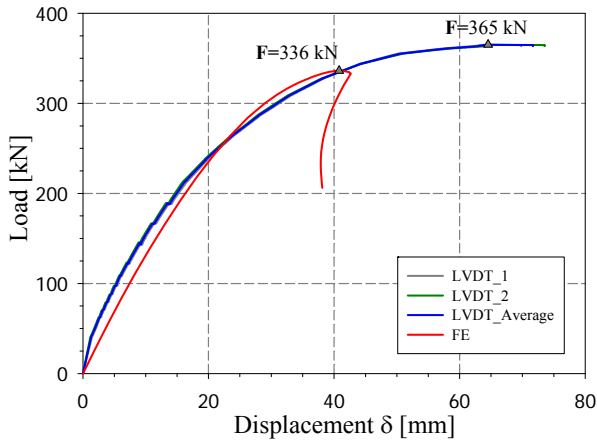
Column positioning



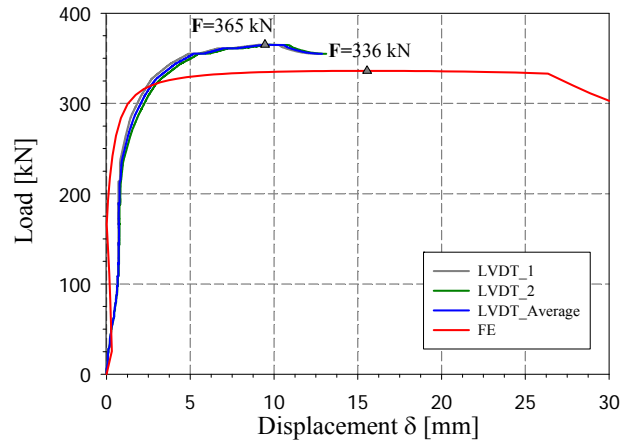
Endplates positions



Main buckling tests

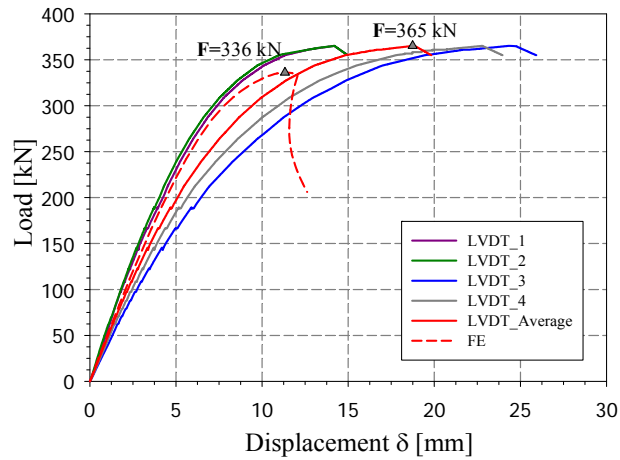


Lateral displacement

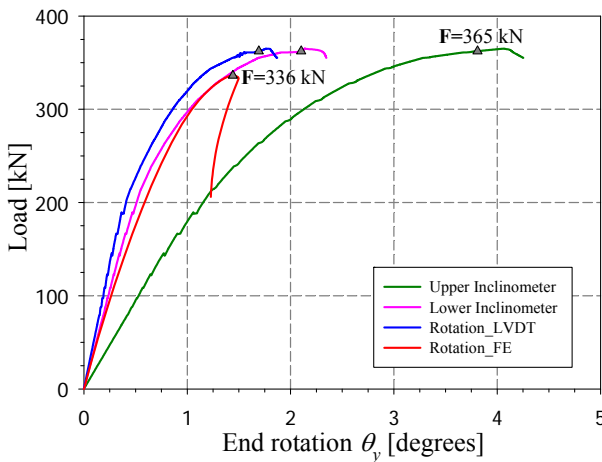


Transversal displacement

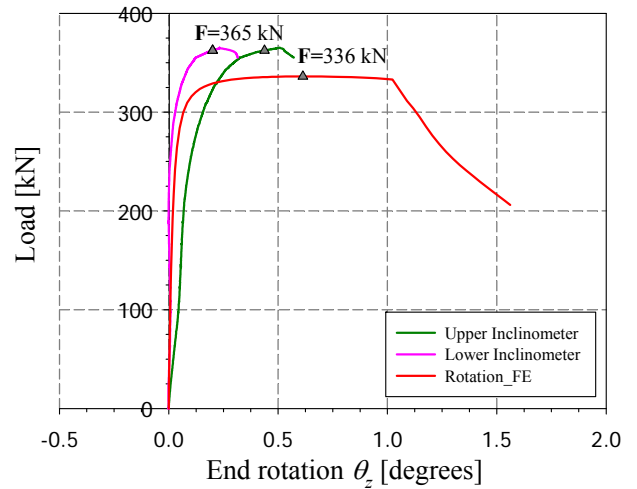
LVDT recording mid-span displacement



LVDTs recording axial shortening

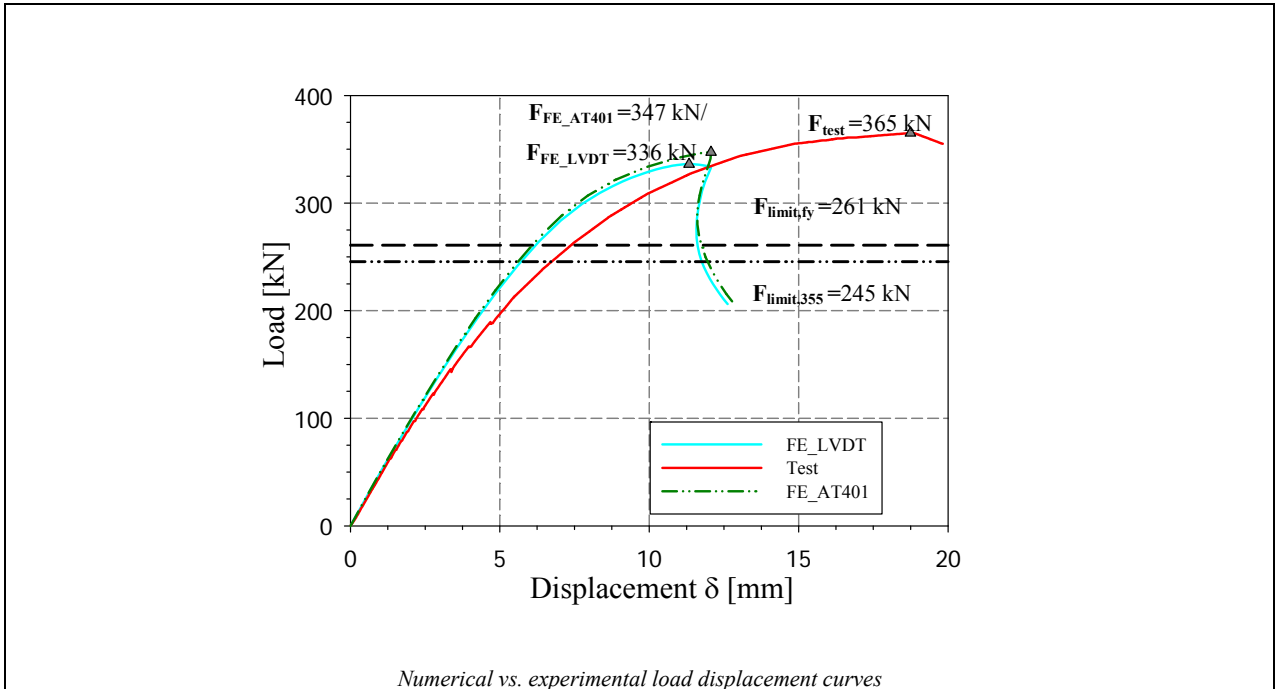


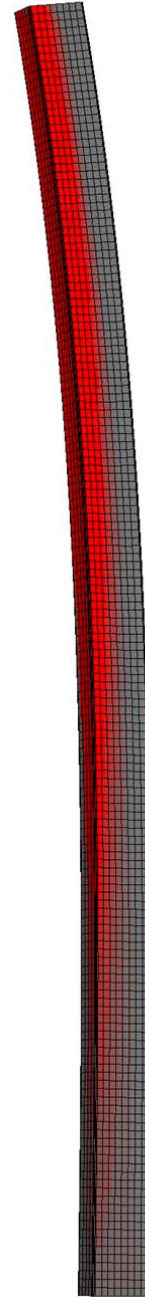
Rotation along major axis



Rotation along minor axis

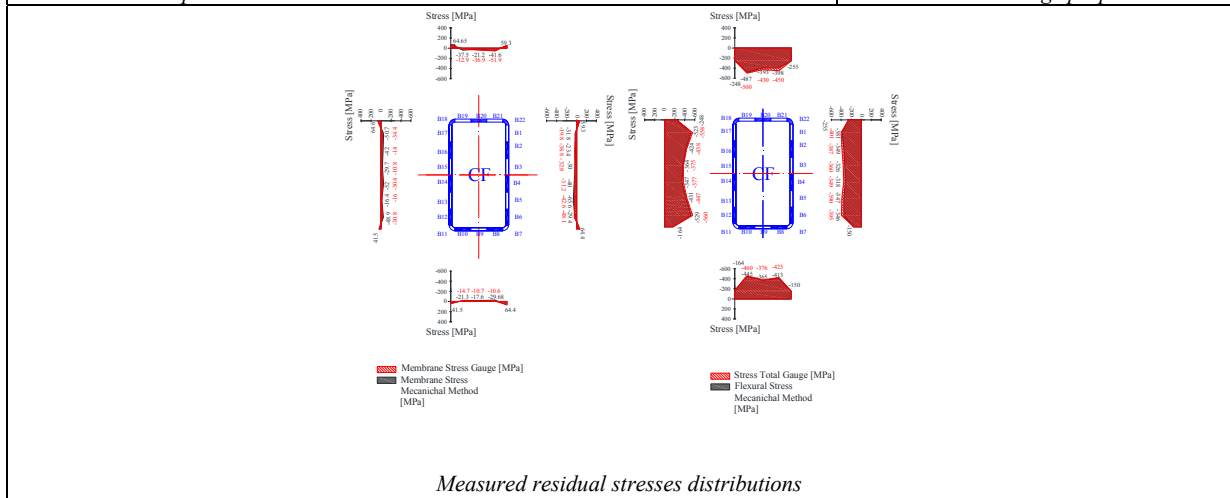
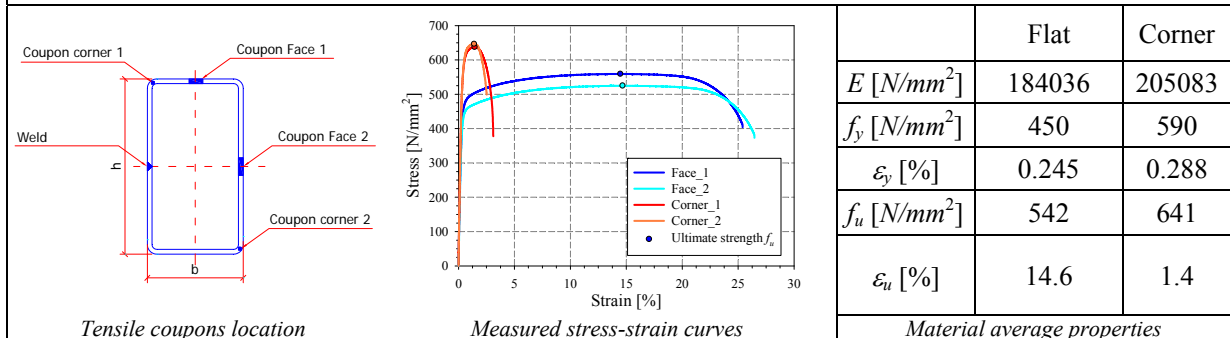
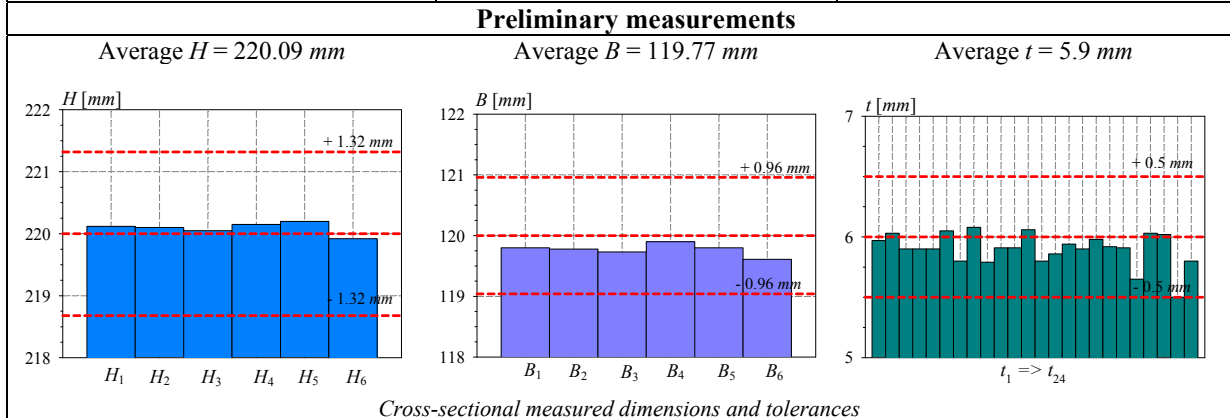
Column end rotations

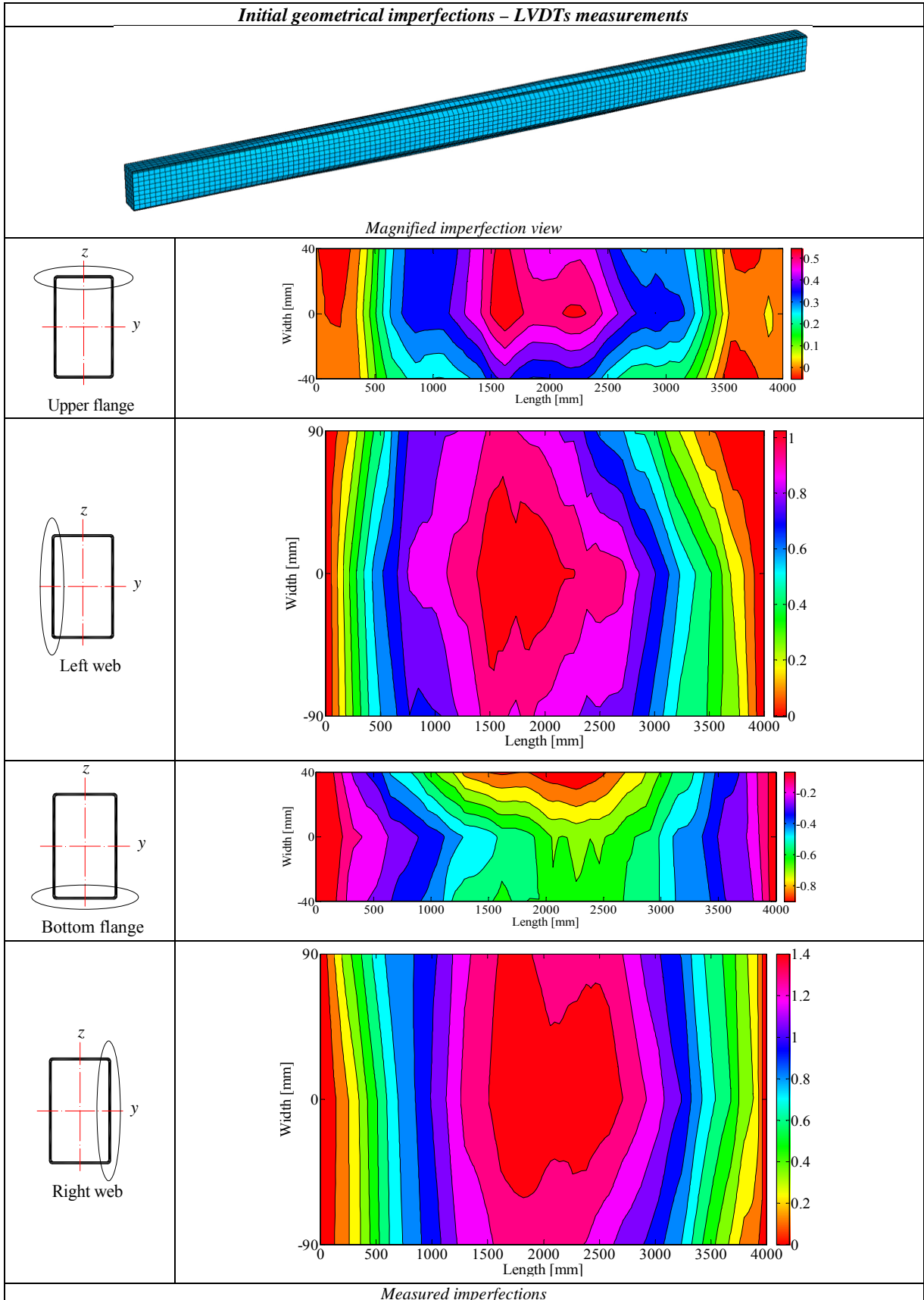


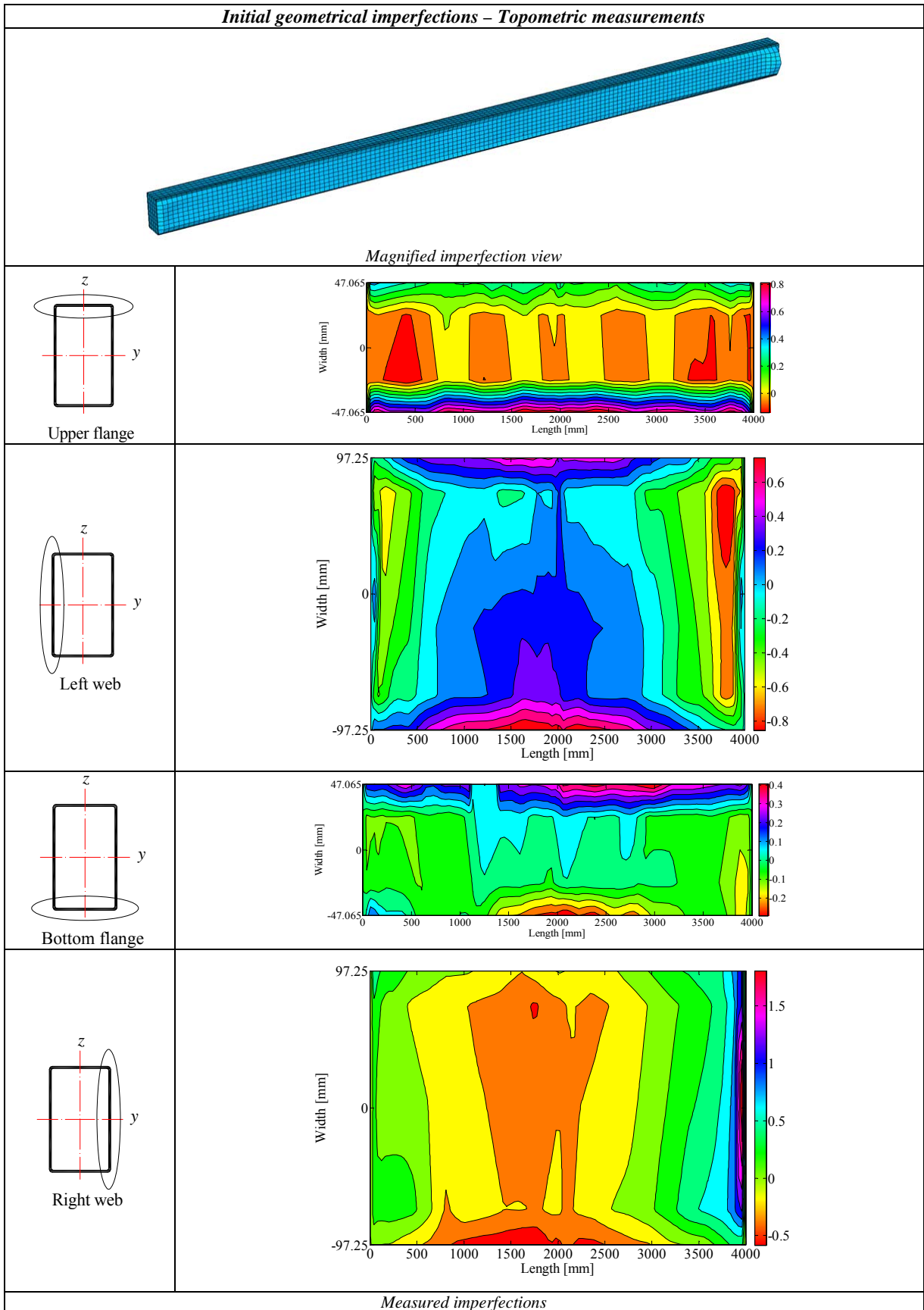


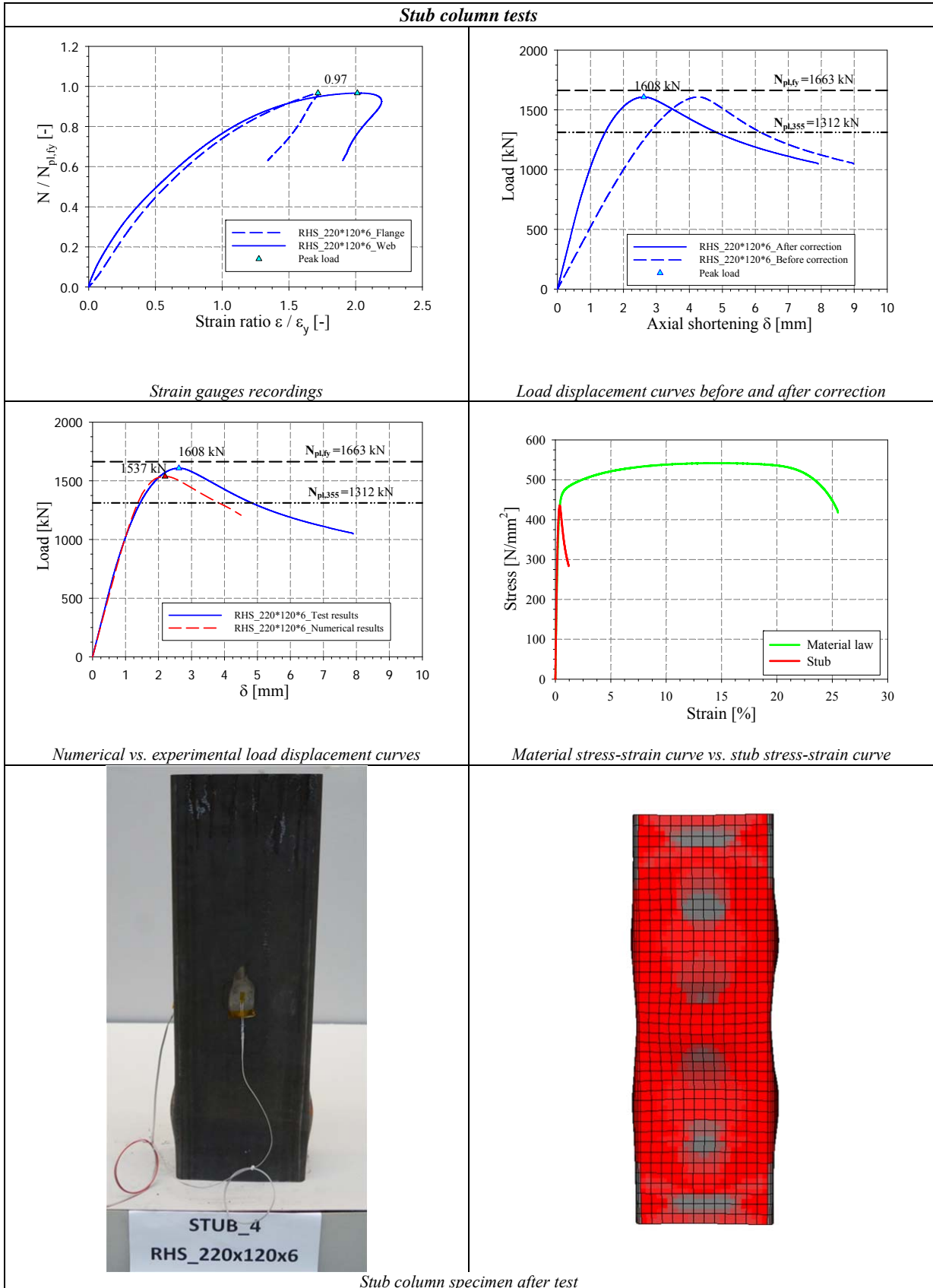
Buckling specimen after test

Test #: 4		
Specimen name	Shape	Details
RHS_S355CF_220x120x6		<p>Shape: Rectangular Hollow Section</p> <p>Nominal yield limit: 355 N/mm²</p> <p>Length = 4000 mm</p> <p>H = 220 mm B = 120 mm t = 6 mm</p> <p>Fabrication process: Cold-Formed</p> <p>Load case: 60%N+40%M_y</p> <p>Moment distribution: Constant</p>

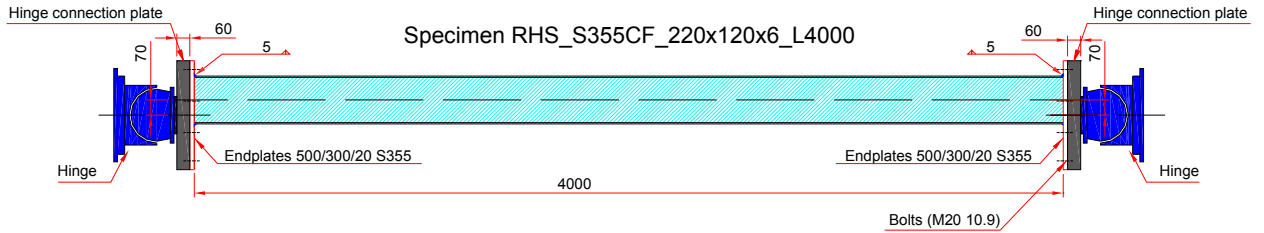




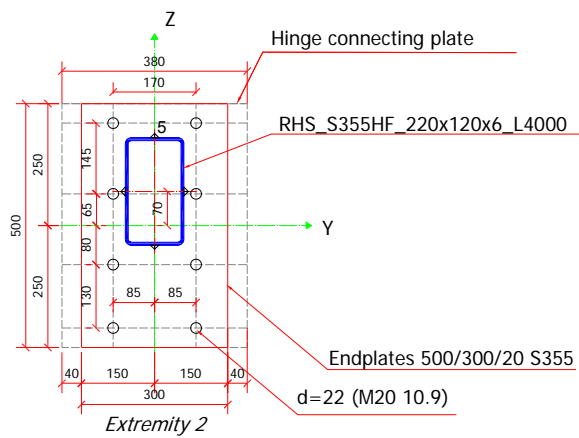
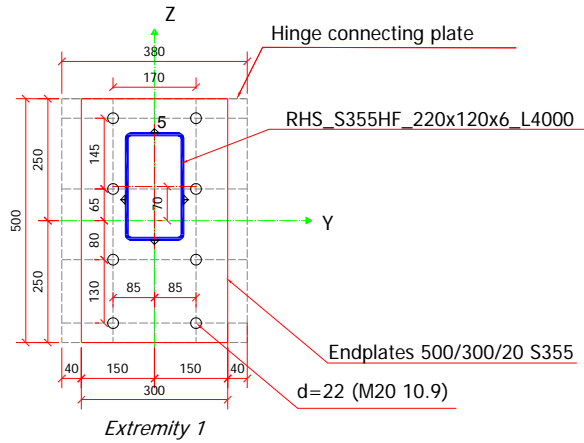


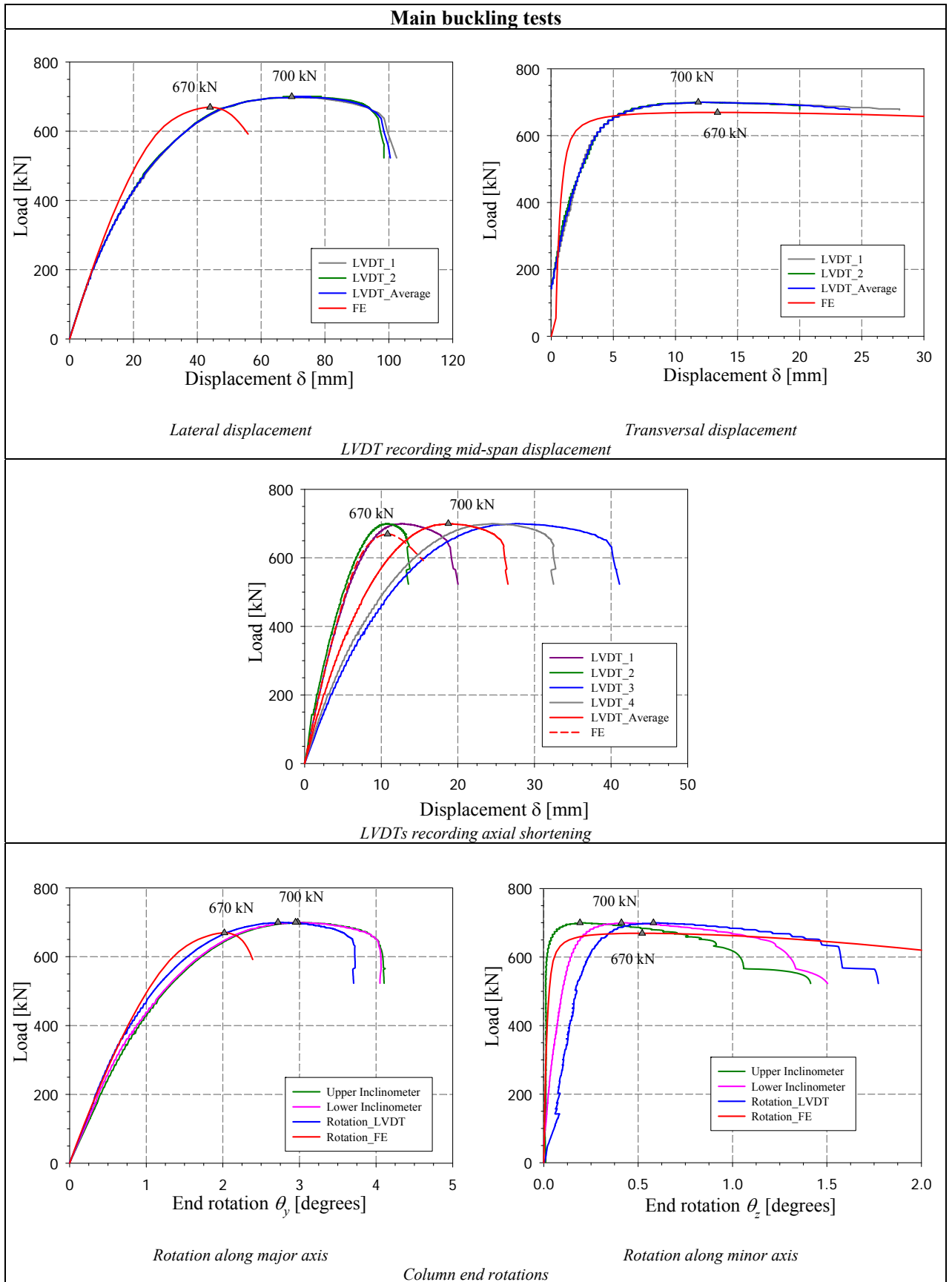


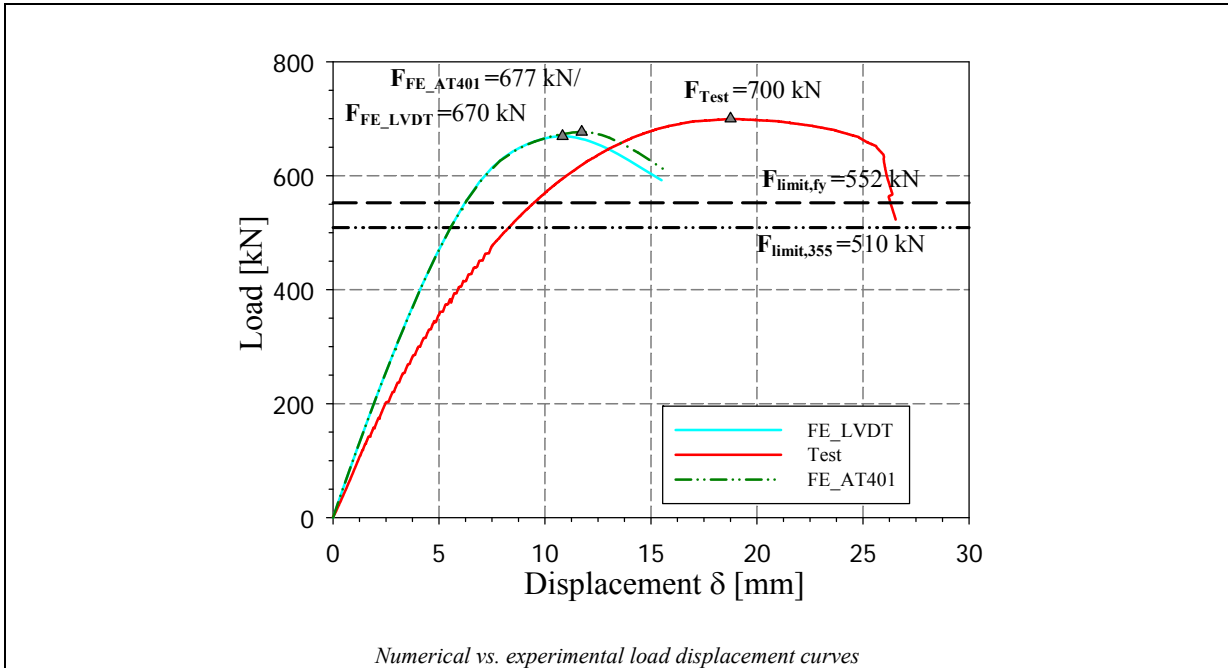
Column positioning

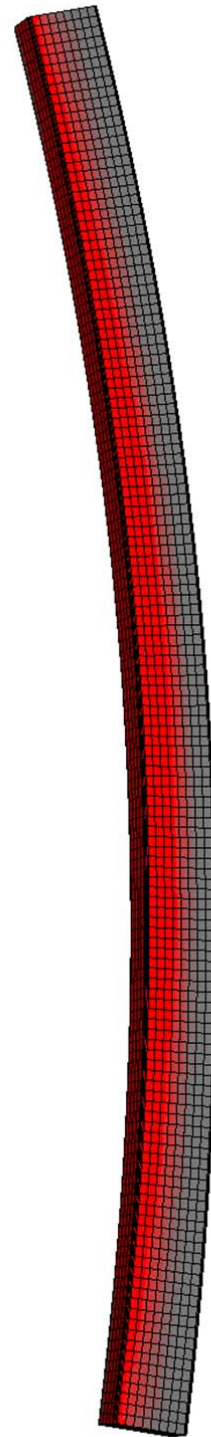


Endplates positions





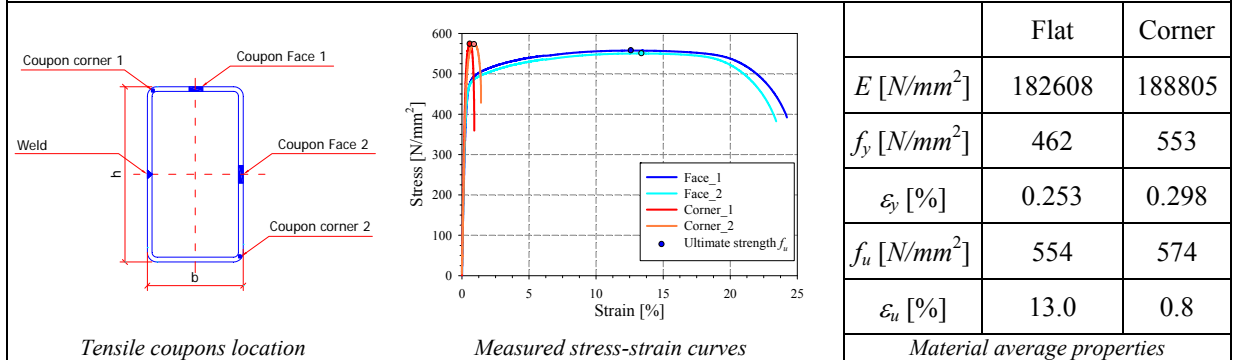
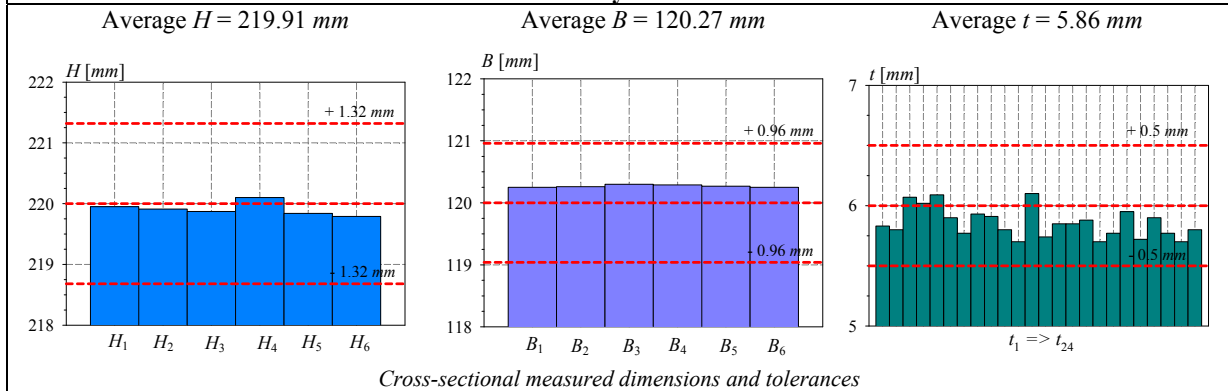


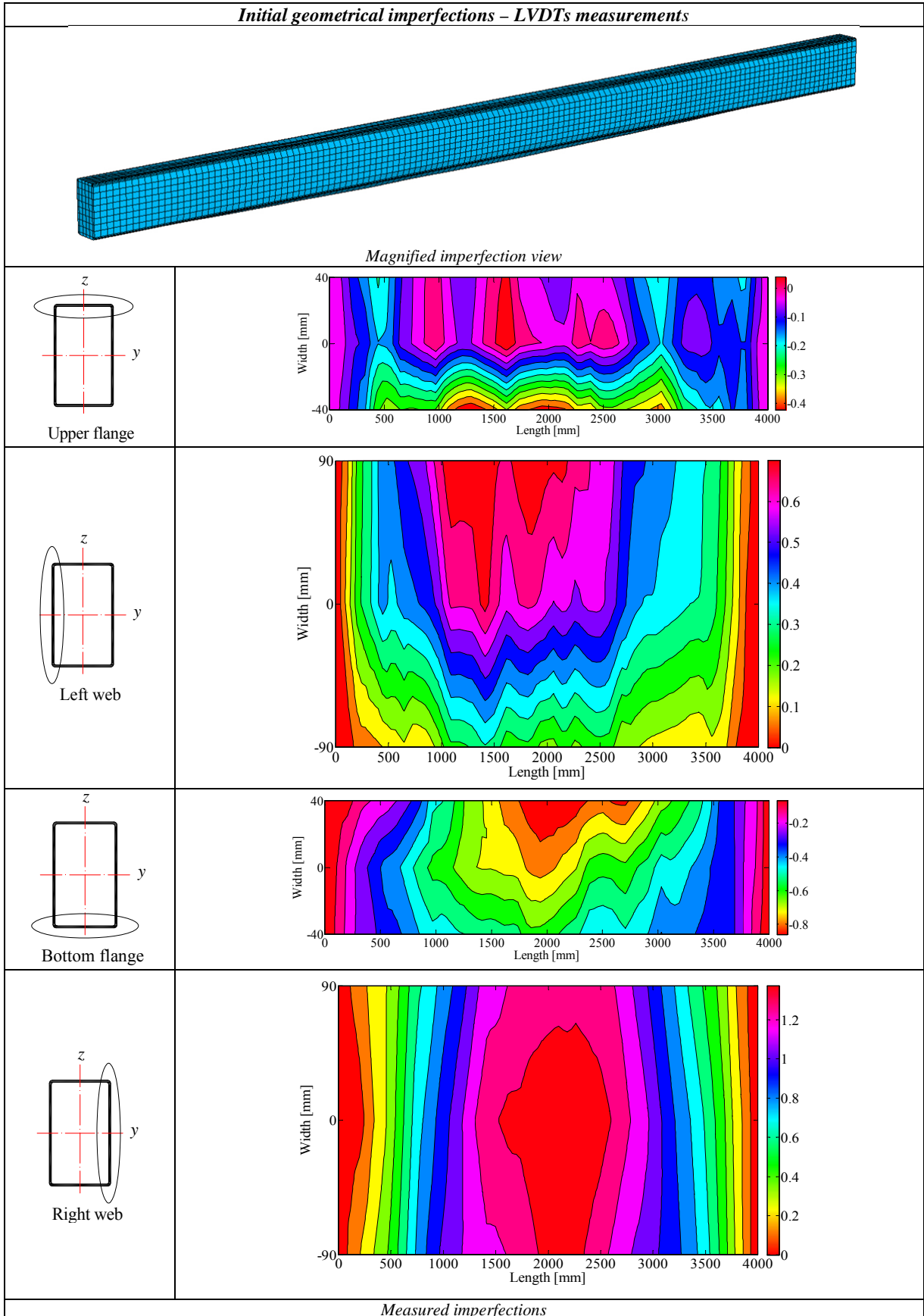


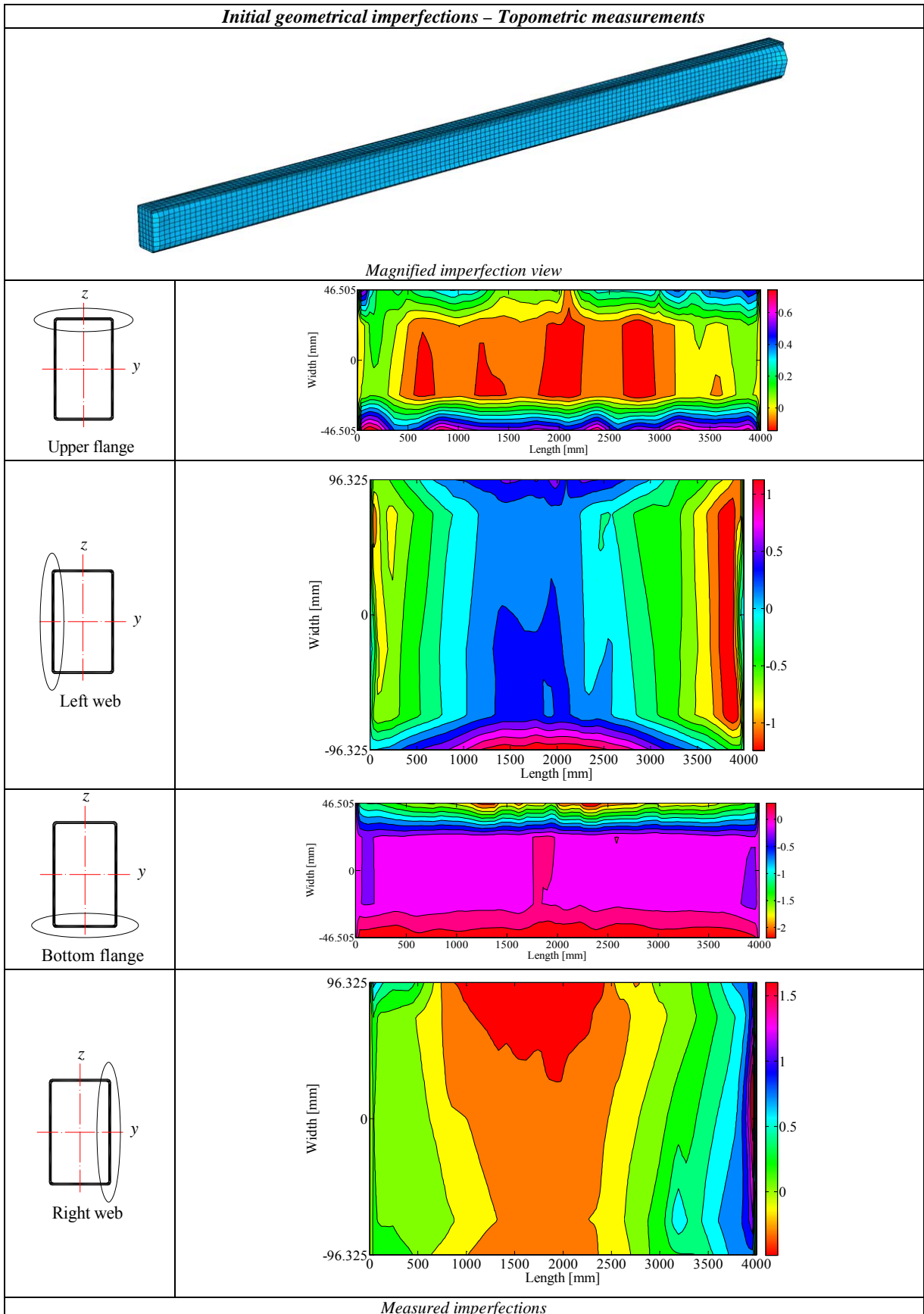
Buckling specimen after test

Test #: 5		
Specimen name	Shape	Details
RHS_S355CF_220x120x6		Shape: Rectangular Hollow Section Nominal yield limit: 355 N/mm^2 Length = 4000 mm $H = 220 \text{ mm}$ $B = 120 \text{ mm}$ $t = 6 \text{ mm}$ Fabrication process: Cold-Formed Load case: $40\%N + 30\%M_y + 30\%M_z$ Moment distribution: Constant

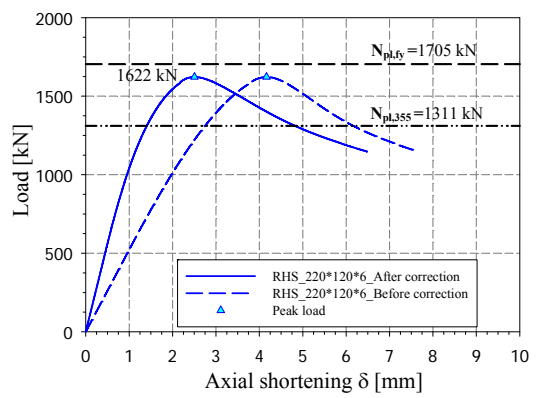
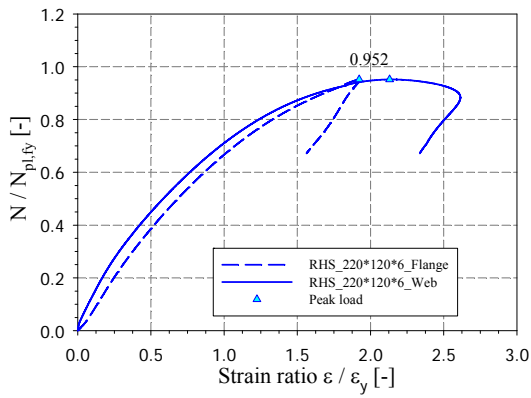
Preliminary measurements



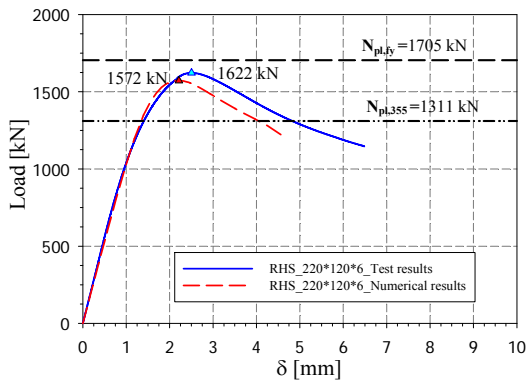




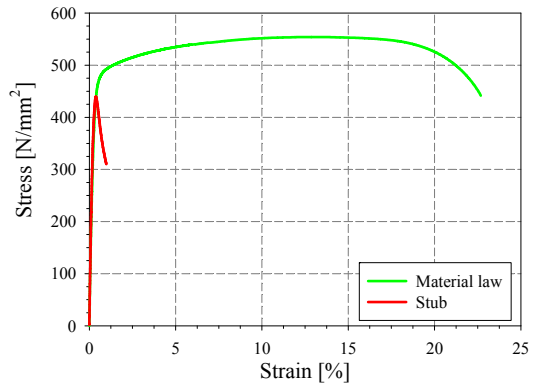
Stub column tests



Strain gauges recordings

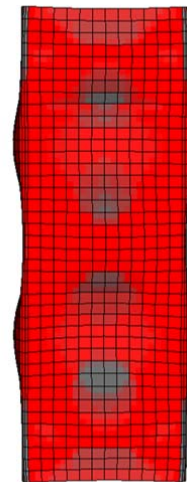


Load displacement curves before and after correction



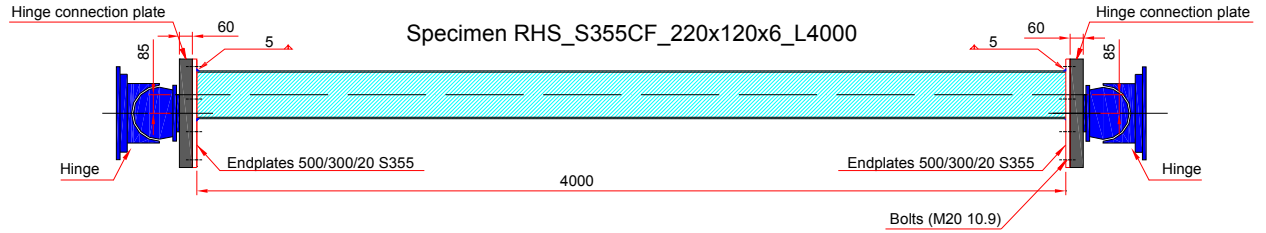
Numerical vs. experimental load displacement curves

Material stress-strain curve vs. stub stress-strain curve

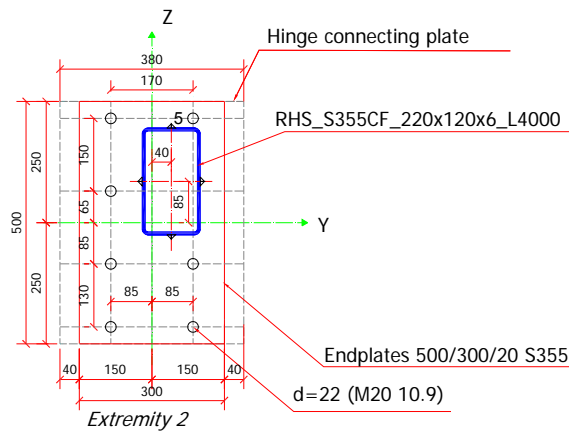
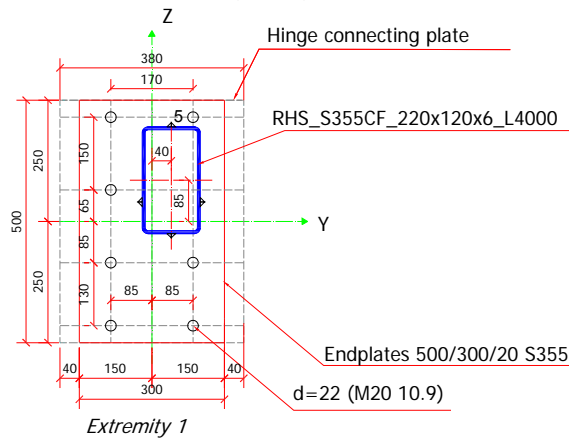


Stub column specimen after test

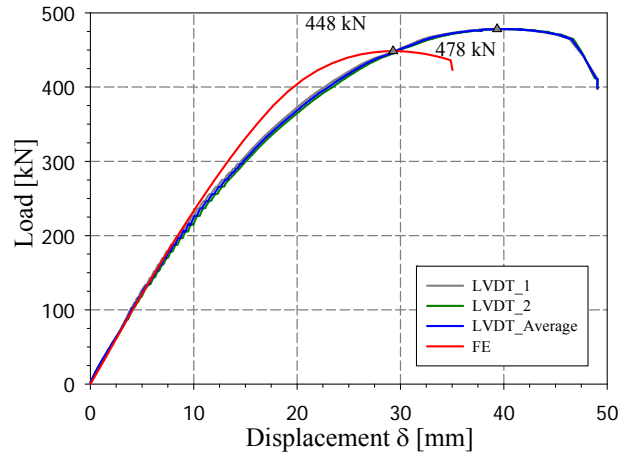
Column positioning



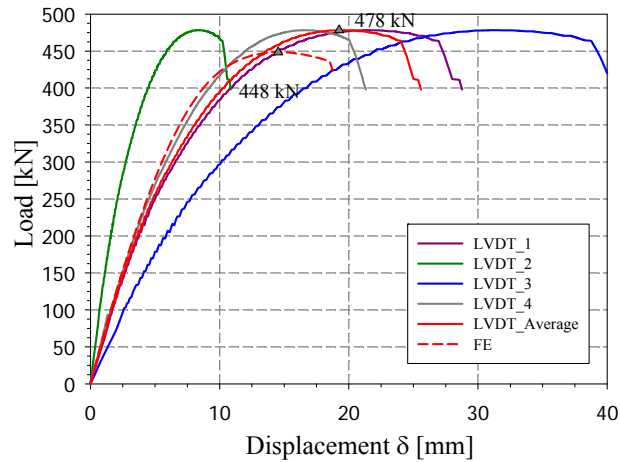
Endplates positions



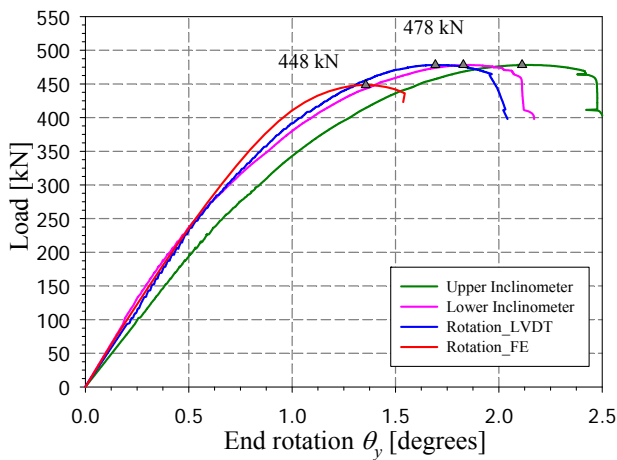
Main buckling tests



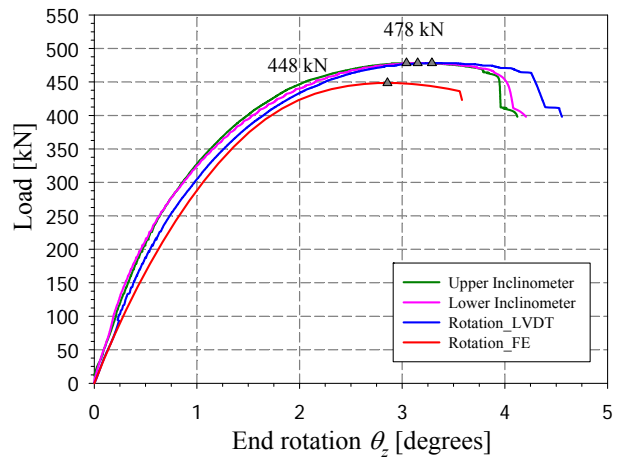
*Lateral displacement
LVDT recording mid-span displacement*



LVDTs recording axial shortening

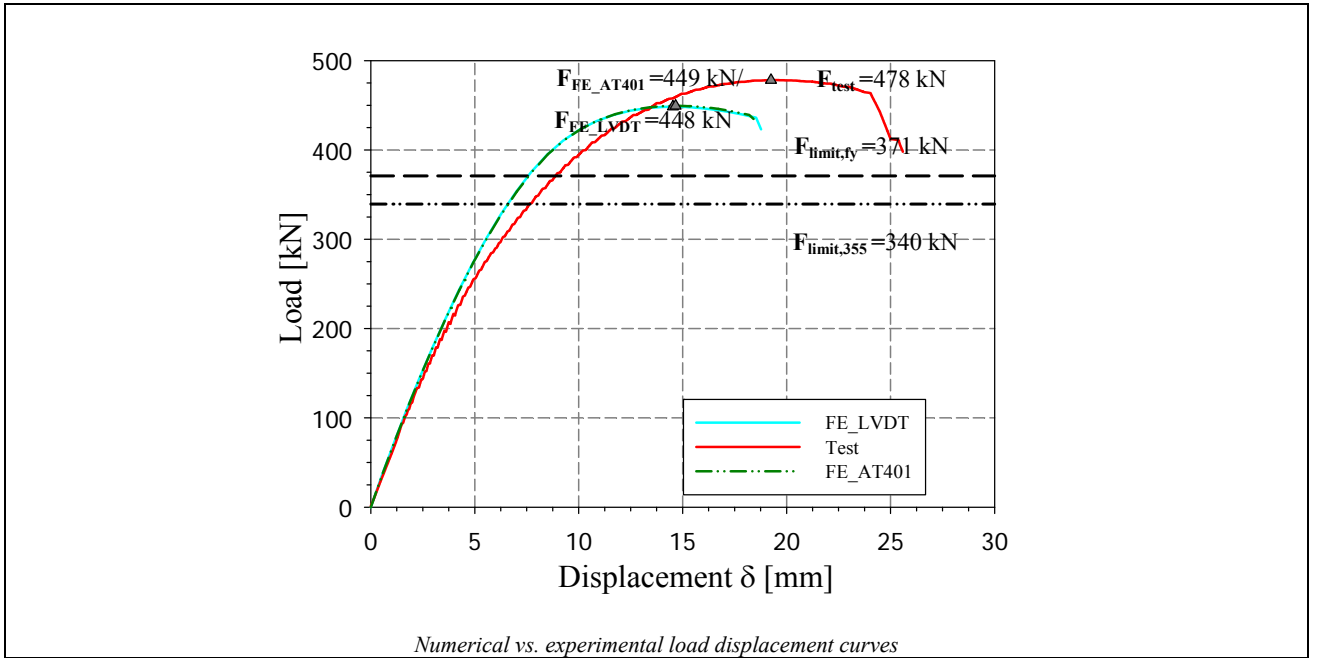


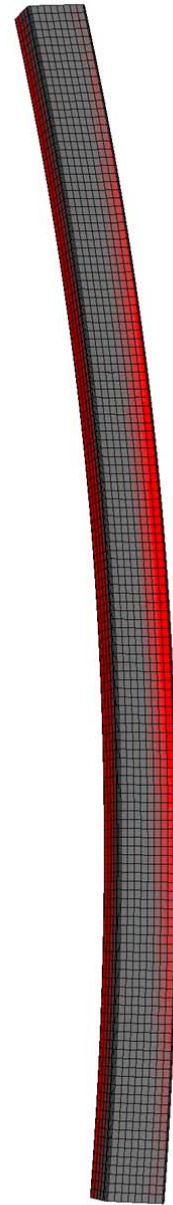
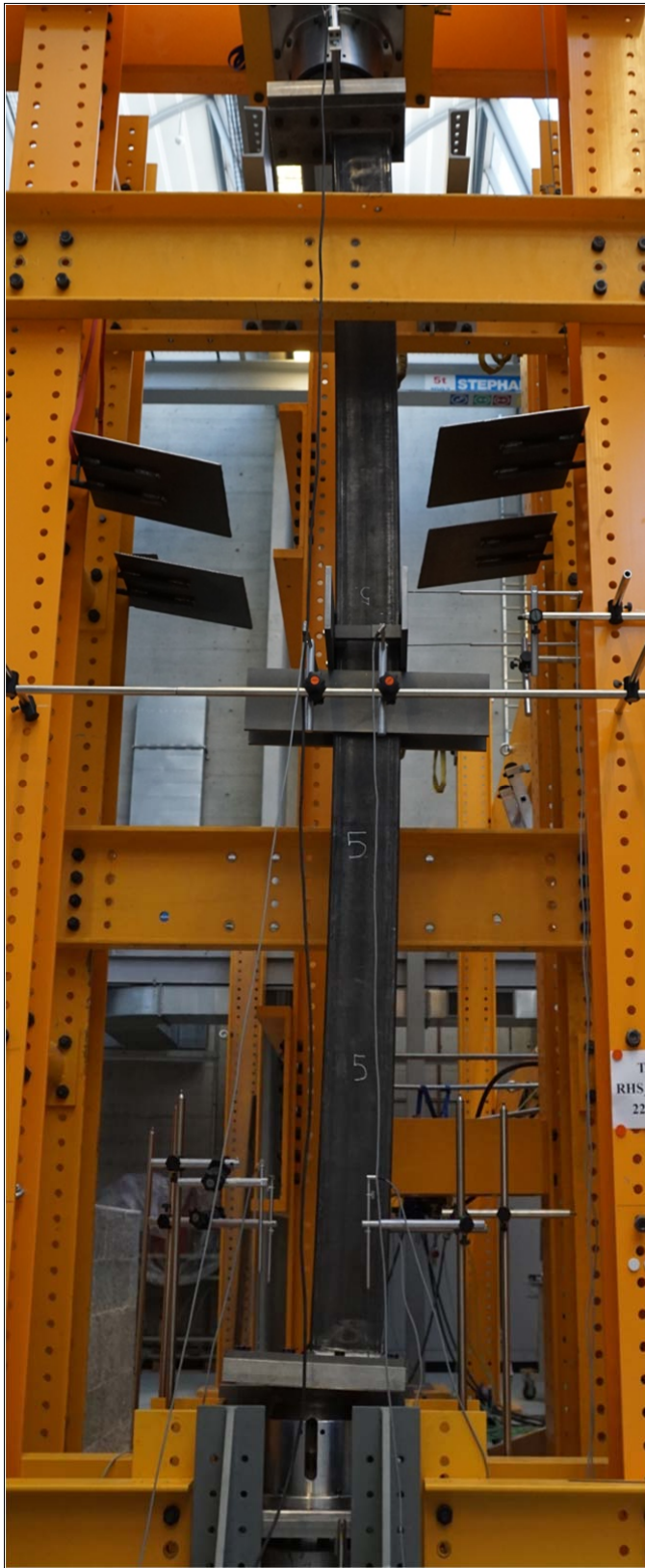
Rotation along major axis



Rotation along minor axis

Column end rotations

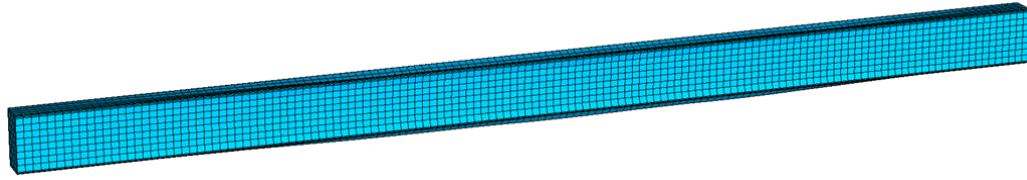




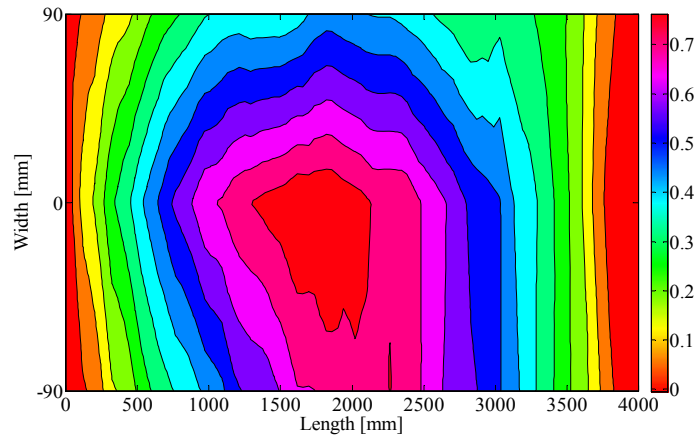
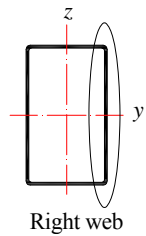
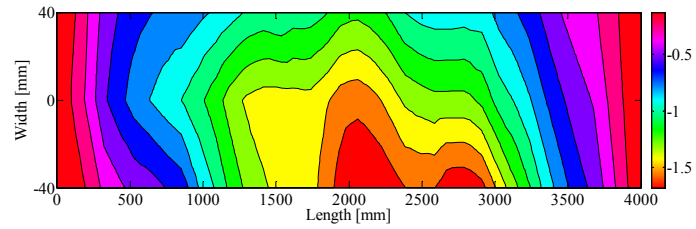
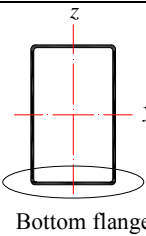
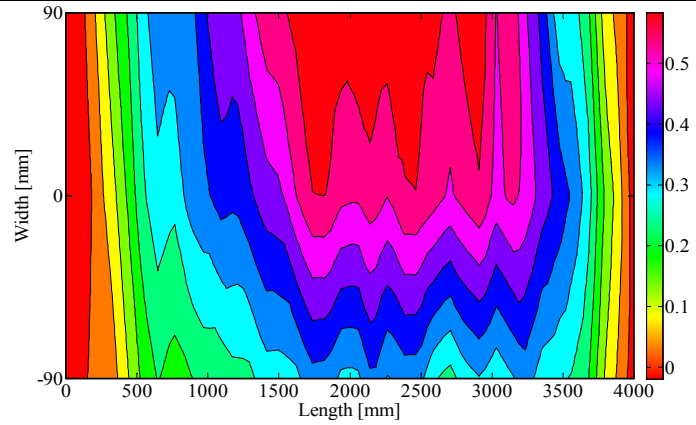
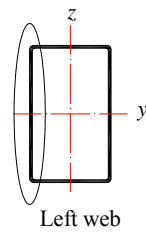
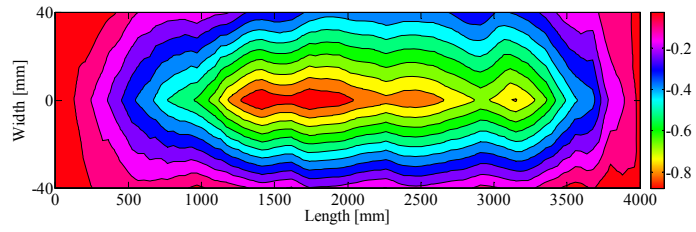
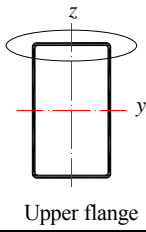
Buckling specimen after test

Test #: 6																				
Specimen name	Shape	Details																		
RHS_S355CF_220x120x6		<p>Shape: Rectangular Hollow Section</p> <p>Nominal yield limit: 355 N/mm²</p> <p>Length = 4000 mm</p> <p>H = 220 mm B = 120 mm t = 6 mm</p> <p>Fabrication process: Cold-Formed</p> <p>Load case: 60%N+40%M_y</p> <p>Moment distribution: Triangular</p>																		
Preliminary measurements																				
Average H = 219.9 mm	Average B = 119.78 mm	Average t = 5.83 mm																		
<i>Cross-sectional measured dimensions and tolerances</i>																				
		<table border="1"> <thead> <tr> <th></th> <th style="text-align: center;">Flat</th> <th style="text-align: center;">Corner</th> </tr> </thead> <tbody> <tr> <td>E [N/mm²]</td> <td style="text-align: center;">196156</td> <td style="text-align: center;">183191</td> </tr> <tr> <td>f_y [N/mm²]</td> <td style="text-align: center;">448</td> <td style="text-align: center;">585</td> </tr> <tr> <td>ϵ_y [%]</td> <td style="text-align: center;">0.229</td> <td style="text-align: center;">0.320</td> </tr> <tr> <td>f_u [N/mm²]</td> <td style="text-align: center;">553</td> <td style="text-align: center;">624</td> </tr> <tr> <td>ϵ_u [%]</td> <td style="text-align: center;">14.6</td> <td style="text-align: center;">1.5</td> </tr> </tbody> </table>		Flat	Corner	E [N/mm ²]	196156	183191	f_y [N/mm ²]	448	585	ϵ_y [%]	0.229	0.320	f_u [N/mm ²]	553	624	ϵ_u [%]	14.6	1.5
	Flat	Corner																		
E [N/mm ²]	196156	183191																		
f_y [N/mm ²]	448	585																		
ϵ_y [%]	0.229	0.320																		
f_u [N/mm ²]	553	624																		
ϵ_u [%]	14.6	1.5																		
<i>Tensile coupons location</i>	<i>Measured stress-strain curves</i>	<i>Material average properties</i>																		

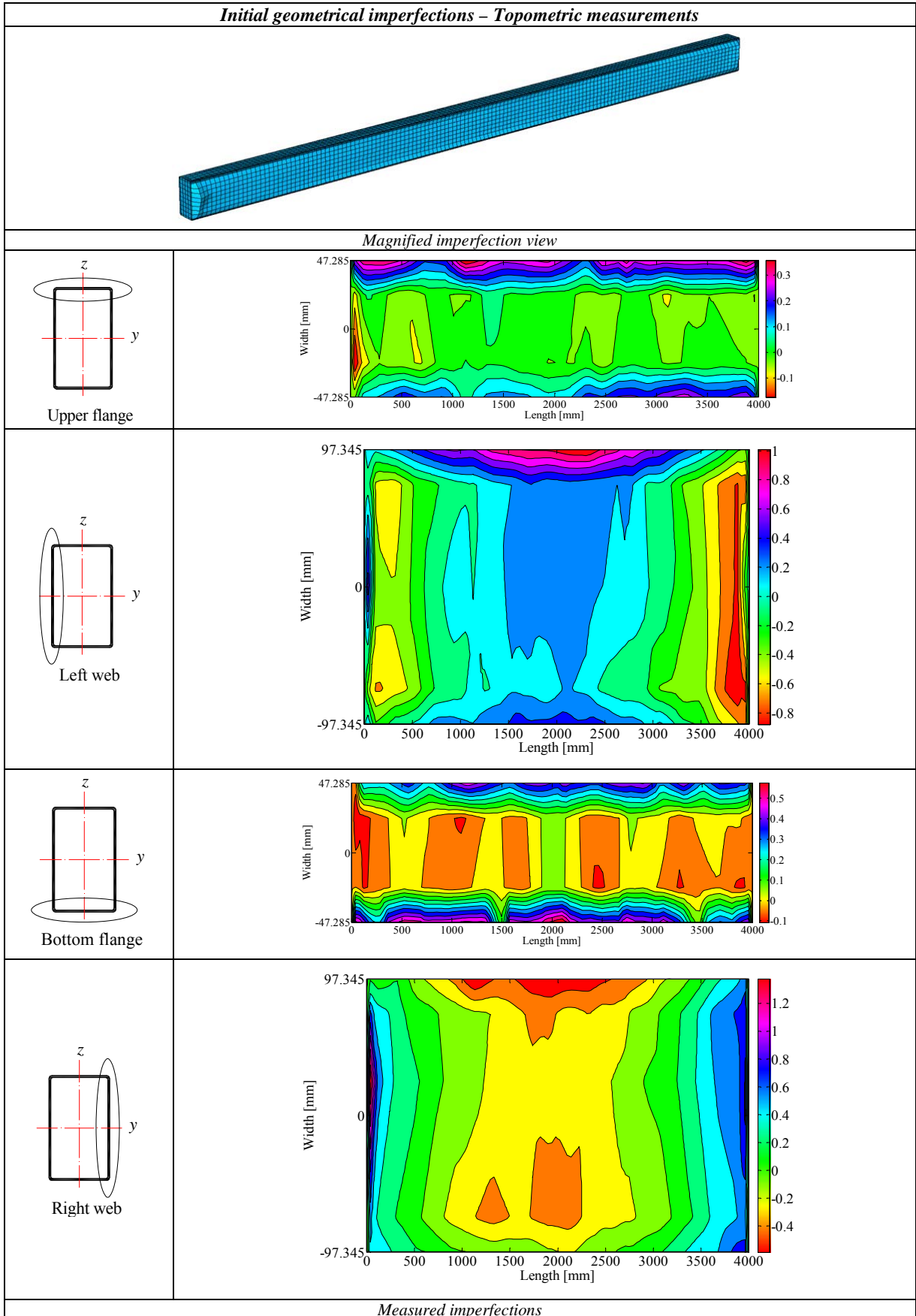
Initial geometrical imperfections – LVDTs measurements



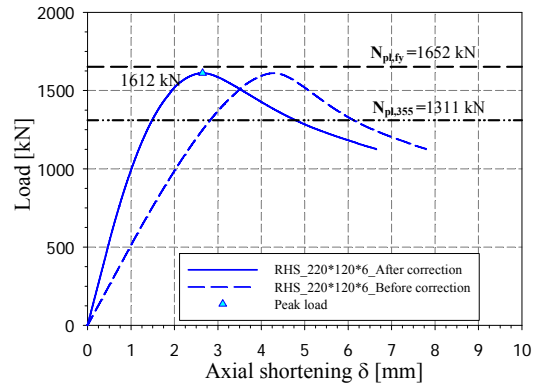
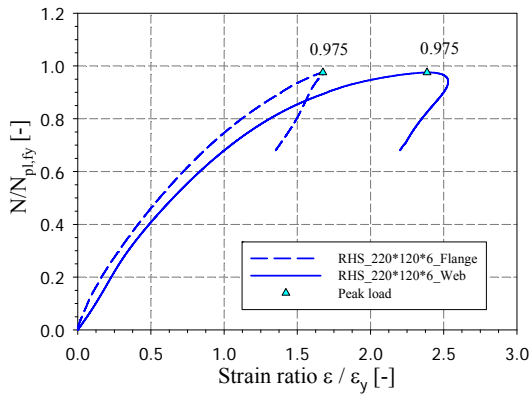
Magnified imperfection view



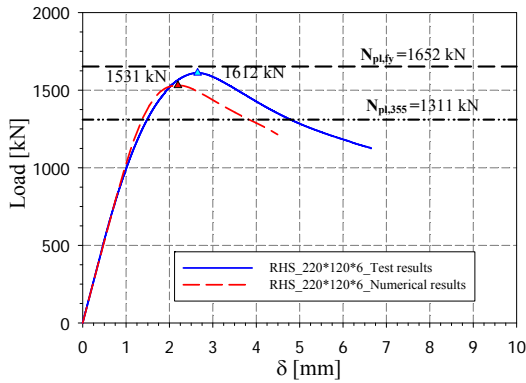
Measured imperfections



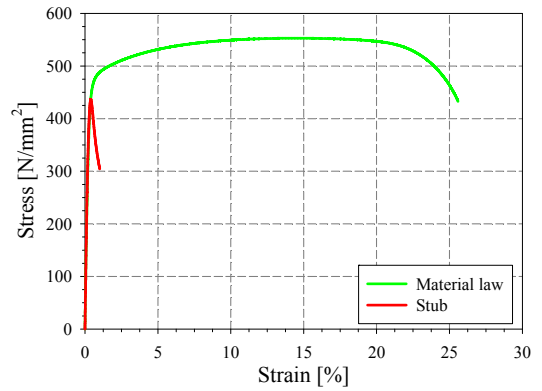
Stub column tests



Strain gauges recordings

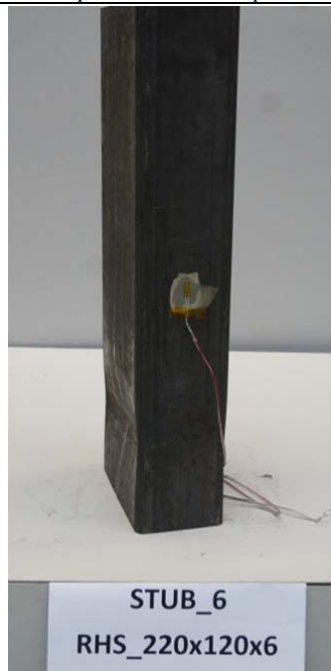


Load displacement curves before and after correction



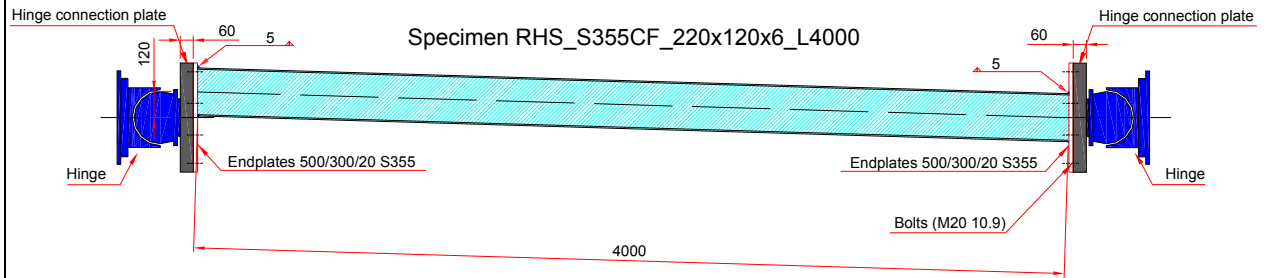
Numerical vs. experimental load displacement curves

Material stress-strain curve vs. stub stress-strain curve

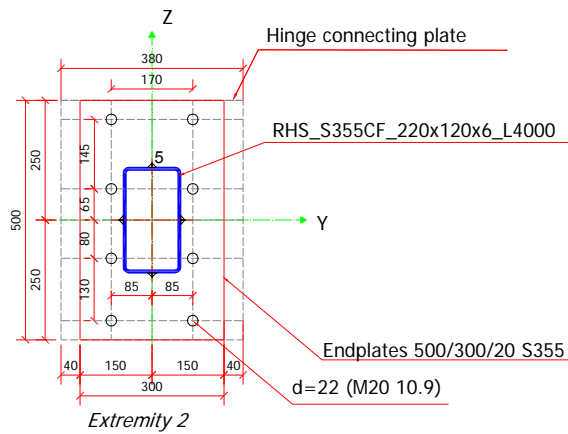
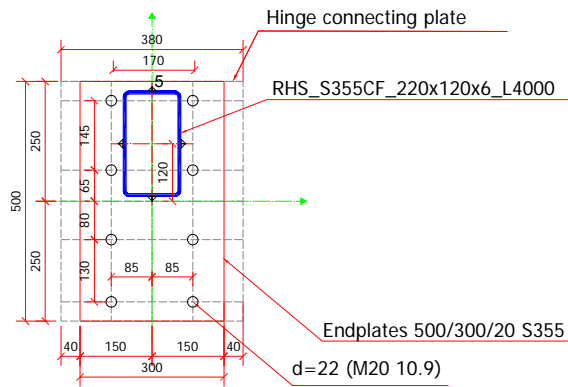


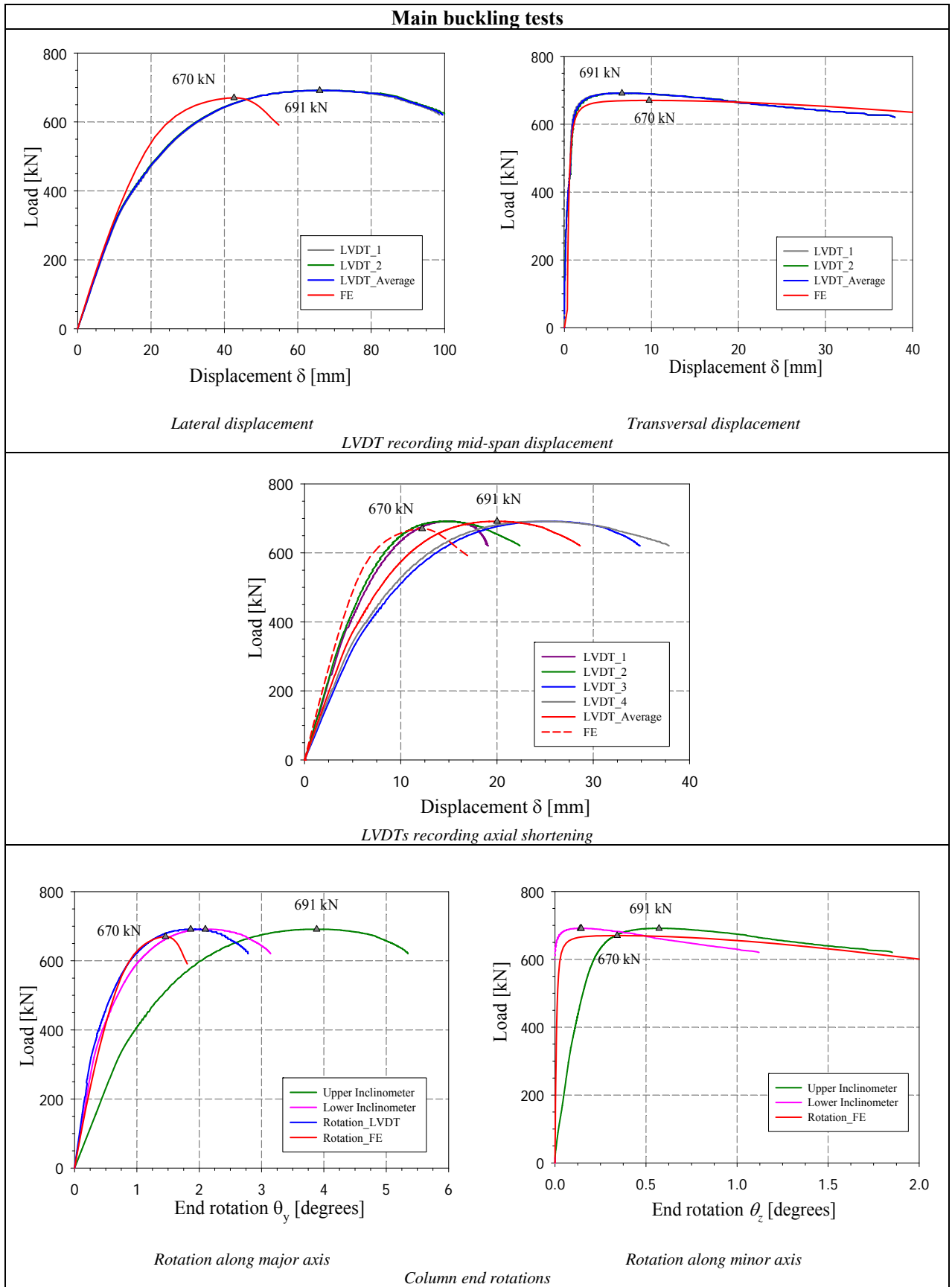
Stub column specimen after test

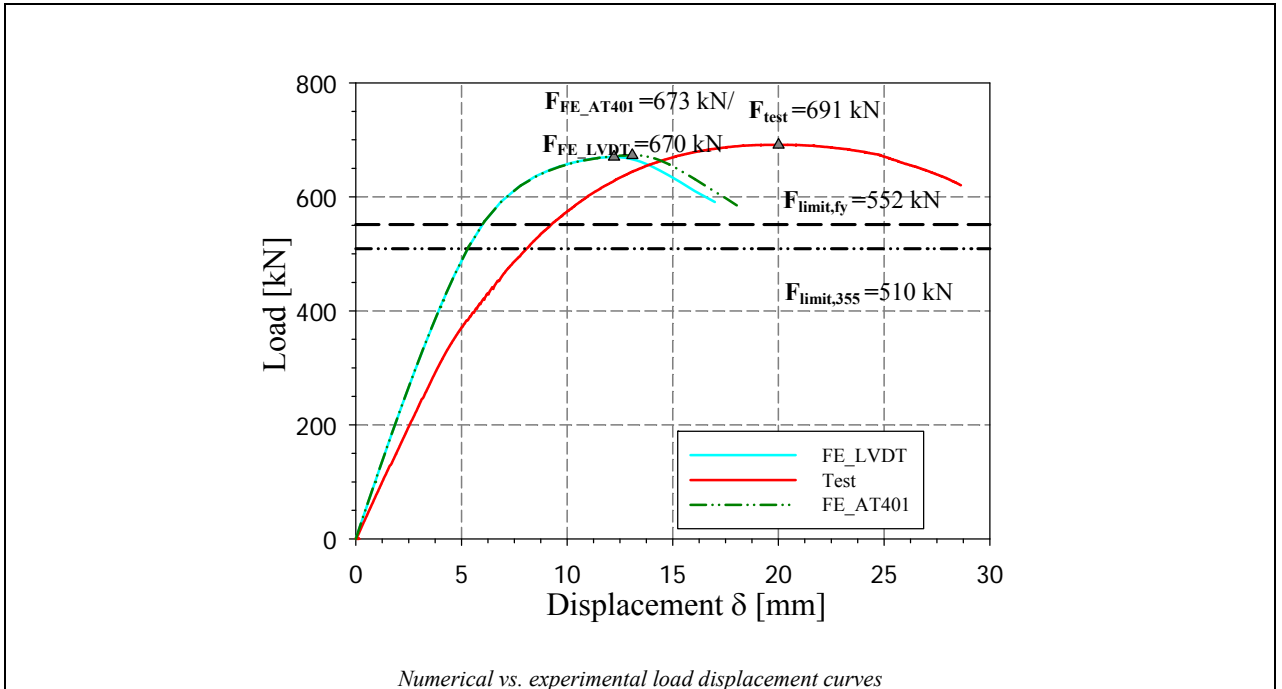
Column positioning

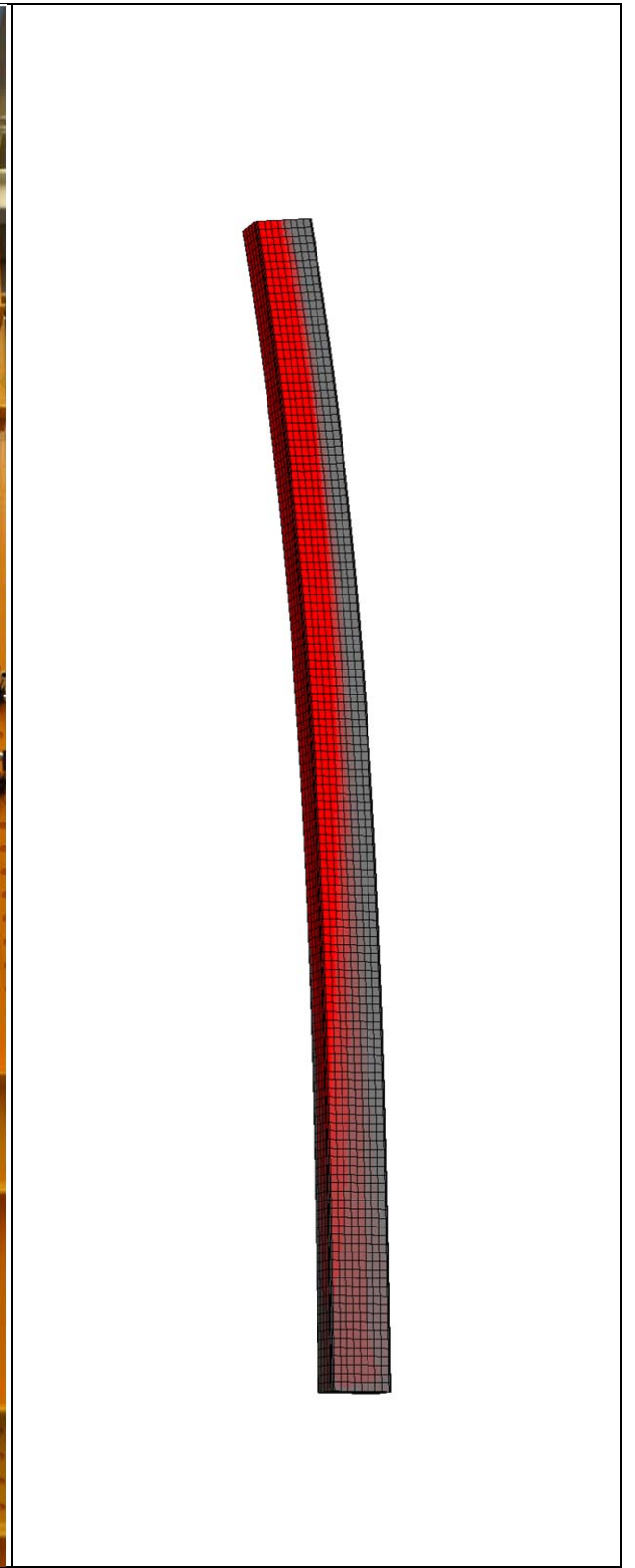


Endplates positions

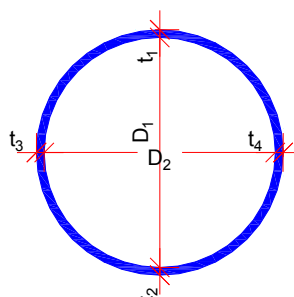
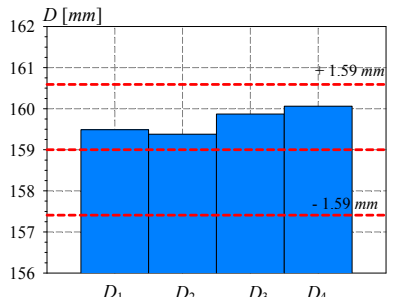
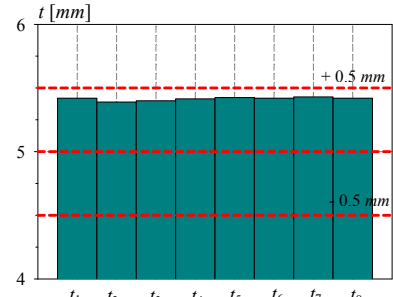
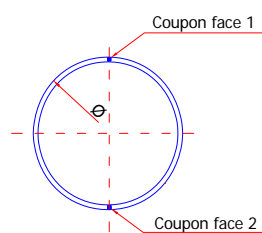
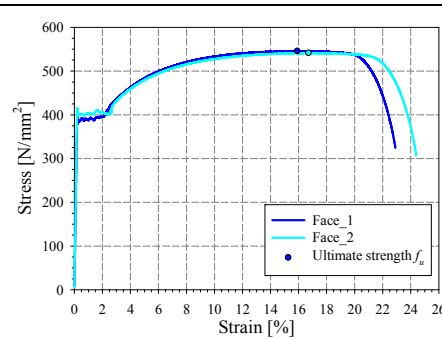


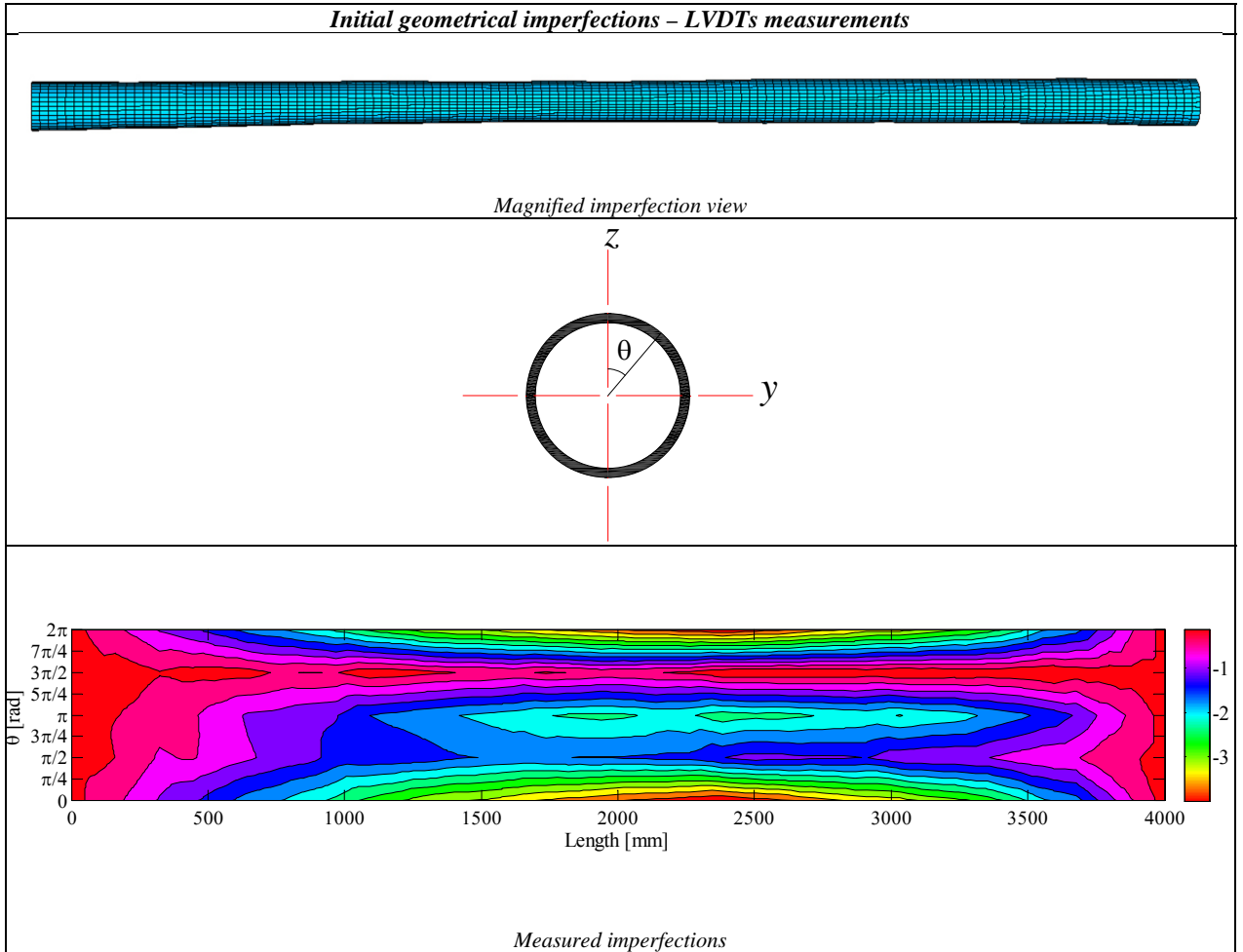




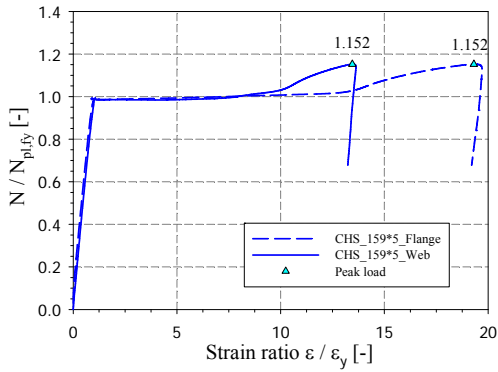


Buckling specimen after test

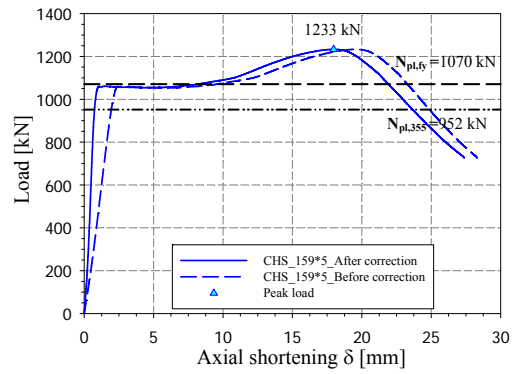
Test #: 7														
Specimen name	Shape	Details												
CHS_S355HR_159x5		<p>Shape: Circular Hollow Section</p> <p>Nominal yield limit: 355 N/mm^2</p> <p>Length = 4000 mm</p> <p>Load case: 50%N+50%M_y</p> <p>$D = 159$ mm $t = 5$ mm</p> <p>Fabrication process: Hot-Rolled</p> <p>Moment distribution: Constant</p>												
Preliminary measurements														
<p>Average $D = 159.8$ mm</p> 		<p>Average $t = 5.42$ mm</p> 												
Cross-sectional measured dimensions and tolerances														
 <p>Tensile coupons location</p>	 <p>Measured stress-strain curves</p>	<table border="1"> <thead> <tr> <th></th> <th>Average</th> </tr> </thead> <tbody> <tr> <td>E [N/mm^2]</td> <td>205050</td> </tr> <tr> <td>f_y [N/mm^2]</td> <td>399</td> </tr> <tr> <td>ϵ_y [%]</td> <td>0.195</td> </tr> <tr> <td>f_u [N/mm^2]</td> <td>543</td> </tr> <tr> <td>ϵ_u [%]</td> <td>16.3</td> </tr> </tbody> </table> <p>Material average properties</p>		Average	E [N/mm^2]	205050	f_y [N/mm^2]	399	ϵ_y [%]	0.195	f_u [N/mm^2]	543	ϵ_u [%]	16.3
	Average													
E [N/mm^2]	205050													
f_y [N/mm^2]	399													
ϵ_y [%]	0.195													
f_u [N/mm^2]	543													
ϵ_u [%]	16.3													



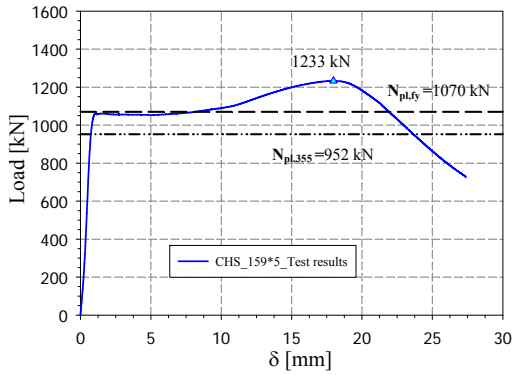
Stub column tests



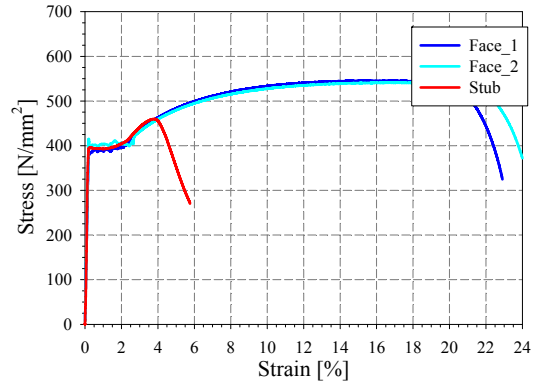
Strain gauges recordings



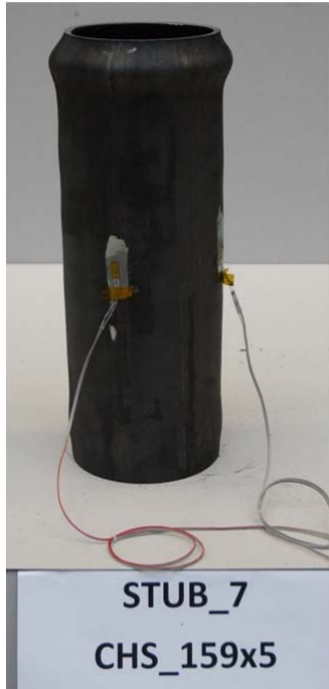
Load displacement curves before and after correction



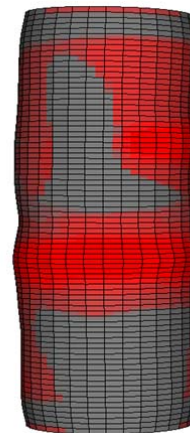
Load displacement curve

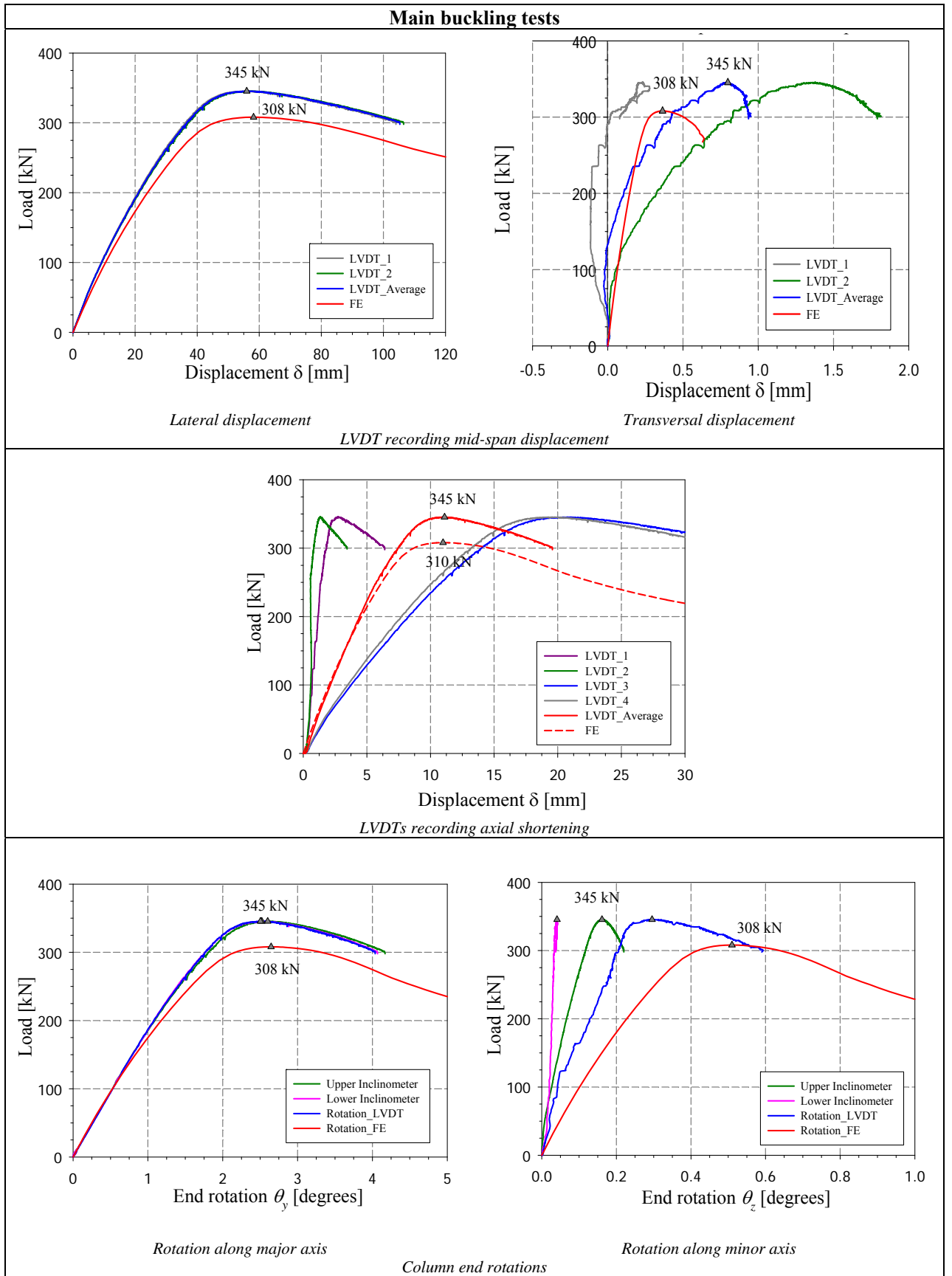


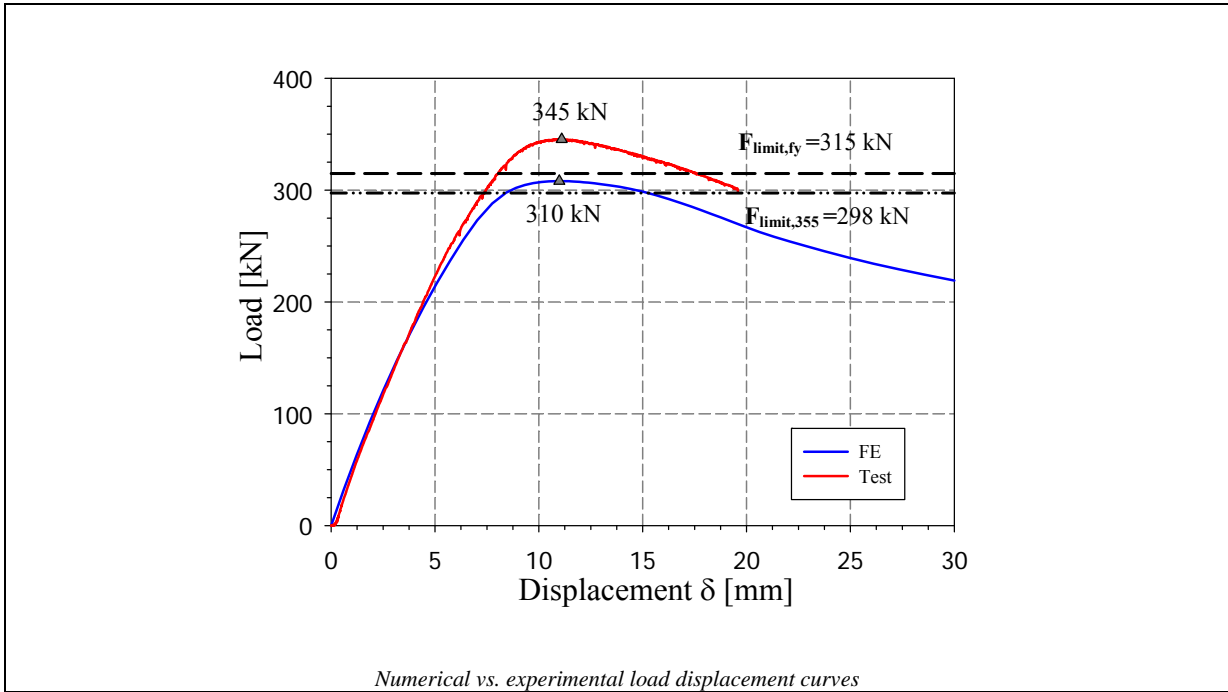
Material stress-strain curve vs. stub stress-strain curve

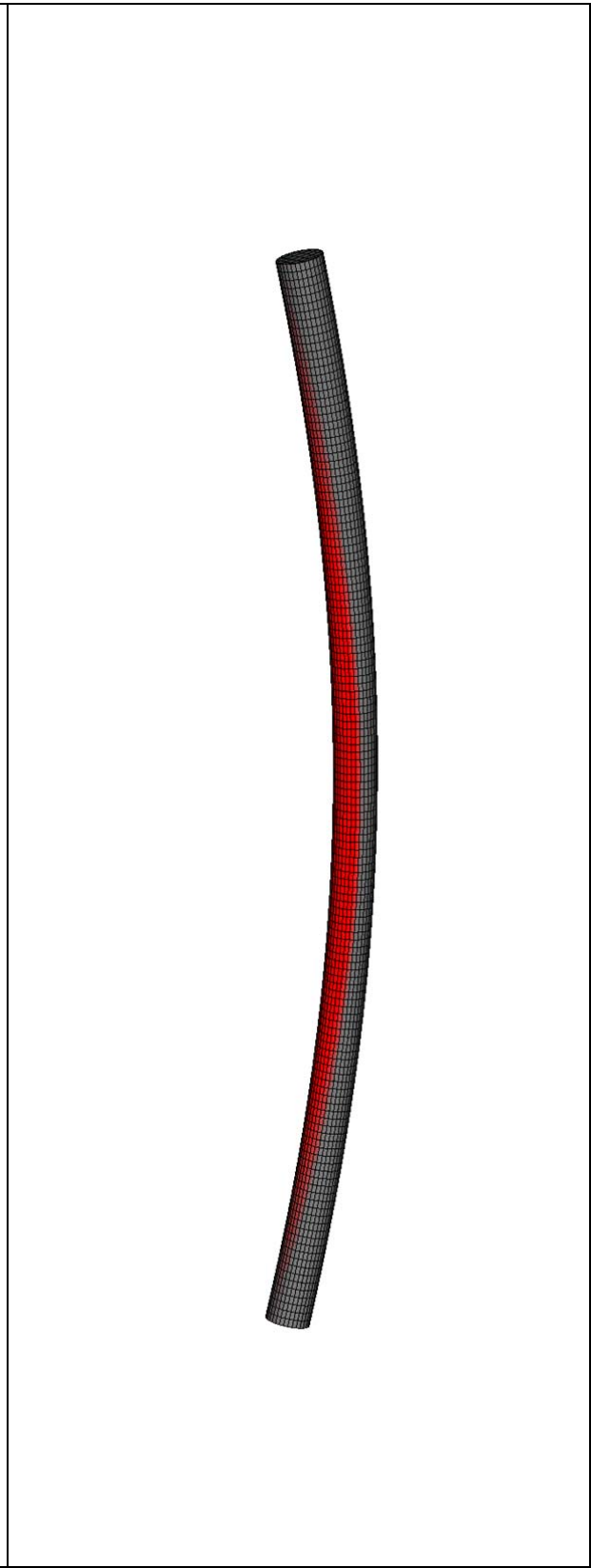


Stub column specimen after test

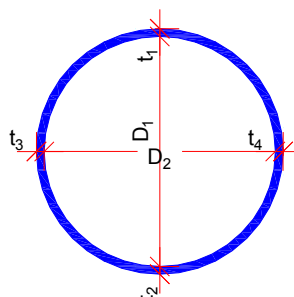
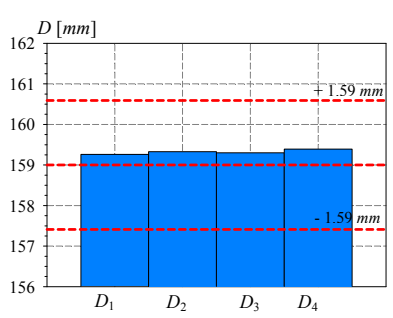
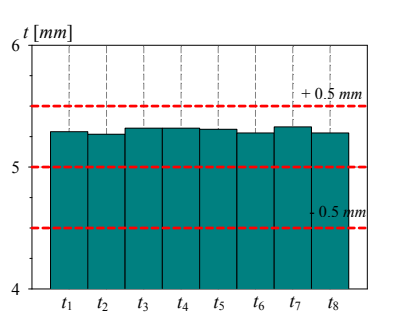
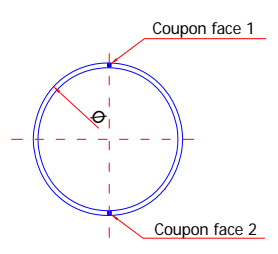
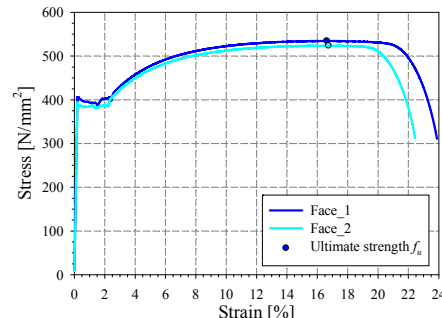








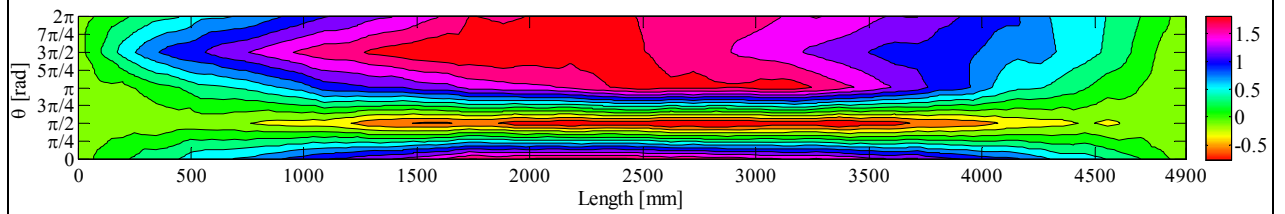
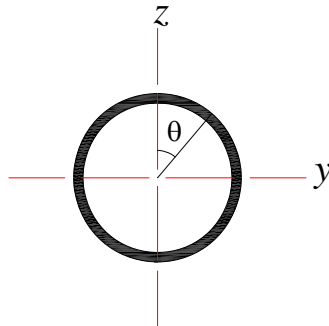
Buckling specimen after test

Test #: 8														
Specimen name	Shape	Details												
CHS_S355HR_159x5		<p>Shape: Circular Hollow Section</p> <p>Nominal yield limit: 355 N/mm²</p> <p>Length = 4900 mm</p> <p>Load case: 50%N+50%M_y</p> <p>D = 159 mm t = 5 mm</p> <p>Fabrication process: Hot-Rolled</p> <p>Moment distribution: Constant</p>												
Preliminary measurements														
<p>Average D = 159.3 mm</p> 		<p>Average t = 5.3 mm</p> 												
Cross-sectional measured dimensions and tolerances														
 <p><i>Tensile coupons location</i></p>	 <p><i>Measured stress-strain curves</i></p>	<table border="1"> <thead> <tr> <th></th> <th>Average</th> </tr> </thead> <tbody> <tr> <td>E [N/mm²]</td> <td>198508</td> </tr> <tr> <td>f_y [N/mm²]</td> <td>393</td> </tr> <tr> <td>ϵ_y [%]</td> <td>0.198</td> </tr> <tr> <td>f_u [N/mm²]</td> <td>529</td> </tr> <tr> <td>ϵ_u [%]</td> <td>16.7</td> </tr> </tbody> </table> <p><i>Material average properties</i></p>		Average	E [N/mm ²]	198508	f_y [N/mm ²]	393	ϵ_y [%]	0.198	f_u [N/mm ²]	529	ϵ_u [%]	16.7
	Average													
E [N/mm ²]	198508													
f_y [N/mm ²]	393													
ϵ_y [%]	0.198													
f_u [N/mm ²]	529													
ϵ_u [%]	16.7													

Initial geometrical imperfections – LVDTs measurements

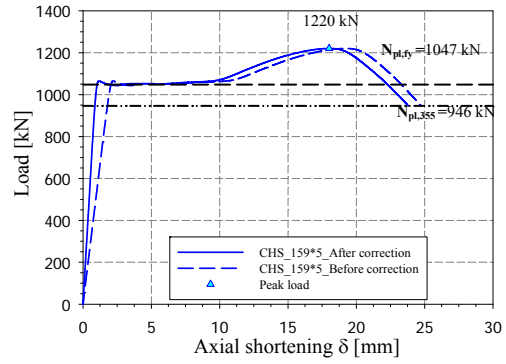
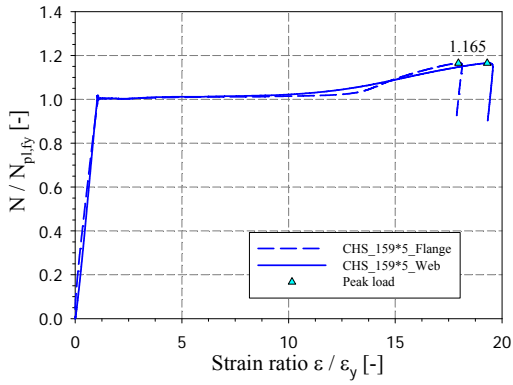


Magnified imperfection view

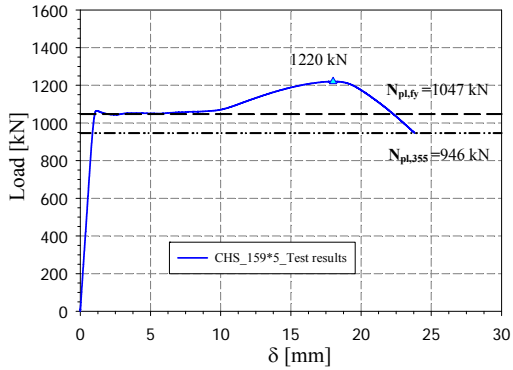


Measured imperfections

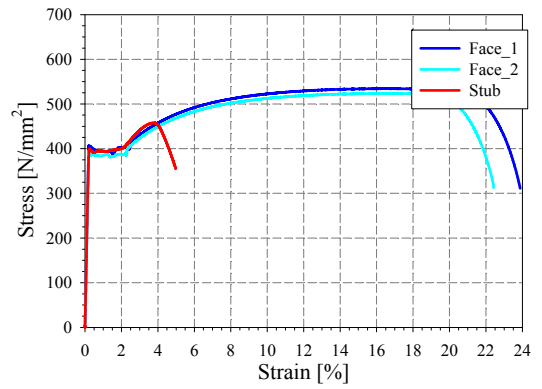
Stub column tests



Strain gauges recordings

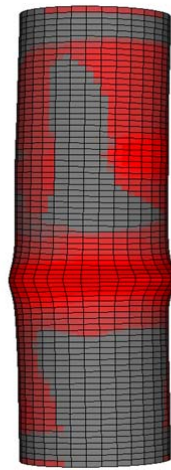
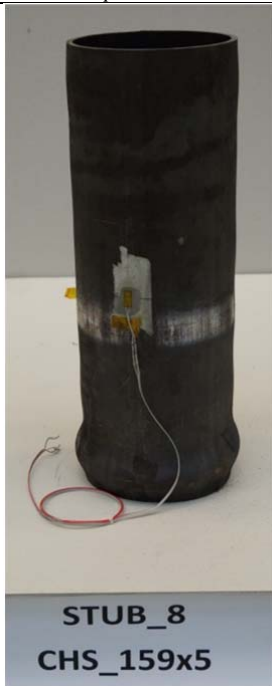


Load displacement curves before and after correction



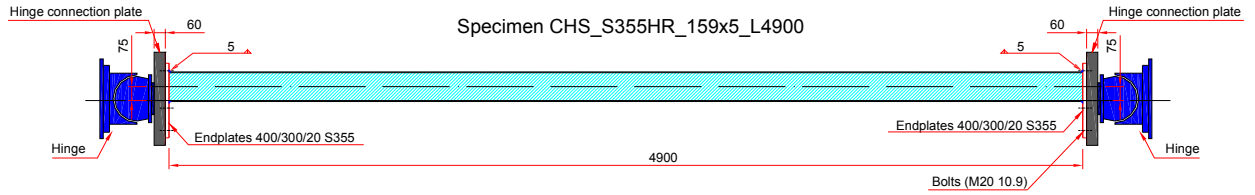
Load displacement curve

Material stress-strain curve vs. stub stress-strain curve

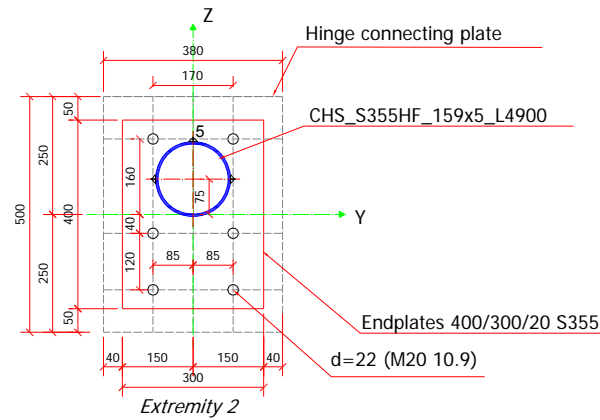
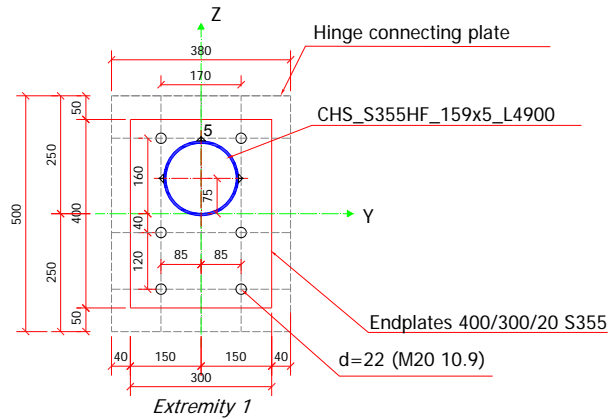


Stub column specimen after test

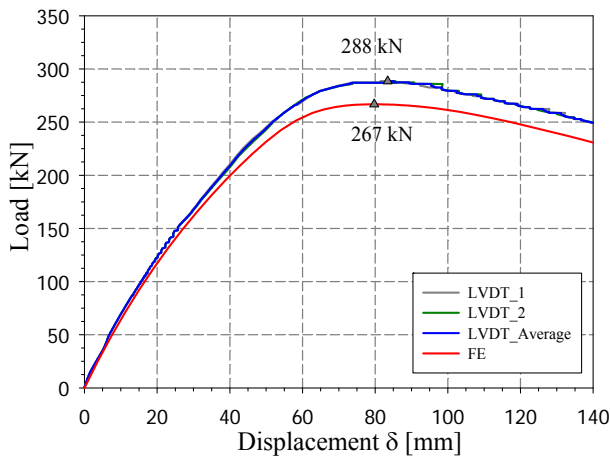
Column positioning



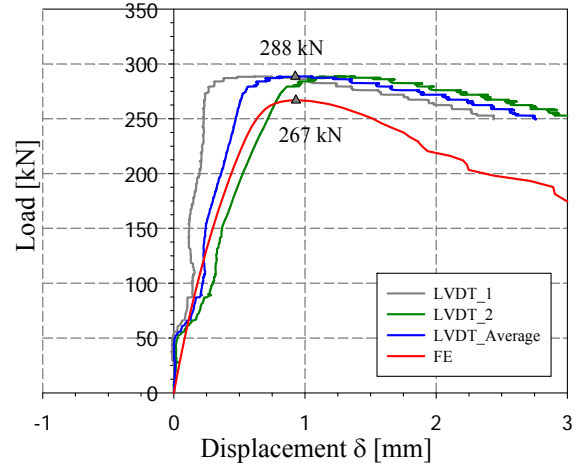
Endplates positions



Main buckling tests

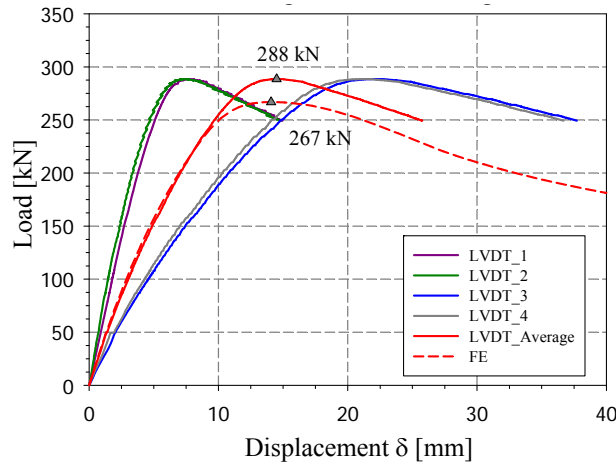


Lateral displacement

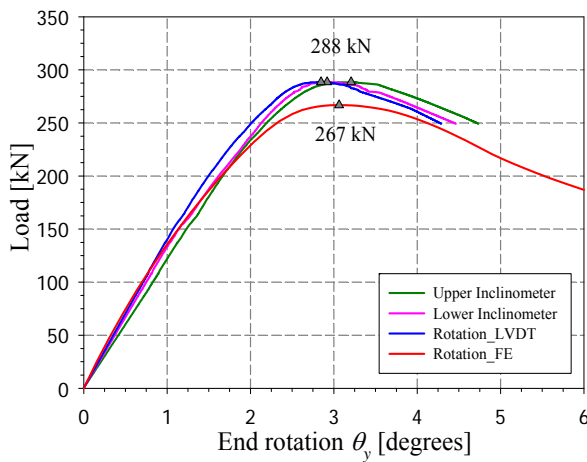


Transversal displacement

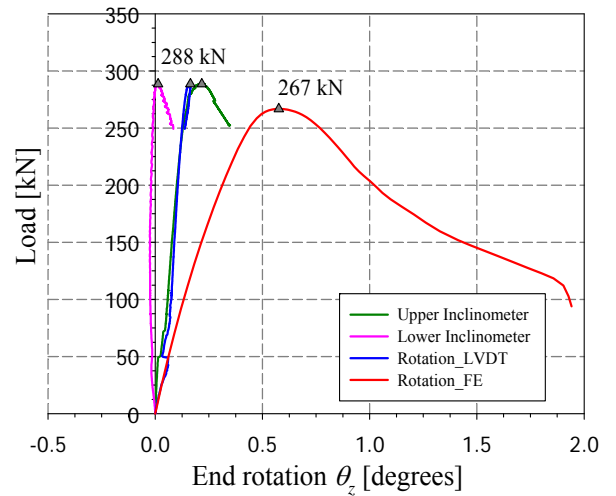
LVDT recording mid-span displacement



LVDTs recording axial shortening

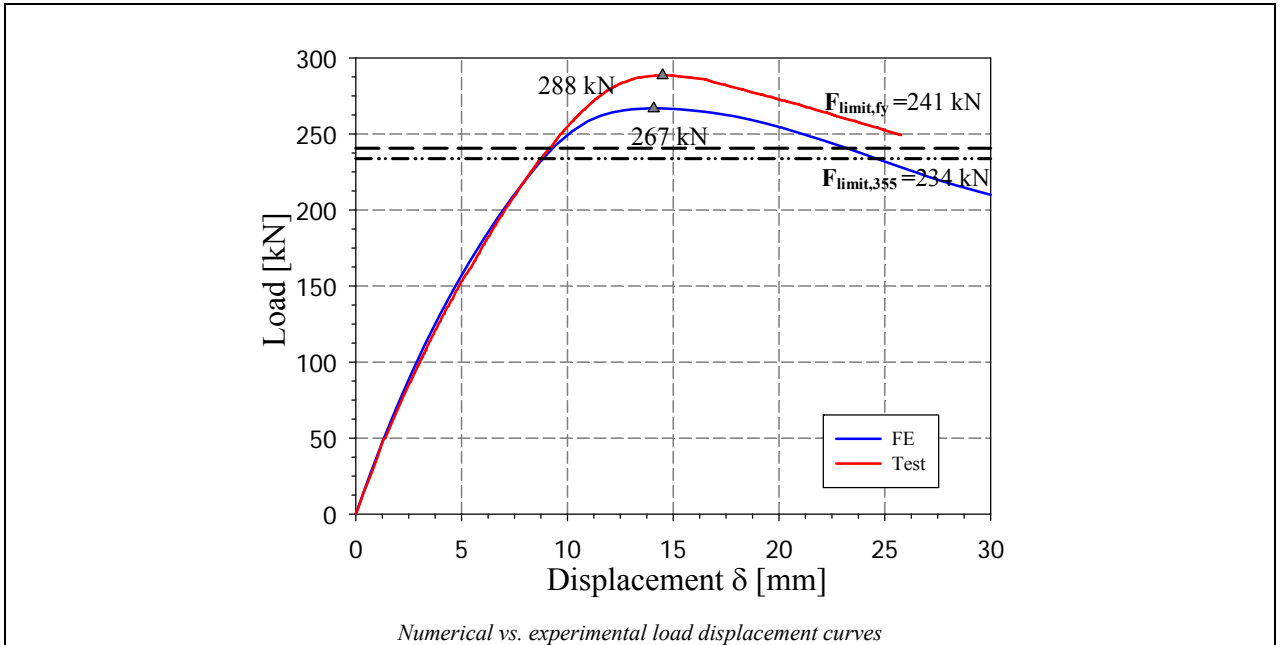


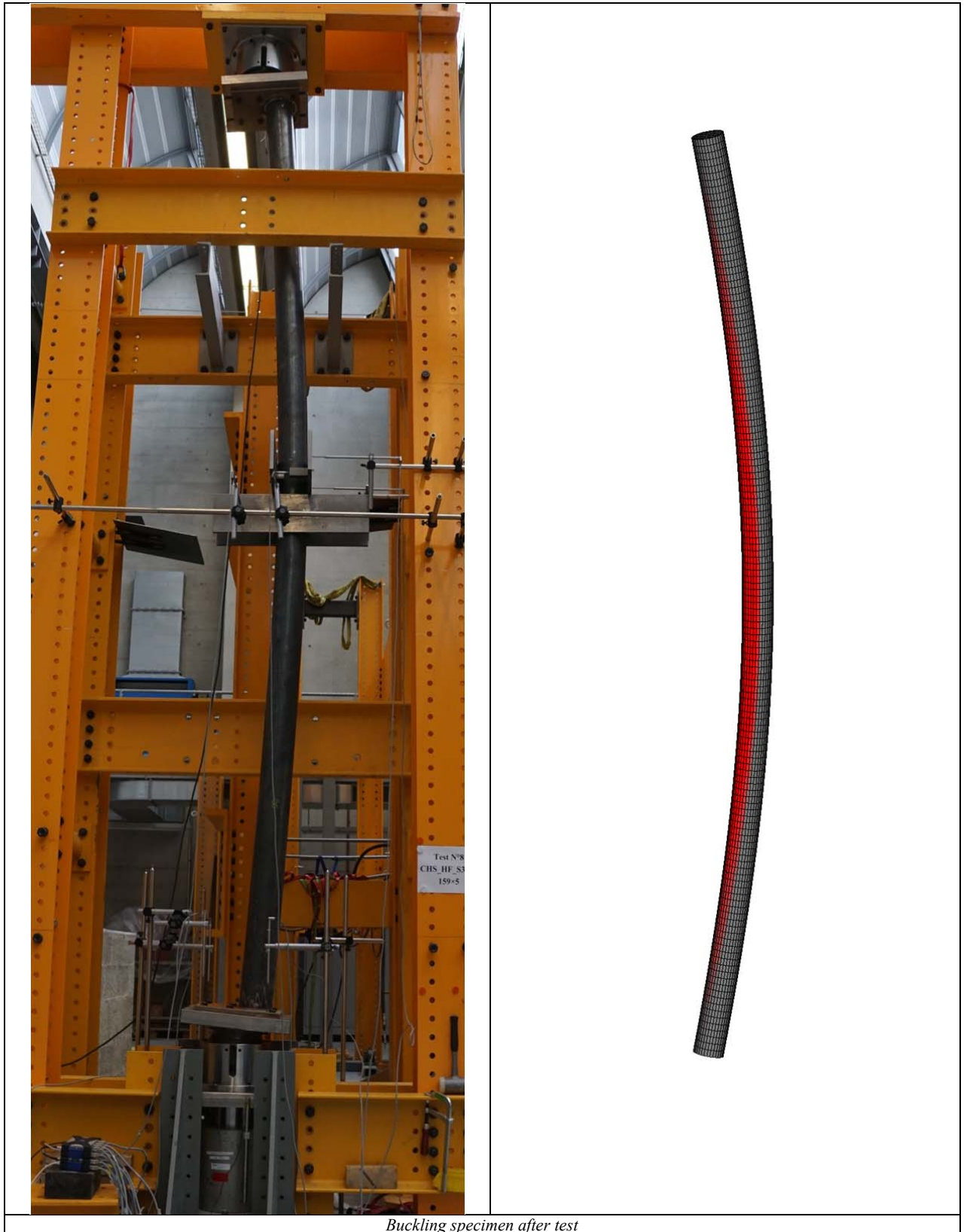
Rotation along major axis



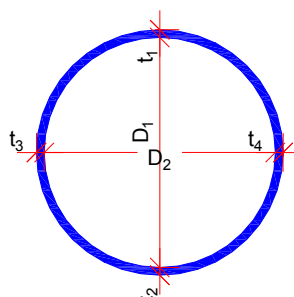
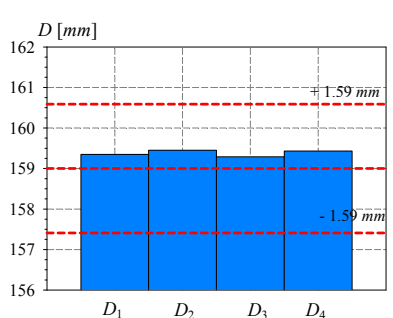
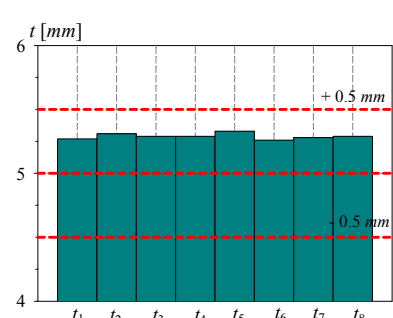
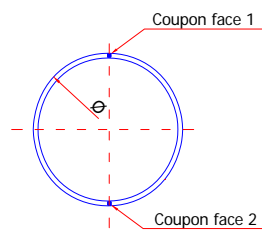
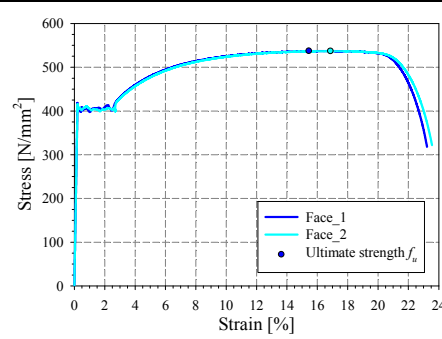
Rotation along minor axis

Column end rotations

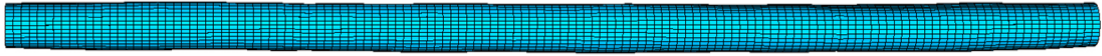




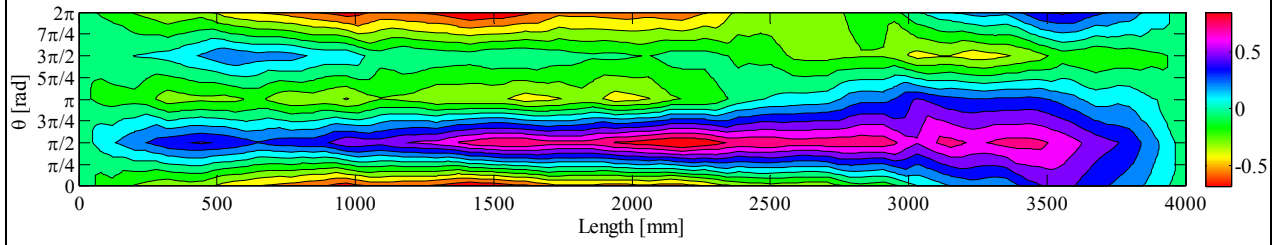
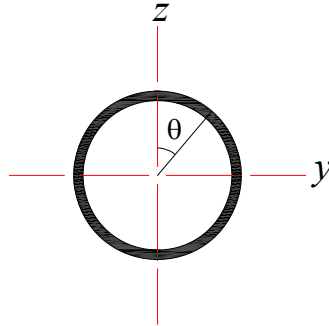
Buckling specimen after test

Test #: 9																
Specimen name	Shape	Details														
CHS_S355HR_159x5		<p>Shape: Circular Hollow Section</p> <p>Nominal yield limit: 355 N/mm^2</p> <p>Length = 4000 mm</p> <p>Load case: 50%N+50%M_y</p> <p>$D = 159$ mm $t = 5$ mm</p> <p>Fabrication process: Hot-Rolled</p> <p>Moment distribution: Triangular</p>														
Preliminary measurements																
Average $D = 159.4$ mm	Average $t = 5.3$ mm															
																
Cross-sectional measured dimensions and tolerances																
 <p style="text-align: center;"><i>Tensile coupons location</i></p>	 <p style="text-align: center;"><i>Measured stress-strain curves</i></p>	<table border="1" style="width: 100%; border-collapse: collapse;"> <thead> <tr> <th></th> <th style="text-align: center;">Average</th> </tr> </thead> <tbody> <tr> <td>E [N/mm^2]</td> <td style="text-align: center;">202187</td> </tr> <tr> <td>f_y [N/mm^2]</td> <td style="text-align: center;">405</td> </tr> <tr> <td>ϵ_y [%]</td> <td style="text-align: center;">0.201</td> </tr> <tr> <td>f_u [N/mm^2]</td> <td style="text-align: center;">537</td> </tr> <tr> <td>ϵ_u [%]</td> <td style="text-align: center;">16.2</td> </tr> <tr> <td colspan="2" style="text-align: center;"><i>Material average properties</i></td> </tr> </tbody> </table>		Average	E [N/mm^2]	202187	f_y [N/mm^2]	405	ϵ_y [%]	0.201	f_u [N/mm^2]	537	ϵ_u [%]	16.2	<i>Material average properties</i>	
	Average															
E [N/mm^2]	202187															
f_y [N/mm^2]	405															
ϵ_y [%]	0.201															
f_u [N/mm^2]	537															
ϵ_u [%]	16.2															
<i>Material average properties</i>																

Initial geometrical imperfections – LVDTs measurements

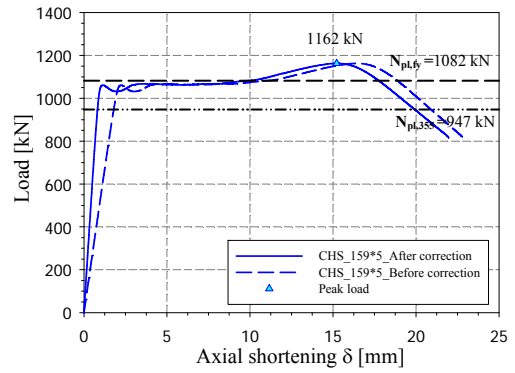
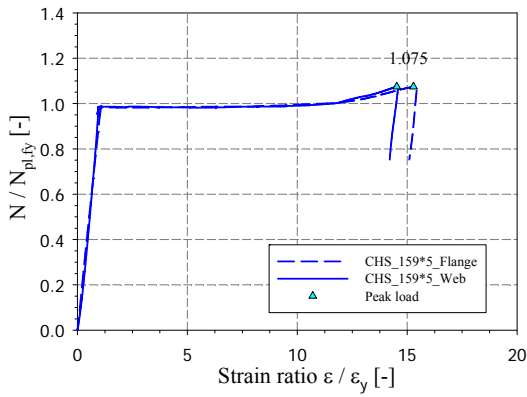


Magnified imperfection view

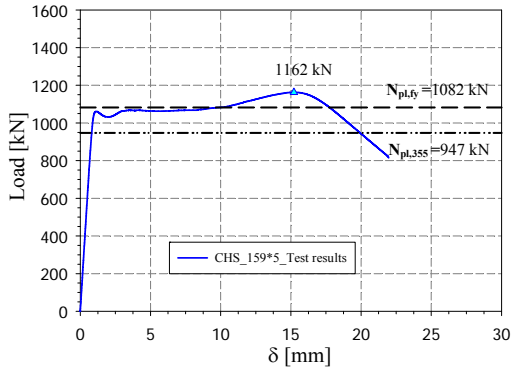


Measured imperfections

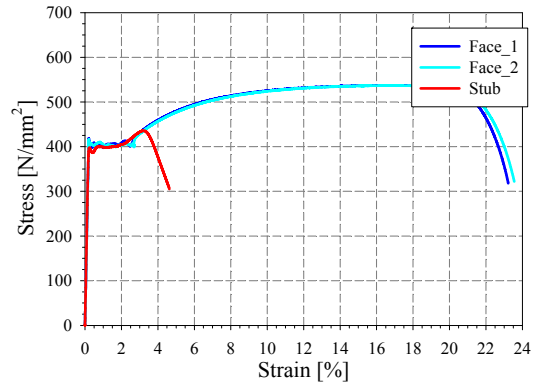
Stub column tests



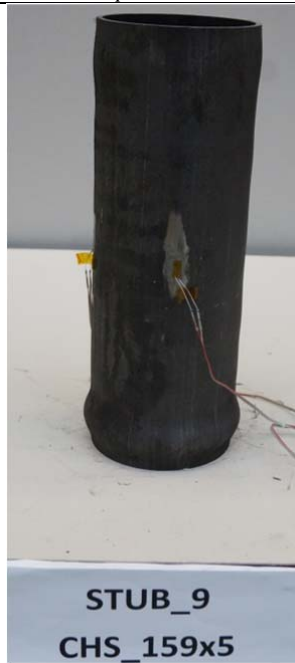
Strain gauges recordings



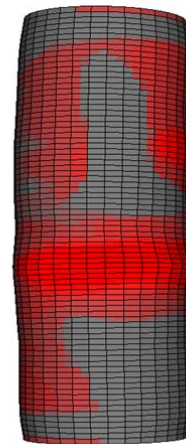
Load displacement curves before and after correction



Load displacement curve

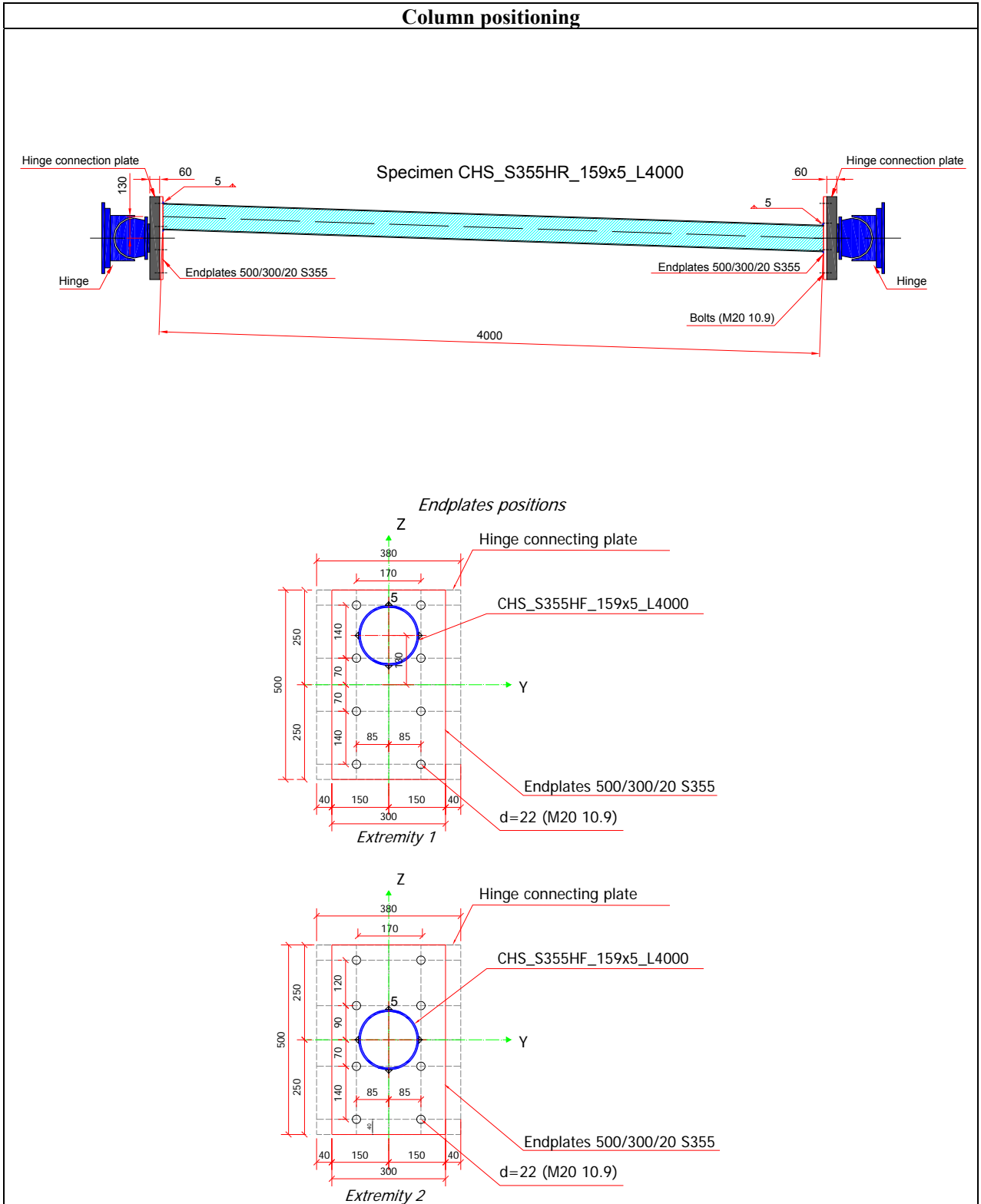


Material stress-strain curve vs. stub stress-strain curve

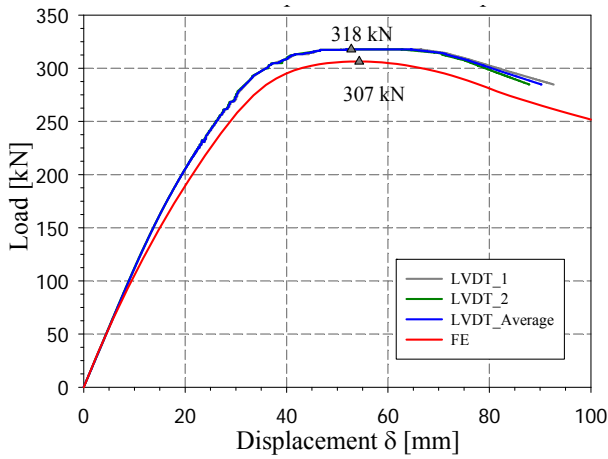


Stub column specimen after test

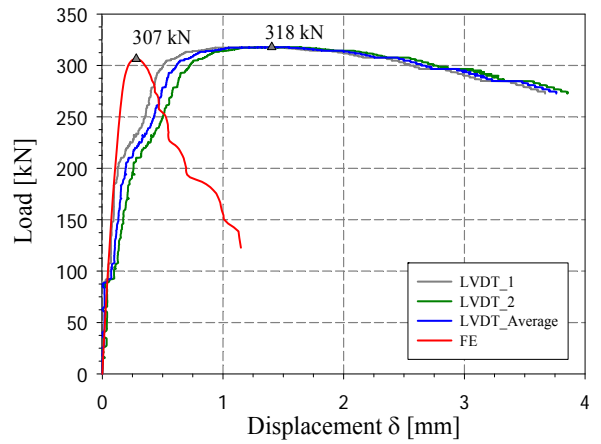
Column positioning



Main buckling tests

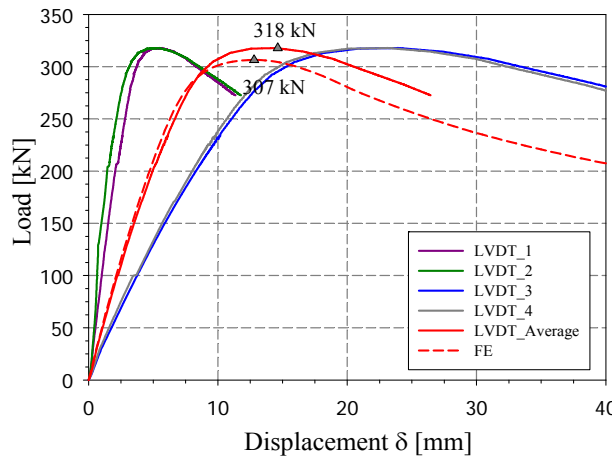


Lateral displacement

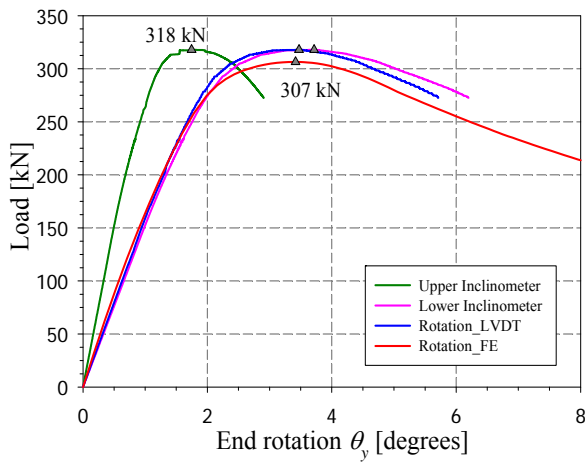


Transversal displacement

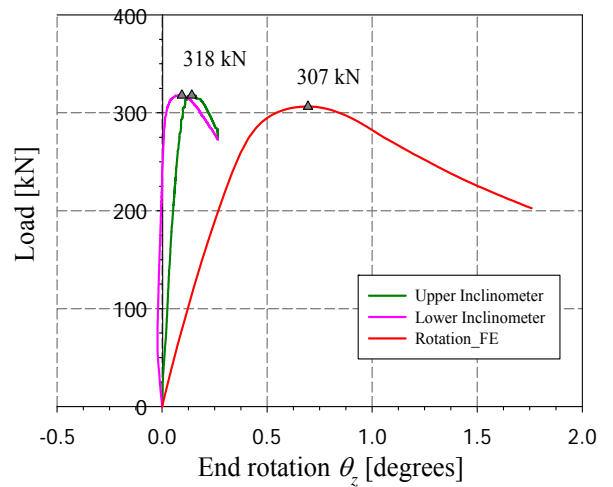
LVDT recording mid-span displacement



LVDTs recording axial shortening

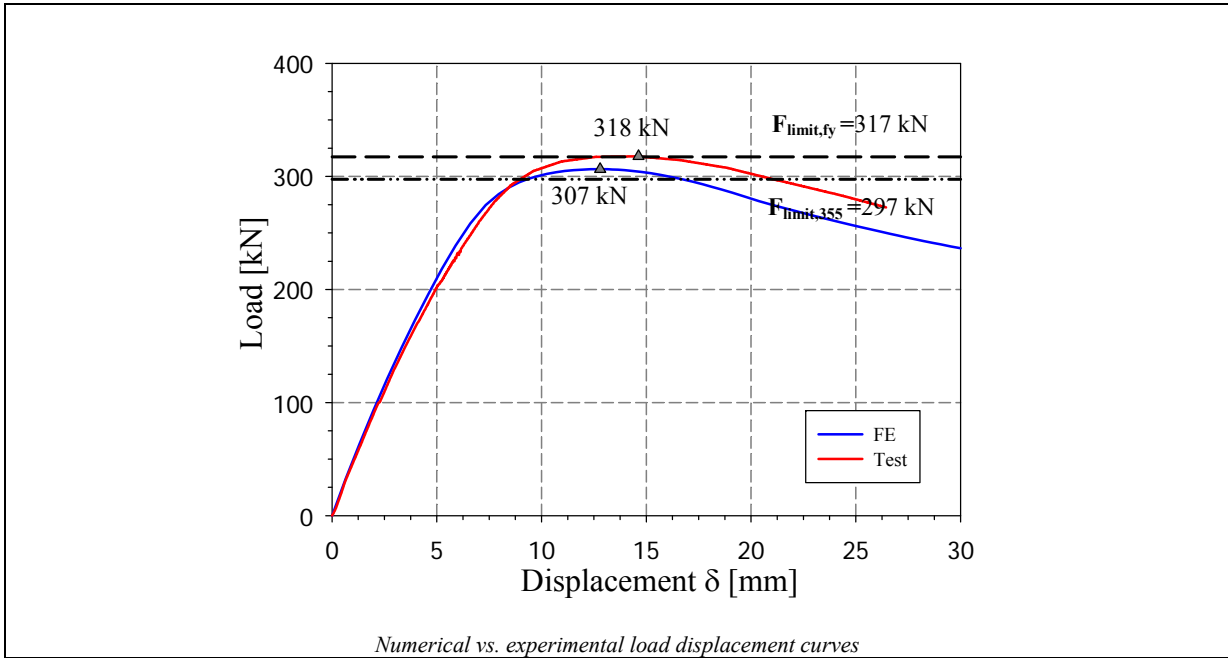


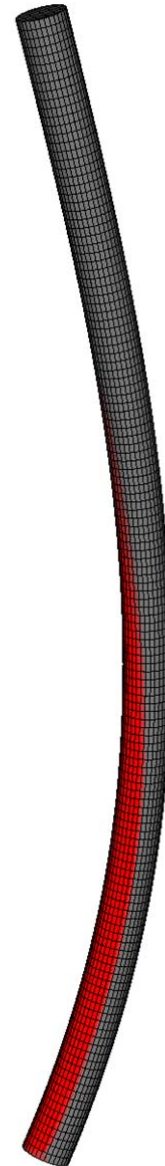
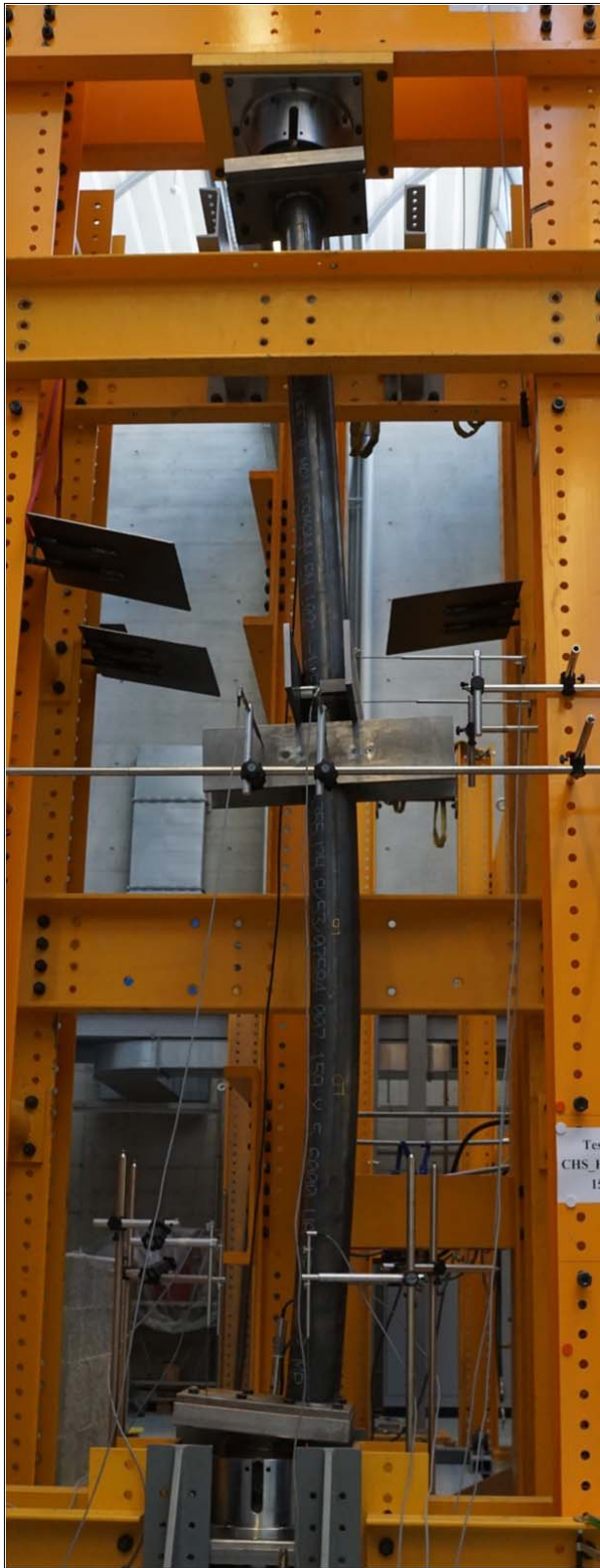
Rotation along major axis



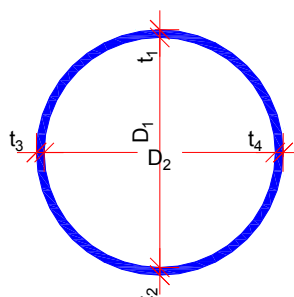
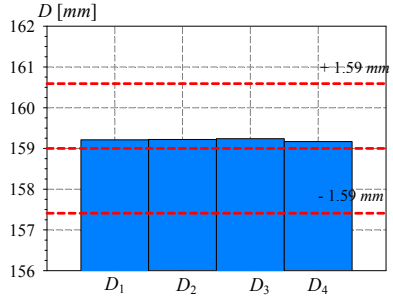
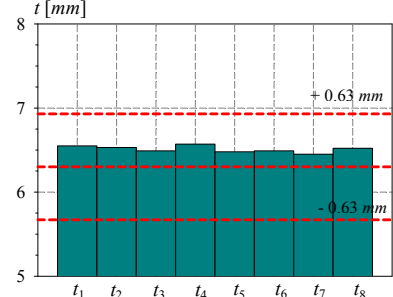
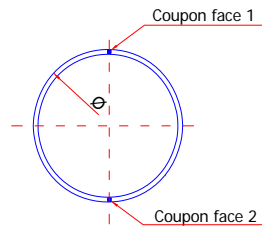
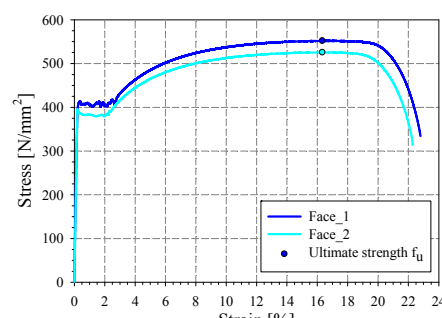
Rotation along minor axis

Column end rotations

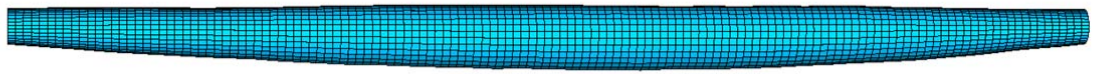




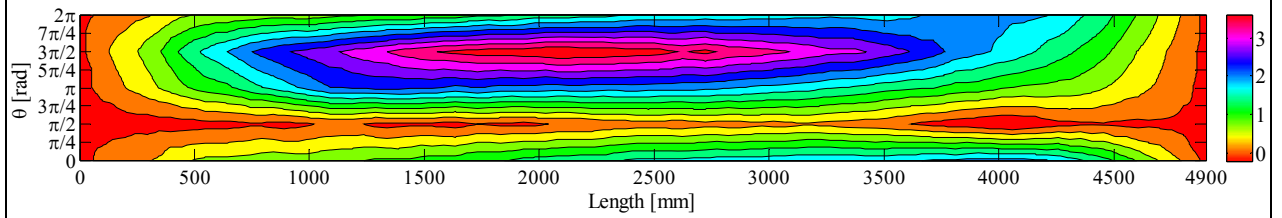
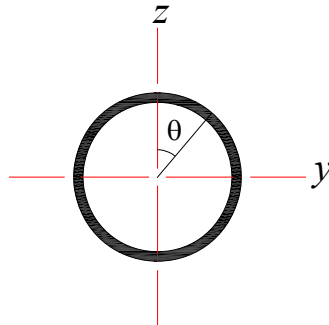
Buckling specimen after test

Test #: 10																
Specimen name	Shape	Details														
CHS_S355HR_159x6.3		<p>Shape: Circular Hollow Section</p> <p>Nominal yield limit: 355 N/mm²</p> <p>Length = 4900 mm</p> <p>Load case: 50%N+50%M_y</p> <p><i>D</i> = 159 mm <i>t</i> = 6.3 mm</p> <p>Fabrication process: Hot-Rolled</p> <p>Moment distribution: Constant</p>														
Preliminary measurements																
Average <i>D</i> = 159.2 mm	Average <i>t</i> = 6.51 mm															
																
<i>Cross-sectional measured dimensions and tolerances</i>																
 <p style="text-align: center;"><i>Tensile coupons location</i></p>	 <p style="text-align: center;"><i>Measured stress-strain curves</i></p>	<table border="1" style="width: 100%; border-collapse: collapse;"> <thead> <tr> <th></th> <th style="text-align: center;">Average</th> </tr> </thead> <tbody> <tr> <td><i>E</i> [N/mm²]</td> <td style="text-align: center;">198884</td> </tr> <tr> <td><i>f_y</i> [N/mm²]</td> <td style="text-align: center;">396</td> </tr> <tr> <td><i>ε_y</i> [%]</td> <td style="text-align: center;">0.199</td> </tr> <tr> <td><i>f_u</i> [N/mm²]</td> <td style="text-align: center;">539</td> </tr> <tr> <td><i>ε_u</i> [%]</td> <td style="text-align: center;">16.4</td> </tr> <tr> <td colspan="2" style="text-align: center;"><i>Material average properties</i></td> </tr> </tbody> </table>		Average	<i>E</i> [N/mm ²]	198884	<i>f_y</i> [N/mm ²]	396	<i>ε_y</i> [%]	0.199	<i>f_u</i> [N/mm ²]	539	<i>ε_u</i> [%]	16.4	<i>Material average properties</i>	
	Average															
<i>E</i> [N/mm ²]	198884															
<i>f_y</i> [N/mm ²]	396															
<i>ε_y</i> [%]	0.199															
<i>f_u</i> [N/mm ²]	539															
<i>ε_u</i> [%]	16.4															
<i>Material average properties</i>																

Initial geometrical imperfections – LVDTs measurements

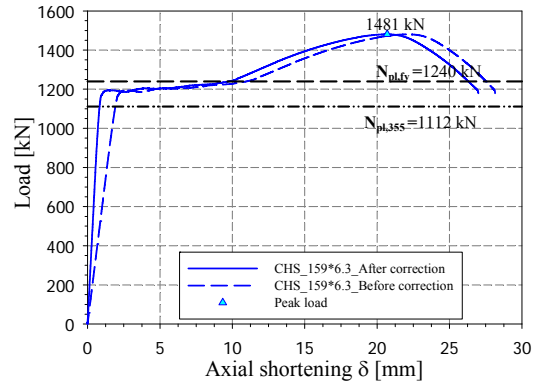
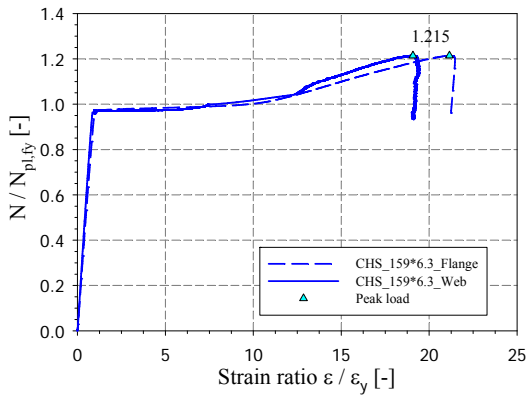


Magnified imperfection view



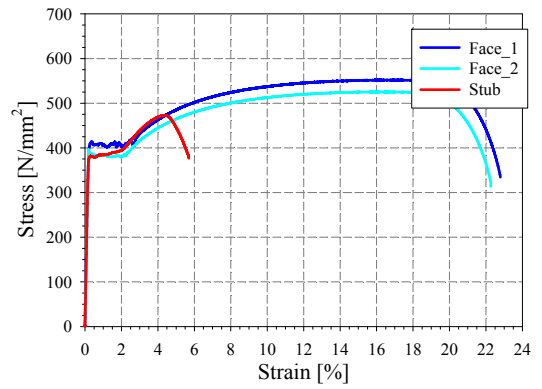
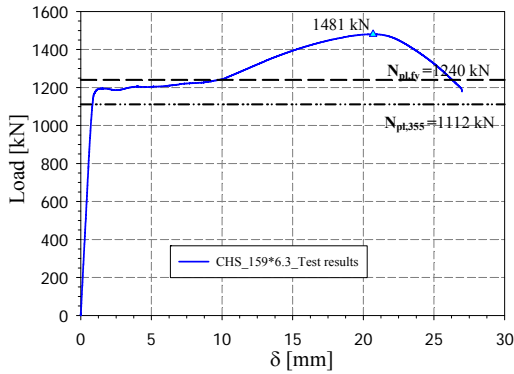
Measured imperfections

Stub column tests



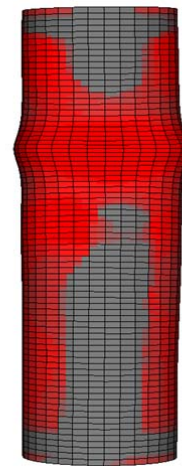
Strain gauges recordings

Load displacement curves before and after correction



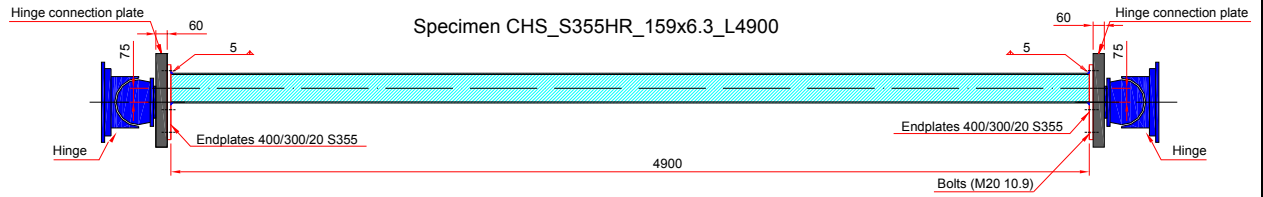
Load displacement curves

Material stress-strain curve vs. stub stress-strain curve

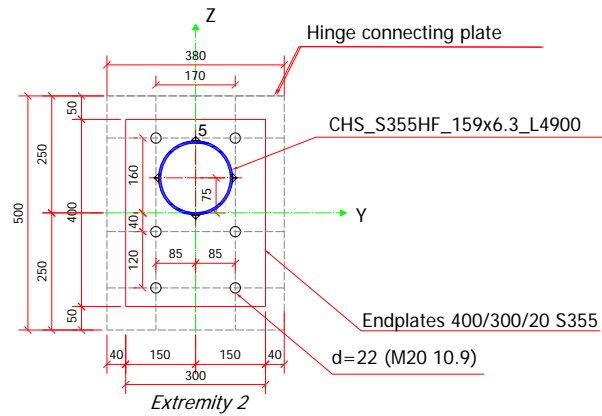
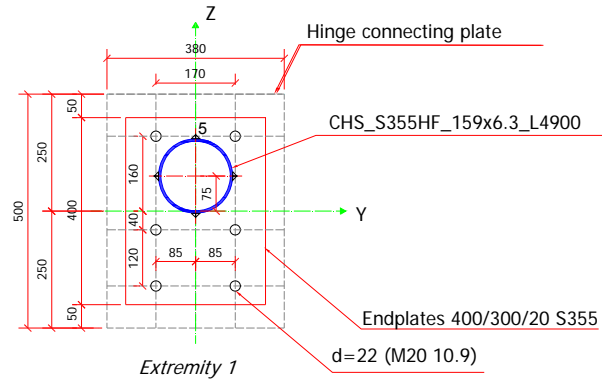


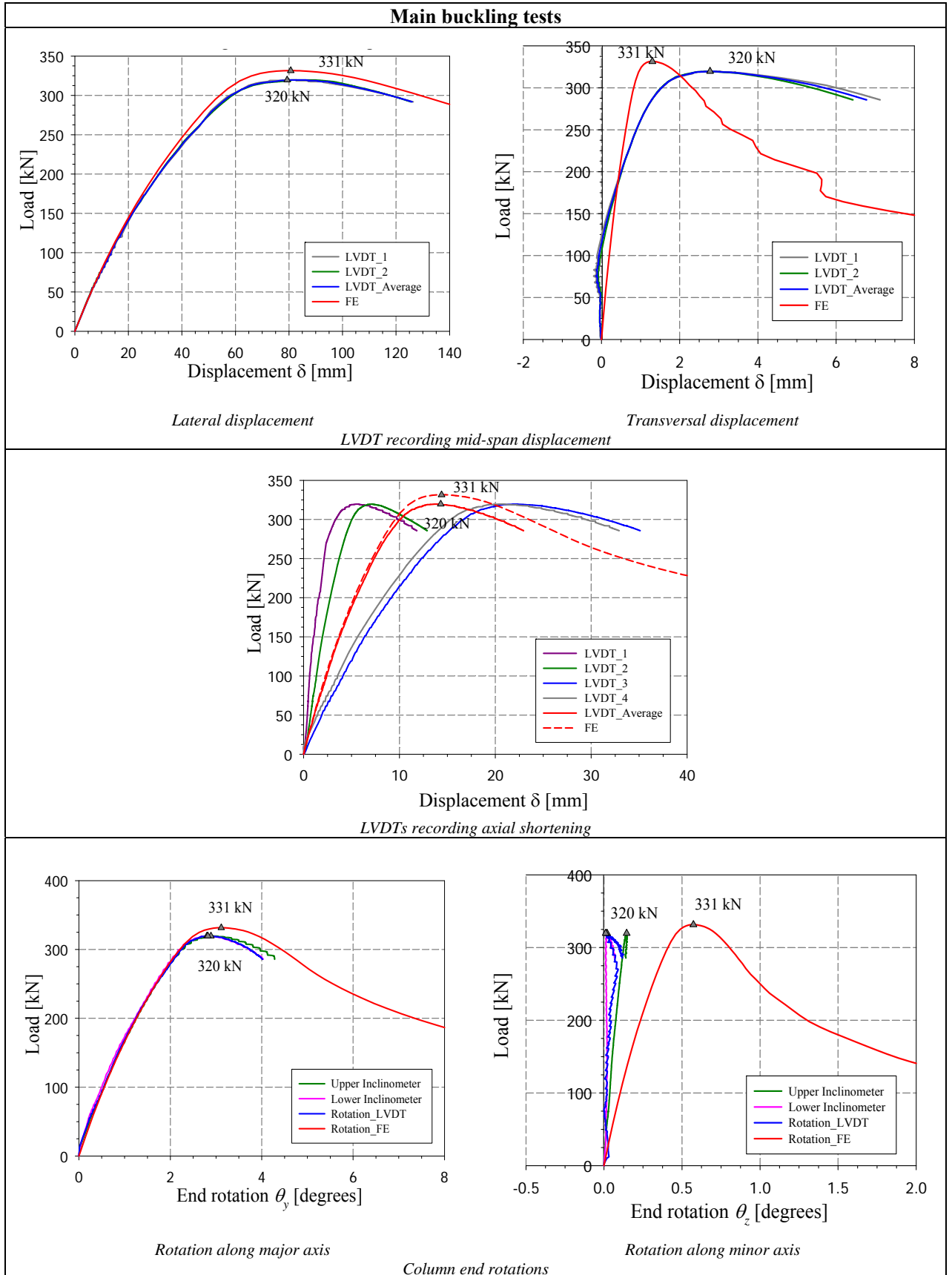
Stub column specimen after test

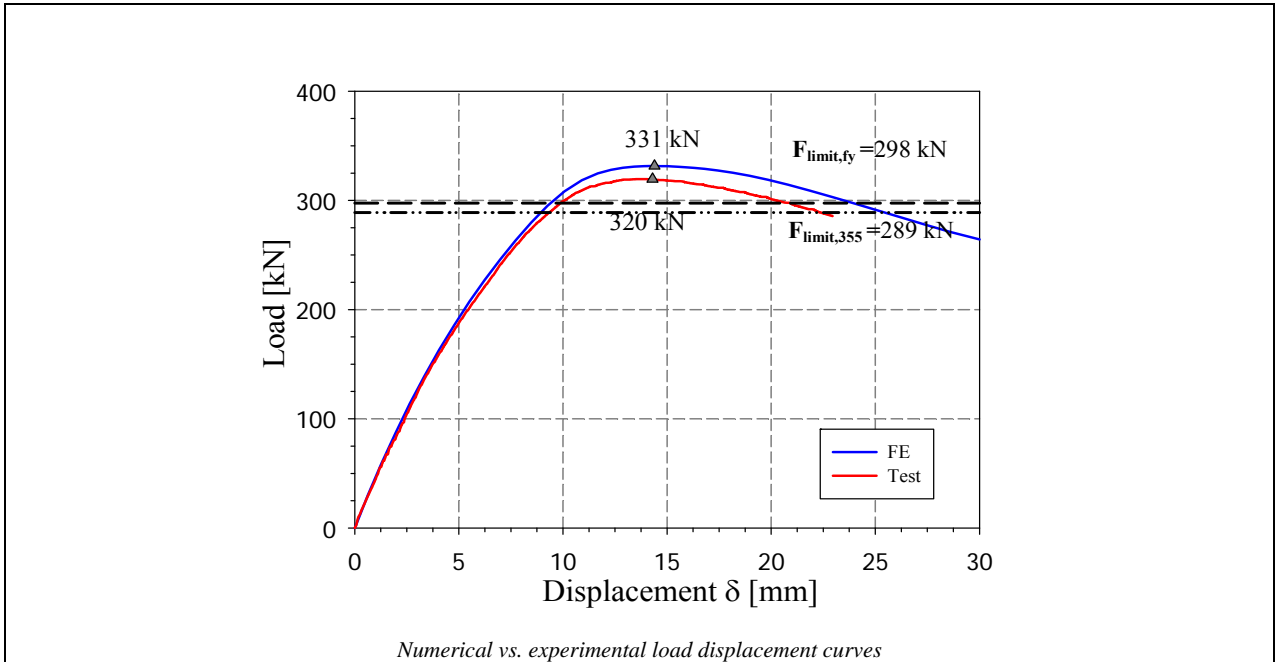
Column positioning

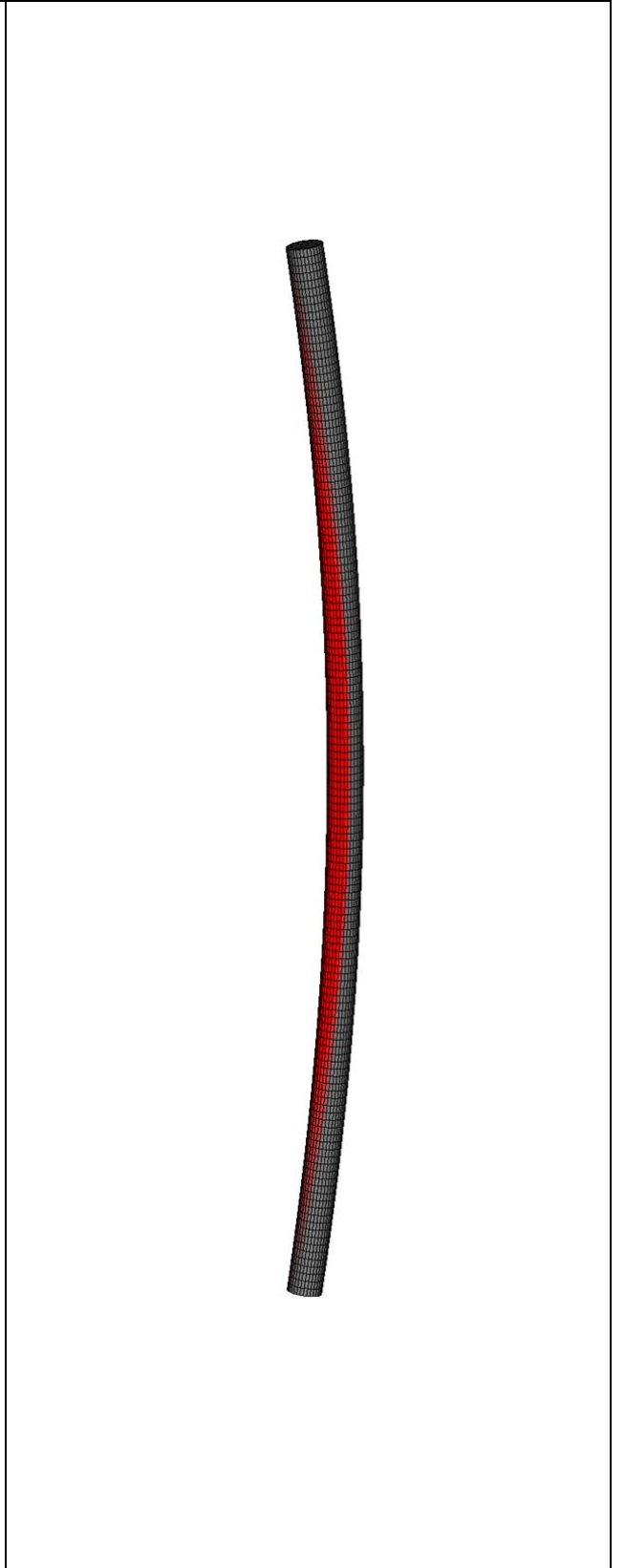


Endplates positions

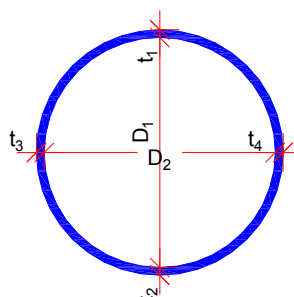
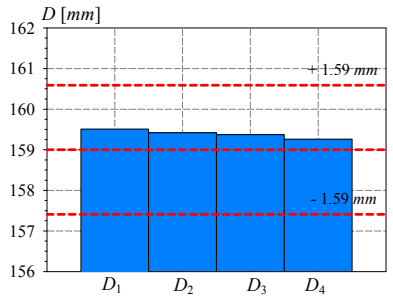
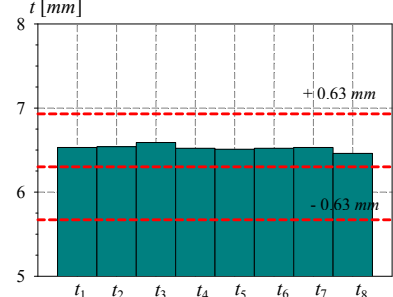
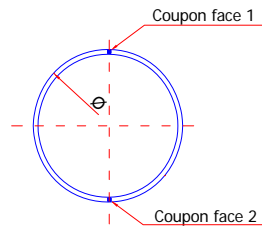
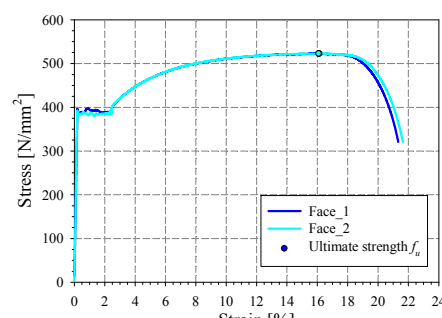








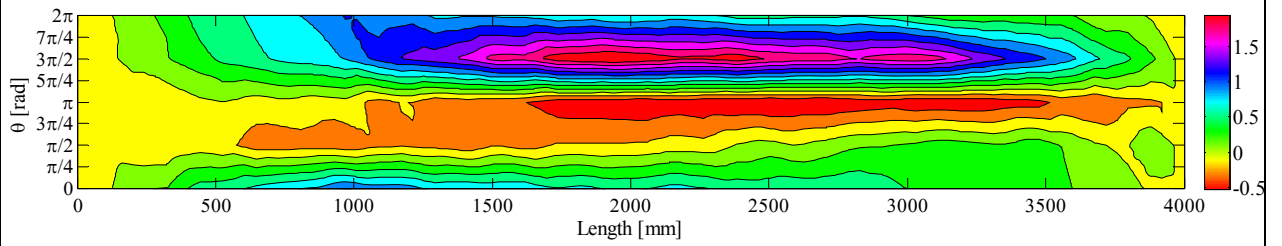
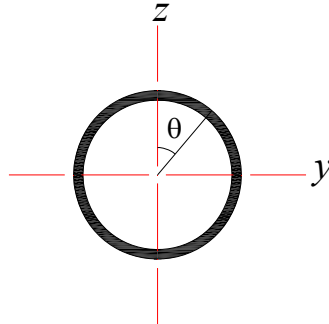
Buckling specimen after test

Test #: 11																
Specimen name	Shape	Details														
CHS_S355HR_159x6.3		<p>Shape: Circular Hollow Section</p> <p>Nominal yield limit: 355 N/mm²</p> <p>Length = 4000 mm</p> <p>Load case: 33%N+33%M_y+33%M_z</p> <p><i>D</i> = 159 mm <i>t</i> = 6.3 mm</p> <p>Fabrication process: Hot-Rolled</p> <p>Moment distribution: Constant</p>														
Preliminary measurements																
Average <i>D</i> = 159.4 mm		Average <i>t</i> = 6.53 mm														
																
<i>Cross-sectional measured dimensions and tolerances</i>																
 <p style="text-align: center;"><i>Tensile coupons location</i></p>	 <p style="text-align: center;"><i>Measured stress-strain curves</i></p>	<table border="1" style="width: 100%; border-collapse: collapse;"> <thead> <tr> <th></th> <th style="text-align: center;">Average</th> </tr> </thead> <tbody> <tr> <td><i>E</i> [N/mm²]</td> <td style="text-align: center;">202739</td> </tr> <tr> <td><i>f_y</i> [N/mm²]</td> <td style="text-align: center;">389</td> </tr> <tr> <td><i>ε_y</i> [%]</td> <td style="text-align: center;">0.192</td> </tr> <tr> <td><i>f_u</i> [N/mm²]</td> <td style="text-align: center;">522</td> </tr> <tr> <td><i>ε_u</i> [%]</td> <td style="text-align: center;">16.1</td> </tr> <tr> <td colspan="2" style="text-align: center;"><i>Material average properties</i></td> </tr> </tbody> </table>		Average	<i>E</i> [N/mm ²]	202739	<i>f_y</i> [N/mm ²]	389	<i>ε_y</i> [%]	0.192	<i>f_u</i> [N/mm ²]	522	<i>ε_u</i> [%]	16.1	<i>Material average properties</i>	
	Average															
<i>E</i> [N/mm ²]	202739															
<i>f_y</i> [N/mm ²]	389															
<i>ε_y</i> [%]	0.192															
<i>f_u</i> [N/mm ²]	522															
<i>ε_u</i> [%]	16.1															
<i>Material average properties</i>																

Initial geometrical imperfections – LVDTs measurements

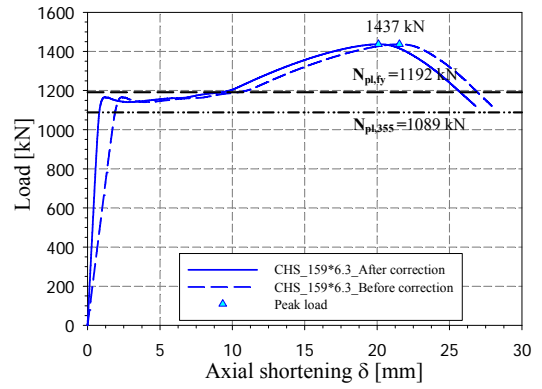
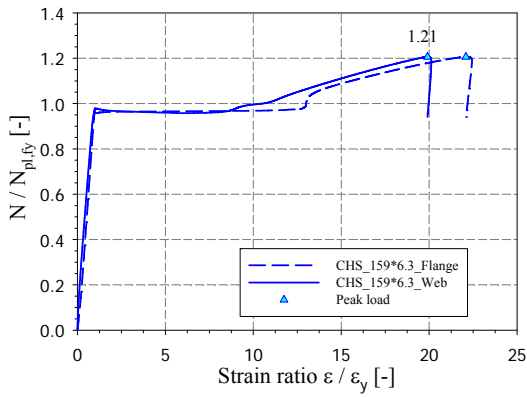


Magnified imperfection view



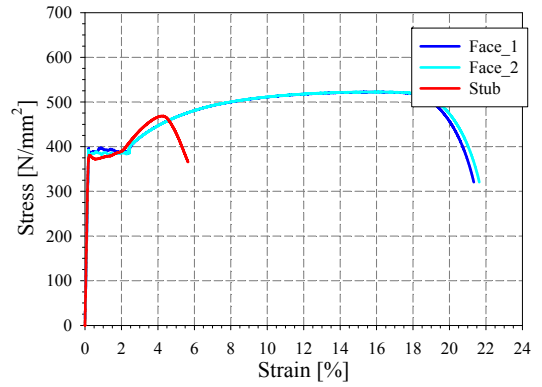
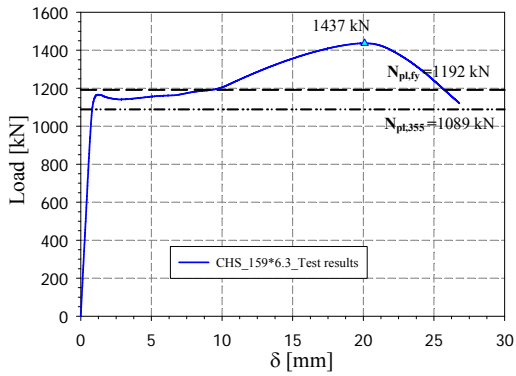
Measured imperfections

Stub column tests



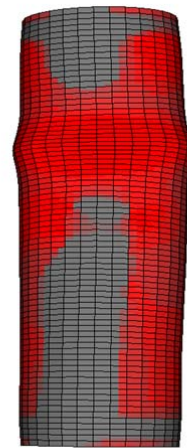
Strain gauges recordings

Load displacement curves before and after correction



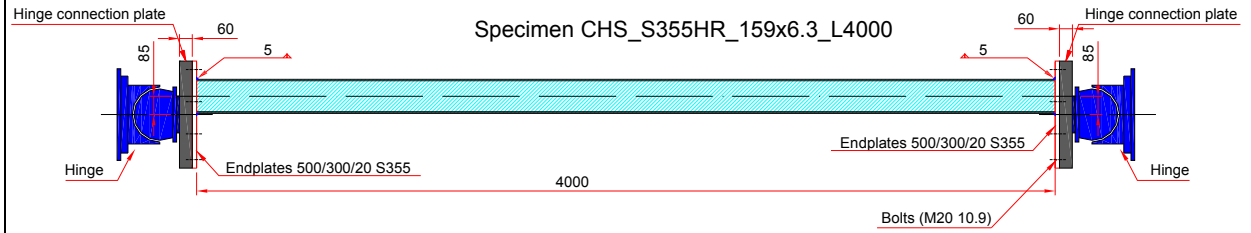
Load displacement curve

Material stress-strain curve vs. stub stress-strain curve

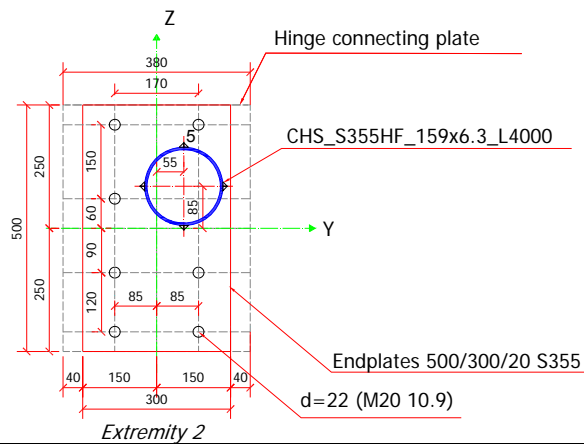
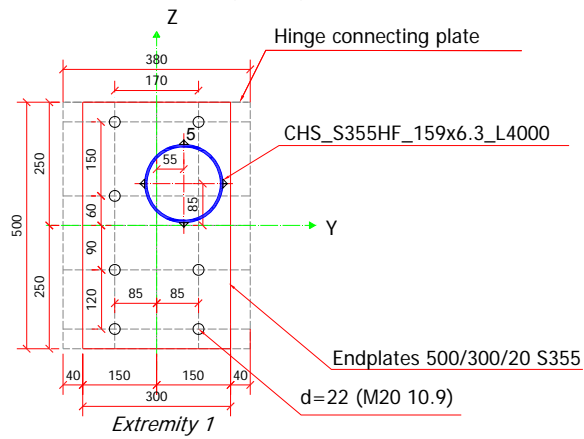


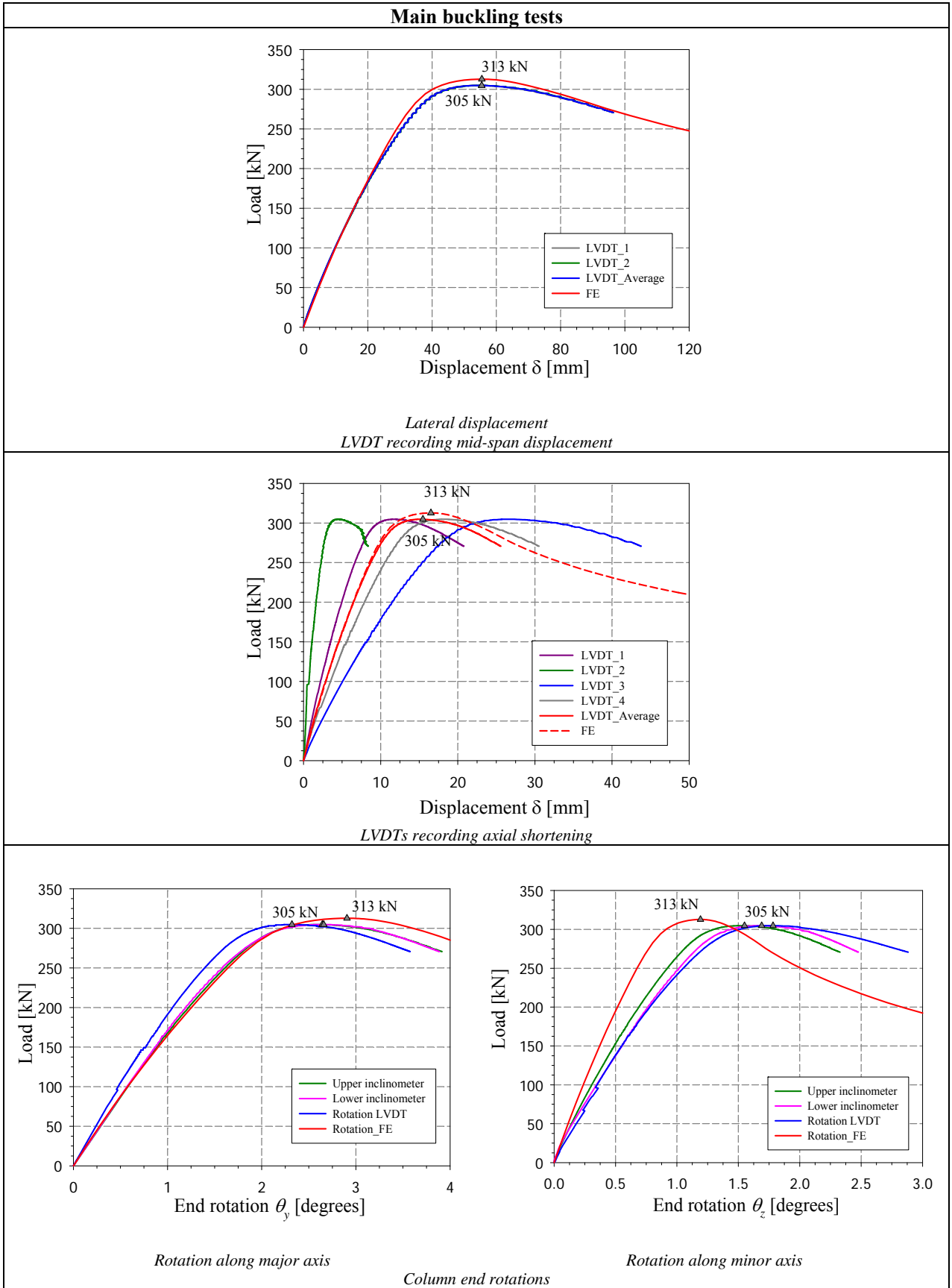
Stub column specimen after test

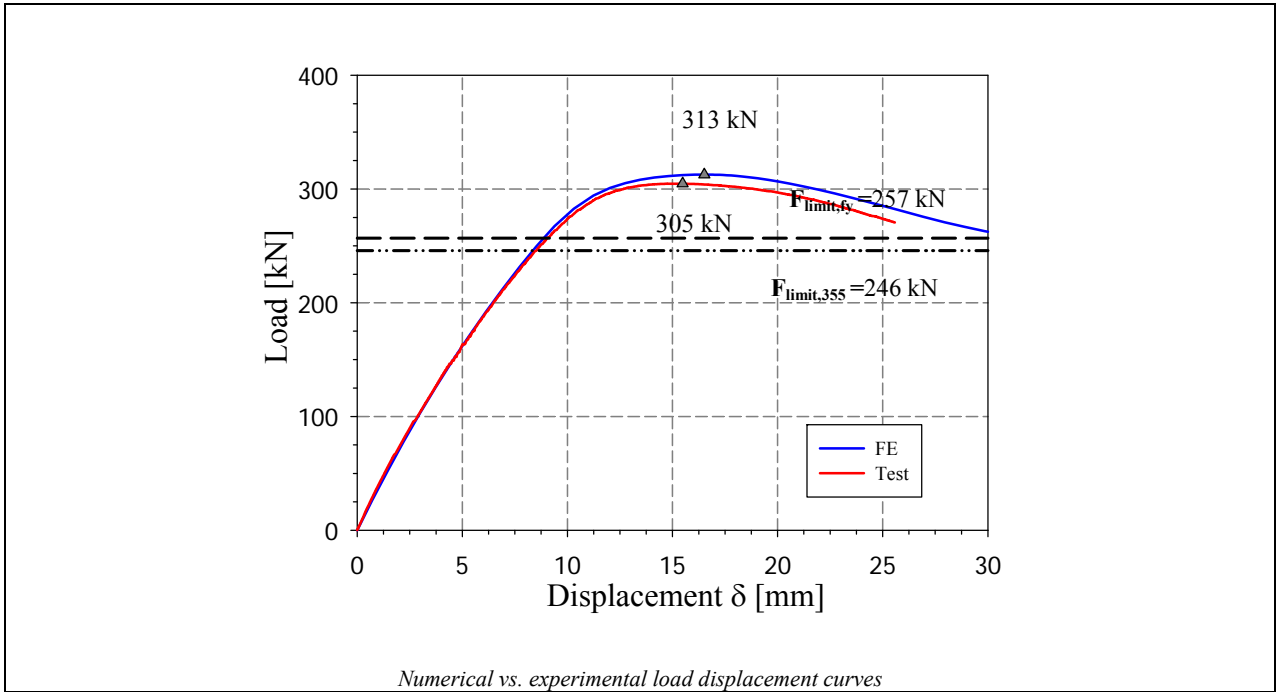
Column positioning



Endplates positions

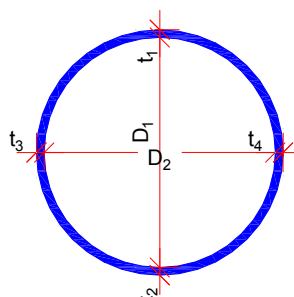
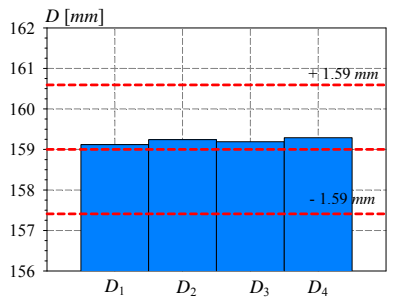
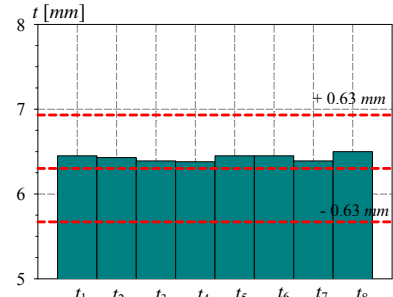
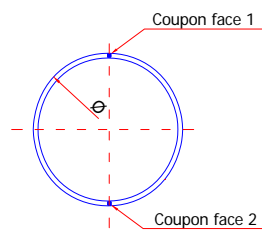
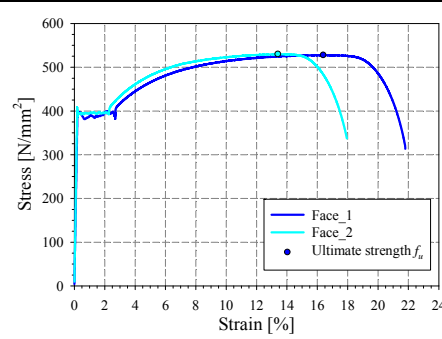








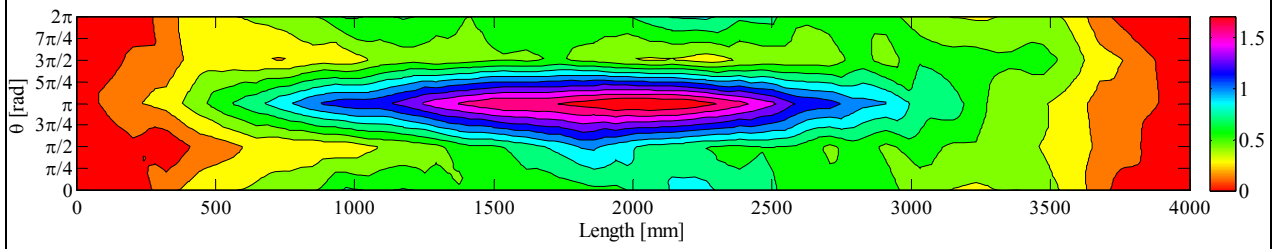
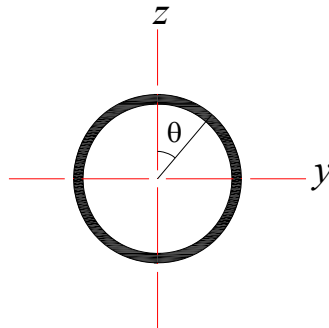
Buckling specimen after test

Test #: 12																
Specimen name	Shape	Details														
CHS_S355HR_159x6.3		<p>Shape: Circular Hollow Section</p> <p>Nominal yield limit: 355 N/mm^2</p> <p>Length = 4000 mm</p> <p>Load case: 50%N+50%M_y</p> <p>$D = 159$ mm $t = 6.3$ mm</p> <p>Fabrication process: Hot-Rolled</p> <p>Moment distribution: Triangular</p>														
Preliminary measurements																
Average $D = 159.2$ mm		Average $t = 6.4$ mm														
																
<i>Cross-sectional measured dimensions and tolerances</i>																
 <p style="text-align: center;"><i>Tensile coupons location</i></p>	 <p style="text-align: center;"><i>Measured stress-strain curves</i></p>	<table border="1" style="width: 100%; border-collapse: collapse;"> <thead> <tr> <th style="width: 60%;"></th> <th style="width: 40%; text-align: center;">Average</th> </tr> </thead> <tbody> <tr> <td>E [N/mm^2]</td> <td style="text-align: center;">206449</td> </tr> <tr> <td>f_y [N/mm^2]</td> <td style="text-align: center;">394</td> </tr> <tr> <td>ϵ_y [%]</td> <td style="text-align: center;">0.191</td> </tr> <tr> <td>f_u [N/mm^2]</td> <td style="text-align: center;">529</td> </tr> <tr> <td>ϵ_u [%]</td> <td style="text-align: center;">14.9</td> </tr> <tr> <td colspan="2" style="text-align: center;"><i>Material average properties</i></td> </tr> </tbody> </table>		Average	E [N/mm^2]	206449	f_y [N/mm^2]	394	ϵ_y [%]	0.191	f_u [N/mm^2]	529	ϵ_u [%]	14.9	<i>Material average properties</i>	
	Average															
E [N/mm^2]	206449															
f_y [N/mm^2]	394															
ϵ_y [%]	0.191															
f_u [N/mm^2]	529															
ϵ_u [%]	14.9															
<i>Material average properties</i>																

Initial geometrical imperfections – LVDTs measurements

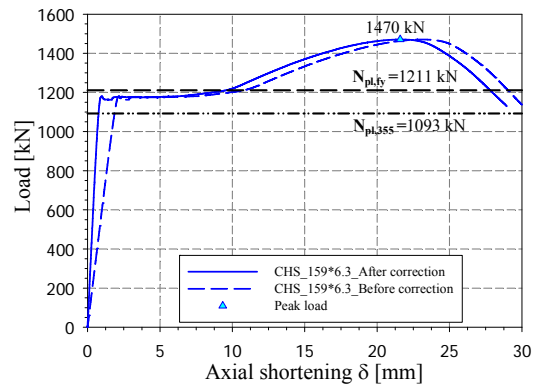
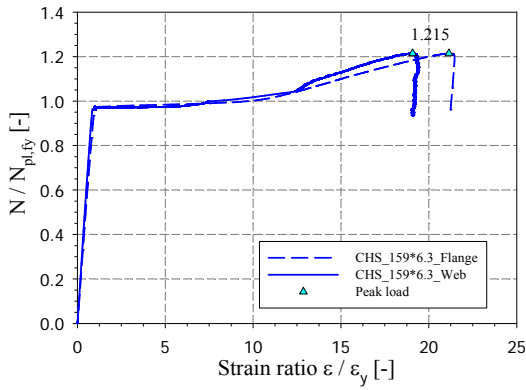


Magnified imperfection view



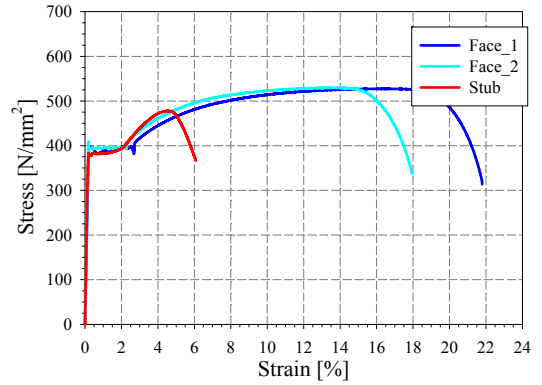
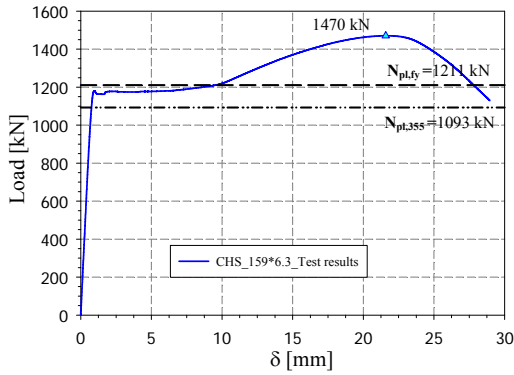
Measured imperfections

Stub column tests



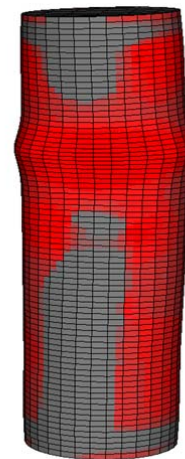
Strain gauges recordings

Load displacement curves before and after correction



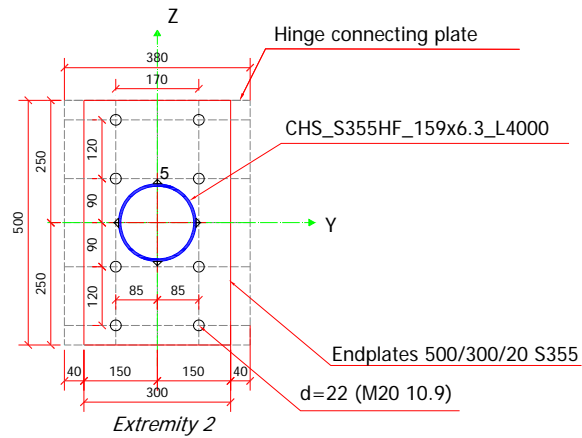
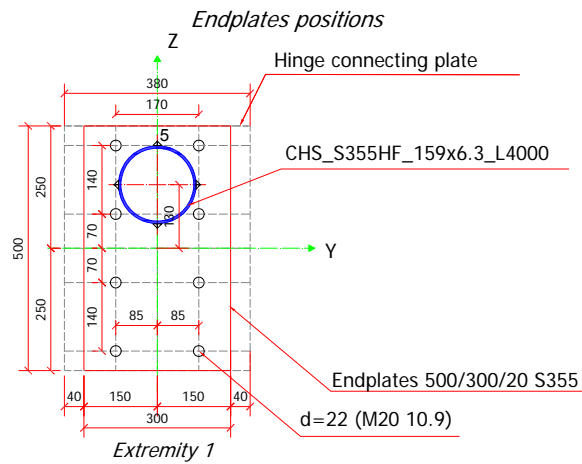
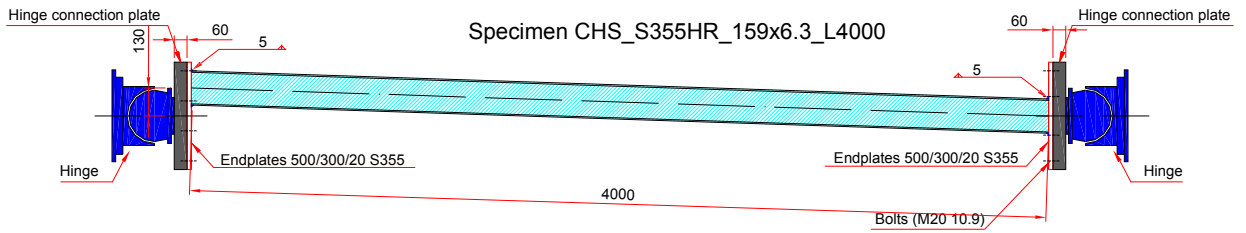
Load displacement curves

Material stress-strain curve vs. stub stress-strain curve

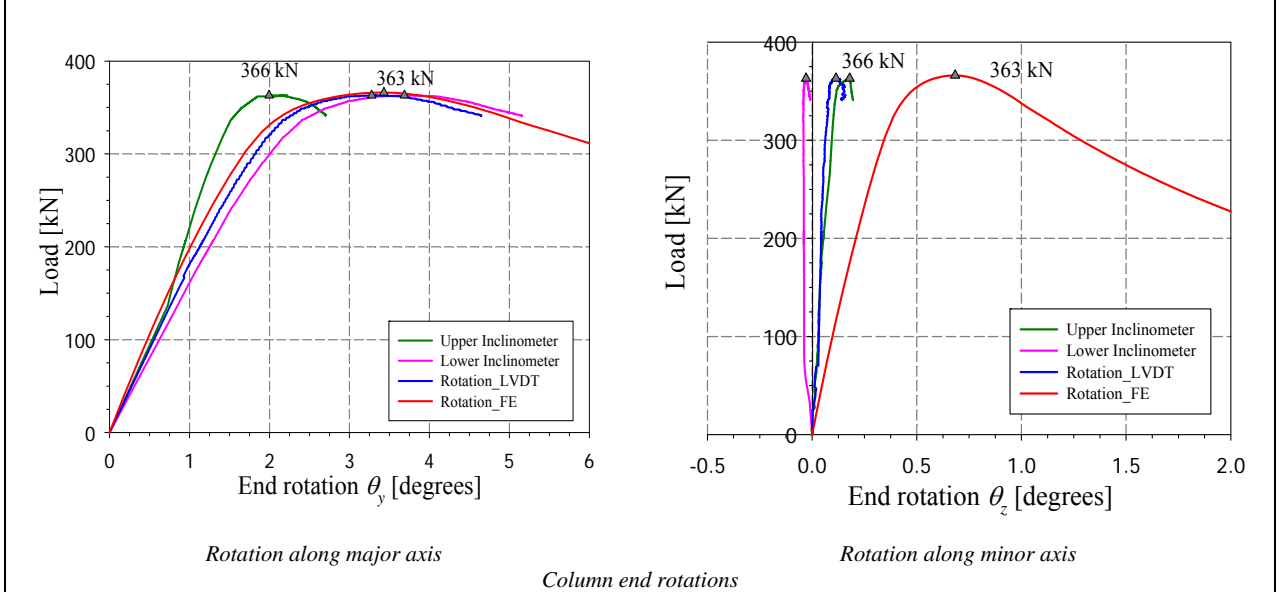
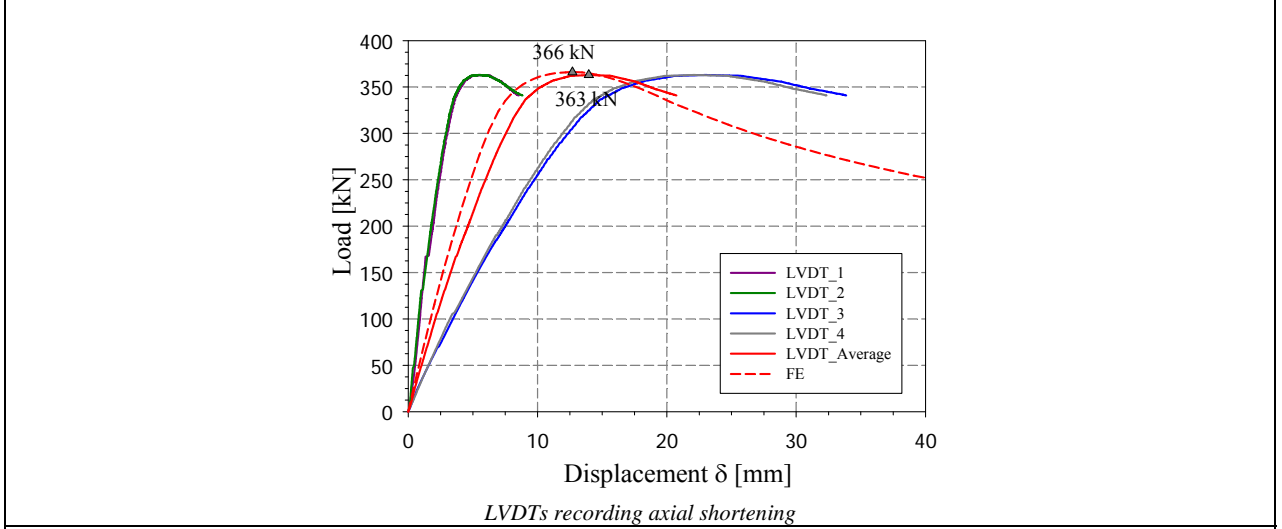
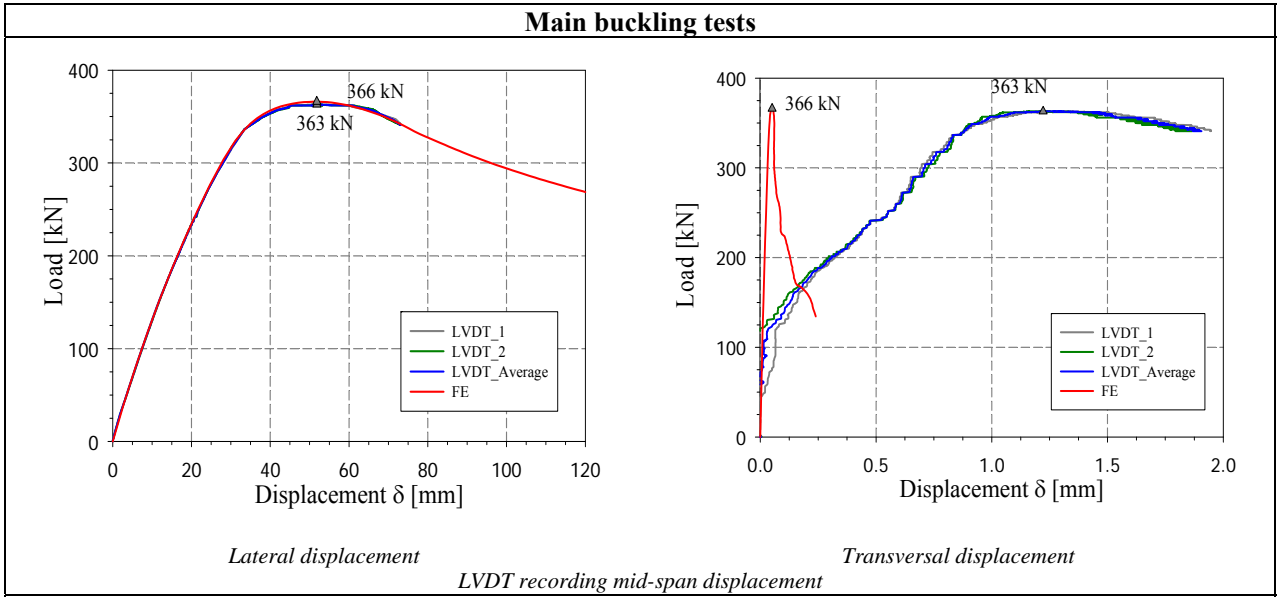


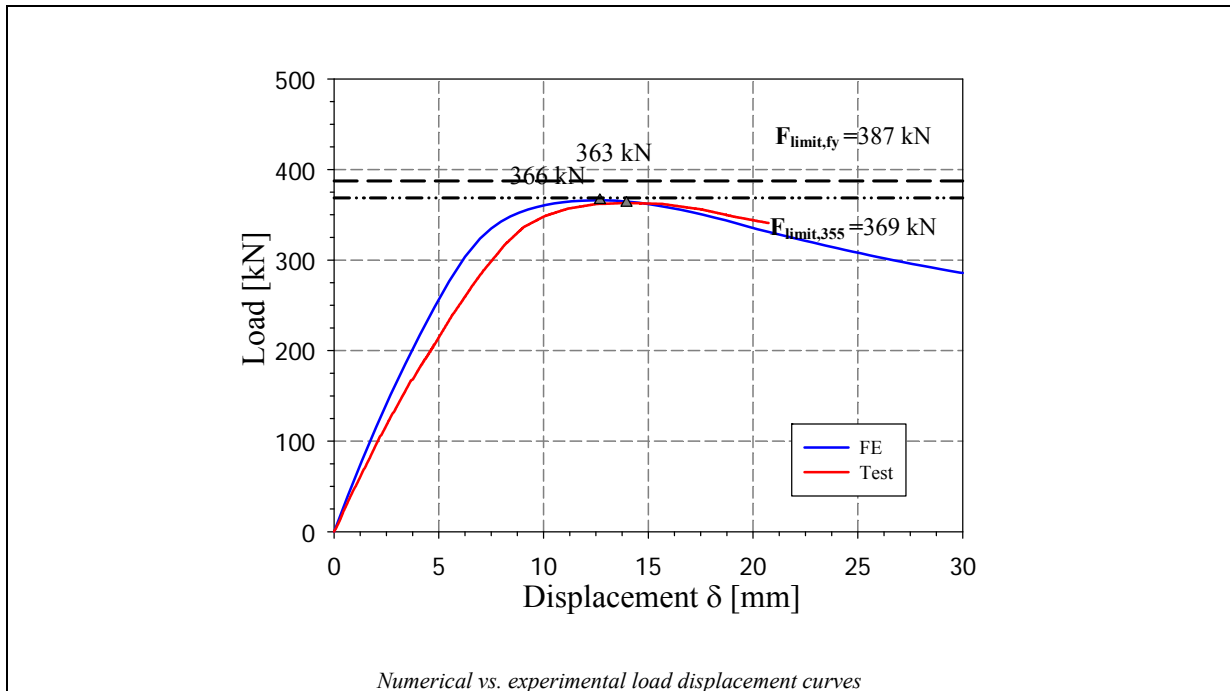
Stub column specimen after test

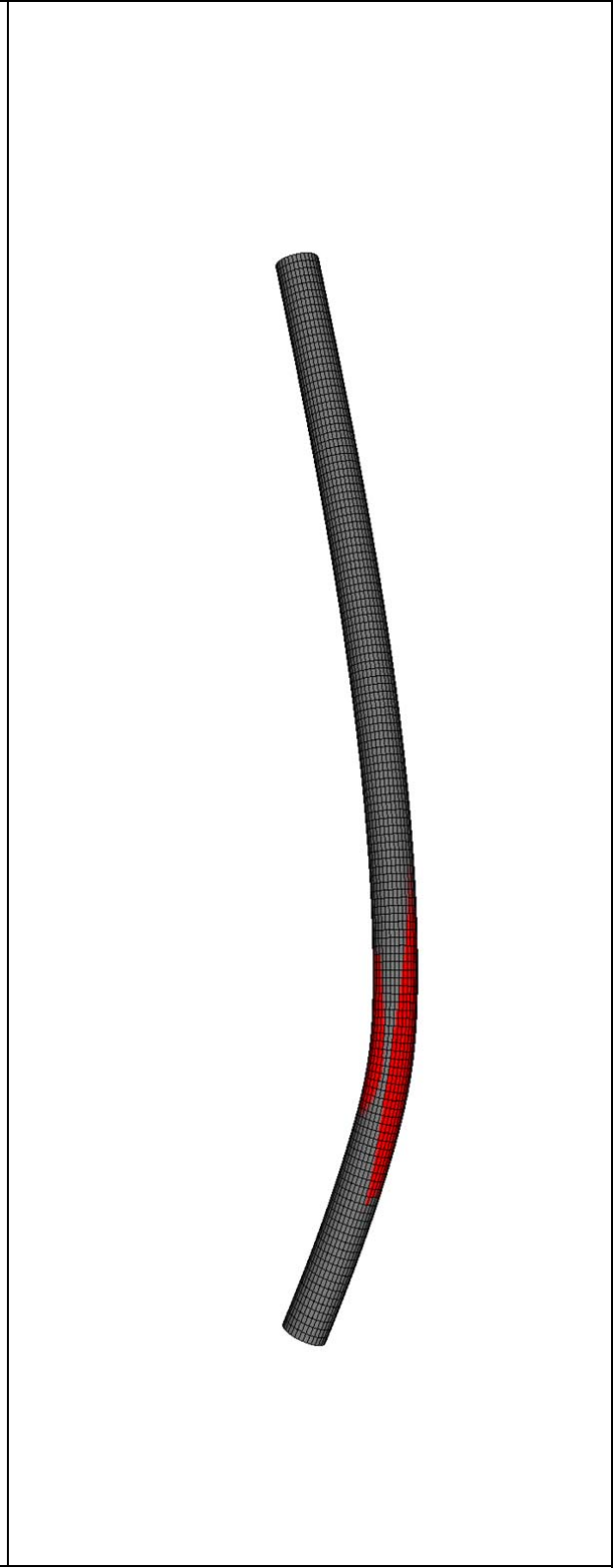
Column positioning



Main buckling tests







Buckling specimen after test

10. Liste of Figures

Figure 1 – Resistance – stability interaction for flexural buckling	1
Figure 2 – Principles and application steps of proposed “Overall Interaction Concept”	2
Figure 3 – Deflection column due to applied compressive load	7
Figure 4 – First three modes of buckling	8
Figure 5 – Historical review of buckling	9
Figure 6 – Simply supported member with initial imperfection	10
Figure 7 – Curves proposed by the CECM in 1970.....	13
Figure 8 – Curves proposed by the CECM in 1978.....	15
Figure 9 – Upper and lower bounds of buckling curves.....	17
Figure 10 – Schematic representation of the Ayrton-Perry approach.....	21
Figure 11 – Section notation and designation.....	27
Figure 12 – Local buckling curves.....	29
Figure 13 – Definition of equivalent width value.....	30
Figure 14 – Actual 2 nd order bending moment and the associated sinusoidal equivalent	32
Figure 15 – Cutting plan and use of a 4900 mm, CHS 159x5 column.....	48
Figure 16 – Cutting procedure	48
Figure 17 – Eccentricities limitations depending on the cross-section shape and end plates dimensions – a) CHS 159x5 / CHS 159x6.3 – b) RHS 200x100x4 – c) RHS 220x120x6.....	51
Figure 18 – Numerical member results tested under combined loadings for – a) CHS 159x6.3 – b) CHS 159x5 – c) RHS 200x100x4 – d) RHS 220x120x6.....	54
Figure 19 – Measurement of cross-section dimensions of circular and rectangular sections.....	58
Figure 20 – Measured dimensions for various cross-sections.....	59
Figure 21 – Measured cross-sectional dimensions and tolerances – RHS CF 200x100x4 T1	60
Figure 22 – Measured cross-sectional dimensions and tolerances – CHS HR 159x6.3 T12	60
Figure 23 – Extraction of coupons from – a) CHS sections – b) RHS sections	61
Figure 24 – Tensile coupons extracted from – a) flat faces of cold-formed RHS sections – b) corners of cold-formed RHS sections – c) corners of hot-rolled CHS	62
Figure 25 – Typical dimensions of tensile coupons (dimensions in mm).....	62
Figure 26 – Setup of tensile coupon tests	63
Figure 27 – Example of some tested coupons	64
Figure 28 – Tensile coupons locations.....	64
Figure 29 – Typical example of engineering stress-strain curves for – a) hot-rolled CHS 159x5 – b) cold-formed RHS 220x120x6	65
Figure 30 –Initial geometrical imperfections measuring procedure	70
Figure 31 – LVDTs transversal displacements – a) <i>Position A</i> – b) <i>Position B</i> – c) <i>Position C</i>	71
Figure 32 – LVDTs transversal displacements for – a) RHS 200x100x4– b) RHS 220x120x6.....	71
Figure 33 – LVDTs displacements along the beam length (top view).....	72
Figure 34 – Extrapolated measurements near the loading plates	73

Figure 35 – Measurement of geometrical imperfections - Resetting the LVDTs to zero.....	73
Figure 36 – Step 1 procedure	73
Figure 37 – Step 2 procedure	74
Figure 38 – Step 3 procedure	74
Figure 39 – Step 4 procedure	74
Figure 40 – Step 5 procedure	74
Figure 41 – Step 6 procedure	74
Figure 42 – Correction of measured geometrical imperfections by an 8-steps procedure	76
Figure 43 – Imperfect shape of specimen RHS CF 200x100x4 T2 (magnified)	76
Figure 44 – Measured out-of-flatness isolines of imperfection magnitudes obtained for each plate of the RHS CF 200x100x4 T2 specimen.....	79
Figure 45 – Beam positions and measured sections	80
Figure 46 – Points distribution for each beam section	80
Figure 47 – Measurement of geometrical imperfections – Topometric procedure.....	81
Figure 48 – Imperfect shape of specimen RHS CF 200x100x4 T1 (magnified)	81
Figure 49 – Measured out-of-flatness isolines of imperfection magnitudes obtained for each plate of the RHS CF 200x100x4 T1 specimen.....	83
Figure 50 – Initial deformations along the length of the RHS CF 200x100x4 T2 specimen at the mid-width of each plate obtained by using the LVDT and the laser tracker procedures.....	84
Figure 51 – Principles of the sectioning method	85
Figure 52 – Use of material for different preliminary tests and measurements.....	86
Figure 53 – Strain gauges and 100 <i>mm</i> -spaced circular marks locations – Circular imprint	87
Figure 54 – Location of the strips in the hollow sections with the adopted labeling system	87
Figure 55 – Invar' bar with 100 <i>mm</i> basis	88
Figure 56 – Strip length and curvature measurements	88
Figure 57 – Geometrical deformation due to residual stresses.....	89
Figure 58 – Electrical strain measurements	91
Figure 59 – Mechanical and electrical measured stresses – a) membrane (right column) – b) flexural/total (left column) stresses of RHS CF 220x120x6	92
Figure 60 – Mechanical and electrical measured stresses – a) membrane (right column) – b) flexural/total (left column) stresses of RHS CF 200x100x4	92
Figure 61 – Adopted block representation for the calculation of the non-equilibrated stresses for specimens – a) RHS CF 220x120x6 – b) RHS CF 200x100x4	94
Figure 62 – General stub-column test setup	96
Figure 63 – Failure shapes of all stub columns.....	97
Figure 64 – Stub column test results – RHS CF 220x120x6 T5 – a) load displacement curve before and after correction – b) strain gauges measurements	98
Figure 65 Stub column test results – CHS HR 159x6.3 T11 – a) load displacement curve before and after correction – b) strain gauges measurements	99
Figure 66 – Material vs. stub stress-strain curves – a) RHS CF 200x100x4 T1 – b) CHS HR 159x5 T7	99

Figure 67 – Beam-column profiles	101
Figure 68 – End plates welded at both extremities – a) RHS CF 200x100x4 T2 (constant bending moment distribution) – b) RHS CF 200x100x4 T3 (triangular bending moment distribution).....	102
Figure 69 – Typical example of column positioning for the cases of – a) constant bending moment distribution – b) triangular bending moment distribution	103
Figure 70 – Front view of test setup.....	104
Figure 71 – Side view of test setup	105
Figure 72 – Overall view of test setup	106
Figure 73 – End plate fixed to bottom hinge plate	107
Figure 74 – Hinge detail.....	107
Figure 75 – Embedded support designed to resist shear forces.....	110
Figure 76 – Upper column end connection.....	110
Figure 77 – Measurement of displacements in mid-span cross-section.....	111
Figure 78 – LVDTs and specimen positions on bottom end plates.....	112
Figure 79 – Measurement of axial shortening	112
Figure 80 – Typical axial shortening curves (CHS HR 159x6.3 T11).....	113
Figure 81 – Typical load-rotation curves along major and minor axes (CHS HR 159x6.3 T11)	114
Figure 82 – Mid-span cross-section lateral and transversal displacements (RHS CF 220x120x6 T6).....	114
Figure 83 – Deformed shape of specimen CHS HR 159x5 T8	115
Figure 84 – Mesh <i>Type II</i> selected for G.M.N.I.A. calculations	117
Figure 85 – Detail view of the corner modelling.....	117
Figure 86 – Finite element model assumptions	118
Figure 87 – Applied load with shifted truss center corresponding to different load cases [3]	118
Figure 88 – Material stress strain laws adopted in F.E. calculations for specimens – a) RHS CF 220x120x6 T4 – b) RHS CF 200x100x4 T2.....	119
Figure 89 – F.E. peak loads vs. experimental loads.	122
Figure 90 – Graphical representation of – a) F_{TEST} / F_{FE_AT401} – b) $F_{FE_AT401} / F_{FE_LVDT}$	122
Figure 91 – Numerical vs. experimental axial load displacement curves of specimens – a) CHS HR 159x6.3 T11 – b) CHS HR 159x5 T9 – c) CHS HR 159x6.3 T12 – d) RHS CF 220x120x6 T4.....	124
Figure 92 – Numerical vs. experimental mid-span displacements for specimen RHS CF 220x120x6 T6– a) lateral displacement – b) transversal displacement.....	124
Figure 93 – Numerical vs. experimental beam end rotation for specimen CHS HR 159x6.3 T11 along – a) major-axis bending – b) weak-axis bending.....	124
Figure 94 – General view of test setup.....	125
Figure 95 – Rectangular shape model with end plate.....	126
Figure 96 – F.E. peak loads vs. experimental loads.	130
Figure 97 – Numerical vs. experimental axial load displacement curves of specimens – a) R275_BU_5– b) R275_BU_6– c) S355_BU_6 – d) S355_BU_3	131
Figure 98 – Elastic-perfectly plastic with 2% strain hardening adopted material law	134
Figure 99 – Reductions of wall thickness and weight with increasing strength of steel	135

Figure 100 – Typical stress-strain curves for different steel grades.....	135
Figure 101 – Investigated stress-strain laws	137
Figure 102 – Stress-strain curve for $f_y = 690 \text{ N/mm}^2$	139
Figure 103 – Residual stresses distribution (ensuring auto equilibrium) for tubular hot-formed profiles – shell model.....	139
Figure 104 – Mesh density study for rectangular sections – a) <i>Type I</i> – b) <i>Type II</i> – c) <i>Type III</i> – d) <i>Type IV</i> ...	141
Figure 105 – Mesh density study for square sections – a) <i>Type I</i> – b) <i>Type II</i> – c) <i>Type III</i> – d) <i>Type IV</i>	141
Figure 106 – Mesh density studies – Results for RHS sections	142
Figure 107 – Mesh density studies – Results for SHS sections	143
Figure 108 – Loading and support conditions	144
Figure 109 – Local geometrical imperfections adopted for both square and rectangular hollow sections (magnified view).....	144
Figure 110 – Imperfections <i>shapes</i> and <i>amplitudes</i> cases adopted – a) Type 1: Sine period equal to the average of plates – b) Type 2: Sine wave per-plate	146
Figure 111 – Magnified view of local imperfections introduced through sine curve with respect to – a) averaged period – b) per-plate periods	146
Figure 112 – Members dimensions and geometry – a) RHS_220x120x10 – b) RHS_300x200x8 – a) RHS_200x100x5 – b) RHS_450x250x8.....	148
Figure 113 – Local imperfection sensitivity under pure compression	148
Figure 114 – Local imperfection sensitivity under major-axis bending	149
Figure 115 – Global imperfection sensitivity under pure compression	151
Figure 116 – Magnified view of imperfections introduced as based on the first eigenmode.....	152
Figure 117 – Magnified initial global geometric imperfections.....	152
Figure 118 – Load path representation.....	153
Figure 119 – Cross-section dimensions adopted in the load-path sensitivity	155
Figure 120 – Comparison of G.M.N.I.A. results for the SHS_120x120x8 of $L = 4000$ – a) m_z vs. m_y diagram – b) n vs. m_y diagram.....	156
Figure 121 – Comparison of G.M.N.I.A. results for the SHS_120x120x8 of $L = 7000$ – a) m_z vs. m_y diagram – b) n vs. m_y diagram.....	156
Figure 122– Comparison of G.M.N.I.A. results for the SHS_260x260x7.1 of $L = 4000$ – a) m_z vs. m_y diagram – b) n vs. m_y diagram	156
Figure 123 – Comparison of G.M.N.I.A. results for the SHS_260x260x7.1 of $L = 7000$ – a) m_z vs. m_y diagram – b) n vs. m_y diagram	157
Figure 124 – Comparison of G.M.N.I.A. results for the SHS_200x200x5 of $L = 4000$ – a) m_z vs. m_y diagram – b) n vs. m_y diagram.....	157
Figure 125 – Comparison of G.M.N.I.A. results for the SHS_200x200x5 of $L = 7000$ – a) m_z vs. m_y diagram – b) n vs. m_y diagram.....	157
Figure 126– Comparison of G.M.N.I.A. results for the SHS_300x300x6.3 of $L = 4000$ – a) m_z vs. m_y diagram – b) n vs. m_y diagram	158

Figure 127 – Comparison of G.M.N.I.A. results for the SHS_300x300x6.3 of $L = 7000$ – a) m_z vs. m_y diagram – b) n vs. m_y diagram.....	158
Figure 128– Comparison of G.M.N.I.A. results for the RHS_220x120x10 of $L = 4000$ – a) m_z vs. m_y diagram – b) n vs. m_y diagram.....	158
Figure 129 – Comparison of G.M.N.I.A. results for the RHS_220x120x10 of $L = 7000$ – a) m_z vs. m_y diagram – b) n vs. m_y diagram.....	159
Figure 130– Comparison of G.M.N.I.A. results for the RHS_300x200x8 of $L = 4000$ – a) m_z vs. m_y diagram – b) n vs. m_y diagram.....	159
Figure 131 – Comparison of G.M.N.I.A. results for the RHS_300x200x8 of $L = 7000$ – a) m_z vs. m_y diagram – b) n vs. m_y diagram.....	159
Figure 132 – Comparison of G.M.N.I.A. results for the RHS_200x100x5 of $L = 4000$ – a) m_z vs. m_y diagram – b) n vs. m_y diagram.....	160
Figure 133 – Comparison of G.M.N.I.A. results for the RHS_200x100x5 of $L = 7000$ – a) m_z vs. m_y diagram – b) n vs. m_y diagram.....	160
Figure 134 – Comparison of G.M.N.I.A. results for the RHS_450x250x8 of $L = 4000$ – a) m_z vs. m_y diagram – b) n vs. m_y diagram.....	160
Figure 135 – Comparison of G.M.N.I.A. results for the RHS_450x250x8 of $L = 7000$ – a) m_z vs. m_y diagram – b) n vs. m_y diagram.....	161
Figure 136 – G.M.N.I.A. results for the load case $n = 0.7$ $\alpha = 50^\circ$ – a) Rectangular hollow sections – b) Square hollow sections.....	162
Figure 137 – G.M.N.I.A. results for the load case $n = 0.3$ $\alpha = 50^\circ$ – a) Rectangular hollow sections – b) Square hollow sections.....	162
Figure 138 – G.M.N.I.A. results for the load case $n = 0.7$ $\alpha = 70^\circ$ – a) Rectangular hollow sections – b) Square hollow sections.....	163
Figure 139 – Loading and support conditions (note that corners are also precisely accounted for in the beam models, however not represented in the above picture).....	164
Figure 140 – Beam model in FINELg.....	164
Figure 141 – Elastic-perfectly plastic hardening adopted material law with – a) 2% strain for normal steel grade – b) 0.45% strain for $f_y = 690 \text{ N/mm}^2$	165
Figure 142 – Residual stresses distribution (ensuring auto equilibrium) for hot-formed profiles – beam model.....	165
Figure 143 – Magnified view of global initial imperfections introduced in the beam F.E. model.....	166
Figure 144 – Deformed shape and yield pattern at failure and load-shortening behaviour using beam models.....	166
Figure 145 – Selection of load cases for $N+M_y+M_z$ combined situations – a) class 1-2 – b) class 3 – c) class 4.....	168
Figure 146 – Discretization in fibres for a rectangular hollow section by Matlab tool (each circle represents the centroid of a fibre).....	170
Figure 147 – R_{STAB,CS_FINELg} , R_{STAB,CS_CUFSM} and R_{STAB,CS_TH} graphical representation in function of b/t ratio.....	173
Figure 148 – $R_{STAB,MB_FINELg} / R_{STAB,MB_ABAQUS}$ graphical representation as a function of member length.....	177
Figure 149 – FEM-treatment of corners zones for hollow sections – a) beam models – b) shell models.....	178
Figure 150 – Numerical results for beam members (global instabilities accounted for).....	179
Figure 151 – Numerical results for shell members (both local and global instabilities accounted for).....	181

Figure 152 – Shell numerical results including the interaction formula linking both local and global instabilities	182
Figure 153 – Numerical results for members under combined loading $N+M_y$ and $N+M_z$ for square and rectangular sections – a) constant bending moment distribution – b) triangular bending moment distribution..	184
Figure 154 – Numerical results for members of class 1 sections under combined loading – a) RHS – b) SHS .	185
Figure 155 – Numerical results for members with rectangular sections and different steel grades under $N+M_y+M_z$	186
Figure 156 – Numerical results for members with rectangular sections and different steel grades under $N+M_y$	186
Figure 157 – Numerical results for members with rectangular sections and different steel grades under $N+M_z$	187
Figure 158 – Numerical results for members under compression and biaxial bending.....	188
Figure 159 – Numerical results for members under compression – a) Major-axis bending – b) Minor-axis bending.....	189
Figure 160 – Numerical results for member with class 1 rectangular sections under compression with mono-axial bending – a) $N+M_y$ – b) $N+M_z$	190
Figure 161 – Numerical results for member with different relative axial force ratios under – a) compression with biaxial bending – b) compression with major-axis bending – c) compression with minor-axis bending	192
Figure 162 – F.E. results for class 3 rectangular and square sections under compression and mono-axial bending $N+M_z$	193
Figure 163 – Influence of the degree of biaxial bending in square sections.....	194
Figure 164 – Numerical results for members under different load cases by varying the degrees of biaxial bending	196
Figure 165 – Comparison of numerical capacity with Eurocode 3 resistances	198
Figure 166 – Manufacturing processes – a) press-braking – b) roll-forming	200
Figure 167 – Typical stress-strain curves – a) S355 – b) S460	202
Figure 168 – Adopted material laws for – a) flat faces – b) corner regions	203
Figure 169 – Loading and support conditions	204
Figure 170 – Mesh <i>Type II</i> selected for G.M.N.I.A. calculations.....	205
Figure 171 – Selection of load cases for $N+M_y+M_z$ combined situations – a) class 1-2 – b) class 3 – c) class 4	207
Figure 172 – Numerical results for members obtained for – a) hot-rolled SHS– b) cold-formed SHS.....	208
Figure 173 – Numerical results for members obtained for – a) hot-rolled RHS– b) cold-formed RHS.....	209
Figure 174 – Numerical results for members under combined loading $N+M_y$ and $N+M_z$ for square and rectangular sections – a) constant bending moment distribution – b) triangular bending moment distribution..	210
Figure 175 – Numerical results for cold-formed members tested under different steel grades	212
Figure 176 – Numerical results for members under compression and biaxial bending.....	213
Figure 177 – Numerical results for member under compression – a) Major-axis bending – b) Minor-axis bending	214
Figure 178 – Numerical results for members with different relative axial force ratios under – a) compression with biaxial bending – b) compression with major-axis bending – c) compression with minor-axis bending.....	215
Figure 179 – Numerical results for members under different load cases by varying the degrees of biaxial bending	217

Figure 180 – Comparison of tensile, stub and member tests under pure compression for specimens – a) RHS CF 220x120x6 T4 – b) CHS HR 159x6.3 T10	220
Figure 181 – Zoomed graphs for small strains for specimens – a) RHS CF 220x120x6 T4 – b) CHS HR 159x6.3 T10	220
Figure 182 – Stress-strain behaviour of corresponding coupon fibers.....	221
Figure 183 – Fibers reaching the strain-hardening stage for a “cross-section” case	222
Figure 184 – Von Mises stresses at failure for the case of RHS 220x120x10 cross-section tested under compression and – a) constant bending moment distribution – b) triangular bending moment distribution.....	223
Figure 185 – Von Mises stresses at failure for the case of RHS 220x120x10 member tested under compression and – a) constant bending moment distribution – b) triangular bending moment distribution	224
Figure 186 – Allowance of 10% strain-hardening for the particular case of hot-rolled RHS tested under compression and triangular bending moment where $n = N_{Ed} / N_{b,Rd} = 0.3$	225
Figure 187 – Collected test results and comparison with Eurocode buckling curves	227
Figure 188 – Experimental results relative to section classes obtained by omitting χ_{CS} for – a) hot-rolled SHS and RHS – b) cold-formed SHS and RHS.....	227
Figure 189 – Experimental results relative to section classes obtained by considering χ_{CS} for – a) hot-rolled SHS and RHS – b) cold-formed SHS and RHS.....	229
Figure 190 – Experimental results relative to pure compression load cases – a) hot-rolled SHS and RHS – b) cold-formed SHS and RHS	229
Figure 191 – Experimental results relative to compression with mono-axial bending load cases for – a) hot-rolled SHS and RHS – b) cold-formed SHS and RHS.....	229
Figure 192 – Experimental results under combined loading for – a) hot-rolled SHS and RHS – b) cold-formed SHS and RHS	230
Figure 193 – Experimental results under combined loading for – a) hot-rolled SHS and RHS – b) cold-formed SHS and RHS	231
Figure 194 – Experimental and numerical test results relative to pure compression load cases for – a) hot-rolled sections – b) cold-formed sections.....	233
Figure 195 – Experimental and numerical test results relative to cold-formed sections tested under compression and triangular bending moment $N+M_z$	233
Figure 196 – Experimental and numerical test results relative to members subjected to compression and constant biaxial bending moment ($N+M_y+M_z$) for– a) hot-rolled sections – b) cold-formed sections.....	234
Figure 197 – Experimental and numerical test results relative to members subjected to compression and constant major-axis bending moment ($N+M_y$) for– a) hot-rolled sections – b) cold-formed sections	234
Figure 198 – Experimental and numerical test results relative to members subjected to compression and constant minor-axis bending moment ($N+M_z$) for– a) hot-rolled sections – b) cold-formed sections	234
Figure 199 – Numerical member results of hot-rolled SHS and RHS of steel grades $f_y = 235 N/mm^2$ and $f_y = 355 N/mm^2$, tested under N – a) shell results – b) beam results.....	236
Figure 200 – Numerical member results of hot-rolled SHS and RHS of steel grade $f_y = 690 N/mm^2$ tested under N – a) shell results – b) beam results.....	236

Figure 201 – Additional shell numerical member results of hot-rolled SHS and RHS of different steel grades under compression	238
Figure 202 – Shell numerical member results of cold-formed SHS and RHS of different steel grades under compression	239
Figure 203 – Additional shell numerical member results of cold-formed SHS and RHS of different steel grades under compression	239
Figure 204 – Variation of α factors based on the yield stress f_y of cold-formed sections, tested under compression	240
Figure 205 – Numerical member results of very slender SHS and RHS of different steel grades under compression– a) hot-rolled – b) cold-formed	242
Figure 206 – Deformed shape / yield pattern at failure of RHS_450x250x8 of steel grade $f_y = 690 N/mm^2$ obtained by using shell models	243
Figure 207 – Simply supported member with initial imperfection	243
Figure 208 – Maximum and initial deflexions reached at mid-span for hot-rolled sections	244
Figure 209 – Maximum and initial deflexions reached at mid-span for cold-formed sections	244
Figure 210 – $R_{REAL, MB} / R_{REAL, CS}$ graphical representation as a function of λ_{CS+MB}	247
Figure 211 – Numerical member results for hot-rolled “exaggerated” slender sections under compression	249
Figure 212 – Numerical member results for cold-formed “exaggerated” slender sections under compression ..	250
Figure 213 – Comparison of the analytical factors α with the adopted ones (obtained through the best-fit procedure) of hot-rolled sections in compression	250
Figure 214 – Comparison of the analytical factors α with the adopted ones (obtained through the best-fit procedure) of cold-formed sections in compression	251
Figure 215 – Comparison of the analytical results to the FEM results – a) hot-rolled sections – b) cold-formed sections	252
Figure 216 – Numerical member results for hot-rolled “exaggerated” slender sections of steel grade $f_y = 235 N/mm^2$ tested under compression – a) proposed O.I.C. curves – b) fitted factors	253
Figure 217 – Selection of load cases for $N+M_y+M_z$ combined situations – a) class 1-2 – b) class 3 – c) class 4 ..	254
Figure 218 – Numerical member results of hot-rolled SHS of steel grades $f_y = 235 N/mm^2$ and $f_y = 355 N/mm^2$ under $N+M_z$ and $\psi = 0$ – a) shell results – b) beam results	255
Figure 219 – Numerical member results of hot-rolled SHS of steel grade $f_y = 690 N/mm^2$ under $N+M_z$ and $\psi = 0$ – a) shell results – b) beam results	256
Figure 220 – Numerical member results of hot-rolled SHS of steel grade $f_y = 235 N/mm^2$ tested under different values of axial force ratio n	257
Figure 221 – Numerical member results of hot-rolled RHS of steel grades $f_y = 235 N/mm^2$ and $f_y = 355 N/mm^2$ under $N+M_z$ and $\psi = 0$ – a) shell results – b) beam results	258
Figure 222 – Numerical member results of hot-rolled RHS of steel grade $f_y = 690 N/mm^2$ under $N+M_z$ and $\psi = 0$ – a) shell results – b) beam results	258
Figure 223 – Comparison of the relative slenderness of different cross-section with various aspect ratios subjected to a weak and a strong axis bending moment [3]	259

Figure 224 – Numerical member results of hot-rolled RHS of steel grade $f_y = 235 \text{ N/mm}^2$ tested under different values of axial force ratio n	260
Figure 225 – Numerical member results of cold-formed SHS of different steel grades – a) $f_y = 235 \text{ N/mm}^2$ and $f_y = 355 \text{ N/mm}^2$ – b) $f_y = 690 \text{ N/mm}^2$	261
Figure 226 – Numerical member results of cold-formed SHS of steel grade $f_y = 235 \text{ N/mm}^2$ under different values of axial force ratio n	261
Figure 227 – Numerical member results of cold-formed RHS of different steel grades – a) $f_y = 235 \text{ N/mm}^2$ and $f_y = 355 \text{ N/mm}^2$ – b) $f_y = 690 \text{ N/mm}^2$	262
Figure 228 – Numerical member results of cold-formed RHS of steel grade $f_y = 235 \text{ N/mm}^2$ under different values of axial force ratio n	263
Figure 229 – Numerical member results of hot-rolled RHS of steel grades $f_y = 235 \text{ N/mm}^2$ and $f_y = 355 \text{ N/mm}^2$ under $N+M_y$ and $\psi = 0$ – a) shell results – b) beam results.....	264
Figure 230 – Numerical member results of hot-rolled RHS of steel grade $f_y = 690 \text{ N/mm}^2$ under $N+M_y$ and $\psi = 0$ – a) shell results – b) beam results.....	265
Figure 231 – Numerical member results of hot-rolled RHS of steel grade $f_y = 235 \text{ N/mm}^2$ tested under different values of axial force ratio n	265
Figure 232 – Numerical member results of cold-formed RHS of different steel grades – a) $f_y = 235 \text{ N/mm}^2$ and $f_y = 235 \text{ N/mm}^2$ – b) $f_y = 690 \text{ N/mm}^2$	266
Figure 233 – Numerical member results of cold-formed RHS tested under different values of axial force ratio n for $f_y = 235 \text{ N/mm}^2$	267
Figure 234 – Numerical member results obtained for different degrees of biaxial bending values and $\psi = 0$ for – a) cold-formed SHS – b) hot-rolled SHS.....	269
Figure 235 – Numerical member results obtained for different degrees of biaxial bending values and $\psi = 0$ for – a) cold-formed RHS – b) hot-rolled RHS	270
Figure 236 – Numerical member results of hot-rolled SHS of steel grades $f_y = 235 \text{ N/mm}^2$ and $f_y = 355 \text{ N/mm}^2$, under $N+M_y+M_z$ and $\psi = 0$ – a) shell results – b) beam results	271
Figure 237 – Numerical member results of hot-rolled SHS of steel grade $f_y = 690 \text{ N/mm}^2$ under $N+M_y+M_z$ and $\psi = 0$ – a) shell results – b) beam results.....	271
Figure 238 – Numerical member results of hot-rolled SHS of steel grade $f_y = 235 \text{ N/mm}^2$ tested under different values of axial force ratio n	271
Figure 239 – Variation of α factor based on $\Omega_{y/z}$ for the case of hot-rolled SHS of steel grades $f_y = 235 \text{ N/mm}^2$ and $f_y = 355 \text{ N/mm}^2$, tested under compression and triangular bending moment.....	272
Figure 240 – Numerical shell and beam member results for hot-rolled RHS of steel grades $f_y = 235 \text{ N/mm}^2$ and $f_y = 355 \text{ N/mm}^2$ under $N+M_y+M_z$	274
Figure 241 – Numerical shell and beam member results of hot-rolled RHS of steel grade $f_y = 690 \text{ N/mm}^2$ under $N+M_y+M_z$	275
Figure 242 – Numerical member results for hot-rolled rectangular sections of steel grade $f_y = 235 \text{ N/mm}^2$ tested under different values of axial force ratio n	276

Figure 243 – Variation of α factor based on $\Omega_{y/z}$ for the case of hot-rolled RHS of steel grades $f_y = 235 \text{ N/mm}^2$ and $f_y = 355 \text{ N/mm}^2$, tested under compression and triangular bending moment.....	277
Figure 244 – Numerical member results of cold-formed SHS under different steel grades – a) $f_y = 235 \text{ N/mm}^2$ and $f_y = 355 \text{ N/mm}^2$ – b) $f_y = 690 \text{ N/mm}^2$	278
Figure 245 – Numerical member results of cold-formed SHS tested under different values of axial force ratio n for $f_y = 235 \text{ N/mm}^2$	279
Figure 246 – Numerical member results of cold-formed RHS of steel grades $f_y = 235 \text{ N/mm}^2$ and $f_y = 355 \text{ N/mm}^2$, under $N+M_y+M_z$	281
Figure 247 – Numerical member results of cold-formed RHS of steel grade $f_y = 690 \text{ N/mm}^2$ under $N+M_y+M_z$	282
Figure 248 – Numerical member results of cold-formed RHS of steel grade $f_y = 235 \text{ N/mm}^2$ tested under different values of axial force ratio n	282
Figure 249 – Numerical member results of hot-rolled SHS of steel grades $f_y = 235 \text{ N/mm}^2$ and $f_y = 355 \text{ N/mm}^2$ under $N+M_z$ with $\psi = 1$ and $n = 0.7$ – a) shell results – b) beam results.....	286
Figure 250 – Numerical member results of hot-rolled SHS of steel grade $f_y = 690 \text{ N/mm}^2$ under $N+M_z$ with $\psi = 1$ and $n = 0.7$ – a) shell results – b) beam results.....	286
Figure 251 – Numerical member results of hot-rolled SHS of steel grades $f_y = 235 \text{ N/mm}^2$ and $f_y = 355 \text{ N/mm}^2$, under $N+M_z$ with $\psi = 1$ and $n = 0.3$ – a) shell results – b) beam results.....	287
Figure 252 – Numerical member results of hot-rolled SHS of steel grade $f_y = 690 \text{ N/mm}^2$ under $N+M_z$ with $\psi = 1$ and $n = 0.3$ – a) shell – b) beam results.....	287
Figure 253 – Numerical member results of hot-rolled SHS of steel grade $f_y = 235 \text{ N/mm}^2$ tested under different values of axial force ratio n	287
Figure 254 – Numerical member results of hot-rolled SHS derived according to the parameter η_z under different steel grades – a) $f_y = 235 \text{ N/mm}^2$ – b) $f_y = 355 \text{ N/mm}^2$ – c) $f_y = 690 \text{ N/mm}^2$	289
Figure 255 – Numerical member results for hot-rolled SHS of steel grade $f_y = 235 \text{ N/mm}^2$ derived according to the parameter η_z	290
Figure 256 – Numerical member results of hot-rolled RHS of steel grades $f_y = 235 \text{ N/mm}^2$ and $f_y = 355 \text{ N/mm}^2$ under $N+M_z$ with $\psi = 1$ and $n = 0.7$ – a) shell results – b) beam results.....	292
Figure 257 – Numerical member results of hot-rolled RHS of steel grade $f_y = 690 \text{ N/mm}^2$ under $N+M_z$ with $\psi = 1$ and $n = 0.7$ – a) shell results – b) beam results.....	292
Figure 258 – Numerical member results for hot-rolled RHS of grades $f_y = 235 \text{ N/mm}^2$ and $f_y = 355 \text{ N/mm}^2$ under $N+M_z$ with $\psi = 1$ and $n = 0.3$ – a) shell results – b) beam results.....	293
Figure 259 – Numerical member results for hot-rolled RHS of steel grade $f_y = 690 \text{ N/mm}^2$ under $N+M_z$ with $\psi = 1$ and $n = 0.3$ – a) shell results – b) beam results.....	293
Figure 260 – Numerical member results for hot-rolled RHS of steel grade $f_y = 235 \text{ N/mm}^2$ tested under different values of axial force ratio n	293
Figure 261 – Numerical member results for hot-rolled RHS derived according to the parameter η_z under different steel grades – a) $f_y = 235 \text{ N/mm}^2$ – b) $f_y = 355 \text{ N/mm}^2$ – c) $f_y = 690 \text{ N/mm}^2$	294

Figure 262 – Numerical member results of hot-rolled RHS of steel grade $f_y = 235 \text{ N/mm}^2$ derived according to the parameter η_z	295
Figure 263 – Numerical member results of cold-formed SHS of steel grades $f_y = 235 \text{ N/mm}^2$ and $f_y = 355 \text{ N/mm}^2$ under $N+M_z$ with $\psi = 1$ with – a) $n = 0.7$ – b) $n = 0.3$	296
Figure 264 – Numerical member results for cold-formed SHS of steel grade $f_y = 690 \text{ N/mm}^2$ under $N+M_z$ with $\psi = 1$ with – a) $n = 0.7$ – b) $n = 0.3$	296
Figure 265 – Numerical member results for cold-formed SHS of steel grade $f_y = 235 \text{ N/mm}^2$ tested under different values of axial force ratio n	296
Figure 266 – Numerical member results of cold-formed SHS derived according to the parameter η_z under different steel grades – a) $f_y = 235 \text{ N/mm}^2$ – b) $f_y = 355 \text{ N/mm}^2$ – c) $f_y = 690 \text{ N/mm}^2$	297
Figure 267 – Numerical member results of cold-formed SHS of steel grade $f_y = 235 \text{ N/mm}^2$ derived according to the parameter η_z	299
Figure 268 – Numerical member results of cold-formed RHS of steel grades $f_y = 235 \text{ N/mm}^2$ and $f_y = 355 \text{ N/mm}^2$, tested under $N+M_z$ with $\psi = 1$ and under different axial force level – a) $n = 0.7$ – b) $n = 0.3$	300
Figure 269 – Numerical member results of cold-formed RHS of steel grade $f_y = 690 \text{ N/mm}^2$ tested under $N+M_z$ with $\psi = 1$ and under different axial force level – a) $n = 0.7$ – b) $n = 0.3$	300
Figure 270 – Numerical member results of cold-formed RHS of steel grade $f_y = 235 \text{ N/mm}^2$ tested under different values of axial force ratio n	300
Figure 271 – Numerical member results of cold-formed RHS derived according to the parameter η_z under different steel grades – a) $f_y = 235 \text{ N/mm}^2$ – b) $f_y = 355 \text{ N/mm}^2$ – c) $f_y = 690 \text{ N/mm}^2$	301
Figure 272 – Numerical member results of cold-formed RHS of steel grade $f_y = 235 \text{ N/mm}^2$ derived according to the parameter η_z	302
Figure 273 – Numerical member results of hot-rolled RHS of steel grades $f_y = 235 \text{ N/mm}^2$ and $f_y = 235 \text{ N/mm}^2$ tested under $N+M_y$ with $\psi = 1$ and $n = 0.7$ – a) shell results – b) beam results	304
Figure 274 – Numerical member results of hot-rolled RHS of steel grade $f_y = 690 \text{ N/mm}^2$ tested under $N+M_y$ with $\psi = 1$ and $n = 0.7$ – a) shell results – b) beam results	304
Figure 275 – Numerical member results of hot-rolled RHS of steel grades $f_y = 235 \text{ N/mm}^2$ and $f_y = 235 \text{ N/mm}^2$ tested under $N+M_y$ with $\psi = 1$ and $n = 0.3$ – a) shell results – b) beam results	305
Figure 276 – Numerical member results of hot-rolled RHS of steel grade $f_y = 690 \text{ N/mm}^2$ tested under $N+M_y$ with $\psi = 1$ and $n = 0.3$ – a) shell results – b) beam results	305
Figure 277 – Numerical member results of hot-rolled RHS of steel grade $f_y = 235 \text{ N/mm}^2$ tested under different values of axial force ratio n	305
Figure 278 – Numerical member results of hot-rolled RHS derived according to the parameter η_y for different steel grades – a) $f_y = 235 \text{ N/mm}^2$ – b) $f_y = 355 \text{ N/mm}^2$ – c) $f_y = 690 \text{ N/mm}^2$	306
Figure 279 – Numerical member results of hot-rolled RHS of steel grade $f_y = 235 \text{ N/mm}^2$ derived according to the parameter η_y	308

Figure 280 – Numerical member results of cold-formed RHS of steel grades $f_y = 235 \text{ N/mm}^2$ and $f_y = 235 \text{ N/mm}^2$ tested under $N+M_y$ with $\psi = 1$ and under different axial force level – a) $n = 0.7$ – b) $n = 0.3$	309
Figure 281 – Numerical member results of cold-formed RHS of steel grade $f_y = 690 \text{ N/mm}^2$ tested under $N+M_y$ with $\psi = 1$ and under different axial force level – a) $n = 0.7$ – b) $n = 0.3$	309
Figure 282 – Numerical member results of cold-formed RHS of steel grade $f_y = 235 \text{ N/mm}^2$ tested under different values of axial force ratio n	309
Figure 283 – Numerical member results of cold-formed RHS derived according to the parameter η_y under different steel grades – a) $f_y = 235 \text{ N/mm}^2$ – b) $f_y = 355 \text{ N/mm}^2$ – c) $f_y = 690 \text{ N/mm}^2$	310
Figure 284 – Numerical member results of cold-formed RHS of steel grade $f_y = 235 \text{ N/mm}^2$ derived according to the parameter η_y	312
Figure 285 – Numerical member results obtained for different degrees of biaxial bending values and $\psi = 1$ for – a) cold-formed SHS – b) hot-rolled SHS	314
Figure 286 – Numerical member results obtained for different degrees of biaxial bending values and $\psi = 1$ for – a) cold-formed RHS – b) hot-rolled RHS	315
Figure 287 – Numerical member results of hot-rolled SHS of steel grades $f_y = 235 \text{ N/mm}^2$ and $f_y = 355 \text{ N/mm}^2$ tested under $N+M_y+M_z$, $\psi = 1$ and $n = 0.7$ – a) shell results – b) beam results	315
Figure 288 – Numerical member results of hot-rolled SHS of steel grade $f_y = 690 \text{ N/mm}^2$ tested under $N+M_y+M_z$, $\psi = 1$ and $n = 0.7$ – a) shell results – b) beam results	316
Figure 289 – Numerical member results of hot-rolled SHS of steel grades $f_y = 235 \text{ N/mm}^2$ and $f_y = 355 \text{ N/mm}^2$ tested under $N+M_y+M_z$, $\psi = 1$ and $n = 0.3$ – a) shell results – b) beam results	316
Figure 290 – Numerical member results of hot-rolled SHS of steel grade $f_y = 690 \text{ N/mm}^2$ tested under $N+M_y+M_z$, $\psi = 1$ and $n = 0.3$ – a) shell results – b) beam results	316
Figure 291 – Numerical member results of hot-rolled SHS of steel grade $f_y = 235 \text{ N/mm}^2$ tested under different values of axial force ratio n	317
Figure 292 – Numerical member results for hot-rolled SHS of steel grade $f_y = 235 \text{ N/mm}^2$ tested under different values of axial force ratio n and derived as a function of the parameters $\Omega_{y/z}$ and η_y	318
Figure 293 – Defined limits of the parameters $\Omega_{y/z}$ and η_y between <i>Type I</i> , <i>Type II</i> and the transition curves	319
Figure 294 – Variation of α based on $\Omega_{y/z}$ for <i>Type I</i> curves, relative to HR SHS of steel grades $f_y = 235 \text{ N/mm}^2$ and $f_y = 355 \text{ N/mm}^2$, tested under compression and constant bending moment distribution.	320
Figure 295 – Numerical member results for hot-rolled RHS of steel grades $f_y = 235 \text{ N/mm}^2$ and $f_y = 355 \text{ N/mm}^2$ tested under $N+M_y+M_z$, $\psi = 1$ and $n = 0.7$ – a) shell results – b) beam results	324
Figure 296 – Numerical member results of hot-rolled RHS of steel grade $f_y = 690 \text{ N/mm}^2$ tested under $N+M_y+M_z$, $\psi = 1$ and $n = 0.7$ – a) shell results – b) beam results	325
Figure 297 – Numerical member results of hot-rolled RHS of steel grades $f_y = 235 \text{ N/mm}^2$ and $f_y = 355 \text{ N/mm}^2$ tested under $N+M_y+M_z$, $\psi = 1$ and $n = 0.3$ – a) shell results – b) beam results	326

Figure 298 – Numerical member results of hot-rolled RHS of steel grade $f_y = 690 \text{ N/mm}^2$ tested under $N+M_y+M_z$, $\psi = 1$ and $n = 0.3$ – a) shell results – b) beam results	327
Figure 299 – Numerical member results of hot-rolled RHS of steel grade $f_y = 235 \text{ N/mm}^2$ tested under different values of axial force ratio n	328
Figure 300 – Numerical member results of hot-rolled RHS of steel grade $f_y = 235 \text{ N/mm}^2$ derived as a function of the parameters $\Omega_{y/z}$ and η_y	329
Figure 301 – Variation of α based on $\Omega_{y/z}$ for <i>Type I</i> curves, relative to HR RHS of steel grades $f_y = 235 \text{ N/mm}^2$ and $f_y = 355 \text{ N/mm}^2$, tested under compression and constant bending moment distribution.	330
Figure 302 – Numerical member results of cold-formed SHS of steel grades $f_y = 235 \text{ N/mm}^2$ and $f_y = 355 \text{ N/mm}^2$ tested under $N+M_y+M_z$ with $\psi = 1$ and under different axial force level – a) $n = 0.7$ – b) $n = 0.3$	333
Figure 303 – Numerical member results of cold-formed SHS of steel grade $f_y = 690 \text{ N/mm}^2$ under $N+M_y+M_z$ with $\psi = 1$ and under different axial force level – a) $n = 0.7$ – b) $n = 0.3$	333
Figure 304 – Numerical member results of cold-formed SHS of steel grade $f_y = 235 \text{ N/mm}^2$ tested under different values of axial force ratio n	334
Figure 305 – Numerical member results for cold-formed SHS of steel grade $f_y = 235 \text{ N/mm}^2$ derived as a function of the parameters $\Omega_{y/z}$ and η_y	335
Figure 306 – Variation of α based on $\Omega_{y/z}$ for <i>Type I</i> curves, relative to CF SHS of steel grades $f_y = 235 \text{ N/mm}^2$ and $f_y = 355 \text{ N/mm}^2$, tested under compression and constant bending moment distribution.	336
Figure 307 – Numerical member results for cold-formed RHS of steel grades $f_y = 235 \text{ N/mm}^2$ and $f_y = 355 \text{ N/mm}^2$ tested under $N+M_y+M_z$, $\psi = 1$ and $n = 0.7$	340
Figure 308 – Numerical member results for cold-formed RHS of steel grade $f_y = 690 \text{ N/mm}^2$, tested under $N+M_y+M_z$, $\psi = 1$ and $n = 0.7$	340
Figure 309 – Numerical member results for cold-formed RHS of steel grades $f_y = 235 \text{ N/mm}^2$ and $f_y = 355 \text{ N/mm}^2$ tested under $N+M_y+M_z$, $\psi = 1$ and $n = 0.3$	341
Figure 310 – Numerical member results of cold-formed RHS of steel grade $f_y = 690 \text{ N/mm}^2$ tested under $N+M_y+M_z$, $\psi = 1$ and $n = 0.3$	342
Figure 311 – Numerical member results of cold-formed RHS of steel grade $f_y = 235 \text{ N/mm}^2$ tested under different values of axial force ratio n	342
Figure 312 – Numerical member results for cold-formed RHS of steel grade $f_y = 235 \text{ N/mm}^2$ tested under different values of axial force ratio n and derived as a function of the parameters $\Omega_{y/z}$ and η_y	344
Figure 313 – Variation of α based on $\Omega_{y/z}$ for <i>Type I</i> curves, relative to CF RHS of steel grades $f_y = 235 \text{ N/mm}^2$ and $f_y = 355 \text{ N/mm}^2$, tested under compression and constant bending moment distribution.	345
Figure 314 – Linear regression between – a) $\alpha - \psi$ – b) $\lambda_0 - \psi$	348
Figure 315 – Numerical member results of hot-rolled and cold-formed SHS of steel grades $f_y = 235 \text{ N/mm}^2$ and $f_y = 690 \text{ N/mm}^2$ tested under compression and mono-axial bending with different end-moment values	350
Figure 316 – Numerical member results of hot-rolled and cold-formed SHS of steel grades $f_y = 235 \text{ N/mm}^2$ and $f_y = 690 \text{ N/mm}^2$ tested under $N+M_y+M_z$	351

Figure 317 – Numerical member results of hot-rolled and cold-formed RHS of steel grades $f_y = 235 \text{ N/mm}^2$ and $f_y = 690 \text{ N/mm}^2$ tested under combined loading $N+M_z$	352
Figure 318 – Numerical member results of hot-rolled and cold-formed RHS of steel grades $f_y = 235 \text{ N/mm}^2$ and $f_y = 690 \text{ N/mm}^2$ tested under $N+M_y$	353
Figure 319 – Numerical member results of hot-rolled and cold-formed RHS of steel grades $f_y = 235 \text{ N/mm}^2$ and $f_y = 690 \text{ N/mm}^2$ tested under $N+M_y+M_z$	356
Figure 320 – Linear transition between $\alpha - h / b$	356
Figure 321 – Hot-rolled, pure compression – a) Comparison of proposal and EC3 results with FEM results – b) Frequency distributions (total number of results: 1056).....	360
Figure 322 – Cold-formed, pure compression – a) Comparison of Proposal and EC3 results with FEM results – b) Frequency distributions (total number of results: 1056).....	360
Figure 323 – Hot-rolled, $N+M_z$ – a) Comparison of Proposal and EC3 results with FEM results – b) Frequency distributions (total number of results: 1160).....	360
Figure 324 – Cold-formed, $N+M_z$ – a) Comparison of Proposal and EC3 results with FEM results – b) Frequency distributions (total number of results: 1160).....	361
Figure 325 – Hot-rolled, $N+M_y$ – a) Comparison of Proposal and EC3 results with FEM results – b) Frequency distributions (total number of results: 1304).....	361
Figure 326 – Cold-formed, $N+M_y$ – a) Comparison of Proposal and EC3 results with FEM results – b) Frequency distributions (total number of results: 1304).....	361
Figure 327 – Hot-rolled, $N+M_y+M_z$, $\psi = 1$ – a) Comparison of Proposal and EC3 results with FEM results – b) Frequency distributions (total number of results: 4576).....	362
Figure 328 – Cold-formed, $N+M_y+M_z$, $\psi = 1$ – a) Comparison of Proposal and EC3 results with FEM results – b) Frequency distributions (total number of results: 4576).....	362
Figure 329 – Hot-rolled, $N+M_y+M_z$, $\psi = 0$ – a) Comparison of Proposal and EC3 results with FEM results – b) Frequency distributions (total number of results: 4207).....	362
Figure 330 – Cold-formed, $N+M_y+M_z$, $\psi = 0$ – a) Comparison of Proposal and EC3 results with FEM results – b) Frequency distributions (total number of results: 4207).....	363
Figure 331 – Hot-rolled, $N+M_y+M_z$, $\psi = -0.33 / 0.33 / 0.67$ – a) Comparison of Proposal and EC3 results with FEM results – b) Frequency distributions (total number of results: 384).....	363
Figure 332 – Cold-formed, $N+M_y+M_z$, $\psi = -0.33 / 0.33 / 0.67$ – a) Comparison of Proposal and EC3 results with FEM results – b) Frequency distributions (total number of results: 384).....	363
Figure 333 – Hot-rolled, $N+M_y+M_z$, $n = 0.3$ – a) Comparison of Proposal and EC3 results with FEM results – b) Frequency distributions (total number of results: 4368).....	364
Figure 334 – Cold-formed, $N+M_y+M_z$, $n = 0.3$ – a) Comparison of Proposal and EC3 results with FEM results – b) Frequency distributions (total number of results: 4368).....	364
Figure 335 – Hot-rolled, $N+M_y+M_z$, $n = 0.7$ – a) Comparison of Proposal and EC3 results with FEM results – b) Frequency distributions (total number of results: 3988).....	364
Figure 336 – Cold-formed, $N+M_y+M_z$, $n = 0.7$ – a) Comparison of Proposal and EC3 results with FEM results – b) Frequency distributions (total number of results: 3988).....	365

Figure 337 – Principles and application steps of the Overall Interaction Concept.....	366
Figure 338 – Defined limits for <i>Type I</i> , <i>Type II</i> and <i>Transition curves</i>	368
Figure 339 – Hot-rolled, $N+M_y+M_z$ – a) Comparison of proposal and EC3 results with FEM results – b) Frequency distributions (total number of results: 8796).....	378
Figure 340 – Hot-rolled, $N+M_z$ – a) Comparison of proposal and EC3 results with FEM results – b) Frequency distributions (total number of results: 1052).....	378
Figure 341 – Hot-rolled, $N+M_y$ – a) Comparison of proposal and EC3 results with FEM results – b) Frequency distributions (total number of results: 1241).....	378
Figure 342 – Cold-formed, $N+M_y+M_z$ – a) Comparison of proposal and EC3 results with FEM results – b) Frequency distributions (total number of results: 8796).....	379
Figure 343 – Cold-formed, $N+M_z$ – a) Comparison of proposal and EC3 results with FEM results – b) Frequency distributions (total number of results: 1052).....	379
Figure 344 – Cold-formed, $N+M_y$ – a) Comparison of proposal and EC3 results with FEM results – b) Frequency distributions (total number of results: 1241).....	379
Figure 345 – Member tested under compression and biaxial bending moment	380
Figure 346 – Stress distribution	381
Figure 347: Application steps of the Overall Interaction Concept.....	385
Figure 348 – Member tested under compression and biaxial bending moment	387
Figure 349 – Member tested under compression and biaxial bending moment	392
Figure 350 – Member tested under compression and biaxial bending moment	396
Figure 351 – Internal compressed elements.....	399
Figure 352 – Section notation and designations for cold-formed RHS and SHS	421
Figure 353 – Comparison of test stress-strain curves vs. simple R.-O. equation with fitted n value – a) S355 (S3, S16, S25 specimens) – b) S460 (S47, S48, S50).....	423
Figure 354 – Simple and double R.-O. calculated parameters – a) welded faces – b) flat faces.	424
Figure 355 – Simple and double R.-O. calculated parameters for corners.	424
Figure 356 – Simple R.-O. n parameter for flat faces from steel grades S355 and S460.....	424
Figure 357 – Experimental vs. fitted double R.-O. material curves – a) S19 specimen – b) S47 specimen.....	426
Figure 358 – Double R.-O. coefficients for flat faces S355 and S460 – a) n parameter $\sigma \leq \sigma_{0.2}$ – b) m parameter $\sigma > \sigma_{0.2}$	426
Figure 359 – Experimental and analytical stress-strain curves for different steel grades – a) SHS 100x100x3 – b) SHS100x100x8.....	427
Figure 360 – Deformed shapes and yield patterns at failure – a) under major-axis bending moment – b) under axial compression	428
Figure 361 – F.E. results – a) sections in compression – b) sections under major-axis bending	428
Figure 362 – SHS100x100x5 cross-section carrying capacity a) moment-rotation curves – b) load-shortening behaviour of section loaded in compression	429
Figure 363 – Simple and double R.-O. calculated parameters for high strength steel tensile tests.....	430
Figure 364 – F.E. results – a) sections in compression – b) sections under major-axis bending	431

Figure 365 – Comparison of G.M.N.I.A. results for the RHS_220x120x10 of $L = 5500$ – a) m_z vs. m_y diagram – b) n vs. m_y diagram	433
Figure 366 – Comparison of G.M.N.I.A. results for the RHS_300x200x8 of $L = 5500$ – a) m_z vs. m_y diagram – b) n vs. m_y diagram.....	434
Figure 367 – Comparison of G.M.N.I.A. results for the RHS_200x100x5 of $L = 5500$ – a) m_z vs. m_y diagram – b) n vs. m_y diagram.....	434
Figure 368 – Comparison of G.M.N.I.A. results for the RHS_450x250x8 of $L = 5500$ – a) m_z vs. m_y diagram – b) n vs. m_y diagram.....	434
Figure 369 – Comparison of G.M.N.I.A. results for the SHS_120x120x8 of $L = 5500$ – a) m_z vs. m_y diagram – b) n vs. m_y diagram.....	435
Figure 370 – Comparison of G.M.N.I.A. results for the SHS_260x260x7.1 of $L = 5500$ – a) m_z vs. m_y diagram – b) n vs. m_y diagram	435
Figure 371 – Comparison of G.M.N.I.A. results for the SHS_200x200x5 of $L = 5500$ – a) m_z vs. m_y diagram – b) n vs. m_y diagram.....	435
Figure 372 – Comparison of G.M.N.I.A. results for the SHS_300x300x6.3 of $L = 5500$ – a) m_z vs. m_y diagram – b) n vs. m_y diagram	436
Figure 373 – Principles and application steps of the Overall Interaction Concept.....	437

11. Liste of Tables

Table 1 – Cross-sectional shapes corresponding to the curves a, b and c proposed by the CECM in 1970.....	13
Table 2 – Parameters proposed by Baar for buckling curves.....	14
Table 3 – Parameters proposed by Young for buckling curves.....	18
Table 4 – Parameters proposed by Unger and Linder for buckling curves.....	19
Table 5 – Parameters proposed by the project revision of DIN 4114.....	19
Table 6 – Parameters proposed the Merchant-Rankine with plateau formula.....	20
Table 7 – Imperfection factor for buckling curves.....	24
Table 8 – Imperfection factor for buckling curves.....	25
Table 9 – Imperfection factor β	30
Table 10 – Equivalent uniform moment factors C_m	34
Table 11 – Equivalent moment factor C_m	37
Table 12 – Delivered sections properties.....	48
Table 13 – Proportion of adopted loadings.....	49
Table 14 – Test program for buckling tests.....	56
Table 15 – Measured material properties.....	67
Table 16 – Initial local maximum out-of-plane magnitude measured along the member length.....	77
Table 17 – Initial global maximum out-of-plane magnitude measured along the member length.....	77
Table 18 – Maximum out-of-plane magnitude measured at mid-width of the upper flange plate.....	83
Table 19 – Maximum out-of-plane magnitude measured at mid-width of the right web plate.....	83
Table 20 – Maximum out-of-plane magnitude measured at mid-width of the bottom flange plate.....	83
Table 21 – Maximum out-of-plane magnitude measured at mid-width of the left web plate.....	84
Table 22 – Percentage of non-equilibrated stresses.....	94
Table 23 – Stub column test results.....	98
Table 24 – Test program summary.....	102
Table 25 – Measured specimens' dimensions and obtained ultimate loads for all tested specimens.....	116
Table 26 – Comparison of numerical and experimental ultimate loads.....	120
Table 27 – Comparisons of F_{FE_AT401} with F_{FE_LVDT} and F_{TEST}	121
Table 28 – “Semi-Comp” test program for member buckling.....	126
Table 29 – Measured dimensions and material properties.....	127
Table 30 – Initial local maximum magnitude measured along the member length.....	128
Table 31 – Initial global maximum magnitude measured along the member length.....	129
Table 32 – Comparison of numerical and experimental ultimate loads from “Semi-Comp” project [4].....	129
Table 33 – Obtained results for tubular sections.....	137
Table 34 – Comparisons of R_{RESIST_EC3} with R_{RESIST_MATLAB} and $R_{RESIST_LESCOUARCH}$	171
Table 35 – Comparison of R_{STAB,CS_TH} with R_{STAB,CS_FINELg} and R_{STAB,CS_CUFSM}	173
Table 36 – Comparisons of R_{STAB,MB_ABAQUS} with R_{STAB,MB_FINELg} for different section shapes.....	176

Table 37 – Values of the fracture elongations ε_{\max} determined from the stress-strain, stub column and buckling tests curves.....	221
Table 38 – Design curves for the case of hot-rolled and cold-formed members subjected to pure compression	241
Table 39 – Design curves for the case of hot-rolled and cold-formed members subjected to compression with triangular minor-axis bending.....	263
Table 40 – Design curves for the case of hot-rolled and cold-formed members subjected to compression and triangular major-axis bending.....	268
Table 41 – Design curves for the case of hot-rolled and cold-formed members subjected to compression with triangular biaxial bending.....	284
Table 42 – Design curves for the case of hot-rolled and cold-formed members subjected to compression with constant minor-axis bending.....	302
Table 43 – Design curves for the case of hot-rolled and cold-formed members subjected to compression with constant major-axis bending.....	312
Table 44 – Design curves for the case of hot-rolled square members subjected to compression with biaxial constant bending moment.....	322
Table 45 – Design curves for the case of hot-rolled RHS members subjected to compression with biaxial constant bending moment.....	332
Table 46 – Design curves for the case of cold-formed SHS members subjected to compression with biaxial constant bending moment.....	338
Table 47 – Design curves for the case of cold-formed RHS members subjected to compression with biaxial constant bending moment.....	346
Table 48 – Comparison between FEM, EC3 and proposal results for all treated load cases.....	357
Table 49 – Proposed O.I.C. design curves for hot-rolled members tested under combined loadings with the corresponding bending moment – a) $\psi = 0$ – b) $\psi = 1$	370
Table 50 – Proposed O.I.C. design curves for cold-formed members tested under combined loadings with the corresponding bending moment – a) $\psi = 0$ – b) $\psi = 1$	372
Table 51 – Proposed O.I.C. design curves for hot-rolled members tested under combined loadings with the corresponding bending moment – a) $\psi = 0$ – b) $\psi = 1$	375
Table 52 – Proposed O.I.C. design curves for cold-formed members tested under combined loadings with the corresponding bending moment – a) $\psi = 0$ – b) $\psi = 1$	376
Table 53 – Comparison between FEM, EC3 and proposal results for all treated load cases.....	377
Table 54 – Cross-section characteristics.....	380
Table 55 – Loading.....	381
Table 56 – Material properties.....	381
Table 57 – Cross-section characteristics.....	387
Table 58 – Loading.....	388
Table 59 – Material properties.....	388
Table 60 – Cross-section characteristics.....	392
Table 61 – Loading.....	393

Table 62 – Material properties	393
Table 63 – Cross-section characteristics	396
Table 64 – Loading	397
Table 65 – Material properties	397
Table 66 – Summary of the gathered test data.....	416
Table 67 – Coupon tests extracted from cold-formed hollow sections of normal steel grades.....	421
Table 68 – Calculated n values through simple R.-O. formulation.....	424
Table 69 – Examples of fitted values for n coefficient – sections S5 and S6.....	425
Table 70 – Calculated n and m values through double R.-O. formulation.....	426
Table 71 – Coupon test results used within present study.....	430
Table 72 – Load combination launched numerically – a) rectangular sections – b) circular sections	432